

A Wiley-Science Wise Co-Publication



Photonics Volume 1

# FUNDAMENTALS OF PHOTONICS AND PHYSICS

David L. Andrews



WILEY

# **PHOTONICS**



# **PHOTONICS**

---

## **Scientific Foundations, Technology and Applications**

Fundamentals of Photonics and Physics

Volume I

*Edited by*

**DAVID L. ANDREWS**

School of Chemical Sciences  
University of East Anglia  
Norwich, UK

**WILEY**

Copyright © 2015 by John Wiley & Sons, Inc. All rights reserved.

Published by John Wiley & Sons, Inc., Hoboken, New Jersey.

Published simultaneously in Canada.

No part of this publication may be reproduced, stored in a retrieval system, or transmitted in any form or by any means, electronic, mechanical, photocopying, recording, scanning, or otherwise, except as permitted under Section 107 or 108 of the 1976 United States Copyright Act, without either the prior written permission of the Publisher, or authorization through payment of the appropriate per-copy fee to the Copyright Clearance Center, Inc., 222 Rosewood Drive, Danvers, MA 01923, (978) 750-8400, fax (978) 750-4470, or on the web at [www.copyright.com](http://www.copyright.com). Requests to the Publisher for permission should be addressed to the Permissions Department, John Wiley & Sons, Inc., 111 River Street, Hoboken, NJ 07030, (201) 748-6011, fax (201) 748-6008, or online at <http://www.wiley.com/go/permissions>.

**Limit of Liability/Disclaimer of Warranty:** While the publisher and author have used their best efforts in preparing this book, they make no representations or warranties with respect to the accuracy or completeness of the contents of this book and specifically disclaim any implied warranties of merchantability or fitness for a particular purpose. No warranty may be created or extended by sales representatives or written sales materials. The advice and strategies contained herein may not be suitable for your situation. You should consult with a professional where appropriate. Neither the publisher nor author shall be liable for any loss of profit or any other commercial damages, including but not limited to special, incidental, consequential, or other damages.

For general information on our other products and services or for technical support, please contact our Customer Care Department within the United States at (800) 762-2974, outside the United States at (317) 572-3993 or fax (317) 572-4002.

Wiley also publishes its books in a variety of electronic formats. Some content that appears in print may not be available in electronic formats. For more information about Wiley products, visit our web site at [www.wiley.com](http://www.wiley.com).

***Library of Congress Cataloging-in-Publication Data:***

Fundamentals of photonics and physics / edited by David L. Andrews.

    pages cm. – (Photonics ; volume I)

Includes bibliographical references and index.

ISBN 978-1-118-22553-0 (cloth)

1. Photonics. 2. Photons. 3. Optics. I. Andrews, David L., 1952–  
TA1520.F86 2015  
621.36'5–dc23

2014041293

Printed in the United States of America

10 9 8 7 6 5 4 3 2 1

# CONTENTS

|   |             |
|---|-------------|
| <b>List of Contributors</b>   | <b>xi</b>   |
| <b>Preface</b>  | <b>xiii</b> |
| <b>1 A Photon in Perspective</b>  | <b>1</b>    |
| <i>David L. Andrews</i>   |             |
| 1.1 Introduction, 1   |             |
| 1.2 Foundations, 3  |             |
| 1.3 Medium Issues, 8  |             |
| 1.4 Photon Localization and Wavefunction, 10                                |             |
| 1.5 The Quantum Vacuum and Virtual Photons, 12                              |             |
| 1.6 Structured Light, 15  |             |
| 1.7 Photon Number Fluctuations and Phase, 18                                |             |
| 1.8 The Reality of Photonics, 20  |             |
| Acknowledgments, 20   |             |
| References, 20  |             |
| <b>2 Coherence and Statistical Optics</b>                                   | <b>27</b>   |
| <i>Mayukh Lahiri</i>  |             |
| 2.1 Introduction, 27  |             |
| 2.2 Classical Theory of Optical Coherence in the Space-Time Domain, 28      |             |
| 2.3 Classical Theory of Optical Coherence in the Space-Frequency Domain, 34 |             |
| 2.4 Cross-Spectrally Pure Optical Fields, 38                                |             |

|          |  |            |
|----------|--|------------|
| 2.5      | Polarization Properties of Stochastic Beams,                 | 43         |
| 2.6      | Remarks on Partially Coherent and Partially Polarized Beams, | 51         |
| 2.7      | Basics of Quantum Theory of Optical Coherence,               | 52         |
| 2.8      | Concluding Remarks,  | 55         |
|          | Acknowledgments,   | 56         |
|          | References,  | 56         |
| <b>3</b> | <b>Light Beams with Spatially Variable Polarization</b>      | <b>61</b>  |
|          | <i>Enrique J. Galvez</i>                                     |            |
| 3.1      | Introduction,  | 61         |
| 3.2      | Poincaré Modes of Beams,                                     | 62         |
| 3.3      | Experimental Approaches,                                     | 69         |
| 3.4      | Polarization Singularities,                                  | 70         |
| 3.5      | Conclusion,  | 73         |
|          | Acknowledgments,   | 73         |
|          | References,  | 73         |
| <b>4</b> | <b>Quantum Optics</b>  | <b>77</b>  |
|          | <i>Howard Carmichael</i>                                     |            |
| 4.1      | Introduction,  | 77         |
| 4.2      | Fundamentals,  | 78         |
| 4.3      | Open Systems: Inputs and Outputs,                            | 87         |
| 4.4      | Photon Counting,   | 95         |
| 4.5      | Cavity and Circuit QED,                                      | 105        |
|          | References,  | 111        |
| <b>5</b> | <b>Squeezed Light</b>  | <b>121</b> |
|          | <i>A. I. Lvovsky</i>   |            |
| 5.1      | What is Squeezed Light?,                                     | 121        |
| 5.2      | Salient Features of Squeezed States,                         | 128        |
| 5.3      | Detection,   | 136        |
| 5.4      | Preparation,   | 141        |
| 5.5      | Applications in Quantum Information,                         | 148        |
| 5.6      | Applications in Quantum Metrology,                           | 154        |
| 5.7      | Conclusion and Outlook,                                      | 157        |
|          | References,  | 158        |
| <b>6</b> | <b>Electromagnetic Theory of Materials</b>                   | <b>165</b> |
|          | <i>Tom G. Mackay</i>   |            |
| 6.1      | Preamble,  | 165        |
| 6.2      | Macroscopic Viewpoint,                                       | 166        |
| 6.3      | Constitutive Dyadics,  | 171        |

|          |   |            |
|----------|---|------------|
| 6.4      | Linear Materials,   | 178        |
| 6.5      | Nonlinear Materials,  | 194        |
| 6.6      | Closing Remarks,  | 198        |
|          | References,   | 199        |
| <b>7</b> | <b>Surface and Cavity Nanophotonics</b>                             | <b>205</b> |
|          | <i>Mohamed Babiker</i>  |            |
| 7.1      | Introduction,   | 205        |
| 7.2      | Basic Formalism,  | 207        |
| 7.3      | Dipole Emitter Near Edge,   | 211        |
| 7.4      | Quantum Correlations,   | 215        |
| 7.5      | Entanglement,   | 217        |
| 7.6      | Wedge Cavities,   | 219        |
| 7.7      | Conclusions,  | 223        |
|          | Acknowledgments,  | 225        |
|          | References,   | 225        |
| <b>8</b> | <b>Quantum Electrodynamics</b>                                      | <b>229</b> |
|          | <i>A. Salam</i>   |            |
| 8.1      | Introduction,   | 229        |
| 8.2      | Molecular QED: Principle of Minimal Electromagnetic Coupling,       | 231        |
| 8.3      | Multipolar Hamiltonian,   | 235        |
| 8.4      | One-Photon Absorption,  | 241        |
| 8.5      | Emission of Light: Spontaneous and Stimulated Processes,            | 244        |
| 8.6      | Linear Light-Scattering: The Kramers–Heisenberg Dispersion Formula, | 246        |
| 8.7      | Chiroptical Effects,  | 251        |
| 8.8      | Two-Photon Absorption,  | 255        |
| 8.9      | Nonlinear Light-Scattering: Sum-Frequency and Harmonic Generation,  | 258        |
| 8.10     | Resonance Energy Transfer,  | 261        |
| 8.11     | van der Waals Dispersion Energy,                                    | 264        |
| 8.12     | Radiation-Induced Interparticle Forces,                             | 266        |
| 8.13     | Summary and Outlook,  | 269        |
|          | References,   | 271        |
| <b>9</b> | <b>Multiphoton Processes</b>  | <b>279</b> |
|          | <i>Angus J. Bain</i>  |            |
| 9.1      | Introduction,   | 279        |
| 9.2      | Molecular Two-Photon Absorption: Basic Principles,                  | 282        |
| 9.3      | Molecular Two-Photon Fluorescence,                                  | 289        |
| 9.4      | Applications and Future Prospects,                                  | 307        |

|  |            |
|--|------------|
| 9.5 Conclusions, 309<br>Acknowledgments, 311<br>References, 311  |            |
| <b>10 Orbital Angular Momentum</b>   | <b>321</b> |
| <i>Emma Wisniewski-Barker and Miles J. Padgett</i>   |            |
| 10.1 Historical Introduction, 321<br>10.2 Creating Beams with OAM, 324<br>10.3 Micro-Manipulation through the Use of OAM, 327<br>10.4 Beam Transformations, 329<br>10.5 Measuring Beams with OAM, 332<br>10.6 OAM in Classical Imaging, 333<br>10.7 OAM in Nonlinear and Quantum Optics, 333<br>10.8 Conclusions, 335<br>References, 335 |            |
| <b>11 Introduction to Helicity and Electromagnetic Duality Transformations in Optics</b>   | <b>341</b> |
| <i>Ivan Fernandez-Corbaton and Gabriel Molina-Terriza</i>  |            |
| 11.1 Introduction, 341<br>11.2 Symmetries and Operators, 342<br>11.3 Electromagnetic Duality, 344<br>11.4 Optical Helicity and Electromagnetic Duality Symmetry, 346<br>11.5 Duality Symmetry in Piecewise Homogeneous and Isotropic Media, 347<br>11.6 Applications of the Framework, 351<br>11.7 Conclusions, 359<br>References, 360   |            |
| <b>12 Slow and Fast Light</b>  | <b>363</b> |
| <i>Robert W. Boyd and Zhimin Shi</i>   |            |
| 12.1 Introduction, 363<br>12.2 Mechanisms of Slow Light, 364<br>12.3 Physics with Slow and Fast Light, 367<br>12.4 Some Applications of Slow and Fast Light, 374<br>12.5 Fundamental Limits on Slow Light, 379<br>References, 381  |            |
| <b>13 Attosecond Physics: Attosecond Streaking Spectroscopy of Atoms and Solids</b>  | <b>387</b> |
| <i>Uwe Thumm, Qing Liao, Elisabeth M. Bothschafter, Frederik Süßmann, Matthias F. Kling, and Reinhard Kienberger</i>   |            |
| 13.1 Introduction, 387<br>13.2 Time-Resolved Photoemission from Atoms, 393   |            |

- 13.3 Streaked Photoemission from Solids, 407
- 13.4 Attosecond Streaking from Nanostructures, 425
- 13.5 Conclusions, 432
- Acknowledgments, 434
- References, 434

**Index** **443**



# LIST OF CONTRIBUTORS

**David L. Andrews**, School of Chemistry, University of East Anglia, Norwich, UK

**Mohamed Babiker**, Department of Physics, University of York, York, UK

**Angus J. Bain**, Department of Physics and Astronomy, University College London, London, UK

**Elisabeth M. Bothschafter**, Max-Planck Institut für Quantenoptik, Garching, Germany

Physik Department, Ludwig-Maximilians-Universität, Garching, Germany

**Robert W. Boyd**, The Institute of Optics, University of Rochester, Rochester, NY, USA

Department of Physics and Astronomy, University of Rochester, Rochester, NY, USA

Department of Physics and School of Electrical Engineering and Computer Science, University of Ottawa, Ottawa, ON, Canada

**Howard Carmichael**, Department of Physics, University of Auckland, Auckland, New Zealand

**Ivan Fernandez-Corbaton**, Department of Physics and Astronomy, Macquarie University, Sydney, Australia

**Enrique J. Galvez**, Department of Physics and Astronomy, Colgate University, Hamilton, NY, USA

**Reinhard Kienberger**, Max-Planck Institut für Quantenoptik, Garching, Germany  
Physik Department, Technische Universität München, Garching, Germany

**Matthias F. Kling**, Max-Planck Institut für Quantenoptik, Garching, Germany  
Physik Department, Ludwig-Maximilians-Universität, Garching, Germany

**Mayukh Lahiri**, IQOQI, University of Vienna, Vienna, Austria

**Qing Liao**, J.R. Macdonald Laboratory, Physics Department, Kansas-State University, Manhattan, KS, USA

**A. I. Lvovsky**, Institute for Quantum Information Science, University of Calgary, Calgary, Canada  
Russian Quantum Center, Skolkovo, Moscow, Russia

**Tom G. Mackay**, School of Mathematics, University of Edinburgh, Edinburgh, UK  
Department of Engineering Science and Mechanics, Pennsylvania State University, University Park, PA, USA

**Gabriel Molina-Terriza**, Department of Physics and Astronomy, Macquarie University, Sydney, Australia

**Miles J. Padgett**, School of Physics and Astronomy, University of Glasgow, SUPA, Glasgow, UK

**A. Salam**, Department of Chemistry, Wake Forest University, Winston-Salem, NC, USA

**Zhimin Shi**, Department of Physics, University of South Florida, Tampa, FL, USA

**Frederik Süßmann**, Max-Planck Institut für Quantenoptik, Garching, Germany  
Physik Department, Ludwig-Maximilians-Universität, Garching, Germany

**Uwe Thumm**, J.R. Macdonald Laboratory, Physics Department, Kansas-State University, Manhattan, KS, USA

**Emma Wisniewski-Barker**, School of Physics and Astronomy, University of Glasgow, SUPA, Glasgow, UK

# PREFACE

Since its inception, the term “photonics” has been applied to increasingly wide realms of application, with connotations that distinguish it from the broader-brush terms “optics” or “the science of light.” The briefest glance at the topics covered in these volumes shows that such applications now extend well beyond an obvious usage of the term to signify phenomena or mechanistic descriptions involving photons. Those who first coined the word partly intended it to convey an aspiration that new areas of science and technology, based on microscale optical elements, would one day develop into a comprehensive range of commercial applications as familiar and distinctive as electronics. The fulfilment of that hope is amply showcased in the four present volumes, whose purpose is to capture the range and extent of photonics science and technology.

It is interesting to reflect that in the early 1960s, the very first lasers were usually bench-top devices whose only function was to emit light. In the period of growth that followed, most technical effort was initially devoted to increasing laser stability and output levels, often with scant regard for possibilities that might be presented by truly photon-based processes at lower intensities. The first nonlinear optical processes were observed within a couple of years of the first laser development, while quantum optics at first grew slowly in the background, then began to flourish more spectacularly several years later. A case can be made that the term “photonics” itself first came into real prominence in 1982, when the trade publication that had previously been entitled *Optical Spectra* changed its name to *Photonics Spectra*. At that time the term still had an exotic and somewhat contrived ring to it, but it acquired a new respectability and wider acceptance with the publication of Bahaa Saleh and Malvin Teich’s definitive treatise, *Fundamentals of Photonics*, in 1991. With the passage of time, the increasing pace of development has been characterized by the striking

progress in miniaturization and integration of optical components, paving the way for fulfilment of the early promise. As the laser industry has evolved, parallel growth in the optical fiber industry has helped spur the continued push toward the long-sought goal of total integration in optical devices.

Throughout the commissioning, compiling, and editing that have led to the publication of these new volumes, it has been my delight and privilege to work with many of the world's top scientists. The quality of the product attests to their commitment and willingness to devote precious time to writing chapters that glow with authoritative expertise. I also owe personal thanks to the ever-professional and dependable staff of Wiley, without whose support this project would never have come to fruition. It seems fitting that the culmination of all this work is a sequence of books published at the very dawning of the UNESCO International Year of Light. Photonics is shaping the world in which we live, more day by day, and is now ready to take its place alongside electronics, reshaping modern society as never before.

DAVID L. ANDREWS

*Norwich, UK, July 2014*

---

# 1

---

## A PHOTON IN PERSPECTIVE

DAVID L. ANDREWS

*School of Chemistry, University of East Anglia, Norwich, UK*

### 1.1 INTRODUCTION

It is a familiar, fundamental truth of modern Physics that light is composed of *photons*, entities known as elementary particles despite possessing both particle- and wave-like attributes. Readers of these volumes on Photonics will accede with the view that numerous properties and interactions of light are only fully comprehensible when represented and formulated in terms of photons. Indeed, in order to understand certain processes, there simply appears to be no viable alternative. This is not only the case with observations such as the photoelectric effect that have played a pivotal role in familiar scientific history; in optics there is a wealth of recent and developing applications that also hinge on other, specifically photon-borne properties. Many properties of light appear to manifest directly corresponding attributes of the individual photons. Other qualities, of course, reflect ensemble characteristics that can emerge only in a beam comprising numerous photons—but there too we find phenomena dependent on statistical properties which can only make sense by reference to photon distributions. There is a rich and deeply embedded relationship between photons and the modern science of light.

The word *photon* has not yet reached its centenary; it was in fact coined in 1926 by a thermodynamics researcher named Lewis [1], who surprisingly introduced it to describe “not light but [that which] plays an essential part in every process of radiation.” However, the emergence of a reasonably fully fledged photon concept can be traced back much earlier, to 1905, where it first surfaced in Einstein’s explanation of a frequency threshold for photoelectric emission. Using the term *Lichtquant*, “light

---

*Photonics: Scientific Foundations, Technology and Applications, Volume I*, First Edition.

Edited by David L. Andrews.

© 2015 John Wiley & Sons, Inc. Published 2015 by John Wiley & Sons, Inc.

quantum,” Einstein wrote: “When a light ray spreads out from a point source, the energy is not distributed continuously over an increasing volume [wave theory of light], but consists of a finite number of energy quanta that are localized at points in space, move without dividing, and can only be absorbed or generated as complete units” [2].

With subsequent success in explaining the line spectra of atoms, this quantum concept rapidly gained an apparently incontrovertible status—and given the passage of time, one might suppose that there would now be little left to discover, little scope for debate over what the photon truly is. However, the nature of that reality has never been simple to explain. It is telling that Lamb, an early pioneer of modern optical spectroscopy, would jest that it should be necessary to be granted a license before being allowed to use the word *photon* [3]. Following the arrival of the laser [4] and the subsequent emergence of the derivative term “photonics” in the 1960s, the distinctive and sometimes paradoxical nature of the photon has become more than ever evident. The state of knowledge even a quarter of a century ago is a pale shadow of the current understanding; many of the issues discussed in the following were unheard of even at that time [5]. What we now understand about photons has certainly become very much richer, certainly less simple, than Einstein’s original conception.

It powerfully illustrates the wide diversity of interpretation that, as more and more exotic phenomena have been identified, specially coined descriptors have been introduced to identify and qualify particular kinds of behavior with which photons can be associated. So we now find in the literature terms that would seem to signify various distinctive kinds of photon, if such a thing were possible. Examples abound: we read of photons whose character is *dressed* [6], *ballistic* or *snake-like* [7,8], *electric* or *magnetic* [9, 10], *entangled* and *heralded* [11, 12], *dipole* or *quadrupole* [13, 14], *real* or *virtual* [15, 16] ... there is literature on *biphotons* [17]—and so the list goes on. Different kinds of system or physical effect certainly manifest different attributes of the photon, but it is evident that various scientific communities and practitioners who share the use of the term would not find themselves in full agreement on every aspect of what a photon is. Far from becoming a fixture in modern physics, the notion of a photon has, if anything, become more of a quandary as time goes by. Many of those who research such matters would be drawn to agree with Loudon, author of one of the classic books on the quantum theory of light, that “it is no longer so straightforward to explain what is meant by a photon” [18].

It is also remarkable that, in the centenary year of the photon concept, 2005, a major international conference with the title *What is a Photon?* could attract wide-ranging contributions and stimulate debate amongst leading scientists from across the globe [19]. Indeed, that initial meeting spawned an ongoing series of conferences and discussions in which the truth and character of the photon continues to be the subject of highly active deliberation. So it seems fitting, in this first chapter of the series on Photonics, to attempt an objective assessment of which, if any, of those photon attributes are incontrovertible, representing a common ground for interpretation—and also to provide a certain perspective on some of the more intricate and less well-settled issues. As we shall see, even the momentum or information content of a photon, or the existence of its wavefunction, are not entirely uncontroversial.

## 1.2 FOUNDATIONS

### 1.2.1 Modes of Optical Propagation

To lay the foundations for a discussion of the most unequivocal photon properties, it will first be helpful to recall some established ground from classical optics—which will also serve to introduce some key definitions. It has been known, since the pioneering work of Maxwell, that light entails the propagation of mutually associated, oscillatory electric and magnetic induction fields, which we shall call  $\mathbf{e}$  and  $\mathbf{b}$ , respectively (lowercase symbols being used, as is common, to signify fields in a microscopic regime). In free space these fields propagate at a speed  $c$ , and they oscillate at a common frequency  $\nu$ , in phase with each other. The simplest case, polarized monochromatic light, can be regarded as a fundamental mode of excitation for the radiation field—an optical mode that is conveniently characterized by two quantities: a wavevector  $\mathbf{k}$  and a polarization  $\eta$ . The former is a vector in conventional three-dimensional space, pointing in the direction of propagation such that the triad of vectors  $\mathbf{e}$ ,  $\mathbf{b}$ , and  $\mathbf{k}$  together form a right-handed, mutually orthogonal set; its magnitude is  $k = 2\pi\nu/c = 2\pi/\lambda$ , where  $\lambda$  is the optical wavelength.

The second mode attribute, the polarization  $\eta$ , which designates the disposition of the electromagnetic oscillations, is most often a label rather than a directly quantifiable variable. Plane (or linear) and circular polarizations are the most familiar forms: circular polarizations in particular occupy a privileged position with regard to some of the ancillary properties to be examined below. The terms “linear” and “circular” are usually taken as referring to a projection of the electric field vector locus, in a plane normal to the direction of propagation. Any more general, conventional form of polarization can be conceived as a variant of an elliptical form, and defined as such by the values of three classical *Stokes parameters*  $S_1$ ,  $S_2$ , and  $S_3$ . The corresponding polarization state can then be regarded as mapping the coordinates of a particular position on the surface of a Poincaré sphere [20] whose axes are defined by those three parameters. The fourth Stokes parameter  $S_0$ , representing the extensive property of intensity, does not carry over to the case of individual photons, since the intensity of light will necessarily be related to the population of photons in a given volume. Equally, any *degree of polarization* will signify the relative photon populations of different polarization states. More intricate forms of polarization state exist in *vector beams*, such as those with electric vectors that are radially or azimuthally directed with respect to the direction of beam propagation. Structured light of this and other kinds is to be discussed in Section 1.6.

Secured as solutions to Maxwell’s equations, the propagating electric and magnetic fields of each optical mode oscillate with a phase factor  $\exp[i(\mathbf{k}\cdot\mathbf{r} - \omega t)]$ , where  $\omega = 2\pi\nu$ . The form of this factor is such that a complete set of optical modes  $(\mathbf{k}, \eta)$ —a set of infinite extent for light in free space—can be regarded as the individual components of a Fourier expansion for the radiation field. Summed over all modes, the total electromagnetic energy is accordingly expressible as a Hamiltonian cast as a volume integral of the energy density: see ① in Table 1.1, where  $\epsilon_0$  is the vacuum electric permittivity. The transverse designation of the electric field vector

**TABLE 1.1 Key equations and significance**

| Reference | Equation  | Significance   |
|-----------|---|--|
| ①         | $H_{\text{rad}} = \frac{\epsilon_0}{2} \int \{ \mathbf{e}^{\perp 2}(\mathbf{r}) + c^2 \mathbf{b}^2(\mathbf{r}) \} d^3 r$  | Hamiltonian is a volume integral of an energy density that is quadratic in the transverse electric and magnetic fields |
| ②         | $E = nhv (\equiv n\hbar ck)$  | Electromagnetic energy is quantized in units whose magnitude is determined by the optical frequency                    |
| ③         | $I = (n/V) hc^2 / \lambda$  | For a given wavelength, irradiance is linearly proportional to the number of photons per unit volume                   |
| ④         | $H_{\text{rad}}  n(\mathbf{k}, \eta)\rangle = \left( n_{k,\eta} + \frac{1}{2} \right) \hbar ck  n(\mathbf{k}, \eta)\rangle$   | Schrödinger equation for light; each mode delivers an integer number of photon energies plus a ground state energy     |
| ⑤         | $\mathbf{S}_{\text{rad}} = \epsilon_0 \int \{ \mathbf{e}^\perp(\mathbf{r}) \times \mathbf{a}(\mathbf{r}) \} d^3 r$  | Spin angular momentum is the volume integral of an operator cross product of the electric field and vector potential   |
| ⑥         | $E^2 = p^2 c^2 + m_0^2 c^4$   | General equation from special relativity theory, linking energy with momentum and rest mass                            |
| ⑦         | $v_g = c/[n(v) + v dn(v)/dv]$   | Group velocity differs from the phase velocity by an additional term in the denominator                                |
| ⑧         | $H = H_{\text{mat}} + H_{\text{int}} + H_{\text{rad}}$  | Quantum electrodynamical Hamiltonian comprising terms for matter, matter-radiation coupling, and the radiation itself  |
| ⑨         | $L = \epsilon_0 \int \mathbf{e}_i^\perp(\mathbf{r}) (\mathbf{r} \times \nabla) \cdot \mathbf{a}_i(\mathbf{r}) d^3 r$  | Orbital angular momentum operator which, together with spin, accounts for the total angular momentum                   |
| ⑩         | $\chi = \frac{\epsilon_0}{2} \{ \mathbf{e}(\mathbf{r}) \cdot \nabla \times \mathbf{e}(\mathbf{r}) + c^2 \mathbf{b}(\mathbf{r}) \cdot \nabla \times \mathbf{b}(\mathbf{r}) \}$ | Optical chirality density derives from projections of the curls of both the electric and magnetic fields               |

is a reminder that the defining expression applies in charge-free regions so that there are no static (longitudinal) electric fields: the magnetic induction field is necessarily transverse, too. Consequently, in each free-space mode, both fields oscillate in directions perpendicular to the propagation wavevector.

It is interesting to observe the imperative for the energy density to take the mathematical structure exhibited by ①. One clear interpretive consequence of the photoelectric effect is that photons have a directly additive energy, requiring a set of evenly spaced energy levels for each optical mode. In fact, the quadratic dependence of ① on conjugate pair variables  $e^\perp$  and  $\mathbf{b}$  is necessary in order for quantization to provide energy levels forming exactly such an evenly spaced, infinite set. Without this, the notion of a photon could not arise: there would not be a linear relationship between the quantum number and the total electromagnetic energy. So, it has transpired that the very existence of photons proves the energy density to be quadratic in both the electric and magnetic fields [21].

### 1.2.2 Quantum Foundations

In principle the theory of quantized light begins with the simple electromagnetic energy equation ②,  $E = nhv$ , signifying a number  $n$  of discrete quanta, with each individual photon energy given by  $hv \equiv \hbar ck$  ( $\hbar = h/2\pi$  is the Dirac constant, and  $h$  is Planck's constant). This formula represents the first step toward the modern, comprehensive theory of quantum optics—a theory that in fully fledged form is nonetheless as different in character from its origins as is modern quantum mechanics from Bohr's atomic theory. Equation ② also provides the basis for another, equally useful but lesser known formula ③, that directly relates beam irradiance  $I$  (optical power per unit area) to the mean number of photons  $n$  within a volume  $V$ . For example, how likely is it, at any instant, to find a single photon within a cube the size of the wavelength? This equation shows that for a laser emitting 532 nm wavelength radiation, the necessary conditions would require an intensity of around  $7 \times 10^8 \text{ W m}^{-2}$ ; that is about half a million times more intense than the average intensity of sunlight on the Earth's surface. The yet much smaller instantaneous probability of finding a photon in the volume of a molecule, under ambient conditions, goes some way to explaining why our comprehension of the photon has been so much advanced by the invention of the laser.

The optical wavevector and polarization, which together define the optical mode  $(\mathbf{k}, \eta)$ , characterize photons in terms of five degrees of freedom. Typically, three (for example, three Cartesian components) can serve to define the wavevector and the other two the polarization (such as a latitude and longitude on the Poincaré sphere). We now recognize that specifying these mode parameters will serve to determine the unit values of all *extensive* quantities—those that directly scale with the number of quanta within a given volume. This is true not only for energy, but also *linear momentum* and *spin angular momentum*. The photon momentum is given by  $\hbar\mathbf{k}$ , whilst the spin is determined by polarization state. In Section 1.3, we shall note issues that arise for photons propagating through material media. For the moment, we simply observe that *beam* attributes, such as measures of linewidth

or coherence, are not extensive quantities as they are meaningful only for photons collectively.

### 1.2.3 Developing Quantum Optics

To put the theory on a firmer footing, since the photon is unequivocally a quantum entity, it is now appropriate to formulate a proper quantum mechanical depiction, cast in terms of state vectors and wavefunctions. The majority of light beams in the real world do not have a well-defined value for the number of photons (we shall return to this in Section 1.7), but it will be helpful to focus at the outset on states that do—noting that a variety of other radiation states are nonetheless possible [22]. For a specific optical mode  $(\mathbf{k}, \eta)$ , a number state with  $n$  photons is designated  $|n(\mathbf{k}, \eta)\rangle$  in the standard Dirac notation. Here, it is important to recognize that the wavefunction for the two-photon state,  $|2(\mathbf{k}, \eta)\rangle$ , will *not* be expressible as a product of one-photon  $|1(\mathbf{k}, \eta)\rangle$  state functions. This is not necessarily surprising; in much the same way, the wavefunction for a  $2s$  electron in the hydrogen atom cannot be represented as a product of  $1s$  wavefunctions. The latter refutation only seems more obvious because atomic energy levels have non-uniform energy spacing. In this respect, the fact that the energy of a state with  $n$  photons scales directly with  $n$  can be potentially misleading, if wrongly taken to indicate that each of those  $n$  photons has a separate identity [23].

The quantum optical equations for light propagating in a vacuum, in which the electric and magnetic fields are promoted to operator status, are based on developing the radiation Hamiltonian into operator form, from the usual classical expression for the spatially integrated energy density, ①. The Schrödinger equation ④ for a single electromagnetic mode can then be constructed. The quantum radiation states  $|n(\mathbf{k}, \eta)\rangle$  are eigenstates of the radiation Hamiltonian; for each mode they form a complete basis set, in terms of which other states of the same optical mode can be expressed through use of the quantum expansion postulate. More generally, the eigenstate basis for any polychromatic radiation can be cast as a product,  $|n_1(\mathbf{k}_1, \eta_1)\rangle \otimes |n_2(\mathbf{k}_2, \eta_2)\rangle \otimes |n_3(\mathbf{k}_3, \eta_3)\rangle \dots$ . To develop the terminology, it follows that the number of photons  $n_{k,\eta}$  can be interpreted as the occupancy, or *occupation number*, of the corresponding optical mode. It also transpires that each term in the free-space equation ①, of electric and magnetic origin, delivers an equal half-contribution to the total mode energy  $(n_{k,\eta} + \frac{1}{2})\hbar ck$ . It is therefore reasonable to consider the photon “conveying” quanta that comprise conjoined electric and magnetic elements of the electromagnetic field.

Just as the electromagnetic energy density is promoted to operator form in quantum optics, so too are other key observables. It can be shown that all physically meaningful observables—properties whose determination can leave the radiation field unchanged—are associated with operators that are bilinear in the electromagnetic fields [24, 25]. An important, further example is the operator for spin angular momentum ⑤, the volume integral of a vector product between the transverse electric field  $\mathbf{e}^\perp(\mathbf{r})$  and the vector potential  $\mathbf{a}(\mathbf{r})$ : the latter is related to the electric and magnetic fields by  $\mathbf{b}(\mathbf{r}) = \nabla \times \mathbf{a}(\mathbf{r})$ ;  $\mathbf{e}(\mathbf{r}) = -\dot{\mathbf{a}}(\mathbf{r})$ . The spin operator and the quantum

Hamiltonian together support a set of common optical eigenstates, the latter comprising the two circular polarization states for each wavevector  $\mathbf{k}$ . In the usual optics convention, the angular momentum is taken to have a positive sense of rotation for left-circular polarization (the electric and magnetic vectors describing an anticlockwise helix, as the light propagates towards the observer) and a negative sign for right circularity. It is only photons of specifically left- and/or right-handed circularity, for which both energy and spin can be precisely quantified. The spin angular momentum operator then delivers an eigenvalue that is an integer multiple of  $\hbar$ , the multiplier corresponding to the difference in numbers of left- and right-hand photons in the beam. The result is consistent with spin angular momentum values of  $\pm\hbar$ , per photon, in the direction of  $\mathbf{k}$ .

### 1.2.4 Boson Statistics

The hallmark integer spin associated with the circular polarization states for the photon, its value one unit of  $\hbar$ , has a powerful foundational significance. It marks out the photon as a particular kind of elementary particle: a boson, subject to Bose–Einstein distribution laws. In the parlance of elementary particle physics, the photon is the gauge boson for electromagnetism. This designation is distinct from fermions (half-integer spin particles such as electrons) which satisfy Fermi–Dirac statistics. The contrast is stark: boson states have wavefunctions that are symmetric on exchange of any two components. In consequence, Bose–Einstein statistics impose no limitation on the number of particles that can be accommodated in a single quantum state. In the case of photons, this is one of the principal reasons that strongly coherent laser light is achievable. In the nature of boson character we also find a deeper reason for the previously noted fact that the quantum state vector for a beam conveying two or more identical photons is not separable as a product of wavefunctions for photons individually—this despite the fact that photon energies appear directly additive, and there is no electrodynamic coupling between the photons themselves.

As an aside, this categorization of photons as a type of elementary *particle* raises the question of whether they have any other “material” attributes. Certainly, the photon is a *stable* elementary particle: there is no limit on how long a photon can live, and we can detect light from a distant star that has taken billions of years to reach the earth. In the realm of optics, two other fundamental properties would be charge and mass: both are zero. The former is unsurprising; the latter is reconciled with non-zero momentum on recognition of the special relativistic equation ④ connecting energy  $E$ , rest mass  $m_0$ , and momentum  $p$ . For the single photon  $E = h\nu$ ; with  $m_0 = 0$  we simply retrieve  $p = h\nu/c$ , consistent with the magnitude  $h/\lambda$  of the momentum vector  $\hbar\mathbf{k}$ . One does have to exercise caution in this regard, however; Einstein famously showed that mass will indeed be conveyed (in the form of energy) from an emitter to an absorber [26]. While relativistic issues are in scope, it is also interesting to note a curious implication of the *proper time* formula from special relativity. This shows that for a hypothetical observer moving along with the light, the photon lifetime is actually zero: at the speed of light, all times are equal. So the times of photon emission and detection, however remote, are in this sense simultaneous.

### 1.3 MEDIUM ISSUES

Before proceeding further, it is instructive to consider how some of the above material, essentially formulated for propagation in a vacuum, needs to be extended—indeed to some extent reinterpreted—for light passing through a material medium. The issues that arise at this stage are not specifically associated with the quantum nature of light; such concerns will be addressed in later sections. However, the modification by matter of electromagnetic propagation does impinge on the way in which photons are understood. It also transpires that one must take special care with the interpretation of issues that might seem to impinge on causality—the tenet of special relativity that no information can be transmitted faster than the vacuum speed of light, that is, the signal velocity  $\neq c$ .

#### 1.3.1 Speed of Propagation

To introduce this topic we can begin by focusing on the simplest and most familiar aspect, the reduction of light's speed in inverse proportion to the refractive index  $n(v)$ . As each photon propagates into a material medium, it continues onward with an unchanged energy and frequency, but its wavelength is generally shorter so that the product of frequency and wavelength is diminished. Within the medium, the light thus has a *phase velocity* given by  $c/n(v)$ , and generally  $n(v) > 1$ . In some condensed matter, phase velocities in the X-ray region can in fact exceed  $c$ , through a refractive index that is a little below unity. However, measurements based on detection at different locations will not escape from the strict conditions of relativistic causality: information cannot be transmitted faster than the speed of light. It is usually argued that the positional uncertainty associated with a precise wavelength (and hence precise photon momentum) precludes causality violation.

The frequency or wavelength dependence of the refractive index means that the velocity varies in a characteristic way across the absorption spectrum of each material. The intricate form of this velocity dependence is captured by the familiar *dispersion curves*, which plot optical frequency against wavenumber  $k$ . In frequency regions well away from material absorption bands, these curves display an approximately linear response with a slope approaching the vacuum speed of light  $c$ —but this line separates off into paired asymptotes of zero slope in the vicinity of each absorption frequency, namely,  $\omega$ . The quantum interpretation is instructive, for in the regions of diminished slope which appear above and below each resonant frequency, photon behavior seamlessly changes to that of a *polariton* [27].

Polaritons, also sometimes termed *dressed* or *medium-dressed* photons, are associated with strong interactions between the propagating radiation and electronic excitations of the material, usually through electric dipole coupling. In photonic terms, we can understand the onset of this change in behavior: as the optical frequency approaches resonance with an optical absorption band, the local electronic polarizability (or linear susceptibility) correspondingly exhibits a rapid escalation in magnitude. In consequence, the optical fields drive increasingly strong, oscillatory motions in the local electronic distribution, slowing down forward propagation. When

exact resonance is reached and the radiation can be halted by actual absorption, the photon energy is taken up in effecting a local electronic transition to a corresponding excited state. This excitation may itself propagate through the material by successive processes of resonant energy transfer, the fulfillment of local energy conservation at each step permitting a small delay in the forward progression. What is remarkable is that there is a continuum of such behavior, the photon acquiring a progressively modified character as its own electromagnetic fields are “dressed” by those of the material it encounters.

In passing it is worth noting that, as its name suggests, the *group velocity* <sup>⑦</sup> is a concept designed for application to beams of light with a frequency spread. It is here, for media exhibiting exotic dispersion features, that the much-vaunted cases of *slow light* arise. It is indeed remarkable that, since the speed of light is generally so far beyond the reach of any material motion, beams of light can be slowed to essentially zero velocity [28]. At the other extreme is a phenomenon that has earned the oxymoron *superluminal light*, in which it is observed that the peak intensity components of short radiation pulses entering and emerging from suitably tailored media are separated by a shorter time interval than the vacuum speed of light would allow. Nonetheless, one cannot meaningfully interpret this as the composite effect of individually “superluminal photons”; it is an ensemble effect associated with the interference between photons in modes spanning the broad range of wavelengths present in short pulses of light. So the term “superluminal” might be applied in a limited sense to the beam, but not its constituent photons. The need for this caution appears salutary; as Chiao and Milonni have pointed out “[In many] classic texts on optics and electromagnetism … it is incorrectly implied that a group velocity greater than  $c$  would contradict the special theory of relativity” [29]. Nothing could be further from reality; no information can be conveyed at this speed. Issues that arise in the less “real” world of virtual photons will be considered in Section 1.5.

### 1.3.2 Momentum

It is somewhat alarming to find that a persuasive resolution has only very recently been found, to a long-standing controversy over the electromagnetic momentum of light propagating through a material medium. The controversy dates back to the early years of the twentieth century, when the photon concept was yet in its infancy. The full development of that concept made the central question much simpler to frame, but not to solve. In modern parlance the essence of the issue can be posed thus: is the linear momentum of a photon diminished or increased from its free space value? Specifically, one might argue that since the speed of light is reduced by a factor of  $n(v)$  in a medium, the linear momentum of each photon should suffer a corresponding loss, and the momentum per photon would be  $h\nu/n(v)c$ . On the other hand, since that reduced speed is associated with a proportionate decrease in the wavelength, it might equally be supposed that the inverse relationship between the wavelength and momentum should signify an increase in the latter, giving a photon momentum  $n(v)h\nu/c$ . The argument over which is the correct formula has become known as the Abraham–Minkowski controversy, respectively named after the two individuals

whose formulations would support each of these apparently irreconcilable conclusions. The recently proffered solution to this enigma [30] centers on an assertion that the Abraham momentum signifies a *kinetic* quantity directly relating time derivative of a positional measurement, whilst the Minkowski version is the correct mathematical formula for *canonical* momentum, in the sense of Lagrangian mechanics. It is not yet clear how widely accepted this resolution will prove to be.

### 1.3.3 Directedness of Propagation

In the sphere of time-gated imaging, other descriptors signifying a distinctive manner of propagation can be found associated with photons. The terms *ballistic* and *snake-like* [7, 8] were originally introduced to signify a distinction between components of light that, in the former case, emerged from transmission through a complex (often biological) sample without significant scattering, compared to components emerging after multiple scattering events within the sample. The longer, more meandering pathway of the optical energy in the latter case, which suggests the sinuous description, also correlates with a delayed emergence from the sample. This enables the “ballistic” signal—which of course has a far greater capacity to produce images that resolve interior structures—to be cleanly captured by time gating. The classic illustration is imaging bone through tissue [31].

The terminology was never meant to suggest that there are indeed two different kinds of photon in the source radiation; the difference in behavior simply represents two opposite extremes within a statistical distribution of photon passage events. Nevertheless, there is a clear inference that still demands attention: interpreting every scattering event as a photon path deviation implies photons that continue to exist, but with changed propagation vector. Yet, since the initial and emergent states for each such interaction relate to quanta of excitation in different radiation modes, it is essentially meaningless to regard the input and output as the *same* photon. More correctly, one has to regard each scattering event as the annihilation of one photon and the creation of another.

## 1.4 PHOTON LOCALIZATION AND WAVEFUNCTION

There is a concise measurement-based interpretation, unattributed but popularly ascribed to one of the pioneers of optical coherence theory, asserting that: “A photon is what a photodetector does.” It is a viewpoint that is not far removed from Bohr’s initial stance on the status of quantized radiation [32]. In the spirit of this succinct depiction, various calculational methods have been demonstrated that can deliver a spatially localized visualization of photon propagation—there are numerous examples [33]. Some such representations have didactic value. Nonetheless, a more accurate description of what any conventional (or quantum) photodetector does is that it responds to the electromagnetic field of impinging radiation, thereby registering its quantum energy. It is indeed entirely consistent with the modern path integral formulation of quantum mechanics in which theoretical derivations do not

presume to describe what intervenes between setup and measurement, but instead make allowance for all possibilities. The post-interpretation of such calculations in terms of specific photon attributes is notoriously misleading; it is impossible to measure the path a photon has taken.

### 1.4.1 Localization

The results of double-slit experiments conducted at low intensities, which reveal interference effects even when a single photon is present, unequivocally show that photons have an essential spatial delocalization. Any more direct measurement that is localized by the physical extent of a detector cannot be interpreted as signifying localization of the photon itself. For example, since the process of light absorption involves photon capture, it clearly effects a collapse of the state function for the radiation field. It is salutary to recall the view of Mandel and Wolf, who pointed out that attempts for whatever purposes to build a picture of “localized photons” are fraught with danger, for “a photon has no precise position no matter what the state may be” [34]. It is essential to keep in mind the notion of photons having a significant degree of delocalization; one has to resist any temptation to think of the photon as in any sense a point particle.

The most significant exceptions to the apparently inexorable process of state collapse in most photon measurements are experiments designed to provide “quantum non-demolition” measurements on the optical field [35, 36], specifically aiming to circumvent the usual limitations associated with quantum measurement. One means of achieving this is to deploy a form of interaction whose effective Hamiltonian commutes with the Hamiltonian driving the system dynamics. In one such scheme based on the optical Kerr effect [37], a beam of throughput radiation emerges unchanged despite bringing about a modification to a second beam, coincident with it in the nonlinear medium. Such a process can both serve to signify the presence of photons in the former beam and also in principle to quantify, without changing, their number. It has been suggested that non-demolition principles can be extended to the detection of single photons, [38, 39] but the viability of some techniques at this level has been contested [40]. Certainly, no such measurements can determine with arbitrary precision in space or time exactly where any individual photon can be found.

### 1.4.2 Wavefunction

Authors who deploy the term “photon wavefunction” usually seem to have in mind a quantum amplitude relating to a spatial distribution of the associated electric field, though we have to bear in mind that there is more to the photon than its electric field! To conceive a more specific “electric field wavefunction” basically indicates a confusion between wavefunctions and operators.

Certainly, the quantum state of radiation comprising a single photon must have a wavefunction—as indeed will a radiation state with any number of photons—yet it is not in general correct or meaningful to conceive a *photon wavefunction*. The important difference between the two propositions, seemingly minor in their verbal

expression, was first touched on in Section 1.2.3. The notion is almost defensible for a one-photon state, where the distinction from state vector does not produce major problems, and in this sense it can be found utilized in areas of application concerned with quantum effects that are significant only at very low levels of intensity. But as soon as we have two or more photons, the notion of a wavefunction for either component is inadmissible. It would seem inadvisable to use, as if it were generally applicable, a concept that is defensible only for one-photon states.

Direct insights into the specifically quantum nature of light are afforded by observations of processes such as spontaneous parametric down-conversion—essentially the time-inverse of sum-frequency or second harmonic generation. When single photons are suitably converted into pairs that propagate off in different directions, the detection of non-classical correlations between the polarization states of the two components signifies quantum entanglement [41, 42]. Radiation produced in this manner is often referred to as comprising *entangled photons* [11, 43] or *biphotons* [17]; the possibility of deducing information concerning one photon component, from a measurement made on the other, also leads to the latter being described as a *heralded photon* [12].

Numerous other experiments in quantum optics underscore the more general inseparability of two-photon states, perhaps most categorically in the Hong-Ou-Mandel effect [44]. When a single photon is intercepted by a beam splitter, the result is a state of the radiation field with one well-defined quantum of energy: this state can be cast as a linear superposition of “reflected” and “transmitted” states, for which each has a distinct photon character since two different modes are involved. Experiments on the output generally provide results consistent with a linear combination of outcomes, again signifying quantum entanglement [45]. What is observed is certainly the collapse of a quantum state, but arguably not “a photon” in the sense we have established. Recognizing that linear combinations of states are not the same as linear combinations of particles gets to the heart of the distinction between the wavefunction for a state comprising one photon, and a “photon wavefunction.”

All such results undermine the best intentioned attempts to portray the quantum mechanical nature of the photon by reference to “its” wavefunction: even the most ardent proponents of this concept will usually admit to the implication of a significant degree of controversy [46]. It has in fact been shown that the contrivance of any “photon wavefunction” approach can indeed only produce results already described by standard quantum electrodynamics [47].

## 1.5 THE QUANTUM VACUUM AND VIRTUAL PHOTONS

### 1.5.1 Vacuum Fluctuations

The  $\frac{1}{2}\hbar ck = \frac{1}{2}\hbar\nu$  energy term on the right in ④ invites attention, for it represents the residual energy of an optical mode with zero occupancy, that is, a state in which no photons are present. The totality of such ground-state contributions signifies the energy associated with *vacuum fluctuations*, the physical consequences of which extend from spontaneous emission to Casimir forces [48]. For any given mode

$(\mathbf{k}, \eta)$ , the vacuum energy of the state  $|n(\mathbf{k}, \eta)\rangle$ , though linearly dependent on  $n$ , is *not proportional* to  $n$ . For example, that energy is exactly the same,  $1/2\hbar\nu$ , for both the  $|1(\mathbf{k}, \eta)\rangle$  and  $|2(\mathbf{k}, \eta)\rangle$  states. This non-additivity of ground-state energies is yet another feature serving to underscore the fact that there is not a separate wavefunction for each of the photons, in a multiphoton state.

The implication of the non-zero vacuum term is that every radiation mode has an irreducible ground state energy, consistent with quantum fluctuations in the electric and magnetic fields, and representing as such the vacuum expectation value of the radiation Hamiltonian ① when no observable light is present. The fact that this vacuum energy is infinite, when summed over all radiation modes and integrated over space, raises some interesting philosophical issues, though it is not a practical problem. A directly significant implication is that, consistent with quantum uncertainty, it is possible to create and then destroy photons for brief intervals of time. These photons, whose fleeting lives begin and end as energy is borrowed from and returned to the vacuum fluctuations, are not experimentally observable: they are accordingly termed *virtual photons*.

### 1.5.2 Virtual Photons in Action

There are essentially two distinct types of application based on virtual photon calculations. One is for energies, the other for interactions: both arise from the following. In general, the quantum electrodynamical Hamiltonian for a region of space containing matter of any kind, ⑧, comprises three terms. Two terms designate the quantum energy operators for matter and for the radiation field (the latter only arises in quantum operator form because we are dealing with photons). The presence of the other term, which represents coupling between the matter and the radiation, means that neither the eigenstates of  $H_{\text{mat}}$ , nor those of  $H_{\text{rad}}$ , are stationary states of the full Hamiltonian  $H$ . Accordingly,  $H_{\text{int}}$  will act as a perturbation on those eigenstates to produce energy shifts and transitions. Each action of  $H_{\text{int}}$  will create or annihilate a photon—and since no photon created from the vacuum can be sustained beyond the spatial and temporal limits decreed by the Uncertainty Principle, it follows that measurable energy shifts and rates of transition between states of the same total energy must be associated with the emergence and disappearance of virtual photons.

In the realm of elementary particles, all electromagnetic interactions are considered to be mediated by the interparticle propagation of such virtual photons. The absence of any interparticle term in the Hamiltonian ⑧—which is exact when cast in multipolar form [49]—means that there is no other means of coupling between separate particles. In the sphere of single-particle interactions, calculations based on the virtual photon premise also provide values for fundamental properties in precise agreement with experiment, for widely varying physical parameters. The most notable example is the fine-structure constant—one of the fundamental constants in the Standard Model of particle physics—whose value based on virtual photon calculations agrees with experiment at an unparalleled level of precision, better than 1 ppb (part per billion) [50].

One key feature of the virtual photon representation is its intrinsic accommodation of causal constraints from special relativity, which precludes instantaneous or any

other superluminal forms of coupling. In this context it is worth clarifying a misleading remark by Feynman, suggesting that by virtue of quantum uncertainty a virtual photon might propagate faster than light [51]. In fact, by evaluating measurable quantities associated with the duly retarded electromagnetic fields, an analysis by Power and Thirunamachandran [24] proved strict adherence to relativistic causality. Another notable feature is a quantum mechanical aspect, enshrined in the mathematics of mode summation for each virtual photon. Enforcing summation over all wavevectors and polarizations is consistent with the principle of summing over every quantum variable for unobserved intermediate states. In some “self-energy” applications, the term *virtual photon cloud* [52] is sometimes used as a reminder that for such calculations there is no constraint over the position or momentum of each virtual photon interaction—indeed it is as if such photons constantly emerge from, and retreat into, the space surrounding each material particle. Matter is universally suffused with virtual light. Moreover, the diffuse spatial character of the photon means that it is conceivable for a photon to be created and annihilated by the same material particle.

### 1.5.3 Virtual Photon Propagation

To better appreciate the propagative characteristics associated with virtual photon coupling, it proves instructive to consider the result of calculations on the simplest two-site process. Known as *resonance energy transfer*, this affords the mechanism for electronic excitation to pass between electrically neutral, independent particles [53]. The initial and final states for the system thus differ through vector displacement of the electronic energy  $\Delta E$  from the donor to the acceptor site. The principal contribution to the quantum amplitude entails the creation of a virtual photon at one center and its subsequent annihilation at the other. It highlights the seemingly paradoxical nature of virtual photons that the calculation includes important contributions from virtual photons of all energies and all directions of propagation, not only those travelling in the same direction as the displacement of the acceptor from the energy donor. Most counterintuitively, account must also be taken of virtual photons propagating from the acceptor to the donor [15, 54].

The result reveals that the character of the energy transfer slowly changes between asymptotic forms, as the distance  $R$  between the donor and acceptor increases. In the *near-field* region, where  $R \ll \hbar c / \Delta E$ , the net quantum amplitude exhibits an inverse cubic dependence on distance, the rate thus falling off as  $R^{-6}$ . This is the result familiarly known as *Förster* (or *fluorescence*) *energy transfer* [55], often termed “radiationless” because there is no direct observation of light emission by the donor. But for distances  $R \gg \hbar c / \Delta E$ , the amplitude moves toward an  $R^{-1}$  asymptote, leading to a rate that exhibits an inverse square dependence on distance. The latter result exactly accords with the acceptor capturing a “real” photon—one that has been released in spontaneous emission by the donor. In fact, in not only these features, but every respect, it turns out that as distance increases there is a smooth transition from virtual to real photon behavior [56, 57]. This can be understood as another manifestation of the Uncertainty Principle, corresponding to the increasingly tight constraints on energy (and momentum) conservation as the coupling photons travel

for longer (and over larger distances). The result lends a fresh interpretation to the supposed distinction between real and virtual photons. By considering the life of a photon as it propagates from its source of creation toward the site of its annihilation at a detector, it becomes evident that every such photon in principle exhibits virtual traits. As has been remarked in the context of elementary particle physics, “In a sense every photon is virtual, being emitted and then sooner or later being absorbed” [58].

Such a perspective also lends new insights into the physical origin and form of the electromagnetic fields in the immediate vicinity of a photon emitter. For example, it emerges that the electric field produced by an electric dipole emitter has some properties that disappear on propagation beyond the near-field region. An example of such evanescent features is the fact that the electric field has longitudinal, as well as the conventional transverse, character with respect to the displacement of a detector from the source [15]. Related, and yet more striking, is the fact that there is a small but significant effective variation of wavelength close to the source [59]. Caution must be exercised in interpreting such near-field behavior as evidence of exotic properties of the virtual photon itself: in vacuum, the virtual photons always propagate with transverse electric fields and a constant wavelength—but measurable near-field properties will always be a result of summing over a range of virtual photons with different directions and wavelengths [60].

#### 1.5.4 Casimir Forces

A fascinating link between the seemingly disconnected topics of vacuum fluctuations and virtual photons is afforded by the phenomena known as Casimir forces which are observed to occur between electrically neutral, non-polar species separated by micro- or nano-scale distances. One particular form of this coupling, which arises between molecules, is commonly designated the Casimir–Polder interaction [61]. This is manifested as a modification to the more familiar London or “dispersion” potential, changing it from an inverse sixth power dependence on separation  $R$  to an inverse seventh power—an exotic feature that has been convincingly proven by experiment [62, 63]. Another manifestation of similar origins, manifested as a sharply distance-dependent attractive force between parallel conducting surfaces [64], represents a feature that has to be corrected for in the design of nanoelectromechanical systems [65–67]. Here, the result is a negative pressure that varies with the inverse fourth power of  $R$ . Surprisingly, it is possible to derive equivalent expressions for such forces either by considering the effect of matter on the vacuum radiation field, or by formulating the interaction potential in terms of virtual photon exchange [49, 68].

### 1.6 STRUCTURED LIGHT

#### 1.6.1 Complex Modes and Vector Beams

In recent years, the field of optics has undergone what can only be regarded as little short of a revolution, through the development of new structural forms of optical beam. Discovering a capacity to engineer beams with non-uniform, intricately crafted

wave-fronts, polarization behavior, and phase structures has stimulated the emergence of new theory and visions of wide-ranging new applications [69]. Although it might have been supposed that some attributes could only be supported in beams comprising a high density of photons, it transpires that most novel features are interpretable as reflecting the properties of individual photons. Indeed, there are experiments demonstrating that individual photons convey full information on the structure of complex beams [70, 71]. Recalling the intrinsic delocalization of photons makes it a little easier to comprehend how one photon might have the capacity to convey such properties. Some of the most important examples of wave-front structures are the complex optical modes associated with Laguerre–Gaussian, Airy, and Bessel beams [72, 73]; many similar photonic issues arise in connection with so-called polarized “vector” beams, as for example those with radial or azimuthal polarization [74].

### 1.6.2 Chirality and Angular Momentum

The most widely studied forms of structured beam are Laguerre–Gaussian modes, often known as *optical vortices*, which propagate with a helically twisted wave-front. The helical structure is characterized by an azimuthal quantum number,  $l$ , the integer number of twists in the wave-front per unit wavelength. Detailed analysis shows that any such mode with an occupation number  $n$  carries an axial angular momentum of  $n\hbar l$ , equivalent to  $\hbar l$  per photon. Thus,  $l$  acquires the status of an orbital angular momentum quantum number, for which a positive sign once again denotes left helicity and a negative sign, right. Generally, in order to convey orbital angular momentum, light must have a topological charge [75], and experiments demonstrate in a direct way that single photons carry the helical-mode information [76]. Surprisingly, it also transpires that not just integer but even fractional values of the orbital angular momentum per photon are attainable [77, 78].

The observation of optical beams conveying such quantized orbital angular momentum, independent of any circularity of polarization, is now understood as exhibiting a partitioning of a total angular momentum  $\mathbf{J}$  for the optical field. The quantum operator for  $\mathbf{J}$  not only comprises the spin term given by ⑤, as shown by Mandel and Wolf [34], but also includes an orbital term  $\mathbf{L}$  ⑨. It is encouraging to observe that issues of gauge dependence in the standard formulation, deployed to effect this separation of spin and orbital angular momentum components, can in fact be fully circumvented in a photon-based representation [79].

The association between helical wave-front structure and orbital angular momentum correctly suggests that both are involved with intrinsic measures of electromagnetic chirality. First addressed in work by Lipkin, a variety of such optical chirality measures have been discovered and all of them shown to be connected with the conservation of polarization in the electromagnetic field [80]. Foremost amongst these measures is an “optical chirality density” ⑩. In a quantum optical analysis, it has recently been proven that an essentially infinite hierarchy of such helicity measures [81] reduces to a common physically meaningful quantity: all are linearly dependent on the difference between the number of photons with opposite polarization circularity [25].

### 1.6.3 Multipole Emission

There exists much confusion in the literature over the issue of whether a photon conveys any kind of imprint of the symmetry character for the electronic decay transition in which it was originally released. For example, there is a prevalent notion that a photon emitted in an electric dipole transition might have an undefined yet measurably different character from the one emitted in an electric quadrupole transition, even given identical wavelengths and polarizations. This has given rise to the cavalier use of terms such as *dipole* or *quadrupole* photon [13, 14]. Similar conjectures also give rise to the terms *electric* photon or *magnetic* photon [9, 10]. The latter are more obviously misnomers; Maxwell's electromagnetism equations ensure that it is not possible for light to have one kind of field without the other. The origin of all such descriptors is mostly attributable to the theory of atomic transitions, in which the spherical symmetry of atoms generally leads to mutually exclusive selection rules for electric dipole (E1) and electric quadrupole (E2) transitions. Although similar kinds of mutual exclusion occur in any centrosymmetric systems, most molecules exhibit transitions that can be both E1 and E2 allowed, with no distinction between the resulting final states. However, there are much deeper and more general factors that undermine the notion of photons with multipolar character.

The decay of an atom or molecule by a particular multipolar transition can be detected, through absorption of the released photon, in an excitation process of a potentially different multipolar character [82–84]. This is a direct physical interpretation of a finite quantum amplitude, despite a non-correspondence in multipoles. In fact, retracting a detector from the immediate vicinity of the source produces a decreasing angular uncertainty in photon propagation direction, consistent with an angular quantum uncertainty principle, [85] and thus reflected in an increasing range of integer values for the measured angular momentum. Indeed, the emission of a photon in an electric quadrupole decay will generally produce a larger signal for dipole detection than for quadrupole detection. The corollary that follows, on considering time-reversal arguments, is that it is no more meaningful to designate such a photon as a “quadrupole” photon than a “dipole” photon: both are equally redundant descriptors. Of course there are differences according to the multipolar order of each process, emission, and detection, in terms of spatial distribution and not least the intensity (signified by the detection rate); the theory reveals the detail. But the inference of a particular multipolarity in any particular detected photon has no basis.

### 1.6.4 Information in a Photon

In the field of spin optics, standard methods provide for two independent degrees of freedom to be communicated by photon polarization. Circular states of opposing handedness are the most obvious candidates, though any two states corresponding to diametrically opposite positions on the Poincaré sphere would provide a suitable basis. However, complex light with structured wave-fronts or vector polarization offer additional degrees of freedom, enabling individual photons to convey a far greater

information content than was previously considered possible [86]. Nonetheless, one must entertain reservations about the extent to which any individual photon can convey structural information. The truth that there is an infinite range of mathematically orthogonal Laguerre–Gaussian modes, for example, has been taken by some to suggest that in principle each photon might convey the information content of an entire image. Such notions have to be tempered by an appreciation of the practical requirement for a detector that is already preconfigured with information on the sought image.

There are many more realistic propositions for methods that could deploy individual photons to encode information on beam structure—particularly topological charge. It has been shown that the necessary modal information can be encoded in single-photon states and resolved by beam tomography [87]. Such studies have stimulated the conception of numerous schemes for quantum communication and data handling applications, although there are daunting practical issues to be taken into account; a useful survey has been provided by Franke-Arnold and Jeffers [88]. One attractive possibility is to selectively divert a mixed-mode beam into components with different orbital angular momentum content; a variety of innovative sorting and detection schemes have been reported [34–36]. One frequently overlooked issue is the outworking of the previously mentioned uncertainty relation that links angle and orbital angular momentum, and which is associated with a non-zero commutator for the two corresponding operators [85, 89]. All schemes for quantum information processing based on photon orbital angular momentum [90] are ultimately limited by this feature, which has been convincingly demonstrated by photon correlations in down-conversion [91]. It is surprising that this principle, particularly relevant to low-number states, has seemingly received very little consideration in the literature to date.

## 1.7 PHOTON NUMBER FLUCTUATIONS AND PHASE

As noted earlier, it should not be inferred that all of the properties of light beams are, like intensity and other extensive quantities, equivalent to the summative effect of individual photons; an obvious exception is the conventional linewidth. Nonetheless, there are numerous other beam attributes with specific photonic measures and interpretations, such as phase, degrees of coherence, and autocorrelation functions.

### 1.7.1 Coherence and Fluctuations

For a variety of reasons, every beam of light exhibits fluctuations of intensity. It is clear enough that a constant beam would require an unattainable degree of control over the temporal regularity of individual photon emission events in its source. However, the nature of the intensity fluctuations reflects important statistical features of the source. For example, a perfect thermal source releases photons with a chaotic phase, whose number distribution (directly corresponding to an intensity distribution) accordingly follows Bose–Einstein statistics. Conversely, a perfectly coherent source delivers photons with a Poisson number distribution [92].

It also has to be recognized that no source has the capacity to deliver photons that all have precisely the same wavelength—not least because this would fall foul of quantum uncertainty in the energy released through each photon emission event. In consequence there is a coherence length, essentially determined by the inverse of the beam linewidth expressed in wavenumber terms [93]; this represents a maximum distance over which the electromagnetic field oscillations of the copropagating photons are meaningfully held in phase. At any instant in time, different portions of the beam will therefore experience different degrees of constructive and destructive interference, correlating with the observed intensity fluctuations. This is indeed the principle that is exploited to achieve laser mode locking, a technique that is widely used to produce ultrashort pulses of light [94].

Under the high levels of intensity produced by ultrashort pulsed lasers, where multiphoton absorption and other nonlinear optical process can occur, interactions with matter generally depend not only on the mean irradiance but also on other higher moments of the intensity distribution. For example, two-photon absorption processes depend on the degree of second-order coherence,  $g^{(2)}$  [18]. To understand the quantum basis for such features, we have to go beyond a simple number state representation.

### 1.7.2 Phase

Whilst it is possible to ascribe fluctuations in beam intensity to essentially stochastic interference between modes of different wavelength and frequency, there are other, more fundamental aspects of phase that arise at the quantum level. Each photon carries a phase  $\exp(i\mathbf{k} \cdot \mathbf{r} - \omega t)$ , referring the space coordinate  $\mathbf{r}$  and time  $t$  to the position and time for photon creation (or annihilation, if the displacements in space and time are taken with a negative sign). This “absolute” phase, which is conveyed by the electromagnetic field operators in the Heisenberg representation [92], nonetheless has little practical significance unless optical interference is engaged in some observable. When two or more photons are present in a system, one can consider issues of relative phase between them—yet only if the individual number of photons in each relevant mode is not completely determined: see p. 495 in Reference 34. This constraint arises for an important fundamental reason: the quantum operators for photon number and phase do not commute. The mathematical formulation of a quantum phase operator is itself fraught with difficulties [95]. Partly, but not wholly, this is due to the physical equivalence of waveforms shifted by an integer number of wavelengths; this is a subject of active research [96].

Loudon [18] gives a nice picture of the implications: if the exact number of photons in a given optical mode is precisely known, then one can extract precisely no phase information. Conversely, if one entertains quantum modes with an exact phase, then their photon number occupancy becomes infinitely uncertain. There are, however, quantum optical states that lie between the extremes represented by number and phase states. An important example is the “minimum uncertainty” state known as a coherent state [92]. Generally considered closest in form to a classical wave, and taken as a good representation of a stable laser beam, it leads to a Poisson distribution

of photon numbers. Although it is perfectly straightforward to formulate theory for processes such as photon absorption, using a coherent state representation for the light, there are curious implications for the photon concept. For example, the mean number of photons in the beam after photon absorption appears to be unchanged. On the other hand, observed quantum interferences between different processes, such as between single- and two-photon absorption in molecules [97], or three- and five-photon ionization of atoms [98], cannot be represented by number states precisely because the final states for each alternative possibility differ.

## 1.8 THE REALITY OF PHOTONICS

In the specific technical sense encountered earlier, it becomes apparent that no photon can ever be regarded as entirely “real.” But, in the broader everyday sense of reality, one can also pose the more philosophical question of whether the photon is real. Perhaps surprisingly, not all exponents of quantum optics or quantum electrodynamics are willing to be drawn on what such photon reality means in the case of optical effects. Power (author of a classic textbook [99] on QED), for example, held that the electromagnetic fields should ultimately be considered closest to irreducible reality. Yet whether it is fields or photons in terms of which we elect to describe phenomena, neither can represent what is actually measured. The surest ground is where theory can explain or predict actual observations, based on given conditions. We need not venture into the quagmire territory of quantum measurement theory [100]; it suffices that all of the observations filling the pages of these volumes, and the applications on which they are based, are fully explicable in photonic terms. The modern concept of the photon, with multiple interpretations and widely differing subsidiary connotations, supports an astonishingly rich and diverse range of phenomena. A strong case can be made that in the modern world, Photonics has become more real than the photon.

## ACKNOWLEDGMENTS

I gratefully acknowledge insights I have gained from numerous friends, co-workers, and correspondents, over many years. From my research group I thank David Bradshaw, Matthew Coles, and Mathew Williams for a meticulous reading of this chapter; I also especially thank Mohamed Babiker and Rodney Loudon for a number of insightful comments. Research in quantum electrodynamics at the University of East Anglia is funded by the Leverhulme Trust and the U.K. Engineering and Physical Sciences Research Council.

## REFERENCES

- [1] G. N. Lewis, “The conservation of photons,” *Nature (Lond.)* **118**, 874–875 (1926).
- [2] A. Einstein, “Über einen die Erzeugung und Verwandlung des Lichtes betreffenden heuristischen Gesichtspunkt [On a heuristic viewpoint concerning the production and transformation of light],” *Ann. Phys.* **17**, 132–148 (1905).

- [3] P. R. Berman and V. S. Malinovsky, *Principles of Laser Spectroscopy and Quantum Optics* (Princeton University Press, Princeton, NJ, 2011), p. 2.
- [4] T. H. Maiman, “Stimulated optical radiation in ruby,” *Nature* **187**(4736), 493–494 (1960).
- [5] R. Kidd, J. Ardini, and A. Anton, “Evolution of the modern photon,” *Am. J. Phys.* **57**, 27–35 (1989).
- [6] M. Ohtsu, “Nanophotonics: dressed photon technology for qualitatively innovative optical devices, fabrication, and systems,” *Progr. Nanophoton.* **1**, 1–58 (2011).
- [7] K. Yoo and R. R. Alfano, “Time-resolved coherent and incoherent components of forward light scattering in random media,” *Opt. Lett.* **15**, 320–322 (1990).
- [8] S. Farsiu, J. Christofferson, B. Eriksson, P. Milanfar, B. Friedlander, A. Shakouri, and R. Nowak, “Statistical detection and imaging of objects hidden in turbid media using ballistic photons,” *Appl. Opt.* **46**, 5805–5822 (2007).
- [9] Y. Koma, M. Koma, E. M. Ilgenfritz, T. Suzuki, and M. I. Polikarpov, “Duality of gauge field singularities and the structure of the flux tube in Abelian-projected SU(2) gauge theory and the dual Abelian Higgs model,” *Phys. Rev. D* **68**, 094018 (2003).
- [10] R. S. Lakes, “Experimental test of magnetic photons,” *Phys. Lett. A* **329**, 298–300 (2004).
- [11] W. Tittel, J. Brendel, H. Zbinden, and N. Gisin, “Quantum cryptography using entangled photons in energy-time Bell states,” *Phys. Rev. Lett.* **84**, 4737–4740 (2000).
- [12] C. I. Osorio, N. Bruno, N. Sangouard, H. Zbinden, N. Gisin, and R. T. Thew, “Heralded photon amplification for quantum communication,” *Phys. Rev. A* **86**, 023815 (2012).
- [13] V. B. Berestetskii, E. M. Lifshitz, and L. P. Pitaevskii, *Quantum Electrodynamics*, 2nd ed. (Butterworth, London, 1982), pp. 15–16.
- [14] A. M. Ellis, “Spectroscopic selection rules: the role of photon states,” *J. Chem. Ed.* **76**, 1291–1294 (1999).
- [15] D. L. Andrews and D. S. Bradshaw, “Virtual photons, dipole fields and energy transfer: a quantum electrodynamical approach,” *Eur. J. Phys.* **25**, 845–858 (2004).
- [16] C. M. Wilson, G. Johansson, A. Pourkabirian, M. Simoen, J. R. Johansson, T. Duty, F. Nori, and P. Delsing, “Observation of the dynamical Casimir effect in a superconducting circuit,” *Nature (Lond.)* **479**, 376–379 (2011).
- [17] A. V. Burlakov, M. V. Chekhova, O. A. Karabutova, D. N. Klyshko, and S. P. Kulik, “Polarization state of a biphoton: quantum ternary logic,” *Phys. Rev. A* **60**, 4209–4212 (1999).
- [18] R. Loudon, *The Quantum Theory of Light*, 3rd ed. (Oxford University Press, Oxford, 2000).
- [19] D. S. Roychoudhuri, A. F. Kracklauer, and K. Creath, *The Nature of Light. What Is a Photon?* (CRC Press, Boca Raton, FL, 2008).
- [20] H. Poincaré, *Théorie Mathématique de la Lumière [Mathematical Theory of Light]* (Gauthiers-Villars, Paris, 1892), Vol. 2, Chap. 12.
- [21] D. L. Andrews and L. C. Dávila Romero, “A back-to-front derivation: the equal spacing of quantum levels is a proof of simple harmonic oscillator physics,” *Eur. J. Phys.* **30**, 1371–1380 (2009).
- [22] H. J. Carmichael, *Statistical Methods in Quantum Optics 1* (Springer, Berlin, 1999), Chap. 3.

- [23] D. L. Andrews, “The irreducible photon,” *Proc. SPIE* **7421**, 742109 (2009).
- [24] E. A. Power and T. Thirunamachandran, “Quantum electrodynamics with non-relativistic sources. 4. Poynting vector, energy densities, and other quadratic operators of the electromagnetic field,” *Phys. Rev. A* **45**, 54–63 (1992).
- [25] M. M. Coles and D. L. Andrews, “Photonic measures of helicity: optical vortices and circularly polarized reflection,” *Opt. Lett.* **38**, 869–871 (2013).
- [26] A. Einstein, “Ist die Trägheit eines Körpers von seinem Energieinhalt abhängig? [Is the inertia of a body dependent on its energy content?]”, *Ann. Phys.* **18**, 639–641 (1905).
- [27] U. Fano, “Atomic theory of electromagnetic interactions in dense materials,” *Phys. Rev.* **103**, 1202–1218 (1956).
- [28] R. Zhang, S. R. Garner, and L. V. Hau, “Creation of long-term coherent optical memory via controlled nonlinear interactions in Bose-Einstein condensates,” *Phys. Rev. Lett.* **103**, 233602 (2009).
- [29] R. Y. Chiao and P. W. Milonni, “Fast light, slow light,” *Optics & Photonics News*, June 2002, pp. 26–30.
- [30] S. M. Barnett and R. Loudon, “The enigma of optical momentum in a medium,” *Phil. Trans. R. Soc.* **368**, 927–939 (2010).
- [31] M. E. Zevallos, S. K. Gayen, B. B. Das, M. Alrubaiee, and R. R. Alfano, “Picosecond electronic time-gated imaging of bones in tissues,” *IEEE J. Sel. Top. Quant. Electron.* **5**, 916–922 (1999).
- [32] M. Born, *The Born-Einstein Letters* (Walker and Co., New York, 1971).
- [33] M. Ligare and R. Oliveri, “The calculated photon: visualization of a quantum field,” *Am. J. Phys.* **70**, 58–66 (2002).
- [34] L. Mandel and E. Wolf, *Optical Coherence and Quantum Optics* (University Press, Cambridge, 1995).
- [35] P. Grangier, J. A. Levenson, and J.-P. Poizat, “Quantum non-demolition measurements in optics,” *Nature* **396**, 537–542 (1998).
- [36] S. Gleyzes, S. Kuhr, C. Guerlin, J. Bernu, S. Deleglise, U. B. Hoff, M. Brune, J. M. Raimond, and S. Haroche, “Quantum jumps of light recording the birth and death of a photon in a cavity,” *Nature* **446**, 297–300 (2007).
- [37] N. Imoto, H. A. Haus, and Y. Yamamoto, “Quantum nondemolition measurement of the photon number via the optical Kerr effect,” *Phys. Rev. A* **32**, 2287–2292 (1985).
- [38] B. R. Johnson, M. D. Reed, A. A. Houck, D. I. Schuster, L. S. Bishop, E. Ginossar, J. M. Gambetta, L. DiCarlo, L. Frunzio, S. M. Girvin, et.al., “Quantum non-demolition detection of single microwave photons in a circuit,” *Nat. Phys.* **6**, 663–667 (2010).
- [39] D. Englund, A. Majumdar, M. Bajcsy, A. Faraon, P. Petroff, and J. Vučković, “Ultrafast photon-photon interaction in a strongly coupled quantum dot-cavity system,” *Phys. Rev. Lett.* **108**, 093604 (2012).
- [40] B. Fan, A. F. Kockum, J. Combes, G. Johansson, I. Hoi, C. M. Wilson, P. Delsing, G. J. Milburn, and T. M. Stace, “Breakdown of the cross-Kerr scheme for photon counting,” *Phys. Rev. Lett.* **110**, 053601 (2013).
- [41] Y. Shih, “Entangled biphoton source—property and preparation,” *Rep. Prog. Phys.* **66**, 1009–1044 (2003).
- [42] J. Fan, M. D. Eisaman, and A. Migdall, “Bright phase-stable broadband fiber-based source of polarization-entangled photon pairs,” *Phys. Rev. A* **76**, 043836 (2007).

- [43] R. Horodecki, P. Horodecki, M. Horodecki, and K. Horodecki, “Quantum entanglement,” *Rev. Mod. Phys.* **81**, 865–942 (2009).
- [44] C. K. Hong, Z. Y. Ou, and L. Mandel, “Measurement of subpicosecond time intervals between two photons by interference,” *Phys. Rev. Lett.* **59**, 2044–2046 (1987).
- [45] C. C. Gerry and P. L. Knight, *Introductory Quantum Optics* (Cambridge University Press, Cambridge, 2005).
- [46] I. Bialynicki-Birula, “Photon wave function,” *Progr. Opt.* **36**, 245–294 (1996).
- [47] F. Tamburini and D. Vicino, “Photon wave function: a covariant formulation and equivalence to QED,” *Phys. Rev. A* **78**, 052116 (2008).
- [48] P. W. Milonni, *The Quantum Vacuum: An Introduction to Quantum Electrodynamics* (Academic Press, San Diego, CA, 1994).
- [49] D. P. Craig and T. Thirunamachandran, *Molecular Quantum Electrodynamics* (Dover, New York, 1998).
- [50] G. Gabrielse, D. Hanneke, T. Kinoshita, M. Nio, and B. Odom, “New determination of the fine structure constant from the electron  $g$  value and QED,” *Phys. Rev. Lett.* **97**, 030802 (2006).
- [51] R. P. Feynman, *QED: The Strange Theory of Light and Matter* (Princeton University Press, Princeton, NJ, 1985), p. 89.
- [52] G. Compagno, R. Passante, and F. Persico, “The role of the cloud of virtual photons in the shift of the ground state of a hydrogen atom,” *Phys. Lett. A* **98**, 253–255 (1983).
- [53] D. L. Andrews and A. A. Demidov (ed.) *Resonance Energy Transfer* (John Wiley & Sons, Chichester, 1999).
- [54] D. L. Andrews, C. Curutchet, and G. D. Scholes, “Resonance energy transfer: beyond the limits,” *Laser Photon. Rev.* **5**, 114–123 (2011).
- [55] T. Förster, “Energiewanderung und Fluoreszenz [Energy migration and fluorescence],” *Naturwissenschaften* **33**, 166–175 (1946).
- [56] D. L. Andrews, “A unified theory of radiative and radiationless molecular energy transfer,” *Chem. Phys.* **135**, 195–201 (1989).
- [57] G. J. Daniels, R. D. Jenkins, D. S. Bradshaw, and D. L. Andrews, “Resonance energy transfer: the unified theory revisited,” *J. Chem. Phys.* **119**, 2264–2274 (2003).
- [58] F. Halzen and A. D. Martin, *Quarks and Leptons* (John Wiley & Sons, New York, 1984), p. 140.
- [59] E. M. Rice, D. S. Bradshaw, K. Saadi, and D. L. Andrews, “Identifying the development in phase and amplitude of dipole and multipole radiation,” *Eur. J. Phys.* **33**, 345–358 (2012).
- [60] R. P. Feynman, “Mathematical formulation of the quantum theory of electromagnetic interaction,” *Phys. Rev.* **80**, 440–457 (1950).
- [61] H. B. G. Casimir and D. Polder, “The influence of retardation of the London-van der Waals forces,” *Phys. Rev.* **73**, 360–372 (1948).
- [62] C. I. Sukenik, M. G. Boshier, D. Cho, V. Sandoghdar, and E. A. Hinds, “Measurement of the Casimir-Polder force,” *Phys. Rev. Lett.* **70**, 560–563 (1993).
- [63] H. Bender, Ph. W. Courteille, C. Marzok, C. Zimmerman, and S. Slama, “Direct measurement of intermediate-range Casimir-Polder potentials,” *Phys. Rev. Lett.* **104**, 083201 (2010).

- [64] H. B. G. Casimir, “On the attraction between two perfectly conducting plates,” *Proc. Kom. Ned. Akad. Wetensch. B* **51**, 793–796 (1948).
- [65] H. B. Chan, V. A. Aksyuk, R. N. Kleiman, P. J. Bishop, and F. Capasso, “Quantum mechanical actuation of microelectromechanical systems by the Casimir force,” *Science* **291**, 1941–1944 (2001).
- [66] G. J. Maclay, H. Fearn, and P. W. Milonni, “Of some theoretical significance: implications of Casimir effects,” *Eur. J. Phys.* **22**, 463–469 (2001).
- [67] C. Genet, A. Lambrecht, and S. Reynaud, “The Casimir effect in the nanoworld,” *Eur. Phys. J. Spec. Top.* **160**, 183–193 (2008).
- [68] E. A. Power, “Casimir-Polder potential from first principles,” *Eur. J. Phys.* **22**, 453–461 (2001).
- [69] D. L. Andrews (ed.) *Structured Light and Its Applications: An Introduction to Phase-Structured Beams and Nanoscale Optical Forces* (Academic Press, Burlington, MA, 2008).
- [70] J. Leach, M. J. Padgett, S. M. Barnett, S. Franke-Arnold, and J. Courtial, “Measuring the orbital angular momentum of a single photon,” *Phys. Rev. Lett.* **88**, 257901 (2002).
- [71] E. J. Galvez, L. E. Coyle, E. Johnson, and B. J. Reschovsky, “Interferometric measurement of the helical mode of a single photon,” *New J. Phys.* **13**, 053017 (2011).
- [72] G. A. Siviloglou, J. Broky, A. Dogariu, and D. N. Christodoulides, “Observation of accelerating Airy beams,” *Phys. Rev. Lett.* **99**, 23–26 (2007).
- [73] K. Dholakia and W. M. Lee, “Optical trapping takes shape: the use of structured light fields,” *Adv. At. Mol. Opt. Phys.* **56**, 261–337 (2008).
- [74] E. J. Galvez, “Vector beams in free space,” in *The Angular Momentum of Light*, edited by D. L. Andrews and M. Babiker (Cambridge University Press, Cambridge, 2013), Chap. 3.
- [75] M. S. Soskin, V. N. Gorshkov, M. V. Vasnetsov, J. T. Malos, and N. R. Heckenberg, “Topological charge and angular momentum of light carrying optical vortices,” *Phys. Rev. A* **56**, 4046–4057 (1997).
- [76] E. J. Galvez, L. E. Coyle, E. Johnson, and B. J. Reschovsky, “Interferometric measurement of the helical mode of a single photon,” *New J. Phys.* **13**, 053017 (2011).
- [77] J. Leach, E. Yao, and M. J. Padgett, “Observation of the vortex structure of a non-integer vortex beam,” *New J. Phys.* **6**, 71–78 (2004).
- [78] J. B. Gotte, S. Franke-Arnold, and R. Zambrini, “Quantum formulation of fractional orbital angular momentum,” *J. Mod. Opt.* **54**, 1723–1738 (2007).
- [79] I. Bialynicki-Birula and Z. Bialynicka-Birula, “Canonical separation of angular momentum of light into its orbital and spin parts,” *J. Opt.* **13**, 064014 (2011).
- [80] D. M. Lipkin, “Existence of a new conservation law in electromagnetic theory,” *J. Math. Phys.* **5**, 696–700 (1964).
- [81] R. P. Cameron, S. M. Barnett, and A. M. Yao, “Optical helicity, optical spin and related quantities in electromagnetic theory,” *New J. Phys.* **14**, 53050 (2012).
- [82] G. D. Scholes and D. L. Andrews, “Damping and higher multipole effects in the quantum electrodynamical model for electronic energy transfer in the condensed phase,” *J. Chem. Phys.* **107**, 5374–5384 (1997).
- [83] A. Salam, “A general formula for the rate of resonant transfer of energy between two electric multipole moments of arbitrary order using molecular quantum electrodynamics,” *J. Chem. Phys.* **122**, 044112 (2005).

- [84] D. L. Andrews, “Optical angular momentum: multipole transitions and photonics,” *Phys. Rev. A* **81**, 033825 (2010).
- [85] J. B. Götte and S. M. Barnett, “Quantum formulation of angle and orbital angular momentum,” in *The Angular Momentum of Light*, edited by D. L. Andrews and M. Babiker (Cambridge University Press, Cambridge, 2012), pp. 135–161.
- [86] J. C. Garcia-Escartin and P. Chamorro-Posada, “Quantum multiplexing with the orbital angular momentum of light,” *Phys. Rev. A* **78**, 062320 (2008).
- [87] J. T. Barreiro, T.-C. Wei, and P. G. Kwiat, “Remote preparation of single-photon ‘hybrid’ entangled and vector-polarization states,” *Phys. Rev. Lett.* **105**, 030407 (2010).
- [88] S. Franke-Arnold and J. Jeffers, “Orbital angular momentum in quantum communication and information,” in *Structured Light and Its Applications*, edited by D. L. Andrews (Academic Press, Burlington, MA, 2008), pp. 271–293.
- [89] D. T. Pegg, J. A. Vaccaro, and S. M. Barnett, “Quantum-optical phase and canonical conjugation,” *J. Mod. Opt.* **37**, 1703–1710 (1990).
- [90] G. Gibson, J. Courtial, M. J. Padgett, M. Vasnetsov, V. Pas’ko, V. S. M. Barnett, and S. Franke-Arnold, “Free-space information transfer using light beams carrying orbital angular momentum,” *Opt. Exp.* **12**, 5448–5456 (2004).
- [91] J. Leach, B. Jack, J. Romero, A. K. Jha, A. M. Yao, S. Franke-Arnold, D. G. Ireland, R. W. Boyd, S. M. Barnett, and M. J. Padgett, “Quantum correlations in optical angle-orbital angular momentum variables,” *Science* **329**, 662–665 (2010).
- [92] W. H. Louisell, *Quantum Statistical Properties of Radiation* (John Wiley & Sons, New York, 1973).
- [93] B. E. A. Saleh and M. C. Teich, *Fundamentals of Photonics* (John Wiley & Sons, New York, 1991).
- [94] D. L. Andrews, *Lasers in Chemistry*, 3rd ed. (Springer, Berlin, 1997).
- [95] S. M. Barnett and D. T. Pegg, “Phase in quantum optics,” *J. Phys. A: Math. Gen.* **19**, 3849–3862 (1986).
- [96] S. M. Barnett and J. A. Vaccaro (eds), *The Quantum Phase Operator: A Review* (CRC Press, Boca Raton, FL, 2007).
- [97] S. Lin, I. D. Hands, D. L. Andrews, and S. R. Meech, “Optically induced second harmonic generation by six-wave mixing: a novel probe of solute orientational dynamics,” *J. Phys. Chem. A* **103**, 3830–3836 (1999).
- [98] C. Chen, Y.-Y. Yin, and D. S. Elliott, “Interference between optical transitions,” *Phys. Rev. Lett.* **64**, 507–510 (1990).
- [99] E. A. Power, *Introductory Quantum Electrodynamics* (Longmans, London, 1964).
- [100] M. Namiki, S. Pascazio, and H. Nakazato, *Decoherence and Quantum Measurements* (World Scientific, Singapore, 1997).



---

# 2

---

## COHERENCE AND STATISTICAL OPTICS

MAYUKH LAHIRI

*IQOQI, University of Vienna, Vienna, Austria*

### 2.1 INTRODUCTION

In traditional optics, an electric field is usually represented by a deterministic function. Although a deterministic model is useful for the analysis of many problems, it cannot be used to explain certain physical phenomena which arise from the random fluctuations present in optical fields. Optical coherence and optical polarization are two examples of such phenomena. The theory of statistical optics has been being developed to explain and analyze these types of properties of light.

The theory of optical coherence has its root in the Young's interference experiment which shows that light emerging from two pinholes may interfere and produce a fringe pattern [1]. Coherence is often regarded as the ability of light to interfere. Many years ago, Zernike introduced the concept of degree of coherence in terms of the visibility of fringes produced in a Young's interference experiment [2]. On the other hand, studies on polarization properties of light began with Bartholinus' observation of double refraction in calcite crystals. On an apparent view it may seem that coherence and polarization properties of light are unrelated. However, works of many distinguished scientists have revealed that the two properties are intimately related and that both can be viewed as manifestation of random fluctuations of optical fields. Detailed descriptions of the history of the subject can be found in References 3–7.

In this chapter, we discuss the key foundations of the classical theory of optical coherence and polarization. We also discuss some recent developments in this subject

---

*Photonics: Scientific Foundations, Technology and Applications, Volume I*, First Edition.

Edited by David L. Andrews.

© 2015 John Wiley & Sons, Inc. Published 2015 by John Wiley & Sons, Inc.

and provide important references for further reading of enthusiastic readers. In the end, we briefly discuss the foundations of the quantum theory of optical coherence.

## 2.2 CLASSICAL THEORY OF OPTICAL COHERENCE IN THE SPACE-TIME DOMAIN

Light being an electromagnetic wave is always associated with electric and magnetic fields. The effects of the magnetic field can be neglected for the purpose of studying coherence properties of light. The electric field vector  $\mathcal{E}(\mathbf{r}; t)$  is a real quantity. Let us express it in the form of a Fourier integral

$$\mathcal{E}(\mathbf{r}; t) = \int_{-\infty}^{\infty} \tilde{\mathcal{E}}(\mathbf{r}; \omega) e^{-i\omega t} d\omega = \int_0^{\infty} \tilde{\mathcal{E}}(\mathbf{r}; \omega) e^{-i\omega t} d\omega + \int_0^{\infty} \tilde{\mathcal{E}}(\mathbf{r}; -\omega) e^{i\omega t} d\omega, \quad (2.1)$$

where  $\omega$  denotes the frequency. Since  $\mathcal{E}(\mathbf{r}; t)$  is real, one must have  $\tilde{\mathcal{E}}(\mathbf{r}; \omega) = \tilde{\mathcal{E}}^*(\mathbf{r}; -\omega)$ , where the asterisk denotes complex conjugate. The result implies that the negative frequency part  $\tilde{\mathcal{E}}(\mathbf{r}; -\omega)$  does not contain any information that is not already contained in the positive frequency part  $\tilde{\mathcal{E}}(\mathbf{r}; \omega)$ . Because of this, one may omit the negative frequency part and can replace  $\mathcal{E}(\mathbf{r}; t)$  by the complex quantity

$$\mathbf{E}(\mathbf{r}; t) = \int_0^{\infty} \tilde{\mathcal{E}}(\mathbf{r}; \omega) e^{-i\omega t} d\omega. \quad (2.2)$$

$\mathbf{E}(\mathbf{r}; t)$  is called the complex analytic signal associated with the real electric field vector [8, Section 3.1]. The concept of complex analytic signal was originally introduced by Gabor [9].  $\mathbf{E}(\mathbf{r}; t)$  is also called the complex electric field vector.

As already mentioned, a deterministic model of optical fields is not sufficient for analyzing coherence and polarization properties of light. A systematic description of statistical properties of light requires to assume that the complex electric field vector  $\mathbf{E}(\mathbf{r}; t)$  is random in nature. Every component of such a field can be represented by statistical ensembles  $\{E_i(\mathbf{r}; t)\}$ , where  $i = x, y, z$  represents three arbitrary mutually orthogonal directions in space. The simplest or lowest order<sup>1</sup> correlation properties of light in the space-time domain are characterized by a  $3 \times 3$  correlation matrix  $\tilde{\Gamma}(\mathbf{r}_1, \mathbf{r}_2; t_1, t_2)$ , whose elements are given by

$$\Gamma_{ij}(\mathbf{r}_1, \mathbf{r}_2; t_1, t_2) \equiv \langle E_i^*(\mathbf{r}_1; t_1) E_j(\mathbf{r}_2; t_2) \rangle, \quad (i = x, y, z; j = x, y, z), \quad (2.3)$$

where the angular brackets denote ensemble average. The matrix  $\tilde{\Gamma}(\mathbf{r}_1, \mathbf{r}_2; t_1, t_2)$  is often referred to as the mutual coherence matrix (to be abbreviated by MC matrix). We assume that the random process is statistically stationary, at least, in the wide

---

<sup>1</sup>Lowest order correlation properties are often called the second-order ones in the classical theory and the first-order ones in the quantum theory.

sense [8, Section 2.2]. This means that elements  $\Gamma_{ij}(\mathbf{r}_1, \mathbf{r}_2; t_1, t_2)$  of the MC matrix depend on  $t_1$  and  $t_2$  only through the difference  $\tau = t_2 - t_1$ , that is,

$$\tilde{\Gamma}(\mathbf{r}_1, \mathbf{r}_2; t_1, t_2) \equiv \tilde{\Gamma}(\mathbf{r}_1, \mathbf{r}_2; \tau) = [\langle E_i^*(\mathbf{r}_1; t) E_j(\mathbf{r}_2; t + \tau) \rangle]. \quad (2.4)$$

Clearly, for stationary fields choice of the origin of time is not important, as one would expect.

For statistically stationary fields one needs to interpret the transition from  $\mathcal{E}(\mathbf{r}; t)$  to its analytic signal  $\mathbf{E}(\mathbf{r}; t)$  with more caution. It is because the sample functions of a stationary random processes are not square integrable. However, precise justification of an analytic signal can still be given in the framework of a generalized function theory ([10]; see also [8, Section 3.1.3]), which is outside the scope of this chapter.

### 2.2.1 Degree of Coherence in the Space-Time Domain

Coherence refers to the ability of light to interfere. Simplest manifestation of coherence properties of light is the visibility of fringes produced in a Young's interference experiment (Fig. 2.1). In 1938, Zernike [2] defined the degree of coherence of a wave field by the maximum value of visibility in the interference pattern produced by it under the “best circumstances”<sup>2</sup>. Zernike did not take into account the time difference between the fields arriving from the pinholes. Consequently, his theory could not address some interesting aspects of the subject. This theory was later generalized by Wolf [11], as he introduced the time difference into the analysis. In this section we discuss the Zernike–Wolf formulation of the theory [5, Chap. 10; 8, Chap. 4; 12, Chap. 3].

For the sake of simplicity, we first address the subject by the use of a scalar theory. We assume that each component of the electric field vector behaves in the same way, so that it is sufficient to consider only one of them. This assumption holds for the

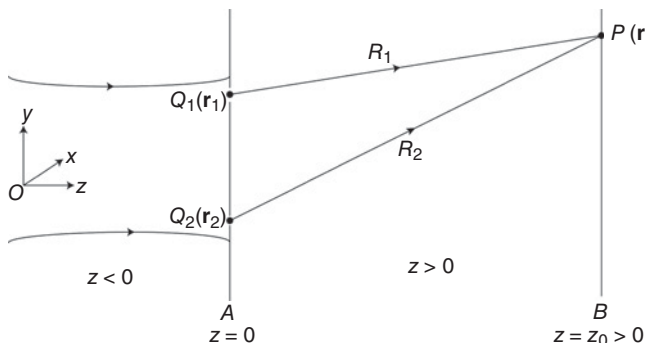


**FIGURE 2.1** Geometry of a Young's interference experiment.

<sup>2</sup>By the term “best circumstances” Zernike meant that the intensities of the two interfering beams were equal and that only small path difference was introduced between them.

light generated by many optical sources such as the extended thermal sources, which radiate unpolarized light. A randomly fluctuating complex scalar field at a point  $P(\mathbf{r})$ , at a time  $t$ , can be represented by a statistical ensemble  $\{V(\mathbf{r}; t)\}$  of realizations. The MC matrix, defined by Eq. (2.4), then reduces to a correlation function given by

$$\Gamma(\mathbf{r}_1, \mathbf{r}_2; \tau) \equiv \langle V^*(\mathbf{r}_1; t)V(\mathbf{r}_2; t + \tau) \rangle. \quad (2.5)$$

The correlation function,  $\Gamma(\mathbf{r}_1, \mathbf{r}_2; \tau)$ , is known as the *mutual coherence function* (MC function).

The average intensity  $I(\mathbf{r})$  of light at a point  $P(\mathbf{r})$ , apart from a constant factor depending on the choice of units, is given by  $\langle |V(\mathbf{r}; t)|^2 \rangle$ . From Eq. (2.5) it follows that

$$I(\mathbf{r}) \equiv \langle |V(\mathbf{r}; t)|^2 \rangle = \Gamma(\mathbf{r}, \mathbf{r}; 0). \quad (2.6)$$

Clearly, for statistically stationary light the average intensity does not depend on time.

Let us now consider a Young's interference experiment (Fig. 2.1). Suppose that a light beam is incident from the half-space  $z < 0$  onto an opaque screen  $A$ , placed in the plane  $z = 0$  containing two pinholes  $Q_1(\mathbf{r}_1)$  and  $Q_2(\mathbf{r}_2)$ . We assume that the beam is incident normally on the screen  $A$ . In general, interference fringes will be formed on screen  $B$ , placed in a plane  $z = z_0 > 0$ , some distance behind the screen  $A$ . The complex random field  $V(\mathbf{r}; t)$  at a point  $P(\mathbf{r})$  on the screen  $B$ , and at time  $t$ , is generated by the superposition of fields arriving from the two pinholes. If the light takes times  $t_1 = R_1/c$  and  $t_2 = R_2/c$  to travel to the point  $P(\mathbf{r})$  from the pinholes  $Q_1(\mathbf{r}_1)$  and  $Q_2(\mathbf{r}_2)$ , respectively ( $c$  is the speed of light), one has

$$V(\mathbf{r}; t) = \mathcal{K}_1 V(\mathbf{r}_1; t - t_1) + \mathcal{K}_2 V(\mathbf{r}_2; t - t_2). \quad (2.7)$$

Here  $\mathcal{K}_1$  and  $\mathcal{K}_2$  are two purely imaginary constant factors, which take into account the diffraction at the pinholes. Their explicit forms can be obtained from Huygen–Fresnel principles (see, e.g., [5, Section 8.2]). On using Eqs. (2.5)–(2.7), one finds that the average intensity at the point  $P(\mathbf{r})$  is given by the expression

$$I(\mathbf{r}) = |\mathcal{K}_1|^2 I(\mathbf{r}_1) + |\mathcal{K}_2|^2 I(\mathbf{r}_2) + 2\text{Re} \left\{ \mathcal{K}_1^* \mathcal{K}_2 \Gamma(\mathbf{r}_1, \mathbf{r}_2; \tau) \right\}, \quad (2.8)$$

where  $\tau \equiv t_2 - t_1 = (R_2 - R_1)/c$  is the time difference between the fields arriving at  $P(\mathbf{r})$  from pinholes  $Q_1(\mathbf{r}_1)$  and  $Q_2(\mathbf{r}_2)$ . It follows from Eq. (2.8) that if one blocks the pinhole  $Q_1(\mathbf{r}_1)$ , the intensity distribution on the screen  $B$  is given by  $I^{(1)}(\mathbf{r}) = |\mathcal{K}_1|^2 I(\mathbf{r}_1)$ . Similarly, if the other pinhole  $Q_2(\mathbf{r}_2)$  is closed, the intensity distribution on the screen  $B$  becomes  $I^{(2)}(\mathbf{r}) = |\mathcal{K}_2|^2 I(\mathbf{r}_2)$ . Evidently the quantities  $I^{(1)}(\mathbf{r})$  and  $I^{(2)}(\mathbf{r})$  represent the contributions to the total intensity at the point  $P(\mathbf{r})$  from the

pinholes  $Q_1(\mathbf{r}_1)$  and  $Q_2(\mathbf{r}_2)$ , respectively. If we assume that these two contributions are equal, that is,  $I^{(1)}(\mathbf{r}) = I^{(2)}(\mathbf{r}) = I^{(0)}(\mathbf{r})$ , we find that

$$I(\mathbf{r}) = 2I^{(0)}(\mathbf{r}) \left\{ 1 + \left| \frac{\Gamma(\mathbf{r}_1, \mathbf{r}_2; \tau)}{\sqrt{I(\mathbf{r}_1)}\sqrt{I(\mathbf{r}_2)}} \right| \cos [\alpha(\mathbf{r}_1, \mathbf{r}_2; \tau)] \right\}, \quad (2.9)$$

where  $\alpha(\mathbf{r}_1, \mathbf{r}_2; \tau) = \arg \{ \Gamma(\mathbf{r}_1, \mathbf{r}_2; \tau) \}$ . It readily follows from Eq. (2.9) that the visibility  $\mathcal{V}$  of the fringes around the point,  $P(\mathbf{r})$ , is

$$\mathcal{V} \equiv \frac{I_{\max} - I_{\min}}{I_{\max} + I_{\min}} = \left| \frac{\Gamma(\mathbf{r}_1, \mathbf{r}_2; \tau)}{\sqrt{I(\mathbf{r}_1)}\sqrt{I(\mathbf{r}_2)}} \right|. \quad (2.10)$$

The degree of coherence in the space-time domain is defined by the normalized MC function [5, Chap. 10]

$$\gamma(\mathbf{r}_1, \mathbf{r}_2; \tau) \equiv \frac{\Gamma(\mathbf{r}_1, \mathbf{r}_2; \tau)}{\sqrt{I(\mathbf{r}_1)}\sqrt{I(\mathbf{r}_2)}}, \quad (2.11)$$

which appears inside the modulus sign in Eq. (2.10). The visibility of fringes is always bounded by zero and by unity and so is the modulus of the degree of coherence. It can also be proved explicitly by the use of the Cauchy–Schwarz inequality that

$$0 \leq |\gamma(\mathbf{r}_1, \mathbf{r}_2; \tau)| \leq 1. \quad (2.12)$$

When  $|\gamma(\mathbf{r}_1, \mathbf{r}_2; \tau)| = 1$ , sharpest possible fringes are obtained and the light is said to be spatially completely coherent at the pair of points  $Q_1(\mathbf{r}_1)$  and  $Q_2(\mathbf{r}_2)$ , for the time delay  $\tau$ . In the other extreme case, when  $\gamma(\mathbf{r}_1, \mathbf{r}_2; \tau) = 0$ , no fringe is obtained and the light is said to be spatially incoherent at the two points, for the time delay  $\tau$ . In the intermediate case  $0 < |\gamma(\mathbf{r}_1, \mathbf{r}_2; \tau)| < 1$ , the light is said to be *partially coherent* at the pair of points. It is to be noted that the degree of coherence is, in general, a complex quantity. Its phase is also a meaningful physical quantity and can be, in principle, determined from the measurements of positions of maximum and minimum in the fringe pattern (see, e.g., [8, p. 167]).

The MC function obeys certain propagation laws which make it possible to study changes in correlation properties of light on propagation. These propagation laws are known as the Wolf equations. For propagation in free space, they are given by [8, Section 4.4.1]

$$\nabla_1^2 \Gamma(\mathbf{r}_1, \mathbf{r}_2; \tau) = \frac{1}{c^2} \frac{\partial^2}{\partial \tau^2} \Gamma(\mathbf{r}_1, \mathbf{r}_2; \tau), \quad (2.13a)$$

$$\nabla_2^2 \Gamma(\mathbf{r}_1, \mathbf{r}_2; \tau) = \frac{1}{c^2} \frac{\partial^2}{\partial \tau^2} \Gamma(\mathbf{r}_1, \mathbf{r}_2; \tau), \quad (2.13b)$$

where  $\nabla_1^2$  and  $\nabla_2^2$  are Laplacian operators acting with respect to the points  $\mathbf{r}_1$  and  $\mathbf{r}_2$ , respectively. These equations imply that the state of coherence of light may change on propagation<sup>3</sup>.

The scalar theory discussed thus far can be generalized to vector fields. If we restrict ourselves to a light beam propagating along a particular direction (positive  $z$ -direction, say), the  $3 \times 3$  MC matrix, defined by Eq. (2.4), reduces to a  $2 \times 2$  MC matrix

$$\vec{\Gamma}(\mathbf{r}_1, \mathbf{r}_2; \tau) \equiv [\Gamma_{lm}(\mathbf{r}_1, \mathbf{r}_2; \tau)] \equiv [\langle E_l^*(\mathbf{r}_1; t) E_m(\mathbf{r}_2; t + \tau) \rangle], \quad (l = x, y; m = x, y). \quad (2.14)$$

It is convenient to represent the electric field vector by a column matrix, that is, by

$$\mathbf{E}(\mathbf{r}; t) \equiv \begin{pmatrix} E_x(\mathbf{r}; t) \\ E_y(\mathbf{r}; t) \end{pmatrix} = (E_x(\mathbf{r}; t) \quad E_y(\mathbf{r}; t))^T, \quad (2.15)$$

where the superscript  $T$  denotes transpose of a matrix. Equation (2.14) can now be expressed as

$$\vec{\Gamma}(\mathbf{r}_1, \mathbf{r}_2; \tau) = \langle \mathbf{E}^*(\mathbf{r}_1; t) \circ \mathbf{E}^T(\mathbf{r}_2; t + \tau) \rangle, \quad (2.16)$$

where the symbol “ $\circ$ ” denotes matrix multiplication. The average intensity at a point  $P(\mathbf{r})$  is given by

$$I(\mathbf{r}) \equiv \langle |E_x(\mathbf{r}; t)|^2 \rangle + \langle |E_y(\mathbf{r}; t)|^2 \rangle = \text{tr} \vec{\Gamma}(\mathbf{r}, \mathbf{r}; 0), \quad (2.17)$$

where  $\text{tr}$  represents trace of a matrix. Following a procedure similar to that used for scalar fields, one obtains the following formula for the degree of coherence<sup>4</sup> [13]:

$$\gamma(\mathbf{r}_1, \mathbf{r}_2, \tau) \equiv \frac{\text{tr} \vec{\Gamma}(\mathbf{r}_1, \mathbf{r}_2, \tau)}{\sqrt{I(\mathbf{r}_1)I(\mathbf{r}_2)}}, \quad (2.18)$$

where  $|\gamma(\mathbf{r}_1, \mathbf{r}_2, \tau)|$  is directly related to the visibility of fringes produced in a Young's interference experiment. Again, one can define the complete coherence by  $|\gamma(\mathbf{r}_1, \mathbf{r}_2; \tau)| = 1$ , the complete incoherence by  $\gamma(\mathbf{r}_1, \mathbf{r}_2; \tau) = 0$ , and the partial coherence by  $0 < |\gamma(\mathbf{r}_1, \mathbf{r}_2; \tau)| < 1$ .

---

<sup>3</sup>Considerable amount of research has been done for understanding the nature of this change. For further details see, for example, [8, Section 4.4.]

<sup>4</sup>There exist other definitions of degree of coherence for beam-like vector fields. One of them was introduced in Reference 14. The same concept was also extended to the frequency domain in Reference 15, which lead to some discussions on what should be an appropriate definition of degree of coherence for beam-like vector fields (see, for example, [16, 17]). Later other approaches to define the degree of coherence were also proposed [18–20].

### 2.2.2 Complete Spatial Coherence in the Time Domain

The concept of complete spatial coherence is often confused with monochromaticity. Although the difference between them has been pointed out in many scholarly publications (see, e.g., [5, 8, 12, 21, 22]), the misconception persists. In this section we discuss the difference between spatially coherent light and monochromatic light.

We consider scalar fields for simplicity. Suppose that an optical field is spatially coherent, at a pair of points  $\mathbf{r}_1$  and  $\mathbf{r}_2$ , for a value of  $\tau = \tau_0$ , that is,  $|\gamma(\mathbf{r}_1, \mathbf{r}_2, \tau_0)| = 1$ . From Eqs. (2.5) and (2.11), one readily finds that

$$|\langle V^*(\mathbf{r}_1; t)V(\mathbf{r}_2; t + \tau_0) \rangle| = \sqrt{I(\mathbf{r}_1)}\sqrt{I(\mathbf{r}_2)}. \quad (2.19)$$

Now applying the Cauchy–Schwarz inequality to  $V(\mathbf{r}_1; t)$  and  $V(\mathbf{r}_2; t + \tau_0)$ , and using Eq. (2.6), one obtains

$$|\langle V^*(\mathbf{r}_1; t)V(\mathbf{r}_2; t + \tau_0) \rangle| \leq \sqrt{I(\mathbf{r}_1)}\sqrt{I(\mathbf{r}_2)}, \quad (2.20)$$

where we have used the fact that for stationary fields  $\langle |V(\mathbf{r}_2; t + \tau_0)|^2 \rangle = \langle |V(\mathbf{r}_2; t)|^2 \rangle = I(\mathbf{r}_2)$ . The expression on the both sides of inequality (2.20) are equal to each other if and only if the ratio  $V(\mathbf{r}_2; t + \tau_0)/V(\mathbf{r}_1; t)$  is independent of  $t$ , that is, if and only if

$$V(\mathbf{r}_2; t + \tau_0) = \mathcal{A}^{(\tau_0)}(\mathbf{r}_1, \mathbf{r}_2)V(\mathbf{r}_1; t), \quad (2.21)$$

where  $\mathcal{A}^{(\tau_0)}(\mathbf{r}_1, \mathbf{r}_2)$  is a time-independent, generally complex quantity. From Eqs. (2.19) and (2.20) it, therefore, follows that *an optical field is spatially completely coherent at a pair of points  $\mathbf{r}_1$  and  $\mathbf{r}_2$  for a value of  $\tau = \tau_0$ , if and only if Eq. (2.21) is true*. This result has important physical significance. It implies that although the field at the two points are represented by two random quantities  $V(\mathbf{r}_1; t)$  and  $V(\mathbf{r}_2; t + \tau_0)$ , their ratio is a deterministic time-independent quantity  $\mathcal{A}^{(\tau_0)}(\mathbf{r}_1, \mathbf{r}_2)$ . Clearly, spatial coherence ( $|\gamma(\mathbf{r}_1, \mathbf{r}_2, \tau_0)| = 1$ ) requires that the random field at the two points *fluctuates in unison* when a suitable time delay,  $\tau_0$ , is introduced between them. Figure 2.2 provides a pictorial description of fluctuations in unison. It is evident that one does not need a monochromatic field to achieve complete spatial coherence. It is not the monochromaticity, but the *fluctuations in unison* that is the essence of complete spatial coherence<sup>5</sup>. The concept of fluctuations in unison is often referred to as the concept of statistical similarity. For more on the concept of statistical similarity see References 24–26.

Let us note that  $\mathcal{A}^{(\tau_0)}(\mathbf{r}_1, \mathbf{r}_2)$  is a measurable quantity. From Eqs. (2.5), (2.6), (2.11), and (2.21), it readily follows that [24]

$$|\mathcal{A}^{(\tau_0)}(\mathbf{r}_1, \mathbf{r}_2)| = \sqrt{\frac{I(\mathbf{r}_2)}{I(\mathbf{r}_1)}}, \quad \arg \{\mathcal{A}^{(\tau_0)}(\mathbf{r}_1, \mathbf{r}_2)\} = \arg \{\gamma(\mathbf{r}_1, \mathbf{r}_2; \tau_0)\}. \quad (2.22)$$

---

<sup>5</sup>The idea of fluctuations in unison is due to Verdet [23].

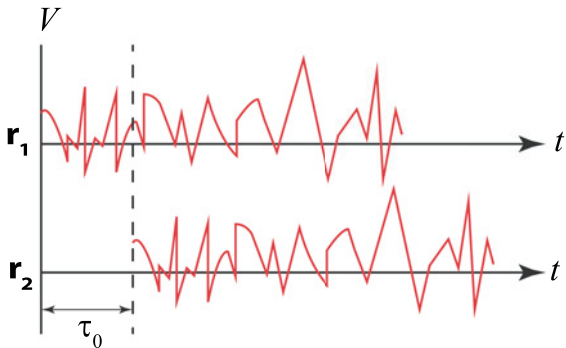


**FIGURE 2.2** Illustrating statistical similarity between the randomly fluctuating field at a pair of points  $\mathbf{r}_1$  and  $\mathbf{r}_2$ . The temporal dependence of the field at the two points are identical except a multiplicative factor and a constant time delay  $\tau_0$ .

### 2.3 CLASSICAL THEORY OF OPTICAL COHERENCE IN THE SPACE-FREQUENCY DOMAIN

The classical theory of optical coherence was originally introduced in the space-time domain [2, 11]. However, there are certain types of problems, which turn out to be very difficult to solve by the use of this formulation. For example, problems involving change in coherence properties of light on propagation through various media and the problems involving scattering of light present considerable difficulties in the time domain. In order to address such problems, the space-frequency formulation of the theory has been introduced [27–29]. In this section, we briefly discuss the theory of spatial coherence in the frequency domain.

Although a stationary random function  $V(\mathbf{r}; t)$  is not Fourier integrable within the framework of the ordinary function theory, it is reasonable to assume that the Fourier transform of the MC function  $\Gamma(\mathbf{r}_1, \mathbf{r}_2; \tau)$  exists<sup>6</sup>. One can then define a function  $W(\mathbf{r}_1, \mathbf{r}_2; \omega)$ , which together with  $\Gamma(\mathbf{r}_1, \mathbf{r}_2; \tau)$  form a Fourier transform pair, that is,

$$W(\mathbf{r}_1, \mathbf{r}_2; \omega) = \frac{1}{2\pi} \int_{-\infty}^{\infty} \Gamma(\mathbf{r}_1, \mathbf{r}_2; \tau) e^{i\omega\tau} d\tau, \quad (2.23a)$$

$$\Gamma(\mathbf{r}_1, \mathbf{r}_2; \tau) = \int_0^{\infty} W(\mathbf{r}_1, \mathbf{r}_2; \omega) e^{-i\omega\tau} d\omega. \quad (2.23b)$$

The lower limit of the integration in Eq. (2.23b) is 0, because  $\Gamma(\mathbf{r}_1, \mathbf{r}_2; \tau)$  is a complex analytic signal. The quantity  $W(\mathbf{r}_1, \mathbf{r}_2; \omega)$  is called the cross-spectral density function (to be abbreviated by CSD function). It can be shown with the help of coherent mode

<sup>6</sup>A rigorous explanation can be given using the Wiener–Khintchine theorem, an account of which can be found in Section 2.4 of Reference 8.

representation that  $W(\mathbf{r}_1, \mathbf{r}_2; \omega)$  is also a correlation function [8, Section 4.7.2], that is, it can be represented in the form

$$W(\mathbf{r}_1, \mathbf{r}_2; \omega) = \langle U^*(\mathbf{r}_1; \omega)U(\mathbf{r}_2; \omega) \rangle, \quad (2.24)$$

where  $U(\mathbf{r}; \omega)$  is a typical member of a suitably constructed ensemble of monochromatic realizations, all of frequency  $\omega$ .

The spectral density  $S(\mathbf{r}; \omega)$  at a point  $\mathbf{r}$ , at frequency  $\omega$ , is given by the formula

$$S(\mathbf{r}; \omega) = W(\mathbf{r}, \mathbf{r}; \omega) = \langle |U(\mathbf{r}; \omega)|^2 \rangle. \quad (2.25)$$

From Eqs. (2.23b) and (2.25) it readily follows that

$$\int_0^\infty S(\mathbf{r}; \omega) d\omega = \Gamma(\mathbf{r}, \mathbf{r}; 0) = I(\mathbf{r}). \quad (2.26)$$

Clearly,  $S(\mathbf{r}; \omega)$  can be regarded as equivalent to the average intensity at a particular frequency. The normalized spectral density  $\mathcal{S}(\mathbf{r}; \omega)$  is given by the formula

$$\mathcal{S}(\mathbf{r}; \omega) = \frac{S(\mathbf{r}; \omega)}{\int_0^\infty S(\mathbf{r}; \omega) d\omega} = \frac{S(\mathbf{r}; \omega)}{I(\mathbf{r})}. \quad (2.27)$$

It is to be noted that the spectral density of a field can change on propagation even through free space [30, 31]. This discovery is one of the many successes of the theory of optical coherence in the space-frequency domain.

### 2.3.1 Degree of Coherence in the Space-Frequency Domain

The spectral degree of coherence  $\mu(\mathbf{r}_1, \mathbf{r}_2; \omega)$ , that is, the spatial degree of coherence at frequency  $\omega$ , is defined by the expression [8, Section 4.3.2]

$$\mu(\mathbf{r}_1, \mathbf{r}_2; \omega) \equiv \frac{W(\mathbf{r}_1, \mathbf{r}_2; \omega)}{\sqrt{S(\mathbf{r}_1, \omega)} \sqrt{S(\mathbf{r}_2, \omega)}}. \quad (2.28)$$

It can be readily shown that  $0 \leq |\mu(\mathbf{r}_1, \mathbf{r}_2; \omega)| \leq 1$ . When  $|\mu(\mathbf{r}_1, \mathbf{r}_2; \omega)| = 1$ , the field is said to be *spectrally* completely coherent at the pair of points  $\mathbf{r}_1$  and  $\mathbf{r}_2$ , at the frequency  $\omega$ . If  $\mu(\mathbf{r}_1, \mathbf{r}_2; \omega) = 0$ , the field is said to be *spectrally* completely incoherent at the two points, at that frequency. In the intermediate case, it is said to be spectrally partially coherent at those points, at frequency  $\omega$ .

The physical significance of  $\mu(\mathbf{r}_1, \mathbf{r}_2; \omega)$  can be elucidated by a Young's interference experiment (Fig. 2.1). However, one now needs to separately analyze the fringe visibility produced by each frequency component that is present in the spectrum. This situation can be realized by imagining that the incident light is filtered to have only

one frequency  $\omega$  before reaching the pinholes. Under the assumption that contributions from the two pinholes are equal, the spectral density  $S(\mathbf{r}; \omega)$ , at a point  $P(\mathbf{r})$  on the screen  $B$ , is given by the expression [8, Section 4.3.2]

$$S(\mathbf{r}; \omega) = S^{(1)}(\mathbf{r}; \omega) \left\{ 1 + |\mu(\mathbf{r}_1, \mathbf{r}_2; \omega)| \cos [\arg \{\mu(\mathbf{r}_1, \mathbf{r}_2; \omega)\} - \delta] \right\}. \quad (2.29)$$

Here  $S^{(1)}(\mathbf{r}; \omega)$  is the contribution of light reaching at  $P(\mathbf{r})$  from either of the two pinholes and  $\delta = \omega(R_2 - R_1)/c$ . The formula (2.29) is known as the *spectral intensity law*. One can readily show that  $|\mu(\mathbf{r}_1, \mathbf{r}_2; \omega)|$  is equal to the visibility of the fringes associated with the frequency component  $\omega$ . A prescription of measuring modulus and phase of  $\mu(\mathbf{r}_1, \mathbf{r}_2; \omega)$  can be found in Reference 32.

Like the MC function, the CSD function also obeys certain propagation laws which are given by [8, Section 4.4.1]

$$\nabla_1^2 W(\mathbf{r}_1, \mathbf{r}_2; \omega) + k^2 W(\mathbf{r}_1, \mathbf{r}_2; \omega) = 0, \quad (2.30a)$$

$$\nabla_2^2 W(\mathbf{r}_1, \mathbf{r}_2; \omega) + k^2 W(\mathbf{r}_1, \mathbf{r}_2; \omega) = 0. \quad (2.30b)$$

These equations show that the spectral degree of coherence of light can change due to propagation.

The theory can also be generalized to the vector fields. For an optical beam propagating along a particular direction, one can define a  $2 \times 2$  matrix, known as the cross-spectral density matrix (CSD matrix), which is the Fourier transform of the  $2 \times 2$  MC matrix [12, Chap. 9]:

$$\vec{W}(\mathbf{r}_1, \mathbf{r}_2; \omega) \equiv \frac{1}{2\pi} \int_{-\infty}^{\infty} \vec{\Gamma}(\mathbf{r}_1, \mathbf{r}_2; \tau) \exp[i\omega\tau] d\tau, \quad (2.31a)$$

$$\vec{\Gamma}(\mathbf{r}_1, \mathbf{r}_2; \tau) = \int_0^{\infty} \vec{W}(\mathbf{r}_1, \mathbf{r}_2; \omega) \exp[-i\omega\tau] d\omega. \quad (2.31b)$$

As in the scalar case, it can be shown that each element of the CSD matrix is a correlation function [12, Chap. 9], i.e.,

$$W_{ij}(\mathbf{r}_1, \mathbf{r}_2; \omega) = \langle E_i^*(\mathbf{r}_1; \omega) E_j(\mathbf{r}_2; \omega) \rangle, \quad (2.32)$$

where  $E_i(\mathbf{r}; \omega)$  is a typical member of an ensemble of monochromatic realizations. Each element of a CSD matrix obeys definite propagation laws which are analogous to Eqs. (2.30), viz.,

$$\nabla_1^2 \vec{W}(\mathbf{r}_1, \mathbf{r}_2; \omega) + k^2 \vec{W}(\mathbf{r}_1, \mathbf{r}_2; \omega) = 0, \quad (2.33a)$$

$$\nabla_2^2 \vec{W}(\mathbf{r}_1, \mathbf{r}_2; \omega) + k^2 \vec{W}(\mathbf{r}_1, \mathbf{r}_2; \omega) = 0. \quad (2.33b)$$

The spectral density  $S(\mathbf{r}; \omega)$  of a vector field is given by the expression [12, Chap. 9]

$$S(\mathbf{r}; \omega) = \text{tr} \vec{W}(\mathbf{r}, \mathbf{r}; \omega), \quad (2.34)$$

and the spectral degree of coherence is given by the expression<sup>7</sup> [12, Chap. 9]

$$\mu(\mathbf{r}_1, \mathbf{r}_2; \omega) = \frac{\text{tr} \overrightarrow{W}(\mathbf{r}_1, \mathbf{r}_2; \omega)}{\sqrt{S(\mathbf{r}_1; \omega)} \sqrt{S(\mathbf{r}_2; \omega)}}. \quad (2.35)$$

Elements of the CSD matrix are measurable quantities. A theoretical prescription to determine them was proposed in Reference 33. Later they were also experimentally determined for a laser beam [34].

### 2.3.2 Complete Spatial Coherence in the Frequency Domain

The concept of statistical similarity, which is discussed in Section 2.2.2, can also be extended to elucidate complete spatial coherence in the frequency domain [35]. For simplicity, we once again restrict our analysis to scalar fields. If the field is spectrally completely coherent at the pair of points  $(\mathbf{r}_1, \mathbf{r}_2)$ , at frequency  $\omega$ , that is, if  $|\mu(\mathbf{r}_1, \mathbf{r}_2; \omega)| = 1$ , it readily follows from Eqs. (2.24), (2.25), and (2.28) that

$$|\langle U^*(\mathbf{r}_1; \omega)U(\mathbf{r}_2; \omega) \rangle|^2 = \left\langle |U(\mathbf{r}_1; \omega)|^2 \right\rangle \left\langle |U(\mathbf{r}_2; \omega)|^2 \right\rangle. \quad (2.36)$$

Applying the Cauchy–Schwarz inequality to the random quantities  $U(\mathbf{r}_1; \omega)$  and  $U(\mathbf{r}_2; \omega)$  one obtains

$$|\langle U^*(\mathbf{r}_1; \omega)U(\mathbf{r}_2; \omega) \rangle|^2 \leq \left\langle |U(\mathbf{r}_1; \omega)|^2 \right\rangle \left\langle |U(\mathbf{r}_2; \omega)|^2 \right\rangle. \quad (2.37)$$

The expressions on both sides of this inequality are equal to each other if and only if the ratio  $U(\mathbf{r}_2; \omega)/U(\mathbf{r}_1; \omega)$  is a deterministic function, that is, if and only if the following relation holds:

$$U(\mathbf{r}_2; \omega) = \mathcal{B}(\mathbf{r}_1, \mathbf{r}_2; \omega)U(\mathbf{r}_1; \omega), \quad (2.38)$$

where  $\mathcal{B}(\mathbf{r}_1, \mathbf{r}_2; \omega)$  is a deterministic function of its arguments. From Eqs. (2.36) and (2.37), it is clear that complete spectral coherence at a pair of points  $(\mathbf{r}_1, \mathbf{r}_2)$ , at frequency  $\omega$ , requires the random quantities  $U(\mathbf{r}_1; \omega)$  and  $U(\mathbf{r}_2; \omega)$  to obey the relation (2.38) and vice versa<sup>8</sup>. Using Eqs. (2.24), (2.25), (2.28), and (2.38), one can show that

$$|\mathcal{B}(\mathbf{r}_1, \mathbf{r}_2; \omega)| = \sqrt{\frac{S(\mathbf{r}_2; \omega)}{S(\mathbf{r}_1; \omega)}}, \quad \arg \{\mathcal{B}(\mathbf{r}_1, \mathbf{r}_2; \omega)\} = \arg \{\mu(\mathbf{r}_1, \mathbf{r}_2; \omega)\}. \quad (2.39)$$

Clearly,  $\mathcal{B}(\mathbf{r}_1, \mathbf{r}_2; \omega)$  is a measurable quantity.

The relation (2.38), which plays a role analogous to the relation (2.21), can be regarded as the statistical similarity relation in the space–frequency domain. It elucidates the concept of complete spectral coherence at a pair of points. However, the

<sup>7</sup>Other definitions of the degree of coherence are also proposed as discussed in footnote 4 of Section 2.2.1.

<sup>8</sup>The proof of sufficiency is straightforward: Using Eqs. (2.28) and (2.38), one readily finds that  $|\mu(\mathbf{r}_1, \mathbf{r}_2; \omega)| = 1$ .

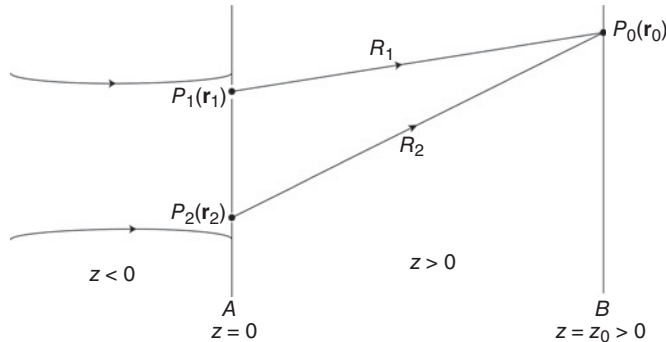


**FIGURE 2.3** A Young's interference experiment.

statistical similarity relations in the space-time and in the space-frequency domains must not be confused with each other. It must be noted that no temporal parameter is involved in Eq. (2.38). This equation cannot, therefore, be interpreted as the fluctuations of the optical field in unison. In fact, the statistical similarity relations in the two domains have different physical significance. We elucidate this point further in the next section.

## 2.4 CROSS-SPECTRALLY PURE OPTICAL FIELDS

When two light beams of the same normalized spectral distribution are superposed, they produce a new beam whose normalized spectral distribution is, in general, different from that of the parent beams [36–38]. Mandel, however, showed that it is possible to obtain certain conditions under which the normalized spectral distribution is not affected by superposition [39]. An optical field obeying these conditions is called a cross-spectrally pure field<sup>9</sup>. A field that is not cross-spectrally pure cannot generate the same spectral distribution in a superposition experiment; such a field is called spectrally impure field. Mandel also introduced a degree of cross-spectral purity [39]. In this section we, however, restrict ourselves only to the cross-spectrally pure fields.

Let us consider a Young's interference experiment (Fig. 2.3), in which the pinholes are located at the points,  $P_1(\mathbf{r}_1)$  and  $P_2(\mathbf{r}_2)$ . A field is said to be cross-spectrally pure at the pair of points  $\mathbf{r}_1$  and  $\mathbf{r}_2$  if it satisfies the following two conditions ([40]; see also [8, Section 4.5.1]):

1. The normalized spectral densities of the light at the two points,  $P_1(\mathbf{r}_1)$  and  $P_2(\mathbf{r}_2)$ , are equal to each other at all frequencies present in its spectrum, that

<sup>9</sup>The term “pure” was used in analogy with its usage in genetics.

is,  $\mathcal{S}(\mathbf{r}_1; \omega) = \mathcal{S}(\mathbf{r}_2; \omega)$  for all  $\omega$ . Using Eq. (2.27), this condition can be expressed as

$$\frac{S(\mathbf{r}_1; \omega)}{I(\mathbf{r}_1)} = \frac{S(\mathbf{r}_2; \omega)}{I(\mathbf{r}_2)}, \quad \forall \omega. \quad (2.40)$$

2. There exists a point  $P_0(\mathbf{r}_0)$  on the screen  $B$ , around which the normalized spectral density is equal to that at the pinholes for all frequencies present in the spectrum of the light, that is,  $\mathcal{S}(\mathbf{r}_0; \omega) = \mathcal{S}(\mathbf{r}_1; \omega) = \mathcal{S}(\mathbf{r}_2; \omega)$  for all possible values of  $\omega$ . Using the formulas for intensity and spectral density at the point  $P_0(\mathbf{r}_0)$ , this condition can be expressed in the form

$$\mu(\mathbf{r}_1, \mathbf{r}_2; \omega) = \gamma(\mathbf{r}_1, \mathbf{r}_2; \tau_0) \exp [i\omega\tau_0], \quad \forall \omega, \quad (2.41)$$

where  $\tau_0 = (R_2 - R_1)/c$  is confined to a range  $\Delta\tau \ll 1/\Delta\omega$ ,  $\Delta\omega$  being the frequency-width of the spectrum.

We now show that the concept of cross-spectral purity plays an important role in distinguishing between complete spatial coherence in the time and frequency domains [41, 42]. First we establish that if  $|\gamma(\mathbf{r}_1, \mathbf{r}_2; \tau_0)| = 1$ , the field is cross-spectrally pure at the pair of points  $\mathbf{r}_1$  and  $\mathbf{r}_2$ . Let us recall that if  $|\gamma(\mathbf{r}_1, \mathbf{r}_2; \tau_0)| = 1$ , the statistical similarity relation (2.21) in the space-time domain holds and vice versa. It follows from Eqs. (2.5), (2.21), and (2.23a) that in this case, for all values of  $\omega$  present in the spectrum,

$$W(\mathbf{r}_1, \mathbf{r}_2; \omega) = \exp [i\omega\tau_0] \mathcal{A}^{(\tau_0)}(\mathbf{r}_1, \mathbf{r}_2) S(\mathbf{r}_1; \omega) = \exp [i\omega\tau_0] \frac{S(\mathbf{r}_2; \omega)}{\{\mathcal{A}^{(\tau_0)}(\mathbf{r}_1, \mathbf{r}_2)\}^*}. \quad (2.42)$$

This formula immediately leads to the relation

$$S(\mathbf{r}_1; \omega) = \frac{S(\mathbf{r}_2; \omega)}{|\mathcal{A}^{(\tau_0)}(\mathbf{r}_1, \mathbf{r}_2)|^2}. \quad (2.43)$$

Using Eqs. (2.22) and (2.43), one then finds that  $S(\mathbf{r}_1; \omega)/I(\mathbf{r}_1) = S(\mathbf{r}_2; \omega)/I(\mathbf{r}_2)$ , that is, such a field satisfies the first condition [Eq. (2.40)] of cross-spectrally purity. From Eqs. (2.21), (2.28), and (2.42) it follows that

$$\mu(\mathbf{r}_1, \mathbf{r}_2; \omega) = \exp [i\omega\tau_0] \frac{\mathcal{A}^{(\tau_0)}(\mathbf{r}_1, \mathbf{r}_2)}{|\mathcal{A}^{(\tau_0)}(\mathbf{r}_1, \mathbf{r}_2)|}. \quad (2.44)$$

Here we have used the fact that  $\sqrt{z/z^*} = z/|z|$ , for any complex number  $z$ . It is thus clear that in this case  $|\mu(\mathbf{r}_1, \mathbf{r}_2; \omega)| = 1 = |\gamma(\mathbf{r}_1, \mathbf{r}_2; \tau_0)|$ , for all frequencies  $\omega$  present in the spectrum. Now using Eqs. (2.22) and (2.44), one finds that

$\mu(\mathbf{r}_1, \mathbf{r}_2; \omega) = \gamma(\mathbf{r}_1, \mathbf{r}_2; \tau_0) \exp[i\omega\tau_0]$ , that is, the second condition [Eq. (2.41)] of cross-spectral purity is also satisfied. Thus we have established that complete spatial coherence in the time domain always ensures cross-spectral purity<sup>10</sup>.

We now show that complete spectral coherence ( $|\mu(\mathbf{r}_1, \mathbf{r}_2; \omega)| = 1$ ) for all frequency  $\omega$ , at a pair of points, does not ensure cross-spectral purity. We recall that if  $|\mu(\mathbf{r}_1, \mathbf{r}_2; \omega)| = 1$ , the statistical similarity relation (2.38) in the space-frequency domain holds and vice versa. From Eq. (2.39), it readily follows that the ratio

$$\frac{S(\mathbf{r}_2; \omega)}{S(\mathbf{r}_1; \omega)} = |\mathcal{B}(\mathbf{r}_1, \mathbf{r}_2; \omega)|^2, \quad (2.45)$$

in general, depends on  $\omega$ . However, the first condition of cross-spectral purity (Eq. 2.40) requires that the ration  $S(\mathbf{r}_2; \omega)/S(\mathbf{r}_1; \omega)$  must be independent of frequency  $\omega$ . Hence complete spectral coherence ( $|\mu(\mathbf{r}_1, \mathbf{r}_2; \omega)| = 1$ ) does not always imply cross-spectral purity.

From the foregoing discussion of this section, it is clear that the concept of cross-spectral purity can be used to elucidate the difference between complete spatial coherence in the time and frequency domains. It is also clear that statistical similarity relations in the space-time and in the space-frequency domains are not equivalent to each other; the former ensures cross-spectral purity, whereas the latter does not.

#### 2.4.1 Application of Coherence Theory in Structure Determination of Random Media

Determining structures of objects has been a subject of interest because of its applications in various branches of science, for example, in physics, chemistry, biology, medicine, etc. The subject originated in the classic x-ray diffraction technique introduced in works of Laue, Friedrich, Knipping, W. H. Bragg, W. L. Bragg, and Ewald in the early part of the previous century ([43–48]; for a collection of important papers on this topic, see Reference 49). In the usual reconstruction techniques, the refractive index (often equivalent to the electric permittivity) of a medium is assumed to be a deterministic function of position. Such a medium can be characterized by the so-called scattering potential, which is defined at a point  $\mathbf{r}'$  by the formula [5, Section 13.1.1]

$$F(\mathbf{r}'; \omega) = \frac{k^2}{4\pi} [n^2(\mathbf{r}'; \omega) - 1], \quad (2.46)$$

where  $n(\mathbf{r}', \omega)$  is the refractive index of the medium at frequency  $\omega$ .

However, there exists a type of media whose refractive indices vary randomly with position and time. They are generally called random media (see, for example, Reference 50). Blood cells, certain types of biological tissues, rain drops, clouds, etc.,

---

<sup>10</sup>The converse is, in general, not true; a cross-spectrally pure field can be partially coherent.

are some examples of such media. The usual reconstruction technique does not apply to them. We now discuss a theory of determining the structure of random media.

We consider a random medium which can be effectively represented by an ensemble of sample media. Such a random medium may be characterized by the correlation function of its scattering potential at two points  $\mathbf{r}'_1$  and  $\mathbf{r}'_2$ , that is, by [12, Section 6.3]

$$C_F(\mathbf{r}'_1, \mathbf{r}'_2; \omega) = \langle F^*(\mathbf{r}'_1; \omega)F(\mathbf{r}'_2; \omega) \rangle_m, \quad (2.47)$$

where the angular brackets with subscript  $m$  denote the average taken over the ensemble of sample media. We assume that  $C_F$  is a well-behaved deterministic function.

Suppose that a spectrally coherent plane light wave, propagating in a direction specified by a real unit vector  $\mathbf{s}_0$ , is incident on the medium which occupies a finite domain  $D$  in space (see Fig. 2.4). The CSD function of the incident light at a pair of points  $\mathbf{r}_1$  and  $\mathbf{r}_2$  is given by the formula

$$W^{(i)}(\mathbf{r}_1, \mathbf{r}_2, \mathbf{s}_0; \omega) = S^{(i)}(\omega) \exp [ik\mathbf{s}_0 \cdot (\mathbf{r}_2 - \mathbf{r}_1)], \quad (2.48)$$

where  $S^{(i)}(\omega)$  is the spectral density of the incident light. We assume that the medium is a weak scatterer, so that the scattering may be analyzed within the accuracy of the first Born approximation [5, Section 13.1.2]. The CSD function of the scattered light in the

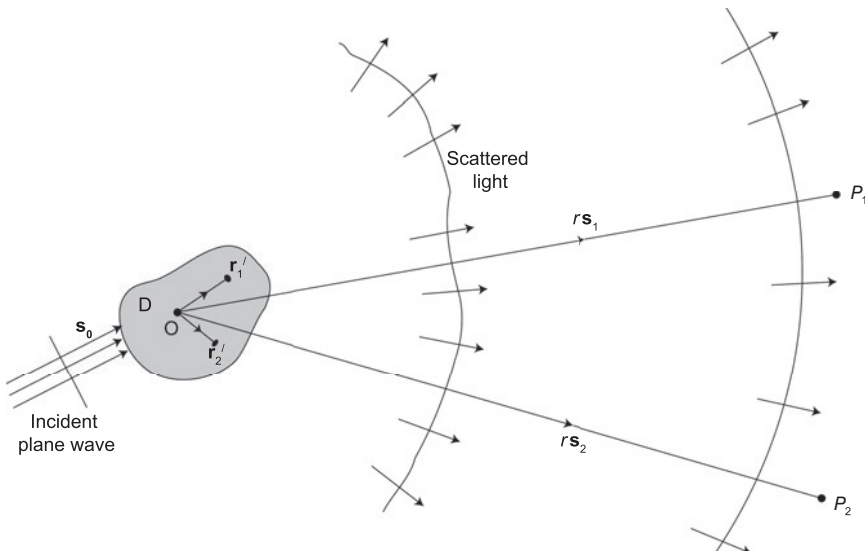


**FIGURE 2.4** A coherent plane wave propagating along  $\mathbf{s}_0$  is scattered by a random medium  $D$ .  $P_1(r\mathbf{s}_1)$  and  $P_2(r\mathbf{s}_2)$  are two points in the far zone.

far zone, at two points specified by position vectors  $r\mathbf{s}_1$  and  $r\mathbf{s}_2$ , ( $|\mathbf{s}_1|^2 = 1, |\mathbf{s}_2|^2 = 1$ ), is given by the formula [12, Section 6.3.2]

$$W_s^{(\infty)}(r\mathbf{s}_1, r\mathbf{s}_2, \mathbf{s}_0; \omega) = \frac{S^{(i)}(\omega)}{r^2} \widetilde{C}_F[-k(\mathbf{s}_1 - \mathbf{s}_0), k(\mathbf{s}_2 - \mathbf{s}_0); \omega]. \quad (2.49)$$

Here

$$\widetilde{C}_F[\mathbf{K}_1, \mathbf{K}_2; \omega] = \int_D \int_D C_F(\mathbf{r}'_1, \mathbf{r}'_2; \omega) \exp[-i(\mathbf{K}_1 \cdot \mathbf{r}'_1 + \mathbf{K}_2 \cdot \mathbf{r}'_2)] d^3 r'_1 d^3 r'_2 \quad (2.50)$$

is the six-dimensional Fourier transform of the correlation function of the scattering potential, and

$$\mathbf{K}_1 = -k(\mathbf{s}_1 - \mathbf{s}_0), \quad \mathbf{K}_2 = k(\mathbf{s}_2 - \mathbf{s}_0). \quad (2.51)$$

The vectors  $\mathbf{K}_1$  and  $\mathbf{K}_2$  are analogous to the momentum transfer vector of the quantum mechanical theory of potential scattering. From Eqs. (2.51) it follows that when the unit vector  $\mathbf{s}_1$  varies over all possible directions and the direction  $\mathbf{s}_0$  of incidence is kept fixed, the end points of the vectors  $\mathbf{K}_1$  move on the surface of a sphere of radius  $k$  centered at the point  $k\mathbf{s}_0$  (see Fig. 2.5). Similarly, with  $\mathbf{s}_0$  kept fixed and the direction  $\mathbf{s}_2$  changing, the end points of the vector  $\mathbf{K}_2$  move on the surface of another sphere of radius  $k$  centered at the point with position vector  $-k\mathbf{s}_0$ . Each of these spheres are analogous to the classic Ewald sphere of reflection used in the theory of X-ray diffraction of crystals. It is clear from Eqs. (2.51) that  $0 \leq |\mathbf{K}_1| \leq 2k = 4\pi/\lambda$  and

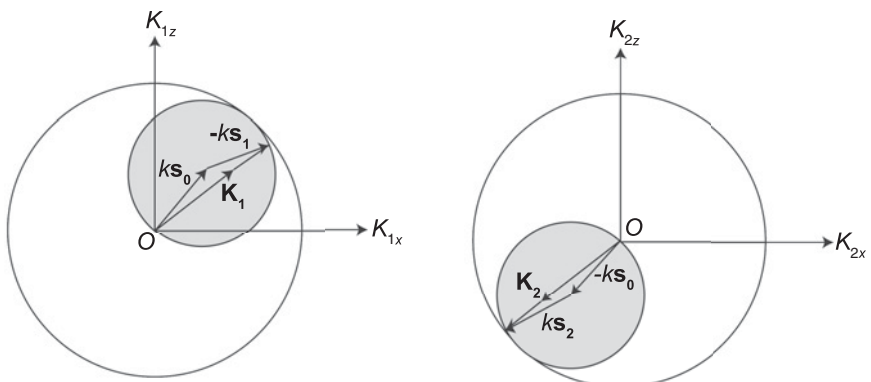


**FIGURE 2.5** The shaded spheres are analogous to the “Ewald’s spheres of reflection” for a particular direction  $\mathbf{s}_0$  of incidence of a plane wave, with wave number  $k$ . These spheres are the region of accessible Fourier components for a particular direction of incidence  $\mathbf{s}_0$ . The large spheres are analogous to the Ewald’s limiting sphere. Adapted from Reference 51.

$0 \leq |\mathbf{K}_2| \leq 2k = 4\pi/\lambda$ , where  $\lambda$  is the wavelength corresponding to the frequency  $\omega$ . Figure 2.5 illustrates the domain of the accessible Fourier components of the two-point spatial correlation function of the scattering potential for a particular direction of incidence  $\mathbf{s}_0$ . However, it follows from Eqs. (2.51) that  $\mathbf{K}_1$  and  $\mathbf{K}_2$  are coupled, because both depend on the vector  $\mathbf{s}_0$ . In fact, it can be shown that they obey the inequality [51]

$$|\mathbf{K}_1 + \mathbf{K}_2| = k|\mathbf{s}_2 - \mathbf{s}_1| \leq \frac{4\pi}{\lambda}. \quad (2.52)$$

Therefore, the Fourier components associated with  $\mathbf{K}_1$  and  $\mathbf{K}_2$  cannot be treated independently. Nonetheless, as  $\mathbf{s}_0$  is varied, the vectors  $(\mathbf{K}_1, \mathbf{K}_2)$  sweep out a continuous, albeit complicated six-dimensional volume  $V(\mathbf{K}_1, \mathbf{K}_2)$  in the Fourier space. Equation (2.49) makes it possible to express the six-dimensional Fourier transform of the correlation function of the scattering potential in terms of the CSD function of the scattered far field. Using Eqs. (2.49) and (2.50), one can obtain an approximation,  $\mathcal{C}_F(\mathbf{r}'_1, \mathbf{r}'_2; \omega)$ , of the correlation function of the scattering potential in terms of the inverse Fourier transform of the CSD function:

$$\begin{aligned} \mathcal{C}_F(\mathbf{r}'_1, \mathbf{r}'_2; \omega) &= \frac{r^2}{(2\pi)^6 S^{(i)}(\omega)} \iint_{V(\mathbf{K}_1, \mathbf{K}_2)} W_s^{(\infty)}(r\mathbf{s}_1, r\mathbf{s}_2, \mathbf{s}_0; \omega) \\ &\quad \exp[i(\mathbf{K}_1 \cdot \mathbf{r}'_1 + \mathbf{K}_2 \cdot \mathbf{r}'_2)] d^3 K_1 d^3 K_2. \end{aligned} \quad (2.53)$$

Evaluation of the integral can be computationally involved in some cases. However, it can be fairly straightforward when the medium possesses certain spatial symmetry.

## 2.5 POLARIZATION PROPERTIES OF STOCHASTIC BEAMS

To analyze the polarization properties of light, one needs to consider the vector nature of the fluctuating electric field. The foundations of the subject was laid down by Stokes in 1852. He described the polarization properties of a light beam in terms of certain parameters, now known as Stokes parameters ([52]; see also [5, 53, 54]). In 1892, Poincaré developed a rigorous mathematical treatment of optical polarization [55]. He introduced the concept of Poincaré sphere, which conveniently represented the state of polarization of a light beam. In the 1930s, a matrix treatment of optical polarization was introduced by Wiener who showed that a relationship may exist between field correlations and polarization properties of light [56]. Later Wolf used the matrix formulation for systematic studies of polarization properties of statistically stationary light beams<sup>11</sup> [57]. For beam-like optical fields, the Stokes–Poincaré representation is equivalent to the Wiener–Wolf matrix representation. In this section, we briefly discuss the matrix representation of the theory.

---

<sup>11</sup>A detailed historical description of the development of the subject can be found in Reference 7.

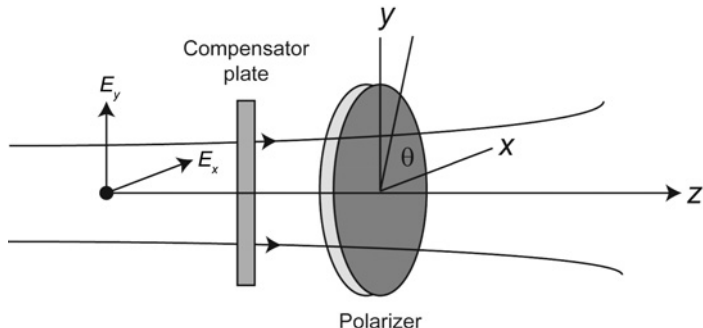


**FIGURE 2.6** A light beam passing through a compensator followed by a polarizer.

### 2.5.1 Matrix Formulation of the Theory of Polarization

Let us consider a statistically stationary light beam propagating along a particular direction. Without any loss of generality, we choose the direction to be along positive  $z$ -axis. As already mentioned [see Eq. (2.14)], in this case the simplest correlation properties of the beam are characterized by the  $2 \times 2$  MC matrix,  $\tilde{\Gamma}(\mathbf{r}_1, \mathbf{r}_2; \tau)$ . Let us define a matrix  $\tilde{J}(\mathbf{r}) \equiv \tilde{\Gamma}(\mathbf{r}, \mathbf{r}; 0)$ . It readily follows from Eq. (2.14) that [5, Section 10.9.1]

$$\tilde{J}(\mathbf{r}) \equiv [J_{ij}(\mathbf{r})] \equiv [\langle E_i^*(\mathbf{r}; t) E_j(\mathbf{r}, t) \rangle], \quad i = x, y, \quad j = x, y. \quad (2.54)$$

The elements of  $\tilde{J}(\mathbf{r})$  are *equal-time* correlation functions of statistically stationary field components and, therefore, have no temporal dependence. This matrix,  $\tilde{J}(\mathbf{r})$ , is often called the coherency matrix. The coherency matrix can characterize the polarization properties of light at a point in space, in the time domain. All the Stoke's parameters can be expressed in terms of its elements [5, Section 10.9.3].

Suppose that the beam passes through a compensator, followed by a polarizer (see Fig. 2.6). The axis of the polarizer makes an angle,  $\theta$ , say, with a chosen  $x$ -direction, so that the electric field vector after passing through the polarizer becomes linearly polarized along a direction making an angle  $\theta$  with the positive  $x$ -axis. The compensator introduces phase delays  $\epsilon_1$  and  $\epsilon_2$  in the  $x$  and the  $y$  components of the electric field, respectively. The average intensity of the light emerging from the polarizer, apart from a constant factor, is given by the expression [5, Section 10.9.1]

$$I(\theta, \epsilon) = J_{xx} \cos^2 \theta + J_{yy} \sin^2 \theta + 2\sqrt{J_{xx}} \sqrt{J_{yy}} \cos \theta \sin \theta |j_{xy}| \cos(\beta_{xy} - \epsilon), \quad (2.55)$$

where  $j_{xy} = J_{xy}/\sqrt{J_{xx}J_{yy}}$ ,  $\epsilon = \epsilon_2 - \epsilon_1$ ,  $\beta_{xy}$  is the argument of  $j_{xy}$ , and dependence on  $\mathbf{r}$  is suppressed for brevity. With the help of this intensity law, it is possible to determine

the elements of the coherency matrix [5, Section 10.9.1], viz.,

$$J_{xx} = I(0, 0), \quad (2.56a)$$

$$J_{yy} = I(\pi/2, 0), \quad (2.56b)$$

$$J_{xy} = \frac{1}{2} [I(\pi/4, 0) - I(3\pi/4, 0)] + \frac{i}{2} [I(\pi/4, \pi/2) - I(3\pi/4, \pi/2)], \quad (2.56c)$$

$$J_{yx} = \frac{1}{2} [I(\pi/4, 0) - I(3\pi/4, 0)] - \frac{i}{2} [I(\pi/4, \pi/2) - I(3\pi/4, \pi/2)]. \quad (2.56d)$$

### 2.5.2 Unpolarized, Polarized, and Partially Polarized Light Beam

If a light beam is unpolarized, the intensity of the light emerging from the polarizer (Fig. 2.6) must be independent of  $\theta$  and  $e$ . From Eq. (2.55), it follows that this will be the case if  $|j_{xy}| = 0$  and  $J_{xx} = J_{yy}$ . Clearly, the coherency matrix of an unpolarized beam has the form [5, Section 10.9.1]

$$\vec{J}^{(u)}(\mathbf{r}) = J_{xx}^{(u)}(\mathbf{r}) \begin{pmatrix} 1 & 0 \\ 0 & 1 \end{pmatrix}. \quad (2.57)$$

In the other extreme case when  $|j_{xy}| = 1$ , the light is completely polarized. One can show that the elements of the corresponding coherency matrix factorize in the form [5, Section 10.9.1]

$$J_{ij}^{(p)}(\mathbf{r}) = \mathcal{E}_i^*(\mathbf{r}) \mathcal{E}_j(\mathbf{r}), \quad (i = x, y; j = x, y), \quad (2.58)$$

where  $\mathcal{E}_i(\mathbf{r})$  is a time-independent deterministic function of position. One can notice that the coherency matrix of a polarized beam is identical with that of a monochromatic electric field  $\mathbf{E}(\mathbf{r}; t) = \mathcal{E}_i(\mathbf{r}) e^{-i\omega t}$ . However, a polarized light beam must not be confused with a monochromatic beam. A light beam of any bandwidth becomes polarized after passing through a polarizer. It can also be shown that if a light beam is filtered to become very narrowband, its degree of polarization might not be equal to unity [58]. We elaborate this point later in Section 2.5.4. Any optical beam, which is neither unpolarized nor polarized, is said to be partially polarized. In other words, its coherency matrix cannot be expressed either in the form (2.57) or in the form (2.58). However, such a coherency matrix can always be uniquely decomposed into the sum of two matrices, one representing an unpolarized field and the other representing a polarized one [5, Section 10.9.2], that is,

$$\vec{J}(\mathbf{r}) = \vec{J}^{(u)}(\mathbf{r}) + \vec{J}^{(p)}(\mathbf{r}). \quad (2.59)$$

Consequently, the average intensity [ $I(\mathbf{r}) \equiv \text{tr}\vec{J}(\mathbf{r})$ ] of any light beam, at a point, has contributions from a completely unpolarized part and from a completely polarized

part. The degree of polarization<sup>12</sup>, at a point  $\mathbf{r}$ , is defined as the ratio of the average intensity of the polarized part to the total average intensity at that point [57]. It is given by the expression<sup>13</sup> [5, Section 10.9.2]

$$\mathcal{P}(\mathbf{r}) \equiv \frac{I^{(p)}(\mathbf{r})}{I(\mathbf{r})} = \sqrt{1 - \frac{4\text{Det}\vec{J}(\mathbf{r})}{[\text{tr}\vec{J}(\mathbf{r})]^2}}, \quad (2.60)$$

where Det denotes the determinant. It is evident that the degree of polarization is always bounded between zero and unity, that is,

$$0 \leq \mathcal{P}(\mathbf{r}) \leq 1. \quad (2.61)$$

It can be readily checked by the use of Eqs. (2.57) and (2.60) that if the light is unpolarized at a point  $\mathbf{r}$ , the degree of polarization  $\mathcal{P}(\mathbf{r}) = 0$ . Similarly from Eqs. (2.58) and (2.60), it follows that the condition,  $\mathcal{P}(\mathbf{r}) = 1$ , implies complete polarization at the point  $\mathbf{r}$ .

### 2.5.3 Statistical Similarity and Complete Polarization

It was pointed out in Section 2.2.2 that the complete spatial coherence can be viewed as the statistical similarity between fluctuating fields at a pair of points. Analogously, one can show that the statistical similarity between two mutually orthogonal components of the fluctuating transverse electric vector at a certain point, implies that the beam is completely polarized at that point. It was shown in Reference 25 that if  $\mathcal{P}(\mathbf{r}) = 1$ , the following relation holds and vice versa<sup>14</sup>:

$$E_y(\mathbf{r}, t) = A(\mathbf{r})E_x(\mathbf{r}, t), \quad (2.62)$$

where  $A(\mathbf{r})$  is a deterministic, generally complex function of position.

Modulus and phase of  $A(\mathbf{r})$  are given by the expressions

$$|A(\mathbf{r})| = \frac{J_{yy}(\mathbf{r})}{J_{xx}(\mathbf{r})}, \quad \arg \{A(\mathbf{r})\} = \arg \{J_{xy}(\mathbf{r})\}. \quad (2.63)$$

Equation (2.62) has an important physical significance. It implies that complete polarization at a point in the beam is achieved if and only if the two mutually orthogonal components of the random electric vector, at that point, *fluctuate in unison*. Figure 2.7 illustrates the statistical similarity between two mutually orthogonal field components.

<sup>12</sup>If the optical field is not beam-like, it is quite challenging to provide an appropriate definition of the degree of polarization. Several definitions have been proposed by different research groups (see, for example, [59–63]; see also [64]).

<sup>13</sup>In the Poincaré sphere representation,  $\mathcal{P}(\mathbf{r})$  represents the distance between the center of the sphere and the point representing the state of polarization.

<sup>14</sup>Analogous relations can also be obtained for complete polarization in the space-frequency domain [65, 66].

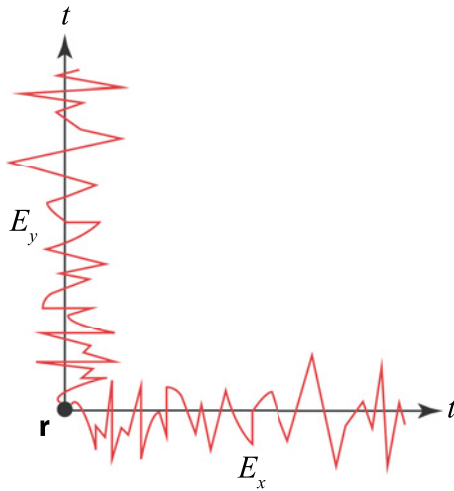


**FIGURE 2.7** Illustrating statistical similarity between two randomly fluctuating orthogonal field components at a point  $\mathbf{r}$ . The temporal dependence of the field components is identical except a multiplicative factor.

It is clear that the concept of statistical similarity elucidates both complete spatial coherence and complete polarization. However, a difference should be noted between the two. In case of complete spatial coherence, one is allowed to accommodate a constant time difference,  $\tau_0$ , in the statistical similarity relations (see Eq. 2.21 and Fig. 2.2). But in the case of complete polarization no time difference can be accommodated in the statistical similarity relation (see Eq. 2.62 and Fig. 2.7).

#### 2.5.4 Polarization Properties of Light in the Frequency Domain

The theory of optical polarization can also be formulated in the space-frequency domain (see, for example, [12, Section 9.2]). The central quantity in that formulation is the *equal-point* CSD matrix<sup>15</sup>  $\overline{W}(\mathbf{r}, \mathbf{r}; \omega)$ . We refer to the matrix  $\overline{W}(\mathbf{r}, \mathbf{r}; \omega)$  as the *spectral polarization matrix* (SP matrix). Following a procedure similar to that discussed in Section 2.5.2, one can obtain general forms of the SP Matrix for unpolarized and polarized light beams. It can be shown that if a light beam is unpolarized, at a frequency  $\omega$ , its SP matrix has the form

$$\overline{W}^{(u)}(\mathbf{r}, \mathbf{r}; \omega) = W_{xx}^{(u)}(\mathbf{r}, \mathbf{r}; \omega) \begin{pmatrix} 1 & 0 \\ 0 & 1 \end{pmatrix}. \quad (2.64)$$

Similarly one can also show that each element of the SP matrix of a completely polarized beam can be factorized in the form

$$W_{ij}^{(p)}(\mathbf{r}, \mathbf{r}; \omega) = \mathcal{E}_i^*(\mathbf{r}; \omega) \mathcal{E}_j(\mathbf{r}; \omega), \quad (i = x, y; j = x, y), \quad (2.65)$$

where  $\mathcal{E}_i(\mathbf{r}; \omega)$  is *not* a random quantity.

<sup>15</sup>See Eqs. (2.31) and (2.32) for definition of the CSD matrix.

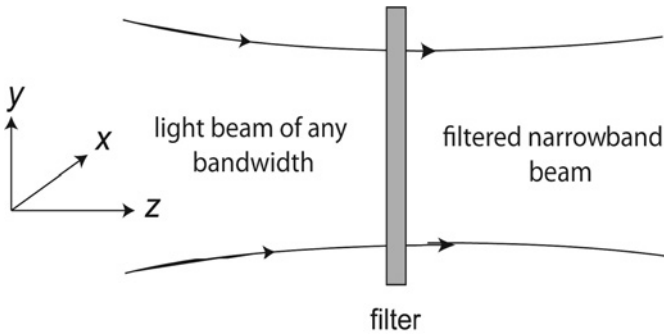


**FIGURE 2.8** An optical beam passing through a narrowband filter (adapted from Reference 58).

It can be proved that the SP matrix of a partially polarized beam, at a point  $\mathbf{r}$ , can always be uniquely decomposed into a polarized and an unpolarized parts, that is,

$$\overrightarrow{W}(\mathbf{r}, \mathbf{r}; \omega) = \overrightarrow{W}^{(u)}(\mathbf{r}, \mathbf{r}; \omega) + \overrightarrow{W}^{(p)}(\mathbf{r}, \mathbf{r}; \omega). \quad (2.66)$$

The spectral degree of polarization (the degree of polarization at a frequency  $\omega$ ) may be introduced in a manner similar to that used in the space-time domain analysis. It is given by the expression [12, Section 9.2]

$$\mathcal{P}(\mathbf{r}; \omega) \equiv \sqrt{1 - \frac{4\text{Det}\overrightarrow{W}(\mathbf{r}, \mathbf{r}; \omega)}{[\text{tr}\overrightarrow{W}(\mathbf{r}, \mathbf{r}; \omega)]^2}}. \quad (2.67)$$

We now discuss the physical significance of the spectral degree of polarization.

Suppose that a statistically stationary electromagnetic beam of arbitrary bandwidth propagates along the positive  $z$ -direction. Suppose further that this beam passes through a linear filter (see Fig. 2.8) and becomes narrowband, with mean frequency  $\omega_0$ . We assume that the effective bandwidth  $\Delta\omega$  of the filtered beam is small compared to its mean frequency  $\omega_0$ , that is,  $\Delta\omega/\omega_0 \ll 1$ .

Let

$$\overline{T}^{(\omega_0)}(\mathbf{r}; \omega) = \begin{pmatrix} T_{xx}^{(\omega_0)}(\mathbf{r}; \omega) & T_{xy}^{(\omega_0)}(\mathbf{r}; \omega) \\ T_{yx}^{(\omega_0)}(\mathbf{r}; \omega) & T_{yy}^{(\omega_0)}(\mathbf{r}; \omega) \end{pmatrix} \quad (2.68)$$

be the transmission matrix of the filter. Such a transformation matrix is generally called a Jones matrix (see, for example, [67, Chap. 9]. Representing the field vectors by column matrices, one can show that each member of the ensemble of the monochromatic realizations of the electric field of the transmitted beam is given by the expression

$$\mathbf{E}^{(\omega_0)}(\mathbf{r}; \omega) = \overline{T}^{(\omega_0)}(\mathbf{r}; \omega) \circ \mathbf{E}(\mathbf{r}; \omega), \quad (2.69)$$

where the superscript  $\omega_0$  indicates that the beam is filtered around that frequency and the product on the right-hand side represents matrix multiplication. By the use of Eqs. (2.32) and (2.69), the CSD matrix of the narrowband beam emerging from the filter can be shown to be given by the formula [68]

$$\overline{W}^{(\omega_0)}(\mathbf{r}_1, \mathbf{r}_2; \omega) = \overline{T}^{(\omega_0)\dagger}(\mathbf{r}_1; \omega) \circ \overline{W}(\mathbf{r}_1, \mathbf{r}_2, \omega) \circ \overline{T}^{(\omega_0)}(\mathbf{r}_2; \omega). \quad (2.70)$$

On using Eqs. (2.31b) and (2.70), the elements of the MC matrix of the filtered narrowband beam are found to be given by

$$\Gamma_{ij}^{(\omega_0)}(\mathbf{r}_1, \mathbf{r}_2; \tau) = \sum_k \sum_l \int_0^\infty T_{ik}^{(\omega_0)*}(\mathbf{r}_1; \omega) T_{jl}^{(\omega_0)}(\mathbf{r}_2; \omega) W_{kl}(\mathbf{r}_1, \mathbf{r}_2; \omega) \exp[-i\omega\tau] d\omega. \quad (2.71)$$

Because of the assumption that  $\Delta\omega/\omega_0 \ll 1$ , the quantity  $W_{kl}(\mathbf{r}_1, \mathbf{r}_2; \omega)$  does not change appreciably as function of frequency  $\omega$  over the narrow bandwidth  $\omega_0 - \Delta\omega/2 \leq \omega \leq \omega_0 + \Delta\omega/2$ , and so is approximately equal to  $W_{kl}(\mathbf{r}_1, \mathbf{r}_2; \omega_0)$ . From Eq. (2.71) it then follows that

$$\begin{aligned} \Gamma_{ij}^{(\omega_0)}(\mathbf{r}_1, \mathbf{r}_2; \tau) &\approx \sum_k \sum_l W_{kl}(\mathbf{r}_1, \mathbf{r}_2; \omega_0) \\ &\quad \int_{\omega_0 - \Delta\omega/2}^{\omega_0 + \Delta\omega/2} T_{ik}^{(\omega_0)*}(\mathbf{r}_1; \omega) T_{jl}^{(\omega_0)}(\mathbf{r}_2; \omega) \exp[-i\omega\tau] d\omega. \end{aligned} \quad (2.72)$$

If one assumes that the filter is homogeneous and isotropic, the elements of the transmission matrix are of the form

$$T_{ij}^{(\omega_0)}(\mathbf{r}; \omega) = T^{(\omega_0)}(\omega) \delta_{ij}, \quad (2.73)$$

where  $\delta_{ij}$  is the Kronecker symbol. From Eqs. (2.72) and (2.73), one then has

$$\Gamma_{ij}^{(\omega_0)}(\mathbf{r}, \mathbf{r}; 0) \approx W_{ij}(\mathbf{r}, \mathbf{r}; \omega_0) \int_{\omega_0 - \Delta\omega/2}^{\omega_0 + \Delta\omega/2} |T^{(\omega_0)}(\omega)|^2 d\omega. \quad (2.74)$$

Using Eqs. (2.60), (2.67), and (2.74) we see at once that

$$\mathcal{P}^{(\omega_0)}(\mathbf{r}) \approx \mathcal{P}(\mathbf{r}; \omega_0), \quad (2.75)$$

where  $\mathcal{P}^{(\omega_0)}(\mathbf{r})$  denotes the degree of polarization in the space-time domain of the narrowband beam of mean frequency  $\omega_0$ . Equation (2.75) implies that if a statistically stationary electromagnetic beam of arbitrary bandwidth is filtered to become narrowband of mean frequency  $\omega_0$ , the space-time degree of polarization of the filtered beam is equal to the spectral degree of polarization at the frequency  $\omega_0$ .

Equation (2.75) also implies that even if a stochastic light beam is filtered to a very narrow frequency range, its degree of polarization may *not* be equal to unity; *its value would depend on the spectral polarization properties of the original beam*. On the other hand, a monochromatic deterministic field *is always completely polarized* [5, Section 1.4.2], that is, its degree of polarization is unity at every point. Thus from Eq. (2.75) one may conclude that, as regards the polarization properties, a narrowband electromagnetic beam cannot, in general, be approximated by the usual monochromatic model [58].

### 2.5.5 Remarks on Polarization Properties of Light in Time and Frequency Domains

It is clear from the discussion of Section 2.5.4 that the spectral degree of polarization,  $\mathcal{P}(\mathbf{r}; \omega)$ , characterizes polarization properties of the beam at a frequency  $\omega$ . However, when all frequencies present in the spectrum are taken into account, the space-time degree of polarization,  $\mathcal{P}(\mathbf{r})$ , represents the polarization properties of the beam. Since the spectrum of an optical field is always distributed over a finite non-zero frequency range, it is reasonable to ask whether a beam can exhibit different polarization properties at different frequencies present in its spectrum. By investigating the connection between  $\mathcal{P}(\mathbf{r})$  and  $\mathcal{P}(\mathbf{r}; \omega)$  in further detail, one can show that the answer to this question is affirmative [69, 70].

The space-time degree of polarization  $\mathcal{P}(\mathbf{r})$  is obtained from the coherency matrix  $[\tilde{J}(\mathbf{r}) = \tilde{\Gamma}(\mathbf{r}, \mathbf{r}; 0)]$ , which does *not* depend on time delay  $\tau$ . On the other hand, the spectral degree of polarization  $\mathcal{P}(\mathbf{r}; \omega)$  is obtained from the SP matrix  $\tilde{W}(\mathbf{r}, \mathbf{r}; \omega)$ , which is the Fourier transform of  $\tilde{\Gamma}(\mathbf{r}, \mathbf{r}; \tau)$ . One may, therefore, expect that the formulas (2.60) and (2.67) do not provide the same information as regards the polarization properties of a beam. It can be established that even if a beam is spectrally polarized at a point and at every frequency, its space-time degree of polarization may not be unity at that point [70]. It can also be shown that  $\mathcal{P}(\mathbf{r}; \omega)$  may vary with frequency  $\omega$  and, therefore, may not be equal to  $\mathcal{P}(\mathbf{r})$  [70, 71]. However,  $\mathcal{P}(\mathbf{r}; \omega)$  would be independent of  $\omega$  and would be equal to  $\mathcal{P}(\mathbf{r})$  if the following conditions hold [71]:

$$\frac{S_x(\mathbf{r}; \omega)}{I_x(\mathbf{r})} = \frac{S_y(\mathbf{r}; \omega)}{I_y(\mathbf{r})}, \forall \omega, \quad (2.76a)$$

$$w_{xy}(\mathbf{r}, \mathbf{r}; \omega) = j_{xy}(\mathbf{r}), \forall \omega, \quad (2.76b)$$

where  $S_x(\mathbf{r}; \omega) = W_{xx}(\mathbf{r}, \mathbf{r}; \omega)$ ,  $S_y(\mathbf{r}; \omega) = W_{yy}(\mathbf{r}, \mathbf{r}; \omega)$ ,  $w_{xy}(\mathbf{r}; \omega) = W_{xy}(\mathbf{r}, \mathbf{r}; \omega)/\sqrt{S_x(\mathbf{r}; \omega)S_y(\mathbf{r}; \omega)}$ , and  $j_{xy}(\mathbf{r}) = J_{xy}(\mathbf{r})/\sqrt{J_{xx}(\mathbf{r})J_{yy}(\mathbf{r})}$ . Equation (2.76a) implies that the normalized spectral densities associated with the  $x$  and the  $y$  components of the field, at a point  $\mathbf{r}$ , are equal to each other for all frequencies present in the spectrum. Equation (2.76b) implies that the normalized space-frequency correlation function of the two mutually orthogonal transverse field components is always equal to the normalized space-time correlation function of the field components.

## 2.6 REMARKS ON PARTIALLY COHERENT AND PARTIALLY POLARIZED BEAMS

It has been mentioned in the beginning of Section 2.5 that polarization properties of a beam can also be analyzed by employing the Stokes–Poincaré formulation. This formulation does not require explicit use of correlation functions of optical field components. Since polarization properties of light have been traditionally studied by the use of this formulation, the importance of statistical fluctuations in the theory of optical polarization has not been properly emphasized for quite some time. The Wiener–Wolf matrix formulation shows that the polarization property of a light beam can be viewed as manifestation of field correlations and thus opens up the possibility of investigating the connection between the coherence and the polarization properties of light.

We have seen that polarization properties of light beams are usually characterized by correlation matrices which depend on a single point,  $\mathbf{r}$ , in space. For example, the spectral polarization properties are described by the SP matrix  $\overline{W}(\mathbf{r}, \mathbf{r}; \omega)$  that is obtained from the CSD matrix,  $\overline{W}(\mathbf{r}_1, \mathbf{r}_2; \omega)$ , by setting  $\mathbf{r}_1 = \mathbf{r}_2 \equiv \mathbf{r}$ . Elements of  $\overline{W}(\mathbf{r}_1, \mathbf{r}_2; \omega)$ , which are functions of two points in space, obey definite propagation laws [see Eq. (2.33)]. However, it is not possible to obtain any such propagation equation for the elements of the SP matrix. This implies that if the SP matrix,  $\overline{W}(\mathbf{r}, \mathbf{r}; \omega)$ , is specified at every point at a secondary source plane, it is, in general, *not* possible to determine the SP matrix at an arbitrary point in the beam. However, if the CSD matrix is specified at every pair of points in a secondary source plane, the SP matrix can be determined at any point in the beam. It is thus clear that although the degree of polarization is defined at a single point, knowledge of *two-point* correlation functions is required for having a deeper insight into the polarization properties of a beam.

Inclusion of the two-point CSD matrix in the theory of optical polarization leads to some interesting observations. The most notable one is probably the discovery that the state of polarization of a beam can change on propagation even through free space [72]. Furthermore, it has been recently shown that unlike the elements of the SP matrix, the elements of the CSD matrix cannot, in general, be expressed in factorized form [73, 74]. Similarly, although the SP matrix of an unpolarized beam is proportional to unit matrix, the CSD matrix is, in general, not so [75]. It is also not possible to decompose the CSD matrix of a partially polarized beam into a polarized and an unpolarized parts, whereas it is possible for the SP matrix [76].

Since elements of two-point correlation matrices can also characterize the spatial coherence of a beam, it gives an indication that spatial coherence and polarization might be related to each other. In fact, many years ago, Wolf called for a unified treatment of the theories of partial coherence and partial polarization [77]. Later it was shown that a two-point correlation matrix can be used to study both spatial coherence and polarization of a quasi-monochromatic light beam [78, 79]. Not long ago, Wolf proposed a unified theory of coherence and polarization of optical beams in the space-frequency domain [80]. The essence of the unified theory lies in the fact

that if the CSD matrix is known at a cross-section of a beam, its spatial coherence and polarization properties can be determined at all cross-sections. This theory also reveals that the propagation law of CSD matrix governs the changes in spectrum, state of coherence and state of polarization of a beam on propagation [81].

Investigation of physical phenomena involving partially coherent and partially polarized optical beams is an active field of research. It has not only led to many interesting results, but also has opened up new research directions. Recently, it has been revealed that some mathematical techniques, which are applied to study quantum entanglement, can also be used in the field of optical coherence and polarization (see, for example, [82, 83]).

## 2.7 BASICS OF QUANTUM THEORY OF OPTICAL COHERENCE

The classical theory of statistical optics does not take into account the effects of measurements. It is, therefore, not useful to analyze certain types of problems, especially the ones, which are related to the detection of single or few light quanta. Such problems can be dealt in the framework of the quantum theory of light. Studies in this subject began with Dirac's quantization of electromagnetic fields [84]. Later Glauber introduced the quantum theory of statistical optics [21, 22]. The subject, being quite vast and important, requires to be dealt in detail with proper attention. The readers are encouraged to read References 8 and 22 for further details. In this section, we briefly discuss the basics of quantum theory of optical coherence to show how some of the concepts introduced in the classical coherence theory can be incorporated into the quantum mechanical version of the theory.

It is well known that in quantum theory any measurable quantity is associated with a Hermitian operator. The Hermitian operator representing a quantized electric field may be expressed in the form<sup>16</sup> [8, Section 10.4.5]

$$\hat{\mathbf{E}}(\mathbf{r}, t) = i \sum_{\mathbf{k}} \sum_s \left( \frac{1}{2} \hbar \omega \right)^{\frac{1}{2}} \left[ \hat{a}_{\mathbf{k},s} C_{\mathbf{k},s} \epsilon_{\mathbf{k},s} e^{i(\mathbf{k} \cdot \mathbf{r} - \omega t)} - \hat{a}_{\mathbf{k},s}^\dagger C_{\mathbf{k},s}^* \epsilon_{\mathbf{k},s}^* e^{-i(\mathbf{k} \cdot \mathbf{r} - \omega t)} \right], \quad (2.77)$$

where the wave vectors  $\mathbf{k}$  labels plane wave modes,  $|\mathbf{k}| = k = \omega/c$ ,  $C_{\mathbf{k},s}$  is a constant, and  $\epsilon_{\mathbf{k},s}$  ( $s = 1, 2$ ) are mutually orthonormal base vectors obeying the conditions<sup>17</sup>

$$\mathbf{k} \cdot \epsilon_{\mathbf{k},s} = 0, \quad \epsilon_{\mathbf{k},s}^* \cdot \epsilon_{\mathbf{k},s'} = \delta_{ss'}, \quad \epsilon_{\mathbf{k},1} \times \epsilon_{\mathbf{k},2} = \mathbf{k}/k. \quad (2.78)$$

<sup>16</sup>Here the field is expanded in discrete modes. Such a representation is useful and appropriate in many cases, for example, when treating an electric field inside a cavity. In more general situations, a continuous mode representation may be employed (see [8, Section 10.10]).

<sup>17</sup>The unit base vectors  $\epsilon_{k1}$ ,  $\epsilon_{k2}$  may be chosen to be complex for general expansion of the field, for example, for resolving the field into two orthogonal components of elliptic polarization.

In the expansion (2.77),  $\hat{a}_{\mathbf{k},s}$  and  $\hat{a}_{\mathbf{k},s}^\dagger$  are the photon annihilation and the photon creation operators, respectively, for the mode labeled by  $\mathbf{k}$  and  $s$ . These operators obey the well-known commutation relations (see, e.g., [8, Section 10.3])

$$[\hat{a}_{\mathbf{k},s}, \hat{a}_{\mathbf{k}',s'}^\dagger] = \delta_{\mathbf{k}\mathbf{k}'}^3 \delta_{ss'}, \quad [\hat{a}_{\mathbf{k},s}, \hat{a}_{\mathbf{k}',s'}] = 0, \quad [\hat{a}_{\mathbf{k},s}^\dagger, \hat{a}_{\mathbf{k}',s'}^\dagger] = 0, \quad (2.79)$$

where  $\delta_{ij}$  is the Kronecker symbol. It is evident from Eq. (2.77) that the electric field operator consists of a positive frequency part

$$\hat{\mathbf{E}}^{(+)}(\mathbf{r}, t) = i \sum_{\mathbf{k}} \sum_s \left( \frac{1}{2} \hbar \omega \right)^{\frac{1}{2}} \hat{a}_{\mathbf{k},s} C_{\mathbf{k},s} \epsilon_{\mathbf{k},s} e^{i(\mathbf{k} \cdot \mathbf{r} - \omega t)} \quad (2.80)$$

and a negative frequency part  $\hat{\mathbf{E}}^{(-)}(\mathbf{r}, t)$ , where  $\hat{\mathbf{E}}^{(-)}(\mathbf{r}; t) = \{\hat{\mathbf{E}}^{(+)}(\mathbf{r}; t)\}^\dagger$ .

The positive and the negative frequency parts of the field operator  $\hat{\mathbf{E}}(\mathbf{r}; t)$  may be introduced in an alternative manner. Let us represent  $\hat{\mathbf{E}}(\mathbf{r}; t)$  as a Fourier integral<sup>18</sup>

$$\hat{\mathbf{E}}(\mathbf{r}; t) = \int_{-\infty}^{\infty} \hat{\mathbf{e}}(\mathbf{r}; \omega) e^{-i\omega t} d\omega. \quad (2.81)$$

Using the Hermitian property of  $\hat{\mathbf{E}}(\mathbf{r}; t)$ , one readily finds that  $\hat{\mathbf{e}}^\dagger(\mathbf{r}; \omega) = \hat{\mathbf{e}}(\mathbf{r}; -\omega)$ . One can now express Eq. (2.81) in the form

$$\hat{\mathbf{E}}(\mathbf{r}; t) = \int_0^{\infty} \hat{\mathbf{e}}(\mathbf{r}; \omega) e^{-i\omega t} d\omega + \int_0^{\infty} \hat{\mathbf{e}}(\mathbf{r}; -\omega) e^{i\omega t} d\omega. \quad (2.82)$$

The first terms on the right is the positive frequency part  $\hat{\mathbf{E}}^{(+)}(\mathbf{r}; t)$  of the electric field operator and the second terms is the negative frequency part  $\hat{\mathbf{E}}^{(-)}(\mathbf{r}; t)$  of the field operator. One can notice that Eq. (2.82) is analogous to Eq. (2.1). Clearly, the classical analogue of  $\hat{\mathbf{E}}^{(+)}(\mathbf{r}; t)$  is the complex analytic signal of a real electric field. However, the operator  $\hat{\mathbf{E}}^{(+)}(\mathbf{r}; t)$ , which consists of photon annihilation operators, has deeper physical significance than its classical counterpart.

The state of the field may be characterized by a state vector  $|i\rangle$  in the Fock space or, more generally, by a density operator<sup>19</sup>  $\hat{\rho} = \{\langle i | i \rangle\}_{\text{average}}$ , where the average is

---

<sup>18</sup>In absence of a Fourier integral, the positive and negative frequency parts of the field may be represented by the formulas [21]

$$\hat{\mathbf{E}}^{(+)}(\mathbf{r}; t) = \lim_{\eta \rightarrow 0+} \frac{1}{2\pi i} \int_{-\infty}^{\infty} \frac{\hat{\mathbf{E}}(\mathbf{r}, t - \tau)}{\tau - i\eta} d\tau,$$

$$\hat{\mathbf{E}}^{(-)}(\mathbf{r}; t) = - \lim_{\eta \rightarrow 0+} \frac{1}{2\pi i} \int_{-\infty}^{\infty} \frac{\hat{\mathbf{E}}(\mathbf{r}, t - \tau)}{\tau + i\eta} d\tau.$$

<sup>19</sup>For a discussion on density operator, see Reference 85.

taken over an appropriate ensemble. The expectation value  $\langle \hat{O} \rangle$  of any operator  $\hat{O}$  is defined, in the usual way, as

$$\langle \hat{O} \rangle = \text{tr} \left\{ \hat{\rho} \hat{O} \right\} = \text{tr} \left\{ \hat{O} \hat{\rho} \right\}. \quad (2.83)$$

Let us now consider detection of a photon by a photo-detector at a space-time point  $(\mathbf{r}, t)$ . We assume the photo-detector to be ideal in the sense that it is of negligible size and has a frequency-independent photo absorbtion probability. Suppose that due to the detection of a photon the field goes from the initial state  $|i\rangle$  to the final state  $|f\rangle$ . Since, in the quantum mechanical interpretation, a photon can be detected only by annihilating (absorbing) it, the probability associated with this process is given by  $|\langle f | \hat{\mathbf{E}}^{(+)}(\mathbf{r}; t) | i \rangle|^2$ . The counting rate in the detector is obtained by summing over all the final states, which can be reached from  $|i\rangle$  by absorption of a photon. Because the states that cannot be reached in this process do not contribute to the result, one can extend the summation over a complete set of final states. The counting rate of the detector then becomes proportional to

$$\sum_f |\langle f | \hat{\mathbf{E}}^{(+)}(\mathbf{r}; t) | i \rangle|^2 = \langle i | \hat{\mathbf{E}}^{(-)}(\mathbf{r}; t) \cdot \hat{\mathbf{E}}^{(+)}(\mathbf{r}; t) | i \rangle, \quad (2.84)$$

where the dot ( $\cdot$ ) denotes scalar product. If one considers the random fluctuations associated with light, that is, if one allows the possibility of having a statistical ensemble of initial states  $|i\rangle$ , one leads to a more general expression involving the density operator. The average counting rate of a photo-detector placed at a position  $\mathbf{r}$  at time  $t$  then becomes proportional to

$$\mathcal{R}(\mathbf{r}; t) \equiv \text{tr} \left\{ \hat{\rho} \hat{\mathbf{E}}^{(-)}(\mathbf{r}; t) \cdot \hat{\mathbf{E}}^{(+)}(\mathbf{r}; t) \right\} = \left\langle \hat{\mathbf{E}}^{(-)}(\mathbf{r}; t) \cdot \hat{\mathbf{E}}^{(+)}(\mathbf{r}; t) \right\rangle. \quad (2.85)$$

The classical counterpart of  $\mathcal{R}(\mathbf{r}; t)$  is the average intensity discussed earlier.

The first(lowest)-order correlation properties of light may be specified by a  $3 \times 3$  correlation matrix [21]

$$\begin{aligned} \overline{G}^{(1)}(\mathbf{r}, t; \mathbf{r}', t') &\equiv \left[ G_{\mu\nu}^{(1)}(\mathbf{r}, t; \mathbf{r}', t') \right] \\ &\equiv \left[ \text{tr} \left\{ \hat{\rho} \hat{E}_\mu^{(-)}(\mathbf{r}, t) \hat{E}_\nu^{(+)}(\mathbf{r}', t') \right\} \right], \end{aligned} \quad (2.86)$$

where  $\mu, \nu$  label the mutually orthogonal components of the electric field operator. It is important to note that  $\hat{\mathbf{E}}^{(-)}(\mathbf{r}; t)$  and  $\hat{\mathbf{E}}^{(+)}(\mathbf{r}; t)$  do not commute with each other. The order in which they appear in Eqs. (2.85) and (2.86) must, therefore, be strictly maintained.

For the sake of simplicity, let us neglect the polarization properties of the light. In this case, with a suitable choice of axes, only one element  $G_{\mu\mu}^{(1)}(\mathbf{r}, t; \mathbf{r}', t')$  (no

summation over repeated indices) of  $\tilde{G}^{(1)}(\mathbf{r}, t; \mathbf{r}', t')$  would completely characterize the first-order correlation properties of the field in the space-time domain. We omit the suffix  $\mu$  and write

$$G^{(1)}(\mathbf{r}, t; \mathbf{r}', t') = \text{tr} \left\{ \hat{\rho} \hat{E}^{(-)}(\mathbf{r}; t) \hat{E}^{(+)}(\mathbf{r}'; t') \right\}. \quad (2.87)$$

The first-order coherence properties of light, in the space-time domain, are characterized by the correlation function  $\tilde{G}^{(1)}(\mathbf{r}, t; \mathbf{r}', t')$ . One can define the first-order degree of coherence by the formula [21]

$$g^{(1)}(\mathbf{r}, t; \mathbf{r}', t') \equiv \frac{G^{(1)}(\mathbf{r}, t; \mathbf{r}', t')}{\sqrt{G^{(1)}(\mathbf{r}, t; \mathbf{r}, t)} \sqrt{G^{(1)}(\mathbf{r}', t'; \mathbf{r}', t')}}. \quad (2.88)$$

The modulus of  $g^{(1)}(\mathbf{r}, t; \mathbf{r}', t')$  may be shown to be bounded by zero and unity [21], that is,

$$0 \leq |g^{(1)}(\mathbf{r}, t; \mathbf{r}', t')| \leq 1. \quad (2.89)$$

It can be shown that this quantity is related to fringe visibility in interference experiments (see, e.g., [22, Section 2.7.2]). Complete first-order coherence is characterized by the condition  $|g^{(1)}(\mathbf{r}, t; \mathbf{r}', t')| = 1$ , and complete first-order incoherence by  $g^{(1)}(\mathbf{r}, t; \mathbf{r}', t') = 0$ . Although Eq. (2.88) looks similar to Eq. (2.11), one must appreciate the fact that the quantum mechanical formulation is much more effective as one goes to a low-intensity range where one needs to consider the effects of absorption or emission of one or few numbers of photons.

## 2.8 CONCLUDING REMARKS

We have discussed the classical theory of optical coherence both in the space-time and the space-frequency domains. We have shown how coherence properties of light can be used in inverse-scattering problems to determine structures of random media. There are, of course, many other applications of the coherence theory in imaging science, for example, in microscopy and tomography. The space-frequency formulation of the theory is often used to study the change of correlation properties of light on propagation and on scattering. These studies led to the discovery of some interesting physical phenomena. Two examples of such phenomena are correlation-induced spectral changes on propagation [31] and on scattering [86]. Recently, it has also been shown that coherence properties of light can change on refraction and on reflection at a planar interface separating two media [87] and furthermore on propagation through a stratified medium [88].

We have provided a brief discussion of the quantum theory of optical coherence in the space-time domain. Although not included in this chapter, the theory can also be formulated in the space-frequency domain [89].

We have also given an overview of the classical theory of optical polarization. Although we have not discussed the quantum theory of optical polarization, a noticeable amount of work has been done on this subject. The quantum mechanical operators for the classical Stokes parameters have been introduced by Fano [90]. Some implications of quantum theory on polarization properties of light have been briefly discussed by Glauber [21]. Further work on nonclassical optical polarization has also been done by Luis [91, 92]. Recently, the Wiener–Wolf formulation of the theory of optical polarization has been explored in the quantum domain [93]. Polarization properties of light generated by superposition in a single-photon interference experiment have also been analyzed; the analysis reveals that wave–particle duality can play an important role in determining the polarization properties of the light generated by superposition [94].

Coherence and statistical optics is an important branch of optics. In this chapter, we have restricted ourselves to the lowest order correlation properties of light. However, optical phenomena involving higher order correlation functions are also important topics of research both in classical and quantum optics.

## ACKNOWLEDGMENTS

The author thanks Professor Emil Wolf for many helpful discussions. This work was carried out during the author's stay at the Department of Physics and Astronomy, University of Rochester, NY, USA and was supported by the US Air Force Office of Scientific Research under grant No. FA9550-12-1-0284.

## REFERENCES

- [1] T. Young, “An account of some cases of the production of colours, not hitherto described,” *Phil. Trans. Roy. Soc. Lond.* **92**, 387 (1802).
- [2] F. Zernike, “The concept of degree of coherence and its application and its application to optical problems,” *Physica* **5**, 785 (1938).
- [3] E. T. Whittaker, *A History of the Theories of Aether and Electricity: From the Age of Descartes to the Close of the Nineteenth Century* (Longmans, Green, and Co., London, 1910).
- [4] E. T. Whittaker, *A History of the Theories of Aether and Electricity, Vol. 2: The Modern Theories, 1900-1926* (Harper, 1960).
- [5] M. Born and E. Wolf, *Principles of Optics*, 7th ed. (Cambridge University Press, Cambridge, 1999).
- [6] E. Wolf, “The influence of Young's interference experiment on the development of statistical optics,” *Prog. Opt.* **50**, 251 (2007).
- [7] C. Brosseau, “Polarization and coherence optics: historical perspective, status, and future directions,” *Prog. Opt.* **54**, 149 (2010).
- [8] L. Mandel and E. Wolf, *Optical Coherence and Quantum Optics* (Cambridge University Press, Cambridge, 1995).

- [9] D. Gabor, “Theory of communication”, *J. Inst. Elec. Eng.* (London) **93**, Pt. III, 429 (1946).
- [10] N. Wiener, “Generalized harmonic analysis”, *Acta Math.* **55**, 117 (1930).
- [11] E. Wolf, “A macroscopic theory of interference and diffraction of light from finite sources II. Fields with a spectral range of arbitrary width,” *Proc. Roy. Soc. (London) A* **230**, 246 (1955).
- [12] E. Wolf, *Introduction to the Theory of Coherence and Polarization of Light* (Cambridge University Press, Cambridge, 2007).
- [13] B. Karczewski, “Coherence theory of the electromagnetic field,” *Nuovo Cimento* **30**, 906 (1963).
- [14] J. Tervo, T. Setälä, and A. T. Friberg, “Degree of coherence for electromagnetic fields,” *Opt. Exp.* **11**, 1137 (2003).
- [15] T. Setälä, J. Tervo, and A. T. Friberg, “Complete electromagnetic coherence in the space-frequency domain,” *Opt. Lett.* **29**, 328 (2004).
- [16] E. Wolf, “Comment on complete electromagnetic coherence in the space-frequency domain,” *Opt. Lett.* **29**, 1712 (2004).
- [17] T. Setälä, J. Tervo, and A. T. Friberg, “Reply to comment on complete electromagnetic coherence in the space-frequency domain,” *Opt. Lett.* **29**, 1713 (2004).
- [18] P. Réfrégier, “Mutual information-based degrees of coherence of partially polarized light with Gaussian fluctuations,” *Opt. Lett.* **30**, 3117 (2005).
- [19] P. Réfrégier and F. Goudail “Invariant degrees of coherence of partially polarized light,” *Opt. Exp.* **13**, 6051 (2005).
- [20] A. Luis, “Degree of coherence for vectorial electromagnetic fields as the distance between correlation matrices,” *J. Opt. Soc. Am. A* **24**, 1063 (2007)
- [21] R. J. Glauber, “The quantum theory of optical coherence” *Phys. Rev.* **130**, 2529 (1963).
- [22] R. J. Glauber, *Quantum Theory of Optical Coherence (Selected Papers and Lectures)* (WILEY-VCH Verlag GmbH & Co. KGaA, Weinheim, 2007).
- [23] E. Verdet, “Etude sur la constitution de la lumiere non polarisée et de la lumiere partiellement polarisée,” *Annales scientifiques de l'E.N.S.* **2**, 291 (1865).
- [24] S. Ponomarenko, H. Roychowdhury, and E. Wolf, “Physical significance of complete spatial coherence of optical fields,” *Phys. Lett. A* **345**, 10–12 (2005).
- [25] H. Roychowdhury and E. Wolf, “Statistical similarity and the physical significance of complete spatial coherence and complete polarization of random electromagnetic beams”, *Opt. Commun.* **248**, 327 (2005).
- [26] E. Wolf, “Statistical similarity as a unifying concept of the theories of coherence and polarization of light”, *Opt. Commun.* **283**, 4427 (2010).
- [27] E. Wolf, “New spectral representation of random sources and of the partially coherent fields that they generate”, *Opt. Commun.* **38**, 3 (1981).
- [28] E. Wolf, “New theory of partial coherence in the space-frequency domain. Part I: spectra and cross spectra of steady-state sources,” *J. Opt. Soc. Am.* **72**, 343 (1982).
- [29] E. Wolf, “New theory of partial coherence in the space-frequency domain. Part II: steady-state fields and higher-order correlations,” *J. Opt. Soc. Am. A* **3**, 76 (1986).
- [30] E. Wolf, “Invariance of the spectrum of light on propagation,” *Phys. Rev. Lett.* **56**, 1370 (1986).

- [31] E. Wolf, “Non-cosmological redshifts of spectral lines” *Nature* **326**, 363 (1987).
- [32] D. F. V. James and E. Wolf, “Determination of the degree of coherence of light from spectroscopic measurements”, *Opt. Commun.* **145**, 1 (1998).
- [33] H. Roychowdhury and E. Wolf, “Determination of the electric cross-spectral density matrix of a random electromagnetic beam”, *Opt. Commun.* **226**, 57 (2003).
- [34] B. Kanseri and H. Kandpal, “Experimental determination of electric cross-spectral density matrix and generalized Stokes parameters for a laser beam,” *Opt. Lett.* **33**, 2410 (2010).
- [35] M. Lahiri and E. Wolf, “Implications of complete coherence in the space-frequency domain,” *Opt. Lett.* **36**, 2423 (2011).
- [36] W. P. Alford and A. Gold, “Laboratory measurement of the velocity of light,” *Amer. J. Phys.* **56**, 481 (1957).
- [37] M. P. Givens, “Photoelectric detection of interference between two Light beams having a large path difference,” *J. Opt. Soc. Am.* **51**, 1030 (1961).
- [38] L. Mandel, “Interference and the Alford and Gold effect,” *J. Opt. Soc. Am.* **52**, 1335 (1962).
- [39] L. Mandel, “Spectral coherence and the concept of cross-spectral purity,” *J. Opt. Soc. Am.* **51**, 1342 (1961).
- [40] L. Mandel and E. Wolf, “Concept of cross-spectral purity in coherence theory,” *J. Opt. Soc. Am.* **66**, 529 (1976).
- [41] M. Lahiri and E. Wolf, “Relationship between complete coherence in the space-time and in the space-frequency domains,” *Phys. Rev. Lett.* **105**, 063901 (2010).
- [42] M. Lahiri and E. Wolf, “Statistical similarity and cross-spectral purity of stationary stochastic fields,” *Opt. Lett.* **37**, 963 (2012).
- [43] W. Friedrich, P. Knipping, and M. von Laue, Sitzungsberichte d. Bayer (Akademie der Wissenschaften), 1912), p. 303.
- [44] W. H. Bragg, “X rays and crystals,” *Nature* **90**, 219 (1912).
- [45] W. L. Bragg, “The specular reflection of X rays,” *Nature* **90**, 410 (1912).
- [46] W. L. Bragg, “The diffraction of short electromagnetic waves by a crystal,” *Proc. Camb. Phil. Soc.* **17**, 43 (1913).
- [47] P. P. Ewald, “Zur Theorie der Interferenzen der Röntgenstrahlen in Kristallen,” *Phys. Zeit.* **14**, 465 (1913).
- [48] P. P. Ewald, “Das “reziproke Gitter” in der Strukturtheorie,” *Zeit. f. Krist.* **56**, 129 (1921).
- [49] G. E. Bacon, *X-ray and Neutron Diffraction* (Pergamon Press, 1966).
- [50] A. Ishimaru, *Wave Propagation and Scattering in Random Media* (Academic Press, New York, 1978), Vols. 1 and 2.
- [51] M. Lahiri, E. Wolf, D. G. Fischer, and T. Shirai, “Determination of correlation functions of scattering potentials of stochastic media from scattering experiments,” *Phys. Rev. Lett.* **102**, 123901 (2009).
- [52] G. G. Stokes, “On the composition and resolution of streams of polarized light from different sources,” *Trans. Cambr. Phil. Soc.* **9**, 399 (1852).
- [53] C. Brosseau, *Fundamentals of Polarized Light: A Statistical Optics Approach* (Wiley, 1995).
- [54] E. Collett, *Polarized Light : Fundamentals and Applications* (Marcel Dekker, New York, 1993).

- [55] H. Poincaré, *Théorie Mathématique de la Lumière: Vol. 2* (Georges Carré, Paris, 1892).
- [56] N. Wiener, “Coherency matrices and quantum theory”, *J. Math. Phys. (M.I.T.)* **7**, 109 (1927–1928).
- [57] E. Wolf, “Coherence properties of partially polarized electromagnetic radiation”, *Nuovo Cimento* **13**, 1165 (1959).
- [58] M. Lahiri and E. Wolf, “Does a light beam of very narrow bandwidth always behave as a monochromatic beam?” *Phys. Lett. A* **374**, 997 (2010).
- [59] T. Setälä, A. Shevchenko, M. Kaivola, and A. T. Friberg, “Degree of polarization for optical near fields,” *Phys. Rev. E* **66**, 016615 (2002).
- [60] J. Ellis, A. Dogariu, S. Ponomarenko, and E. Wolf, “Degree of polarization of statistically stationary electromagnetic fields,” *Opt. Commun.* **248**, 333–337 (2005).
- [61] A. Luis, “Degree of polarization for three-dimensional fields as a distance between correlation matrices,” *Opt. Commun.* **253**, 10–14 (2005).
- [62] M. R. Dennis, “A three-dimensional degree of polarization based on Rayleigh scattering,” *J. Opt. Soc. Am. A* **24**, 2065 (2007).
- [63] X.-F. Qian and J. H. Eberly, “Entanglement and classical polarization states,” *Opt. Lett.* **36**, 4110 (2011).
- [64] C. Brosseau and A. Dogariu, “Symmetry properties and polarization descriptors for an arbitrary electromagnetic wavefield,” *Prog. Opt.* **49**, 315 (2006).
- [65] M. Lahiri, “Contributions to the Theories of Coherence and Polarization of Light,” Doctoral thesis, University of Rochester, (2012).
- [66] J. Chen, Y. Chen, F. Chen, Y. Xin, Y. Wang, Q. Zhao, and M. Zhou, “Physical significance of complete coherence and complete polarization of random electromagnetic beams in the space-frequency domain,” *Opt. Las. Tech.* **47**, 174 (2013).
- [67] E. L. O’Neill, *Introduction to Statistical Optics* (Addison-Wesley Publication Company, Inc., 1963)
- [68] O. Korotkova and E. Wolf, “Effects of linear non-image-forming devices on spectra and on coherence and polarization properties of stochastic electromagnetic beams: part-I General theory,” *J. Mod. Opt.* **52**, 2659 (2005).
- [69] M. Lahiri, “Polarization properties of stochastic light beams in the space-time and space-frequency domains,” *Opt. Lett.* **34**, 2936 (2009).
- [70] T. Setälä, F. Nunziata, and A. T. Friberg, “Differences between partial polarizations in the space-time and space-frequency domains,” *Opt. Lett.* **34**, 2924 (2009).
- [71] M. Lahiri, “Concept of purity in the theory of optical polarization,” *Opt. Lett.* **38**, 866 (2013).
- [72] D. F. V. James, “Change in polarization of light beams on propagation in free space,” *J. Opt. Soc. Am. A* **11**, 1641 (1994).
- [73] F. Gori, “Partially correlated sources with complete polarization,” *Opt. Lett.* **33**, 2818–2820 (2008).
- [74] M. Lahiri and E. Wolf, “Cross-spectral density matrix of polarized light beams,” *Opt. Lett.* **34**, 557 (2009).
- [75] F. Gori, J. Tervo, and J. Turunen, “Correlation matrices of completely unpolarized beams,” *Opt. Lett.* **34**, 1447–1449 (2009).
- [76] E. Wolf, “Can a light beam be considered to be the sum of a completely polarized and a completely unpolarized beam?” *Opt. Lett.* **33**, 642 (2008).

- [77] E. Wolf, “Optics in terms of observable quantities,” *Nuovo Cimento* **12**, 884 (1954).
- [78] F. Gori, “Matrix treatment for partially polarized, partially coherent beams,” *Opt. Lett.* **23**, 241 (1998).
- [79] F. Gori, M. Santarsiero, S. Vicalvi, R. Borghi, and G. Guattari, “Beam coherence-polarization matrix,” *Pure Appl. Opt.* **7**, 941 (1998).
- [80] E. Wolf, “Unified theory of coherence and polarization of random electromagnetic beams,” *Phys. Lett. A* **312**, 263 (2003).
- [81] E. Wolf, “Correlation-induced changes in the degree of polarization, the degree of coherence, and the spectrum of random electromagnetic beams on propagation” *Opt. Lett.* **28**, 1078 (2003).
- [82] B. N. Simon, S. Simon, F. Gori, M. Santarsiero, R. Borghi, N. Mukunda, and R. Simon, “Nonquantum entanglement resolves a basic issue in polarization optics,” *Phys. Rev. Lett.* **104**, 023901 (2010).
- [83] K. H. Kagalwala, G. D. Giuseppe, A. F. Abouraddy, and B. E. A. Saleh, “Bell’s measure in classical optical coherence,” *Nat. Phot.* **7**, 72–78 (2013).
- [84] P. A. M. Dirac, *The Principles of Quantum Mechanics*, 4th ed. (Oxford University Press, Oxford, 1957).
- [85] U. Fano, “Description of states in quantum mechanics by density matrix and operator techniques,” *Rev. Mod. Phys.* **29**, 74 (1957).
- [86] E. Wolf, J. T. Foley, and F. Gori, “Frequency shifts of spectral lines produced by scattering from spatially random media,” *J. Opt. Soc. Am. A* **6**, 1142 (1989).
- [87] M. Lahiri and E. Wolf, “Theory of refraction and reflection with partially coherent electromagnetic beams,” *Phys. Rev. A* **86**, 043815 (2012).
- [88] M. Lahiri and E. Wolf, “Propagation of electromagnetic beams of any state of spatial coherence and polarization through multilayered stratified media,” *J. Opt. Soc. Am. A* **30**, 2547 (2013).
- [89] M. Lahiri and E. Wolf, “Quantum theory of optical coherence of non-stationary light in the space-frequency domain ,” *Phys. Rev. A* **82**, 043837 (2010).
- [90] U. Fano, “A Stokes-parameter technique for the treatment of polarization in quantum mechanics”, *Phys. Rev.* **93**, 121 (1954).
- [91] A. Luis, “Degree of polarization in quantum optics,” *Phys. Rev. A* **66**, 013806 (2002).
- [92] A. Luis, “Nonclassical polarization states,” *Phys. Rev. A* **73**, 063806 (2006).
- [93] M. Lahiri and E. Wolf, “Quantum analysis of polarization properties of optical beams,” *Phys. Rev. A* **82**, 043805 (2010).
- [94] M. Lahiri, “Wave-particle duality and partial polarization of light in single-photon interference experiments,” *Phys. Rev. A* **83**, 045803 (2011).

---

# 3

---

## LIGHT BEAMS WITH SPATIALLY VARIABLE POLARIZATION

ENRIQUE J. GALVEZ

*Department of Physics and Astronomy, Colgate University, Hamilton, NY, USA*

### 3.1 INTRODUCTION

Polarization optics is a mature field of photonics technology. The fundamentals are amply treated in countless textbooks and journal articles. Yet, new developments have come forward that deserve revisiting new treatments and manipulation of polarization that are opening new research topics and creating new applications. The purpose of this chapter is to bring attention to emerging aspects of polarization optics that bring new impetus to established principles and proven technologies.

These new developments are connected to the polarization of optical beams. As it is well known, the uniform polarization of an optical beam can be understood in terms of well-characterized states of the electromagnetic field. A modern field of research and technology involves the study of spatial modes of the electromagnetic field, which only 20 years ago led to the discovery of orbital angular momentum [1, 2], a form of angular momentum that is encoded in wavefronts that have a helical shape. There is renewed interest in spatial modes: some old, such as Hermite–Gauss [3]; some also old but seen in a new light, such as Laguerre–Gauss [4]; and some novel, such as Bessel– [5], Mathieu– [6], Ince–Gaussian [7], and rediscovered Airy beams [8]. These are just salient examples, of a vibrant growing collection of beam studies, known as Complex Light or Structured Light [9].

In parallel with these researches has come the study of the forces that optical beams can exert on matter, and the applications of these, channeled mainly through a modern

device: optical tweezers. Spatial modes and polarization are currently used to exert forces and torques to trap, manipulate, channel, sort, bind, and spin material particles of various compositions, sizes, and shapes. Research in complex light has also made inroads in finding new ways to encode information, both quantum mechanical [10] and classical [11].

The emergence of multi-modal beams, of combined spatial mode and polarization, topic of this chapter, has interesting features and applications that are only starting to be realized. Such multi-modal beams result in optical beams that exhibit transverse modes where the polarization state varies from point to point. It is a class of beams that had its beginnings in vector beams, with notable cases being radial and azimuthal vector beams [12], where the mode consists of a field of linearly polarized states pointing either radially outward or perpendicularly to the radial direction, respectively. Further work has produced more elaborate manifestations, with multi-modes exhibiting all polarization states, also referred to as full-Poincaré, or simply Poincaré modes, because they contain single or multiple mappings of the Poincaré sphere, onto points along the transverse mode of the beam.

This class of beams falls under an interesting new category of optical beams, called singular beams. These are beams that contain points in their transverse mode where one or more parameters of the polarization state, or wave attribute, are undefined or singular. Polarization singularities emerged in theoretical treatments that have preceded experiments [13–16]. Only recently, different technologies have been able to produce singular beams of various forms, as is described later in more detail. In this chapter we will describe their main characteristics framed in terms of state superpositions, which in itself is a method of production of singular beams.

In the second section we review the formalism of polarization and mode. The third section covers the methods of production of singular beams, and the fourth section discusses the studies of polarization singularities.

## 3.2 POINCARÉ MODES OF BEAMS

There are two aspects to the discussion presented here. One involves a polarization component, and the other a spatial mode component. So we divide this section into three subsections: 3.2.1, to discuss polarization; 3.2.2, to discuss spatial modes; and 3.2.3, to discuss the combined spatial-polarization mode.

### 3.2.1 States of Polarization

The Poincaré sphere is the fundamental graphical object to represent the states of polarization. A unique point on the surface of the sphere represents a pure state of polarization. Major states are the north and south poles of the sphere, which represent the states of right and left circular polarization, respectively. We use the convention in optics for these states, in which at any given time the electric field of the light describes a right-handed corkscrew along the propagation direction. Conversely, when looking into the beam, the electric field rotates clockwise in any plane that is

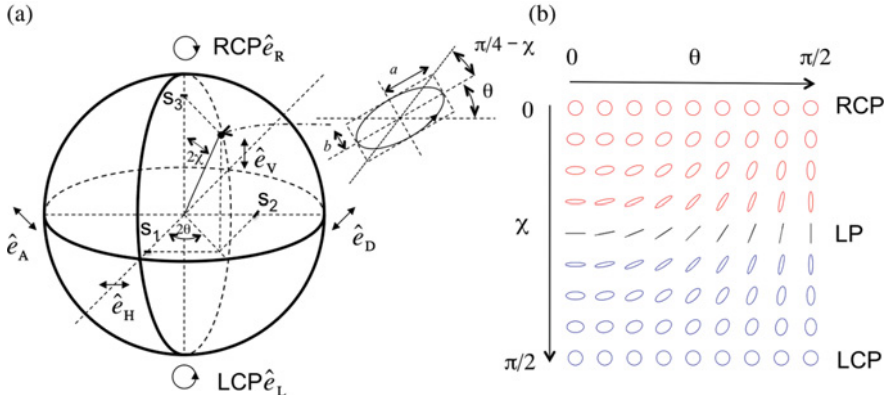


**FIGURE 3.1** (a) Poincaré sphere and (b) states of polarization as a function of the angles  $\chi$  and  $\theta$ . Right- and left-handed ellipses are colored red and blue, respectively. (For a color version of this figure, see the color plate section.)

transverse to the propagation direction [17, 18]. Points along the equator of the sphere are those representing all the orientations of linear polarization, with antipodes having orthogonal orientations. The northern and southern hemispheres represent points of right-handed and left-handed elliptical polarization, respectively, with the ratio of the semiminor to the semimajor axes decreasing when going from a pole to the equator along a meridian, and with semimajor axis orientation varying when going around the sphere along a parallel. The Poincaré sphere is shown in Figure 3.1a.

The sphere is centered at the origin of a set of coordinate axes that is aligned with three pairs of polarization eigenstates, as shown in Figure 3.1a. The ends of one axis denote the right- and left-handed circular polarization states by  $\hat{e}_R$  and  $\hat{e}_L$ , respectively. A second axis is aligned with the  $x$ - and  $y$ -linearly polarized states, which we refer to, respectively, as horizontally and vertically polarized light, and denote respectively as  $\hat{e}_H$  and  $\hat{e}_V$ . The third axis is aligned with the linearly polarized states oriented at 45 degrees to the horizontal axis, defined as diagonal,  $\hat{e}_D = 2^{-1/2}(\hat{e}_H + \hat{e}_V)$ ; and antidiagonal,  $\hat{e}_A = 2^{-1/2}(-\hat{e}_H + \hat{e}_V)$ .

We can represent any state of polarization by superpositions of eigenstates. Using the circular basis, we express it as

$$\hat{e} = \hat{e}_R e^{i\theta} \cos \chi + \hat{e}_L e^{-i\theta} \sin \chi. \quad (3.1)$$

This notation is convenient for the reasons illustrated in Figure 3.1. The variable  $\chi$ , which is half the polar angle of the sphere, determines the ratio of the amplitudes of the two circular polarization components, and consequently, the ellipticity of the state of polarization, defined as

$$\epsilon = \tan(\pi/4 - \chi) = \frac{b}{a}, \quad (3.2)$$

where  $b$  and  $a$  are the semiminor and semimajor axes of the ellipse, respectively.

Note a few important consequences: when the two circularly polarized eigenstates have the same amplitude (i.e.,  $\chi = \pi/4$ ), the total polarization is linear; and when either eigenstate dominates ( $0 < \chi < \pi/4$  or  $\pi/4 < \chi < \pi/2$ ), the polarization is elliptical of the same handedness as the dominant eigenstate, and with ellipticity given by Eq. (3.2); and circular polarization states result when one of the eigenstates has zero amplitude. The angle  $\theta$ , half of the phase difference between the two eigenstates, is the orientation of the semimajor axis of the ellipse (or orientation of linear polarization) regardless of the value of the ellipticity. A map of polarization states in terms of the variables  $\chi$  and  $\theta$  is shown in Figure 3.1b.

We could equally represent states in terms of the other two mentioned pairs of eigenstates, either the conventional linear horizontal and vertical:

$$\hat{e} = \hat{e}_H e^{i\varphi} \cos \eta + \hat{e}_V e^{+i\varphi} \sin \eta, \quad (3.3)$$

or the diagonal and antidiagonal:

$$\hat{e} = \hat{e}_D e^{i\alpha} \cos \xi + \hat{e}_A e^{+i\alpha} \sin \xi, \quad (3.4)$$

where  $2\chi$ ,  $2\eta$ , and  $2\xi$  are the angles that  $\hat{e}$  makes with the three axes, as shown in Figure 3.2. The normalized Stokes parameters  $s_1$ ,  $s_2$ , and  $s_3$  are the coordinates of the radius vector representing the state of polarization,  $\hat{e}$ . Therefore, we can express them as

$$s_1 = \cos 2\eta = \cos^2 \eta - \sin^2 \eta = \frac{I_H - I_V}{I_0}, \quad (3.5)$$

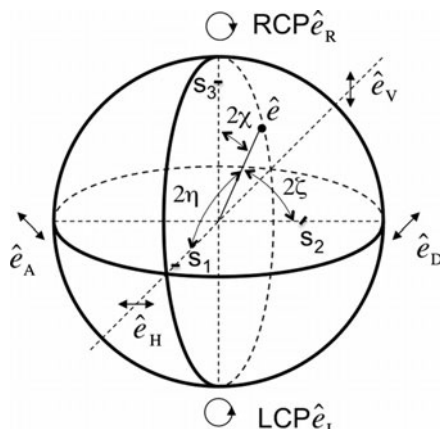


**FIGURE 3.2** Poincaré sphere showing the angles that define the Stokes parameters of a particular state of polarization  $\hat{e}$ .

where  $I_H$  and  $I_V$  are the intensities of the light that would be transmitted through H and V polarizers, respectively, and  $I_0 = I_H + I_V$  is the total intensity (assuming totally coherent light). Similarly, the other parameters are given by

$$s_2 = \cos 2\xi = \frac{I_D - I_A}{I_0} \quad (3.6)$$

and

$$s_3 = \cos 2\chi = \frac{I_R - I_L}{I_0}, \quad (3.7)$$

where  $I_D$ ,  $I_A$ ,  $I_R$ ,  $I_L$  are the intensities past filters that transmit, respectively, D, A, R, and L states. Thus, the six intensity measurements can be used to define state  $\hat{e}$ . Indeed, this is a standard method of polarimetry.

### 3.2.2 Spatial Modes

As mentioned earlier, there are numerous families of spatial modes that have been studied in recent years. None have attracted as much attention as Laguerre–Gauss (LG) modes. Their intrinsic interest is that via the orbital angular momentum that they can carry, they add a novelty that was not present when spatial modes were first studied, as part of the development of lasers. Our discussion is going to be limited to LG beams, but we should be mindful that there is a rich variety of beams that can be used. We focus on LG beams because they are symmetric, which provide a convenient setting for the production of Poincaré beams.

The scalar portion of the amplitude of an LG beam is given in cylindrical coordinates as [1, 4]

$$\text{LG}_p^\ell = A_{p,\ell} r^{|\ell|} e^{i\ell\phi} G L_p^{|\ell|} W, \quad (3.8)$$

where

$$A_{p,\ell} = \left( \frac{p! 2^{|\ell|+1}}{\pi(|\ell|+p)!} \right)^{1/2} \frac{1}{w^{|\ell|+1}} \quad (3.9)$$

is a constant that normalizes the integrated amplitude;

$$G = e^{-r^2/w^2} \quad (3.10)$$

is the Gaussian envelope, with  $w$  being the beam width (or spot). The term  $L_p^{|\ell|}$  is the associated Laguerre polynomial, which is a function of  $2r^2/w^2$ . The last term of Eq. (3.8) is

$$W = e^{-i(x^2+y^2)/(2R)-i\varphi}. \quad (3.11)$$

The first part of the exponential corrects for the curvature of the wavefront, which is often neglected for simplicity, but which accounts for the spiral patterns in the fringes of measured beams. The second term in the exponential is the Gouy phase, given by

$$\varphi = (2p + |\ell| + 1) \tan^{-1}(z/z_R), \quad (3.12)$$

where  $z_R$  is the Rayleigh range. For a pure mode the Gouy phase is an overall term that has no effect, but in a superposition it leads to a relative phase between the component modes, leading often to the transverse rotation of the mode about the beam center as the beam propagates [19].

LG modes are multiringed, with  $p$  nodes between  $r = 0$  and  $r = \infty$ . Commonly used LG modes have  $p = 0$  and exhibit a classic single-ring or “doughnut” shape. The radius of the ring (where amplitude is maximum) is given by

$$r_\ell = \left( \frac{\ell}{2} \right)^{1/2} w, \quad (3.13)$$

and so it increases with  $\ell$ , also known as the topological charge of the mode. Figure 3.3b shows the diffraction pattern produced by a forked amplitude grating (a), where the diffraction orders  $n$  are LG modes with  $n = \ell$ .

The most important element of the LG modes is the azimuthal phase, given by  $\ell\phi$ . Transverse phase maps for LG modes are given in the bottom of Figure 3.3b. The points in the beam that have the same phase, that is, the wavefront, make surfaces that consist of  $\ell$ -intertwined helices. These tilted wavefronts are able to exert torques on irregularly shaped objects [20]. Absorption of LG light also gives rise to particle rotation. In the quantum limit, single photons carry the entire mode of the field [21], and an angular momentum given by  $\ell\hbar$  [1]. This is in addition to the angular momentum that it may have due to right or left circular polarization ( $-\hbar$  or  $+\hbar$ , respectively). Finally, LG beams are also interesting because they carry an interesting type of scalar optical singularity: an optical vortex. This is a point in the

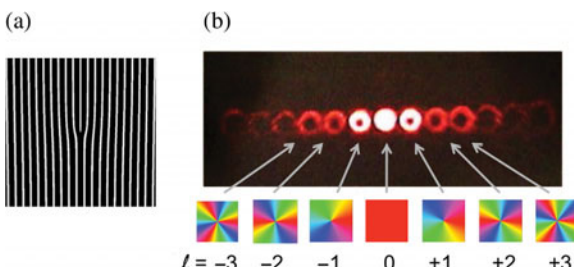


**FIGURE 3.3** (a) Forked amplitude grating used to produce LG modes in (b). Each order has a different topological phase, shown below in colored phase maps, where each color is a unique phase (modulo  $2\pi$ ). (For a color version of this figure, see the color plate section.)

transverse plane where the intensity is zero, and where the phase is multiply defined. The topological charge of the vortex is  $\ell$ , the multiple of  $2\pi$  that the phase advances on a closed loop about the vortex [2]. Vortices of varying charge are seen at the center of the colored phase maps of Figure 3.3b. In three dimensions, the vortices propagate as lines of darkness, which may not only move and rotate, but also form loops and knots [22–24].

Since LG modes are a complete set of functions, they can be used to create other modes via their superposition. Another important family is that of Hermite–Gauss (HG) modes, which we will not discuss here in detail. They are solutions of the paraxial equation in Cartesian coordinates. These modes are commonly produced by lasers with a rectangular symmetry, but carry no orbital angular momentum. An interesting new type of beams, called Ince–Gaussian beams, is a hybrid mixture of LG and HG modes [7]. Another class of beams not discussed here is nondiffracting Bessel beams [5].

### 3.2.3 Poincaré Modes

The new development in polarization optics of the last 10 years is the generation and use of optical beams that are not in a unique state of polarization. Instead, the polarization varies across the profile of the beam [25]. The label Poincaré beams or modes are a compelling one, but not unique. These types of beams are also known as beams with space-variant polarization, vector beams, and also singular beams. The latter comes owing to the polarization singularities that they contain, as mentioned below.

These types of modes have been recognized for a longtime. As seen in Eqs. (3.1), (3.3), and (3.4), a general state of polarization is constructed with a pair of orthogonal states of polarization with varying amplitudes and relative phases. Spatial modes exhibit space-variant amplitudes and phases, so superpositions of distinct spatial modes in orthogonal states lead to modes with a spatially varying polarization state.

Interest in these types of beams gained momentum with radially polarized beams. These are beams where the electric field is linearly polarized along the radial direction [26]. It was recognized that when focused, they generate an axial electric field at the center of the waist, which could potentially be used for charge particle acceleration [27]. A similar counterpart is the azimuthally polarized beam, where the linear polarization of the beam is at every point perpendicular to the radial direction, and which produces an axial magnetic field when focused [28]. Radial vector beams also gain interest for particle manipulation owing to their smaller waist [29]. These linearly polarized beams have been known as vector beams and constitute a subset of the class that we call Poincaré beams.

A general expression for a mode with space-variant polarization is given by a nonseparable superposition of spatial modes and polarization:

$$V = (a_1 M_1 \hat{e}_1 + a_2 M_2 \hat{e}_2), \quad (3.14)$$

where  $a_1$  and  $a_2$  are normalized complex amplitudes,  $M_1$  and  $M_2$  are orthogonal spatial modes, and  $\hat{e}_1$  and  $\hat{e}_2$  are orthogonal polarization eigenstates. If we use a particular case, LG spatial modes with unit-norm amplitudes, we get a Poincaré mode [30]:

$$V = \frac{1}{\sqrt{2}}(LG_{p_1}^{\ell_1} e^{i\alpha} \hat{e}_R + LG_{p_2}^{\ell_2} e^{-i\alpha} \hat{e}_L). \quad (3.15)$$

The case of vector beams corresponds to the setting  $p_1 = p_2 = 0$ ,  $\ell_1 = -\ell_2 = 1$ , and  $\alpha = 0$  for radial or  $\alpha = \pi/2$  for azimuthal modes [31].

Equation (3.15) can be rewritten in the following form:

$$V = NGWe^{i(\ell_1 + \ell_2)\phi/2} (\cos \chi e^{i\theta} \hat{e}_R + \sin \chi e^{-i\theta} \hat{e}_L), \quad (3.16)$$

where

$$\chi = \tan^{-1} \frac{A_{p_2, \ell_2} r^{|\ell_2|} L_{p_2}^{|\ell_2|}}{A_{p_1, \ell_1} r^{|\ell_1|} L_{p_1}^{|\ell_1|}}, \quad (3.17)$$

and

$$\theta = (\ell_1 - \ell_2)\phi/2 + \alpha, \quad (3.18)$$

with  $N$  being a normalization constant. Equations (3.17) and (3.18) reveal that the ellipticity of the states composing the mode depends only on the radial coordinate, and their orientation depends only on the transverse angular coordinate.

Let us understand this in more detail with an example. Figure 3.4a shows the pattern of polarization states for the case  $p_1 = p_2 = 0$  and  $\ell_1 = 0$  and  $\ell_2 = -1$ . Mode  $LG_0^0$  is the fundamental Gaussian beam, which peaks at  $r = 0$  and decreases to zero

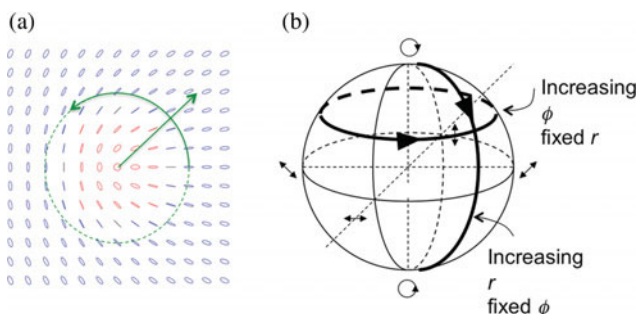


**FIGURE 3.4** (a) Lemon polarization pattern formed by a superposition of LG modes, one with topological charges 1 and 0, in opposite states of circular polarization. (b) Illustration of the mapping of the beam pattern onto the Poincaré sphere. Right- and left-handed ellipses are colored red and blue, respectively. (For a color version of this figure, see the color plate section.)

at  $r = \infty$  following the Gaussian function of Eq. (3.10). (We also note that  $L_0^0 = 1$ .) The mode  $LG_0^1$  is, as mentioned earlier, a ring. Between  $r = 0$  and  $w/\sqrt{2}$  we have that  $|LG_0^0| > |LG_0^{-1}|$ , and so the mode is composed of right-handed ellipses, with  $r = 0$  containing the state of right circular polarization and with ellipticity increasing as a function of  $r$ . At  $r = w/\sqrt{2}$  the amplitudes of the spatial modes are equal, and so specify a ring of linearly polarized states. At greater radii, the mode is dominated by left-handed ellipses, with ellipticity increasing to left circular polarization at  $r = \infty$ . Every point in the transverse plane has a distinct polarization state. In essence, the mode is a mapping of the Poincaré sphere onto the transverse plane of the mode. Figure 3.4b depicts the way the modes are mapped: a radial trajectory from  $r = 0$  is equivalent to following a meridian on the sphere, from the north pole to the south pole; and a circular trajectory centered about  $r = 0$  counter-clockwise, corresponds to following a parallel on the sphere from west to east.

### 3.3 EXPERIMENTAL APPROACHES

Early work with beams with space-variant polarization focused on radial vector beams [12]. These have been produced in free space using superposition HG or LG beams of opposite polarization [32], essentially creating a superposition such as the one represented by Eq. (3.14). It consists of a polarization interferometer, where each arm has one state of linear polarization (horizontal and vertical), and in each arm a distinct spatial mode is encoded. This can be accomplished with the use of polarizing beam splitters, both in the separation of orthogonal components and in their recombination. In the case of radial vector beams we need either a superposition of first-order HG modes,  $HG_{10}$  and  $HG_{01}$ , in orthogonal linear polarization eigenstates or first-order LG modes,  $LG_0^{+1}$  and  $LG_0^{-1}$ , in orthogonal circular polarization eigenstates (for a review of experiments, see References [12] and [31]). The spatial modes were prepared either directly from laser emission (in the case of HG modes, and rotating one of them) or by the use of diffractive optical elements, such as spiral phase plates or forked gratings. Poincaré beams have been produced using this basic scheme, by using high-order LG modes, implementing Eq. (3.16) [30]. Circular or elliptical polarization eigenstates can be prepared after the polarization interferometer using standard waveplates. Since the states leaving the interferometer are orthogonal, the unitary transformation of one of them into an elliptical state automatically prepares the other in the orthogonal state [33]. The previous method is limited by the availability of diffractive optical elements. A more flexible device uses a spatial light modulator (SLM) for encoding the two modes, and encode in principle any superposition [34].

This can be accomplished with the setup of Figure 3.5, which is basically a polarization interferometer with the SLM serving as one of the reflective elements of the interferometer. In the case shown, a single SLM was also used to encode both spatial modes. Briefly, the laser beam is expanded and split by a non-polarizing beam splitter. The two parallel beams are incident on the SLM, which diffracts them with two separate patterns encoded in the same SLM. The polarization of both beams is the same due to the polarization sensitivity of the SLM. After the SLM,

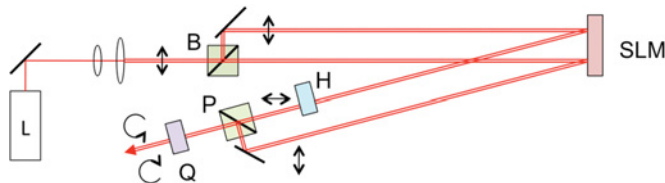


**FIGURE 3.5** Apparatus to create Poincaré modes. It uses beam splitters that are unpolarized (B), polarized (P), half (H), and quarter (Q) waveplates to manipulate the polarization and an SLM to encode the spatial modes.

the polarization of one of the components is rotated via a half-wave plate. The two beams are merged with a polarizing beam splitter. A quarter-wave plate after the interferometer transforms the two linear polarizations into circular eigenstates.

A second class of production methods uses single elements that optically generate the spatial-polarization state. The earliest type of element was used specifically for producing radial vector beams. It used an optical element that consisted of a mosaic of half-wave plates with fast axes oriented appropriately [35, 36]. Other devices that rotate the polarization in a smoother way have been developed. Sub-wavelength gratings have been used to create vector beams via their space-variant patterning designs [37]. It has been shown that few-mode optical fibers can be used to produce vector beams [38–40], and more recently, spun fibers have been used as well [41].

Liquid crystals have emerged as powerful method to manipulate phase, via SLMs. However, engineered liquid crystal cells can also be used to smoothly rotate the polarization to generate radially or azimuthally polarized beams from an incident linearly polarized beam [42]. More recently, the interaction of liquid crystals with polarized light has been used to couple the spin (polarization) and orbital (spatial) modes of light. A new device that has attracted attention is called the “q-plate,” which also uses an engineered liquid crystal cell [43, 44], but which can be electrically or thermally tuned to produce a greater variety of mode–polarization combinations [45]. The nonlinearity of liquid crystals can also be exploited for the purpose of spin–orbit coupling via cross-phase-modulation [46]. Self-induced nonlinearity of liquid crystals [47] and other crystals [48] can also be used for the same purpose. The greater array of polarization singularities exhibited by Poincaré beams has been achieved in a very unique way using stress birefringence [49].

There is a growing interest in the generation of polarization patterns and the study of singularities in birefringent [50–52], nematic [53], and anisotropic [54, 55] media. This work complements the studies of polarization singularities in speckle fields [56–58].

### 3.4 POLARIZATION SINGULARITIES

In the past 20 years much work has been done on scalar singularities, such as optical vortices [59]. That work is still evolving and finding applications. As the work with

scalar singularities matures, there is a growing interest on vector singularities [60]. In terms of the polarization of light, polarization singularities manifest as places where the parameters of the polarization ellipse are undefined. In the case of Figure 3.4a, the central point is known as a C-point, where the orientation of the semimajor axis of the ellipse is undefined [14, 15]. Surrounding it are ellipses, whose semimajor axis rotates counter-clockwise by 180 degrees per counter-clockwise turn around the C-point. An important morphological characteristic of the field of ellipses that surround the C-point is that there is a single line originating from the C-point where all the ellipses have an orientation in the radial direction. This type of C-point is known as a lemon [14, 15]. The singularity index denotes the winding of the field of ellipses around the C-point. It is defined as [61]

$$I_C = \frac{\Delta\theta}{2\pi}. \quad (3.19)$$

If  $\theta$  is the orientation of the ellipses around a C-point (see Eq. 3.18), then we define  $\Delta\theta$  as the change in  $\theta$  per turn around the singularity. Thus, for the lemon  $I_C = +1/2$ .

Shown in Figure 3.6a is another type of C-point, known as a star. It is constructed with Eq. (3.15) and  $\ell_1 = 0$  and  $\ell_2 = +1$ , or with  $\ell_1 = -1$  and  $\ell_2 = 0$ . In this case, the semimajor axis of the surrounding ellipses rotates clockwise by 180 degrees per counter-clockwise turn around the C-point, and thus having  $I_C = -1/2$ . This type of singularity has three lines that are oriented radially. Figure 3.6b shows a measurement of a Poincaré beam prepared using the setup of Figure 3.5. The states of the beam were measured using Stokes polarimetry, as described in the section 3.2.1. A third type of C-point is part lemon and part star, and so it is called monstar [14]. Surrounding this type of C-point is a field of ellipses that have a semimajor axis that rotates in the same sense as those of the lemon, but have three lines where the semimajor axes of the ellipses are radially oriented.

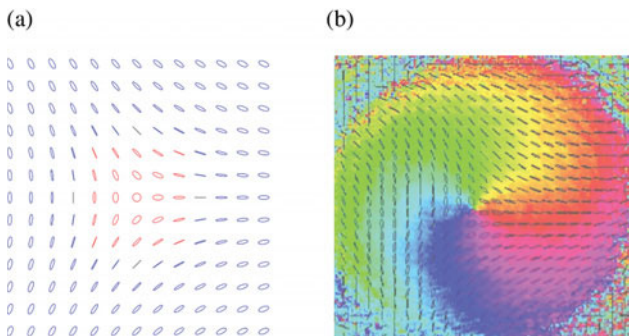


**FIGURE 3.6** (a) Polarization-state map for a star pattern, created by the superposition of LG modes with topological charges 1 and 0, in opposite circular polarization states, but the reverse combination as Figure 3.4. (b) Measured polarization field for the pattern corresponding to a star, taken with the setup of Figure 3.5. The color map is the phase of the Stokes field  $\sigma_{12}$ . (For a color version of this figure, see the color plate section.)

The field of polarization singularities can be viewed from a different perspective, in terms of the Stokes parameters. If we define the complex scalar field as [61–65]

$$\sigma_{12} = s_1 + is_2, \quad (3.20)$$

and similarly with the other pairwise combinations of Stokes parameters, then the phase of the Stokes field  $\Phi = \arg(\sigma_{12})$  will reveal C-points at a dislocation. In the case of  $\sigma_{12}$ , the phase will also be the orientation of the semimajor axis of the ellipses in the field. Figure 3.6b shows a color map of  $\sigma_{12}$  [66].

Another type of polarization singularity is the L-line, which is a linearly polarized boundary of regions of opposite elliptical handedness [13]. For example, in Figures 3.4a and 3.6a, L-lines are the circles that contain linearly polarized states. Under certain conditions we can have a field of states that have the same ellipticity. One such case is that of a field of linearly polarized states with distinct orientations at different angles, as shown in Figure 3.7a [30, 63]. The central point is also known as a vector singularity, or V-point. If we define the singularity index for this point similarly to Eq. (3.19), then  $I_V = +3$ . It can be constructed using Eq. (3.15) with  $\ell_1 = +3$  and  $\ell_2 = -3$ . It does not show any other state of polarization because modes  $LG_0^{+3}$  and  $LG_0^{-3}$  have the same radial dependence (see Eq. 3.8), so the opposite states of polarization in Eq. (3.1) always have the same amplitude (in absolute value, or  $\chi = \pi/4$ ). If instead of circular polarization eigenstates we have linear polarization eigenstates, we get the pattern shown in Figure 3.7b, The central point is singular as well, because it has all ellipticities of diagonal and antidiagonal orientations.

Polarization singularities are sensitive to perturbations: other fields [61] and inhomogeneities in the medium [54, 55, 67]. This leads to the motion of the singularities and the breakup of singularities of high index, as illustrated by the polarization

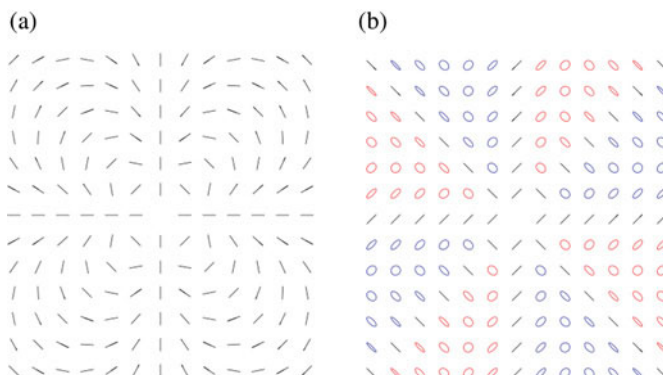


**FIGURE 3.7** (a) Polarization patterns produced by the superposition of  $LG_0^{+3}$  and  $LG_0^{-3}$  modes in circular polarization eigenstates. (b)  $LG_0^{+2}$  and  $LG_0^{-2}$  modes in linear polarization eigenstates. The central points are singular. Regions of right- and left-handed ellipticity are colored red and blue, respectively. (For a color version of this figure, see the color plate section.)

pattern of clear sky [68]. Polarization singularities in partially coherent light also show interesting results [69].

### 3.5 CONCLUSION

An emerging development of space-variant polarization of light beams constitutes a significant fundamental advance in an otherwise mature field of polarization optics. Polarization singularities hold much promise in optical diagnosis [70], as a technique where singularities become sensitive probes of perturbations to the wave field. On the fundamental side, work on polarization effects in three dimensions has only started [71, 72] and holds promise of more interesting developments.

### ACKNOWLEDGMENTS

We thank G. Milione and F. De Zela for stimulating discussions. This work was funded by National Science Foundation and U.S. Air Force.

### REFERENCES

- [1] L. Allen, M. W. Beijersbergen, R. J. C. Spreeuw, and J. P. Woerdman, “Orbital angular momentum of light and the transformation of Laguerre-Gauss modes,” *Phys. Rev. A* **92**, 8185–8189 (1992).
- [2] L. Allen, S. M. Barnett, and M. J. Padgett, Eds., *Optical Angular Momentum* (Institute of Physics, Bristol, 2003).
- [3] A. E. Siegman, *Lasers* (University Science Books, Mill Valley, CA, 1986).
- [4] M. W. Beijersbergen, L. Allen, H. E. L. O. van der Veen, and J. P. Woerdman, “Astigmatic laser mode converters and transfer of orbital angular momentum,” *Opt. Commun.* **96**, 123–132 (1993).
- [5] J. Durnin, J. J. Miceli, Jr., and J. H. Eberly, “Diffraction-free beams,” *Phys. Rev. Lett.* **58**, 1499–1501 (1987).
- [6] J. C. Gutierrez-Vega, M. D. Iturbe-Castillo, and S. Chavez-Cerda, “Alternative formulation for invariant optical fields: mathieu beams,” *Opt. Lett.* **25**, 1493–1495 (2000).
- [7] M. A. Bandres and J. C. Gutierrez-Vega, “Ince-Gaussian beams,” *Opt. Lett.* **29**, 144–146 (2004).
- [8] G. A. Siviloglou, J. Broky, A. Dogariu, and D. N. Christodoulides, “Observation of accelerating airy beams,” *Phys. Rev. Lett.* **99**, 213901 (2007).
- [9] D. Andrews, *Structured Light and Its Applications: An Introduction to Phase-Structured Beams and Nanoscale Optical Forces* (Academic Press-Elsevier, Burlington, 2008).
- [10] A. Mair, A. Vaziri, G. Weihs, and A. Zeilinger, “Entanglement of the orbital angular momentum states of photons,” *Nature (London)* **412**, 313–316 (2001).
- [11] G. Gibson, J. Courtial, M. Padgett, M. Vasnetsov, V. Pas’ko, S. M. Barnett, and S. Franke-Arnold, “Free-space information transfer using light beams carrying orbital angular momentum,” *Opt. Express* **12**, 5448–5456 (2004).

- [12] Q. Zhan, “Cylindrical vector beams: from mathematical concepts to applications,” *Adv. Opt. Photon.* **1**, 1–57 (2009).
- [13] J. F. Nye, “Line singularities in wave fields,” *Proc. R. Soc. Lond. A* **387**, 105–132 (1983).
- [14] J. F. Nye, “Lines of circular polarization in electromagnetic wave fields,” *Proc. R. Soc. Lond. A* **389**, 279–290 (1983).
- [15] J. F. Nye, *Natural Focusing and Fine Structure of Light* (Institute of Physics, Bristol, 1999).
- [16] M. V. Berry and M. R. Dennis, “Polarization singularities in isotropic random vector waves,” *Proc. R. Soc. Lond. A* **457**, 141–155 (2001).
- [17] M. Born and E. Wolf, *Principles of Optics*, 7th ed. (Cambridge University Press, Cambridge, 2010).
- [18] W. A. Shurcliff, *Polarized Light* (Harvard University Press, Cambridge, 1966).
- [19] S. M. Baumann, D. M. Kalb, L. H. MacMillan, and E. J. Galvez, “Propagation dynamics of optical vortices due to Gouy phase,” *Opt. Express* **17**, 9818–9827 (2009).
- [20] A. I. Bishop, T. A. Niemen, N. R. Heckenberg, and H. Rubinsztein-Dunlop, “Optical microrheology using rotating laser-trapped particles,” *Phys. Rev. Lett.* **42**, 198104 (2004).
- [21] E. J. Galvez, L. E. Coyle, E. Johnson, and B. J. Reschovsky, “Interferometric measurement of the helical mode of a single photon,” *New J. Phys.* **13**, 053017 (2011).
- [22] M. V. Berry and M. R. Dennis, “Knotted and linked phase singularities in monochromatic waves,” *Proc. R. Soc. Lond. A* **457**, 2251–2263 (2001).
- [23] M. V. Berry and M. R. Dennis “Knotting and unknotting of phase singularities: Helmholtz waves, paraxialwaves and waves in 2+1 spacetime,” *J. Phys. A* **34**, 8877–8888 (2001).
- [24] J. Leach, M. R. Dennis, J. Courtial, and M. J. Padgett, “Vortex knots in light,” *New J. Phys.* **7**, 1–11 (2005).
- [25] T. Brown, “Unconventional polarization states: beam propagation, focusing, and imaging,” *Prog Optics* **56**, 81–129 (2011).
- [26] Y. Mushiake, K. Matsumura, N., and Nakajima, “Generation of radially polarized optical beam mode by laser oscillation,” *Proc. IEEE* **60**, 1107–1109 (1972).
- [27] J. R. Fontana, and R. H. Pantell, “A high-energy laser accelerator for using the inverse Cherenkov effect,” *J. Appl. Phys.* **54**, 4285–4288 (1983).
- [28] K. S. Youngsworth and T. G. Brown, “Focusing of high numerical aperture cylindrical vector beams,” *Opt. Express* **7**, 77–87 (2000).
- [29] S. Quabis, R. Dorn, M. Eberler, O. Glöckl, and G. Leuchs, “Focusing light to a tighter spot,” *Opt. Commun.* **179**, 1–7 (2000).
- [30] E. J. Galvez, S. Khadka, W. H. Schubert, and S. Nomoto, “Poincaré-beam patterns produced by nonseparable superpositions of Laguerre-Gauss and polarization modes of light,” *Appl. Opt.* **51**, 2925–2934 (2012).
- [31] E. J. Galvez, “Vector beams in free space,” in *The Angular Momentum of Light*, edited by D. L. Andrews and M. Babiker (Cambridge University Press, Cambridge, 2012).
- [32] S. C. Tidwell, D. H. Ford, and W. D. Kimura, “Generating radially polarized beams interferometrically,” *Appl. Opt.* **29**, 2234–2239 (1990).
- [33] E. J. Galvez and S. Khadka, “Poincaré modes of light,” *Proc. SPIE* **8274**, 82740Y 1–8 (2012).
- [34] C. Maurer, A. Jesacher, S. Fürhapter, S. Bernet, and M. Ritsch-Marte, “Tailoring of arbitrary optical vector beams,” *New J. Phys.* **9**, 78–1–20 (2007).

- [35] S. Quabis, R. Dorn, and G. Leuchs, "Generation of a radially polarized doughnut mode of high quality," *Appl. Phys. B* **81**, 597–600 (2005).
- [36] G. Machavariani, Y. Lumer, I. Moshe, A. Meir, and S. Jackel, "Efficient extracavity generation of radially and azimuthally polarized beams," *Opt. lett.* **32**, 1468–1470 (2007).
- [37] Z. Bomzon, G. Biener, V. Kleiner, and E. Hasman, "Radially and azimuthally polarized beams generated by space variant dielectric subwavelength gratings," *Opt. Lett.* **27**, 285–287 (2002).
- [38] G. Volpe and D. Petrov, "Generation of cylindrical vector beams with few-mode fibers excited by Laguerre-Gaussian beams," *Opt. Commun.* **237**, 89–95 (2004).
- [39] S. Ramachandran, P. Kristensen, and M. F. Yan, "Generation and propagation of radially polarized beams in optical fibers," *Opt. Lett.* **34**, 2525–2527 (2009).
- [40] N. K. Viswanathan and V. V. G. Inavalli, "Generation of optical vector beams using a two-mode fiber," *Opt. Lett.* **34**, 1189–1191 (2009).
- [41] G. Milione, H. I. Sztul, R. R. Alfano, and D. A. Nolan, "Stokes polarimetry of a hybrid vector beam from a spun elliptical core optical fiber," *Proc. SPIE* **7613**, 761305–761310 (2009).
- [42] M. Stalder and M. Schadt, "Linearly polarized light with axial symmetry generated by liquid-crystal polarization converters," *Opt. Lett.* **21**, 1948–1950 (1996).
- [43] L. Maruuucci, C. Manzo, and D. Paparo, "Optical spin-to-orbital angular momentum conversion in inhomogeneous anisotropic media," *Phys. Rev. Lett.* **96**, 163905 (2006).
- [44] E. Karimi, S. Slussarenko, L. Marrucci, and E. Santamato, "Polarization-controlled evolution of light transverse modes and associated Pancharatnam geometric phase in orbital angular momentum," *Phys. Rev. A* **81**, 053813 (2010).
- [45] F. Cardano, E. Karimi, S. Slussarenko, L. Marrucci, C. de Lisio, and E. Santamato, "Polarization pattern of vector vortex beams generated by q-plates with different topological charges," *Appl. Opt.* **51**, C1–C6 (2012).
- [46] E. Brasselet, "Spin-orbit optical cross-phase-modulation," *Phys. Rev. A* **82**, 063836 (2010).
- [47] M. El Ketara and E. Brasselet, "Self-induced nonlinear spin-orbit interaction of light in liquid crystals," *Opt. Lett.* **37**, 602–604 (2012).
- [48] S. Mosca, B. Canuel, E. Karimi, B. Piccirillo, L. Marrucci, R. De Rosa, E. Genin, L. Milano, and E. Santamato, "Photon self-induced spin-to-orbital conversion in a terbium-gallium-garnet crystal at high laser power," *Phys. Rev. A* **82**, 043806 (2010).
- [49] A. M. Beckley, T. G. Brown, and M. A. Alonso, "Full Poincaré beams," *Opt. Express* **18**, 10777–10785 (2010).
- [50] A. V. Volyar and T. A. Fadeyeva, "Decay and fusion pf polarization umbilics in a singular beam passed through a crystal," *Opt. Spectrosc.* **95**, 792–799 (2003).
- [51] F. Flossmann, U. T. Schwarz, M. Maier, and M. R. Dennis, "Polarization singularities from unfolding optical vortex through a birefringent crystal," *Phys. Rev. Lett.* **95**, 253901 (2005).
- [52] T. A. Fadeyeva, V. G. Shvedov, Y. V. Izdebskaya, A. V. Volyar, E. Brasselet, D. N. Neshev, A. S. Desyatnikov, W. Krolikowski, and Y. S. Kivshar, "Spatially engineered polarization states and optical vortices in uniaxial crystal," *Opt. Express* **18**, 10848–10863 (2010).
- [53] I. O. Buinyi, V. G. Denisenko, and M. S. Soskin, "Topological structure in polarization resolved conoscopic patterns for nematic liquid crystal cells," *Opt. Commun.* **282**, 143–155 (2010).

- [54] K. Y. Bliokh, A. N. Kleiner, and E. Hasman, “Singular polarimetry: evolution of polarization singularities in electromagnetic waves propagating in weakly anisotropic medium,” *Opt. Express* **16**, 695–709 (2008).
- [55] V. Ponevchinsky, A. I. Goncharuk, V. I. Vasilev, N. I. Lebovka, and M. S. Soskin, “Optical singularities induced in a nematic-cell by carbon nanotubes,” *Proc. SPIE* **7613**, 761306 (2010).
- [56] R. I. Egorov, M. S. Soskin, and I. Freund, “Experimental optical diabolos,” *Opt. Lett.* **31**, 2048–2050 (2006).
- [57] V. Vasil’ev and M. S. Soskin, “Topological and morphological transformations of developing singular paraxial vector light fields,” *Opt. Commun.* **281**, 5527–5540 (2008).
- [58] F. Flossmann, K. O’Holleran, M. R. Dennis, and M. J. Padgett, “Polarization singularities in 2D and 3D speckle fields,” *Phys. Rev. Lett.* **100**, 203902 1–4 (2008).
- [59] M. S. Soskin and M. V. Vasnetsov, “Singular optics,” *Prog. Optics* **42**, 219–276 (2001).
- [60] M. R. Dennis, K. O’Holleran, M. J. Padgett, “Singular optics: optical vortices and polarization singularities,” *Prog. Optics* **53**, 293–363 (2009).
- [61] I. Freund, “Polarization singularity indices in Gaussian laser beams,” *Opt. Commun.* **201**, 251–270 (2002).
- [62] I. Freund, “Poincaré vortices,” *Opt. Lett.* **26**, 1996–1998 (2001).
- [63] I. Freund, “Polarization flowers,” *Opt. Commun.* **199**, 47–63 (2001).
- [64] I. Freund, “Stokes singularity relations,” *Opt. Lett.* **27**, 545–547 (2002).
- [65] M. R. Dennis, “Polarization singularities in paraxial vector fields: morphology and statistics,” *Opt. Commun.* **213**, 201–221 (2002).
- [66] E. J. Galvez, B. L. Rojec, and K. R. McCullough, “Understanding optical singularities: understanding the duality of C-points and optical vortices,” *Proc. SPIE* **8637**, 863706 (2013).
- [67] O. V. Angelsky, Y. Y. Tomka, A. G. Ushenko, Y. G. Ushenko, and Y. A. Ushenko, “Investigation if 2D Mueller marix structure of biological tissues for preclinical diagnostics of their pathological states,” *J. Phys. D* **38**, 4227–4235 (2005).
- [68] M. V. Berry, M. R. Dennis, and R. L. Lee Jr., “Polarization singularities in the clear sky,” *New J. Phys.* **6**, 162 1–14 (2004).
- [69] A. A. Chernyshov, C. V. Felde, H. V. Bogatyryova, P. V. Polyanskii, and M. S. Soskin, “Vector singularities of the combined beams assembled from mutually incoherent orthogonally polarized components,” *J. Opt. A* **11**, 094010 (2009).
- [70] O. V. Angelsky, P. V. Polyanskii, I. I. Mokhum, C. Y. Zenkova, H. V. Bogatyryova, C. V. Felde, V. T. Bachinskiy, T. M. Boichuk, and A. G. Ushenko, “Optical coherence measurements: polarization and coherence of light fields,” in *Modern Metrology Concerns*, edited by L. Cocco (InTech, 2012).
- [71] I. Freund, “Möbius strips and twisted ribbons in intersecting Gauss Laguerre beams,” *Opt. Commun.* **284**, 3816–3845 (2011).
- [72] M. R. Dennis, “Fermionic out-of-plane structure of polarization singularities,” *Opt. Lett.* **36** 3765–3767 (2011).

---

# 4

---

## QUANTUM OPTICS

HOWARD CARMICHAEL

*Department of Physics, University of Auckland, Auckland, New Zealand*

### 4.1 INTRODUCTION

It is often said that optics is an enabling science. Quantum optics might be seen to hold a similar position in the field of photonics. If not “enabling” in the very same sense, it does provide background on the quantum mechanical nature of light across a wide range of topics which fall, perhaps more directly, within the gamut of photonics. There is overlap with so many chapters in the first three volumes of this work that no purpose is served by choosing amongst them to make a list. Choosing, however, is precisely the challenge faced when one begins to map out a chapter on a subject that already fills many well-regarded books [1–3]. My choice has been to organize material around four broad themes, each judged a central thread in quantum optics or in what it provides as background to the wide sweep of photonics. The chapter starts out in Section 4.2 with a review of the simple quantum mechanics encountered in any quantum optics discussion: the quantum mechanics of the harmonic oscillator and the two-level system or qubit, along with their interaction. Then the quantum mechanics of light must deal with irreversible photon exchange, photo-emissive sources, and loss. Section 4.3 covers the topic by taking up the theme of open quantum systems, treating issues like inputs and outputs, Lindblad master equations, and the quantum regression procedure. Next, the notion of classical versus nonclassical fields is central to understanding the “quantum” in quantum optics. It arises through measurement, photoelectric detection. It is addressed in Section 4.4, where the heading is photon

counting and the topics covered include photon antibunching, homodyne/heterodyne detection, squeezed light, and quantum trajectories. Finally, in Section 4.5, the theme is cavity and circuit QED. It is in this context that the quantum side of light is brought most vividly to attention, and perhaps where one sees most clearly that someday an important branch of photonics will be optical engineering with single photons.

For all that is left out of this synopsis, and that is a great deal, I trust I can rely on other chapters of this multi-volume work.

## 4.2 FUNDAMENTALS

### 4.2.1 Quantum Mechanics of the Harmonic Oscillator

The quantum mechanics of light is essentially the quantum mechanics of the harmonic oscillator, after the manner of Dirac [4]. Although quantum optics deals with the creation and annihilation of photons and is formally a part of quantum electrodynamics, it limits attention to nonrelativistic energies (1 eV, even 1  $\mu\text{eV}$ , not 1 MeV) so there is no creation and annihilation of mass. Each mode of the electromagnetic field is quantized as a formal harmonic oscillator, whose elementary properties we first recall.

**4.2.1.1 Hamiltonian and Observables** The Hamiltonian of one mode of the field, with frequency  $\omega$ , is conveniently written

$$H = \hbar\omega(X^2 + Y^2), \quad (4.1)$$

with the observables  $X$  and  $Y$  related to position and momentum operators,  $q$  and  $p$ , of a harmonic oscillator of unit mass:

$$X = \sqrt{\frac{\omega}{2\hbar}}q, \quad Y = \frac{1}{\sqrt{2\hbar\omega}}p. \quad (4.2)$$

Operators that annihilate and create photons are the ladder operators

$$a = X + iY, \quad a^\dagger = X - iY. \quad (4.3)$$

The canonical commutation relation,  $[q, p] = i\hbar$ , is equivalently

$$[X, Y] = -\frac{i}{2}, \quad [a, a^\dagger] = 1, \quad (4.4)$$

the latter the boson commutation relation of quantum field theory. The form of the Hamiltonian encountered most often in quantum optics is

$$H = \hbar\omega \left( N + \frac{1}{2} \right), \quad (4.5)$$

with  $N = a^\dagger a$  the photon number operator. It is commonly written with the ground state or vacuum energy,  $\hbar\omega/2$ , omitted.

**4.2.1.2 Energy Spectrum and Photon Number** Let  $|E\rangle$  denote an eigenket of  $H$  with eigenvalue  $E$ . It is straightforward to show that  $a^\dagger|E\rangle$  is also an eigenket, eigenvalue  $E + \hbar\omega$ , and so is  $a|E\rangle$ , with eigenvalue  $E - \hbar\omega$ . Applying  $a^\dagger$  and  $a$  repeatedly generates a ladder of energies stepping away from  $E$  in units of  $\hbar\omega$ . With regard to repeated application of  $a$ , it is necessary to impose the requirement that the energy does not go negative. This constraint nails down the absolute position of the energy ladder. In summary, energy eigenkets may be labeled by an nonnegative integer  $n$ , with

$$H|n\rangle = \hbar\omega \left( n + \frac{1}{2} \right) |n\rangle. \quad (4.6)$$

The Fock states  $|n\rangle$ ,  $n = 0, 1, 2, \dots$ , are eigenkets of the photon number operator  $N$ :

$$N|n\rangle = n|n\rangle. \quad (4.7)$$

Furthermore, it may be shown that if  $|n\rangle$  denotes the normalized eigenket, then

$$a|n\rangle = \sqrt{n}|n\rangle, \quad a^\dagger|n\rangle = \sqrt{n+1}|n+1\rangle. \quad (4.8)$$

The observable  $N$  counts the number of photons of frequency  $\omega$ , which are annihilated by  $a$  and created by  $a^\dagger$ . The state  $|0\rangle$  of zero photon number is the vacuum state.

**4.2.1.3 Rotation, Displacement, and Squeeze** Elementary manipulations of the harmonic oscillator operators and states are carried out by unitary rotation, displacement, and squeeze operators:

$$R(\theta) = \exp(i\theta a^\dagger a), \quad D(\alpha) = \exp(\alpha a^\dagger - \alpha^* a), \quad (4.9)$$

and

$$S(\xi) = \exp \left[ \frac{1}{2} (\xi^* a^2 - \xi a^{\dagger 2}) \right], \quad (4.10)$$

where  $\theta$  is a real parameter (angle) and both  $\alpha$  and  $\xi$  are arbitrary complex numbers. The unitary transformation of operators is conveniently provided by the transformation of the annihilation operator:

$$R^\dagger(\theta)aR(\theta) = e^{i\theta}a, \quad D^\dagger(\alpha)aD(\theta) = a + \alpha, \quad (4.11)$$

and, writing  $\xi = re^{i2\theta}$ ,  $r$  and  $\theta$  real parameters,

$$S^\dagger(\xi)aS(\xi) = a \cosh r - e^{i2\theta}a^\dagger \sinh r. \quad (4.12)$$

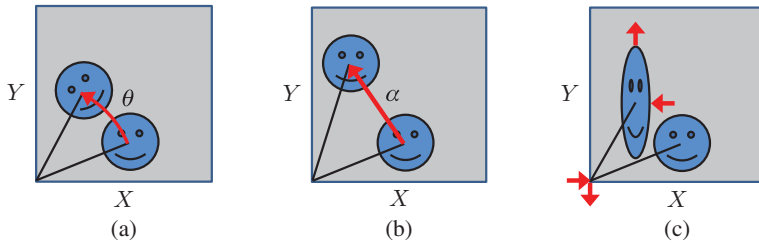


**FIGURE 4.1** Mapping of phase-space regions for the harmonic oscillator through (a) a rotation, (b) a displacement, and (c) a squeeze (in the  $X$ -direction).

Alternatively, in the case of the squeeze, the coordinate system is first rotated,  $e^{-i\theta}a = X_\theta + iY_\theta$ , and then the shrinking and stretching of the transformation is apparent:

$$S^\dagger(\xi)X_\theta S(\xi) = e^{-r}X_\theta, \quad S^\dagger(\xi)Y_\theta S(\xi) = e^rY_\theta. \quad (4.13)$$

The three transformations are illustrated by mapping regions in the phase space of the harmonic oscillator in Figure 4.1.

The form of Hamiltonian  $H$  shows that the free motion of the harmonic oscillator is continuous rotation at frequency  $\omega$ . The important physical role played by displacements comes from their connection to the coherent states. Applying  $D(\alpha)$  to the equation  $a|0\rangle = 0$ ,

$$[D(\alpha)aD^\dagger(\alpha)]D(\alpha)|0\rangle = 0 \Rightarrow aD(\alpha)|0\rangle = \alpha D(\alpha)|0\rangle. \quad (4.14)$$

From this  $a$  has eigenket  $D(\alpha)|0\rangle$ , a coherent state, for any complex  $\alpha$ :

$$a|\alpha\rangle = \alpha|\alpha\rangle, \quad |\alpha\rangle = D(\alpha)|0\rangle. \quad (4.15)$$

Coherent states are prepared by quasiresonant driving of a damped harmonic oscillator (Section 4.3.2.3). They are central to Glauber's theory of coherence and the distinction between classical and nonclassical fields (Section 4.4.2). Their Fock state expansion, following from the eigenvalue equation, is

$$|\alpha\rangle = e^{-|\alpha|^2/2} \sum_{n=0}^{\infty} \frac{\alpha^n}{\sqrt{n!}} |n\rangle. \quad (4.16)$$

The physical significance of the squeeze transformation comes from squeezed light (Section 4.4.3.2) and related phenomena (Section 4.4.3.3).

#### 4.2.2 The Electromagnetic Field

As is recounted in any standard textbook, the general solution to Maxwell's equations, in the absence of charges and currents, may be expanded as a Fourier series

in space and time. The expansion in space introduces mode functions, conveniently taken to correspond to plane running waves. Such mode functions arise, along with a countable set of wavevectors, by adopting periodic boundary conditions. The free space dispersion relation relates space and time; it assigns a frequency  $\omega$  and harmonically oscillating coefficient to each one of the modes. These coefficients become harmonic oscillator annihilation operators when the field is quantized. For simplicity details are given for the electric field operator only and only in 1D.

**4.2.2.1 Expansion in 1D** The free electromagnetic field expanded with periodic boundary conditions, period  $L$ , has electric field operator

$$\mathbf{E}(z, t) = \mathbf{E}^{(+)}(z, t) + \mathbf{E}^{(-)}(z, t), \quad (4.17)$$

with  $\mathbf{E}^{(-)}$  the adjoint of  $\mathbf{E}^{(+)}$ , and positive frequency part

$$\mathbf{E}^{(+)}(z, t) = i \sum_{j, \xi} \hat{\mathbf{e}}_{j, \xi} \sqrt{\frac{\hbar \omega_j}{2\epsilon_0 c A L}} a_{j, \xi} \exp[-i(\omega_j t - k_j z)]. \quad (4.18)$$

The mode with annihilation operator  $a_{j, \xi}$  has wavenumber  $k_j = j2\pi/L$ ,  $j$  an integer, frequency  $\omega_j = |k_j|c$ , and unit polarization vector  $\hat{\mathbf{e}}_{j, \xi}$ ; the area  $A$  serves as an effective cross-section for the “plane-wave” modes.

**4.2.2.2 Energy Density and Photon Flux** Due to its high frequency, it is not possible to measure the electric field in quantum optics directly. Measurements rely in one way or another on photon counting (Section 4.4). It is therefore often convenient to introduce photon flux units. A plane electromagnetic wave,  $E(z, t) = 2E_0 \cos(\omega t - kz)$ , has energy density  $U = 2\epsilon_0 E_0^2$ . The units of the scaled field

$$\mathcal{E}(z, t) = \sqrt{\frac{2\epsilon_0 c A}{\hbar \omega}} E(z, t) \quad (4.19)$$

are  $t^{-1/2}$ . The scaled intensity,  $|\mathcal{E}|^2$ , has units of photon flux (photons per second through cross-section  $A$ ). Strictly, the frequency dependence of the photon energy demands a different scale factor for every mode. A quasi-monochromatic field may nevertheless be cast in photon flux units by writing the electric field operator as

$$\mathcal{E}^{(+)}(z, t) = i \sqrt{\frac{c}{L}} \sum_{j, \xi} \hat{\mathbf{e}}_{j, \xi} a_{j, \xi} \exp[-i(\omega_j t - k_j z)]. \quad (4.20)$$

Dropping the frequency dependence is acceptable as an approximation across all occupied modes.

### 4.2.3 Phase-Space Representations of the Quantum State

Fock state expansions of a ket vector or, more generally, a density operator are widely used to represent the quantum state of an electromagnetic field mode. Other representations can be more useful, though; not the standard position and momentum representations but representations that in a sense fall in between. There are many options (in fact infinitely many), but all are representations in phase space, that is, involve functions of both  $X$  and  $Y$  (read here as numbers). Three are commonly used in quantum optics. Two are derived from the following elementary properties of the coherent states: (i) coherent states satisfy the completeness relation

$$\int d^2\alpha |\alpha\rangle\langle\alpha| = \pi; \quad (4.21)$$

and (ii) unlike Fock states, which as eigenstates of a Hermitian operator are orthogonal,

$$|\langle\alpha|\beta\rangle|^2 = \exp(-|\alpha - \beta|^2) \neq 0. \quad (4.22)$$

**4.2.3.1 The  $Q$  or Husimi Function** The  $Q$  or Husimi function [5] is defined as the diagonal coherent state matrix element of the density operator  $\rho$ . When normalized so that its integral over the complex plane is unity,

$$Q(\alpha, \alpha^*) = \pi^{-1} \langle\alpha|\rho|\alpha\rangle. \quad (4.23)$$

The function is clearly positive definite, and for pure state  $|\psi\rangle$  is the squared inner product  $|\langle\alpha|\psi\rangle|^2/\pi$ . It is tempting to read it as the probability for coherent state  $|\alpha\rangle$  to be occupied. The apparent ready interpretation is not permitted, though, as coherent states are not orthogonal to one another. The  $Q$  function is a quasi-probability density. It allows operator averages placed in antinormal order ( $a$ 's to the left and  $a^\dagger$ 's to the right) to be calculated as phase-space integrals (use Eq. 4.21 and properties of the trace):

$$\langle a^p a^{\dagger q} \rangle = \int d\alpha^2 \alpha^p \alpha^{*q} Q(\alpha, \alpha^*). \quad (4.24)$$

**4.2.3.2 The  $P$  Function** The  $P$  function plays a featured role in Glauber's coherence theory [6–8], where for some field states it maps quantum mechanical correlation functions to classical expressions. It underlies the distinction made in quantum optics between so-called classical versus nonclassical fields (Section 4.4.2.1).

The  $P$  function allows operator averages in normal order ( $a^\dagger$ 's to the left and  $a$ 's to the right) to be calculated as phase-space integrals. Given the nonorthogonality of coherent states, a purely diagonal coherent state expansion of  $\rho$  may be posited,

$$\rho = \int d^2\alpha P(\alpha, \alpha^*) |\alpha\rangle\langle\alpha|. \quad (4.25)$$

It is then easy to show that

$$\langle a^{\dagger q} a^p \rangle = \int d^2\alpha \alpha^p \alpha^{*q} P(\alpha, \alpha^*). \quad (4.26)$$

The  $P$  function need not be positive definite and it may or may not exist as an ordinary function. Its potential nonexistence is appreciated from the alternate definition of  $P$  as the 2D Fourier transform of the characteristic function

$$\chi_N(z, z^*) = \text{tr} \left( \rho e^{iz^* a^\dagger} e^{iz a} \right). \quad (4.27)$$

The Fock state  $|1\rangle$ , for example, has  $\chi_N(z, z^*) = 1 - z^* z$ . This is not a square integrable function and has no Fourier transform in the usual sense. Generalized functions, or the generalized  $P$  representations of Drummond and Gardiner [9], are needed in a case like this. Sudarshan's optical equivalence theorem [10] accepts  $P$  as a generalized function (tempered distribution).

**4.2.3.3 The Wigner Function** The Wigner function [11] may be defined as the Fourier transform of a different characteristic function:

$$W(\alpha, \alpha^*) = \pi^{-2} \int d^2z \chi_S(z, z^*) e^{-iz^* \alpha^*} e^{-iz \alpha}, \quad (4.28)$$

with

$$\chi_S(z, z^*) = \text{tr} \left( \rho e^{i(z^* a^\dagger + za)} \right) = e^{-z^* z/2} \chi_N(z, z^*). \quad (4.29)$$

The prefactor  $e^{-z^* z/2}$  ensures that the Fourier transform always exists as an ordinary function, though  $W$  need not be positive definite. It is in a sense intermediate between  $Q$  and  $P$ , allowing for the evaluation of symmetrically ordered (Weyl ordered) operator averages, for example,

$$\int d^2\alpha \alpha \alpha^* W(\alpha, \alpha^*) = \frac{1}{2} (\langle a^\dagger a \rangle + \langle aa^\dagger \rangle). \quad (4.30)$$

Having met with two characteristic functions it will come as no surprise that the  $Q$  function is the Fourier transform of a third,  $\chi_A(z, z^*)$ , defined by interchanging the exponentials in Eq. (4.27).

The Wigner function is often the object reconstructed in quantum state tomography (Section 4.4.3.3). It presents a particularly accessible route to the quantum features of a field mode, as it is always an ordinary function and displays its quantum side by becoming negative. Its fringes, as in the examples of Figure 4.2, are a form of quantum interference, closely related to the concept of interference in phase space [12, 13]. The  $Q$  function contains the same information, but smeared out by a convolving of

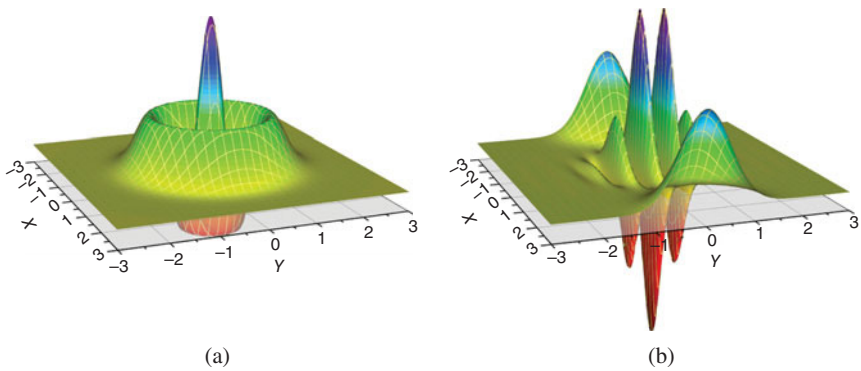


**FIGURE 4.2** Wigner functions for (a) the Fock state  $|2\rangle$  and (b) the coherent state superposition  $|3\rangle - |-3\rangle$ . (For a color version of this figure, see the color plate section.)

$W$  against a Gaussian. The  $P$  function exists only as generalized function for the examples of Figure 4.2.

#### 4.2.4 Two-State System or Qubit

With the growth of the field of quantum information, the two-state system has acquired elevated status as the fundamental “bit” of information, the qubit. It has a longer history in quantum optics, though, employed as the simplest approximation to a material resonance beyond the Lorenz oscillator model. Its nonharmonic character leads to a number of topical markers in quantum optics, including the Mollow spectrum (Section 4.3.3.4), photon antibunching (Section 4.4.2.2), and the Jaynes–Cummings model (Section 4.5.1). Many of the basics return to the physics of the original (and genuine) two-state system, electron spin.

**4.2.4.1 Pauli Operators** Pauli operators are familiar from the study of spin- $\frac{1}{2}$ , where the spin operator is written  $s = \hbar\boldsymbol{\sigma}/2$ , with the three Pauli operators the components of  $\boldsymbol{\sigma}$ . Their common matrix representation makes the  $z$ -component diagonal, which gives

$$\sigma_x \leftrightarrow \begin{pmatrix} 0 & 1 \\ 1 & 0 \end{pmatrix}, \quad \sigma_y \leftrightarrow \begin{pmatrix} 0 & -i \\ i & 0 \end{pmatrix}, \quad \sigma_z \leftrightarrow \begin{pmatrix} 1 & 0 \\ 0 & -1 \end{pmatrix}. \quad (4.31)$$

They satisfy commutation and anticommutation relations,

$$[\sigma_i, \sigma_j] = 2i\sigma_k, \quad [\sigma_i, \sigma_j]_+ = 2\delta_{ij}, \quad (4.32)$$

with  $i, j, k$  a cyclic permutation of  $x, y, z$ . By combining  $\sigma_x$  and  $\sigma_y$  raising and lowering operators,

$$\sigma_+ = \frac{1}{2} (\sigma_x + i\sigma_y) \leftrightarrow \begin{pmatrix} 0 & 1 \\ 0 & 0 \end{pmatrix} \quad \text{and} \quad \sigma_- = \frac{1}{2} (\sigma_x - i\sigma_y) \leftrightarrow \begin{pmatrix} 0 & 0 \\ 1 & 0 \end{pmatrix} \quad (4.33)$$

are obtained, along with their commutation relations:

$$[\sigma_+, \sigma_-] = \sigma_z, \quad [\sigma_{\pm}, \sigma_z] = \mp 2\sigma_{\pm}. \quad (4.34)$$

**4.2.4.2 Rotations and the Bloch Sphere** From their association with angular momentum, Pauli operators generate rotations. Since we most generally consider a pseudo-spin in quantum optics, the rotation is usually not one in 3-space. Rotation through an angle  $\varphi$  about axis  $\hat{\mathbf{n}}$  is generated by the unitary operator

$$R(\hat{\mathbf{n}}, \varphi) = \exp\left(-i\frac{\boldsymbol{\sigma} \cdot \hat{\mathbf{n}}}{2}\varphi\right) = \cos(\varphi/2)\mathbb{1} - i\sin(\varphi/2)\boldsymbol{\sigma} \cdot \hat{\mathbf{n}}. \quad (4.35)$$

An arbitrary ket vector  $|\psi\rangle$  written as

$$|\psi\rangle = \cos(\theta/2)e^{i\phi/2}|+\rangle + \sin(\theta/2)e^{-i\phi/2}|-\rangle, \quad (4.36)$$

with  $| \pm \rangle$  the eigenkets of  $\sigma_z$ , is defined by the angles  $\theta$  and  $\phi$ . It may thus be represented on the Bloch (unit) sphere by the Bloch vector [14]

$$\langle \boldsymbol{\sigma} \rangle = (\sin \theta \cos \phi, \sin \theta \sin \phi, \cos \theta)^T. \quad (4.37)$$

The components of the Bloch vector are expectations of the respective Pauli operators. A rotated ket  $|\psi'\rangle = R(\hat{\mathbf{n}}, \varphi)|\psi\rangle$  is represented by a rotated Bloch vector. From  $\langle \psi' | \boldsymbol{\sigma} | \psi' \rangle = \langle \psi | \boldsymbol{\sigma}' | \psi \rangle$ ,  $\langle \boldsymbol{\sigma} \rangle$  rotates through angle  $\varphi$  about axis  $\hat{\mathbf{n}}$ .

## 4.2.5 Electric Dipole Interaction

**4.2.5.1 Hamiltonian and Coupling Strength** In view of the long wavelength of light on the scale of an atom, interactions with matter are generally treated in the electric dipole approximation. Only if the electric dipole transition is forbidden, is it necessary to consider the much weaker electric quadrupole or magnetic dipole terms. The interaction Hamiltonian in the electric dipole approximation is

$$H_I = -\mathbf{d} \cdot \mathbf{E}(\mathbf{r}_a), \quad (4.38)$$

where the dipole operator  $\mathbf{d} = -e \sum_j (\mathbf{r}_j - \mathbf{r}_a)$  sums over electron positions relative to a positive nuclear charge at  $\mathbf{r}_a$ , and  $\mathbf{E}(\mathbf{r}_a)$  is the electric field operator at the location of the nucleus. When considering a quasiresonant transition between a lower state  $|-\rangle$  and upper state  $|+\rangle$ , the dipole operator expands as  $\mathbf{d} = \boldsymbol{\mu}_{+-}|-\rangle\langle|+| + \boldsymbol{\mu}_{+-}|+\rangle\langle|-|$ , with  $\boldsymbol{\mu}_{+-} = \boldsymbol{\mu}_{-+}^*$  the atomic dipole matrix element; diagonal elements (permanent dipole moments) are assumed by symmetry to vanish. For one field mode (wavevector  $\mathbf{k}$ , frequency  $\omega = kc$ , polarization  $\hat{\mathbf{e}}$ ),

$$\mathbf{E}(\mathbf{r}_a) = i\hat{\mathbf{e}} \sqrt{\frac{\hbar\omega}{2\epsilon_0 V}} (ae^{i\mathbf{k} \cdot \mathbf{r}_a} - a^\dagger e^{-i\mathbf{k} \cdot \mathbf{r}_a}). \quad (4.39)$$

It is usual in quantum optics to also make the rotating wave approximation, where photon creation (annihilation) simultaneous with atomic excitation (deexcitation) is neglected, in which case

$$H_I = i\hbar g(e^{i\varphi} a\sigma_+ - e^{-i\varphi} a^\dagger\sigma_-), \quad (4.40)$$

where the phase  $\varphi$  depends on the atomic position and the phase of  $\hat{\mathbf{e}} \cdot \boldsymbol{\mu}_{+-}$ , and

$$g = \sqrt{\frac{\omega}{2\hbar\epsilon_0 V}} |\hat{\mathbf{e}} \cdot \boldsymbol{\mu}_{+-}| \quad (4.41)$$

is the dipole coupling constant. As the rotating wave approximation requires  $g$  to be small relative to the frequency of the transition, it is not necessarily such a good approximation—or can even be a bad approximation—in the context of cavity and circuit QED. Beyond strong coupling (Section 4.5.3) there is a regime of ultrastrong coupling where the rotating wave approximation fails [15].

**4.2.5.2 Classical Drive: Optical Bloch Equations** For a classical drive,  $E(z, t) = \hat{\mathbf{e}}E \sin(\omega t - kz)$ , the interaction Hamiltonian carries over with the photon annihilation operator replaced by the time-dependent complex amplitude  $\alpha(t) = |\alpha| \exp(-i\omega t)$ , where  $|\alpha|$  defines the Rabi frequency [16]

$$\Omega = 2g|\alpha| = \frac{|\hat{\mathbf{e}} \cdot \boldsymbol{\mu}_{+-}|}{\hbar} E. \quad (4.42)$$

Adding the free Hamiltonian  $H_A = \hbar\omega_a\sigma_z/2$ , Heisenberg equations yield the equation of motion satisfied by the Bloch vector,

$$\langle \dot{\boldsymbol{\sigma}} \rangle = \mathbf{B}_{\text{eff}}(t) \times \langle \boldsymbol{\sigma} \rangle, \quad (4.43)$$

with

$$\mathbf{B}_{\text{eff}}(t) = (\Omega \sin(\omega t - \varphi), \Omega \cos(\omega t - \varphi), \omega_a)^T \quad (4.44)$$

an effective rotating magnetic field. The equation is familiar from Bloch's treatment of nuclear induction [14]. The response is easy to recover in a frame rotating at the frequency of the drive: the Bloch vector  $\langle \boldsymbol{\sigma}' \rangle = (u, v, w)$  precesses about the now stationary  $\mathbf{B}_{\text{eff}} = (0, \Omega, \omega_a - \omega)$ , that is, the two-state system executes a Rabi oscillation (Fig. 4.3).

Applications in optics may encounter energy damping and dephasing of the atomic dipole moment. In that case terms  $-\gamma_\perp \langle \sigma_x \rangle$ ,  $-\gamma_\perp \langle \sigma_y \rangle$ , and  $-\gamma_\parallel (\langle \sigma_z \rangle + 1)$  damp the respective Bloch vector components, with  $\gamma_\perp = 1/T_2$  and  $\gamma_\parallel = 1/T_1$  in the notation of Bloch.

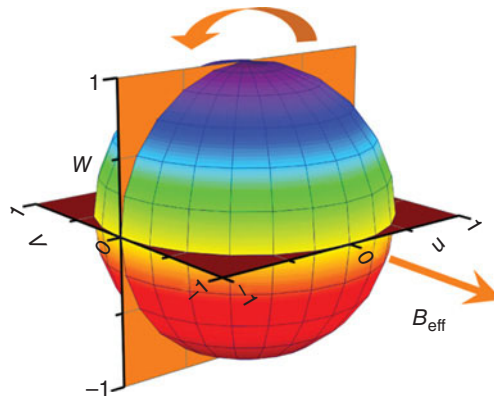


**FIGURE 4.3** The Bloch sphere: for on-resonance driving the precessing Bloch vector describes a circle in a plane parallel to the orange ( $u,w$ )-plane. (For a color version of this figure, see the color plate section.)

### 4.3 OPEN SYSTEMS: INPUTS AND OUTPUTS

Sources of light emit photons, whether they be laser sources, sources of filtered chaotic (thermal) light, or something more exotic emitting a stream of antibunched photons or a beam of squeezed light. Such sources are open quantum systems, often built around a driven or pumped material system inside an optical resonator. Quantum optics has made major contributions to the repository of concepts and methods used to analyze open quantum systems and their outputs. Most of this work makes a Markov approximation, which enormously simplifies the treatment and provides for a broad range of interconnecting techniques and applications. The product may be thought of as a low energy scattering theory, something to connect input optical drives and pumping—or input vacuum fields—to output optical fields. While each fundamental tool is based either on the Heisenberg picture or on the Schrödinger picture, in practice applications generally rely on a combination of both views.

#### 4.3.1 Heisenberg Picture

Senitzky [17, 18] pioneered the Heisenberg picture approach to dissipation in a paper published in the year of the first operational laser. The developed form used in quantum optics to relate inputs to outputs is due to Collett and Gardiner [19, 20] and appeared some 25 years later, stimulated by the need to understand squeezed light. At its center is the quantum Langevin equation and its relation to the input field that drives it and the output field for which it is the source.

**4.3.1.1 Model in 1D** Considering one mode of the single-input optical cavity illustrated in Figure 4.4 and the 1D expansion of the electric field operator in

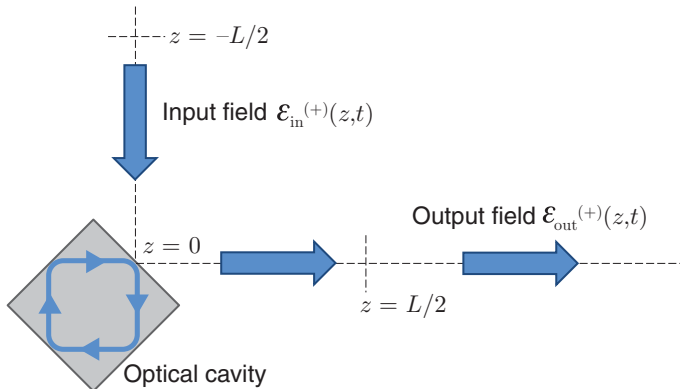


**FIGURE 4.4** Schematic of an open system (lossy cavity mode) as a scattering scenario in 1D.

Section 4.2.2, the coupling of light through the input–output mirror is modeled with Hamiltonian

$$H = \hbar\omega_c a^\dagger a + \sum_j \hbar\omega_j b_j^\dagger b_j + \hbar g \sum_j (ab_j^\dagger + a^\dagger b_j), \quad (4.45)$$

where the input field operator ( $z < 0$ ), in photon flux units, is

$$\mathcal{E}_{\text{in}}^{(+)}(z, t) = \xi(t - z/c), \quad \xi(t) = i\sqrt{\frac{c}{L}} \sum_j b_j e^{-i\omega_j t}. \quad (4.46)$$

The cavity has resonance frequency  $\omega_c$  and energy damping rate  $2\kappa = Tc/\ell$ , with  $\ell$  the cavity length and  $T$  the mirror transmission coefficient. Fermi's golden rule sets the phenomenological coupling coefficient at  $g = \sqrt{2\kappa} \sqrt{L/c}$  (density of states  $L/2\pi c$ ), and  $[\xi(t'), \xi^\dagger(t'')] = \delta(t' - t'')$  (in the  $L \rightarrow \infty$  limit) so  $\mathcal{E}_{\text{in}}^{(+)}(z, t)$  and  $\mathcal{E}_{\text{in}}^{(-)}(z, t)$  obey the commutation relation of a free field.

**4.3.1.2 Quantum Langevin Equation and Output Field** The quantum Langevin equation is the Heisenberg equation of motion for annihilation operator  $a$  with the response of modes  $b_j$  formally eliminated in favor of an integral (up to time  $t$ ) over  $a$  and the free oscillation  $b_j \exp(-i\omega_j t)$ . The assumed frequency-independent mode density and coupling  $g$  allow the sum over  $\exp[-i\omega_j(t - t')]$  (extended to negative  $\omega_j$ ) to yield a  $\delta$ -function and the integral over  $a$  to be evaluated. The resulting equation is

$$\frac{da}{dt} = -(\kappa + i\omega_c)a - \sqrt{2\kappa}\xi(t). \quad (4.47)$$

The same sum taken over the formal solution for  $b_j(t)$  yields the output field operator ( $z > 0$ )

$$\mathcal{E}_{\text{out}}^{(+)}(z, t) = \xi(t - z/c) + \sqrt{2\kappa}a(t - z/c), \quad (4.48)$$

and at the discontinuity (input–output mirror),

$$\mathcal{E}^{(+)}(0, t) = \xi(t) + \frac{1}{2}\sqrt{2\kappa}a(t). \quad (4.49)$$

Formal integration of Eq. (4.47) gives results for commutators  $[a(t'), a^\dagger(t'')]$  and  $[\xi(t'), a^\dagger(t'')]$  such that  $\mathcal{E}_{\text{out}}^{(-)}(z, t)$  and  $\mathcal{E}_{\text{out}}^{(+)}(z, t)$  also obey the commutation relation of a free field.

### 4.3.2 Schrödinger Picture

As is commonly the case in quantum mechanics, Heisenberg equations of motion can be difficult to solve. The Langevin equation above raises no problem as the chosen example of a freely decaying cavity mode yields a linear equation. The more interesting situation, however, is where the cavity mode also interacts with a material system—atom, quantum dot, nonlinear crystal—and the Heisenberg picture yields a coupled set of nonlinear operator equations. In such a situation the Schrödinger picture is likely preferred for making calculations, though the Heisenberg connection between input and output fields is still used. Mollow’s calculation [21] of the power spectrum of resonance fluorescence (Section 4.3.3.4) is an early example of the method; the operator input–output relation is first provided, Eqs. (2.11) and (2.12), and a master equation, Eq. (3.9), is then introduced.

**4.3.2.1 Lindblad Master Equation** The master equation is an autonomous equation of motion for the reduced density operator of the cavity mode  $\rho = \text{tr}_B(\chi)$ ; the trace is over all modes  $b_j$ , and the density operator  $\chi$  satisfies the Schrödinger (Liouville) equation with Hamiltonian  $H$ . The explicit form depends on the state of the input field through correlation functions. Considering broadband chaotic light, for example, photon number  $n_b$  per mode, the relevant correlation functions are

$$\langle \xi^\dagger(t')\xi(t'') \rangle = n_b\delta(t' - t''), \quad \langle \xi(t')\xi^\dagger(t'') \rangle = (n_b + 1)\delta(t' - t''), \quad (4.50)$$

and the master equation is

$$\frac{d\rho}{dt} = -i\omega_c[a^\dagger a, \rho] + \kappa(n_b + 1)\mathcal{L}[a]\rho + \kappa n_b\mathcal{L}[a^\dagger]\rho. \quad (4.51)$$

Terms appear describing incoherent pumping and decay, expressed through the Lindblad superoperator (the dot shows where the argument goes)

$$\mathcal{L}[\eta] = 2\eta \cdot \eta^\dagger - \eta^\dagger \eta \cdot - \cdot \eta^\dagger \eta. \quad (4.52)$$

The Lindblad form is generic to all physically acceptable reduced evolutions. It obviously preserves the trace of  $\rho$  but, more particularly, ensures that it evolves under a completely positive map [22].

**4.3.2.2 Rate Equations: The Pauli Master Equation** The derivation of Eq. (4.51) is largely a familiar exercise in time-dependent perturbation theory. Its most immediate content is a rate equation that might be reached equally well from Fermi's golden rule:

$$\frac{d\rho_{n,n}}{dt} = 2\kappa(n_b + 1)[(n + 1)\rho_{n+1,n+1} - n\rho_{n,n}] + 2\kappa n_b[n\rho_{n-1,n-1} - (n + 1)\rho_{n,n}], \quad (4.53)$$

where  $\rho_{n,n} = \langle n|\rho|n\rangle$  is the probability for  $n$  photons in the cavity. The term with coefficient  $2\kappa(n_b + 1)(n + 1)$  is the rate of stimulated plus spontaneous emission, taking  $n + 1$  photons to  $n$ , while the term with coefficient  $2\kappa n_b n$  is the rate of absorption, taking  $n - 1$  photons to  $n$ . Equating transition rates between neighboring energy levels—for example, first and last terms (or second and third)—yields the steady-state photon number distribution,

$$\rho_{n,n} = \frac{n_b^n}{(n_b + 1)^{n+1}}, \quad (4.54)$$

of chaotic light. An equation like Eq. (4.53) balancing incoherent transitions in and out of a quantum state is an example of a Pauli master equation [23].

**4.3.2.3 Coherent Drive** The signature of quantum optics is coherence. As an operator equation, the Lindblad master equation can deal with coherent driving as well. Setting one mode of the reservoir, frequency  $\omega$ , in coherent state  $|i\beta\rangle$ , the input field  $\xi(t)$  gains a nonzero mean:

$$-\sqrt{2\kappa}\langle\xi(t)\rangle = \varepsilon e^{-i\omega t}, \quad \varepsilon = \sqrt{2\kappa}\sqrt{\frac{c}{L}}\beta. \quad (4.55)$$

If all other modes  $b_j$  are in the vacuum state, the master equation is

$$\frac{d\rho}{dt} = -i\omega_c[a^\dagger a, \rho] + \varepsilon [ae^{i\omega t} - a^\dagger e^{-i\omega t}, \rho] + \kappa \mathcal{L}[a]\rho, \quad (4.56)$$

with the drive interaction appearing at first order. Its solution shows the cavity filling up with coherent light. For initial state  $|0\rangle$ , the state at time  $t$  is the coherent state  $|\alpha(t)\rangle = D(\alpha(t))|0\rangle$ ,

$$\alpha(t) = \frac{\varepsilon e^{-i\omega t}}{\kappa + i(\omega_c - \omega)}(1 - e^{-\kappa t}). \quad (4.57)$$

### 4.3.3 Quantum Regression

The master equation is solved for a quantum state of the cavity mode, most generally, a mixed state  $\rho(t)$ . Output field properties such as the power spectrum (Section 4.3.3.4), spectrum of squeezing (Section 4.4.3.2), and photon counting statistics (Sections 4.3.3.3 and 4.4), are not accessible from  $\rho(t)$  alone. They depend on correlation functions, whose computation relies on a strategy for evaluating two- (or multi-) time operator averages. The strategy is the quantum regression procedure of Lax [24–26]. It may be set out in two different, though equivalent, forms.

**4.3.3.1 Solve the Master Equation Twice** The master equation accounts only for one-time averages of the intracavity field operators, for example,

$$\langle a(t) \rangle = \text{tr}[a\rho(t)]. \quad (4.58)$$

Nonetheless, a Lindblad master equation describes a Markov process. This means that the same equation of motion can provide multi-time averages with an appropriate change made to its initial condition. The situation is analogous to writing a two-time joint probability density  $P(x_2, t_2 \wedge x_1, t_1)$  as  $P(x_2, t_2|x_1, t_1)P(x_1, t_1)$ , where both the one-time density and conditional density obey the same equation of motion.

Working from the one-time average  $\langle a(t) \rangle$  as an example, the quantum regression procedure calls for the master equation to be solved a second time, as an equation in  $\tau > 0$ , to evaluate a two-time average

$$\langle A(t)a(t + \tau)B(t) \rangle = \text{tr}[aR_{B\rho(t)A}(\tau)]. \quad (4.59)$$

The operators  $A$  and  $B$  are arbitrary and the quantity  $R_{B\rho(t)A}(\tau)$  obeys the master equation with initial condition

$$R_{B\rho(t)A}(0) = B\rho(t)A. \quad (4.60)$$

**4.3.3.2 In the Manner of Lax** Lax sets the procedure out in a different way [24–26]. Staying with the same example, he starts with the equation of motion for the one-time average,

$$\frac{d\langle a \rangle}{dt} = -(\kappa + i\omega_c)\langle a \rangle. \quad (4.61)$$

The quantum regression procedure then asserts that the angle brackets may be removed throughout, the time argument changed from  $t$  to  $t + \tau$ , and then any operators  $A(t)$  and  $B(t)$  may be inserted before replacing the angle brackets. The result is an equation of motion for a correlation function,

$$\frac{d\langle A(t)a(t + \tau)B(t) \rangle}{d\tau} = -(\kappa + i\omega_c)\langle A(t)a(t + \tau)B(t) \rangle, \quad (4.62)$$

which can be solved if the average at  $\tau = 0$  is known. The procedure extends to the less trivial case where one-time averages obey a set of coupled equations (Section 4.3.3.4).

Equations (4.61) and (4.62) both follow from Eq. (4.47), where one sees that the regression procedure relies on the fact that the input field  $\xi(t + \tau)$  is uncorrelated with operators of the cavity evaluated at an earlier time, that is,  $\langle A(t)\xi(t + \tau)B(t)\rangle = \langle A(t)B(t)\rangle\langle\xi(t + \tau)\rangle = 0$ .

**4.3.3.3 Hanbury Brown and Twiss** The photon bunching effect of Hanbury Brown and Twiss serves well as a first example of the quantum regression procedure. For their application in astronomy they considered the correlation of two light intensities recorded at different points in space [27–30]. The bunching of thermal light is captured just as well, however, by the correlation of intensities displaced in time.

Consider a modification of Figure 4.4 with the cavity open at both ends, decay rates  $\gamma$  (left) and  $\kappa$  (right). Broadband chaotic (thermal) light is input from the left and a filtered output field transmitted to the right; the input field to the right is in the vacuum state. The equation of motion for the mean number of photons in the cavity is

$$\frac{d\langle N \rangle}{dt} = -2(\gamma + \kappa)\langle N \rangle + 2\gamma n_b, \quad (4.63)$$

from which, according to the quantum regression procedure in its second form, the intensity correlation function in the longtime (stationary) limit obeys the equation of motion

$$\frac{\langle a^\dagger(0)N(\tau)a(0) \rangle}{d\tau} = -2(\gamma + \kappa)\langle a^\dagger(0)N(\tau)a(0) \rangle + 2\gamma n_b\langle N(\infty) \rangle. \quad (4.64)$$

The solution is

$$\lim_{t \rightarrow \infty} \langle a^\dagger(0)N(\tau)a(0) \rangle = \langle N(\infty) \rangle^2 (1 + e^{-2(\gamma+\kappa)|\tau|}), \quad (4.65)$$

with  $\langle N(\infty) \rangle = \gamma n_b / (\gamma + \kappa)$ . It exhibits photon bunching (Section 4.4.2.2).

**4.3.3.4 The Mollow Spectrum** The power spectrum of quasi-elastic scattering from a two-state system driven by monochromatic laser light, that is, the spectrum of resonance fluorescence, provides a second notable application of the quantum regression procedure. Mollow [21] used this method to calculate the spectrum in 1969 (following some erroneous calculations). Schuda et al. [31] experimentally verified his result in 1974. Although of 40-year vintage, the Mollow spectrum continues to be encountered along new experimental pathways, for example, in experiments with quantum dots inside microcavities [32] and in circuit QED [33].

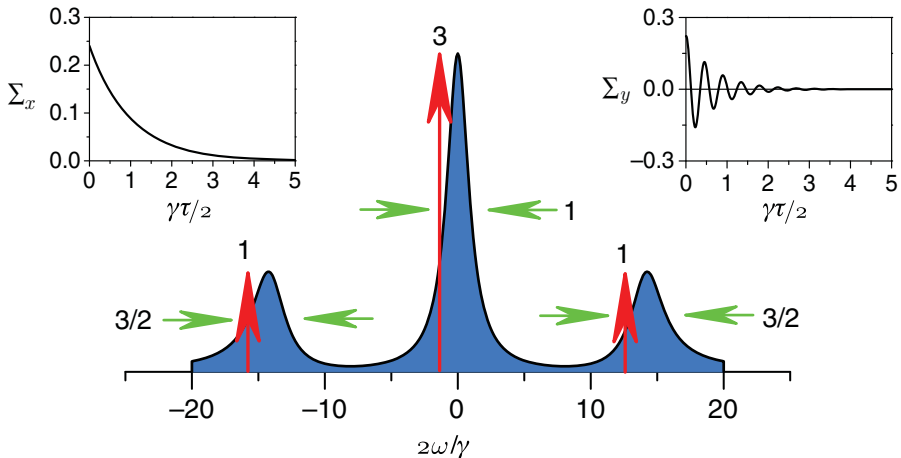


**FIGURE 4.5** Incoherent part of the Mollow spectrum for radiative decay and strong drive ( $\gamma_{\parallel} = 2\gamma_{\perp} = \gamma$  and  $\Omega \gg \gamma$ ). Fourier transforms of the correlation functions  $\Sigma_{x,y}(\tau) = \langle \Delta\sigma_+(0)\Delta\sigma_{x,y}(\tau) \rangle$  contribute the central peak ( $\Sigma_x$ ) and sidebands ( $\Sigma_y$ ).

The spectrum is the Fourier transform of the autocorrelation of the dipole moment,  $\langle \sigma_+(t)\sigma_-(t+\tau) \rangle$ , of the driven two-state system. It is calculated by applying the quantum regression procedure to the optical Bloch equations (Section 4.2.5.2): for arbitrary operators  $A$  and  $B$  in the longtime limit,

$$\frac{d\langle A\sigma'(\tau)B \rangle}{d\tau} = \begin{pmatrix} -\gamma_{\perp} & -z & y \\ z & -\gamma_{\perp} & -x \\ -y & x & -\gamma_{\parallel} \end{pmatrix} \langle A\sigma'(\tau)B \rangle - \gamma_{\parallel} \begin{pmatrix} 0 \\ 0 \\ 1 \end{pmatrix} \langle AB \rangle, \quad (4.66)$$

where  $\sigma'$  refers to a frame of reference rotating at the frequency of the drive, so that  $\mathbf{B}_{\text{eff}}(t) \rightarrow (x, y, z) = (0, \Omega, \omega_a - \omega)$ , with  $\Omega$  the Rabi frequency. The required autocorrelation is calculated with  $A = \sigma'_+$  and  $B = \mathbb{1}$ .

Figure 4.5 illustrates the main features of the dipole autocorrelation and the incoherent (inelastic) part of the Mollow spectrum. There are two pieces to the autocorrelation: the first shows the decay of fluctuations in quadrature to the drive and contributes the central spectral peak; the second shows the modulated (at the Rabi frequency) decay of fluctuations in phase with the drive and contributes the Mollow sidebands. The three-peak structure may also be understood from a dressed-state point of view (Section 4.5.1.2).

#### 4.3.4 Quantum Jumps

The quantum jump is rooted in the time of the old quantum theory and finds expression in master equations of the Pauli type (Section 4.3.2.2), where the dynamic is one of incoherent transitions (jumps) between stationary states. Operator master equations

combine coherent and incoherent evolution, with the jump part buried in the Lindblad superoperator  $\mathcal{L}[\xi]$ . The connection is fully elaborated in quantum trajectory theory (Section 4.4.4). It is reach most directly in elementary form from a Dyson expansion of the solution  $\rho(t)$  to a Lindblad master equation.

**4.3.4.1 Dyson Expansion for the Master Equation** For a simplest example (Eq. 4.51 with  $n_b = 0$ ), the superoperator on the right-hand side may be separated into two pieces mimicking the free Hamiltonian and interaction Hamiltonian of time-dependent perturbation theory:

$$-i\omega_c[a^\dagger a, \cdot] + \kappa\mathcal{L}[a] = \mathcal{L}_0 + \mathcal{L}_J, \quad (4.67)$$

with

$$\mathcal{L}_0 = -i\omega_c[a^\dagger a, \cdot] - \kappa[a^\dagger a, \cdot]_+, \quad \mathcal{L}_J = 2\kappa a \cdot a^\dagger. \quad (4.68)$$

In the open systems context,  $\mathcal{L}_0$  might be called the null-measurement (no-jump) superoperator, with  $\mathcal{L}_J$  the jump superoperator. The Dyson expansion sums over the number of quantum jumps (photons lost) up to time  $t$ :

$$\rho(t) = \sum_{n=0}^{\infty} \int_0^t dt_n \cdots \int_0^{t_2} dt_1 \mathcal{N}(t, t_n) \mathcal{L}_J \dots \mathcal{L}_J \mathcal{N}(t_1, 0) \rho(0), \quad (4.69)$$

where  $\mathcal{N}(t_k, t_{k-1}) = \exp[\mathcal{L}_0(t_k - t_{k-1})]$ . It is clear that  $\mathcal{L}_J$  extracts one photon from the cavity. The other part of the original  $\kappa\mathcal{L}[a]$ , the anticommutator in  $\mathcal{L}_0$ , effectively adds an imaginary part to the energy.

**4.3.4.2 À la Dehmelt** In a short abstract published in 1975 in the *Bulletin of the American Physical Society* [34], Hans Dehmelt outlined his “electron shelving” scheme. He conceived it as a method of amplification for monitoring the state (ground or excited) of a weak metastable transition, by recording the fluorescence from a simultaneously driven strong dipole-allowed transition: the electron is in the shared ground state if the fluorescence is “on” and the weak excited state if “off” [Fig. 4.6a]. With continuous driving of both transitions, spontaneous switching of the fluorescence “on” and “off” records quantum jumps between the ground and metastable state. Such switching was subsequently observed [35–37], and electron shelving is now widely used as a monitor of qubit states in the field of quantum information. Quantum jumps in single molecules [38] and in a single-electron cyclotron [39] have been seen; in a reversal typical of microwave cavity QED (Section 4.5.1.1) where a stream of Rydberg atoms monitors the photon state, quantum jumps of photons have also been reported [40].

Quantum jumps as inferred from the on–off switching of a measurement record are related to, though distinct from, the formal jumps employed by quantum trajectory theory (Section 4.4.4). The latter are the discrete events written into the record (e.g., the recording of one count in fluorescence), while the former are inferred from

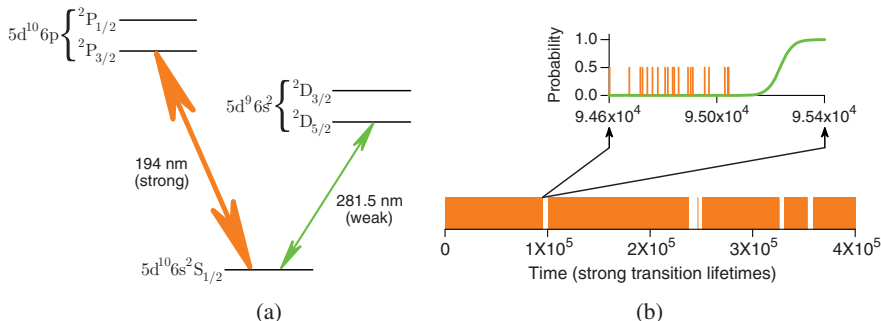


**FIGURE 4.6** (a) Level scheme used for the realization of quantum jumps in Mercury II [37]. (b) The probability to occupy the weak excited state evolves continuously (green curve) in a quantum trajectory simulation (Section 4.4.4.2). (*For a color version of this figure, see the color plate section.*)

the latter, or more precisely from their absence, that is, from the null-measurement inference [41]: if no fluorescence count is being recorded over an extended interval of time, then the electron is increasingly likely to be shelved. When the drive light is incoherent, as it is in the theoretical treatment of Cook and Kimble [42], jumps within the atom might be adopted as primary events. When the drive is coherent that option is withdrawn. Whatsoever is the state of the atom is then an inference, drawn from a continuous Schrödinger evolution conditioned upon whatever information is (or may be) recorded in the environment. The inferred passage to the shelved state is continuous, as in Figure 4.6, a jump only in coarse-grained time, the course-graining set by the bandwidth of the monitoring scheme.

## 4.4 PHOTON COUNTING

Photon or photo-electron counting is the basis of most measurements of light. Even when there is no counting of individual photons, recording at the level of photon counts is fundamental to an understanding of shot-noise-limited and sub-shot-noise measurements. A related and recurring theme in quantum optics is the distinction drawn between classical and nonclassical fields. Of course, all radiation is quantum mechanical in theory. A line of demarcation may nonetheless be defined; it is drawn from the theory of photon counting.

### 4.4.1 Basics

**4.4.1.1 Glauber Coherence Theory and the Kelley-Kleiner Formula** Glauber coherence theory [6–8] is built around the normally ordered correlation functions (more generally with space-time arguments)

$$G^{(n)}(t_1, \dots, t_n, t_{n+1}, \dots, t_{2n}) = \langle E^{(-)}(t_1) \dots E^{(-)}(t_n) E^{(+)}(t_{n+1}) \dots E^{(+)}(t_{2n}) \rangle.$$

An optical field is coherent at order  $n$  if  $G^{(n)}$  factorizes as a  $2n$ -fold product. The normal ordering of operators means the field is coherent to all orders when it is in

a multi-mode coherent state. First-order coherence and second-order coherence are most commonly discussed, often for a time-stationary field, where one introduces the normalized autocorrelation of the electric field, or degree of first-order coherence,

$$g^{(1)}(\tau) = \frac{G^{(1)}(\tau)}{G^{(1)}(0)}, \quad G^{(1)}(\tau) = \lim_{t \rightarrow \infty} G^{(1)}(t, t + \tau), \quad (4.70)$$

whose Fourier transform is the optical spectrum, and the autocorrelation of intensity, or degree of second-order coherence,

$$g^{(2)}(\tau) = \frac{G^{(2)}(\tau)}{[G^{(1)}(0)]^2}, \quad G^{(2)}(\tau) = \lim_{t \rightarrow \infty} G^{(2)}(t, t + \tau, t + \tau, t), \quad (4.71)$$

which plays an important role in the characterization of photon statistics. Glauber based his correlation functions on considerations of photoelectron counting. The time-symmetric ones ( $t_{2n-k} = t_{k+1}$ ) are, aside from a scale factor, *nonexclusive* photoelectron counting probability densities, that is, rates for photoelectron counts at times  $t_1, \dots, t_n$ , without regard to the number of counts that may or may not occur at other times. They enter in this capacity into the probability for counting  $n$  photoelectrons between  $t$  and  $t + T$ :

$$P(n) = \left\langle : \frac{[\Omega(t, t + T)]^n}{n!} \exp[-\Omega(t, t + T)] : \right\rangle. \quad (4.72)$$

This quantum-averaged Poisson distribution is known as the Kelley–Kleiner formula [43]. It is a Poisson distribution in the integrated photon flux operator  $\Omega(t, t + T) = \eta \int_t^{t+T} dt' \mathcal{E}^{(-)}(t') \mathcal{E}^{(+)}(t')$ , where  $\eta < 1$  is the quantum efficiency. The double dots indicate normal ordering of the field operators.

**4.4.1.2 Shot Noise and the Fano Factor** Normal ordering means that the integrated photon flux operator  $\Omega(t, t + T)$  is replaced by a number when the field is coherent to all orders (multi-mode coherent state). The photon counting distribution is then a regular Poisson distribution with variance equal to the mean. The residual fluctuation in the number of counts is the shot noise traditionally associated with the random conversion of a light flux into a flux of discrete (countable) photoelectric pulses. The semiclassical treatment of photoelectric detection (Section 4.4.2.1) sets this shot-noise level as a barrier; sub-shot-noise detection is not possible. The barrier may be broken in quantum mechanics (Sections 4.4.2.2 and 4.4.3.2). The Fano factor [44] is a simple relative measure of deviations from the shot-noise level.

For light that is not fully coherent, factorial moments of  $n$  are calculated as derivatives w.r.t.  $y$  of the generating function  $\langle : \exp\{-[y\Omega(t, t + T)]\} : \rangle$ . Considering a stationary field and the cavity model of Section 4.3, the photon number count variance is

$$\langle \Delta n^2 \rangle = \langle n \rangle + (\eta 2\kappa)^2 \langle N(\infty) \rangle^2 \int_t^{t+T} dt' \int_t^{t+T} dt'' [g^{(2)}(|t' - t''|) - 1], \quad (4.73)$$

and for a counting interval short compared to the correlation time,

$$\langle \Delta n^2 \rangle - \langle n \rangle = (\eta 2\kappa T)^2 [\langle \Delta N^2(\infty) \rangle - \langle N(\infty) \rangle]. \quad (4.74)$$

Counts may be super-Poisson or sub-Poisson according to whether the photon number distribution of the light inside the cavity is super-Poisson or sub-Poisson, though the degree of departure from a Poisson distribution depends on the factor  $\eta 2\kappa T$ , the mean number of counts per intracavity photon. The Fano factor is a simple ratio,

$$F = \frac{\langle \Delta n^2 \rangle}{\langle n \rangle}, \quad (4.75)$$

which quantifies the departure from a Poisson. Mandel's  $Q = F - 1$  [45] does an equivalent job. The semiclassical treatment of photoelectric detection limits  $Q$  to nonnegative values.

#### 4.4.2 Classical and Nonclassical Fields

**4.4.2.1 Mandel Formula: The  $P$  Function and BKS** Mandel discussed photoelectron counting and its relation to photon statistics as early as 1959 [46, 47]. His arguments are semiclassical, in so far as the light is viewed as a classical Maxwell wave with fluctuating intensity, and its intensity (averaged over an optical cycle) governs the rate at which photoelectrons are created—at random in accord with Fermi's golden rule. The Mandel counting formula looks like Eq. (4.72), but with the quantum average replaced by an average over the classical random variable  $\Omega(t, t + T)$ . For stationary intensity fluctuations, the average is a time average.

Mandel's semiclassical result is recovered from the full quantum treatment if the state of the field may be represented by a  $P$  function (Section 4.2.3.2) that is an ordinary function and positive definite. It is then a statistical mixture over coherent states and the normal ordering of Eq. (4.72) recasts the quantum average as a classical average. Sudarshan's optical equivalence theorem [10] extends this connection to all field states by admitting  $P$  functions as generalized functions. The extension is a formal (not operational) one.

The existence of an ordinary positive definite  $P$  function defines what in quantum optics is called a classical field. Nonexistence defines a nonclassical field. It is interesting to note as a historical aside that classical fields are those whose behavior in photoelectric detection is consistent with the so-called BKS proposal [48], the last valiant effort of Bohr to save the idea of light as a classical wave. Glauber coherence theory and the  $P$  function formalize the failure, in general, of the BKS proposal *vis à vis* photoelectric detection.

**4.4.2.2 Photon Antibunching and Single-Photon Sources** The photon bunching of Hanbury Brown and Twiss (Section 4.3.3.3) stimulated much of the early work on photon counting. Both Mandel [46] and Glauber [6, 7] open their seminal papers

with references to Hanbury Brown and Twiss. Photon “bunching” refers to a tendency of photoelectrons to be produced in bunches in photoelectric detection; photon “antibunching” to a tendency toward photoelectrons equally spaced in time. These tendencies are revealed in the intensity autocorrelation,  $g^{(2)}(\tau)$ , whose behavior sets the variance of the photon counting distribution (Section 4.4.1.2). The light is bunched when the autocorrelation decays to unity from an initial value greater than one (e.g., Eq. 4.65); when it approaches unity from a smaller initial value—that is, it rises to unity from below—it is antibunched.

In photon counting terms, the intensity autocorrelation is proportional to the probability to detect a pair of photons separated by  $\tau$ ; it measures the delayed photon coincidence rate. Thus the ideal antibunched light source emits a stream of single-photon pulses regularly spaced in time. Due largely to interests in the field of quantum information, a great deal of effort has gone into the realization of this ideal in recent years [49].

The first observation of antibunched light employed scattering from a single two-state atom. The experiment by Kimble et al. [50] followed a flurry of theoretical work on the photon statistics of resonance fluorescence [51–54]. Although photons are scattered one at a time in this one-atom system, their timing and direction are unpredictable, a deficiency for a practical light source. The example nevertheless serves to illustrate matters of principle. Figure 4.7 compares a simulated (at unit

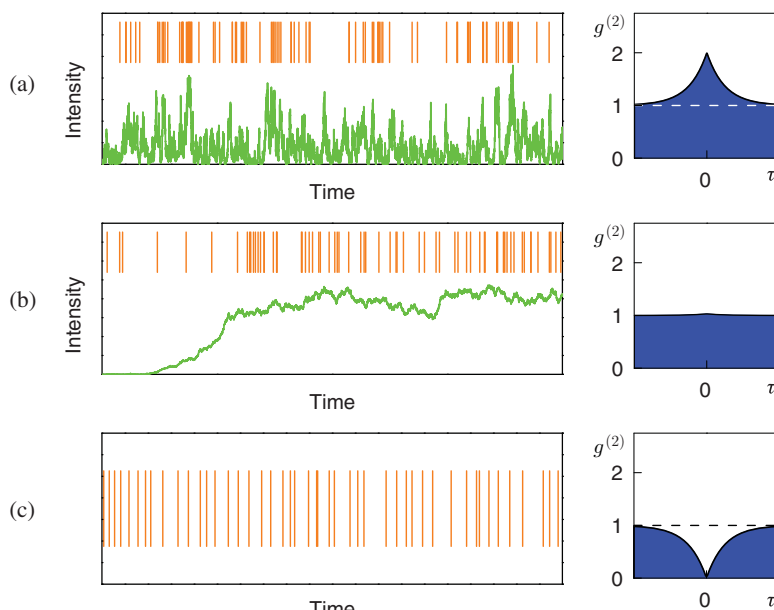


**FIGURE 4.7** Simulated photon counting sequences: (a) filtered thermal light, (b) laser turn-on, and (c) resonance fluorescence. Green curves plot the a priori rate of events (classical intensity); an event rate for resonance fluorescence must include back-action (Section 4.4.4.2). (For a color version of this figure, see the color plate section.)

efficiency) detection time series for resonance fluorescence with similar series for filtered thermal light (Section 4.3.3.3) and a simple laser model. It is noticeably more regular. It is also nonclassical, in so far as it cannot be generated as a point process from a fluctuating rate of events (classical intensity) as the others can.

#### 4.4.3 Homodyne/Heterodyne Detection

Homodyne and heterodyne detection are methods of demodulation originally developed for applications in the RF. Stable lasers extend these methods into the optical domain [55], where balanced homodyne detection, in particular, is the method of choice for measuring optical squeezing [56]. It provides access to the observables mapped by the squeeze transformation (Section 4.2.1.3) and is therefore a fundamental tool in the field of continuous variable quantum information. Heterodyne detection, although less widely used in quantum optics, is an important measurement technique in circuit QED (Section 4.5.1.1).

Homodyne and heterodyne detection superpose the signal field of interest with a local oscillator field prior to making a photon counting measurement. They may be seen and analyzed as applications of the photon counting theory of Glauber and Kelley–Kleiner (Section 4.4.1.1), with its explicit normal ordering of operators. The square of a quadrature amplitude, like  $X = \frac{1}{2}(a + a^\dagger)$ , is not a normally ordered operator. It therefore has a nonzero vacuum average, coming from the commutator  $[a, a^\dagger] = 1$ , that is, from the vacuum fluctuations. Squeezing is all about reducing this vacuum average. One might then ask: how can a measurement of optical squeezing, which relates to a nonzero vacuum average, emerge from the explicit normal ordering of the Glauber and Kelley–Kleiner theory? The story in detail is a little involved [57], but boils down to the fact that shot noise appears in the semiclassical treatment of photoelectric detection too. Its story is carried by the underlying Poisson structure of the photon counting formula and need not be associated with a vacuum state operator average. Vacuum fluctuation bookkeeping [56, 58] is simpler, though, and is used in this section.

**4.4.3.1 Simple Single-Mode Scheme** In a simple single-mode model, balanced homodyne/heterodyne detection is described by the mapping of a signal mode  $a$  and local oscillator mode  $b$  through the arrangement of beam splitters in Figure 4.8a. The mapping at the initial 50/50 beam splitter is expressed through the unitary transformation of annihilation operators

$$B^\dagger(\lambda) \begin{pmatrix} a \\ b \end{pmatrix} B(\lambda) = \begin{pmatrix} \cos \lambda & i \sin \lambda \\ i \sin \lambda & \cos \lambda \end{pmatrix} \begin{pmatrix} a \\ b \end{pmatrix}, \quad (4.76)$$

$B(\lambda) = \exp[i\lambda(ab^\dagger + a^\dagger b)]$ , with  $\lambda = \pi/4$ . The other beam splitters add vacuum modes  $v_1$  and  $v_2$  to account for nonunit detection efficiency  $\eta$ . These modes combine with the outputs of the 50/50 beam splitter through similar transformations, with  $\cos \lambda = \sqrt{\eta}$ ,  $\sin \lambda = \sqrt{1 - \eta}$ . Local oscillator mode  $b$  is in a coherent state

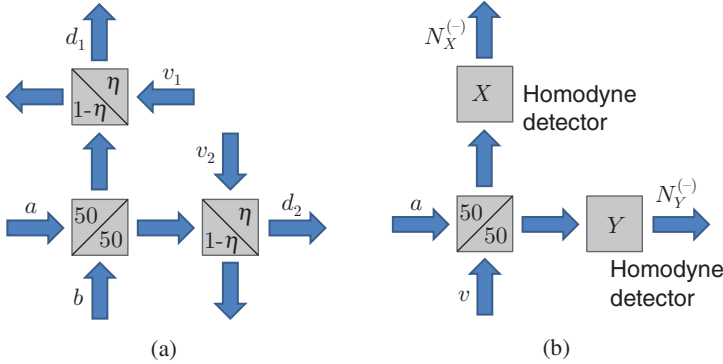


**FIGURE 4.8** Inputs and outputs for (a) homodyne detection and (b) heterodyne detection (as a dual homodyne scheme).

$|\beta\rangle$  of large amplitude, and by subtraction the reduced photon number difference  $N^{(-)}(t) = \langle\beta|d_1^\dagger(t)d_1(t) - d_2^\dagger(t)d_2(t)|\beta\rangle$  is measured, where output modes  $d_1$  and  $d_2$  are defined in Figure 4.8a. Keeping terms of order  $\beta$  only, the photon number difference is

$$N^{(-)}(t) = i\eta[\beta(t)a^\dagger(t) - \beta^*(t)a(t)] + \sqrt{\eta(1-\eta)}[\beta(t)v^\dagger(t) + \beta^*(t)v(t)], \quad (4.77)$$

$\beta(t) = \beta \exp(-i\omega t)$ , where  $v$  is a linear combination of  $v_1$  and  $v_2$ .

Balanced homodyne detection matches the local oscillator frequency to the frequency of the signal, and the relevant vacuum mode  $v$  is similarly matched. Then setting the local oscillator phase  $\theta$ , writing  $\beta = -i|\beta|e^{i\theta}$ ,

$$N^{(-)} = 2\eta|\beta|X_\theta - i\sqrt{\eta(1-\eta)}|\beta|(v^\dagger - v), \quad (4.78)$$

where  $X_\theta$  denotes the quadrature amplitude of the signal field in the local-oscillator-selected rotating frame:  $e^{i\theta} \exp(i\omega_a t) a(t) = X_\theta + iY_\theta$ . At unit detector efficiency the vacuum term is zero. It then follows that moments of homodyne detection data yield the symmetrically ordered moments of the operator  $X_\theta$ , that is, moments of the Wigner function (Section 4.2.3.3).

Balanced heterodyne detection works in a similar way, but introduces a frequency offset  $\Delta$  between the local oscillator and signal. This provides for a modulated photon number difference,

$$N^{(-)}(t) = \eta|\beta|(e^{-i\Delta t}a^\dagger - e^{i\Delta t}a) + \sqrt{\eta(1-\eta)}|\beta|(e^{-i\Delta t}v^\dagger + e^{i\Delta t}v), \quad (4.79)$$

which may be demodulated to recover both the signal amplitude and phase. The demodulation effectively measures two quadrature amplitudes at once, and therefore calls for further signal splitting. For clarity, the overall scheme may be analyzed using

the dual homodyne setup of Figure 4.8b. Considering unit detection efficiency for simplicity,

$$N_X^{(-)} = |\beta|(X + X_v), \quad N_Y^{(-)} = |\beta|(Y + Y_v), \quad (4.80)$$

where  $a = X + iY$  and  $v = X_v + iY_v$ . The effective number operator after demodulation is

$$\left(N_X^{(-)}\right)^2 + \left(N_Y^{(-)}\right)^2 = |\beta|^2(aa^\dagger + v^\dagger v). \quad (4.81)$$

Operationally the number operator  $v^\dagger v$  may be dropped, and the result shows how moments of heterodyne detection data yield quantum averages of signal field operators placed in antinormal order, that is, moments of the  $Q$  function (Section 4.2.3.1).

**4.4.3.2 Squeezed Light** Harmonic oscillator minimum uncertainty states of unequal uncertainty were known before they attracted wide attention in quantum optics, beginning in the 1970s, with the recognition of their potential to improve performance in optical communications [55]. Many early references appear in a paper by Yuen that looks ahead in this direction [59]. Squeezed states today are the foundation of continuous variable quantum information. In the simple single-mode scheme, squeezing is described by the squeeze transformation of Eq. (4.13) and generated, ideally, through the two-photon interaction of parametric down conversion, which realizes the squeeze operator. The physical implication is seen with  $a_{j\xi} \rightarrow e^{i\theta}(X_\theta + iY_\theta)$  in the expansion of the electric field, Eqs. (4.17) and (4.18): the amplitude and its quantum fluctuations of the  $\sin(\omega_j t - k_j t - \theta)$  oscillation is reduced, while for the  $\cos(\omega_j t - k_j t - \theta)$  oscillation they increase. The reduced fluctuations are seen in balanced homodyne detection, where Eq. (4.78) gives a number difference variance (assuming zero mean)

$$\langle N^{(-)}N^{(-)} \rangle = \eta|\beta|^2[4\eta\langle X_\theta^2 \rangle + (1-\eta)]. \quad (4.82)$$

The result is  $\eta|\beta|^2$  (shot noise) if the signal mode is in the vacuum state. When the vacuum is squeezed,  $\langle X_\theta^2 \rangle = e^{-2r}\frac{1}{4}$ , it is less.

The squeezing of light was first observed in 1985 [60] in an experiment that realized the squeeze interaction through four-wave mixing in sodium vapor in an optical cavity. The next year significantly larger squeezing was achieved in parametric down conversion [61]. Most generally, squeezing experiments call for a multi-mode discussion [62, 63], where shot-noise reduction at RF frequency  $\omega$  is caused by correlated photon pairs, whose frequencies  $\omega_a + \omega$  and  $\omega_a - \omega$  are symmetrically placed with respect to the central signal frequency  $\omega_a$ . For a stationary signal, for example, the output of a parametric oscillator (output coupling rate  $2\kappa$ ), a spectrum of squeezing is defined as the ratio of measured noise power to shot-noise power at frequency  $\omega$ :

$$P_\theta(\omega)/P_{\text{shot}} = 1 + 8\eta\kappa \int_{-\infty}^{\infty} d\tau e^{-i\omega\tau} \langle :X_\theta(t)X_\theta(t+\tau):\rangle, \quad (4.83)$$

where double dots indicate time and normal order. In this formula  $X_\theta$  refers to a lossy cavity mode, while it refers to a mode of the output field in Eq. (4.82); the connection, from Eq. (4.48), adds the delta-function correlation of the input field [57]:  $2\kappa\langle :X_\theta(t)X_\theta(t+\tau):\rangle = \langle X_{\text{out}}^\theta(t)X_{\text{out}}^\theta(t+\tau)\rangle - \frac{1}{4}\delta(\tau)$ .

Squeezed light generation and detection is sensitive to loss, as the above  $\eta$ -dependence shows. Experimental progress toward useful squeezing has nevertheless raised the initial 7% noise reduction [60] to a factor of ten [64]. In the reverse direction, the extremely weak squeezing of single-atom resonance fluorescence [65, 66] is of interest as a fundamental example of nonclassical light, although difficult to measure. It has been observed with one trapped atom in a cavity [67] following an earlier few-atom experiment [68].

**4.4.3.3 Quantum State Tomography and Teleportation** Quantum state tomography refers to the reconstruction of a quantum state, in one representation or another, from repeated measurements made on an ensemble of identically prepared systems. The version originally proposed in quantum optics [69] and realized soon thereafter [70] is a remarkable application of homodyne detection. As shown by Eq. (4.78), the moments of balanced homodyne detection data are moments of the Wigner function; specifically, they are moments of the marginal distribution obtained by integrating out the  $Y_\theta$ -dependence of  $W$  when  $X_\theta$  is measured; a histogram of data values *is* the marginal distribution. The Wigner function can then be reconstructed, as a representation of the quantum state, if marginal distributions are measured for all  $\theta$  (many in practice) and the set inverted with the inverse Radon transformation. This raw idea has seen considerable development [71, 72], with one off-shoot adopted as a standard procedure for characterizing the quantum state of qubits [73] and operations on qubits [74].

Continuous variable quantum teleportation aims not to reconstruct the quantum state of a field mode, but to transfer it between two parties, usually given the names Alice and Bob. Its realization as a protocol in quantum optics [75–77] substitutes field modes that are infinitely squeezed in either  $X$  or  $Y$  for the position and momentum eigenstates in a scheme proposed by Vaidman [78]. Although it is usual to speak about the transfer of a “state”, the protocol is far more accessible seen as a mapping of fields, as sketched in Figure 4.9. Mode  $a$  is an input field sent to Alice and mode  $b$  an output field received by Bob. Modes  $c$  and  $d$  are squeezed, one in  $X$  and the other in  $Y$ . If Alice’s balanced homodyne detector outputs are mapped as operators, in line with Eq. (4.78) (set  $\eta = 1$ ), the overall mapping from Alice to Bob is

$$b = \frac{1}{\sqrt{2}}(c - d) + \left[ a + \frac{1}{\sqrt{2}}(c^\dagger + d^\dagger) \right] = a + \sqrt{2}(X_c - iY_d). \quad (4.84)$$

With  $X_c$  and  $Y_d$  both infinitely squeezed, they are, in effect, zero; so the field received by Bob is the field presented to Alice.

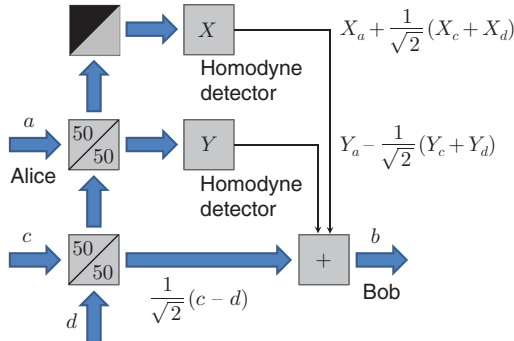


**FIGURE 4.9** Schematic of continuous variable teleportation viewed as a mapping of quantum fields.

#### 4.4.4 Quantum Trajectory Theory

Quantum trajectory theory is built around a relationship between Lindblad loss (Section 4.3.2.1) and photon counting theory, in particular, the Kelley–Kleiner formula (Section 4.4.1.1). It relates the photon counting statistics of output fields to the solution of a Lindblad master equation written as a Dyson expansion (Section 4.3.4.1) [79–81]. Although it is not necessary to follow the photon counting connection to reach the Monte Carlo algorithm that makes quantum trajectories such a useful tool [82], it is fundamental, and important for interpretation and developing variations on the basic theme [83, 84].

**4.4.4.1 Counts for Photoemissive Sources: Davies Meets Lindblad** Some few years after the seminal work of Mandel [46, 47], Glauber [6–8], and Kelley and Kleiner [43], Davies [85, 86] outlined a mathematical description of realistic photon counting (as opposed to instantaneous quantum measurement) within the framework of quantum stochastic processes. While later a disagreement with the traditional approach was claimed [87], the confusion is resolved by noting that the Kelly–Kleiner formula holds for the output fields of an open system [88, 89]; there is an underlying assumption that counted photons have already escaped their source and are not extracted from it by the presence of the detector. Indeed, rather than disagreement there is a close connection between a Davies process and Kelly–Kleiner. Quantum trajectory theory is built upon it.

The Dyson series for the solution to a Lindblad master equation connects the Kelly–Kleiner formula to a Davies quantum stochastic process. In the notation of quantum trajectories, the series is recast as a decomposition of the density operator into a mixture of pure states, each labeled by a history of photon emission times:

$$\rho(t) = \sum_{n=0}^{\infty} \int_0^t dt_n \dots \int_0^{t_2} dt_1 P(\{t_1, \dots, t_n\}) |\psi_{\{t_1, \dots, t_n\}}(t)\rangle \langle \psi_{\{t_1, \dots, t_n\}}(t)|, \quad (4.85)$$

with  $P(\{t_1, \dots, t_n\}) = \langle \bar{\psi}_{\{t_1, \dots, t_n\}}(t) | \bar{\psi}_{\{t_1, \dots, t_n\}}(t) \rangle$  the *exclusive* probability density for emissions at times  $t_1, \dots, t_n$  and none in between these times, and  $|\psi_{\{t_1, \dots, t_n\}}(t)\rangle$  the normalized  $|\bar{\psi}_{\{t_1, \dots, t_n\}}(t)\rangle$ . The Kelley–Kleiner formula uses *nonexclusive* probabilities and does not appear to be connected to this series. It may nevertheless be rewritten in terms of exclusive probabilities for an output field like that of Eq. (4.48). It is then seen (with efficiency  $\eta = 1$ ) to be nothing but the trace of the nested integral of order  $n$  inside the sum. Moreover, equating photon emissions with photon counts, the explicit form of the unnormalized ket,

$$|\bar{\psi}_{\{t_1, \dots, t_n\}}(t)\rangle = N(t, t_n) J \cdots J N(t_1, 0) |\psi(0)\rangle, \quad (4.86)$$

with operators (for the simple example of Section 4.3.4.1)

$$N(t_k, t_{k-1}) = \exp[-(\kappa + i\omega_c)t_k^\dagger a(t_k - t_{k-1})], \quad J = \sqrt{2\kappa}a, \quad (4.87)$$

shows the connection to a Davies process. From an initial ket  $|\psi(0)\rangle$ , the evolution for a given count (emission) sequence passes through a series of null measurement intervals and quantum jumps.

**4.4.4.2 Simulated Detection Records: Master Equation Unravelings** The central object in quantum trajectory theory is the ket  $|\bar{\psi}_{\{t_1, \dots, t_n\}}(t)\rangle$ , with its label of photon count times. Its norm is the exclusive probability density for the specified record of photon counts, and the normalized ket derived from it is the state of the photoemissive light source inferred from, or conditioned upon, the record of photon counts. The expansion of  $\rho(t)$  as a generalized sum over conditional kets is referred to as an unraveling of the master equation. Unravelings provide a route to Monte-Carlo simulation of photon count records and their associated conditional kets; this follows from a simple application of Bayesian inference, whereby, assuming  $|\psi_{\{t_1, \dots, t_n\}}(t)\rangle$  is known, the probability density for photon count  $n+1$  to occur at  $t$  is

$$\frac{\langle \bar{\psi}_{\{t_1, \dots, t_n\}}(t) | J^\dagger J | \bar{\psi}_{\{t_1, \dots, t_n\}}(t) \rangle}{\langle \bar{\psi}_{\{t_1, \dots, t_n\}}(t) | \bar{\psi}_{\{t_1, \dots, t_n\}}(t) \rangle} = 2\kappa \langle \psi_{\{t_1, \dots, t_n\}}(t) | a^\dagger a | \psi_{\{t_1, \dots, t_n\}}(t) \rangle. \quad (4.88)$$

By drawing uniformly distributed random numbers, one decides at each time step whether to use  $J$  or  $N(\Delta t)$  to map the ket, thus generating trajectories (conditional kets and their records) automatically ensemble weighted as the exclusive probability densities dictate.

Master equation unravelings come in infinite variety. The connection with photon counting makes this plain, since a photoemissive light source might alternatively be directed to a homodyne or heterodyne detector or experience some other passive transformation before the final recording of photon counts. Homodyne/heterodyne detection yields a diffusive evolution since a counted photon is far more likely

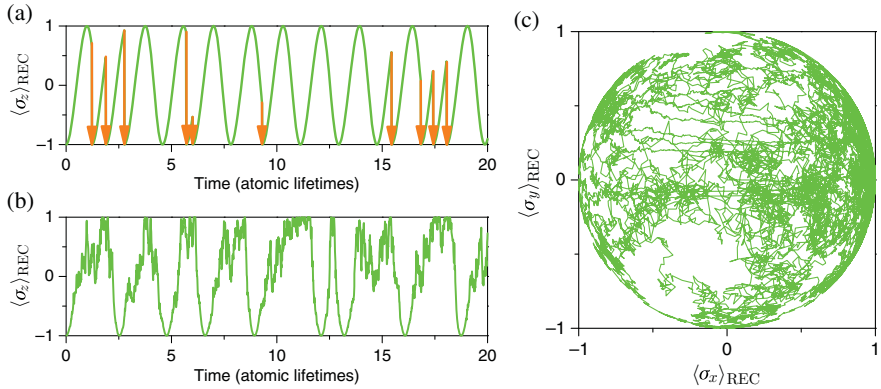


**FIGURE 4.10** Three unravelings of resonance fluorescence: (a) direct detection, (b) in-phase homodyne detection, and (c) heterodyne detection. All curves are projections of a path on the Bloch sphere.

to come from the local oscillator than from the signal. The generated stochastic Schrödinger equation (in the interaction picture and for the simple example of Section 4.3.4.1) is

$$d|\psi'_{\text{REC}}\rangle = \left( -\kappa a^\dagger a dt + \begin{Bmatrix} e^{-i\theta} \\ 1 \end{Bmatrix} \sqrt{2\kappa} adq \right) |\psi'_{\text{REC}}\rangle, \quad (4.89)$$

with record “charge” increment

$$dq = \begin{cases} 2\sqrt{2\kappa}\langle X_\theta \rangle_{\text{REC}} dt + dW & \text{homodyne} \\ \sqrt{2\kappa}\langle a^\dagger \rangle_{\text{REC}} dt + dZ & \text{heterodyne} \end{cases}, \quad (4.90)$$

where  $dW$  and  $dZ = (dW_x + idW_y)/\sqrt{2}$  are Wiener increments. The norm of ket  $|\psi'_{\text{REC}}\rangle$  is arbitrary, though expectations are normalized. Figure 4.10 shows sample trajectories for three different unravelings of resonance fluorescence.

## 4.5 CAVITY AND CIRCUIT QED

The interaction of electromagnetic radiation and matter inside cavities is an old and persistent theme in quantum optics, taking us back to early work on masers and lasers [90, 91], then forward to the recent realization of the Dicke quantum phase transition [92, 93] with a superfluid gas in an optical cavity [94, 95] and the first Bose–Einstein condensation of photons [96]. Cavity and circuit QED claim their special place in this long history by realizing single-photon dipole interaction strengths that

are very large. The goal is achieved either through a cavity design that by spatial confinement achieves high one-photon energy density [97], or by exploiting the large dipole moments of Rydberg atoms or Josephson junctions. Dipole coupling strengths (Section 4.2.5.1) as large or larger than spontaneous emission and cavity decay rates are realized, and in this way, resonances labeled by photon number, not merely cavity modes, are spectroscopically addressable. The spectroscopy is that of the Jaynes–Cummings model.

### 4.5.1 Jaynes–Cummings Model

In 1963 Jaynes and Cummings published a paper containing the model now associated with their names: “Comparison of quantum and semiclassical radiation theories with application to the beam maser” [98]. Although focused on the success of semiclassical Maxwell–Bloch equations for describing light-matter interactions—even at the one photon level—the legacy is a quantum mechanical model for the interaction of a two-state system with one mode of the radiation field. Harry Paul published the same model in 1963 [99]. The interaction is described by the dipole interaction Hamiltonian taken in the rotating wave approximation (Section 4.2.5.1):

$$H_{\text{JC}} = \hbar\omega_c a^\dagger a + \frac{1}{2}\hbar\omega_a \sigma_z + \hbar g(a\sigma_+ + a^\dagger\sigma_-), \quad (4.91)$$

with  $g$  the dipole coupling strength, and  $\omega_c$  and  $\omega_a$  the resonance frequencies of a cavity mode and two-state system (e.g., atom). Most work in cavity and circuit QED is built around realizations of this model, although ultrastrong coupling requires that the rotating wave approximation not be made [15, 100].

**4.5.1.1 Realization: Atoms, Dots, Superconducting Circuits** Attempts to realize the fully quantum mechanical Jaynes–Cummings model, so its semiclassical approximation might be questioned in the lab, begin with superconducting microwave cavities, where the large dipole moments and low spontaneous emission rates of Rydberg atoms mean that coupling to just one photon can overcome losses. This strategy is followed in the micromaser [101, 102], and in a long series of experiments performed in Paris [103]. Optical frequency realizations use either single dipole-trapped atoms [104, 105] or quantum dots [106]. Cavities might be dielectric supermirror Fabry–Perot interferometers [107], microtoroids [108], or of the micropillar or photonic crystal variety [97]. While single-photon coupling well in excess of loss rates is achieved with atoms, loss is not eliminated, and the paradigm is the Jaynes–Cummings model with decay (Section 4.5.2). Realizations in circuit QED [109] complete the circle, returning to the microwave regime. Two-state systems are engineered in a variety of designs from Josephson junctions (superconducting qubits) and interact with superconducting resonators in integrated superconducting circuits. Extremely large dipole coupling relative to loss is achieved, although loss channels are not simply ignored, as they provide for the coupling of electromagnetic signals into and out of the resonator.

**4.5.1.2 Energy Spectrum: Dressed States** The Jaynes–Cummings interaction conserves excitation number. Base kets above the ground state are therefore coupled in pairs. The energy spectrum comprises a ground state energy,  $E_0 = -\frac{1}{2}\hbar\omega_a$ , and an infinite ladder of doublets [Fig. 4.11a]:

$$E_{n,\pm} = \left(n - \frac{1}{2}\right)\hbar\omega_c \pm \hbar\sqrt{\left(\frac{\omega_c - \omega_a}{2}\right)^2 + ng^2}, \quad (4.92)$$

$n = 1, 2, \dots$ . Above the ground state, a twofold degeneracy on resonance is symmetrically split, with level shifts showing characteristic dependence on the square root of the photon number,  $\Delta E_{n,\pm} = \hbar\sqrt{ng}$ . The eigenkets above the ground states are the so-called dressed states,

$$|E_{n,\pm}\rangle = \cos(\theta_{n,\pm}/2)|n-1,+\rangle \pm \sin(\theta_{n,\pm}/2)|n,-\rangle,$$

$$\tan \theta_{n,\pm} = \mp \frac{2\sqrt{ng}}{\omega_c - \omega_a}, \quad 0 < \theta_{n,\pm} < \pi. \quad (4.93)$$

Transitions due to spontaneous emission high up the ladder of dressed states provide a quick path to the main features of the Mollow triplet spectrum of resonance fluorescence [Fig. 4.11b] [110]; although the Mollow spectrum does not rely on quantum aspects of the field (the quantum number  $n$ ) and was derived by Mollow using a classical driving field (Section 4.3.3.4).

The Jaynes–Cummings Hamiltonian with classical drive (Section 4.2.5.2) is time dependent and periodic:

$$H(t) = \frac{1}{2}\hbar\omega_a\sigma_z + \hbar\epsilon(e^{-i\omega t}\sigma_+ + e^{i\omega t}\sigma_-). \quad (4.94)$$

One may speak of dressed states in this context too. They carry over as periodic solutions to the Schrödinger equation with a technical definition taken from Floquet theory [111]. The dressed states

$$|E_{\pm}(t)\rangle = \cos(\theta_{\pm}/2)e^{\frac{1}{2}i\omega t}|+\rangle \pm \sin(\theta_{\pm}/2)e^{-\frac{1}{2}i\omega t}|-\rangle, \\ \tan \theta_{\pm} = \mp \frac{2\epsilon}{\omega - \omega_a}, \quad 0 < \theta_{\pm} < \pi, \quad (4.95)$$

evolve under the periodic Hamiltonian in much the same way as the eigenkets  $|E_{n,\pm}\rangle$  do under the Jaynes–Cummings Hamiltonian: each simply acquires an additional overall phase factor,  $\exp(-i\omega_{\pm}t)$ ,

$$\omega_{\pm} = \pm\sqrt{\left(\frac{\omega - \omega_a}{2}\right)^2 + \epsilon^2}, \quad (4.96)$$

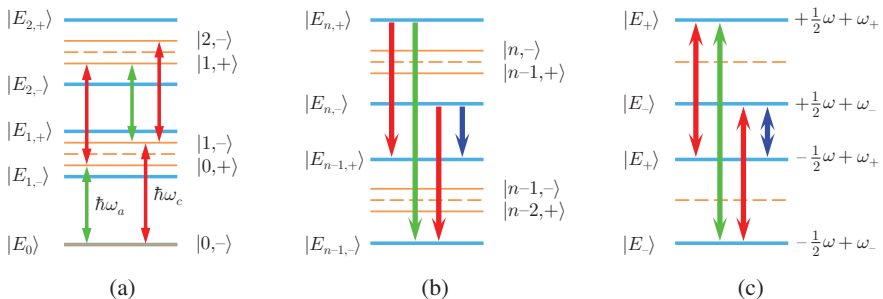


**FIGURE 4.11** Dressed state energies: (a) lower rungs of the Jaynes–Cummings ladder; (b) equally split doublets for  $n \gg 1$ ; (blue, red, green) transitions yield the (lower, center, upper) peaks of the Mollow spectrum (Section 4.3.3.4); (c) quasi-energies show the same transition frequencies as (b). (For a color version of this figure, see the color plate section.)

with  $E_{\pm} = \hbar\omega_{\pm}$  the associated quasienergies [Fig. 4.11c]. The difference frequency  $\omega_+ - \omega_-$  is the generalized Rabi frequency (compare Eq. 4.42).

**4.5.1.3 Quantum Rabi Oscillation: Collapse and Revival** According to the Jaynes–Cummings model, Bloch equations (Section 4.2.5.2) are unable to provide a complete description of the response of a two-state system to a quantum mechanical drive. In place of the Bloch sphere representation of a pseudo-spin (Section 4.2.4.2), a countable infinity of spheres is needed, one for each Jaynes–Cummings doublet (independent coupled two-state manifold). The state of the two-state system plus field is entangled, and there is no definite Rabi frequency, unless the field starts out in an eigenstate of photon number. Most generally, the simple Rabi oscillation response is dramatically altered and depends on the initial state of the field [112]. For a coherent state of amplitude  $\alpha$  and with the two-state system prepared in  $|-\rangle$ , the probability for excitation to  $|+\rangle$  after time  $t$  is ( $\omega_c = \omega_a$ )

$$p_+(t) = e^{-|\alpha|^2} \frac{1}{2} \sum_{n=0}^{\infty} \frac{|\alpha|^{2n}}{n!} [1 - \cos(\sqrt{n}gt)]. \quad (4.97)$$

The anharmonic dependence on photon number causes the quantum Rabi oscillation to collapse, due to dephasing, and at a later time revive [113]. The revival is a direct result of the discrete dependence on photon number; there is collapse but no revival if a Gaussian integral replaces the Poisson sum. This emphatic signature of the quantum nature of the radiation field can be traced through 20 years of experimentation in cavity and circuit QED, from early micromaser experiments [114], to the first definitive demonstration of quantum Rabi oscillation in a microwave field [115] and its analog in the quantized motion of a trapped ion [116], to dramatic results for superconducting qubits [117].

### 4.5.2 Jaynes–Cummings Model with Decay

Experimental measurements are made against a background of spontaneous emission and cavity loss. The Jaynes–Cummings model with decay includes these processes and generally coherent driving of the cavity mode or the two-state system. It is defined by the Lindblad master equation (Sections 4.3.2.1 and 4.3.2.3)

$$\frac{d\rho}{dt} = \frac{1}{i\hbar}[H_{JC}, \rho] + \eta_d \left( \begin{Bmatrix} a \\ \sigma_- \end{Bmatrix} e^{i\omega_d t} - \begin{Bmatrix} a^\dagger \\ \sigma_+ \end{Bmatrix} e^{-i\omega_d t} \right) + \kappa \mathcal{L}[a] + \frac{\gamma}{2} \mathcal{L}[\sigma_-], \quad (4.98)$$

with  $\eta_d$  and  $\omega_d$  the drive amplitude and frequency,  $\gamma$  the spontaneous emission rate, and  $2\kappa$  the energy loss rate for the cavity; Lindblad superoperator  $\mathcal{L}[\xi]$  is defined in Eq. (4.52). If dephasing is an issue, due to phonons in quantum dots, for example, additional Lindblad terms may be added [118]. Experimental observation of quantum Rabi oscillation calls for very large dipole coupling  $g$  relative to loss rates  $\gamma$  and  $\kappa$ . Such strong coupling is one but not the only aim of cavity and circuit QED. Cavities can act as a preferred channel in the perturbative interaction of a two-state system with its electromagnetic environment, thus controlling the rate and direction of photon emission.

**4.5.2.1 The Purcell Effect** The Purcell effect [119] can be understood from a simple application of Fermi’s golden rule to the coupling of a two-state system to a lossy cavity mode. Say the cavity mode has line profile  $(\kappa/\pi)[\kappa^2 + (\omega - \omega_c)^2]^{-1}$ , which, for the sake of the argument, may be read as a box of unit area, width  $\pi\kappa$ , and mode density  $(\pi\kappa)^{-1}$ . Then, with coupling strength  $g$ , Fermi’s golden rule gives a spontaneous emission rate through the cavity channel of  $2\pi g^2(\pi\kappa)^{-1} = 2g^2/\kappa$ . For large enough  $g$ , the net rate  $\gamma + 2g^2/\kappa$  of spontaneous emission can be significantly enhanced, with a significant fraction of photons emitted in a controlled direction. It is required that  $\kappa$  be larger than  $g$  for a photon to escape the cavity before being reabsorbed—justification for Fermi’s golden rule. Nonetheless, the degree of enhancement and directionality can be very high if  $\gamma$  is much smaller than  $g$ .

The first experimental realization of the Purcell effect was made for dye molecules near surfaces as early as 1974 [120]; early experiments in cavities date back many years as well [121, 122]. The topic is still important, however, with the Purcell effect one factor in optimizing the design of quantum dot microlasers and single-photon sources [123, 124]. A factor of equal importance is the related effect of spontaneous emission inhibition [125–127], now commonly realized in photonic crystals [128, 129]. Near perfect control of emission channels is possible in superconducting circuits, as shown, for example, by the demonstration of asymmetric—transmission versus reflection—photon statistics [130] for a near-ideal 1D (artificial) atom [131].

**4.5.2.2 Cooperativity and Saturation Photon Number** The Purcell enhancement factor may be given as a ratio of rates—the rate of spontaneous emission through

the cavity mode to the rate of emission to all other modes. This ratio,  $2C = 2g^2/\gamma\kappa$ , is sometimes termed the single-atom cooperativity. The terminology began with superradiance, and the original sense of “cooperation” hardly carries over to one atom. The meaning relative to the Purcell effect is clear. If a good rather than bad cavity is considered,  $2C$  measures the spoiling of the cavity  $Q$  by absorption:  $\kappa \rightarrow \kappa + 2g^2/\gamma$ . The Jaynes–Cummings model with decay depends on one coupling constant and two decay rates, so a second dimensionless parameter fully defines an operating regime. Often a saturation photon number,  $n_{\text{sat}} = \gamma^2/8g^2$ , is given. At weak coupling  $n_{\text{sat}}$  is large and is the number of cavity photons needed to saturate the two-state system.

### 4.5.3 Strong Coupling

In order to realize controlled coherent interactions, like those required by the field of quantum information, dipole coupling strengths far in excess of spontaneous emission and cavity decay rates are needed. At the threshold of this regime, strong coupling allows the  $\sqrt{n}$ -spectroscopy of the Jaynes–Cummings model to be addressed. Experiments on quantum Rabi oscillation (Section 4.5.1.3) are the earliest in this direction, though direct frequency domain measurements of Jaynes–Cummings spectroscopy had a decade to wait. In all sub-fields of cavity and circuit QED, the first step toward strong coupling is the demonstration of so-called vacuum Rabi splitting.

**4.5.3.1 Vacuum Rabi Splitting** Vacuum-field Rabi splitting [132,133] might more correctly be termed one-photon Rabi splitting, as it refers to the Jaynes–Cummings doublet at the first excited state (Section 4.5.1.2). It may nevertheless be probed with an arbitrarily weak cavity drive, where normal-mode frequencies of the coupled cavity field and two-state polarization are roots to the characteristic equation [134]

$$\det \begin{vmatrix} \Lambda + i\omega_c + \kappa & ig \\ ig & \Lambda + i\omega_a + \gamma/2 \end{vmatrix} = 0. \quad (4.99)$$

The two roots are

$$\Lambda_{\pm} = i\frac{\omega_c + \omega_a}{2} - \frac{1}{2}\left(\kappa + \frac{\gamma}{2}\right) \pm i\sqrt{g^2 + \left[\frac{\omega_c - \omega_a}{2} + i\frac{1}{2}\left(\kappa - \frac{\gamma}{2}\right)\right]^2}, \quad (4.100)$$

and their resolved splitting at the avoided crossing ( $\omega_c = \omega_a$ ) provides direct spectroscopic evidence of strong coupling. The normal modes are sometimes referred to as cavity polaritons.

The first experimental observations were made in optical cavities and with atomic beams [135–137]. The collective polarization of many atoms is coupled to the cavity mode in a setup like this and the dipole coupling strength is collectively enhanced. Observed normal-mode doublets do not demonstrate strong coupling at the one-atom level. One-atom experiments followed after a wait of a decade and a half [138, 139], and along with them the first realization of vacuum Rabi splitting for a single quantum dot in a photonic crystal cavity [140, 141] and in superconducting circuits [142].

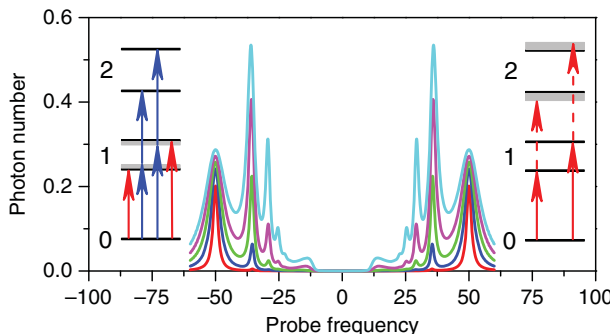


**FIGURE 4.12** Cavity photon number for increasing drive strength (red to cyan); for  $\omega_c = \omega_a$ ,  $\gamma/\kappa = 0$ , and  $g/\kappa = 50$ . One- and two-photon resonances are shown on the left and photon blockade on the right. (For a color version of this figure, see the color plate section.)

**4.5.3.2 Multi-photon Resonance and Photon Blockade** The unique signature of the Jaynes–Cummings spectrum is its  $\sqrt{n}$ -dependence. Unlike vacuum Rabi doublets (cavity polaritons), which are formed when a resonator is coupled to *any* polarizable medium, the  $\sqrt{n}$ -signature holds for *one two-level system* only. It is a feature of the cavity probe transmission spectra at stronger drive, where a sequence of resonances appear due to two-photon, three-photon, four-photon, etc., absorption from the ground to the second, third, fourth, etc., excited states [143], as shown in Figure 4.12. The two-photon resonance was first observed in experiments with a trapped atom coupled to one mode of a Fabry–Perot microcavity [144], and in the same year in superconducting circuits [145]. A second experiment with superconducting circuits [146] observed resonances all the way up to five-photon absorption.

Photon blockade is a related effect which demonstrates the anharmonicity of the Jaynes–Cummings spectrum in a perhaps even more dramatic way. If one cavity polariton (sub-level at the first excited state) is brought to resonance and the dipole coupling is strong, transitions from the first- to the second-excited state are far from resonance (see the inset in Figure 4.12); one photon in the cavity (one polariton) blocks the absorption of a second so that the *dressed* cavity behaves as a two-level system [147]. As an analog of electron physics, the phenomenon is called photon blockade [148]. The dressed cavity exhibits all the phenomenology of resonance fluorescence, including photon antibunching (Section 4.4.2.2) [149], a Mollow spectrum (Section 4.3.3.4) [33], and a phenomenon dubbed “supersplitting” [146], which is related to the drive-induced splitting of the Mollow triplet but measured in heterodyne rather than direct detection.

## REFERENCES

- [1] R. Loudon, *The Quantum Theory of Light*, 3rd ed. (Oxford University Press, Oxford, 2000).

- [2] L. Mandel and E. Wolf, *Optical Coherence and Quantum Optics*, 3rd ed. (Cambridge University Press, Cambridge, 1995).
- [3] H. Paul, *Introduction to Quantum Optics: From Light Quanta to Quantum Teleportation*, English translation by I. Jex (Cambridge University Press, Cambridge, 2004).
- [4] P. A. M. Dirac, “The quantum theory of the emission and absorption of radiation,” *Proc. R. Soc. Lond.* **114**, 243–265 (1927).
- [5] K. Husimi, “Some formal properties of the density matrix,” *Proc. Phys. Math. Soc. Jpn.* **22**, 264–314 (1940).
- [6] R. J. Glauber, “Photon correlations,” *Phys. Rev. Lett.* **10**, 84–86 (1963).
- [7] R. J. Glauber, “The quantum theory of optical coherence,” *Phys. Rev.* **130**, 2529–2539 (1963).
- [8] R. J. Glauber, “Coherent and incoherent states of the radiation field,” *Phys. Rev.* **131**, 2766–2788 (1963).
- [9] P. D. Drummond and C. W. Gardiner, “Generalised  $P$ -representations in quantum optics,” *J. Phys. A* **13**, 2353–2368 (1980).
- [10] E. C. G. Sudarshan, “Equivalence of semiclassical and quantum mechanical descriptions of statistical light beams,” *Phys. Rev. Lett.* **10**, 277–279 (1963).
- [11] E. Wigner, “On the quantum correction for thermodynamic equilibrium,” *Phys. Rev.* **40**, 749–759 (1932).
- [12] W. Schleich, D. F. Walls, and J. A. Wheeler, “Area of overlap and interference in phase space versus Wigner pseudoprobabilities,” *Phys. Rev. A* **38**, 1177–1186 (1988).
- [13] W. Schleich, *Quantum Optics in Phase Space* (Wiley-VCH, Berlin, 2001).
- [14] F. Bloch, “Nuclear induction,” *Phys. Rev.* **70**, 460–474 (1946).
- [15] C. Ciuti and I. Carusotto, “Input-output theory of cavities in the ultrastrong coupling regime: the case of time-independent cavity parameters,” *Phys. Rev. A* **74**, 033811-1–13 (2006).
- [16] I. I. Rabi, “Space quantization in a gyrating magnetic field,” *Phys. Rev.* **51**, 652–654 (1937).
- [17] I. R. Senitzky, “Dissipation in quantum mechanics: the harmonic oscillator,” *Phys. Rev.* **119**, 670–679 (1960).
- [18] I. R. Senitzky, “Dissipation in quantum mechanics: the harmonic oscillator. II,” *Phys. Rev.* **124**, 642–648 (1961).
- [19] M. J. Collett and C. W. Gardiner, “Squeezing of intracavity and traveling-wave light fields produced in parametric amplification,” *Phys. Rev. A* **30**, 1386–1391 (1984).
- [20] C. W. Gardiner and M. J. Collett, “Input and output in damped quantum systems: quantum stochastic differential equations and the master equation,” *Phys. Rev. A* **31**, 3761–3774 (1985).
- [21] B. R. Mollow, “Power spectrum of light scattered by two-level atoms,” *Phys. Rev.* **188**, 1969–1975 (1969).
- [22] G. Lindblad, “On the generators of quantum dynamical semigroups,” *Commun. Math. Phys.* **48**, 119–130 (1976).
- [23] W. Pauli, in *Probleme der Modernen Physik, Arnold Sommerfeld zum 60. Geburtstage gewidmet von seinen Schülern*, edited by P. Debye (Hirzel Verlag, Leipzig, 1928), Vol. 1.
- [24] M. Lax, “Formal theory of quantum fluctuations from a driven system,” *Phys. Rev.* **129**, 2342–2348 (1963).

- [25] M. Lax, “Quantum noise. X. Density-matrix treatment of field and population-difference equations,” *Phys. Rev.* **157**, 213–231 (1967).
- [26] M. Lax, “The Lax-Onsager regression ‘theorem’ revisited,” *Optics Commun.* **179**, 463–476 (2000).
- [27] R. Hanbury Brown and R. Q. Twiss, “Correlation between photons in coherent beams of light,” *Nature* **177**, 27–29 (1956).
- [28] R. Hanbury Brown and R. Q. Twiss, “A test of a new type of stellar interferometer on Sirius,” *Nature* **178**, 1046–1048 (1956).
- [29] R. Hanbury Brown and R. Q. Twiss, “Interferometry of the intensity fluctuations in light I. Basic theory: the correlation between photons in coherent beams of radiation,” *Proc. Roy. Soc. Lond. A* **242**, 300–324 (1957).
- [30] R. Hanbury Brown and R. Q. Twiss, “Interferometry of the intensity fluctuations in light II. An experimental test of the theory for partially coherent light,” *Proc. Roy. Soc. Lond. A* **243**, 291–319 (1958).
- [31] F. Y. Schuda, C. F. Stroud Jr., and M. Hercher, “Observation of the resonant Stark effect at optical frequencies,” *J. Phys. B* **7**, L198–203 (1974).
- [32] S. M. Ulrich, S. Ates, S. Reitzenstein, A. Löffler, A. Forchel, and P. Michler, “Dephasing of triplet-sideband optical emission of a resonantly driven InAs/GaAs quantum dot inside a microcavity,” *Phys. Rev. Lett.* **106**, 247402-1-4 (2011).
- [33] C. Lang, D. Bozyigit, C. Eichler, L. Steffen, J. M. Fink, A. A. Abdumalikov Jr., M. Baur, S. Filipp, M. P. da Silva, A. Blais, et al., “Observation of resonant photon blockade at microwave frequencies using correlation function measurements,” *Phys. Rev. Lett.* **106**, 243601-1-4 (2011).
- [34] H. G. Dehmelt, “Proposed  $10^{14}D\nu < \nu$  laser fluorescence spectroscopy of Tl<sup>+</sup> mono-ion oscillator II (spontaneous quantum jumps),” *Bull. Am. Phys. Soc.* **20**, 60 (1975).
- [35] W. Nagourney, J. Sandberg, and H. Dehmelt, “Shelved optical electron amplifier: observation of quantum jumps,” *Phys. Rev. Lett.* **56**, 2797–2799 (1986).
- [36] Th. Sauter, W. Neuhauser, R. Blatt, and P. E. Toschek, “Observation of quantum jumps,” *Phys. Rev. Lett.* **57**, 1696–1698 (1986).
- [37] J. C. Berquist, R. G. Hulet, W. M. Itano, and D. J. Wineland, “Observation of quantum jumps in a single atom,” *Phys. Rev. Lett.* **57**, 1699–1702 (1986).
- [38] Th. Basché, S. Kummer, and C. Bräuchle, “Direct spectroscopic observation of quantum jumps in a single molecule,” *Nature* **373**, 132–134 (1995).
- [39] S. Peil and G. Gabrielse, “Observing the quantum limit of an electron cyclotron: QND measurements of quantum jumps between Fock states,” *Phys. Rev. Lett.* **83**, 1287–1290 (1999).
- [40] S. Gleyzes, S. Kuhr, C. Guerlin, J. Bernu, S. Deléglise, U. B. Hoff, M. Brune, J.-M. Raimond, and S. Haroche, “Quantum jumps of light recording the birth and death of a photon in a cavity,” *Nature* **446**, 297–300 (2007).
- [41] M. Porri and S. Putterman, “Wave-function collapse due to null measurements: the origin of intermittent atomic fluorescence,” *Phys. Rev. A* **36**, 929–932 (1987).
- [42] R. J. Cook and H. J. Kimble, “Possibility of direct observation of quantum jumps,” *Phys. Rev. Lett.* **54**, 1023–1026 (1985).
- [43] P. L. Kelley and W. H. Kleiner, “Theory of electromagnetic field measurement and photoelectron counting,” *Phys. Rev.* **136**, A316–A334 (1964).

- [44] U. Fano, "Ionization yield of radiations. II. The fluctuations of the number of ions," *Phys. Rev.* **72**, 26–29 (1947).
- [45] L. Mandel, "Sub-Poissonian photon statistics in resonance fluorescence," *Opt. Lett.* **4**, 205–207 (1979).
- [46] L. Mandel, "Fluctuations of photon beams and their correlations," *Proc. Phys. Soc.* **72**, 1037–1048 (1958).
- [47] L. Mandel, "Fluctuations of photon beams: the distribution of the photo-electrons," *Proc. Phys. Soc.* **74**, 233–243 (1959).
- [48] N. Bohr, H. A. Kramers, and J. C. Slater, "The quantum theory of radiation," *Philos. Mag.* **47**, 785–802 (1924).
- [49] M. D. Eisaman, J. Fan, A. Migdall, and S. V. Polyakov, "Single-photon sources and detectors," *Rev. Sci. Instrum.* **82**, 071101-1–25 (2011).
- [50] H. J. Kimble, M. Dagenais, and L. Mandel, "Photon antibunching in resonance fluorescence," *Phys. Rev. Lett.* **39**, 691–695 (1977).
- [51] B. R. Mollow, "Pure-state analysis of resonant light scattering: radiative damping, saturation, and multiphoton effects," *Phys. Rev. A* **12**, 1919–1943 (1975).
- [52] H. J. Carmichael and D. F. Walls, "Proposal for the resonant Stark effect by photon correlation techniques," *J. Phys. B* **9**, L43–L46 (1976).
- [53] H. J. Carmichael and D. F. Walls, "A quantum mechanical master equation treatment of the dynamical Stark effect," *J. Phys. B* **9**, 1199–1219 (1976).
- [54] H. J. Kimble and L. Mandel, "Theory of resonance fluorescence," *Phys. Rev. A* **13**, 2123–2144 (1976).
- [55] H. P. Yuen and J. H. Shapiro, "Optical communication with two-photon coherent states—part III: quantum measurements realizable with photoemissive detectors," *IEEE Trans. Inf. Theory* **IT-26**, 78–92 (1980).
- [56] H. P. Yuen and V. W. S. Chan, "Noise in homodyne and heterodyne detection," *Opt. Lett.* **8**, 177–179 (1983).
- [57] H. J. Carmichael, "Spectrum of squeezing and photocurrent shot noise: a normally ordered treatment," *J. Opt. Soc. Am. B* **4**, 1588–1603 (1987).
- [58] J. H. Shapiro, "Quantum noise and excess noise in optical homodyne and heterodyne receivers," *IEEE J. Quantum Electron.* **QE-21**, 237–250 (1985).
- [59] H. P. Yuen, "Two-photon coherent states of the radiation field," *Phys. Rev. A* **13**, 2226–2243 (1976).
- [60] R. E. Slusher, L. W. Hollberg, B. Yurke, J. C. Mertz, and J. F. Valley, "Observation of squeezed states generated by four-wave mixing in an optical cavity," *Phys. Rev. Lett.* **55**, 2409–2412 (1985).
- [61] L.-A. Wu, H. J. Kimble, J. L. Hall, and H. Wu, "Generation of squeezed states by parametric down conversion," *Phys. Rev. Lett.* **57**, 2520–2523 (1986).
- [62] C. M. Caves and B. L. Schumaker, "New formalism for two-photon quantum optics. I. Quadrature phases and squeezed states," *Phys. Rev. A* **31**, 3068–3092 (1985).
- [63] B. L. Schumaker and C. M. Caves, "New formalism for two-photon quantum optics. II. Mathematical foundation and compact notation," *Phys. Rev. A* **31**, 3093–3111 (1985).
- [64] H. Valbruch, M. Mehmet, S. Chelkowski, B. Hage, A. Franzen, N. Lastzka, S. Großler, K. Danzmann, and R. Schnabel, "Observation of squeezed light with 10-dB quantum-noise reduction," *Phys. Rev. Lett.* **100**, 033602-1–4 (2008).

- [65] D. F. Walls and P. Zoller, “Reduced quantum fluctuations in resonance fluorescence,” *Phys. Rev. Lett.* **47**, 709–711 (1981).
- [66] H. J. Carmichael, “Photon antibunching and squeezing for a single atom in a resonant cavity,” *Phys. Rev. Lett.* **55**, 2790–2793 (1985).
- [67] A. Ourjoumtsev, K. Kubanek, M. Koch, C. Sames, P. W. H. Pinkse, G. Rempe, and K. Murr, “Observation of squeezed light from one atom excited by two photons,” *Nature* **474**, 623–626 (2011).
- [68] G. T. Foster, L. A. Orozco, H. M. Castro-Beltran, and H. J. Carmichael, “Quantum state reduction and conditional time evolution of wave-particle correlations in cavity QED,” *Phys. Rev. Lett.* **85**, 3149–3152 (2000).
- [69] K. Vogel and H. Risken, “Determination of quasiprobability distributions in terms of probability distributions for the rotated quadrature phase,” *Phys. Rev. A* **40**, 2847–2849 (1989).
- [70] D. T. Smithey, M. Beck, M. G. Raymer, and A. Faridani, “Measurement of the Wigner distribution and the density matrix of a light mode using optical homodyne tomography: application to squeezed states and the vacuum,” *Phys. Rev. Lett.* **70**, 1244–1247 (1993).
- [71] A. I. Lvovsky and M. G. Raymer, “Continuous-variable optical quantum-state tomography,” *Rev. Mod. Phys.* **81**, 299–332 (2009).
- [72] M. D’Ariano, M. G. A. Paris, and M. F. Sacchi, “Quantum tomography,” *Adv. Imaging Electron Phys.* **128**, 205–308 (2003).
- [73] J. B. Altepeter, J. R. Jeffrey, and P. G. Kwiat, “Photonic state tomography,” *Adv. At. Mol. Opt. Phys.* **52**, 105–159 (2005).
- [74] I. L. Chuang and M. A. Nielsen, “Prescription for the experimental determination of the dynamics of a quantum black box,” *J. Modern Opt.* **44**, 2455–2467 (1997).
- [75] S. L. Braunstein and H. J. Kimble, “Teleportation of continuous quantum variables,” *Phys. Rev. Lett.* **80**, 869–872 (1998).
- [76] A. Furusawa, J. L. Sørensen, S. L. Braunstein, C. A. Fuchs, H. J. Kimble, and E. S. Polzik, “Unconditional quantum teleportation,” *Science* **282**, 706–709 (1998).
- [77] W. P. Bowen, N. Treps, B. C. Buchler, R. Schnabel, T. C. Ralph, H.-A. Bachor, T. Symul, and P. K. Lam, “Experimental investigation of continuous variable quantum teleportation,” *Phys. Rev. A* **67**, 032302-1–4 (2003).
- [78] L. Vaidman, “Teleportation of quantum states,” *Phys. Rev. A* **49**, 1473–1476 (1994).
- [79] H. J. Carmichael, S. Singh, R. Vyas, and P. R. Rice, “Photoelectron waiting times and atomic state reduction in resonance fluorescence,” *Phys. Rev. A* **39**, 1200–1218 (1989).
- [80] H. J. Carmichael, *An Open Systems Approach to Quantum Optics*, Lecture Notes in Physics, New Series m-Monographs (Springer, Berlin, Heidelberg, 1993), Vol. m18.
- [81] H. J. Carmichael, *Statistical Methods in Quantum Optics 2: Non-Classical Fields* (Springer, Berlin, Heidelberg, 2008).
- [82] J. Dalibard, Y. Castin, and K. Mølmer, “Wave-function approach to dissipative processes in quantum optics,” *Phys. Rev. Lett.* **68**, 580–583 (1992).
- [83] A. Barchielli and M. Gregoratti, *Quantum Trajectories and Measurements in Continuous Time*, Lecture Notes in Physics 782 (Springer, Berlin, Heidelberg, 2009).
- [84] H. M. Wiseman and G. J. Milburn, *Quantum Measurement and Control* (Cambridge University Press, Cambridge, 2010).

- [85] E. B. Davies, “Quantum stochastic processes,” *Commun. Math. Phys.* **15**, 277–304 (1969).
- [86] E. B. Davies, *Quantum Theory of Open Systems* (Academic Press, London, 1976).
- [87] M. D. Srinivas and E. B. Davies, “Photon counting probabilities in quantum optics,” *Opt. Acta* **28**, 981–996 (1981).
- [88] L. Mandel, “Comment on ‘photon counting probabilities in quantum optics’,” *Opt. Acta* **28**, 1447–1450 (1981).
- [89] M. D. Srinivas and E. B. Davies, “What are the photon counting probabilities for open systems—a reply to Mandel’s comments,” *Opt. Acta* **29**, 235–238 (1982).
- [90] A. L. Schawlow and C. H. Townes, “Infrared and optical masers,” *Phys. Rev.* **112**, 1940–1949 (1958).
- [91] M. Scully and W. E. Lamb Jr., “Quantum theory of an optical maser,” *Phys. Rev. Lett.* **16**, 853–855 (1966).
- [92] R. H. Dicke, “Coherence in spontaneous radiation processes,” *Phys. Rev.* **93**, 99–110 (1954).
- [93] K. Hepp and E. H. Lieb, “On the superradiant phase transition for molecules in a quantized radiation field,” *Ann. Phys.* **76**, 360–404 (1973).
- [94] K. Baumann, C. Guerlin, F. Brennecke, and T. Esslinger, “Dicke quantum phase transition with a superfluid gas in an optical cavity,” *Nature* **464**, 1301–1306 (2010).
- [95] F. Dimer, B. Estienne, A. S. Parkins, and H. J. Carmichael, “Proposed realization of the Dicke-model quantum phase transition in an optical cavity QED system,” *Phys. Rev. A* **75**, 031804-1–14 (2007).
- [96] J. Klaers, J. Schmitt, F. Vewinger, and M. Weitz, “Bose-Einstein condensation of photons in an optical microcavity,” *Nature* **468**, 445–448 (2010).
- [97] K. J. Vahala, “Optical microcavities,” *Nature* **424**, 839–846 (2003).
- [98] E. T. Jaynes and F. W. Cummings, “Comparison of quantum and semiclassical radiation theories with application to the beam maser,” *Proc. IEEE* **51**, 89–109 (1963).
- [99] H. Paul, “Induzierte Emission bei starker Einstrahlung,” *Annalen der Physik* **466**, 411–412 (1963).
- [100] T. Niemczyk, F. Deppe, H. Huebl, E. P. Menzel, F. Hocke, M. J. Schwarz, J. J. Garcia-Ripoll, D. Zueco, T. Hümmer, E. Solano, et al., “Circuit quantum electrodynamics in the ultrastrong-coupling regime,” *Nature Phys.* **6**, 772–776 (2010).
- [101] H. Walther, B. T. H. Varcoe, B.-G. Englert, and T. Becker, “Cavity quantum electrodynamics,” *Rep. Prog. Phys.* **69**, 1325–1382 (2006).
- [102] M. O. Scully and M. S. Zubairy, *Quantum Optics* (Cambridge University Press, Cambridge, 1997), Chap. 13.
- [103] J. M. Raimond, M. Brune, and S. Haroche, “Manipulating quantum entanglement with atoms and photons in a cavity,” *Rev. Mod. Phys.* **73**, 565–582 (2001).
- [104] H. Mabuchi and A. C. Doherty, “Cavity quantum electrodynamics: coherence in context,” *Science* **298**, 1372–1377 (2002).
- [105] R. Miller, T. E. Northup, K. M. Birnbaum, A. Boca, A. D. Boozer, and H. J. Kimble, “Trapped atoms in cavity QED: coupling quantized light and matter,” *J. Phys. B* **38**, S551–S565 (2005).
- [106] A. Kiraz, C. Reese, B. Gayral, L. Zhang, W. V. Schoenfeld, B. D. Gerardot, P. M. Petroff, E. L. Hu, and A. Imamoğlu “Cavity-quantum electrodynamics with quantum dots,” *J. Opt. B: Quantum. Semiclass. Opt.* **5**, 129–137 (2003).

- [107] C. J. Hood, H. J. Kimble, and J. Ye, “Characterization of high-finesse mirrors: loss, phase shifts, and mode structure in an optical cavity,” *Phys. Rev. A* **64**, 033804-1–7 (2001).
- [108] D. K. Armani, T. J. Kippenberg, S. M. Spillane, and K. J. Vahala, “Ultra-high-Q toroid microcavity on a chip,” *Nature* **421**, 925–928 (2003).
- [109] R. J. Schoelkopf and S. M. Girvin, “Wiring up quantum systems,” *Nature* **451**, 664–669 (2008).
- [110] C. Cohen-Tannoudji and S. Reynaud, “Dressed-atom description of resonance fluorescence and absorption spectra of a multi-level atom in an intense laser beam,” *J. Phys. B* **10**, 345–363 (1977).
- [111] J. H. Shirley, “Solution of the Schrödinger equation with a Hamiltonian periodic in time,” *Phys. Rev.* **138**, B979–B987 (1965).
- [112] F. W. Cummings, “Stimulated emission of radiation in a single mode,” *Phys. Rev.* **140**, A1051–A1056 (1965).
- [113] J. H. Eberly, N. B. Narozhny, and J. J. Sanchez-Mondragon, “Periodic spontaneous collapse and revival in a simple quantum model,” *Phys. Rev. Lett.* **44**, 1323–1326 (1980).
- [114] G. Rempe, H. Walther, and N. Klein, “Observation of quantum collapse and revival in a one-atom maser,” *Phys. Rev. Lett.* **58**, 353–356 (1987).
- [115] M. Brune, F. Schmidt-Kaler, A. Maali, J. Dreyer, E. Hagley, J. M. Raimond, and S. Haroche, “Quantum Rabi oscillation: a direct test of field quantization in a cavity,” *Phys. Rev. Lett.* **76**, 1800–1803 (1996).
- [116] D. M. Meekhof, C. Monroe, B. E. King, W. M. Itano, and D. J. Wineland, “Generation of nonclassical motional states of a trapped ion,” *Phys. Rev. Lett.* **76**, 1796–1799 (1996).
- [117] M. Hofheinz, E. M. Weig, M. Ansmann, R. C. Bialczak, E. Lucero, M. Neeley, A. D. O’Connell, H. Wang, J. M. Martinis, and A. N. Cleland, “Generation of Fock states in a superconducting quantum circuit,” *Nature* **76**, 310–314 (2008).
- [118] C. Roy and S. Hughes, “Influence of electron-acoustic-photon scattering on intensity power broadening in a coherently driven quantum-dot-cavity system,” *Phys. Rev. X* **1**, 021009-1–19 (2011).
- [119] E. M. Purcell, “Spontaneous emission probabilities at radio frequencies,” *Phys. Rev.* **69**, 681 (1946).
- [120] K. H. Drexhage, “Interaction of light with monomolecular dye layers,” in *Progress in Optics*, edited by E. Wolf (North Holland, Amsterdam, 1974), Vol. XII, pp. 165–232.
- [121] P. Goy, J. M. Raimond, M. Gross, and S. Haroche, “Observation of cavity-enhanced single-atom spontaneous emission,” *Phys. Rev. Lett.* **50**, 1903–1906 (1983).
- [122] D. J. Heinzen, J. J. Childs, J. E. Thomas, and M. S. Feld, “Enhanced and inhibited visible spontaneous emission by atoms in a confocal resonator,” *Phys. Rev. Lett.* **58**, 1320–1323 (1987).
- [123] J. M. Gérard, B. Sermage, B. Gayral, B. Legrand, E. Costard, and V. Thierry-Mieg, “Enhanced spontaneous emission by quantum boxes in a monolithic optical microcavity,” *Phys. Rev. Lett.* **81**, 1110–1113 (1998).
- [124] M. Munsch, J. Claudon, J. Bleuse, N. S. Malik, E. Dupuy, J. M. Gérard, Y. Chen, N. Gregersen, and J. Mørke, “Linearly polarized single-mode spontaneous emission in a photonic nanowire,” *Phys. Rev. Lett.* **108**, 077405-1–5 (2012).

- [125] D. Kleppner, “Inhibited spontaneous emission,” *Phys. Rev. Lett.* **47**, 233–236 (1981).
- [126] G. Gabrielse and H. Dehmelt, “Observation of inhibited spontaneous emission,” *Phys. Rev. Lett.* **55**, 67–70 (1985).
- [127] R. G. Hulet, E. S. Hilfer, and D. Kleppner , “Inhibited spontaneous emission by a Rydberg atom,” *Phys. Rev. Lett.* **55**, 2137–2140 (1985).
- [128] E. Yablonovitch, “Inhibited spontaneous emission in solid state physics and electronics,” *Phys. Rev. Lett.* **58**, 2059–2062 (1987).
- [129] S. John, “Strong localization of photons in certain disordered dielectric superlattices,” *Phys. Rev. Lett.* **58**, 2486–2489 (1987).
- [130] H. J. Carmichael, “Quantum trajectory theory for cascaded open systems,” *Phys. Rev. Lett.* **70**, 2273–2276 (1993).
- [131] I.-C. Hoi, T. Palomaki, J. Lindkvist, G. Johansson, P. Delsing, and C. M. Wilson, “Generation of nonclassical microwave states using an artificial atom in 1D open space,” *Phys. Rev. Lett.* **108**, 263601-1-5 (2012).
- [132] J. J. Sanchez-Mondragon, N. B. Narozhny, and J. H. Eberly, “Theory of spontaneous emission lineshape in an ideal cavity,” *Phys. Rev. Lett.* **51**, 550–553 (1983).
- [133] G. S. Agarwal, “Vacuum-field Rabi splittings in microwave absorption by Rydberg atoms in a cavity,” *Phys. Rev. Lett.* **53**, 1732–1734 (1984).
- [134] H. J. Carmichael, “Quantum fluctuations in absorptive bistability without adiabatic elimination,” *Phys. Rev. A* **33**, 3262–3269 (1986).
- [135] M. G. Raizen, R. J. Thompson, R. J. Brecha, H. J. Kimble, and H. J. Carmichael, “Normal-mode splitting and linewidth averaging for two-state atoms in an optical cavity,” *Phys. Rev. Lett.* **63**, 240–243 (1989).
- [136] Y. Zhu, D. J. Gauthier, S. E. Morin, Q. Wu, H. J. Carmichael, and T. W. Mossberg, “Vacuum Rabi splitting as a feature of linear dispersion theory: analysis and experimental observations,” *Phys. Rev. Lett.* **64**, 2499–2502 (1990).
- [137] R. J. Thompson, G. Rempe, and H. J. Kimble, “Observation of normal-mode splitting for an atom in an optical cavity,” *Phys. Rev. Lett.* **68**, 1132–1135 (1992).
- [138] A. Boca, R. Miller, K. M. Birnbaum, A. D. Boozer, J. McKeever, and H. J. Kimble, “Observation of the vacuum Rabi spectrum for one trapped atom,” *Phys. Rev. Lett.* **93**, 233603-1-4 (2004).
- [139] P. Maunz, T. Puppe, I. Schuster, N. Syassen, P. W. H. Pinkse, and G. Rempe, “Normal-mode spectroscopy of a single-bound-atom-cavity system,” *Phys. Rev. Lett.* **94**, 033002-1-4 (2005).
- [140] Y. Yoshie, A. Scheer, J. Hendrickson, G. Khitrova, H. M. Gibbs, G. Rupper, C. Eli, O. B. Shchekin, and D. G. Deppe, “Vacuum Rabi splitting with a single quantum dot in a photonic crystal nanocavity,” *Nature* **432**, 200–203 (2004).
- [141] G. Khitrova, H. M. Gibbs, M. Kira, S. W. Koch, and A. Scherer, “Vacuum Rabi splitting in semiconductors,” *Nature Phys.* **2**, 81–90 (2006).
- [142] A. Wallraff, D. I. Schuster, A. Blais, L. Frunzio, R.-S. Huang, J. Majer, S. Kumar, S. M. Girvin, and R. J. Schoelkopf, “Strong coupling of a single photon to a superconducting qubit using circuit quantum electrodynamics,” *Nature* **431**, 162–167 (2004).
- [143] H. J. Carmichael, L. Tian, W. Ren, and P. Alsing, “Nonperturbative atom-photon interactions in an optical cavity,” in *Cavity Quantum Electrodynamics, Advances in Atomic Molecular and Optical Physics*, edited by P. R. Berman (Academic Press, Orlando, 1994), pp. 381–423.

- [144] I. Schuster, A. Kubanek, A. Fuhrmanek, T. Puppe, P. W. H. Pineske, K. Murr, and G. Rempe, “Nonlinear spectroscopy of photons bound to one atom,” *Nature Phys.* **4**, 382–385 (2008).
- [145] J. M. Fink, M. Göppel, M. Baur, R. Bianchetti, P. J. Leek, A. Blais, and A. Wallraff, “Climbing the Jaynes-Cummings ladder and observing its  $\sqrt{n}$  nonlinearity in a cavity QED system,” *Nature* **454**, 315–318 (2008).
- [146] L. V. Bishop, J. M. Chow, J. Koch, A. A. Houck, M. H. Devoret, E. Thuneberg, S. M. Girvin, and R. J. Schoelkopf, “Nonlinear response of the vacuum Rabi resonance,” *Nature Phys.* **5**, 105–109 (2009).
- [147] L. Tian and H. J. Carmichael, “Quantum trajectory simulations of two-state behavior in an optical cavity containing one atom,” *Phys. Rev. A* **46**, R6801–R6804 (1992).
- [148] A. Imamoğlu, H. Schmidt, G. Woods, and M. Deutsch, “Strongly interacting photons in a nonlinear cavity,” *Phys. Rev. Lett.* **79**, 1467–1470 (1997).
- [149] K. M. Birnbaum, A. Boca, R. Miller, A. D. Boozer, T. E. Northup, and H. J. Kimble, “Photon blockade in an optical cavity with one trapped atom,” *Nature* **436**, 87–90 (2005).



---

# 5

---

## SQUEEZED LIGHT

A. I. LVOVSKY<sup>1,2</sup>

<sup>1</sup>*Institute for Quantum Information Science, University of Calgary, Calgary, Canada*

<sup>2</sup>*Russian Quantum Center, Skolkovo, Moscow, Russia*

### 5.1 WHAT IS SQUEEZED LIGHT?

#### 5.1.1 Single-Mode Squeezed Light

In squeezed states of light, the noise of the electric field at certain phases falls below that of the vacuum state. This means that, when we turn on the squeezed light, we see *less noise than no light at all*. This apparently paradoxical feature is a direct consequence of quantum nature of light and cannot be explained within the classical framework.

The basic idea of squeezing can be understood by considering the quantum harmonic oscillator, familiar from undergraduate quantum mechanics. Its vacuum state wavefunction in the dimensionless position basis is given by<sup>1</sup>

$$\psi_0(X) = \frac{1}{\pi^{1/4}} e^{-X^2/2}, \quad (5.1)$$

which in the momentum basis corresponds to

$$\tilde{\psi}_0(P) = \frac{1}{\sqrt{2\pi}} \int_{-\infty}^{+\infty} e^{-iPX} \psi_0(X) dX = \frac{1}{\pi^{1/4}} e^{-P^2/2} \quad (5.2)$$

---

<sup>1</sup>We use convention  $[\hat{X}, \hat{P}] = i$  for the quadrature observables.

(so the vacuum state wavefunction is the same in the position and momentum bases). The variance of the position and momentum observables in the vacuum state equals  $\langle 0 | \Delta X^2 | 0 \rangle = \langle 0 | \Delta P^2 | 0 \rangle = 1/2$ .

The wavefunction of the *squeezed-vacuum* state  $|\text{sq}_R\rangle$  with the *squeezing factor*  $R > 0$  is obtained from that of the vacuum state by means of scaling transformation:

$$\psi_R(X) = \frac{\sqrt{R}}{\pi^{1/4}} e^{-(RX)^2/2} \quad (5.3)$$

and

$$\tilde{\psi}_R(P) = \frac{1}{\pi^{1/4} \sqrt{R}} e^{-(P/R)^2/2} \quad (5.4)$$

in the position and momentum bases, respectively. In this state, the variances of the two canonical observables are

$$\langle \Delta X^2 \rangle = 1/(2R^2) \quad \text{and} \quad \langle \Delta P^2 \rangle = R^2/2. \quad (5.5)$$

If  $R > 1$ , the position variance is below that of the vacuum state, so  $|\text{sq}_R\rangle$  is *position-squeezed*; for  $R < 1$  the state is *momentum-squeezed*. In other words, if we prepare multiple copies of  $|\text{sq}_R\rangle$ , and perform a measurement of the squeezed observable on each copy, our measurement results will exhibit less variance than if we performed the same set of measurements on multiple copies of the vacuum state.

More generally, we say that a state of a single harmonic oscillator exhibits (*quadrature*) *squeezing* if the variance of the position, momentum, or any other quadrature<sup>2</sup> in that state exhibits variance below 1/2. In accordance with the uncertainty principle, both position and momentum observables, or any two quadratures associated with orthogonal angles, cannot be squeezed at the same time. For example, in state (5.3) the product  $\langle \Delta X^2 \rangle \langle \Delta P^2 \rangle = 1/4$  is the same as that for the vacuum state.

Squeezing is best visualized by means of the Wigner function—the quantum analog of the phase-space probability density. Figures 5.1a and 5.1b display the Wigner functions of the position- and momentum-squeezed vacuum states, respectively. The squeezing feature becomes apparent when these Wigner functions are compared with those of the vacuum state (Fig. 5.1a). Figure 5.1e and 5.1f show *squeezed coherent states*, which are analogous to the squeezed vacuum except that their Wigner functions are displaced from the phase-space origin akin to the coherent state (Fig. 5.1b).

The state shown in Figure 5.1f is particularly interesting because it exhibits, as a consequence of momentum squeezing, *phase squeezing*—reduction of the uncertainty in the *phase* with respect to a coherent state of the same amplitude. Because the Schrödinger evolution under the standard harmonic oscillator Hamiltonian corresponds to clockwise rotation of the phase space around the origin point, the phase squeezing property is preserved under this evolution. In the same context, the state in Figure 5.1e is sometimes called *amplitude-squeezed*.

---

<sup>2</sup>The field *quadrature* is observable  $\hat{X}_\theta = \hat{X} \cos \theta + \hat{P} \sin \theta$  (where  $\theta$  is a real number known as *quadrature angle*).

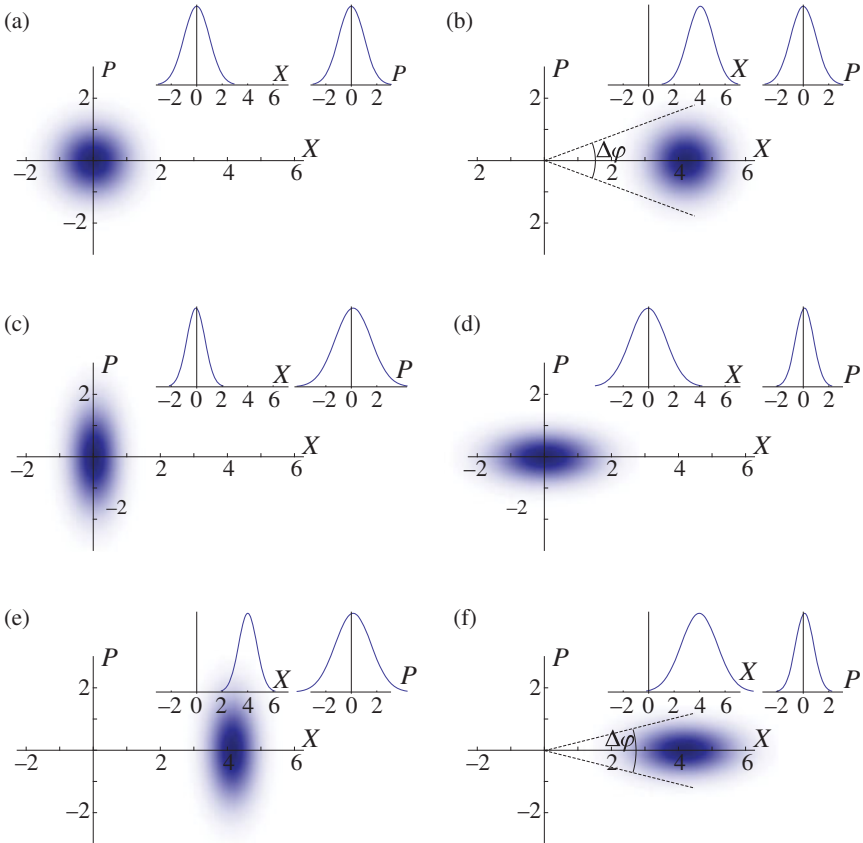


**FIGURE 5.1** Wigner functions of certain single-oscillator states. (a) Vacuum state. (b) Coherent state. (c,d) Position- and momentum-squeezed vacuum states. (e,f) Position- and momentum-squeezed coherent states with real amplitudes. Panels (b) and (f) show the phase uncertainties of the respective states to emphasize the phase squeezing of state (f). Insets show wavefunctions in the position and momentum bases.

According to the quantum theory of light, the Hilbert space associated with a mode of the electromagnetic field is isomorphic to that of the mechanical harmonic oscillator. The role of the position and momentum observables in this context is played by the electric field magnitudes measured at specific phases. For example, the field at phase zero (with respect to a certain reference) corresponds to the position observable, that at phase  $\pi/2$  to the momentum observable, and so on. Accordingly, phase-sensitive measurements of the field marmitude in an electromagnetic wave are affected by quantum uncertainties. For the coherent and vacuum states, this uncertainty is phase-independent and equals  $\sqrt{\hbar\omega/2\epsilon_0V}$  (the *standard quantum limit*, or *SQL*), where  $\omega$  is the optical frequency and  $V$  is the quantization volume [1]. But squeezed optical states exhibit uncertainties below SQL at certain phases.

Depending on whether the mean coherent amplitude of the state is zero or not, squeezed optical states are classified into squeezed vacuum and (*bright*) *squeezed light*. Squeezed coherent states form a subset of bright squeezed light states.

How can one generate optical squeezed states in experiment? Consider the state

$$|\psi\rangle = |0\rangle - \frac{s}{\sqrt{2}} |2\rangle, \quad (5.6)$$

where  $|0\rangle$  and  $|2\rangle$  are photon number (Fock) states and  $s$  is a real positive number. We assume  $s$  to be small, so the norm of state (5.6) is close to one. The mean value of the position operator  $\hat{X} = (\hat{a} + \hat{a}^\dagger)/\sqrt{2}$  in this state is zero while its variance equals

$$\langle \Delta X^2 \rangle = \langle \psi | \frac{(\hat{a} + \hat{a}^\dagger)^2}{2} | \psi \rangle = \frac{1}{2} - s, \quad (5.7)$$

so state  $|\psi\rangle$  is position squeezed for positive  $s$ .

This result illustrates one of the primary methods of producing squeezing. Spontaneous parametric down-conversion (SPDC) is a nonlinear optical process in which a photon of a powerful laser field propagating through a second-order nonlinear optical medium may split into two photons of lower energy. The frequencies, wavevectors, and polarizations of the generated photons are governed by phase-matching conditions. Single-mode squeezing, such as that in the above example, is obtained when SPDC is *degenerate*: the two generated photons are indistinguishable in all their parameters: frequency, direction, and polarization. The quantum state of the optical mode into which the photon pairs are emitted exhibits squeezing (Figure 5.2a).

Aside from being an interesting physical entity by itself, squeezed light has a variety of applications. One of the primary applications of single-mode squeezed light is in precision measurements of distances. Such measurements are typically done by means of interferometry. Quantum phase noise poses an ultimate limit to interferometry, and the application of squeezing (in particular, the phase-squeezed state discussed earlier) permits expanding this limit beyond that fundamental boundary. For example, squeezing is employed in the new generation of gravitational wave detectors.

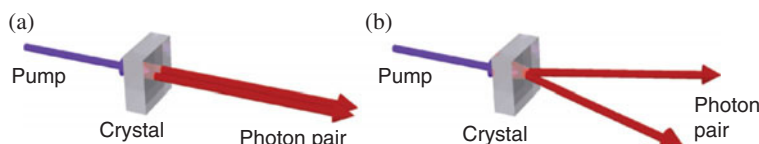


**FIGURE 5.2** Spontaneous parametric down-conversion. (a) Degenerate configuration, leading to single-mode squeezed vacuum. (b) Non-degenerate configuration, leading to two-mode squeezed vacuum.

### 5.1.2 Two-Mode Squeezed Light

A state that is closely related to the single-oscillator squeezed vacuum in its theoretical description and experimental procedures, but quite different in properties is the *two-mode squeezed vacuum* (TMSV), also known as the *twin-beam state*. As the name suggests, this is a state of not one, but two mechanical or electromagnetic oscillators. We introduce this state by first analyzing the tensor product  $|0\rangle \otimes |0\rangle$  of vacuum states of the two oscillators. In the position basis, its wavefunction (Fig. 5.3a),

$$\Psi_{00}(X_a, X_b) = \frac{1}{\sqrt{\pi}} e^{-X_a^2/2} e^{-X_b^2/2}, \quad (5.8)$$

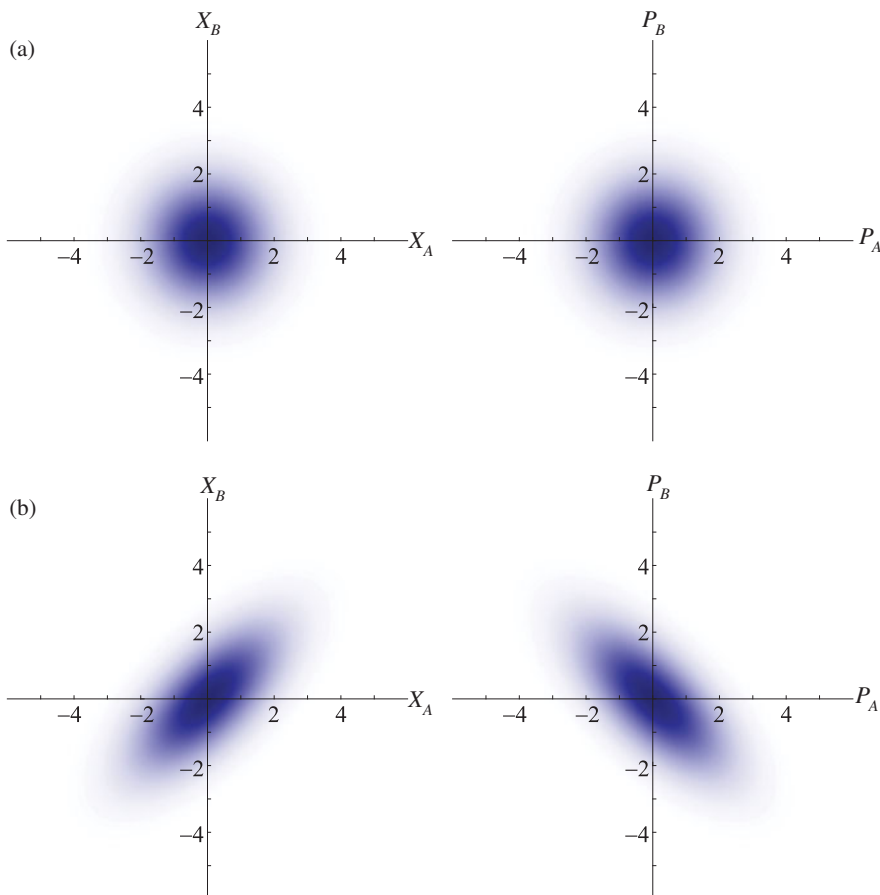


**FIGURE 5.3** Wavefunctions (not Wigner functions!) of two-mode states in the position (left) and momentum (right) bases. (a) The double-vacuum state is uncorrelated in both bases. (b) The two-mode squeezed state with position observables correlated, and momentum observables anticorrelated beyond the standard quantum limit.

can be rewritten as

$$\Psi_{00}(X_a, X_b) = \frac{1}{\sqrt{\pi}} e^{-(X_a - X_b)^2/4} e^{-(X_a + X_b)^2/4}. \quad (5.9)$$

Here,  $X_a$  and  $X_b$  are the position observables of the two oscillators which are traditionally associated with fictional experimentalists Alice and Bob. The meaning of Eq. (5.9) is that the observables  $(X_a - X_b)/\sqrt{2}$  and  $(X_a + X_b)/\sqrt{2}$  have a Gaussian distribution with variance  $1/2$ . This is not surprising because in the double-vacuum state Alice's and Bob's position observables are uncorrelated and both of them have variance  $1/2$ . The behavior of the momentum quadratures in this state is analogous to that of the position.

The wavefunction of the two-mode squeezed vacuum state  $|\text{TMSV}_R\rangle$  is given by

$$\Psi_R(X_a, X_b) = \frac{1}{\sqrt{\pi}} e^{-(X_a + X_b)^2/(4R^2)} e^{-R^2(X_a - X_b)^2/4}, \quad (5.10)$$

where  $R$ , as previously, is the squeezing factor (Figure 5.3c). In contrast to the double-vacuum state, TMSV is an entangled state, and Alice's and Bob's position observables are nonclassically correlated, thanks to that entanglement. For  $R > 1$ , the variance of  $(X_a - X_b)/\sqrt{2}$  is less than  $1/2$ , that is, below the value for the double-vacuum state.

The wavefunction of TMSV in the momentum basis is obtained from Eq. (5.10) by means of Fourier transform by both Alice's and Bob's observables:

$$\tilde{\Psi}_R(P_a, P_b) = \frac{1}{\sqrt{\pi}} e^{-(P_a - P_b)^2/(4R^2)} e^{-R^2(P_a + P_b)^2/4}. \quad (5.11)$$

We see that for  $R > 1$  Alice's and Bob's momenta are anticorrelated, that is, the variance of the sum  $(P_a + P_b)/\sqrt{2}$  is below the level expected from two vacuum states (Fig. 5.3d).

The two-mode squeezed vacuum does not imply squeezing in each individual mode. On the contrary, Alice's and Bob's position and momentum observables in TMSV obey a Gaussian probability distribution with variance

$$\langle \Delta X_a^2 \rangle = \langle \Delta X_b^2 \rangle = \langle \Delta P_a^2 \rangle = \langle \Delta P_b^2 \rangle = \frac{1 + R^4}{4R^2} \quad (5.12)$$

that exceeds that of the vacuum state for any  $R \neq 1$ . In other words, each mode of a TMSV considered individually is in the thermal state. With increasing  $R > 1$ , the uncertainty of individual quadratures increases, while that of the difference of Alice's and Bob's position observables as well as the sum of their momentum observables decreases.

In the extreme case of  $R \rightarrow \infty$ , the wavefunctions of the two-modes squeezed state take the forms

$$\Psi_R(X_a, X_b) \propto \delta(X_a - X_b) \quad \text{and} \quad (5.13)$$

$$\tilde{\Psi}_R(P_a, P_b) \propto \delta(P_a + P_b). \quad (5.14)$$

Both Alice's and Bob's positions are completely uncertain, but at the same time precisely equal, whereas the momenta are uncertain and precisely opposite. This state is the basis of the famous quantum nonlocality paradox in its original formulation of Einstein, Podolsky, and Rosen (EPR) [2]. EPR argued that by choosing to perform either a position or momentum measurement on her portion of the TMSV, Alice remotely prepares either a state with a certain position or one with a certain momentum at Bob's location. But according to the uncertainty principle, certainty of position implies complete uncertainty of momentum, and vice versa. In other words, by choosing the setting of her measurement apparatus, Alice can instantly and remotely, without any interaction, prepare at Bob's station one of two mutually incompatible physical realities. This apparent contradiction to basic principles of causality has lead EPR to challenge quantum mechanics as complete description of physical reality and triggered a debate that continues to this day.

Experimental realization of TMSV is largely similar to that of single-mode squeezing. SPDC is the primary method; however, in contrast to the single-mode case, it is implemented in the non-degenerate configuration. The photons in each generated pair are emitted into two distinguishable modes that become carriers of the TMSV state (Fig. 5.2b).

In order to understand how non-degenerate SPDC leads to squeezing, consider the two-mode state

$$|\Psi\rangle = |0\rangle \otimes |0\rangle + s |1\rangle \otimes |1\rangle, \quad (5.15)$$

that is, a pair of photons has been emitted into Alice's and Bob's modes with amplitude  $s$ . Now if we evaluate the variance of the observable  $(X_a - X_b)/\sqrt{2}$ , we find

$$\frac{1}{2}\langle\Delta(X_a - X_b)^2\rangle = \frac{1}{4}\langle\Psi|(\hat{a} + \hat{a}^\dagger - \hat{b} - \hat{b}^\dagger)^2|\Psi\rangle = \frac{1}{2} - s, \quad (5.16)$$

that is, Alice's and Bob's position observables are correlated akin to TMSV. A similar calculation shows anticorrelation of Alice's and Bob's momentum observables.

Both the single-mode and two-mode squeezed vacuum states are valuable resources in quantum optical information technology. TMSV, in particular, is useful for generating heralded single photons and unconditional quantum teleportation.

## 5.2 SALIENT FEATURES OF SQUEEZED STATES

### 5.2.1 The Squeezing Operator

We now proceed to a more rigorous mathematical description of squeezing. Single-mode squeezing occurs under the action of operator

$$\hat{S}(r) = \exp[(r\hat{a}^2 - r\hat{a}^{\dagger 2})/2], \quad (5.17)$$

where  $r = \ln R$  is the *squeezing parameter*, upon the vacuum state. Note that, for a small  $r$ , the squeezing operator (5.17) acting on the vacuum state generates the state

$$\hat{S}(r)|0\rangle \approx [1 + (r\hat{a}^2 - r\hat{a}^{\dagger 2})/2]|0\rangle = |0\rangle - (r/\sqrt{2})|2\rangle, \quad (5.18)$$

which is consistent with Eq. (5.6) for  $s = r$ .

The action of the squeezing operator can be analyzed as fictitious evolution under Hamiltonian

$$\hat{H} = i\hbar\alpha[\hat{a}^2 - (\hat{a}^{\dagger})^2]/2 \quad (5.19)$$

for time  $t = r/\alpha$  (so that  $\hat{S}(r) = e^{-i(\hat{H}/\hbar)t}$ ). Analyzing this evolution in the Heisenberg picture, we use  $[\hat{a}, \hat{a}^{\dagger}] = 1$  to find that

$$\dot{\hat{a}} = \frac{i}{\hbar}[\hat{H}, \hat{a}] = -\alpha\hat{a}^{\dagger} \quad (5.20)$$

and

$$\dot{\hat{a}}^{\dagger} = -\alpha\hat{a}. \quad (5.21)$$

Now using the expressions for quadrature observables

$$\hat{X} = (\hat{a} + \hat{a}^{\dagger})/\sqrt{2} \quad \text{and} \quad \hat{P} = (\hat{a} - \hat{a}^{\dagger})/\sqrt{2}i, \quad (5.22)$$

we rewrite Eqs. (5.20) and (5.21) as

$$\dot{\hat{X}} = -\alpha X; \quad (5.23a)$$

$$\dot{\hat{P}} = \alpha P. \quad (5.23b)$$

If this evolution continues for time  $t$ , we will have

$$\hat{X}(t) = \hat{S}^{\dagger}(r)\hat{X}(0)\hat{S}(r) = \hat{X}(0)e^{-r}; \quad (5.24a)$$

$$\hat{P}(t) = \hat{S}^{\dagger}(r)\hat{P}(0)\hat{S}(r) = \hat{P}(0)e^r, \quad (5.24b)$$

which correspond to position squeezing by factor  $R = e^r$  and corresponding momentum antisqueezing (Fig. 5.4). If the initial state is vacuum, the evolution will result in a squeezed vacuum state; coherent states will yield squeezed light [3].

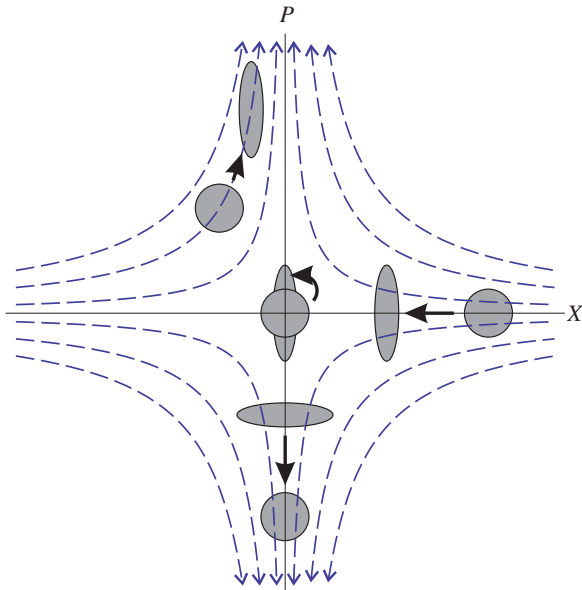


**FIGURE 5.4** Transformation of quadratures under the action of the squeezing Hamiltonian (5.19) with  $\alpha > 0$ . Gray areas show examples of Wigner function transformations with  $r = \alpha t = \ln 2$ , so  $R = 2$ .

The corresponding transformation of the creation and annihilation operators is given by

$$\hat{a}(t) = \hat{a}(0) \cosh r - \hat{a}^\dagger(0) \sinh r; \quad (5.25a)$$

$$\hat{a}^\dagger(t) = \hat{a}^\dagger(0) \cosh r - \hat{a}(0) \sinh r, \quad (5.25b)$$

known as *Bogoliubov transformation*.

Two-mode squeezing is treated similarly. The two-mode squeezing operator is

$$\hat{S}_2(\zeta) = \exp[-\zeta \hat{a}\hat{b} + \zeta^* \hat{a}^\dagger \hat{b}^\dagger]. \quad (5.26)$$

Assuming, again, a real  $\zeta = r$ , introducing the fictitious Hamiltonian and recalling that the creation and annihilation operators associated with different modes commute, we find

$$\hat{a}(t) = \hat{a}(0) \cosh r + \hat{b}(0)^\dagger \sinh r; \quad (5.27a)$$

$$\hat{b}(t) = \hat{b}(0) \cosh r + \hat{a}(0)^\dagger \sinh r; \quad (5.27b)$$

and hence

$$\hat{X}_a(t) \pm \hat{X}_b(t) = [\hat{X}_a(0) \pm \hat{X}_b(0)]e^{\pm r}; \quad (5.28a)$$

$$\hat{P}_a(t) \pm \hat{P}_b(t) = [\hat{P}_a(0) \pm \hat{P}_b(0)]e^{\mp r}. \quad (5.28b)$$

Initially, Alice's and Bob's modes are in vacuum states, and the quadrature observables in these modes are uncorrelated. But as the time progresses, Alice's and Bob's position observables become correlated while the momentum observables become anticorrelated.

### 5.2.2 Photon Number Statistics

An important component in the theoretical description of squeezed light is its decomposition in the photon number basis, that is, calculating the quantities  $\langle n | \text{sq}_R \rangle$  for the single-mode squeezed state and  $\langle mn | \text{TMSV}_R \rangle$  for the two-mode state. Due to non-commutativity of the photon creation and annihilation operators, this calculation turns out surprisingly difficult even for basic squeezed vacuum states, let alone squeezed coherent states and the states that have been affected by losses. Possible approaches to this calculation include the disentangling theorem for SU(1,1) Lie algebra [4], direct calculation of the wavefunction overlap in the position space [5], or transformation of the squeezing operator [6]. Here, we derive the photon number statistics of single- and two-mode squeezed vacuum states by calculating their inner product with coherent states.

The wavefunction of a coherent state with real amplitude  $\alpha$  is

$$\psi_\alpha(X) = \frac{1}{\pi^{1/4}} e^{-(X-\alpha\sqrt{2})^2/2}, \quad (5.29)$$

so its inner product with the position squeezed state (5.3) equals

$$\langle \alpha | \text{sq}_R \rangle = \int_{-\infty}^{+\infty} \psi_\alpha(X) \psi_R(X) dX = \sqrt{\frac{2R}{1+R^2}} e^{-\frac{R^2}{1+R^2}\alpha^2}. \quad (5.30)$$

Now we recall that the coherent state is decomposed into the Fock basis according to

$$|\alpha\rangle = \sum_{n=0}^{\infty} e^{-\alpha^2/2} \frac{\alpha^n}{\sqrt{n!}} |n\rangle, \quad (5.31)$$

so we have

$$\sum_{n=0}^{\infty} \langle n | \text{sq}_R \rangle \frac{\alpha^n}{\sqrt{n!}} = \sqrt{\frac{2R}{1+R^2}} e^{\frac{1-R^2}{2(1+R^2)}\alpha^2}. \quad (5.32)$$

Decomposing the exponent in the right-hand side of the above equation into the Taylor series with respect to  $\alpha$ , we obtain

$$\sum_{n=0}^{\infty} \langle n | \text{sq}_R \rangle \frac{\alpha^n}{\sqrt{n!}} = \sqrt{\frac{2R}{1+R^2}} \sum_{m=0}^{\infty} \left[ \frac{1-R^2}{2(1+R^2)} \right]^m \frac{\alpha^{2m}}{m!}. \quad (5.33)$$

Because this equality must hold for any real  $\alpha$ , each term of the sum in the left-hand side must equal its counterpart in the right-hand side that contains the same power of  $\alpha$ . Hence,  $n = 2m$  and

$$\langle 2m | \text{sq}_R \rangle = \sqrt{\frac{2R}{1+R^2}} \left[ \frac{1-R^2}{2(1+R^2)} \right]^m \frac{\sqrt{(2m)!}}{m!}. \quad (5.34)$$

Since  $R = e^r$ , we have

$$\frac{2R}{1+R^2} = \frac{1}{\cosh r} \quad \text{and} \quad \frac{1-R^2}{1+R^2} = -\tanh r, \quad (5.35)$$

so Eq. (5.34) can be rewritten as

$$|\text{sq}_R\rangle = \frac{1}{\sqrt{\cosh r}} \sum_{m=0}^{\infty} (-\tanh r)^m \frac{\sqrt{(2m)!}}{2^m m!} |2m\rangle. \quad (5.36)$$

We stop here for a brief discussion. First, we note that for  $r \ll 1$ , Eq. (5.36) becomes

$$|\text{sq}_R\rangle = |0\rangle - (r/\sqrt{2}) |2\rangle + O(r^2), \quad (5.37)$$

consistent with Eq. (5.18). Second, note that the squeezed vacuum state (5.36) contains only terms with even photon numbers. This is a fundamental feature of this state; in fact, one of the earlier names for squeezed states has been “two-photon coherent states” [7]. This feature follows from the nature of the squeezing operator (5.17): in its decomposition into the Taylor series creation and annihilation operators occur only in pairs. Pairwise emission of photons is also a part of the physical nature of SPDC: due to energy conservation a pump photon can only split into two photons of half its energy.

We now turn to finding the photon number decomposition of the two-mode squeezed state. We first notice, by looking at Eq. (5.26), that  $|R_{AB}\rangle$  must only contain terms with equal photon numbers in Alice’s and Bob’s modes. This circumstance allows us to significantly simplify the algebra. We proceed along the same

route as outlined above, calculating the overlap of  $|\text{TMSV}_R\rangle$  with the tensor product  $|\alpha\alpha\rangle$  of identical coherent states  $|\alpha\rangle$  in Alice's and Bob's channels using Eqs. (5.10) and (5.29):

$$\langle\alpha\alpha| \text{TMSV}_R\rangle = \int_{-\infty}^{+\infty} \psi_\alpha(X_a)\psi_\alpha(X_b)\Psi_R(X_a, X_b)dX_a dX_b = \frac{2R}{1+R^2} e^{-\frac{2}{1+R^2}\alpha^2}. \quad (5.38)$$

Decomposing the coherent states in the left-hand side into the Fock basis according to Eq. (5.31) and keeping only the terms with equal photon numbers, we have

$$\sum_{n=0}^{\infty} \langle nn| \text{TMSV}_R\rangle \frac{\alpha^{2n}}{n!} = \frac{2R}{1+R^2} e^{-\frac{1-R^2}{1+R^2}\alpha^2}. \quad (5.39)$$

Now writing the Taylor series for the right-hand side and using Eq. (5.35), we obtain

$$|\text{TMSV}_R\rangle = \sum_{n=0}^{\infty} \frac{1}{\cosh r} \tanh^n r |nn\rangle. \quad (5.40)$$

Similar to the single-mode squeezing, it is easy to verify that the above result is consistent with state (5.15) for small  $r$ . Remarkably, the energy spectrum of TMSV follows Boltzmann distribution with mean photon number in each mode  $\langle n \rangle = \sinh^2 r$ . This is in agreement with our earlier observation that Alice's and Bob's portions of TMSV considered independently of their counterpart are in the thermal state, that is, the state whose photon number distribution obeys Boltzmann statistics with the temperature given by  $e^{-\hbar\omega/kT} = \tanh r$ .

While the present analysis is limited to pure squeezed vacuum states, photon number decompositions of squeezed coherent states and squeezed states that have undergone losses can be found in the literature [8, 9]. In contrast to pure squeezed vacuum states, these decompositions have nonzero terms associated with nonpaired photons. The origin of these terms is easily understood. If a one- or two-mode squeezed vacuum state experiences a loss, it may happen that one of the photons in a pair is lost while the other one remains. If the squeezing operator acts on a coherent state, the odd photon number terms will appear in the resulting state because they are present initially.

Photon statistics of both classes of squeezed states have been tested experimentally, as discussed in Section 5.3. An example is shown in Figure 5.5.

### 5.2.3 Interconversion Between Single- and Two-Mode Squeezing

If the modes of the TMSV are overlapped on a symmetric beam splitter, two unentangled single-mode vacuum states will emerge in the output (Fig. 5.6). To see this,

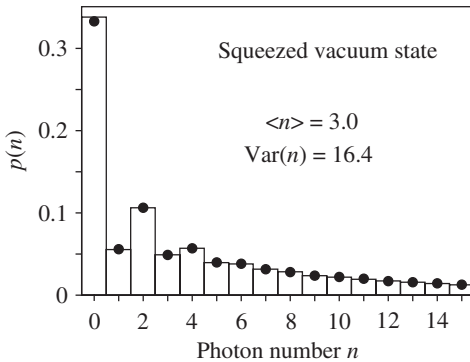


**FIGURE 5.5** Experimentally reconstructed photon number statistics of the squeezed vacuum state. For low photon numbers, the even terms are greater than the odd terms due to pairwise production of photons, albeit the odd term contribution is nonzero due to loss. Reproduced from Reference 10.

we recall the beam splitter transformation

$$\hat{a}' = \tau \hat{a} - \rho \hat{b}; \quad (5.41a)$$

$$\hat{b}' = \tau \hat{b} + \rho \hat{a}, \quad (5.41b)$$

where  $\tau$  and  $\rho$  are the beam splitter amplitude transmissivity and reflectivity, respectively. For a symmetric beam splitter,  $\tau = \rho = 1/\sqrt{2}$ . In writing Eqs. (5.41), we neglected possible phase shifts that may be applied to individual input and output modes [5].

In accordance with the definition (5.22) of quadrature observables, Eqs. (5.41) apply in the same way to the position and momentum of the input and output modes. Applying this to Eqs. (5.28), we find

$$\begin{aligned} \hat{X}'_{a,b} &= [\hat{X}_a(t) \mp \hat{X}_b(t)]/\sqrt{2} \\ &= e^{\mp r} [\hat{X}_a(0) \mp \hat{X}_b(0)]/\sqrt{2} \end{aligned} \quad (5.42)$$

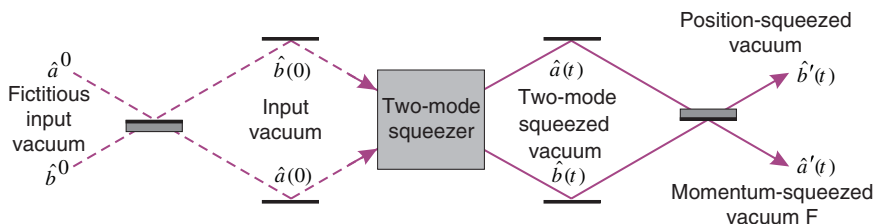


**FIGURE 5.6** Interconversion of the two-mode squeezed vacuum and two single-mode squeezed vacuum states. Dashed lines show a fictitious beam splitter transformation of a pair of vacuum states such that the modes  $\hat{a}'(t), \hat{b}'(t)$  are explicitly single-mode squeezed with respect to modes  $\hat{a}^0, \hat{b}^0$ .

for the output positions and

$$\begin{aligned}\hat{P}'_{a,b} &= [\hat{P}_a(t) \mp \hat{P}_b(t)]/\sqrt{2} \\ &= e^{\pm r}[\hat{P}_a(0) \mp \hat{P}_b(0)]/\sqrt{2}\end{aligned}\quad (5.43)$$

for the momenta. In order to understand what state this corresponds to, let us assume, for the sake of the argument, that vacuum modes  $\hat{a}$  and  $\hat{b}$  at the SPDC input have been obtained from another pair of modes by means of another symmetric beam splitter:

$$\hat{a}^0 = [\hat{a}(0) - \hat{b}(0)]/\sqrt{2} \quad (5.44)$$

$$\hat{b}^0 = [\hat{a}(0) + \hat{b}(0)]/\sqrt{2}. \quad (5.45)$$

Of course, since modes  $\hat{a}(0)$  and  $\hat{b}(0)$  are in the vacuum state, so are  $\hat{a}^0$  and  $\hat{b}^0$ . We then have

$$\begin{aligned}\hat{X}'_{a,b} &= e^{\mp r}\hat{X}_{a,b}^0; \\ \hat{P}'_{a,b} &= e^{\pm r}\hat{P}_{a,b}^0,\end{aligned}\quad (5.46)$$

where superscript 0 associates the quadrature with modes  $\hat{a}^0$  and  $\hat{b}^0$ . We see that modes  $\hat{a}'$  and  $\hat{b}'$  are related to vacuum modes  $\hat{a}^0$  and  $\hat{b}^0$  by means of position and momentum squeezing transformations, respectively.

Because the beam splitter transformation is reversible, it can also be used to obtain a TMSV from two single-mode squeezed vacuum states with squeezing in orthogonal quadratures. This technique has been used, for example, in the experiment on continuous-variable quantum teleportation [11].

#### 5.2.4 Squeezed Vacuum and Squeezed Light

Squeezed vacuum and bright squeezed light are readily converted between each other by means of the phase-space displacement operator [5], whose action in the Heisenberg picture can be written as

$$\hat{D}^\dagger(\alpha)\hat{a}^\dagger\hat{D}(\alpha) = \hat{a} + \alpha. \quad (5.47)$$

This means, in particular, that the position and momentum transform according to

$$\hat{X} \mapsto \hat{X} + \text{Re } \alpha \sqrt{2}; \quad (5.48)$$

$$\hat{P} \mapsto \hat{P} + \text{Im } \alpha \sqrt{2}, \quad (5.49)$$

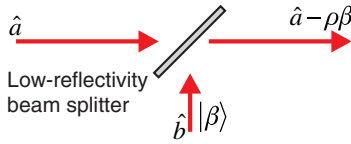


**FIGURE 5.7** Implementation of phase-space displacement.  $\rho \ll 1$  is the beam splitter's amplitude reflectivity.

so, under the action of  $\hat{D}(\alpha)$ , the entire phase space displaces itself, thereby changing the coherent amplitude of the squeezed state without changing the degree of squeezing.

Phase-space displacement can be implemented experimentally by overlapping the signal state with a strong coherent state  $|\beta\rangle$  on a low reflectivity beam splitter (Fig. 5.7). Applying the beam splitter transformation (5.41), we find for the signal mode

$$\hat{a}' = \tau\hat{a} - \rho\hat{b}. \quad (5.50)$$

Given that mode  $\hat{b}$  is in a coherent state (i.e., an eigenstate of  $\hat{b}$ ) and that  $\rho \ll 1$  (i.e.,  $\tau \sim 1$ ), we have

$$\hat{a}' = \hat{a} - \rho\beta \quad (5.51)$$

in analogy to Eq. (5.47). The displacement operation has been used to change the amplitude of squeezed light in many experiments, for example, in Reference 12.

### 5.2.5 Effect of Losses

Squeezed states that occur in practical experiments necessarily suffer from losses present in sources, transmission channels, and detectors. In order to understand the effect of propagation losses on a single-mode squeezed vacuum state, we can use the model in which a lossy optical element with transmission  $T$  is replaced by a beam splitter (Fig. 5.8). At the other input port of the beam splitter, there is a vacuum state. The interference of the signal mode  $\hat{a}$  with the vacuum mode  $\hat{v}$  will produce a mode with operator  $\hat{a}' = \tau\hat{a} - \rho\hat{v}$  (with  $\tau^2 = T$  and  $\rho^2 = 1 - T$  being the beam splitter transmissivity and reflectivity, respectively) in the beam splitter output. Accordingly, we have

$$\hat{X}_{\theta,\text{out}} = \tau\hat{X}_{a,\theta} - \rho\hat{X}_{v,\theta}. \quad (5.52)$$

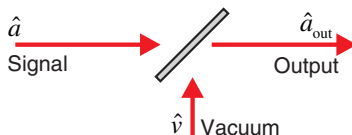


**FIGURE 5.8** The beam splitter model of loss.

Because the quadrature observable of the signal and vacuum states are uncorrelated, and since  $\langle \Delta(X_\theta)^2 \rangle = 1/2$ , it follows that

$$\begin{aligned} \langle \Delta X_{\theta,\text{out}}^2 \rangle &= \tau^2 \langle \Delta(X_{a,\theta})^2 \rangle + \rho^2 \langle \Delta(X_{v,\theta})^2 \rangle \\ &= T \langle \Delta(X_{a,\theta})^2 \rangle + (1 - T)/2. \end{aligned} \quad (5.53)$$

Analyzing Eqs. (5.41) we see that the optical loss alone, no matter how significant it is, cannot eliminate the property of squeezing completely.

Ideal squeezed-vacuum and coherent states have the minimum-uncertainty property: the product of uncertainties  $\langle \Delta X_{\text{out}}^2 \rangle \langle \Delta P_{\text{out}}^2 \rangle$  reaches the theoretical minimum of 1/4. But this is no longer the case in the presence of losses. The deviation of the uncertainty from the minimum can be used to estimate the preparation quality of a squeezed state. Suppose a measurement of a squeezed state yielded the minimum and maximum quadrature uncertainty values of  $\langle \Delta X_{\min}^2 \rangle$  and  $\langle \Delta X_{\max}^2 \rangle$ , respectively. One can assume that the state has been obtained from an ideal (minimum-uncertainty) squeezed state with squeezing  $R$  by means of loss channel with transmissivity  $T$ . Using Eq. (5.5) and solving Eqs. (5.53), one finds  $T$  [13], which one can then compare with the values expected from the setup at hand, and thereby find out if any unexpected losses are present in it.

## 5.3 DETECTION

### 5.3.1 Balanced Homodyne Detection

In order to detect squeezing, we need to perform multiple measurements of the field quadrature, that is, the observable  $\hat{X}_\theta = \hat{X} \cos \theta + \hat{P} \sin \theta = [e^{-i\theta}\hat{A} + e^{i\theta}\hat{A}^\dagger]/\sqrt{2}$ , where  $\hat{A}$  is the annihilation operator of the mode of interest. The task of measuring optical fields in a phase-sensitive fashion may appear daunting, as these fields oscillate at frequencies on a scale of hundreds of terahertz. Fortunately, however, such a measurement can be implemented using a relatively simple interference setup. The technique known as balanced homodyne detection proposed in 1983 by Yuen and Chan [14] and subsequently implemented by Abbas et al. [15] to this day remains the method of choice for quadrature measurements. Reference 16 provides a review of the current state of the art in this area.

Here I start with a brief overview of this technique, in the way it is presented in most textbooks. Subsequently, I will discuss a more complex but important question of identifying the temporal mode whose quadrature is being measured. For simplicity, I will start in the classical language.

Suppose the field to be measured (referred to as *signal*) is centered at frequency  $\Omega$ . We write for the field magnitude  $E(t) \propto a(t)e^{-i\Omega t} + a^*(t)e^{i\Omega t}$ , where  $a(t)$  is slowly varying. For quadrature measurement, this field is overlapped on a symmetric (50:50) beam splitter with a strong laser field at frequency  $\Omega$ , known as the *local oscillator* (*LO*), with amplitude  $a_{\text{LO}}(t)$ :  $E_{\text{LO}}(t) \propto a_{\text{LO}}(t)e^{-i\Omega t+i\theta} + a_{\text{LO}}^*(t)e^{i\Omega t-i\theta}$ . The phase  $\theta$  of

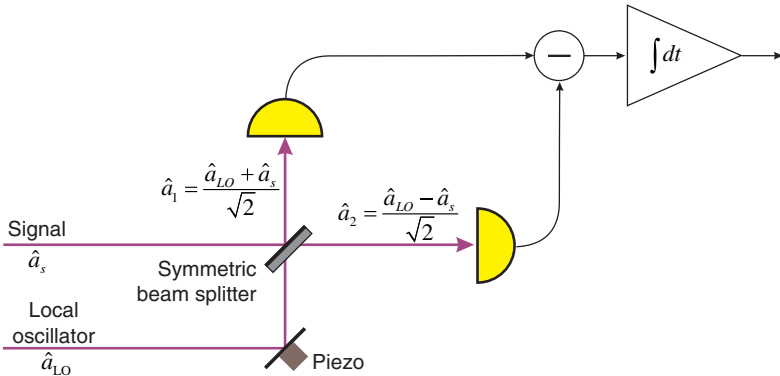


**FIGURE 5.9** The principle of balanced homodyne detection.

the local oscillator is controlled, for example, by a piezoelectric transducer. The two beam splitter output fields impinge onto two photodiodes whose output photocurrents are electronically subtracted (Fig. 5.9).

In order to see how the detector output relates to the signal quadrature, we write the amplitudes of the beam splitter outputs as

$$a_{1,2}(t) = \frac{a_{\text{LO}}(t)e^{i\theta} \pm a(t)}{\sqrt{2}}. \quad (5.54)$$

The detector's output current is then proportional to the intensity difference

$$\begin{aligned} I_-(t) &\propto a_1(t)^* a_1(t) - a_2(t)^* a_2(t) \\ &= a(t)a_{\text{LO}}^*(t)e^{-i\theta} + a^*(t)a_{\text{LO}}(t)e^{i\theta}. \end{aligned} \quad (5.55)$$

Assuming that  $a_{\text{LO}}(t)$  is real (this is a matter of choosing the zero phase reference point), the quantity in the right-hand side of Eq. (5.55) is an instantaneous (or, rather, averaged over the detection electronics' response time) value of the classical quadrature  $a(t)e^{-i\theta} + a^*(t)e^{i\theta}$ .

Switching to quantum treatment, we replace the classical amplitude  $a(t)$  by operator  $\hat{a}(t)$ . This operator is defined as

$$\hat{a}(t) = \frac{1}{\sqrt{2\pi}} \int_{-\infty}^{+\infty} \hat{a}_\omega e^{-i(\omega-\Omega)t} d\omega, \quad (5.56)$$

where  $\hat{a}_\omega$  is the annihilation operator of a plane wave mode of optical frequency  $\omega$  familiar from the electromagnetic field quantization procedure. One can think of  $\hat{a}(t)$  as the annihilation operator of a photon of frequency  $\Omega$  at time moment  $t$ . Such a description is of course unphysical because of the time-frequency uncertainty principle; yet it is quite useful for visualization.

As to the local oscillator, we recall that it is in a high-amplitude coherent state so the relative quantum noise of its amplitude is negligible. Hence, we can continue

to treat the LO amplitude  $a_{\text{LO}}(t)$  as a number, not an operator. Equation (5.55) simplifies to

$$\hat{I}_-(t) \propto \alpha_{\text{LO}}(t)[\hat{a}(t)e^{-i\theta} + \hat{a}^\dagger(t)e^{i\theta}]. \quad (5.57)$$

There are two primary approaches to the acquisition and analysis of the subtraction photocurrent of the homodyne detector. In *time-domain* analysis, the photocurrent is measured using a time-resolving device, such as an oscilloscope. In *frequency-domain* measurements, one instead looks at the electronic spectrum of the photocurrent.

### 5.3.2 Time-Domain Approach

In the time-domain approach, the goal is to measure the quadrature of a limited duration temporal mode defined by annihilation operator

$$\hat{A} = \int_{-\infty}^{+\infty} \varphi(t)\hat{a}(t)dt, \quad (5.58)$$

where  $\varphi(\cdot)$  is some normalized real function of bounded support. Following Eq. (5.57), this measurement can be realized by multiplying the subtraction photocurrent, obtained from the homodyne detector with a constant LO, by the mode function and integrating it over time:

$$\int_{-\infty}^{+\infty} \varphi(t)\hat{I}(t)dt \propto a_{\text{LO}}(\hat{A}e^{-i\theta} + \hat{A}^\dagger e^{i\theta}) = \sqrt{2}a_{\text{LO}}\hat{X}_\theta. \quad (5.59)$$

This approach works if the temporal resolution of the acquisition electronics (typically on a scale of nanoseconds) is fast compared to the duration of the mode of interest, such as in Reference 17.

The opposite extreme that frequently occurs in experimental practice is that the squeezed state is prepared using a pico- or femtosecond pulsed laser, and its temporal mode is defined by the laser pulse. In this case, the quadrature measurement can be accomplished in spite of lack of resolution at the electronic level by using the same laser as the local oscillator. We then have  $a_{\text{LO}}(t) \propto \varphi(t)$  and hence  $\int_{-\infty}^{+\infty} \hat{I}(t) dt \propto \hat{X}_\theta$ . Because of the slow electronics' response, the integration occurs in this setting automatically. The output of the homodyne detector is an electrical pulse whose shape is determined by the response function, and magnitude is proportional to the quadrature [18].

Time-domain homodyne detection permits full reconstruction of the state in the acquisition mode. By varying the local oscillator phase  $\theta$ , one can obtain noise statistics for all quadratures. Probability distributions  $\text{pr}(X_\theta) = \langle X_\theta | \hat{\rho} | X_\theta \rangle$  for all phase angles are sufficient to obtain full information about density operator  $\hat{\rho}$  of the signal, such as its Wigner function or the density matrix in the photon number representation. This method of measuring the quantum state of light is referred to as *optical homodyne tomography* [5, 16].

Homodyne tomography was first proposed in 1989 [19] and implemented experimentally in application to single-mode squeezed vacuum in 1993 [20] and to two-mode squeezed vacuum in 2000 [21].

### 5.3.3 Frequency-Domain Approach

Theoretically, if squeezing is generated in a continuous nonlinear process, it could be observed by measuring the variance of the homodyne detector output photocurrent as a function of the local oscillator phase. In practice, however, this measurement is obscured by various spurious noises produced by either the source or the detector. For example, the reflectivity of the homodyne detector's beam splitter can vary as a function of time due to minute perturbations to its orientation. However small such variation may be, it may affect precise subtraction of the LO amplitudes. As a result, the mean value of the output photocurrent will drift with time, and the drift amplitude can exceed the shot noise level, thereby obscuring the observation of quantum noise (Fig. 5.10).

Fortunately, such technical (classical) noises of the photocurrent can be distinguished from the quantum noise by analyzing their spectral behavior. Technical noises often occur within specific frequency bands; for example, the slow drift of the zero point is limited to low frequencies (Fig. 5.10b). The quantum noise, on the other hand, is “white”: it is constant for all frequencies within the detector's bandwidth (Fig. 5.10a). One can therefore observe squeezing, even in the presence of technical noises, by only looking at those sidebands in which they do not appear (Fig. 5.10c). A further advantage of the frequency-domain method is that, by measuring the quantum noise at different sidebands, one is able to analyze the properties of the source and detector; in particular, measure the spectral band in which the squeezing is present.

We start our theoretical analysis of frequency-domain measurements by finding the Fourier transform of the photocurrent (5.57) using Eq. (5.56):

$$\tilde{\hat{I}}(\nu) = \frac{1}{\sqrt{2\pi}} \int_{-\infty}^{+\infty} \hat{I}(t) e^{i\nu t} dt \propto \hat{a}_{\Omega+\nu} e^{-i\theta} + \hat{a}_{\Omega-\nu}^\dagger e^{i\theta}, \quad (5.60)$$

where  $\nu$  is the electronic frequency. By some algebra, we can express the right-hand side of this equation as

$$\begin{aligned} \hat{a}_{\Omega+\nu} e^{-i\theta} + \hat{a}_{\Omega-\nu}^\dagger e^{i\theta} &= \hat{X}_+ \cos \theta + \hat{P}_+ \sin \theta - i\hat{X}_- \sin \theta + i\hat{P}_- \cos \theta \\ &= \hat{X}_{+, \theta} + i\hat{X}_{-, \pi/2+\theta}, \end{aligned} \quad (5.61)$$

where

$$\hat{X}_{\pm, \theta} = \frac{1}{\sqrt{2}} [\hat{X}_\theta(\Omega + \nu) \pm \hat{X}_\theta(\Omega - \nu)]. \quad (5.62)$$

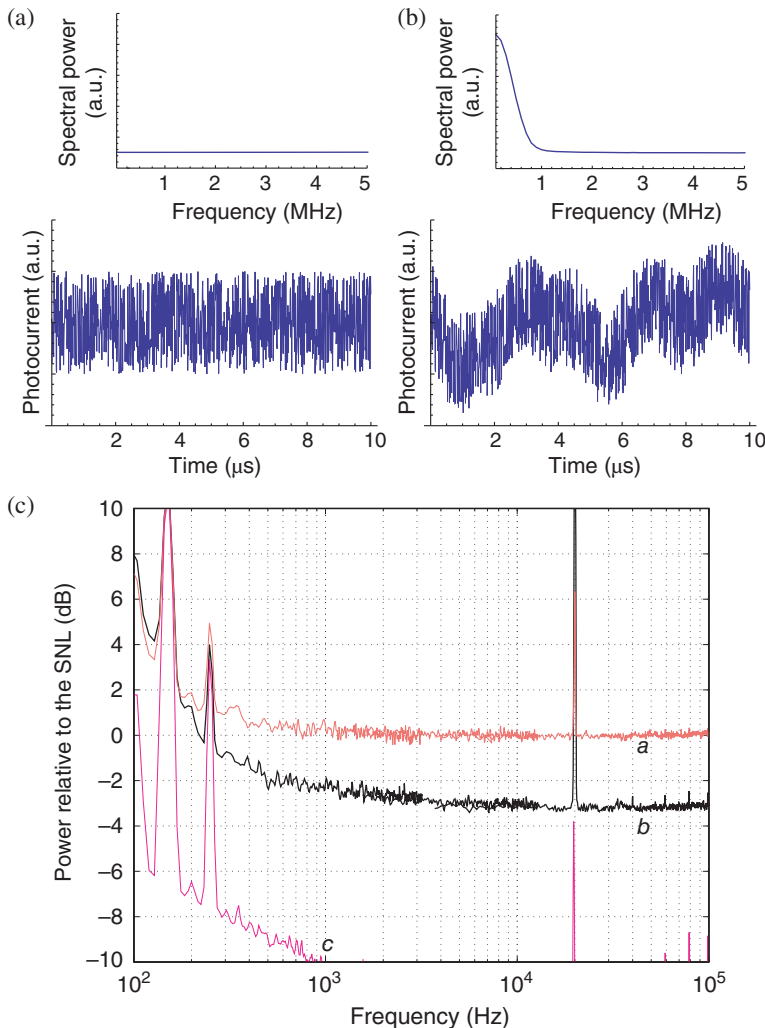


**FIGURE 5.10** Frequency-domain approach to homodyne measurements. (a) Simulated output of a homodyne detector exhibiting noise corresponding to the SQL (bottom). Its spectrum (top) is flat. (b) The same output affected by the drift of the zero point on a time scale of  $2 \mu$ s. Direct variance measurement of the photocurrent will not give SQL. However, the spectral power remains at the SQL level for frequencies above 1 MHz and hence allows observation of squeezing. (c) *Bona fide* spectrum of the homodyne detector from Reference 22 showing similar behavior. Curve *a* corresponds to SQL, *b* to squeezed vacuum, and *c* to the detector's electronic noise (in the absence of LO). The noise peaks arise from harmonics of 50 Hz power line and phase locking signal (20 kHz).

This means that measuring the real and imaginary parts of  $\tilde{I}(\nu)$  is equivalent to subjecting frequency modes  $\Omega + \nu$  and  $\Omega - \nu$  to a beam splitter operation and performing homodyne measurements of the beam splitter outputs at LO phases  $\theta$  and  $\pi/2 + \theta$  [23].

Suppose that the state entering the homodyne detector is squeezed—that is, the noise of  $\hat{I}(t)$  is below the standard quantum limit for a certain local oscillator phase  $\theta$ . But this would also imply that its Fourier transform—both the real and imaginary parts of  $\tilde{I}(\nu)$ —exhibit fluctuations below SQL. This would in turn mean that that observables  $\hat{X}_{+, \theta}$  and  $\hat{X}_{-, \pi/2+\theta}$  exhibit reduced variance at the same time—that is, modes  $\Omega + \nu$  and  $\Omega - \nu$  are in the two-mode squeezed state (cf. Section 5.2.3). In other words, *single-mode squeezing in the time domain is equivalent to two-mode squeezing in the frequency domain*. An explicit experimental demonstration to that effect has been presented by Huntington et al. [24].

Simultaneous measurements of the real and imaginary parts of  $\tilde{I}(\nu)$  are possible using lock-in amplifiers. In this way, one can perform full quantum-state tomography of the modes defined by operators  $(\hat{a}_{\Omega+\nu} \pm \hat{a}_{\Omega-\nu}^\dagger)/\sqrt{2}$ . In a classic work of 1997, Breitbach et al. [10] used this approach for tomography of an extended family of Gaussian states, including coherent, squeezed vacuum, as well as amplitude- and phase-squeezed light states (Fig. 5.11).

It is common to use the electronic spectrum analyzer rather than lock-in amplifiers for frequency-domain measurements. The spectrum analyzer displays the mean squared power of the photocurrent's sideband:

$$\left\langle \left| \tilde{I}(\nu) \right|^2 \propto \hat{X}_{+, \theta}^2 + \hat{X}_{-, \pi/2+\theta}^2 \right\rangle. \quad (5.63)$$

Because observables  $\hat{X}_{+, \theta}$  and  $\hat{X}_{-, \pi/2+\theta}$  are simultaneously squeezed, the spectrum analyzer will show reduced signal at frequency  $\nu$ . In this way, the spectrum analyzer can measure squeezing in spite of being unable to resolve the two terms of Eq. (5.61). This result is consistent with the common sense expectation: if the time-dependent photocurrent  $I(t)$  exhibits reduced noise, so will its frequency spectrum.

An important shortcoming of the spectrum analyzer is that it does not enable quantum state tomography. It provides information about the variance of the quadrature probability distribution, but not the probability distribution itself. This does not matter, however, if the variance (i.e., the amount of squeezing) is the only quantity of interest, and state reconstruction is not the goal.

## 5.4 PREPARATION

In Section 5.2.1, we had a conceptual discussion of a Hamiltonian that squeezes the phase space. But in fact, almost any Hamiltonian that is at least quadratic in the creation and annihilation operators brings about sophisticated trajectories in the phase space and can result in squeezing. Similarly, a Hamiltonian that is bilinear in

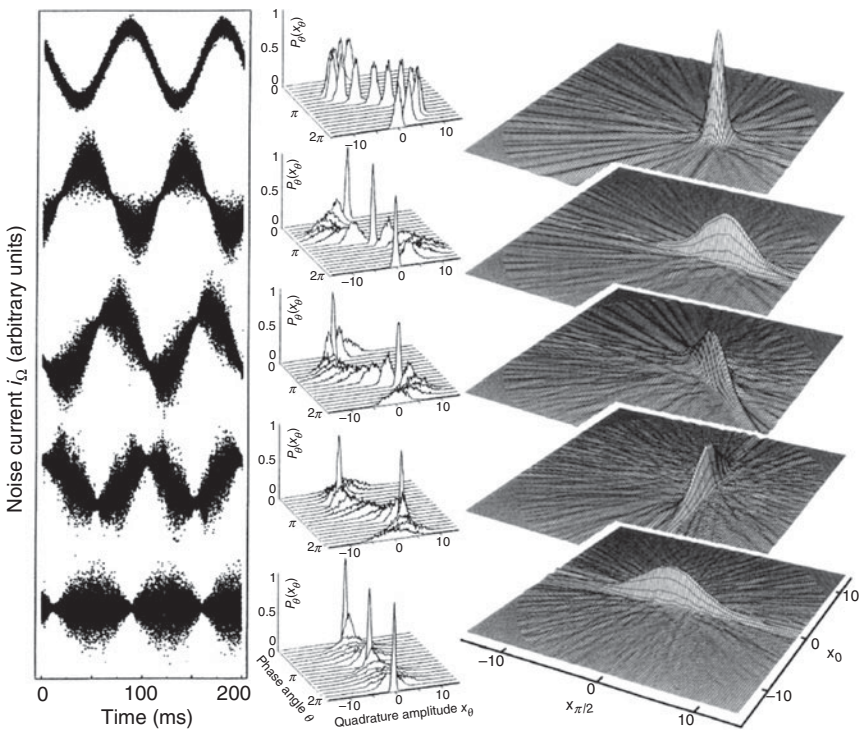


**FIGURE 5.11** Optical homodyne measurements of coherent and squeezed states of light. Top to bottom: coherent state, phase (position) squeezed light,  $45^\circ$  quadrature squeezed light, amplitude (momentum) squeezed light, position squeezed vacuum. Left column: statistics of quadrature measurements obtained with a balanced homodyne detector while the local oscillator phase is varied. Middle column: histograms  $pr(X_\theta)$  of these measurements associated with specific values  $\theta$  of the phase. These histograms are integral projections of the Wigner functions onto vertical planes positioned at angle  $\theta$  with respect to the position axis of the phase space. The histograms are used to reconstruct the Wigner functions (right column) of the corresponding states in a procedure similar to computer tomography scanning in medicine. They were also used to reconstruct the states' density matrices in the photon number basis (Fig. 5.5) by means of the quantum state sampling method [5]. Reproduced from Reference 10.

the creation and annihilation operators of two modes is likely to generate two-mode squeezing. Accordingly, there exist many physical processes that can be employed to prepare single- and two-mode squeezed states of the electromagnetic field.

An important limitation to the above is the requirement that the Hamiltonian evolution that leads to squeezing be not compromised by competing non-unitary processes that increase noise. For example, attempts to achieve squeezing in atomic systems have for a long time met with limited success due to incoherent spontaneous emission into the signal mode, which leads to thermalization of the signal state and loss of squeezing.

Most frequently, squeezing is obtained by nonlinear optical wave-mixing processes, in which pairs of photons are emitted into degenerate (single-mode squeezing) or non-degenerate (two-mode squeezing) modes. An example is spontaneous parametric down-conversion, a three-wave mixing between the pump field and the two photons of squeezed vacuum that occurs due to second-order optical nonlinearity. Another way to generate squeezing is four-wave mixing, a third-order nonlinear process in which two strong waves, interacting with a nonlinear medium, give rise to a pair of photons. Let us discuss these two processes in more detail.

#### 5.4.1 Via Parametric Down-Conversion

In order to mathematically describe nonlinear-optical squeezing, we begin with equations for the propagation of classical electromagnetic fields through a nonlinear medium. We then quantize the fields and replace their amplitudes with corresponding creation and annihilation operators, thereby obtaining their evolution in the Heisenberg picture.

Consider a three-wave mixing process in which a strong *pump* field of frequency  $2\Omega$  interacts with weak *signal* and *idler* fields of frequencies  $\Omega \pm \nu$ , respectively, with  $\nu \ll \Omega$ , in a crystal with effective nonlinearity  $\chi_{\text{eff}}$ . All fields are continuous in time, but the amplitudes<sup>3</sup>  $\epsilon_s(z)$  and  $\epsilon_i(z)$  of the signal and idler change with the propagation distance  $z$  due to the nonlinear interaction. The pump amplitude  $a_p$  is assumed to remain constant because  $\epsilon_p \gg \epsilon_s, \epsilon_i$ , so there is no depletion. We further assume that the crystal is perfectly phase matched for this nonlinear process.

In the slowly varying envelope approximation [25], the equations of motion for the signal and idler fields take the form

$$\frac{\partial}{\partial z} \epsilon_{s,i}(z) = i \frac{(\Omega \pm \nu)}{2\epsilon_0 n c} P_{\text{NL}}(\Omega \pm \nu), \quad (5.64)$$

where  $n$  is the refractive index and the nonlinear polarization amplitude is given by

$$P_{\text{NL}}(\Omega \pm \nu) = 2\epsilon_0 \chi_{\text{eff}} \epsilon_p \epsilon_{i,s}^*(z), \quad (5.65)$$

$\chi_{\text{eff}}$  being the effective nonlinear susceptibility. Without loss of generality, we can define the phase of the pump such that  $ia_p$  is real and positive. Then, solving these equations for propagation length  $L$  under assumption  $\nu \ll \Omega$ , we find

$$\epsilon_s(L) = \epsilon_s(0) \cosh r + \epsilon_i^*(0) \sinh r; \quad (5.66a)$$

$$\epsilon_i(L) = \epsilon_i(0) \cosh r + \epsilon_s^*(0) \sinh r \quad (5.66b)$$

---

<sup>3</sup>The amplitude is defined according to  $E(z, t) = \epsilon(z)e^{ikz - i\omega t} + \text{c.c.}$ , for  $E(z, t)$  being the value of the field in space in time.

with

$$r = \frac{\chi_{\text{eff}}\Omega}{nc} |a_p|L. \quad (5.67)$$

We now quantize the signal and idler fields according to  $\epsilon_{s,i} \rightarrow \hat{a}_{\Omega \pm v}$ , but continue to treat the macroscopic pump field as classical. This leads to

$$\hat{a}_{\Omega \pm v}(L) = \hat{a}_{\Omega \pm v}(0) \cosh r + \hat{a}_{\Omega \mp v}^\dagger(0) \sinh r, \quad (5.68)$$

which is identical to Eqs. (5.27). In other words, if the signal and idler fields of frequencies  $\Omega \pm v$  before the crystal are in the vacuum state, they will be in a two-mode squeezed state after the crystal.

As discussed in the previous section, such a state manifests itself as single-mode squeezing when a homodyne measurement with the local oscillator tuned to frequency  $\Omega$  is performed.

One can readily estimate the amount of squeezing one can obtain. Consider, for example, an  $L = 5$  mm periodically poled potassium titanyl phosphate (PPKTP) crystal with the signal wavelength of  $\lambda = 780$  nm and the pump field of power  $P = 100$  mW focused into a spot of  $w = 50$   $\mu\text{m}$  radius. The relevant effective nonlinear coefficient of PPKTP is  $\chi_{\text{eff}} = 14$  pm  $\text{V}^{-1}$ , refractive index  $n = 1.8$ .

Under these conditions, the pump intensity is  $I_p = P/\pi w^2 = 1.3 \times 10^7 \text{ W m}^{-2}$  and the field amplitude  $|\epsilon_p| = \sqrt{I_p/2n\epsilon_0 c} = 3.6 \times 10^4 \text{ V m}^{-1}$ . Substituting this value into Eq. (5.67), we find  $r = 1.1 \times 10^{-2}$ . We see that the amount of squeezing obtained by a single pass of a continuous-wave pump laser through a nonlinear crystal of a reasonable size is very small.

There are two primary methods of addressing this complication. First, one could use an ultrashort pulsed laser, thereby greatly increasing the pump amplitude. The above theory, developed for continuous-wave pump, has only limited application for pulsed pump; the amount of squeezing strongly depends on the shape  $\varphi(t)$  of the temporal mode chosen for the measurement [13]. Nevertheless, squeezing has been demonstrated in the single-pass pulsed regime as soon as one year after the first experimental observation of squeezed light [26] and the degree of squeezing has been increased to several decibels<sup>4</sup> in subsequent years [27].

The second approach is to place the crystal inside a Fabry-Perot cavity. The cavity can be resonant to the pump light, thereby enhancing the effective pump power, or to the signal, effectively allowing multiple passing of the signal through the crystal, or both. The case when the cavity is resonant to the signal is most common; this configuration is referred to as the *optical parametric oscillator or amplifier (OPO/OPA)*. A theory of squeezing inside an OPA has been developed by Gardiner

---

<sup>4</sup>Decibel (dB) is a common unit of squeezing in experiment. The degree of squeezing in decibels is calculated according to  $10 \log_{10}(2 \langle \Delta X^2 \rangle)$ . The standard quantum limit corresponds to a squeezing of 0 dB, the reduction of quadrature variance by a factor of 2 to about 3 dB, factor of 4 to about 6 dB, factor of 10 to 10 dB, and so on.

and Savage [28] and reviewed, for example, in Reference 8. Without derivation, we present the result for the quadrature noise levels associated with the antisqueezed ( $\vartheta^+ = \pi/2$ ) and squeezed ( $\vartheta^- = 0$ ) quadratures:

$$V^\pm(\nu) = \frac{1}{2} \pm \eta \frac{2\sqrt{P/P_{\text{th}}}}{(\nu/\gamma)^2 + (1 \mp \sqrt{P/P_{\text{th}}})^2}, \quad (5.69)$$

where  $2\gamma$  is the cavity linewidth,  $\eta$  is the overall quantum efficiency,  $P$  is the pump power, and  $P_{\text{th}}$  is the threshold power, that is, the pump power at which the nonlinear process in the cavity leads to macroscopic optical oscillations. By analyzing this result, we see that the squeezing occurs at sideband frequencies  $\nu$  less than or on the order of the cavity linewidth. This is not surprising: the enhancement effect of the cavity is only present within its resonance.

The squeezing is strongest at the threshold point, when the amplification in a single pass through the nonlinear crystal is equal to the loss occurring in a roundtrip of the signal through the cavity, including that at the output coupling mirror. The gain equals  $e^{2r} \approx 1 + 2r$  for  $r \ll 1$ . In the numerical example studied above,  $r = 1.1 \times 10^{-2}$ , so at the threshold point we would have a full roundtrip loss on a scale of  $T = 0.02$ . This loss occurs due to the transmission through the output coupling mirror as well as spurious losses on all other optical elements inside the cavity. Assuming, for example, that the mirror has a transmissivity of 0.015, and the spurious losses add up to 0.005, we find  $\eta = 0.015/(0.015 + 0.005) = 0.75$ , which means that at the threshold, for  $\nu \ll \gamma$ , we will see a variance of  $V^- \approx 1/2 - \eta/2$ , or about 6 dB.

Let us now estimate the bandwidth within which the squeezing is generated. This bandwidth is the same as the cavity linewidth  $\gamma$ , which, in turn, is the ratio of the cavity's free spectral range and finesse. Assuming that the cavity is of a bow-tie configuration (Fig. 5.12) with a full length of  $L_c = 30$  cm, its free spectral range is  $c/L = 1$  GHz. The finesse is  $\pi/T \approx 160$ , so  $\gamma \approx 6$  MHz.

Historically, the first observation of squeezing using an OPA cavity has been achieved by Wu et al. in 1986 [29]. The squeezing reached in that experiment was about 3 dB. Since then, many groups made efforts to further develop this approach. One of the most recent results reported a squeezing of 12.7 dB [30]. This remarkable achievement required the overall quantum efficiency (including that of the OPA cavity, homodyne detection, mode matching, etc.) to approach 95%.

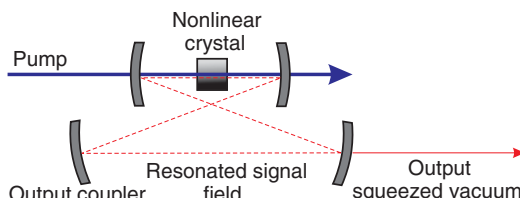


**FIGURE 5.12** Squeezing in an OPA cavity. The cavity mirrors are reflective to the signal field, but transparent to the pump.

OPAs can as well be used successfully to generate two-mode squeezing. The first experiment to that effect was reported by Ou et al. in 1992 [31]. In that work, the signal and idler fields resonated in the cavity were of the same frequency, but different polarizations, and were mixed with one another using polarization optics after exiting the OPA.

### 5.4.2 In Atomic Ensembles

As mentioned above, high optical nonlinearity is at the heart of most squeezing processes. An atom interacting with an optical wave resonant with one of its transitions is an intrinsically nonlinear object. Atoms begin to exhibit nonlinear optical properties at intensity levels on a scale of the saturation intensity, which is many orders of magnitude lower than the intensity levels required for significant nonlinear effects in ferroelectric crystals. Therefore, atomic ensembles have been considered an attractive medium for the preparation of squeezed optical states from early days of quantum optics.

A typical mechanism that leads to the generation of squeezing is four-wave mixing (Fig. 5.13). A  $\Lambda$ -shaped atomic energy level configuration contains two ground states coupled to a single excited state by optical transitions of degenerate or nondegenerate frequencies. This configuration can be found, in particular, in alkali atoms, where the ground level is split into two hyperfine sublevels.

Suppose the atom is initially in ground state  $|b\rangle$ . The pump field of frequency  $\Omega$  excites the  $|a\rangle - |b\rangle$  transition, driving the atom into the other ground state  $|c\rangle$  through Raman scattering, which results in emission of a Stokes photon of frequency  $\Omega - \Delta$ . Level  $|c\rangle$  is in turn excited by the pump field and the atom goes back into  $|b\rangle$ , accompanied by emission of an anti-Stokes photon of frequency  $\Omega + \Delta$ . If the entire

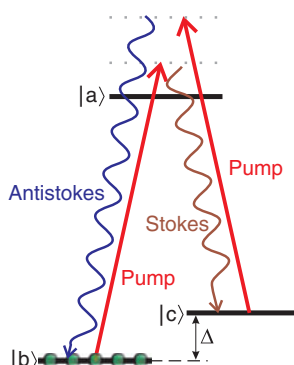


**FIGURE 5.13** Quantum four-wave mixing in an atomic  $\Lambda$  system leads to emission of the Stokes and anti-Stokes photons akin to signal and idler in parametric down-conversion. Two-mode squeezing obtains for non-degenerate and single-mode squeezing for degenerate ground states.

process is coherent, the Stokes and anti-Stokes emission modes will find themselves in the two-mode squeezed state.

This mechanism was used in the very first observation of optical squeezing by Slusher et al. [32]. In that experiment, atomic vapor of sodium has been used and two Fabry-Perot cavities resonant with the pump and the Stokes/anti-Stokes fields have been placed around the vapor sample for amplification. A two-mode squeezed state at frequencies  $\Omega \pm \Delta$  was observed at a  $\sim 0.3$  dB level using a homodyne detector with the local oscillator at frequency  $\Omega$ .

The state observed by Slusher and co-workers did not approach the minimum-uncertainty limit. This is largely due to processes in atoms that occur concurrently to four-wave mixing and lead to incoherent emission into the signal modes, such as Brillouin and incoherent Raman scattering. Further hindrance is presented by various dephasing phenomena such as time-of-flight decoherence that inhibit coherent four-wave mixing. All these processes contribute to the “thermalization” of the optical state in the signal modes and degrade the squeezing.

This appears to be a common problem in experiments using atomic ensembles for squeezing. This is the primary reason that ferroelectric crystals, rather than atomic systems became the workhorse of squeezed light generation. In recent years, however, atomic systems have been revisited and significant squeezing has been demonstrated in experiments involving four-wave mixing [33, 34] and polarization self-rotation [35, 36].

### 5.4.3 In Fibers

Optical fibers are typically made of glass, an amorphous material with inversion symmetry. Accordingly, they normally possess no second-order nonlinearity. However, fibers enable propagation of focused optical wavepackets over long distances, so the effects of third-order (Kerr) nonlinearities on these wavepackets become significant. One of these effects is squeezing.

Squeezing in optical fiber is best explained in terms of the nonlinear refractive index. In a Kerr medium, the refractive index depends on intensity  $I$  of the propagating light according to

$$n = n_0 + n_2 I, \quad (5.70)$$

where  $n_2$  is related to the third-order nonlinear susceptibility  $\chi^{(3)}$ . The phase of light that has propagated through such a material will then depend on the intensity, resulting in the transformation of the Wigner function as illustrated in Figure 5.14. The parts of the Wigner function that are associated with higher and lower intensities becomes shifted in the phase space with respect to each other, resulting in squeezing.

Homodyne detection of squeezing in this configuration is complicated by the macroscopic mean amplitude of the signal required to take advantage of Eq. (5.70). The amplitude could, in principle, be eliminated by means of phase-space displacement (see Section 5.2.4); however, this would require a powerful laser and excellent

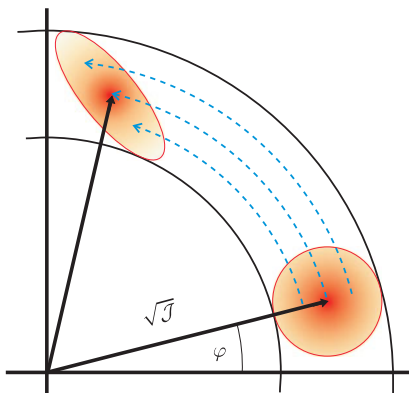


**FIGURE 5.14** Effect of a Kerr medium on a coherent state. Different intensities experience different refractive indices, resulting in quadrature squeezing. From Reference 37.

phase stabilization. A more common detection method involves causing two fiber-squeezed fields to interfere with each other so the resulting phase-space displacement and rotation make one of the resulting fields amplitude-squeezed. Amplitude squeezing is then readily observed by measuring the intensity with a single high-efficiency detector and evaluating the variance of the photocurrent noise.

There are a number of ways such interference can be implemented. For example, in a Sagnac-type interferometer the initial laser pulse impinges on a beam splitter, after which the transmitted and reflected fields enter the fiber from two ends. Upon exiting the fiber, the fields interfere on the same beam splitter, and one of the resulting fields is measured [38]. Alternatively, a polarization-maintaining fiber is used, so that the fields in both polarizations become squeezed at the fiber output. These fields are then brought into interference using waveplates positioned at the output end of the fiber [39].

Squeezing in optical fibers is limited by phase noise associated with thermal fluctuations of the refractive index, in particular guided acoustic wave Brillouin scattering. An additional degrading factor, particularly significant for very short pulses, is Raman scattering [38]. Both these phenomena allow precise theoretical treatment, and can be minimized by wise choice of experimental parameters [40, 41]. As a result, squeezing up to about 7 dB has been obtained [41].

## 5.5 APPLICATIONS IN QUANTUM INFORMATION

Squeezed light is a primary resource in continuous-variable<sup>5</sup> quantum information processing. In addition to fundamental interest such as implementation of the original

<sup>5</sup>The term “continuous-variable” refers to optical quantum information protocols that involve manipulation of a state in phase space, that is, displacement, squeezing, quadrature measurements, and so on. It is usually contrasted with “discrete-variable” methods dealing with manipulating and measuring single photons. This

EPR paradox, it is the basis of many basic applications such as universal quantum computing, dense coding, and quantum key distribution. The limited volume of this manuscript does not permit a comprehensive review of these applications; such a review can be found, for example, in References 42 and 43. Here we will concentrate on only two important examples.

### 5.5.1 Quantum-Optical State Engineering

Lasers generate coherent states and their statistical mixtures — the states of light known as classical. While such states are useful for some applications, many emerging quantum technologies require a supply of optical states that lie outside the classical domain. Nonclassical optical states cannot be achieved by linear-optical manipulation: interference of coherent states necessarily leads to coherent states. Production of nonclassical states therefore requires nonlinear optics.

Parametric down-conversion is a nonlinear phenomenon capable of producing quantum states of light with high efficiencies and with well-defined spatiotemporal properties. This property is unique among existing methods of non-classical light generation (see, e.g., Reference 44). However, the only states that SPDC can produce are the single- and dual-mode squeezed vacua. For this reason, the past decade has seen extensive efforts to use these states as “primitives” to produce (“engineer”) various other states of light. As we see in this section, application of tools such as linear-optical manipulation, interference with coherent states, and conditional measurements allows one to accomplish this task successfully. However small the degree of squeezing may be, even a single squeezed resource permits producing a wide variety of complex optical states [16, 45].

A TMSV with a weak level of squeezing can be used to generate *heralded single photons*. To that end, one channel of that state (idler) is monitored by a single-photon detector. If the detector “clicks,” we know, according to Eq. (5.40), that a photon must have been emitted into the other (signal) channel as well. If the squeezing parameter  $r$  is sufficiently small, the contribution of higher photon numbers in the signal channel can be neglected.

In 2001, this technique was used to generate a heralded single photon in a definite spatiotemporal mode, characterize it using homodyne tomography and, for the first time, observe a negative Wigner function [46]. This method was later extended to generate and measure the two- [47] and three-photon [48, 49] states. In these extensions, the idler channel of SPDC was split into multiple photon detectors, and their coincident “clicks” were required for a heralding event.

A modification of this scheme shown in Figure 5.15 permits producing arbitrary superpositions of photon number states. Prior to detection, the light in the idler channel is mixed with weak ancillary coherent states on beam splitters. In this way, a detector registering a photon “does not know” whether it comes from SPDC or from

---

separation is largely of historical and technological nature; in fact, more and more interesting applications now arise at the boundary between the two domains [16, 88].

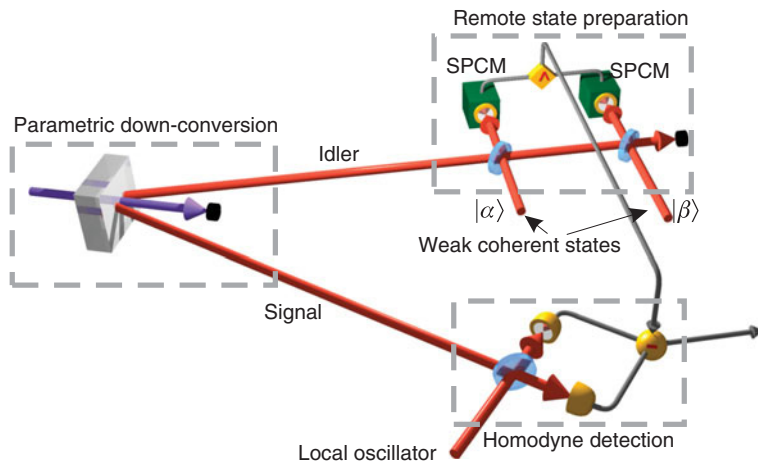


**FIGURE 5.15** Generating arbitrary superpositions of the zero-, one-, and two-photon states. The light in the idler channel of parametric down-conversion is brought into interference with two weak coherent states and subsequently detected by single-photon counting modules (SPCMs). A double “click” heralds the generation of the desired state in the signal channel. (For a color version of this figure, see the color plate section.)

a coherent state. This indistinguishability results in the idler channel of SPDC being effectively projected onto a superposition of Fock states. Thanks to entanglement of the TMSV, this superposition is automatically transferred to the signal channel. The weight of each component of the superposition can be controlled by the amplitudes and phases of the ancilla coherent states. This technique has been demonstrated for superpositions of up to the two- [50] and three-photon [49] terms, but can, in principle, be extended to higher numbers. One of the possible applications of this method is the implementation of the cubic phase gate for universal quantum computation in the continuous-variable setting.

In the above examples, a low magnitude of the squeezing parameter does not degrade the fidelity of engineered quantum states. Quite the contrary, it ensures that the state is not contaminated by higher photon number components. However, low squeezing also reduces the probability of the heralding event, which can make the method unpractical. One must choose the degree of squeezing as a compromise between the fidelity and the state production rate.

In the next example, in contrast, a non-negligible value of squeezing is essential for obtaining the desired state — a superposition  $|\alpha\rangle \pm |-\alpha\rangle$  of two coherent states of opposite amplitudes. This state is of interest to the quantum community because, while being a linear combination of classical states, it is highly nonclassical, and hence reminiscent of the famous “Schrödinger cat” Gedankenexperiment.

Remarkably, the squeezed vacuum is quite similar to the state  $|\alpha\rangle + |-\alpha\rangle$  (“even Schrödinger kitten”) for  $\alpha \lesssim 1$ . To see this, recall the Fock decomposition (5.31) of

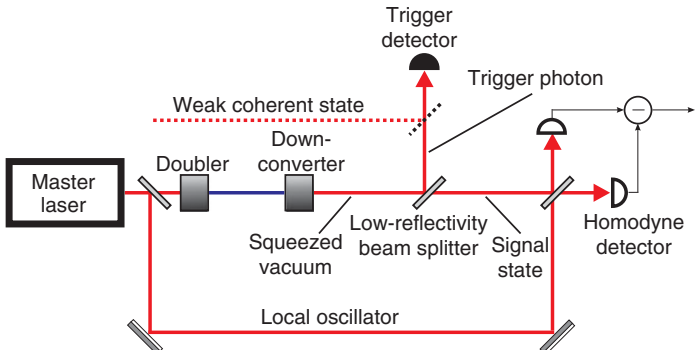


**FIGURE 5.16** Conditional preparation of the “odd Schrödinger kitten” by applying photon annihilation to the squeezed vacuum state (the “even Schrödinger kitten”). The dashed lines shows the additional elements used to generate arbitrary superpositions of states  $|\alpha\rangle$  and  $|-\alpha\rangle$  as in Reference 57.

the coherent state. The sum of two coherent states of opposite amplitudes will contain only even photon number terms,

$$|\alpha\rangle + |-\alpha\rangle \propto |0\rangle + \frac{\alpha^2}{\sqrt{2}} |2\rangle + O(\alpha^4), \quad (5.71)$$

in the same way as the squeezed vacuum state (5.37). With a sufficiently small  $\alpha$ , only the first two terms of these decompositions are significant, and setting  $r = \alpha^2$  makes them mutually identical for the two states.

Because coherent states are eigenstates of the photon annihilation operator  $\hat{a}$ , applying that operator to  $|\alpha\rangle + |-\alpha\rangle$  produces  $\alpha(|\alpha\rangle - |-\alpha\rangle)$ , that is, an “odd Schrödinger kitten.” This idea was implemented experimentally by Wenger et al. [51] and later refined in References 52–55. For photon annihilation, squeezed vacuum produced by means of degenerate SPDC was transmitted through a low reflectivity beam splitter (Fig. 5.16). Detection of a photon in the reflected channel indicates that a photon has been removed from the squeezed vacuum — that is, a photon annihilation event has occurred [56].

If a weak ancilla coherent state is injected into the heralding detector using an additional beam splitter (Fig. 5.16), the heralding photon cannot be definitively traced back to the squeezed state or that ancilla. If the event comes from the squeezed state, the photon subtraction takes place and the signal output is the odd Schrödinger kitten; if it comes from the coherent state, the signal output is the same as the input, that is, the even Schrödinger kitten. Because these two possibilities are indistinguishable, the output state becomes a coherent superposition of the even and odd kittens, with the magnitude and phase of the terms in the superposition dependent on the parameters of the ancilla. In this way, arbitrary superpositions of states  $|\alpha\rangle$  and  $|-\alpha\rangle$  — an optical continuous-variable qubit — are generated [57].

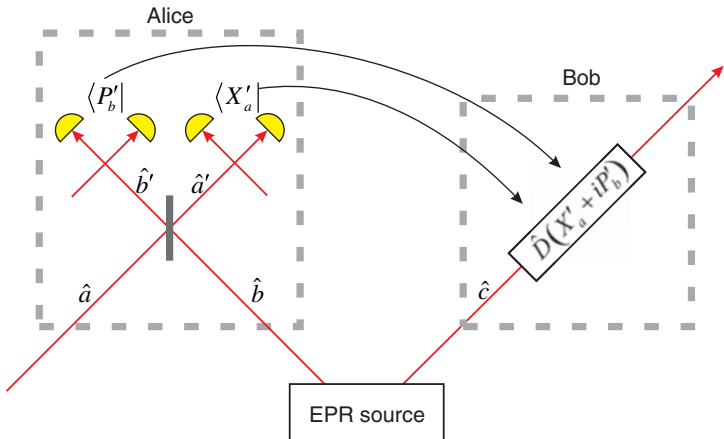


**FIGURE 5.17** The scheme of quantum teleportation. Operator  $\hat{D}(X'_a + iP'_b)$  denotes phase-space displacement.

### 5.5.2 Continuous-Variable Quantum Teleportation

Teleportation is a quantum communication protocol in which a quantum state is transferred between two locations without utilizing any direct quantum communication channel. The transfer is enacted by local interference of the signal state with a portion of the entangled resource shared between the two locations, as well as local measurements, classical communications, and local quantum operations. The teleportation protocol was first proposed for qubits in 1993 by Bennett et al. [58], and for continuous variables in 1994 by Vaidman [59]. The latter protocol utilizes the two-mode squeezed vacuum as the entangled resource; its major advantage is the principal capability of *complete* transfer of a quantum state of an optical mode, independent, in particular, of the number of photons therein.

Figure 5.17 shows the scheme of the protocol. The sender, Alice, has the signal state she wishes to teleport in mode  $\hat{a}$ . In addition, she and the receiver, Bob, share a two-mode squeezed state in modes  $\hat{b}$  and  $\hat{c}$ . In order to perform teleportation, Alice overlaps modes  $\hat{a}$  and  $\hat{b}$  on a symmetric beam splitter and performs position and momentum measurements in its outputs using two homodyne detectors. She then communicates the results of her measurement to Bob via a classical channel. Bob performs phase-space displacement of mode  $\hat{c}$  in accordance with that information, after which the state of this mode becomes identical to the initial state of mode  $\hat{a}$ .

In order to visualize the physics of teleportation, let us think of the signal state as a point  $(X_a, P_a)$  in the phase space (neglect the uncertainty principle for a moment). Further, we assume the initial two-mode squeezing of modes  $\hat{b}$  and  $\hat{c}$  to be infinite:  $X_b = X_c$  and  $P_b = -P_c$ , with both these quantities being completely uncertain. The beam splitter transformation, in accordance with Eqs. (5.41), makes the position in mode  $\hat{a}$  equal to  $X'_a = (X_a - X_b)/\sqrt{2}$  while the momentum in mode  $\hat{b}$  becomes  $P'_b = (P_a + P_b)/\sqrt{2}$ .

Suppose now that the position and momentum of these modes are measured. Let the measurement results be  $X'_a$  and  $P'_b$ , respectively. This means that the position of mode  $\hat{b}$  prior to the beam splitter has been  $X_b = X_a - X'_a \sqrt{2}$  and its momentum  $P_b = -P_a + P'_b \sqrt{2}$ . Because of the infinite two-mode squeezing of modes  $\hat{b}$  and  $\hat{c}$  this implies, in turn, that  $X_c = X_a - X'_a \sqrt{2}$  and  $P_c = P_a - P'_b \sqrt{2}$ .

We see that, after Alice's measurement, the position and momentum of Bob's mode become certain and related to those of the initial state. Furthermore, if Alice communicates the observed values of  $X'_a$  and  $P'_b$  to Bob (via a classical channel), Bob will be able to perform a phase-space displacement operation (see Section 5.2.4) on his mode, obtaining the position and momentum equal to  $X_a$  and  $P_a$ , respectively, that is, identical to those of the initial signal state.

A more rigorous argument can be presented in terms of Wigner functions. Let the initial Wigner function of the signal state be  $W_a(X_a, P_a)$ . The Wigner function of the EPR state shared between Alice and Bob is  $W_{bc}(X_b, P_b, X_c, P_c) \propto \delta(X_b - X_c)\delta(P_b + P_c)$ . The three-mode Wigner function is then  $W_{abc}(X_a, P_a, X_b, P_b, X_c, P_c) = W_a(X_a, P_a)W_{bc}(X_b, P_b, X_c, P_c)$ . After the beam splitter in Alice's channel, it will transform into

$$\begin{aligned} W'_{abc}(X'_a, P'_a, X'_b, P'_b, X_c, P_c) &\propto W_a\left(\frac{X'_a + X'_b}{\sqrt{2}}, \frac{P'_a + P'_b}{\sqrt{2}}\right) \\ &\times \delta\left(\frac{-X'_a + X'_b}{\sqrt{2}} - X_c\right) \delta\left(\frac{-P'_a + P'_b}{\sqrt{2}} + P_c\right), \end{aligned} \quad (5.72)$$

where the primed indices refer to the quadratures of the modes after the beam splitter. A measurement of  $X'_a$  and  $P'_b$  will yield, in mode  $\hat{c}$ ,

$$\begin{aligned} W'_c(X_c, P_c) &= \iint_{-\infty}^{\infty} W'_{abc}(X'_a, P'_a, X'_b, P'_b, X_c, P_c) dP'_a dX'_b \\ &\propto W_a\left(X_c + X'_a \sqrt{2}, P_c + P'_b \sqrt{2}\right). \end{aligned} \quad (5.73)$$

Again, applying displacement to Bob's mode, we recover a state with the Wigner function equal to that of the initial signal that is, the state identical to the initial.

In experimental practice, the teleportation performance is degraded by a number of factors, of which the primary ones are the optical losses, optical phase fluctuations, and imperfect squeezing of the TMSV resource. A variety of performance metrics has been proposed [42, 60–63]. The most common one is the *coherent-state fidelity*, which is the average, over all coherent states  $|\alpha\rangle$ , of the fidelity  $F_c = \langle \alpha | \hat{T}(|\alpha\rangle\langle\alpha|) | \alpha \rangle$ , where  $\hat{T}(|\alpha\rangle\langle\alpha|)$  is the density operator of the teleported state. For a perfect teleportation procedure,  $F_c = 1$ . On the other hand, the best fidelity that can be achieved

without the use of entangled resource, simply by Alice's measuring the position and momentum quadratures of the input state and Bob's recreating a coherent state with the same central position and momentum, is  $F_c = 1/2$ . The value of  $F_c$  reaching a value of  $2/3$ , known as the no-cloning fidelity [62], guarantees that nobody else can have a better copy of the input state than Bob. For this reason, the no-cloning fidelity is of relevance to continuous-variable quantum communication. The value of  $2/3$  is also the minimum required for obtaining teleported states with negative values of the Wigner function.

The first continuous-variable quantum teleportation experiment was reported by Furusawa and colleagues in 1998 [11]. The TMSV resource has been obtained from two single-mode squeezed fields generated as counterpropagating modes in a single OPA cavity. Phase-space displacement was implemented using a low-transmissivity beamsplitter, with the amplitude and phase of the displacement beam regulated by electro-optical modulator. The resulting fidelity,  $F_c = 0.58$ , exceeded the classical benchmark.

Thereafter, numerous efforts have been reported to refine the protocol and teleport increasingly complex quantum states. For example, Takei and colleagues [64] in 2005 demonstrated entanglement swapping (teleportation of one channel of a TMSV state), which is an essential component of quantum repeaters. Yonezawa et al. [65] teleported in 2007 a squeezed vacuum state and obtained, for the first time, squeezing in the output. The first teleportation of states with a negative Wigner function, such as the single photon and "Schrödinger kitten" [52] was implemented in 2011 [66]. This work was followed by unconditional high fidelity teleportation of dual-rail single-photon qubits [67].

## 5.6 APPLICATIONS IN QUANTUM METROLOGY

Squeezed light can be useful in any task that requires precise evaluation of the optical phase. Such tasks occur, for example, in optical communications [68] and metrology [69]. Phase evaluation typically involves an interferometer, and its precision is determined by the phase uncertainty of the fields used. The coherent state, which is readily obtained from lasers, has a phase uncertainty on a scale of the inverse of its amplitude, or inverse square root of its photon number  $1/\sqrt{N}$  (Fig. 5.1b). However, employing nonclassical states has a potential to improve the precision up to the fundamental limit  $\sim 1/N$  established by the Heisenberg uncertainty principle. Among the many approaches leading to this goal [70], phase squeezing is perhaps the most straightforward (Fig. 5.1f). In this section, we discuss a prominent example: the application of squeezed light in gravitational wave detection.

Gravitational waves (GWs) are deformations of the space-time continuum caused by accelerating massive objects. GWs, which propagate at the speed of light, are a primary prediction of Einstein's general relativity, but they have not yet been observed due to their minuscule magnitude. The strongest GWs reaching the Earth are expected to cause deformations on a scale of 1 part in  $10^{20}$ , and their detection constitutes one of the most significant challenges faced by modern physics.

Gravitational wave detectors use a Michelson-type laser interferometer to detect small perturbations to positions of massive, freely suspended mirrors in its two arms. The action of a GW stretches one of the arms and compresses the other, thereby affecting the path-length difference and changing the intensity of the output signal.

At present, the world's most sensitive GW detectors are TAMA in Japan, GEO 600 in Germany, LIGO in the United States and VIRGO in Italy. These detectors utilize a number of techniques in order to enhance their signal.

- The interferometer arms are constructed up to a few kilometers in length in order to increase the absolute displacement of the mirrors.
- Both arms of the interferometer are turned into high-finesse Fabry-Perot cavities by means of additional mirrors placed near the Michelson interferometer beam splitter.
- Massive (tens of kilograms) mirrors are used in order to reduce the radiation pressure noise and the mirrors' Brownian motion.
- Laser powers of up to hundreds of watt are employed to minimize the phase uncertainty.

Further enhancement of any of these parameters would be prohibitive in terms of costs and resources. This is why additional sensitivity improvement associated with squeezing becomes useful. The idea of this improvement was proposed by Caves in 1981 [71] and involves injecting squeezed vacuum into the dark port of the interferometer.

Suppose the interferometer input mode  $\hat{a}$  is fed with a strong laser field in coherent state  $|\alpha\rangle$  (Fig. 5.18a). We assume  $\alpha$  to be real. The other input mode,  $\hat{b}$ , is in the vacuum or squeezed vacuum state. The beam splitter implements the mode transformation according to  $\hat{a}' = (\hat{a} + \hat{b})/\sqrt{2}$ ,  $\hat{b}' = (\hat{a} - \hat{b})/\sqrt{2}$ . Let the interferometer paths be slightly unbalanced in length so that, upon return to the beam splitter, mode  $\hat{b}'$  acquires a small phase shift  $\varphi$  which we wish to evaluate. After interacting, for the second time, on the beam splitter, the modes become  $\hat{a}'' = (\hat{a}' + \hat{b}' e^{i\varphi})/\sqrt{2}$ ,  $\hat{b}'' = (\hat{a}' - \hat{b}' e^{i\varphi})/\sqrt{2}$ . Using  $e^{i\varphi} \approx 1 + i\varphi$ , we find

$$\hat{b}'' = \hat{b} - i\varphi\hat{a}. \quad (5.74)$$

Because  $\varphi$  is small, the second term in Eq. (5.74) effectively results in displacement of the (squeezed) vacuum mode  $\hat{b}$  along the momentum axis by  $\varphi\alpha$  (Fig. 5.18b).

A momentum quadrature measurement performed on mode  $\hat{b}''$  by means of a homodyne detector will yield this value, with an uncertainty equal to the momentum uncertainty of the initial state of mode  $b$ . If this state is momentum squeezed, the measurement sensitivity is enhanced accordingly, as illustrated in Figure 5.18c.

The actual measurement procedure that is currently implemented in GEO 600 [72] and LIGO [73] largely follows the above description. A major challenge is to construct a source capable of generating squeezing in the frequency band compatible with gravitational waves. Typical GWs are produced in the audio range between 150

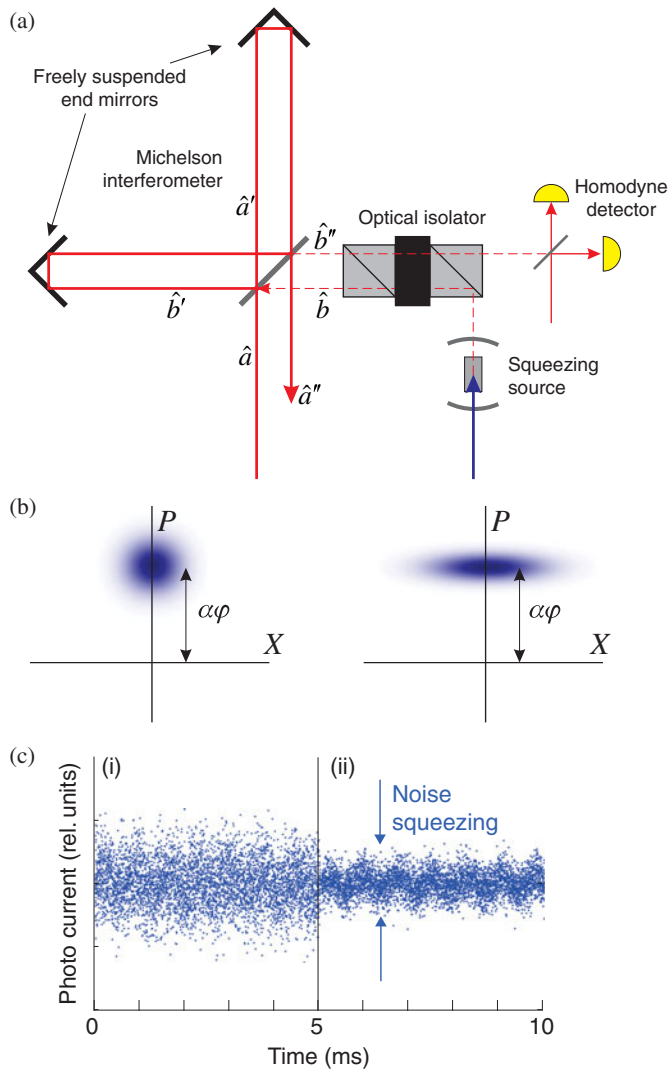


**FIGURE 5.18** Using squeezed vacuum to enhance the sensitivity of interferometric phase detection. (a) Scheme of the setup. The squeezed vacuum is injected through the dark port (mode  $\hat{b}$ ) of the interferometer. An optical isolator is used to separate the input and output modes  $\hat{b}$  and  $\hat{b}''$ , and also to prevent scattering of the macroscopic light inside the interferometer into the squeezed vacuum source. For clarity, the end mirrors are sketched as retroreflectors. (b) The Wigner function of the state in mode  $\hat{b}''$  for the vacuum (left) and squeezed (right) input in mode  $\hat{b}$ . The momentum quadrature measurement by the homodyne detector is proportional to the interferometer path length difference; the measurement precision is enhanced by the initial momentum squeezing of mode  $\hat{b}$ . (c) Simulation from Reference 69 illustrating how squeezing helps revealing a small oscillation. Left, no squeezing; right, squeezing present.

and 300 Hz, whereas most OPA-based squeezing sources built until recently exhibited significant technical noises at frequencies below 1 MHz. A series of breakthroughs achieved over the past decade helped identifying and eliminating the sources of these noises [69].

The primary issue turned out to be macroscopic optical field at the wavelength of the desired squeezing present within the OPA cavity. Mechanical fluctuations of the cavity length (which occur at low frequencies) randomly affect the magnitude and phase of that field and subsequently contaminate the output. The remedy consisted of preventing the ambient laser field from penetrating into the cavity. This included using a field of different frequency to lock the cavity length [74], using an optical isolator to prevent the reflection of the local oscillator from the homodyne detector photodiodes into the OPA cavity [22] and even minimization of scattering from the nearby optical elements [75].

The most recent result on incorporating squeezed light into a GW detector has been reported for LIGO [73]. Enhancement of sensitivity of up to 2.2 dB for frequencies down to 150 Hz is reported. Note that this enhancement is far below the  $>10$  dB degree of squeezing produced by the source employed. This is because of the losses introduced when injecting the squeezed field into the Michelson interferometer, imperfect mode matching with the carrier field, and phase fluctuations. It is expected that the next generation of LIGO (the so-called Advanced LIGO) will address most of these shortcomings [73].

## 5.7 CONCLUSION AND OUTLOOK

Over the past 30 years, the science of squeezed light has experienced enormous progress and made significant influence on the entire field of physics. Its primary effect, in my opinion, was to radically change the physicists' perception of quantum theory of electromagnetic radiation. Prior to the observation of squeezing, it was a largely abstract discipline, having little connection to experimental practice. Observation of squeezing and subsequent development of optical homodyne tomography resulted in techniques of creating, manipulating, and measuring quantum states of light, allowing the postulates of quantum theory of light to be directly tested and applied in experiment.

The second important contribution of squeezing is that to quantum information science. It provided an entangled resource for many quantum information protocols. Additionally, it gave rise to deeper understanding of parametric down-conversion, allowing preparation of other important quantum optical resources such as polarization-entangled photon pairs. As a result, optics has become, for at least a decade, the main test bed for quantum information science, effectively jump starting this field.

What developments can be expected in the next years? We are currently witnessing the emergence of new means of production of squeezing, e.g. by bringing light into interaction with an optomechanical cavity, that is, a optical cavity with one of its elements suspended so as to form on a high quality mechanical resonator [76, 77].

The pressure of light inside the cavity on that resonator results in optical nonlinearities described by equations similar to (5.70), thereby leading to the squeezing. The promise of this new method is the possibility to manufacture on-chip sources of squeezed light, enabling compact optical sensors and new fundamental tests of physics.

In terms of applications, major results are awaited in *gravitational wave detection*. Although squeezed light has already been integrated into some of the detectors, it has not yet been used in actual data acquisition runs. In Advanced LIGO, the squeezing is expected to enhance the sensitivity by up to a factor of ten. Hopefully, such a detector will not only be able to prove the existence of GWs, but also provide information about their spatial distribution and temporal dynamics. This would result in a fundamentally new method for observing the universe, which has a potential to revolutionize the entire field of astronomy.

No less exciting are squeezed light's contributions to quantum information science. Existing techniques of two-mode squeezing and quantum teleportation can be employed for the development of the *continuous-variable quantum repeater* [78], which will dramatically enhance the quantum communication distance leading to global "quantum internet." The unsolved challenges in this domain are long-term storage of squeezed light [79–81] as well as methods of distilling the two-mode squeezed state that has experienced losses [82, 83].

Recently, exciting developments have been reported on creation of *multimode quadrature-entangled states* by simultaneous pumping of multiple spatial [84], spectral [85, 86], or temporal [87] modes of an SPDC arrangement. In this way, a large-scale, individually addressable entangled state is created that may be possible to use in measurement-based quantum computation and other quantum information applications.

## REFERENCES

- [1] R. Loudon and P. Knight, "Squeezed light," *J. Mod. Opt.* **34**, 709–759 (1987).
- [2] A. Einstein, B. Podolsky, and N. Rosen, "Can quantum-mechanical description of physical reality be considered complete?" *Phys. Rev.* **47**, 777–780 (1935).
- [3] K. Schneider, M. Lang, J. Mlynek, and S. Schiller, "Generation of strongly squeezed continuous-wave light at 1064 nm," *Opt. Exp.* **2**, 59–64 (1998).
- [4] V. Buzek and P. L. Knight, *Squeezed States: Basic Principles* (Springer, Berlin, Heidelberg, 2004), pp. 3–32.
- [5] U. Leonhardt, *Measuring the Quantum State of Light*, Cambridge Studies in Modern Optics (Cambridge University Press, 1997).
- [6] B. L. Schumaker and C. M. Caves, "New formalism for two-photon quantum optics. ii. Mathematical foundation and compact notation," *Phys. Rev. A* **31**, 3093–3111 (1985).
- [7] H. P. Yuen, "Two-photon coherent states of the radiation field," *Phys. Rev. A* **13**, 2226–2243 (1976).
- [8] M. Scully and S. Zubairy, *Quantum Optics* (Cambridge University Press, 1997).

- [9] V. V. Dodonov, O. V. Man'ko, and V. I. Man'ko, "Photon distribution for one-mode mixed light with a generic gaussian Wigner function," *Phys. Rev. A* **49**, 2993–3001 (1994).
- [10] G. Breitenbach, S. Schiller, and J. Mlynek, "Measurement of the quantum states of squeezed light," *Nature* **387**, 471–475 (1997).
- [11] A. Furusawa, J. L. Sørensen, S. L. Braunstein, C. A. Fuchs, H. J. Kimble, and E. S. Polzik, "Unconditional quantum teleportation," *Science* **282**, 706–709 (1998).
- [12] R. Schnabel, H. Vahlbruch, A. Franzen, S. Chelkowski, N. Grosse, H.-A. Bachor, W. Bowen, P. Lam, and K. Danzmann, "Squeezed light at sideband frequencies below 100 khz from a single OPA," *Opt. Commun.* **240**, 185–190 (2004).
- [13] W. Wasilewski, A. I. Lvovsky, K. Banaszek, and C. Radzewicz, "Pulsed squeezed light: simultaneous squeezing of multiple modes," *Phys. Rev. A* **73**, 063819 (2006).
- [14] H. P. Yuen and V. W. S. Chan, "Noise in homodyne and heterodyne detection," *Opt. Lett.* **8**, 177–179 (1983).
- [15] G. L. Abbas, V. W. S. Chan, and T. K. Yee, "Local-oscillator excess-noise suppression for homodyne and heterodyne detection," *Opt. Lett.* **8**, 419–421 (1983).
- [16] A. I. Lvovsky and M. G. Raymer, "Continuous-variable optical quantum-state tomography," *Rev. Mod. Phys.* **81**, 299–332 (2009).
- [17] W. Wasilewski, T. Fernholz, K. Jensen, L. S. Madsen, H. Krauter, C. Muschik, and E. S. Polzik, "Generation of two-mode squeezed and entangled light in a single temporal and spatial mode," *Opt. Exp.* **17**, 14444–14457 (2009).
- [18] H. Hansen, T. Aichele, C. Hettich, P. Lodahl, A. I. Lvovsky, J. Mlynek, and S. Schiller, "Ultrasensitive pulsed, balanced homodyne detector: application to time-domain quantum measurements," *Opt. Lett.* **26**, 1714–1716 (2001).
- [19] K. Vogel and H. Risken, "Determination of quasiprobability distributions in terms of probability distributions for the rotated quadrature phase," *Phys. Rev. A* **40**, 2847–2849 (1989).
- [20] D. T. Smithey, M. Beck, M. G. Raymer, and A. Faridani, "Measurement of the Wigner distribution and the density matrix of a light mode using optical homodyne tomography: application to squeezed states and the vacuum," *Phys. Rev. Lett.* **70**, 1244–1247 (1993).
- [21] M. Vasilyev, S.-K. Choi, P. Kumar, and G. M. D'Ariano, "Tomographic measurement of joint photon statistics of the twin-beam quantum state," *Phys. Rev. Lett.* **84**, 2354–2357 (2000).
- [22] K. McKenzie, N. Grosse, W. P. Bowen, S. E. Whitcomb, M. B. Gray, D. E. McClelland, and P. K. Lam, "Squeezing in the audio gravitational-wave detection band," *Phys. Rev. Lett.* **93**, 161105 (2004).
- [23] F. A. Barbosa, A. S. Coelho, K. N. Cassemiro, P. Nussen-zveig, C. Fabre, M. Martinelli, and A. S. Villar, "Beyond spectral homodyne detection: complete quantum measurement of spectral modes of light," *Phys. Rev. Lett.* **111**, 200402 (2013).
- [24] E. H. Huntington, G. N. Milford, C. Robilliard, T. C. Ralph, O. Glöckl, U. L. Andersen, S. Lorenz, and G. Leuchs, "Demonstration of the spatial separation of the entangled quantum sidebands of an optical field," *Phys. Rev. A* **71**, 041802 (2005).
- [25] R. Boyd, *Nonlinear Optics*, (Academic Press, 2003).
- [26] R. E. Slusher, P. Grangier, A. LaPorta, B. Yurke, and M. J. Potasek, "Pulsed squeezed light," *Phys. Rev. Lett.* **59**, 2566–2569 (1987).

- [27] C. Kim and P. Kumar, “Quadrature-squeezed light detection using a self-generated matched local oscillator,” *Phys. Rev. Lett.* **73**, 1605–1608 (1994).
- [28] C. Gardiner and C. Savage, “A multimode quantum theory of a degenerate parametric amplifier in a cavity,” *Opt. Commun.* **50**, 173–178 (1984).
- [29] L.-A. Wu, H. J. Kimble, J. L. Hall, and H. Wu, “Generation of squeezed states by parametric down conversion,” *Phys. Rev. Lett.* **57**, 2520–2523 (1986).
- [30] T. Eberle, S. Steinlechner, J. Bauchrowitz, V. Händchen, H. Vahlbruch, M. Mehmet, H. Maller-Ebhardt, and R. Schnabel, “Quantum enhancement of the zero-area sagnac interferometer topology for gravitational wave detection,” *Phys. Rev. Lett.* **104**, 251102 (2010).
- [31] Z. Y. Ou, S. F. Pereira, H. J. Kimble, and K. C. Peng, “Realization of the einstein-podolsky-rosen paradox for continuous variables,” *Phys. Rev. Lett.* **68**, 3663–3666 (1992).
- [32] R. E. Slusher, L. W. Hollberg, B. Yurke, J. C. Mertz, and J. F. Valley, “Observation of squeezed states generated by four-wave mixing in an optical cavity,” *Phys. Rev. Lett.* **55**, 2409–2412 (1985).
- [33] C. F. McCormick, V. Boyer, E. Arimondo, and P. D. Lett, “Strong relative intensity squeezing by four-wave mixing in rubidium vapor,” *Opt. Lett.* **32**, 178–180 (2007).
- [34] V. Boyer, A. M. Marino, R. C. Pooser, and P. D. Lett, “Entangled images from four-wave mixing,” *Science* **321**, 544–547 (2008).
- [35] J. Ries, B. Brezger, and A. I. Lvovsky, “Experimental vacuum squeezing in rubidium vapor via self-rotation,” *Phys. Rev. A* **68**, 025801 (2003).
- [36] S. Barreiro, P. Valente, H. Failache, and A. Lezama, “Polarization squeezing of light by single passage through an atomic vapor,” *Phys. Rev. A* **84**, 033851 (2011).
- [37] I. Rigas, A. B. Klimov, L. L. Snchez-Soto, and G. Leuchs, “Nonlinear cross-Kerr quasi-classical dynamics,” *New J. of Phys.* **15**, 043038 (2013).
- [38] P. Drummond, R. Shelby, S. Friberg, and Y. Yamamoto, “Quantum solitons in optical fibres,” *Nature* **365**, 307–313 (1993).
- [39] J. Heersink, V. Josse, G. Leuchs, and U. L. Andersen, “Efficient polarization squeezing in optical fibers,” *Opt. Lett.* **30**, 1192–1194 (2005).
- [40] J. F. Corney, P. D. Drummond, J. Heersink, V. Josse, G. Leuchs, and U. L. Andersen, “Many-body quantum dynamics of polarization squeezing in optical fibers,” *Phys. Rev. Lett.* **97**, 023606 (2006).
- [41] R. Dong, J. Heersink, J. F. Corney, P. D. Drummond, U. L. Andersen, and G. Leuchs, “Experimental evidence for raman-induced limits to efficient squeezing in optical fibers,” *Opt. Lett.* **33**, 116–118 (2008).
- [42] S. L. Braunstein and P. van Loock, “Quantum information with continuous variables,” *Rev. Mod. Phys.* **77**, 513–577 (2005).
- [43] U. L. Andersen, G. Leuchs, and C. Silberhorn, “Continuous-variable quantum information processing,” *Laser Photon. Rev.* **4**, 337–354 (2010).
- [44] P. Grangier, B. Sanders, and J. Vuckovic, “Focus on single photons on demand,” *New J. Phys.* **6** (2004).
- [45] F. DellAnno, S. De Siena, and F. Illuminati, “Multiphoton quantum optics and quantum state engineering,” *Phys. Reports* **428**, 53–168 (2006).
- [46] A. I. Lvovsky, H. Hansen, T. Aichele, O. Benson, J. Mlynek, and S. Schiller, “Quantum state reconstruction of the single-photon Fock state,” *Phys. Rev. Lett.* **87**, 050402 (2001).

- [47] A. Ourjoumtsev, R. Tualle-Brouri, and P. Grangier, “Quantum homodyne tomography of a two-photon Fock state,” *Phys. Rev. Lett.* **96**, 213601 (2006).
- [48] M. Cooper, L. J. Wright, C. Soller, and B. J. Smith, “Experimental generation of multi-photon fock states,” *Opt. Exp.* **21**, 5309–5317 (2013).
- [49] M. Yukawa, K. Miyata, T. Mizuta, H. Yonezawa, P. Marek, R. Filip, and A. Furusawa, “Generating superposition of up-to three photons for continuous variable quantum information processing,” *Opt. Exp.* **21**, 5529–5535 (2013).
- [50] E. Bimbard, N. Jain, A. MacRae, and A. Lvovsky, “Quantum-optical state engineering up to the two- photon level,” *Nat. Photon.* **4**, 243–247 (2010).
- [51] J. Wenger, R. Tualle-Brouri, and P. Grangier, “Non-Gaussian statistics from individual pulses of squeezed light,” *Phys. Rev. Lett.* **92**, 153601 (2004).
- [52] A. Ourjoumtsev, R. Tualle-Brouri, J. Laurat, and P. Grangier, “Generating optical Schrödinger kittens for quantum information processing,” *Science* **312**, 83–86 (2006).
- [53] J. S. Neergaard-Nielsen, B. M. Nielsen, C. Hettich, K. Mølmer, and E. S. Polzik, “Generation of a superposition of odd photon number states for quantum information networks,” *Phys. Rev. Lett.* **97**, 083604 (2006).
- [54] K. Wakui, H. Takahashi, A. Furusawa, and M. Sasaki, “Photon subtracted squeezed states generated with periodically poled  $\text{KTiOPO}_4$ ,” *Opt. Exp.* **15**, 3568–3574 (2007).
- [55] T. Gerrits, S. Glancy, T. S. Clement, B. Calkins, A. E. Lita, A. J. Miller, A. L. Migdall, S. W. Nam, R. P. Mirin, and E. Knill, “Generation of optical coherent-state superpositions by number-resolved photon subtraction from the squeezed vacuum,” *Phys. Rev. A* **82**, 031802 (2010).
- [56] R. Kumar, E. Barrios, C. Kupchak, and A. I. Lvovsky, “Experimental characterization of bosonic creation and annihilation operators,” *Phys. Rev. Lett.* **110**, 130403 (2013).
- [57] J. S. Neergaard-Nielsen, M. Takeuchi, K. Wakui, H. Takahashi, K. Hayasaka, M. Takeoka, and M. Sasaki, “Optical continuous-variable qubit,” *Phys. Rev. Lett.* **105**, 053602 (2010).
- [58] C. H. Bennett, G. Brassard, C. Crepeau, R. Jozsa, A. Peres, and W. K. Wootters, “Teleporting an unknown quantum state via dual classical and Einstein-Podolsky-Rosen channels,” *Phys. Rev. Lett.* **70**, 1895–1899 (1993).
- [59] L. Vaidman, “Teleportation of quantum states,” *Phys. Rev. A* **49**, 1473–1476 (1994).
- [60] S. L. Braunstein, C. A. Fuchs, and H. J. Kimble, “Criteria for continuous-variable quantum teleportation,” *J. Mod. Opt.* **47**, 267–278 (2000).
- [61] T. C. Ralph and P. K. Lam, “Teleportation with bright squeezed light,” *Phys. Rev. Lett.* **81**, 5668–5671 (1998).
- [62] F. Grosshans and P. Grangier, “Continuous variable quantum cryptography using coherent states,” *Phys. Rev. Lett.* **88**, 057902 (2002).
- [63] K. Hammerer, M. M. Wolf, E. S. Polzik, and J. I. Cirac, “Quantum benchmark for storage and transmission of coherent states,” *Phys. Rev. Lett.* **94**, 150503 (2005).
- [64] N. Takei, H. Yonezawa, T. Aoki, and A. Furusawa, “High-fidelity teleportation beyond the no-cloning limit and entanglement swapping for continuous variables,” *Phys. Rev. Lett.* **94**, 220502 (2005).
- [65] H. Yonezawa, S. L. Braunstein, and A. Furusawa, “Experimental demonstration of quantum teleportation of broadband squeezing,” *Phys. Rev. Lett.* **99**, 110503 (2007).
- [66] N. Lee, H. Benichi, Y. Takeno, S. Takeda, J. Webb, E. Huntington, and A. Furusawa, “Teleportation of non-classical wave packets of light,” *Science* **332**, 330–333 (2011).

- [67] S. Takeda, T. Mizuta, M. Fuwa, P. van Loock, and A. Fu-rusawa, “Deterministic quantum teleportation of photonic quantum bits by a hybrid technique,” *Nature* **500**, 315–318 (2013).
- [68] R. Slavik, F. Parmigiani, J. Kakande, C. Lundström, M. Sjödin, P. A. Andrekson, R. Weerasuriya, S. Sygle-tos, A. D. Ellis, L. Gröner-Nielsen, et al., “All-optical phase and amplitude regenerator for next-generation telecommunications systems,” *Nat. Photon.* **4**, 690–695 (2010).
- [69] R. Schnabel, N. Mavalvala, D. E. McClelland, and P. K. Lam, “Quantum metrology for gravitational wave astronomy,” *Nat. Commun.* **1**, 121 (2010).
- [70] V. Giovannetti, S. Lloyd, and L. Maccone, “Advances in quantum metrology,” *Nat. Photon.* **5**, 222–229 (2011).
- [71] C. M. Caves, “Quantum-mechanical noise in an interferometer,” *Phys. Rev. D* **23**, 1693 (1981).
- [72] J. Abadie, B. Abbott, R. Abbott, T. Abbott, M. Aber-nathy, C. Adams, R. Adhikari, C. Affeldt, B. Allen, G. Allen, et al., “A gravitational wave observatory operating beyond the quantum shot-noise limit,” *Nat. Phys.* **7**, 962–965 (2011).
- [73] J. Aasi, J. Abadie, B. Abbott, R. Abbott, T. Abbott, M. Abernathy, C. Adams, T. Adams, P. Addesso, R. Adhikari, et al., “Enhanced sensitivity of the ligo gravitational wave detector by using squeezed states of light,” *Nat. Photon.* **7**, 613–619 (2013).
- [74] H. Vahlbruch, S. Chelkowski, B. Hage, A. Franzen, K. Danzmann, and R. Schnabel, “Coherent control of vacuum squeezing in the gravitational-wave detection band,” *Phys. Rev. Lett.* **97**, 011101 (2006).
- [75] H. Vahlbruch, S. Chelkowski, K. Danzmann, and R. Schnabel, “Quantum engineering of squeezed states for quantum communication and metrology,” *New J. Phys.* **9**, 371 (2007).
- [76] A. H. Safavi-Naeini, S. Groöblacher, J. T. Hill, J. Chan, M. Aspelmeyer, and O. Painter, “Squeezed light from a silicon micromechanical resonator,” *Nature* **500**, 185–189 (2013).
- [77] T. P. Purdy, P.-L. Yu, R. W. Peterson, N. S. Kampel, and C. A. Regal, “Strong optomechanical squeezing of light,” *Phys. Rev. X* **3**, 031012 (2013).
- [78] H.-J. Briegel, W. Dür, J. I. Cirac, and P. Zoller, “Quantum repeaters: the role of imperfect local operations in quantum communication,” *Phys. Rev. Lett.* **81**, 5932–5935 (1998).
- [79] K. Honda, D. Akamatsu, M. Arikawa, Y. Yokoi, K. Akiba, S. Nagatsuka, T. Tanimura, A. Furusawa, and M. Kozuma, “Storage and retrieval of a squeezed vacuum,” *Phys. Rev. Lett.* **100**, 093601 (2008).
- [80] J. Appel, E. Figueroa, D. Korystov, M. Lobino, and A. I. Lvovsky, “Quantum memory for squeezed light,” *Phys. Rev. Lett.* **100**, 093602 (2008).
- [81] A. I. Lvovsky, B. C. Sanders, and W. Tittel, “Optical quantum memory,” *Nat. Photon.* **3**, 706–714 (2009).
- [82] H. Takahashi, J. S. Neergaard-Nielsen, M. Takeuchi, M. Takeoka, K. Hayasaka, A. Furusawa, and M. Sasaki, “Entanglement distillation from gaussian input states,” *Nat. Photon.* **4**, 178–181 (2010).
- [83] Y. Kurochkin, A. S. Prasad, and A. Lvovsky, “Distillation of the two-mode squeezed state,” *Phys. Rev. Lett.* **112**, 070402 (2014).
- [84] S. Armstrong, J.-F. Morizur, J. Janousek, B. Hage, N. Treps, P. K. Lam, and H.-A. Bachor, “Programmable multimode quantum networks,” *Nat. Commun.* **3**, 1026 (2012).

- [85] N. C. Menicucci, S. T. Flammia, and O. Pfister, “One-way quantum computing in the optical frequency comb,” *Phys. Rev. Lett.* **101**, 130501 (2008).
- [86] M. Pysher, Y. Miwa, R. Shahrokhsahi, R. Bloomer, and O. Pfister, “Parallel generation of quadripartite cluster entanglement in the optical frequency comb,” *Phys. Rev. Lett.* **107**, 030505 (2011).
- [87] S. Yokoyama, R. Ukai, S. C. Armstrong, C. Sornphiphat-phong, T. Kaji, S. Suzuki, J.-i. Yoshikawa, H. Yonezawa, N. C. Menicucci, and A. Furusawa, “Optical generation of ultra-large-scale continuous-variable cluster states,” *Nature Photonics.* **7**, 982 (2013).
- [88] U. L. Andersen, J. S. Neergaard-Nielsen, P. van Loock, A. Furusawa, Hybrid quantum information processing, arxiv.org/1409.3719



---

# 6

---

## ELECTROMAGNETIC THEORY OF MATERIALS

TOM G. MACKAY

*School of Mathematics, University of Edinburgh, Edinburgh, UK*

*and*

*Department of Engineering Science and Mechanics, Pennsylvania State University,  
University Park, PA, USA*

### 6.1 PREAMBLE

This chapter concerns the theory which underpins the electromagnetic properties of materials. A “material” is taken to be an assembly of a great number of atoms or molecules, each of which is much smaller than the electromagnetic wavelengths under consideration. Accordingly, we employ macroscopic electromagnetic fields, and the materials in question are characterized by their constitutive relations. The structure of these relations is considered for isotropic, anisotropic, and bianisotropic materials; these materials may be either spatially homogeneous or nonhomogeneous. We concentrate on linear materials, but nonlinear materials are described too. Thus, a very wide range of both naturally occurring and artificial materials are included within our scope. The focus of our attention is skewed toward anisotropic and bianisotropic materials; while these are less often described in standard textbook presentations on the electromagnetic properties of materials, they are of increasing importance from a technological viewpoint, particularly given recent rapid developments in the fields pertaining to artificial materials and metamaterials.

In the notation employed, vector quantities are underlined and the overhead  $\hat{\phantom{x}}$  symbol is used to denote a unit vector. In particular, the unit vectors aligned with the

Cartesian axes are written as  $\hat{x}$ ,  $\hat{y}$ , and  $\hat{z}$ . Double underlining and normal (bold) face signify a  $3 \times 3$  ( $6 \times 6$ ) dyadic. The inverse and transpose of a dyadic  $\underline{\underline{Q}}$  are represented by  $\underline{\underline{Q}}^{-1}$  and  $\underline{\underline{Q}}^T$ , respectively. Angular frequency is denoted by  $\omega$  and the permittivity and permeability of free space are written as  $\epsilon_0$  and  $\mu_0$ . The operators  $\text{Re}\{\cdot\}$  and  $\text{Im}\{\cdot\}$  deliver the real and imaginary parts of complex-valued quantities while  $i = \sqrt{-1}$ . SI units are adopted.

## 6.2 MACROSCOPIC VIEWPOINT

A material contains a vast number of atoms and each atom typically contains many charged particles. Accordingly, the determination of the electromagnetic fields—which are functions of both position  $\underline{r}$  and time  $t$  coordinates—inside a material only becomes a tractable problem if we consider fields which are averaged over a volume that is large compared with the volume occupied by a single atom. These fields are called macroscopic fields [1]. In fact, the averaging process should be carried out over both  $\underline{r}$  and  $t$  coordinates; but in practice this may be achieved by spatial averaging alone on account of the finite speed of light.

### 6.2.1 Maxwell Postulates

Electromagnetic fields are governed by the physical principles encapsulated in the Maxwell postulates. From the macroscopic perspective, these are represented by the coupled differential equations [2]

$$\left. \begin{aligned} \nabla \times \underline{\tilde{E}}(\underline{r}, t) + \frac{\partial}{\partial t} \underline{\tilde{B}}(\underline{r}, t) &= \underline{0} \\ \nabla \times \underline{\tilde{B}}(\underline{r}, t) - \epsilon_0 \mu_0 \frac{\partial}{\partial t} \underline{\tilde{E}}(\underline{r}, t) &= \mu_0 \underline{\tilde{J}}(\underline{r}, t) \\ \nabla \cdot \underline{\tilde{E}}(\underline{r}, t) &= \frac{1}{\epsilon_0} \tilde{\rho}(\underline{r}, t) \\ \nabla \cdot \underline{\tilde{B}}(\underline{r}, t) &= 0 \end{aligned} \right\}. \quad (6.1)$$

Herein the macroscopic fields  $\underline{\tilde{E}}(\underline{r}, t)$  and  $\underline{\tilde{B}}(\underline{r}, t)$  are the spatial averages of microscopic electric and magnetic fields, respectively; the macroscopic charge and current densities  $\tilde{\rho}(\underline{r}, t)$  and  $\underline{\tilde{J}}(\underline{r}, t)$  are likewise related to their microscopic counterparts.

When considering materials, it is helpful to distinguish between free charges (which are externally impressed) and bound charges (which are generated by internal mechanisms). Accordingly, let us introduce the polarization  $\underline{\tilde{P}}(\underline{r}, t)$  and magnetization  $\underline{\tilde{M}}(\underline{r}, t)$  macroscopic fields to characterize the

bound source densities. These allow us to define externally impressed source densities as<sup>1</sup>

$$\left. \begin{aligned} \tilde{\rho}_e(\underline{r}, t) &= \tilde{\rho}(\underline{r}, t) + \nabla \cdot \tilde{\underline{P}}(\underline{r}, t) \\ \tilde{\underline{J}}_e(\underline{r}, t) &= \tilde{\underline{J}}(\underline{r}, t) - \frac{\partial}{\partial t} \tilde{\underline{P}}(\underline{r}, t) - \nabla \times \tilde{\underline{M}}(\underline{r}, t) \end{aligned} \right\}. \quad (6.2)$$

In addition, the notions of polarization and magnetization give rise to two more macroscopic fields:

$$\left. \begin{aligned} \tilde{\underline{D}}(\underline{r}, t) &= \epsilon_0 \tilde{\underline{E}}(\underline{r}, t) + \tilde{\underline{P}}(\underline{r}, t) \\ \tilde{\underline{H}}(\underline{r}, t) &= \frac{1}{\mu_0} \tilde{\underline{B}}(\underline{r}, t) - \tilde{\underline{M}}(\underline{r}, t) \end{aligned} \right\}. \quad (6.3)$$

The four macroscopic electromagnetic fields,  $\tilde{\underline{E}}(\underline{r}, t)$ ,  $\tilde{\underline{D}}(\underline{r}, t)$ ,  $\tilde{\underline{B}}(\underline{r}, t)$ , and  $\tilde{\underline{H}}(\underline{r}, t)$ , are piecewise differentiable vector functions of position  $\underline{r}$  and time  $t$ . The fields  $\tilde{\underline{E}}(\underline{r}, t)$  and  $\tilde{\underline{B}}(\underline{r}, t)$  are the *primitive* fields; these are directly measurable quantities which together generate the Lorentz force [2]

$$\tilde{\underline{F}}_{\text{Lor}}(\underline{r}, t) = q \left[ \tilde{\underline{E}}(\underline{r}, t) + \underline{v}(\underline{r}, t) \times \tilde{\underline{B}}(\underline{r}, t) \right] \quad (6.4)$$

acting on a point charge  $q$  (located at  $\underline{r}$ , at time  $t$ ) travelling at velocity  $\underline{v}(\underline{r}, t)$ . The fields  $\tilde{\underline{D}}(\underline{r}, t)$  and  $\tilde{\underline{H}}(\underline{r}, t)$  are the *induction* fields; these develop inside a material in response to the primitive fields. Somewhat confusingly, the primitive fields  $\tilde{\underline{E}}(\underline{r}, t)$  and  $\tilde{\underline{B}}(\underline{r}, t)$  are often called the electric field and magnetic induction, while the induction fields  $\tilde{\underline{D}}(\underline{r}, t)$  and  $\tilde{\underline{H}}(\underline{r}, t)$  are often called the dielectric displacement and magnetic field.

In terms of  $\tilde{\underline{E}}(\underline{r}, t)$ ,  $\tilde{\underline{D}}(\underline{r}, t)$ ,  $\tilde{\underline{B}}(\underline{r}, t)$ , and  $\tilde{\underline{H}}(\underline{r}, t)$ , the mathematical representation of the Maxwell postulates (6.1) is given as

$$\left. \begin{aligned} \nabla \times \tilde{\underline{H}}(\underline{r}, t) - \frac{\partial}{\partial t} \tilde{\underline{D}}(\underline{r}, t) &= \tilde{\underline{J}}_e(\underline{r}, t) \\ \nabla \times \tilde{\underline{E}}(\underline{r}, t) + \frac{\partial}{\partial t} \tilde{\underline{B}}(\underline{r}, t) &= -\tilde{\underline{J}}_m(\underline{r}, t) \\ \nabla \cdot \tilde{\underline{D}}(\underline{r}, t) &= \tilde{\rho}_e(\underline{r}, t) \\ \nabla \cdot \tilde{\underline{B}}(\underline{r}, t) &= \tilde{\rho}_m(\underline{r}, t) \end{aligned} \right\}. \quad (6.5)$$

---

<sup>1</sup>If we replace  $\tilde{\underline{P}}(\underline{r}, t)$  by  $\tilde{\underline{P}}(\underline{r}, t) - \nabla \times \tilde{\underline{A}}(\underline{r}, t)$  and  $\tilde{\underline{M}}(\underline{r}, t)$  by  $\tilde{\underline{M}}(\underline{r}, t) + (\partial/\partial t)\tilde{\underline{A}}(\underline{r}, t)$ , then Eqs. (6.2) would still be satisfied for any differentiable vector function  $\tilde{\underline{A}}(\underline{r}, t)$ . Therefore Eqs. (6.2) do not uniquely specify  $\tilde{\underline{P}}(\underline{r}, t)$  and  $\tilde{\underline{M}}(\underline{r}, t)$ . Indeed, as a consequence, the induction fields  $\tilde{\underline{D}}(\underline{r}, t)$  and  $\tilde{\underline{H}}(\underline{r}, t)$  are not uniquely specified either. However, this gauge freedom is eliminated by the establishment of constitutive relations [3].

Herein the magnetic current and magnetic charge densities  $\tilde{\mathbf{J}}_m(\underline{r}, t)$  and  $\tilde{\rho}_m(\underline{r}, t)$  do not represent physical quantities; they are added for the reasons of mathematical convenience [4]. The source terms on the right side of Eqs. (6.5) satisfy the continuity relations

$$\left. \begin{aligned} \nabla \cdot \tilde{\mathbf{J}}_e(\underline{r}, t) + \frac{\partial}{\partial t} \tilde{\rho}_e(\underline{r}, t) &= 0 \\ \nabla \cdot \tilde{\mathbf{J}}_m(\underline{r}, t) + \frac{\partial}{\partial t} \tilde{\rho}_m(\underline{r}, t) &= 0 \end{aligned} \right\}. \quad (6.6)$$

Observe that the Maxwell divergence postulates (6.5)<sub>3,4</sub> may be derived from the Maxwell curl postulates (6.5)<sub>1,2</sub> under the assumption of source continuity as represented by Eqs. (6.6).<sup>2</sup>

### 6.2.2 Constitutive Relations

In practice, it is the Maxwell curl postulates (6.5)<sub>1,2</sub> that are used to determine the fields inside materials. However, these provide a system of only two linear vector differential equations, whereas there are four vector fields to be determined, namely  $\tilde{\mathbf{E}}(\underline{r}, t)$ ,  $\tilde{\mathbf{B}}(\underline{r}, t)$ ,  $\tilde{\mathbf{D}}(\underline{r}, t)$ , and  $\tilde{\mathbf{H}}(\underline{r}, t)$ . Further information, linking the two primitive vector fields  $\underline{\mathbf{E}}(\underline{r}, t)$  and  $\underline{\mathbf{B}}(\underline{r}, t)$  to the two induction vector fields  $\tilde{\mathbf{D}}(\underline{r}, t)$  and  $\tilde{\mathbf{H}}(\underline{r}, t)$ , is needed to solve the differential equations (6.5)<sub>1,2</sub>. This further information is provided by the constitutive relations which characterize the electromagnetic response of a material. These may be written in the general form [5]

$$\left. \begin{aligned} \tilde{\mathbf{D}} &= \underline{\mathcal{F}} \{ \underline{\mathbf{E}}, \underline{\mathbf{B}} \} \\ \tilde{\mathbf{H}} &= \underline{\mathcal{G}} \{ \underline{\mathbf{E}}, \underline{\mathbf{B}} \} \end{aligned} \right\}, \quad (6.7)$$

where  $\underline{\mathcal{F}}$  and  $\underline{\mathcal{G}}$  are linear functions (possibly incorporating differential/integral operators) of  $\underline{\mathbf{E}}$  and  $\underline{\mathbf{B}}$  for linear materials and nonlinear functions (possibly incorporating differential/integral operators) of  $\underline{\mathbf{E}}$  and  $\underline{\mathbf{B}}$  for nonlinear materials. We shall return to the topic of nonlinear materials in Section 6.5, but for now we concentrate on linear materials.

In general, the induction fields for a material at a certain location  $\underline{r} = \underline{r}_0$  and time  $t = t_0$  depend not only on the primitive fields at  $\underline{r} = \underline{r}_0$  and  $t = t_0$  but also on the primitive fields in the vicinity of  $\underline{r} = \underline{r}_0$  and at times leading up to  $t = t_0$ . Thus, a general linear material is characterized by constitutive relations that are nonlocal with respect to both space and time per [6]

---

<sup>2</sup>The subscripts on (6.5)<sub>1,2</sub> signify the upper two equations in Eqs. (6.5), and the subscripts on (6.5)<sub>3,4</sub> signify the lower two equations in Eqs. (6.5).

$$\left. \begin{aligned} \tilde{\underline{D}}(\underline{r}, t) &= \int_{t'} \int_{\underline{r}'} \left[ \tilde{\epsilon}_{\text{EB}}(\underline{r}', t') \bullet \tilde{\underline{E}}(\underline{r} - \underline{r}', t - t') + \tilde{\xi}_{\text{EB}}(\underline{r}', t') \bullet \tilde{\underline{B}}(\underline{r} - \underline{r}', t - t') \right] d^3 \underline{r}' dt' \\ \tilde{\underline{H}}(\underline{r}, t) &= \int_{t'} \int_{\underline{r}'} \left[ \tilde{\zeta}_{\text{EB}}(\underline{r}', t') \bullet \tilde{\underline{E}}(\underline{r} - \underline{r}', t - t') + \tilde{\mu}^{-1}_{\text{EB}}(\underline{r}', t') \bullet \tilde{\underline{B}}(\underline{r} - \underline{r}', t - t') \right] d^3 \underline{r}' dt' \end{aligned} \right\}, \quad (6.8)$$

where  $\tilde{\epsilon}_{\text{EB}}(\underline{r}, t)$ ,  $\tilde{\xi}_{\text{EB}}(\underline{r}, t)$ ,  $\tilde{\zeta}_{\text{EB}}(\underline{r}, t)$ , and  $\tilde{\mu}^{-1}_{\text{EB}}(\underline{r}, t)$  are  $3 \times 3$  constitutive dyadics (i.e., second-rank Cartesian tensors). Conventionally,  $\tilde{\epsilon}_{\text{EB}}(\underline{r}, t)$  and  $\tilde{\mu}^{-1}_{\text{EB}}(\underline{r}, t)$  are called the permittivity and inverse permeability dyadics, while  $\tilde{\xi}_{\text{EB}}(\underline{r}, t)$  and  $\tilde{\zeta}_{\text{EB}}(\underline{r}, t)$  are called magnetoelectric dyadics.

If electromagnetic wavelengths are of the same order of magnitude as a characteristic length scale in the material, then spatial nonlocality can be an important phenomenon [7]. However, in many commonly encountered scenarios the effects of spatial nonlocality are negligible. On the other hand, temporal nonlocality often leads to readily observable effects in materials. Accordingly, henceforth we shall restrict our attention to spatially local, temporally nonlocal materials described by constitutive relations of the form

$$\left. \begin{aligned} \tilde{\underline{D}}(\underline{r}, t) &= \int_{t'} \left[ \tilde{\epsilon}_{\text{EB}}(\underline{r}, t') \bullet \tilde{\underline{E}}(\underline{r}, t - t') + \tilde{\xi}_{\text{EB}}(\underline{r}, t') \bullet \tilde{\underline{B}}(\underline{r}, t - t') \right] dt' \\ \tilde{\underline{H}}(\underline{r}, t) &= \int_{t'} \left[ \tilde{\zeta}_{\text{EB}}(\underline{r}, t') \bullet \tilde{\underline{E}}(\underline{r}, t - t') + \tilde{\mu}^{-1}_{\text{EB}}(\underline{r}, t') \bullet \tilde{\underline{B}}(\underline{r}, t - t') \right] dt' \end{aligned} \right\}. \quad (6.9)$$

### 6.2.3 Time/Frequency Domain

The constitutive relations (6.9) provide a *time-domain* description. While such a description is physically intuitive, the convolution integrals featuring in Eqs. (6.9) lead to considerable mathematical difficulties when combined with the Maxwell postulates. These difficulties can be bypassed by switching to the *frequency domain*. This involves taking the temporal Fourier transform of Eqs. (6.9); application of the convolution theorem [8] then delivers the frequency-domain constitutive relations as [9]

$$\left. \begin{aligned} \underline{D}(\underline{r}, \omega) &= \epsilon_{\text{EB}}(\underline{r}, \omega) \bullet \underline{E}(\underline{r}, \omega) + \xi_{\text{EB}}(\underline{r}, \omega) \bullet \underline{B}(\underline{r}, \omega) \\ \underline{H}(\underline{r}, \omega) &= \zeta_{\text{EB}}(\underline{r}, \omega) \bullet \underline{E}(\underline{r}, \omega) + \mu^{-1}_{\text{EB}}(\underline{r}, \omega) \bullet \underline{B}(\underline{r}, \omega) \end{aligned} \right\}, \quad (6.10)$$

with  $\omega$  being the angular frequency. The  $\omega$ -dependent terms

$$\begin{aligned} \mathcal{Z}(\underline{r}, \omega) &= \int_{-\infty}^{\infty} \tilde{\mathcal{Z}}(\underline{r}, t) \exp(i\omega t) dt, \\ \left( \mathcal{Z} \in \left\{ \frac{\epsilon}{\epsilon_{EB}}, \frac{\xi}{\epsilon_{EB}}, \frac{\zeta}{\epsilon_{EB}}, \frac{\mu^{-1}}{\epsilon_{EB}}, \underline{E}, \underline{D}, \underline{B}, \underline{H} \right\} \right), \end{aligned} \quad (6.11)$$

are the temporal Fourier transforms of the corresponding  $t$ -dependent terms. In the frequency domain, the Maxwell curl postulates are represented as

$$\begin{cases} \nabla \times \underline{H}(\underline{r}, \omega) + i\omega \underline{D}(\underline{r}, \omega) = \underline{J}_e(\underline{r}, \omega) \\ \nabla \times \underline{E}(\underline{r}, \omega) - i\omega \underline{B}(\underline{r}, \omega) = -\underline{J}_m(\underline{r}, \omega) \end{cases}, \quad (6.12)$$

where the source terms  $\underline{J}_{e,m}(\underline{r}, \omega)$  are the temporal Fourier transforms of  $\underline{J}_{e,m}(\underline{r}, t)$ , defined as in Eq. (6.11) with  $\mathcal{Z} = \underline{J}_{e,m}$ .

There is a price to be paid in terms of physical interpretation for the mathematical simplicity of Eqs. (6.10) as compared to Eqs. (6.9): the frequency-domain terms are complex valued in general, whereas the time-domain terms are real valued. The frequency-domain terms  $\underline{E}(\underline{r}, \omega)$ ,  $\underline{D}(\underline{r}, \omega)$ ,  $\underline{B}(\underline{r}, \omega)$ , and  $\underline{H}(\underline{r}, \omega)$  are called field *phasors*. Since the inverse temporal Fourier transform

$$\begin{aligned} \tilde{\mathcal{Z}}(\underline{r}, t) &= \frac{1}{2\pi} \int_{-\infty}^{\infty} \mathcal{Z}(\underline{r}, \omega) \exp(-i\omega t) d\omega, \\ \left( \mathcal{Z} \in \left\{ \frac{\epsilon}{\epsilon_{EB}}, \frac{\xi}{\epsilon_{EB}}, \frac{\zeta}{\epsilon_{EB}}, \frac{\mu^{-1}}{\epsilon_{EB}}, \underline{E}, \underline{D}, \underline{B}, \underline{H} \right\} \right), \end{aligned} \quad (6.13)$$

is required to be real valued, the symmetry

$$\mathcal{Z}^*(\underline{r}, \omega) = \mathcal{Z}(\underline{r}, -\omega) \quad (6.14)$$

relates  $\mathcal{Z}$  to its complex conjugate  $\mathcal{Z}^*$ ; and it therefore follows that

$$\begin{cases} \operatorname{Re} \{ \mathcal{Z}(\underline{r}, \omega) \} = \operatorname{Re} \{ \mathcal{Z}(\underline{r}, -\omega) \} \\ \operatorname{Im} \{ \mathcal{Z}(\underline{r}, \omega) \} = -\operatorname{Im} \{ \mathcal{Z}(\underline{r}, -\omega) \} \end{cases}, \quad (6.15)$$

where the operators  $\operatorname{Re} \{ \cdot \}$  and  $\operatorname{Im} \{ \cdot \}$  deliver real and imaginary parts, respectively.

In characterizing the electromagnetic properties of materials, it can be convenient to consider  $\underline{E}(\underline{r}, \omega)$  partnered with  $\underline{H}(\underline{r}, \omega)$  instead of  $\underline{B}(\underline{r}, \omega)$ . For example, boundary conditions and the time-averaged Poynting vector are formulated in terms of  $\underline{E}(\underline{r}, \omega)$

partnered with  $\underline{H}(\underline{r}, \omega)$ . Accordingly, it is desirable to express the constitutive relations (6.10) in the form

$$\left. \begin{aligned} \underline{D}(\underline{r}, \omega) &= \underline{\epsilon}_{\text{EH}}(\underline{r}, \omega) \bullet \underline{E}(\underline{r}, \omega) + \underline{\xi}_{\text{EH}}(\underline{r}, \omega) \bullet \underline{H}(\underline{r}, \omega) \\ \underline{B}(\underline{r}, \omega) &= \underline{\zeta}_{\text{EH}}(\underline{r}, \omega) \bullet \underline{E}(\underline{r}, \omega) + \underline{\mu}_{\text{EH}}(\underline{r}, \omega) \bullet \underline{H}(\underline{r}, \omega) \end{aligned} \right\}, \quad (6.16)$$

where

$$\left. \begin{aligned} \underline{\epsilon}_{\text{EH}}(\underline{r}, \omega) &= \underline{\epsilon}_{\text{EB}}(\underline{r}, \omega) - \underline{\xi}_{\text{EB}}(\underline{r}, \omega) \bullet \underline{\mu}_{\text{EB}}(\underline{r}, \omega) \bullet \underline{\zeta}_{\text{EB}}(\underline{r}, \omega) \\ \underline{\xi}_{\text{EH}}(\underline{r}, \omega) &= \underline{\xi}_{\text{EB}}(\underline{r}, \omega) \bullet \underline{\mu}_{\text{EB}}(\underline{r}, \omega) \\ \underline{\zeta}_{\text{EH}}(\underline{r}, \omega) &= -\underline{\mu}_{\text{EB}}(\underline{r}, \omega) \bullet \underline{\zeta}_{\text{EB}}(\underline{r}, \omega) \\ \underline{\mu}_{\text{EH}}(\underline{r}, \omega) &= \underline{\mu}_{\text{EB}}(\underline{r}, \omega) \end{aligned} \right\}. \quad (6.17)$$

The constitutive relations (6.10) are sometimes called the *Boys–Post* constitutive relations, while the constitutive relations (6.16) are sometimes called the *Tellegen* constitutive relations [10]. The subscripts “EB” signify Boys–Post constitutive dyadics, while the subscripts “EH” signify Tellegen constitutive dyadics.

A note of caution should be added here: in writing down Eqs. (6.17) we have assumed  $\underline{\mu}_{\text{EB}}^{-1}(\underline{r}, \omega)$  to be invertible. While this is nearly always the case, instances of singular constitutive dyadics can arise—see Section 6.4 for examples.

## 6.3 CONSTITUTIVE DYADICS

In the most general linear scenario, spatially local materials are specified in the frequency domain by the four constitutive dyadics  $\underline{\epsilon}_{\text{EH}}(\underline{r}, \omega)$ ,  $\underline{\zeta}_{\text{EH}}(\underline{r}, \omega)$ ,  $\underline{\xi}_{\text{EH}}(\underline{r}, \omega)$ , and  $\underline{\mu}_{\text{EH}}(\underline{r}, \omega)$  (or equivalently,  $\underline{\epsilon}_{\text{EB}}(\underline{r}, \omega)$ ,  $\underline{\zeta}_{\text{EB}}(\underline{r}, \omega)$ ,  $\underline{\xi}_{\text{EB}}(\underline{r}, \omega)$ , and  $\underline{\mu}_{\text{EB}}(\underline{r}, \omega)$ ). In other words, up to 36 complex-valued parameters are needed to specify such a material. There are however certain constraints on these parameters and important specializations that reduce the number of independent parameters needed.

### 6.3.1 Constraints

**6.3.1.1 Causality** The principle of causality—namely, that “effect” cannot precede “cause”—must be adhered to by all real materials [11, 12]. In terms of

the time-domain constitutive relations (6.9), this principle is represented by the constraints

$$\left. \begin{array}{l} \tilde{\epsilon}_{\text{EB}}(\underline{r}, t) - \epsilon_0 \delta(t) \underline{I} \equiv 0 \\ \tilde{\xi}_{\text{EB}}(\underline{r}, t) \equiv 0 \\ \tilde{\zeta}_{\text{EB}}(\underline{r}, t) \equiv 0 \\ \mu_0^{-1} \delta(t) \underline{I} - \tilde{\mu}^{-1}(\underline{r}, t) \equiv 0 \end{array} \right\} \quad \text{for } t \leq 0, \quad (6.18)$$

wherein  $\delta(\cdot)$  denotes the Dirac delta function and  $\underline{I}$  is the identity  $3 \times 3$  dyadic. These constraints result in integral relations between the real and imaginary parts of the frequency-dependent constitutive parameters, as follows.

Let the scalar function  $\tilde{f}(\underline{r}, t)$  be an arbitrary component of  $\tilde{\epsilon}_{\text{EB}}(\underline{r}, t) - \epsilon_0 \delta(t) \underline{I}$ ,  $\tilde{\xi}_{\text{EB}}(\underline{r}, t)$ ,  $\tilde{\zeta}_{\text{EB}}(\underline{r}, t)$ , or  $\mu_0^{-1} \delta(t) \underline{I} - \tilde{\mu}^{-1}(\underline{r}, t)$ . Then, in light of the causality constraint (6.18), the temporal Fourier transform of  $\tilde{f}(\underline{r}, t)$  may be written as

$$f(\underline{r}, \omega) = \int_0^\infty \tilde{f}(\underline{r}, t) \exp(i\omega t) dt. \quad (6.19)$$

The Cauchy integral formula delivers the analytic continuation of  $f(\underline{r}, \omega)$  into the upper complex- $\omega$  plane per

$$f(\underline{r}, \omega) = \frac{1}{2\pi i} \oint \frac{f(\underline{r}, s)}{s - \omega} ds, \quad (6.20)$$

wherein the integration paths lie in the upper half of the complex plane, as illustrated in Figure 6.1. In the limit  $|s| \rightarrow \infty$ , the integrand in Eq. (6.20) vanishes, due to the  $\exp(i\omega t)$  term introduced by the integral representation (6.19). The contour integral in Eq. (6.20) therefore simplifies to an integral along the real axis. As the single pole on the real axis at  $s = \omega$  contributes a half-residue to the integration, we find

$$f(\underline{r}, \omega) = \frac{1}{\pi i} \mathcal{P} \int_{-\infty}^{\infty} \frac{f(\underline{r}, s)}{s - \omega} ds, \quad (6.21)$$

with  $\mathcal{P}$  denoting the Cauchy principal value. Taking real and imaginary parts, the Hilbert transforms emerge as

$$\left. \begin{array}{l} \text{Re } \{f(\underline{r}, \omega)\} = \frac{1}{\pi} \mathcal{P} \int_{-\infty}^{\infty} \frac{\text{Im } \{f(\underline{r}, s)\}}{s - \omega} ds \\ \text{Im } \{f(\underline{r}, \omega)\} = -\frac{1}{\pi} \mathcal{P} \int_{-\infty}^{\infty} \frac{\text{Re } \{f(\underline{r}, s)\}}{s - \omega} ds \end{array} \right\}. \quad (6.22)$$

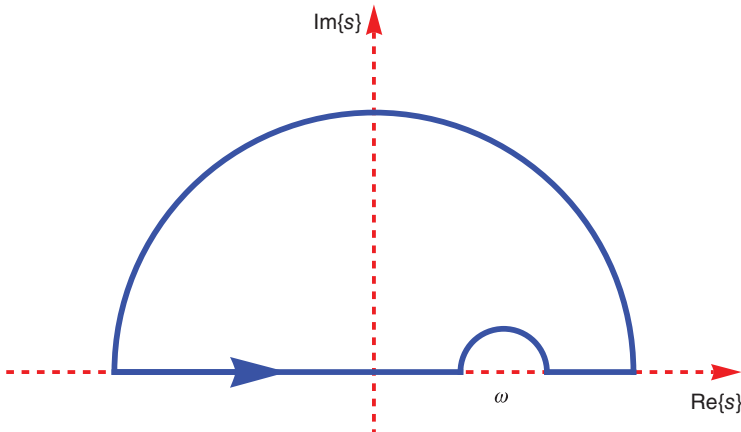


**FIGURE 6.1** An integration path for the right side of Eq. (6.20).

By exploiting the symmetry condition (cf. Eq. (6.14))

$$f(\underline{r}, -\omega) = f^*(\underline{r}, \omega), \quad (6.23)$$

which relates  $f$  to its complex conjugate  $f^*$ , Eqs. (6.22) may be expressed in terms of integrations over positive-valued angular frequency as

$$\left. \begin{aligned} \text{Re } \{f(\underline{r}, \omega)\} &= \frac{2}{\pi} P \int_0^\infty \frac{s \text{Im } \{f(\underline{r}, s)\}}{s^2 - \omega^2} ds \\ \text{Im } \{f(\underline{r}, \omega)\} &= -\frac{2}{\pi} P \int_0^\infty \frac{\omega \text{Re } \{f(\underline{r}, s)\}}{s^2 - \omega^2} ds \end{aligned} \right\}. \quad (6.24)$$

These relations (6.24) are called the Kramers–Kronig relations [13]. While the Kramers–Kronig relations are fundamentally important in the electromagnetic theory of materials, they are also utilized in practical applications such as in experimental determinations of constitutive parameters [14, 15].

The presentation in this section delivered the Kramers–Kronig relations (6.24) for components of the Boys–Post constitutive dyadics. Analogous relations for components of the Tellegen constitutive dyadics may be delivered by implementing the transformations (6.17).

**6.3.1.2 Onsager Relations** The Onsager relations apply to coupled linear phenomena at macroscopic length scales [16–18], but they are derived from the assumption of microscopic reversibility [19]. Since microscopic processes cannot occur in vacuum, the electromagnetic properties of vacuum must first be factored out before applying the Onsager relations to materials. This can be done neatly by means of the frequency-dependent polarization and magnetization vectors  $\underline{P}(\underline{r}, \omega)$  and

$\underline{M}(\underline{r}, \omega)$ , which are the temporal Fourier transforms of  $\tilde{P}(\underline{r}, t)$  and  $\tilde{M}(\underline{r}, t)$  introduced in Eqs. (6.2); these deliver the electromagnetic response of a material relative to the electromagnetic response of free space. In the case of linear homogeneous materials characterized by the Boys–Post constitutive relations (6.10), we have

$$\left. \begin{aligned} \underline{P}(\underline{r}, \omega) &= \left[ \underline{\epsilon}_{\text{EB}}(\omega) - \epsilon_0 \underline{I} \right] \bullet \underline{E}(\underline{r}, \omega) + \underline{\xi}_{\text{EB}}(\omega) \bullet \underline{B}(\underline{r}, \omega) \\ \underline{M}(\underline{r}, \omega) &= -\underline{\zeta}_{\text{EB}}(\omega) \bullet \underline{E}(\underline{r}, \omega) + \left[ \frac{1}{\mu_0} \underline{I} - \underline{\mu}^{-1}(\omega) \right] \bullet \underline{B}(\underline{r}, \omega) \end{aligned} \right\}. \quad (6.25)$$

Suppose now that the material characterized by the constitutive relations (6.25) is subjected to a spatially uniform, magnetostatic field  $\underline{B}_{\text{dc}}$ . The Onsager relations impose the constraints [20]

$$\left. \begin{aligned} \underline{\epsilon}_{\text{EB}}(\omega) \Big|_{\underline{B}_{\text{dc}}} &= \underline{\epsilon}_{\text{EB}}^T(\omega) \Big|_{-\underline{B}_{\text{dc}}} \\ \underline{\xi}_{\text{EB}}(\omega) \Big|_{\underline{B}_{\text{dc}}} &= \underline{\zeta}_{\text{EB}}^T(\omega) \Big|_{-\underline{B}_{\text{dc}}} \\ \underline{\mu}^{-1}(\omega) \Big|_{\underline{B}_{\text{dc}}} &= \left( \underline{\mu}^{-1} \right)_{\text{EB}}^T(\omega) \Big|_{-\underline{B}_{\text{dc}}} \end{aligned} \right\} \quad (6.26)$$

on the Boys–Post constitutive dyadics. Equivalently, the Tellegen constitutive dyadics are constrained as

$$\left. \begin{aligned} \underline{\epsilon}_{\text{EH}}(\omega) \Big|_{\underline{B}_{\text{dc}}} &= \underline{\epsilon}_{\text{EH}}^T(\omega) \Big|_{-\underline{B}_{\text{dc}}} \\ \underline{\xi}_{\text{EH}}(\omega) \Big|_{\underline{B}_{\text{dc}}} &= -\underline{\zeta}_{\text{EH}}^T(\omega) \Big|_{-\underline{B}_{\text{dc}}} \\ \underline{\mu}_{\text{EH}}(\omega) \Big|_{\underline{B}_{\text{dc}}} &= \underline{\mu}_{\text{EH}}^T(\omega) \Big|_{-\underline{B}_{\text{dc}}} \end{aligned} \right\}. \quad (6.27)$$

**6.3.1.3 Post Constraint** The Post constraint relates to linear materials which exhibit magnetoelectric coupling [13]. It is expressed mathematically as

$$\text{tr} \left[ \underline{\zeta}_{\text{EB}}(\underline{r}, \omega) - \underline{\xi}_{\text{EB}}(\underline{r}, \omega) \right] = 0 \quad (6.28)$$

for materials characterized by the Boys–Post constitutive relations (6.10) or as

$$\text{tr} \left\{ \underline{\mu}_{\text{EH}}^{-1}(\underline{r}, \omega) \bullet \left[ \underline{\zeta}_{\text{EH}}(\underline{r}, \omega) + \underline{\xi}_{\text{EH}}(\underline{r}, \omega) \right] \right\} = 0 \quad (6.29)$$

for materials characterized by the Tellegen constitutive relations (6.16). By invoking the Post constraint, the number of independent complex-valued constitutive parameters needed to specify the most general linear material reduces from 36 to 35.

There are several routes to the Post constraint, for example, via the Lorentz covariance of the Maxwell equations [13, 21], a uniqueness requirement [22, 23], and multipole considerations [24]. However, experimental evidence of violation of the Post constraint at low frequencies has been reported [25]. The theoretical predictions and experimental observations have yet to be reconciled [26].

### 6.3.2 Specializations

**6.3.2.1 Lorentz Reciprocity** Suppose that  $\underline{J}_e^p(\underline{r}, \omega)$  and  $\underline{J}_e^q(\underline{r}, \omega)$  represent two frequency-domain electric source current densities, whereas  $\underline{J}_m^p(\underline{r}, \omega)$  and  $\underline{J}_m^q(\underline{r}, \omega)$  represent two frequency-domain magnetic source current densities. The fields  $\underline{E}^p(\underline{r}, \omega)$  and  $\underline{H}^p(\underline{r}, \omega)$  are generated by the sources labelled “p,” while the fields  $\underline{E}^q(\underline{r}, \omega)$  and  $\underline{H}^q(\underline{r}, \omega)$  are generated by the sources labelled “q.” The *reaction* [9, 27]

$$\langle\langle p, q \rangle\rangle = \int_{V_p} [\underline{J}_e^p(\underline{r}, \omega) \cdot \underline{E}^q(\underline{r}, \omega) - \underline{J}_m^p(\underline{r}, \omega) \cdot \underline{H}^q(\underline{r}, \omega)] d^3 r \quad (6.30)$$

characterizes the interaction of the “p” sources with the fields generated by the “q” sources; herein, the integration region  $V_p$  contains the “p” sources. In a similar fashion, the interaction of the “q” sources with the field generated by the “p” sources is characterized by the reaction  $\langle\langle q, p \rangle\rangle$ . The material which supports  $\underline{J}_{e,m}^{p,q}(\underline{r}, \omega)$ ,  $\underline{E}^{p,q}(\underline{r}, \omega)$ , and  $\underline{H}^{p,q}(\underline{r}, \omega)$  is called Lorentz reciprocal provided that the reaction of the “p” fields on the “q” sources is the same as the reaction of the “q” fields on the “p” sources, that is, Lorentz reciprocity is signalled by

$$\langle\langle p, q \rangle\rangle = \langle\langle q, p \rangle\rangle. \quad (6.31)$$

The reaction difference  $\langle\langle p, q \rangle\rangle - \langle\langle q, p \rangle\rangle$  may be calculated by integrating the Maxwell curl postulates (6.12) in conjunction with the Tellegen constitutive relations (6.16). Thus, we find

$$\begin{aligned} \langle\langle p, q \rangle\rangle - \langle\langle q, p \rangle\rangle &= -i\omega \int_{V_p \cup V_q} \left\{ \underline{E}^q(\underline{r}, \omega) \cdot \left[ \underline{\epsilon}_{EH}(\underline{r}, \omega) - \underline{\epsilon}_{EH}^T(\underline{r}, \omega) \right] \cdot \underline{E}^p(\underline{r}, \omega) \right. \\ &\quad + \underline{H}^p(\underline{r}, \omega) \cdot \left[ \underline{\mu}_{EH}(\underline{r}, \omega) - \underline{\mu}_{EH}^T(\underline{r}, \omega) \right] \cdot \underline{H}^q(\underline{r}, \omega) \\ &\quad + \underline{E}^q(\underline{r}, \omega) \cdot \left[ \underline{\xi}_{EH}(\underline{r}, \omega) + \underline{\xi}_{EH}^T(\underline{r}, \omega) \right] \cdot \underline{H}^p(\underline{r}, \omega) \\ &\quad \left. + \underline{H}^p(\underline{r}, \omega) \cdot \left[ \underline{\xi}_{EH}(\underline{r}, \omega) + \underline{\xi}_{EH}^T(\underline{r}, \omega) \right] \cdot \underline{E}^q(\underline{r}, \omega) \right\} d^3 r, \end{aligned} \quad (6.32)$$

wherein both the “p” and the “q” sources lie within the integration domain  $V_p \cup V_q$ . Accordingly, we see that the Tellegen constitutive dyadics of Lorentz–reciprocal materials satisfy the relations [28]

$$\left. \begin{aligned} \underline{\underline{\epsilon}}_{EH}(\underline{r}, \omega) &= \underline{\underline{\epsilon}}_{EH}^T(\underline{r}, \omega) \\ \underline{\underline{\xi}}_{EH}(\underline{r}, \omega) &= -\underline{\underline{\zeta}}_{EH}^T(\underline{r}, \omega) \\ \underline{\underline{\mu}}_{EH}(\underline{r}, \omega) &= \underline{\underline{\mu}}_{EH}^T(\underline{r}, \omega) \end{aligned} \right\}. \quad (6.33)$$

The corresponding relations for the Boys–Post constitutive dyadics are

$$\left. \begin{aligned} \underline{\underline{\epsilon}}_{EB}(\underline{r}, \omega) &= \underline{\underline{\epsilon}}_{EB}^T(\underline{r}, \omega) \\ \underline{\underline{\xi}}_{EB}(\underline{r}, \omega) &= \underline{\underline{\zeta}}_{EB}^T(\underline{r}, \omega) \\ \underline{\underline{\mu}}_{EB}^{-1}(\underline{r}, \omega) &= (\underline{\underline{\mu}}_{EB}^{-1})^T(\underline{r}, \omega) \end{aligned} \right\}. \quad (6.34)$$

Clearly, in the absence of a magnetostatic field, the Lorentz–reciprocity conditions (6.33) and (6.34) are the same as the Onsager relations (6.26) and (6.27).

**6.3.2.2 Dissipative, Nondissipative, and Active Materials** In accordance with the principle of causality, passive materials cannot respond instantaneously to an applied electromagnetic field [29, 30].<sup>3</sup> Dissipation is therefore unavoidable in all passive materials. However, for certain materials, it may well be the case that dissipation is tiny over length scales of interest, within a narrow frequency range at least; under these circumstances such materials may be regarded as nondissipative.

In order to pursue this matter, let us introduce the notion of monochromatic fields. A monochromatic field, which oscillates at an angular frequency  $\omega$ , may be represented by the vector

$$\tilde{\underline{\mathcal{Z}}}_{mono}(\underline{r}, t) = \operatorname{Re} \{ \check{\underline{\mathcal{Z}}}(\underline{r}, \omega) \exp(-i\omega t) \}, \quad (\mathcal{Z} \in \{E, B, D, H\}), \quad (6.35)$$

with the amplitude  $\check{\underline{\mathcal{Z}}}(\underline{r}, \omega) \in \mathbb{C}^3$  in general. The energy flow (i.e., energy per unit area per unit time), averaged over the time period  $2\pi/\omega$ , associated with such a

---

<sup>3</sup>Since it is not a material, free space is excluded from our consideration here.

monochromatic field is provided by the time-averaged Poynting vector for monochromatic fields, namely [29]<sup>4</sup>

$$\langle \check{S}(\underline{r}, \omega) \rangle_t = \frac{1}{2} \operatorname{Re} \left\{ \check{E}(\underline{r}, \omega) \times \check{H}^*(\underline{r}, \omega) \right\}. \quad (6.36)$$

It is the divergence of  $\langle \check{S}(\underline{r}, \omega) \rangle_t$  that is used to establish whether dissipation occurs within a material. By first combining the source-free versions of the Maxwell curl postulates (6.12) and the Tellegen constitutive relations (6.16) to calculate  $\langle \check{S}(\underline{r}, \omega) \rangle_t$ , and then taking the divergence, we find [9]

$$\nabla \bullet \langle \check{S}(\underline{r}, \omega) \rangle_t = \frac{\omega}{4} \left[ \check{E}(\underline{r}, \omega) \check{H}(\underline{r}, \omega) \right]^* \bullet \underline{\underline{m}}(\underline{r}, \omega) \bullet \begin{bmatrix} \check{E}(\underline{r}, \omega) \\ \check{H}(\underline{r}, \omega) \end{bmatrix}, \quad (6.37)$$

wherein the  $6 \times 6$  Hermitian dyadic

$$\underline{\underline{m}}(\underline{r}, \omega) = i \begin{bmatrix} \underline{\underline{\epsilon}}_{EH}(\underline{r}, \omega) - \underline{\underline{\epsilon}}_{EH}^\dagger(\underline{r}, \omega) & \underline{\underline{\xi}}_{EH}(\underline{r}, \omega) - \underline{\underline{\xi}}_{EH}^\dagger(\underline{r}, \omega) \\ \underline{\underline{\zeta}}_{EH}(\underline{r}, \omega) - \underline{\underline{\xi}}_{EH}^\dagger(\underline{r}, \omega) & \underline{\underline{\mu}}_{EH}(\underline{r}, \omega) - \underline{\underline{\mu}}_{EH}^\dagger(\underline{r}, \omega) \end{bmatrix} \quad (6.38)$$

has been introduced, with the superscript  $\dagger$  indicating the conjugate transpose.

Thus, the following three material specializations arise:

- (i) A nondissipative material is characterized by  $\nabla \bullet \langle \check{S}(\underline{r}, \omega) \rangle_t = 0$ . That is, the Tellegen constitutive dyadics for a nondissipative material are required to conform to [29]

$$\left. \begin{array}{l} \underline{\underline{\epsilon}}_{EH}(\underline{r}, \omega) = \underline{\underline{\epsilon}}_{EH}^\dagger(\underline{r}, \omega) \\ \underline{\underline{\xi}}_{EH}(\underline{r}, \omega) = \underline{\underline{\xi}}_{EH}^\dagger(\underline{r}, \omega) \\ \underline{\underline{\mu}}_{EH}(\underline{r}, \omega) = \underline{\underline{\mu}}_{EH}^\dagger(\underline{r}, \omega) \end{array} \right\}, \quad (6.39)$$

---

<sup>4</sup>Parenthetically, the definition of the *Abraham* momentum density for monochromatic fields is the same as that for the time-averaged Poynting vector provided in Eq. (6.36), except for a scalar multiplicative factor. However, the Abraham momentum density is defined differently from the *Minkowski* momentum density; the physical interpretation of these momentum densities is a controversial issue [31].

or, equivalently in terms of Boys–Post constitutive dyadics,

$$\left. \begin{aligned} \underline{\underline{\epsilon}}_{\text{EB}}(\underline{r}, \omega) &= \underline{\underline{\epsilon}}_{\text{EB}}^\dagger(\underline{r}, \omega) \\ \underline{\underline{\xi}}_{\text{EB}}(\underline{r}, \omega) &= -\underline{\underline{\zeta}}_{\text{EB}}^\dagger(\underline{r}, \omega) \\ \underline{\underline{\mu}}_{\text{EB}}^{-1}(\underline{r}, \omega) &= \left( \underline{\underline{\mu}}_{\text{EB}}^{-1} \right)^\dagger(\underline{r}, \omega) \end{aligned} \right\}. \quad (6.40)$$

- (ii) A dissipative material is characterized by  $\nabla \cdot \langle \underline{\underline{S}}(\underline{r}, \omega) \rangle_t < 0$ . The dyadic  $\underline{\underline{m}}(\underline{r}, \omega)$  must be negative definite in order to satisfy this inequality. It follows that a material is dissipative if and only if the two  $3 \times 3$  dyadics [32]

$$\left. \begin{aligned} \underline{\underline{m}}_1(\underline{r}, \omega) &= i \left[ \underline{\underline{\epsilon}}_{\text{EH}}(\underline{r}, \omega) - \underline{\underline{\epsilon}}_{\text{EH}}^\dagger(\underline{r}, \omega) \right] \\ \underline{\underline{m}}_2(\underline{r}, \omega) &= i \left\{ \underline{\underline{\mu}}_{\text{EH}}(\underline{r}, \omega) - \underline{\underline{\mu}}_{\text{EH}}^\dagger(\underline{r}, \omega) \right. \\ &\quad \left. - \left[ \underline{\underline{\zeta}}_{\text{EH}}(\underline{r}, \omega) - \underline{\underline{\xi}}_{\text{EH}}^\dagger(\underline{r}, \omega) \right] \bullet \underline{\underline{m}}_1(\underline{r}, \omega) \bullet \left[ \underline{\underline{\xi}}_{\text{EH}}(\underline{r}, \omega) - \underline{\underline{\zeta}}_{\text{EH}}^\dagger(\underline{r}, \omega) \right] \right\} \end{aligned} \right\}, \quad (6.41)$$

expressed in terms of Tellegen constitutive dyadics, are negative definite. Equivalently, a material is dissipative if and only if the two  $3 \times 3$  dyadics [32]

$$\left. \begin{aligned} \underline{\underline{m}}_3(\underline{r}, \omega) &= i \left[ \underline{\underline{\mu}}_{\text{EH}}(\underline{r}, \omega) - \underline{\underline{\mu}}_{\text{EH}}^\dagger(\underline{r}, \omega) \right] \\ \underline{\underline{m}}_4(\underline{r}, \omega) &= i \left\{ \underline{\underline{\epsilon}}_{\text{EH}}(\underline{r}, \omega) - \underline{\underline{\epsilon}}_{\text{EH}}^\dagger(\underline{r}, \omega) \right. \\ &\quad \left. - \left[ \underline{\underline{\xi}}_{\text{EH}}(\underline{r}, \omega) - \underline{\underline{\zeta}}_{\text{EH}}^\dagger(\underline{r}, \omega) \right] \bullet \underline{\underline{m}}_3(\underline{r}, \omega) \bullet \left[ \underline{\underline{\zeta}}_{\text{EH}}(\underline{r}, \omega) - \underline{\underline{\xi}}_{\text{EH}}^\dagger(\underline{r}, \omega) \right] \right\} \end{aligned} \right\} \quad (6.42)$$

are negative definite.

- (iii) An active material is one that is neither dissipative nor nondissipative, that is, it is characterized by  $\nabla \cdot \langle \underline{\underline{S}}(\underline{r}, \omega) \rangle_t > 0$ .

## 6.4 LINEAR MATERIALS

In this section we survey the commonly encountered classifications (and subclassifications) of linear materials. The constitutive dyadics determine these classifications. Tellegen constitutive dyadics will be used to represent the classifications, on the understanding that the corresponding representations in terms of Boys–Post constitutive dyadics may be readily achieved via Eqs. (6.17). We will largely focus on

homogeneous materials—the constitutive dyadics for these are independent of the space coordinate  $\underline{r}$ —but some notable examples of nonhomogeneous materials are also presented.

### 6.4.1 Isotropic Materials

**6.4.1.1 Dielectric–Magnetic Materials** Mathematically at least, the simplest homogeneous materials are isotropic dielectric–magnetic materials. Their frequency-domain Tellegen constitutive relations

$$\left. \begin{aligned} \underline{D}(\underline{r}, \omega) &= \epsilon(\omega) \underline{E}(\underline{r}, \omega) \\ \underline{B}(\underline{r}, \omega) &= \mu(\omega) \underline{H}(\underline{r}, \omega) \end{aligned} \right\} \quad (6.43)$$

are given in terms of the scalar permittivity  $\epsilon(\omega)$  and scalar permeability  $\mu(\omega)$ . Thus, the field phasors  $\underline{D}$ ,  $\underline{E}$ ,  $\underline{B}$ , and  $\underline{H}$  are parallel for such a material. In the case of a dissipative material, both  $\epsilon$  and  $\mu$  are  $\omega$  dependent and complex valued. Furthermore, as a consequence of the sign convention for the exponent of the temporal Fourier transform kernel in Eq. (6.11), we have that  $\text{Im}\{\epsilon(\omega)\} > 0$  and  $\text{Im}\{\mu(\omega)\} > 0$  for dissipative materials. In the case of an isotropic dielectric material, we have  $\mu(\omega) = \mu_0$ , while in the case of an isotropic magnetic material, we have  $\epsilon(\omega) = \epsilon_0$ . Note that the category of isotropic dielectric materials includes crystals belonging to the cubic crystal system.

There are subtleties lurking in the electromagnetic properties of isotropic dielectric–magnetic materials, despite the mathematical simplicity of their constitutive relations. For example, such a material can support the propagation of uniform plane waves with negative phase velocity—which is a property intimately related to that of negative refraction and one which has been the focus of intense research activity for the past 12 years [33]—provided that the condition [34]

$$\frac{\text{Re}\{\epsilon(\omega)\}}{\text{Im}\{\epsilon(\omega)\}} + \frac{\text{Re}\{\mu(\omega)\}}{\text{Im}\{\mu(\omega)\}} < 0 \quad (6.44)$$

is satisfied at a given angular frequency  $\omega$ .

**6.4.1.2 Isotropic Chiral Materials** By introducing magnetoelectric coupling, more general isotropic materials may be realized. An isotropic chiral material is characterized by the frequency-domain Tellegen constitutive relations [35]

$$\left. \begin{aligned} \underline{D}(\underline{r}, \omega) &= \epsilon(\omega) \underline{E}(\underline{r}, \omega) + \chi(\omega) \underline{H}(\underline{r}, \omega) \\ \underline{B}(\underline{r}, \omega) &= -\chi(\omega) \underline{E}(\underline{r}, \omega) + \mu(\omega) \underline{H}(\underline{r}, \omega) \end{aligned} \right\}. \quad (6.45)$$

Thus, three complex-valued,  $\omega$ -dependent scalars specify such a material: permittivity  $\epsilon$ , permeability  $\mu$ , and the chirality parameter  $\chi$ . The mirror conjugate of the material

characterized by Eqs. (6.45) is characterized by the same constitutive relations and parameters but with  $\chi$  replaced by  $-\chi$ .

Most notably, isotropic chiral materials can distinguish between left-handed and right-handed electromagnetic fields; that is, they exhibit optical activity [36]. However, an equally-proportioned mixture of an isotropic chiral medium and its mirror conjugate does not exhibit optical activity (assuming that no chemical reactions or molecular conformational changes occur); such a mixture—which is known as a *racemic* mixture—is an isotropic dielectric–magnetic material, as specified by the constitutive relations (6.43).

Isotropic chiral materials are Lorentz reciprocal, per the account of Lorentz reciprocity presented in Section 6.3. An isotropic material which is non-Lorentz reciprocal is characterized by the Tellegen constitutive relations

$$\left. \begin{aligned} \underline{D}(\underline{r}, \omega) &= \epsilon(\omega) \underline{E}(\underline{r}, \omega) + \chi_1(\omega) \underline{H}(\underline{r}, \omega) \\ \underline{B}(\underline{r}, \omega) &= \chi_2(\omega) \underline{E}(\underline{r}, \omega) + \mu(\omega) \underline{H}(\underline{r}, \omega) \end{aligned} \right\}, \quad (6.46)$$

with  $\chi_1(\omega) \neq -\chi_2(\omega)$ . Such a material is called a biisotropic material. However, the existence of biisotropic materials is at odds with the Post constraint and is therefore controversial.

#### 6.4.2 Anisotropic Materials

By definition, in anisotropic materials the primitive field phasor  $\underline{E}$  is not aligned with the induction field phasor  $\underline{D}$  and/or the primitive field phasor  $\underline{B}$  is not aligned with the induction field phasor  $\underline{H}$ . Accordingly  $3 \times 3$  dyadics are needed to specify the constitutive properties of anisotropic materials. Manifestations of dielectric anisotropy are widely encountered in crystal optics, while the magnetic properties of many diamagnetic and paramagnetic materials are significantly anisotropic.

**6.4.2.1 Uniaxial Materials** Uniaxial materials are characterized by a single distinguished axis at macroscopic length scales. The crystalline structure or some other underlying microscopic structure (e.g., deriving from the orientation of electromagnetically small component particles) may give rise to the distinguished axis. Suppose that this distinguished axis is aligned with the unit vector  $\hat{\underline{u}}$ .

A uniaxial homogeneous dielectric material is characterized by the frequency-domain Tellegen constitutive relations [29]

$$\left. \begin{aligned} \underline{D}(\underline{r}, \omega) &= \underline{\epsilon}_{\text{uni}}(\omega) \bullet \underline{E}(\underline{r}, \omega) \\ \underline{B}(\underline{r}, \omega) &= \mu_0 \underline{H}(\underline{r}, \omega) \end{aligned} \right\}, \quad (6.47)$$

wherein the  $\omega$ -dependent permittivity dyadic

$$\underline{\epsilon}_{\text{uni}}(\omega) = \epsilon(\omega) \left( \underline{\underline{I}} - \hat{\underline{u}} \hat{\underline{u}} \right) + \epsilon_u(\omega) \hat{\underline{u}} \hat{\underline{u}}. \quad (6.48)$$

The permittivity scalars  $\epsilon(\omega)$ ,  $\epsilon_u(\omega) \in \mathbb{C}$ , while for a dissipative material  $\text{Im}\{\epsilon(\omega)\} > 0$  and  $\text{Im}\{\epsilon_u(\omega)\} > 0$  per the principle of causality. Let us note that uniaxial dielectric materials include crystals belonging to the hexagonal, tetragonal, and trigonal crystal systems.

In an analogous fashion, the Tellegen constitutive relations

$$\left. \begin{aligned} \underline{D}(\underline{r}, \omega) &= \epsilon_0 \underline{E}(\underline{r}, \omega) \\ \underline{B}(\underline{r}, \omega) &= \underline{\mu}_{\text{uni}}(\omega) \bullet \underline{H}(\underline{r}, \omega) \end{aligned} \right\} \quad (6.49)$$

characterize a uniaxial homogeneous magnetic material. The permeability constitutive dyadic has the form

$$\underline{\mu}_{\text{uni}}(\omega) = \mu(\omega) \left( \underline{\underline{I}} - \hat{\underline{u}} \hat{\underline{u}} \right) + \mu_u(\omega) \hat{\underline{u}} \hat{\underline{u}}, \quad (6.50)$$

with the  $\omega$ -dependent parameters  $\mu$  and  $\mu_u$  being located in the upper half of the complex plane for dissipative materials.

The effective union of Eqs. (6.47) and (6.49), namely

$$\left. \begin{aligned} \underline{D}(\underline{r}, \omega) &= \underline{\epsilon}_{\text{uni}}(\omega) \bullet \underline{E}(\underline{r}, \omega) \\ \underline{B}(\underline{r}, \omega) &= \underline{\mu}_{\text{uni}}(\omega) \bullet \underline{H}(\underline{r}, \omega) \end{aligned} \right\}, \quad (6.51)$$

characterizes a uniaxial dielectric–magnetic material.

**6.4.2.2 Biaxial Materials** Generalizing Eq. (6.47), the Tellegen constitutive relations [37]

$$\left. \begin{aligned} \underline{D}(\underline{r}, \omega) &= \underline{\epsilon}_{\text{bi}}^{\text{ortho}}(\omega) \bullet \underline{E}(\underline{r}, \omega) \\ \underline{B}(\underline{r}, \omega) &= \mu_0 \underline{H}(\underline{r}, \omega) \end{aligned} \right\} \quad (6.52)$$

characterize a homogeneous *orthorhombic* biaxial dielectric material. Here, for a suitable orientation of the coordinate axes, the permittivity dyadic has the diagonal form

$$\underline{\epsilon}_{\text{bi}}^{\text{ortho}}(\omega) = \epsilon_x(\omega) \hat{\underline{x}} \hat{\underline{x}} + \epsilon_y(\omega) \hat{\underline{y}} \hat{\underline{y}} + \epsilon_z(\omega) \hat{\underline{z}} \hat{\underline{z}}, \quad (6.53)$$

with  $\text{Im}\{\epsilon_x(\omega)\} > 0$ ,  $\text{Im}\{\epsilon_y(\omega)\} > 0$ , and  $\text{Im}\{\epsilon_z(\omega)\} > 0$  for a dissipative material, in conformity with the principle of causality.

While the diagonal dyadic representation (6.53) is convenient mathematically, it is not especially insightful from a physical viewpoint. The dual-axis symmetry is more clearly highlighted in the equivalent representation [29]

$$\underline{\epsilon}_{\text{bi}}^{\text{ortho}}(\omega) = \epsilon_p(\omega) \underline{\underline{I}} + \epsilon_q(\omega) (\hat{\underline{u}}_m \hat{\underline{u}}_n + \hat{\underline{u}}_n \hat{\underline{u}}_m). \quad (6.54)$$

For nondissipative materials, the permittivity scalars  $\epsilon_p$  and  $\epsilon_q$  are real-valued, and the unit vectors  $\hat{\underline{u}}_m$  and  $\hat{\underline{u}}_n$  are aligned with the *optic ray axes*. In general, there are two different modes of propagation for electromagnetic radiation in a biaxial material, with the rates of energy flow for these modes generally being different. However, the optic ray axes are oriented in the two privileged directions for which there is only one rate of energy flow [37]. One should be careful to distinguish the optic ray axes from the *optic axes* which are oriented in the two privileged directions for which electromagnetic radiation propagates in a biaxial material with only one phase speed. For dissipative materials, the interpretation is more complicated as both  $\epsilon_p$  and  $\epsilon_q$  are complex valued with  $\text{Im}\{\epsilon_p(\omega), \epsilon_q(\omega)\} > 0$ ; in this case there are different pairs of  $(\hat{\underline{u}}_m, \hat{\underline{u}}_n)$  axes associated with  $\text{Re}\{\epsilon_p(\omega), \epsilon_q(\omega)\}$  and  $\text{Im}\{\epsilon_p(\omega), \epsilon_q(\omega)\}$  [38].

More general biaxial dielectric materials are possible [39]. *Monoclinic* and *triclinic* biaxial dielectric materials are characterized by the Tellegen constitutive relations

$$\left. \begin{aligned} \underline{D}(\underline{r}, \omega) &= \left. \begin{aligned} \epsilon_{\text{bi}}^{\text{mono}}(\omega) \\ \epsilon_{\text{bi}}^{\text{tri}}(\omega) \end{aligned} \right\} \bullet \underline{E}(\underline{r}, \omega) \\ \underline{B}(\underline{r}, \omega) &= \mu_0 \underline{H}(\underline{r}, \omega) \end{aligned} \right\}, \quad (6.55)$$

respectively. For suitable orientations of the coordinate axes, the corresponding  $3 \times 3$  permittivity dyadics have the symmetric forms

$$\underline{\epsilon}_{\text{bi}}^{\text{mono}}(\omega) = \epsilon_x(\omega) \hat{\underline{x}} \hat{\underline{x}} + \epsilon_y(\omega) \hat{\underline{y}} \hat{\underline{y}} + \epsilon_z(\omega) \hat{\underline{z}} \hat{\underline{z}} + \epsilon_\alpha(\omega) (\hat{\underline{x}} \hat{\underline{y}} + \hat{\underline{y}} \hat{\underline{x}}) \quad (6.56)$$

and

$$\begin{aligned} \underline{\epsilon}_{\text{bi}}^{\text{tri}}(\omega) &= \epsilon_x(\omega) \hat{\underline{x}} \hat{\underline{x}} + \epsilon_y(\omega) \hat{\underline{y}} \hat{\underline{y}} + \epsilon_z(\omega) \hat{\underline{z}} \hat{\underline{z}} \\ &+ \epsilon_\alpha(\omega) (\hat{\underline{x}} \hat{\underline{y}} + \hat{\underline{y}} \hat{\underline{x}}) + \epsilon_\beta(\omega) (\hat{\underline{x}} \hat{\underline{z}} + \hat{\underline{z}} \hat{\underline{x}}) + \epsilon_\gamma(\omega) (\hat{\underline{y}} \hat{\underline{z}} + \hat{\underline{z}} \hat{\underline{y}}). \end{aligned} \quad (6.57)$$

Herein the  $\omega$ -dependent permittivity scalars  $\epsilon_x, \epsilon_y, \epsilon_z \in \mathbb{C}$  with  $\text{Im}\{\epsilon_x(\omega), \epsilon_y(\omega), \epsilon_z(\omega)\} > 0$  for dissipative materials, per the principle of causality. But the off-diagonal  $\omega$ -dependent scalars  $\epsilon_\alpha, \epsilon_\beta, \epsilon_\gamma \in \mathbb{R}$ .

The permittivity dyadics given in Eqs. (6.53), (6.56), and (6.57) specify biaxial materials which belong to the orthorhombic, monoclinic, and triclinic crystal systems, respectively [39]. The three biaxial crystal systems are distinguished by the symmetries of their primitive unit cells associated with their corresponding Bravais lattices. For the orthogonal crystal system, all three basis vectors of the primitive unit cell are mutually orthogonal; for the monoclinic crystal system, only two of the three basis vectors are orthogonal; and for the triclinic crystal system, none of the three basis vectors are orthogonal [40].

Biaxial magnetic materials are specified in precisely the same way as biaxial dielectric materials. That is, the Tellegen constitutive relations

$$\left. \begin{aligned} \underline{D}(\underline{r}, \omega) &= \epsilon_0 \underline{E}(\underline{r}, \omega) \\ \underline{B}(\underline{r}, \omega) &= \left. \begin{aligned} &\mu_{\equiv \text{bi}}^{\text{ortho}}(\omega) \\ &\mu_{\equiv \text{bi}}^{\text{mono}}(\omega) \\ &\mu_{\equiv \text{bi}}^{\text{tri}}(\omega) \end{aligned} \right\} \bullet \underline{H}(\underline{r}, \omega) \end{aligned} \right\} \quad (6.58)$$

characterize orthorhombic, monoclinic, and triclinic biaxial magnetic materials, respectively, wherein the corresponding permeability dyadics have symmetric forms which are analogous to those presented in Eqs. (6.53), (6.56), and (6.57). Furthermore, the amalgamation of a biaxial dielectric material with a biaxial magnetic material results in a biaxial dielectric–magnetic material which is biaxial with respect to both its dielectric and magnetic properties. The Tellegen constitutive relations

$$\left. \begin{aligned} \underline{D}(\underline{r}, \omega) &= \underline{\epsilon}_{\equiv \text{bi}}(\omega) \bullet \underline{E}(\underline{r}, \omega) \\ \underline{B}(\underline{r}, \omega) &= \underline{\mu}_{\equiv \text{bi}}(\omega) \bullet \underline{H}(\underline{r}, \omega) \end{aligned} \right\} \quad (6.59)$$

characterize such a material, with the symmetric permittivity and permeability dyadics  $\underline{\epsilon}_{\equiv \text{bi}}(\omega)$  and  $\underline{\mu}_{\equiv \text{bi}}(\omega)$ , being of the orthorhombic, monoclinic, or triclinic types.

**6.4.2.3 Gyrotropic Materials** The foregoing examples of uniaxial and biaxial anisotropy are characterized by symmetric permittivity and permeability dyadics. Accordingly, such anisotropic materials are Lorentz reciprocal. As we describe in this section, gyrotropic materials are fundamentally different: they are characterized by anti-symmetric permittivity and/or permeability dyadics and such materials are accordingly non-Lorentz reciprocal.

As a concrete example of a manifestation of gyrotropy, we consider an incompressible plasma of electrons in thermal motion, subjected to a quasistatic magnetic field  $\underline{B}_{\text{qs}} = B_{\text{qs}} \hat{\underline{u}}$  [41]. This magnetic field has strength  $B_{\text{qs}}$  and is applied in the direction of the unit vector  $\hat{\underline{u}}$ . The plasma consists of  $n_{\text{el}}$  electrons per unit volume; the charge density and mass density of the plasma are  $-n_{\text{el}}q_{\text{el}}$  and  $n_{\text{el}}m_{\text{el}}$ , respectively, with

the electronic charge being  $q_{\text{el}} = 1.6022 \times 10^{-19}$  C and the electronic mass being  $m_{\text{el}} = 9.1096 \times 10^{-31}$  kg. The plasma is assumed to be homogeneously distributed in free space, and its density is sufficiently low that collisions between electrons may be neglected. The average electron velocity is  $\bar{\underline{v}}(\underline{r}, t)$ .

The electromagnetic properties of the plasma are described by the time-domain Maxwell curl postulates

$$\left. \begin{aligned} \nabla \times \underline{\tilde{H}}(\underline{r}, t) - \epsilon_0 \frac{\partial}{\partial t} \underline{\tilde{E}}(\underline{r}, t) &= -n_{\text{el}} q_{\text{el}} \bar{\underline{v}}(\underline{r}, t) \\ \nabla \times \underline{\tilde{E}}(\underline{r}, t) + \mu_0 \frac{\partial}{\partial t} \underline{\tilde{H}}(\underline{r}, t) &= \underline{0} \end{aligned} \right\}, \quad (6.60)$$

together with the equation of motion

$$-n_{\text{el}} q_{\text{el}} \left[ \underline{\tilde{E}}(\underline{r}, t) + \bar{\underline{v}}(\underline{r}, t) \times \underline{B}_{\text{qs}} \right] = n_{\text{el}} m_{\text{el}} \frac{\partial}{\partial t} \bar{\underline{v}}(\underline{r}, t). \quad (6.61)$$

By combining Eqs. (6.60) and (6.61) and then comparing with the source-free versions of the Maxwell curl postulates (6.5)<sub>1,2</sub>, the constitutive relations for the plasma are developed as [42]

$$\left. \begin{aligned} \underline{\tilde{D}}(\underline{r}, t) &= \underline{\tilde{\epsilon}}_{\text{gyro}} \cdot \{ \underline{\tilde{E}}(\underline{r}, t) \} \\ \underline{\tilde{H}}(\underline{r}, t) &= \frac{1}{\mu_0} \underline{\tilde{B}}(\underline{r}, t) \end{aligned} \right\}. \quad (6.62)$$

Herein the permittivity dyadic term  $\underline{\tilde{\epsilon}}_{\text{gyro}} \cdot \{ \cdot \}$  is a differential operator defined as

$$\underline{\tilde{\epsilon}}_{\text{gyro}} = \epsilon_0 \underline{\underline{I}} + \epsilon_0 \omega_p^2 \left[ \underline{\underline{I}} \frac{\partial^2}{\partial t^2} - \omega_c \left( \underline{\hat{u}} \times \underline{\underline{I}} \right) \frac{\partial}{\partial t} \right]^{-1}, \quad (6.63)$$

where

$$\omega_p = q_{\text{el}} \left( \frac{n_{\text{el}}}{m_{\text{el}} \epsilon_0} \right)^{1/2} \quad (6.64)$$

is the *plasma frequency*, while

$$\omega_c = q_{\text{el}} \frac{B_{\text{qs}}}{m_{\text{el}}} \quad (6.65)$$

is the *gyrofrequency*; also the following interpretation

$$\left( \frac{\partial}{\partial t} \right)^{-1} f(t) \equiv \int_{-\infty}^t f(s) \, ds \quad (6.66)$$

should be attached to the inverse of the temporal differential operator.

More conveniently, Eq. (6.63) may be re-arranged as [29]

$$\begin{aligned}\underline{\tilde{\epsilon}}_{\text{gyro}} = \epsilon_0 & \left[ \left( \underline{I} - \hat{\underline{u}} \hat{\underline{u}} \right) \left( 1 + \frac{\omega_p^2}{\omega_c^2 + \partial^2/\partial t^2} \right) + \left( \hat{\underline{u}} \times \underline{I} \right) \frac{\omega_p^2 \omega_c}{(\omega_c^2 + \partial^2/\partial t^2) \partial/\partial t} \right. \\ & \left. + \hat{\underline{u}} \hat{\underline{u}} \left( 1 + \frac{\omega_p^2}{\partial^2/\partial t^2} \right) \right],\end{aligned}\quad (6.67)$$

where the interpretation

$$g(t) = \frac{1}{\alpha + \partial^2/\partial t^2} f(t) \iff \left( \alpha + \frac{\partial^2}{\partial t^2} \right) g(t) = f(t) \quad (6.68)$$

should be inferred.

Temporal dispersion is implied by the partial derivative operators appearing in Eqs. (6.63) and (6.67). The differential operator  $\partial/\partial t$  is converted to the multiplicative factor  $-i\omega$  upon taking the temporal Fourier transform. Thus, the time-domain constitutive relations (6.62) correspond to the Tellegen frequency-domain constitutive relations

$$\left. \begin{aligned}\underline{D}(\underline{r}, \omega) &= \underline{\epsilon}_{\text{gyro}}(\omega) \bullet \underline{E}(\underline{r}, \omega) \\ \underline{B}(\underline{r}, \omega) &= \mu_0 \underline{H}(\underline{r}, \omega)\end{aligned}\right\}, \quad (6.69)$$

with the  $\omega$ -dependent permittivity dyadic being given as

$$\begin{aligned}\underline{\epsilon}_{\text{gyro}}(\omega) = \epsilon_0 & \left[ \left( 1 + \frac{\omega_p^2}{\omega_c^2 - \omega^2} \right) \left( \underline{I} - \hat{\underline{u}} \hat{\underline{u}} \right) + \frac{i\omega_p^2 \omega_c}{(\omega_c^2 - \omega^2) \omega} \hat{\underline{u}} \times \underline{I} \right. \\ & \left. + \left( 1 - \frac{\omega_p^2}{\omega^2} \right) \hat{\underline{u}} \hat{\underline{u}} \right].\end{aligned}\quad (6.70)$$

The gyrotropic form (6.70) combines uniaxial anisotropy in the direction of the quasistatic magnetic field, together with antisymmetric terms associated with the plane normal to the magnetic field.

Notice that the gyrotropic plasma characterized by the permittivity dyadic (6.70) is nondissipative. If electron collisions were taken into account then a more realistic characterization may be achieved. In effect, the characterization of such a dissipative plasma could result from replacing  $\omega$  with  $\omega - iv_{dp}$ , with  $v_{dp} \in \mathbb{R}$  being an appropriate damping parameter [6].

Gyrotropy is not exclusively a dielectric phenomenon—magnetic materials, such as ferrites [43], also exhibit gyrotropic behavior. A gyrotropic magnetic material may be characterized by the Tellegen constitutive relations

$$\left. \begin{aligned} \underline{D}(\underline{r}, \omega) &= \epsilon_0 \underline{E}(\underline{r}, \omega) \\ \underline{B}(\underline{r}, \omega) &= \underline{\mu}_{\text{gyro}}(\omega) \bullet \underline{H}(\underline{r}, \omega) \end{aligned} \right\}. \quad (6.71)$$

The  $\omega$ -dependent permeability dyadic herein has the form

$$\underline{\mu}_{\text{gyro}}(\omega) = \mu(\omega) \left( \underline{I} - \hat{\underline{u}} \hat{\underline{u}} \right) + i \mu_g(\omega) \hat{\underline{u}} \times \underline{I} + \mu_u(\omega) \hat{\underline{u}} \hat{\underline{u}}; \quad (6.72)$$

the constitutive parameters  $\mu(\omega)$ ,  $\mu_u(\omega)$ ,  $\mu_g(\omega) \in \mathbb{R}$  for nondissipative materials whereas  $\mu(\omega)$ ,  $\mu_u(\omega)$ ,  $\mu_g(\omega) \in \mathbb{C}$  for dissipative materials.

### 6.4.3 Bianisotropic Materials

In a bianisotropic material,  $\underline{D}(\underline{r}, t)$  is anisotropically coupled to both  $\underline{E}(\underline{r}, t)$  and  $\underline{B}(\underline{r}, t)$ , and  $\underline{H}(\underline{r}, t)$  is anisotropically coupled to both  $\underline{E}(\underline{r}, t)$  and  $\underline{B}(\underline{r}, t)$  [6, 42]. Therefore, in general, a linear bianisotropic material is described by four  $3 \times 3$  constitutive dyadics, as in the Tellegen constitutive relations (6.16).

Bianisotropy crops up in variety of different ways. A number of naturally occurring minerals are bianisotropic at low frequencies and temperatures, albeit the magnitudes of their bianisotropic effects are typically small [44, 45]. Perhaps more significantly from a technological perspective, artificial composite materials and metamaterials can be readily conceptualized which exhibit appreciable bianisotropic effects [46]; indeed, this bianisotropy may be harnessed to realize exotic and potentially useful phenomena such as negative refraction [47]. Other manifestations of bianisotropy arise in relativistic scenarios; here the bianisotropy may be induced by uniform motion [29] or gravitational fields [48].

**6.4.3.1 Uniaxial and Biaxial Materials** The notions of uniaxial and biaxial anisotropy introduced earlier in Section 6.4 for dielectric and magnetic materials generalize in a natural way to bianisotropic scenarios. Accordingly, the general form for the Tellegen constitutive relations of a homogeneous material which is biaxially bianisotropic is [49]

$$\left. \begin{aligned} \underline{D}(\underline{r}, \omega) &= \underline{\epsilon}_{\text{bi}}(\omega) \bullet \underline{E}(\underline{r}, \omega) + \underline{\xi}_{\text{bi}}(\omega) \bullet \underline{H}(\underline{r}, \omega) \\ \underline{B}(\underline{r}, \omega) &= \underline{\zeta}_{\text{bi}}(\omega) \bullet \underline{E}(\underline{r}, \omega) + \underline{\mu}_{\text{bi}}(\omega) \bullet \underline{H}(\underline{r}, \omega) \end{aligned} \right\}, \quad (6.73)$$

where each of the four  $3 \times 3$  constitutive dyadics has the symmetric form

$$\begin{aligned} \underline{\underline{\mathcal{Z}}}_{\text{bi}}(\omega) = & \mathcal{Z}_x(\omega)\hat{x}\hat{x} + \mathcal{Z}_y(\omega)\hat{y}\hat{y} + \mathcal{Z}_z(\omega)\hat{z}\hat{z} + \mathcal{Z}_\alpha(\omega)(\hat{x}\hat{y} + \hat{y}\hat{x}) + \mathcal{Z}_\beta(\omega)(\hat{x}\hat{z} + \hat{z}\hat{x}) \\ & + \mathcal{Z}_\gamma(\omega)(\hat{y}\hat{z} + \hat{z}\hat{y}), \quad (\mathcal{Z} \in \{\epsilon, \xi, \zeta, \mu\}), \end{aligned} \quad (6.74)$$

with the  $\omega$ -dependent constitutive parameters  $\epsilon_{x,y,z}, \xi_{x,y,z}, \zeta_{x,y,z}, \mu_{x,y,z} \in \mathbb{C}$  and  $\epsilon_{\alpha,\beta,\gamma}, \xi_{\alpha,\beta,\gamma}, \zeta_{\alpha,\beta,\gamma}, \mu_{\alpha,\beta,\gamma} \in \mathbb{R}$ . The specialization

$$\mathcal{Z}_{\alpha,\beta,\gamma}(\omega) = 0, \quad (\mathcal{Z} \in \{\epsilon, \xi, \zeta, \mu\}), \quad (6.75)$$

applies to orthorhombic bianisotropic materials, while the specialization

$$\mathcal{Z}_x(\omega) = \mathcal{Z}_y(\omega), \quad (\mathcal{Z} \in \{\epsilon, \xi, \zeta, \mu\}), \quad (6.76)$$

combined with the conditions (6.75) applies to uniaxial bianisotropic materials.

**6.4.3.2 Simultaneously Mirror-Conjugated and Racemic Chiral Materials** A special form of chirality can be exhibited by a certain bianisotropic material wherein both mirror-conjugated and racemic characteristics co-exist. The Tellegen constitutive relations for such a material may be expressed as [50]

$$\left. \begin{aligned} \underline{D}(\underline{r}, \omega) &= \underline{\epsilon}_{\text{MCR}}(\omega) \bullet \underline{E}(\underline{r}, \omega) + \underline{\xi}_{\text{MCR}}(\omega) \bullet \underline{H}(\underline{r}, \omega) \\ \underline{B}(\underline{r}, \omega) &= -\underline{\xi}_{\text{MCR}}(\omega) \bullet \underline{E}(\underline{r}, \omega) + \underline{\mu}_{\text{MCR}}(\omega) \bullet \underline{H}(\underline{r}, \omega) \end{aligned} \right\}, \quad (6.77)$$

where the constitutive dyadics have the diagonal forms

$$\left. \begin{aligned} \underline{\epsilon}_{\text{MCR}}(\omega) &= \epsilon(\omega) \left( \underline{I} - \hat{z}\hat{z} \right) + \epsilon_z(\omega) \hat{z}\hat{z} \\ \underline{\xi}_{\text{MCR}}(\omega) &= \xi(\omega) \left( \hat{x}\hat{x} - \hat{y}\hat{y} \right) \\ \underline{\mu}_{\text{MCR}}(\omega) &= \mu(\omega) \left( \underline{I} - \hat{z}\hat{z} \right) + \mu_z(\omega) \hat{z}\hat{z} \end{aligned} \right\}, \quad (6.78)$$

for a particular orientation of the coordinate axes. This material is uniaxial in terms of its dielectric and magnetic properties, but biaxial in terms of its magnetoelectric properties. Also, the structure of the magnetoelectric dyadic  $\underline{\xi}_{\text{MCR}}(\omega)$  indicates chirality of opposite handedness along the  $x$  and  $y$  coordinate axes while its null-valued  $\hat{z}\hat{z}$  term indicates achirality along the  $z$  coordinate axis. Notably, the magnetoelectric dyadic  $\underline{\xi}_{\text{MCR}}(\omega)$  is singular.

Nature provides some minerals of the type  $\text{RXO}_4$ , where R is a trivalent rare earth, X is either vanadium or arsenic or phosphorus, and O is oxygen [51, 52], which are described by the constitutive relations (6.77) at temperatures below their Néel temperatures. In addition, artificial materials described by the constitutive relations (6.77) may be conceptualized through immersing an array of parallel identical springs in an isotropic dielectric–magnetic host material [53, 54], provided that the linear spring dimensions are sufficiently small compared to the electromagnetic wavelengths. Right- and left-handed springs should be aligned in equal linear densities along the  $x$ - and  $y$ -directions on a square lattice, respectively, while in the  $z$ -direction either no springs at all or equal proportions of left- and right-handed springs should be aligned to simulate either achirality or racemic chirality, respectively [50].

**6.4.3.3 Faraday Chiral Materials** Faraday chiral materials may be conceived as homogenized composite materials (HCMs) [55]. That is, their existence comes about through mixing together two (or more) component materials, where the linear dimensions of the particles that make up the component materials are at least an order of magnitude smaller than the electromagnetic wavelengths involved. If the component materials are anisotropic (or bianisotropic), or if the component particles have asymmetric shapes and a preferred orientation, then the resulting HCM can have a complex anisotropic or bianisotropic structure which represents an amalgamation of the complexities of the component materials. In the case of Faraday chiral materials, the manifestation of bianisotropy is due to one of the component materials being isotropic chiral while the other is a gyrotropic material which supports Faraday rotation [29, 43, 56]. For example, the gyrotropic component material could be a magnetically biased ferrite [57] or it could be a magnetically biased plasma [58]. Gyrotropic materials are non-Lorentz reciprocal and consequently Faraday chiral materials are also non-Lorentz reciprocal.

The frequency-domain Tellegen constitutive relations for a homogeneous Faraday chiral material are [59]

$$\left. \begin{aligned} \underline{D}(\underline{r}, \omega) &= \underline{\epsilon}_{\text{FCM}}(\omega) \cdot \underline{E}(\underline{r}, \omega) + i\underline{\xi}_{\text{FCM}}(\omega) \cdot \underline{H}(\underline{r}, \omega) \\ \underline{B}(\underline{r}, \omega) &= -i\underline{\xi}_{\text{FCM}}(\omega) \cdot \underline{E}(\underline{r}, \omega) + \underline{\mu}_{\text{FCM}}(\omega) \cdot \underline{H}(\underline{r}, \omega) \end{aligned} \right\}. \quad (6.79)$$

The  $3 \times 3$  constitutive dyadics all have same form, namely

$$\underline{\underline{\mathcal{Z}}}_{\text{FCM}}(\omega) = \mathcal{Z}(\omega) \underline{\underline{I}} + [\mathcal{Z}_u(\omega) - \mathcal{Z}(\omega)] \hat{\underline{u}} \hat{\underline{u}} + i\mathcal{Z}_g(\omega) \hat{\underline{u}} \times \underline{\underline{I}}, \quad (\mathcal{Z} \in \{\epsilon, \xi, \mu\}). \quad (6.80)$$

Herein the unit vector  $\hat{\underline{u}}$  is aligned with the direction of the biasing magnetic field for the gyrotropic component material. The  $\omega$ -dependent constitutive parameters  $\epsilon$ ,  $\epsilon_u$ ,  $\epsilon_g$ ,  $\xi$ ,  $\xi_g$ ,  $\xi_u$ ,  $\mu$ ,  $\mu_g$ , and  $\mu_u$  are real valued for a nondissipative Faraday material, otherwise they are nontrivially complex valued.

The constitutive dyadic form in Eq. (6.80) arises in the case where the component materials in the homogenization procedure are composed of spherical particles. More general constitutive dyadic forms for Faraday chiral materials result if the component materials are composed of aligned nonspherical particles [58, 60].

Parenthetically, let us add that a material which is characterized as isotropic chiral by a stationary observer is characterized as Faraday chiral by a uniformly moving observer.

**6.4.3.4 Pseudochiral Materials** A pseudochiral omega material is one characterized by the Tellegen constitutive relations [61].

$$\left. \begin{aligned} \underline{D}(\underline{r}, \omega) &= \underline{\underline{\epsilon}}(\omega) \bullet \underline{E}(\underline{r}, \omega) - \underline{\underline{\xi}}(\omega) \bullet \underline{H}(\underline{r}, \omega) \\ \underline{B}(\underline{r}, \omega) &= \underline{\underline{\xi}}^T(\omega) \bullet \underline{E}(\underline{r}, \omega) + \underline{\underline{\mu}}(\omega) \bullet \underline{H}(\underline{r}, \omega) \end{aligned} \right\}, \quad (6.81)$$

wherein the  $3 \times 3$  constitutive dyadics are of the form

$$\left. \begin{aligned} \underline{\underline{\epsilon}}(\omega) &= \epsilon_x(\omega) \hat{x}\hat{x} + \epsilon_y(\omega) \hat{y}\hat{y} + \epsilon_z(\omega) \hat{z}\hat{z} \\ \underline{\underline{\xi}}(\omega) &= \xi(\omega) \hat{z}\hat{y} \\ \underline{\underline{\mu}}(\omega) &= \mu_x(\omega) \hat{x}\hat{x} + \mu_y(\omega) \hat{y}\hat{y} + \mu_z(\omega) \hat{z}\hat{z} \end{aligned} \right\}, \quad (6.82)$$

for a particular orientation of the coordinate axes. Such a material is orthorhombic biaxial as far as its dielectric and magnetic properties are concerned, and the magnetoelectric coupling is such that the material is Lorentz reciprocal. Notably, the magnetoelectric dyadic  $\underline{\underline{\xi}}(\omega)$  is singular.

A microstructure involving arrays of identically oriented  $\Omega$ -shaped particles embedded in an isotropic dielectric–magnetic host material [62] can give rise to a pseudochiral omega material. For the coordinate axis orientation represented in Eqs. (6.82), the stems of the  $\Omega$ -shaped particles are aligned with the Cartesian  $y$ -axis. We note that constitutive dyadics of the form of Eqs. (6.82) also characterize certain metamaterials which support negative refraction; in this case the microstructure is based on arrays of electromagnetically small split-ring resonators [63].

**6.4.3.5 Motion-Induced Bianisotropy** Consider an inertial reference frame  $\Sigma'$  which moves at constant velocity  $\underline{v} = v\underline{\hat{v}}$  relative to an inertial reference frame  $\Sigma$ . The Lorentz transformation [29]

$$\left. \begin{aligned} \underline{r}' &= \underline{\underline{Y}} \bullet \underline{r} - \gamma \underline{v} t \\ t' &= \gamma \left( t - \frac{\underline{r} \bullet \underline{v}}{c_0^2} \right) \end{aligned} \right\}, \quad (6.83)$$

with

$$\left. \begin{aligned} \underline{\underline{Y}} &= \underline{\underline{I}} + (\gamma - 1) \underline{\hat{v}} \underline{\hat{v}} \\ \gamma &= \left[ 1 - \left( \frac{v}{c_0} \right)^2 \right]^{-\frac{1}{2}} \end{aligned} \right\}, \quad (6.84)$$

relates the spacetime coordinates  $(\underline{r}', t')$  in  $\Sigma'$  to the spacetime coordinates  $(\underline{r}, t)$  in  $\Sigma$ . Here  $c_0 = (\epsilon_0 \mu_0)^{-1/2}$  is the speed of light in free space.<sup>5</sup>

If the Lorentz transformation (6.83) is applied to the time-domain fields  $\tilde{\underline{E}}(\underline{r}, t)$ ,  $\tilde{\underline{B}}(\underline{r}, t)$ ,  $\tilde{\underline{D}}(\underline{r}, t)$ , and  $\tilde{\underline{H}}(\underline{r}, t)$  in the inertial reference frame  $\Sigma$ , then one finds that corresponding fields in inertial reference frame  $\Sigma'$  are given as [29]

$$\left. \begin{aligned} \tilde{\underline{E}}'(\underline{r}', t') &= \gamma \left[ \underline{\underline{Y}}^{-1} \bullet \tilde{\underline{E}}(\underline{r}, t) + \underline{v} \times \tilde{\underline{B}}(\underline{r}, t) \right] \\ \tilde{\underline{B}}'(\underline{r}', t') &= \gamma \left[ \underline{\underline{Y}}^{-1} \bullet \tilde{\underline{B}}(\underline{r}, t) - \frac{1}{c_0^2} \underline{v} \times \tilde{\underline{E}}(\underline{r}, t) \right] \\ \tilde{\underline{D}}'(\underline{r}', t') &= \gamma \left[ \underline{\underline{Y}}^{-1} \bullet \tilde{\underline{D}}(\underline{r}, t) + \frac{1}{c_0^2} \underline{v} \times \tilde{\underline{H}}(\underline{r}, t) \right] \\ \tilde{\underline{H}}'(\underline{r}', t') &= \gamma \left[ \underline{\underline{Y}}^{-1} \bullet \tilde{\underline{H}}(\underline{r}, t) - \underline{v} \times \tilde{\underline{D}}(\underline{r}, t) \right] \end{aligned} \right\}. \quad (6.85)$$

Furthermore, the Maxwell postulates have same form in inertial reference frame  $\Sigma'$  as they have in inertial reference frame  $\Sigma$ . Since they retain their form under the spatiotemporal transformation (6.83), they are said to be *Lorentz covariant*. However, the concepts of isotropy and anisotropy are not invariant under the Lorentz transformation (6.83). In other words, a material which is isotropic or anisotropic in one inertial reference frame is generally biaxotropic in all other inertial reference frames [29]. A further complication is that a homogeneous material which is spatially local but temporally nonlocal in one inertial reference frame is generally spatiotemporally nonlocal in all other inertial reference frames [22, 64].

#### 6.4.4 Nonhomogeneous Materials

Thus far in this section materials have been classified as isotropic, anisotropic, or biaxotropic on the basis of constitutive dyadics which are independent on the position vector  $\underline{r}$ . However, for many materials of theoretical and practical interest, the dependency of their constitutive properties on  $\underline{r}$  is crucial. Of course, nonhomogeneity generally increases the complexity of mathematical descriptions of electromagnetic

<sup>5</sup>In classical electromagnetic theory free space and vacuum are regarded as being equivalent. The nonclassical representation of vacuum is described in Section 6.5.

properties, but for certain nonhomogeneous anisotropic and bianisotropic materials well-developed theoretical descriptions have been established. A selection of such nonhomogeneous materials is presented in the following subsections.

**6.4.4.1 Periodically Nonhomogeneous Materials** Chiral nematic liquid crystals (also known as cholesteric liquid crystals) constitute an especially well-studied class of materials that are both anisotropic and periodically nonhomogeneous. Their crystalline structure consists of helicoidal arrangements of aciculate molecules. This structure endows such liquid crystals with periodically twisted, uniaxial dielectric properties. The Tellegen frequency-domain constitutive relations for chiral nematic liquid crystals may be expressed as [65, 66]

$$\left. \begin{aligned} \underline{D}(r, \omega) &= \underline{\epsilon}_{\text{CNLC}}(z, \omega) \bullet \underline{E}(r, \omega) \\ \underline{B}(r, \omega) &= \mu_0 \underline{H}(r, \omega) \end{aligned} \right\}, \quad (6.86)$$

with the nonhomogeneous permittivity dyadic having the uniaxial form

$$\underline{\epsilon}_{\text{CNLC}}(z, \omega) = \epsilon_a(\omega) \underline{\underline{I}} + [\epsilon_b(\omega) - \epsilon_a(\omega)] \hat{u}(z) \hat{u}(z). \quad (6.87)$$

Herein the orientation of the coordinate axes has been chosen such that rotational axis of  $\underline{\epsilon}_{\text{CNLC}}(z, \omega)$  coincides with the Cartesian  $z$ -axis. The  $\omega$ -dependent, permittivity scalars  $\epsilon_a$  and  $\epsilon_b$  are real valued for the nondissipative case and nontrivially complex valued for dissipative case. The unit vector

$$\hat{u}(z) = \hat{x} \cos \frac{\pi z}{\Omega_{\text{dp}}} \pm \hat{y} \sin \frac{\pi z}{\Omega_{\text{dp}}} \quad (6.88)$$

is defined in terms of the dielectric periodicity along the  $z$ -direction, namely  $2\Omega_{\text{dp}}$ ; structural right-handedness is signalled by choosing the “+” sign, while structural left-handedness is signalled by choosing the “−” sign.

Chiral smectic liquid crystals—which may be regarded as generalizations of their nematic counterparts—are characterized by the constitutive relations which are similar to Eqs. (6.86) except that the corresponding permittivity dyadic has a biaxial form [67].

The helicoidal structure of chiral liquid crystals is analogous to that of chiral sculptured thin films (CSTFs) [68]. Such a film consists of an array of parallel helical nanowires grown on a substrate. CSTFs can be manufactured by vapor deposition methods, with the substrate being rotated at constant circular speed throughout the deposition process. Locally, the dielectric properties of the nanowires may be characterized as orthorhombic biaxial. The helicity of their component nanowires results in CSTFs exhibiting structural chirality. These materials have been extensively studied for the past 17 years or more on account of their technologically promising optical properties [69].

In the case where the component nanowires coil around the direction of the Cartesian  $z$ -axis, a CSTF may be characterized by the Tellegen frequency-domain constitutive relations

$$\left. \begin{aligned} \underline{D}(\underline{r}, \omega) &= \underline{\epsilon}_{\text{CSTF}}(z, \omega) \bullet \underline{E}(\underline{r}, \omega) \\ \underline{B}(\underline{r}, \omega) &= \mu_0 \underline{H}(\underline{r}, \omega) \end{aligned} \right\}. \quad (6.89)$$

The nonhomogeneous permittivity dyadic

$$\underline{\epsilon}_{\text{CSTF}}(z, \omega) = \underline{\underline{S}}(z) \bullet \underline{\underline{S}}(\psi) \bullet \begin{pmatrix} \epsilon_u(\omega) & 0 & 0 \\ 0 & \epsilon_v(\omega) & 0 \\ 0 & 0 & \epsilon_w(\omega) \end{pmatrix} \bullet \underline{\underline{S}}^{-1}(\psi) \bullet \underline{\underline{S}}^{-1}(z) \quad (6.90)$$

is expressible in terms of three complex-valued,  $\omega$ -dependent parameters  $\epsilon_u$ ,  $\epsilon_v$  and  $\epsilon_w$ , along with the rotation and tilt dyadics

$$\underline{\underline{S}}(\psi) = \begin{pmatrix} \cos \psi & 0 & -\sin \psi \\ 0 & 1 & 0 \\ \sin \psi & 0 & \cos \psi \end{pmatrix}, \quad (6.91)$$

$$\underline{\underline{S}}(z) = \begin{pmatrix} \cos \left( \frac{\pi z}{\Omega_{hp}} \right) & -h \sin \left( \frac{\pi z}{\Omega_{hp}} \right) & 0 \\ h \sin \left( \frac{\pi z}{\Omega_{hp}} \right) & \cos \left( \frac{\pi z}{\Omega_{hp}} \right) & 0 \\ 0 & 0 & 1 \end{pmatrix}. \quad (6.92)$$

Herein  $\Omega_{hp}$  is the half-pitch of the helical nanowires,  $h = +1$  signifies structural right-handedness,  $h = -1$  signifies the structural left-handedness, and  $\psi \in [0, \pi/2]$ .

The bianisotropic generalization of the CSTF characterized by Eqs. (6.89) and (6.90) is called a helicoidal bianisotropic material [70]. Its Tellegen frequency-domain constitutive relations may be written as

$$\left. \begin{aligned} \underline{D}(\underline{r}, \omega) &= \underline{\epsilon}_{\text{HBM}}(z, \omega) \bullet \underline{E}(\underline{r}, \omega) + \underline{\xi}_{\text{HBM}}(z, \omega) \bullet \underline{H}(\underline{r}, \omega) \\ \underline{B}(\underline{r}, \omega) &= \underline{\zeta}_{\text{HBM}}(z, \omega) \bullet \underline{E}(\underline{r}, \omega) + \underline{\mu}_{\text{HBM}}(z, \omega) \bullet \underline{H}(\underline{r}, \omega) \end{aligned} \right\}. \quad (6.93)$$

All four of its  $3 \times 3$  nonhomogeneous constitutive dyadics have the form

$$\underline{\underline{\mathcal{Z}}}_{\text{HBM}}(z, \omega) = \begin{pmatrix} \mathcal{Z}_{11}(z, \omega) & \mathcal{Z}_{12}(z, \omega) & \mathcal{Z}_{13}(z, \omega) \\ \mathcal{Z}_{21}(z, \omega) & \mathcal{Z}_{22}(z, \omega) & \mathcal{Z}_{23}(z, \omega) \\ \mathcal{Z}_{31}(z, \omega) & \mathcal{Z}_{32}(z, \omega) & \mathcal{Z}_{33}(z, \omega) \end{pmatrix}, \quad (\mathcal{Z} \in \{\epsilon, \xi, \zeta, \mu\}), \quad (6.94)$$

which decomposes as

$$\underline{\underline{\mathcal{Z}}}_{\text{HBM}}(z, \omega) = \underline{\underline{S}}_z(z) \bullet \underline{\underline{\mathcal{Z}}}_{\text{HBM}}(0, \omega) \bullet \underline{\underline{S}}_z^{-1}(z), \quad (\mathcal{Z} \in \{\epsilon, \xi, \zeta, \mu\}). \quad (6.95)$$

**6.4.4.2 Material Analogues of Curved Spacetime** Although not explicitly stated, we have so far in this chapter been describing electromagnetic theory in flat spacetime. We now extend our presentation by considering the electromagnetic properties of free space in curved spacetime. As we shall elaborate upon shortly, free space in curved spacetime is not electromagnetically isotropic in general—in fact, its electromagnetic properties are equivalent to those of a nonhomogeneous, nondissipative bianisotropic material in flat spacetime.

Conventionally, the curvature of spacetime induced by a gravitational field is characterized by a *metric*, which is a symmetric covariant tensor of rank 2 [71]. Let us introduce the symmetric, real-valued,  $4 \times 4$  matrix  $\underline{\underline{\tilde{g}}}(\underline{r}, t)$  whose components are the same as those of the spacetime metric. In general, the matrix  $\underline{\underline{\tilde{g}}}(\underline{r}, t)$  is both spatially nonhomogeneous and time dependent.

Following the approach of Tamm and others [72–74], by expressing the covariant Maxwell equations in noncovariant form, one finds that the electromagnetic response of free space in curved spacetime is equivalent to that of a certain material in flat spacetime which is described by the Tellegen time-domain constitutive relations [48, 75]

$$\left. \begin{aligned} \underline{\underline{D}}(\underline{r}, t) &= \epsilon_0 \underline{\underline{\tilde{\gamma}}}_{\text{GAV}}(\underline{r}, t) \bullet \underline{\underline{\tilde{E}}}(\underline{r}, t) - \frac{1}{c_0} \underline{\underline{\tilde{\Gamma}}}_{\text{GAV}}(\underline{r}, t) \times \underline{\underline{\tilde{H}}}(\underline{r}, t) \\ \underline{\underline{B}}(\underline{r}, t) &= \mu_0 \underline{\underline{\tilde{\gamma}}}_{\text{GAV}}(\underline{r}, t) \bullet \underline{\underline{\tilde{H}}}(\underline{r}, t) + \frac{1}{c_0} \underline{\underline{\tilde{\Gamma}}}_{\text{GAV}}(\underline{r}, t) \times \underline{\underline{\tilde{E}}}(\underline{r}, t) \end{aligned} \right\}. \quad (6.96)$$

Herein the  $3 \times 3$  dyadic  $\underline{\underline{\tilde{\gamma}}}_{\text{GAV}}(\underline{r}, t)$  has components

$$\left[ \underline{\underline{\tilde{\gamma}}}_{\text{GAV}}(\underline{r}, t) \right]_{\ell m} = - \frac{\left[ -\det \underline{\underline{\tilde{g}}}(\underline{r}, t) \right]^{1/2}}{\left[ \underline{\underline{\tilde{g}}}(\underline{r}, t) \right]_{1,1}} \left[ \underline{\underline{\tilde{g}}}^{-1}(\underline{r}, t) \right]_{\ell+1, m+1}, \quad (\ell, m \in \{1, 2, 3\}), \quad (6.97)$$

while the 3-vector

$$\underline{\underline{\tilde{\Gamma}}}_{\text{GAV}}(\underline{r}, t) = \left( \left[ \underline{\underline{\tilde{g}}}(\underline{r}, t) \right]_{1,1} \right)^{-1} \left( \begin{array}{c} \left[ \underline{\underline{\tilde{g}}}(\underline{r}, t) \right]_{1,2} \\ \left[ \underline{\underline{\tilde{g}}}(\underline{r}, t) \right]_{1,3} \\ \left[ \underline{\underline{\tilde{g}}}(\underline{r}, t) \right]_{1,4} \end{array} \right), \quad (6.98)$$

with  $[\underline{\tilde{g}}(\underline{r}, t)]_{\ell,m}$  representing the  $(\ell, m)$ -th component of  $\underline{\tilde{g}}(\underline{r}, t)$ . Thus, the mathematical description of the electromagnetic properties of free space subjected to a gravitational field is isomorphic to the description for a fictitious material characterized by the constitutive relations (6.96) in the absence of a gravitational field. Accordingly, well-established analytical techniques used to investigate the electromagnetic properties of materials may be implemented in the study of gravitational fields. The nature of the fictitious material characterized by Eqs. (6.96) is determined by the underlying metric. In general, this material is bianisotropic, nondissipative, and non-Lorentz reciprocal, but it does satisfy the Post constraint (6.29) [21]. Its constitutive dyadics are both spatially nonhomogeneous and time varying. The symmetry of the matrix  $\underline{\tilde{g}}(\underline{r}, t)$  implies that the permittivity and permeability dyadics  $\epsilon_0 \underline{\tilde{\gamma}}_{\text{GAV}}(\underline{r}, t)$  and  $\mu_0 \underline{\tilde{\gamma}}_{\text{GAV}}(\underline{r}, t)$ , respectively, are of the orthorhombic biaxial type; furthermore these constitutive dyadics share the same eigenvectors. In the absence of a gravitational field, the matrix  $\underline{\tilde{g}}(\underline{r}, t)$  reduces to the constant diagonal matrix

$$\underline{\tilde{g}}(\underline{r}, t) = \begin{pmatrix} 1 & 0 & 0 & 0 \\ 0 & -1 & 0 & 0 \\ 0 & 0 & -1 & 0 \\ 0 & 0 & 0 & -1 \end{pmatrix}, \quad (6.99)$$

and the constitutive relations (6.96) simplify to the familiar form

$$\left. \begin{aligned} \underline{\tilde{D}}(\underline{r}, t) &= \epsilon_0 \underline{\tilde{E}}(\underline{r}, t) \\ \underline{\tilde{H}}(\underline{r}, t) &= \frac{1}{\mu_0} \underline{\tilde{B}}(\underline{r}, t) \end{aligned} \right\}. \quad (6.100)$$

The formal equivalence between a fictitious material characterized by the constitutive relations (6.96) and gravitationally affected free space opens to the door to the construction of material analogues of curved spacetime, at least in principle. In practice, real materials cannot respond instantaneously as the fictitious material is required to do, nevertheless perhaps useful approximate analogues could be achieved within certain restricted frequency ranges. For example, metamaterial analogues of a spinning cosmic string [76] and Schwarzschild-(anti-)de Sitter spacetime [77] have recently been proposed. In the latter case, the metamaterial in question takes the form of a HCM, with an inverse homogenization procedure [78] being implemented to derive the required constitutive parameters.

## 6.5 NONLINEAR MATERIALS

Our focus so far has largely been on materials wherein the induction fields are linearly proportional to the primitive fields. Let us close this chapter with a brief

outline of the rather more complicated scenario involving nonlinear proportionality. Materials characterized by nonlinear constitutive relations are of tremendous technological importance. Even in the earliest years of electromagnetics, the nonlinear permeability of ferromagnetic materials was much exploited in electrical machines [79], for example. Since nonlinear optical properties are generally exhibited at high light intensities, the invention of the laser resulted in the rapid expansion of the field of nonlinear optics in the 1960s [79, 80].

Let us consider the concept of nonlinearity within the general framework of homogeneous bianisotropic materials. As our starting point, we turn to the frequency-domain versions of the definitions of the induction fields provided in Eqs. (6.3), that is,

$$\left. \begin{aligned} \underline{D}(\underline{r}, \omega) &= \epsilon_0 \underline{E}(\underline{r}, \omega) + \underline{P}(\underline{r}, \omega) \\ \underline{H}(\underline{r}, \omega) &= \frac{1}{\mu_0} \underline{B}(\underline{r}, \omega) - \underline{M}(\underline{r}, \omega) \end{aligned} \right\}, \quad (6.101)$$

with the frequency-domain polarization  $\underline{P}(\underline{r}, \omega)$  and magnetization  $\underline{M}(\underline{r}, \omega)$  being the temporal Fourier transforms of  $\tilde{\underline{P}}(\underline{r}, t)$  and  $\tilde{\underline{M}}(\underline{r}, t)$ , respectively, per Eq. (6.11). For compact presentation, the following 6-vectors are introduced:

$$\underline{\mathbf{N}}(\underline{r}, \omega) = \begin{bmatrix} \underline{P}(\underline{r}, \omega) \\ \underline{M}(\underline{r}, \omega) \end{bmatrix}, \quad \underline{\mathbf{C}}(\underline{r}, \omega) = \begin{bmatrix} \underline{D}(\underline{r}, \omega) \\ \underline{B}(\underline{r}, \omega) \end{bmatrix}, \quad \underline{\mathbf{F}}(\underline{r}, \omega) = \begin{bmatrix} \underline{E}(\underline{r}, \omega) \\ \underline{H}(\underline{r}, \omega) \end{bmatrix}. \quad (6.102)$$

Thus nonlinear constitutive relations may be written in the 6-vector/dyadic notation as [81]

$$\underline{\mathbf{C}}(\underline{r}, \omega) = \underline{\underline{\mathbf{K}}} \cdot \underline{\mathbf{F}}(\underline{r}, \omega) + \underline{\mathbf{N}}(\underline{r}, \omega), \quad (6.103)$$

where

$$\underline{\underline{\mathbf{K}}} = \begin{bmatrix} \epsilon_0 \underline{\underline{I}} & \underline{\underline{0}} \\ \underline{\underline{0}} & \mu_0 \underline{\underline{I}} \end{bmatrix} \quad (6.104)$$

is the  $6 \times 6$  Tellegen constitutive dyadic of free space.

Now we write the 6-vector  $\underline{\mathbf{N}}(\underline{r}, \omega)$  as the sum of linear and nonlinear parts

$$\underline{\mathbf{N}}(\underline{r}, \omega) = \underline{\mathbf{N}}_L(\underline{r}, \omega) + \underline{\mathbf{N}}_{NL}(\underline{r}, \omega). \quad (6.105)$$

The linear contribution

$$\underline{\mathbf{N}}_L(\underline{r}, \omega) = \left[ \underline{\underline{\mathbf{K}}}^L(\omega) - \underline{\underline{\mathbf{K}}} \right] \cdot \underline{\mathbf{F}}(\underline{r}, \omega) \quad (6.106)$$

is specified by the  $6 \times 6$  Tellegen constitutive dyadic  $\underline{\underline{\mathbf{K}}}_L(\omega)$  which characterizes the linear response of the nonlinear material. In the case of a material whose linear properties are characterized by the four  $3 \times 3$  Tellegen constitutive dyadics  $\underline{\underline{\epsilon}}(\omega)$ ,  $\underline{\underline{\xi}}(\omega)$ ,  $\underline{\underline{\zeta}}(\omega)$ , and  $\underline{\underline{\mu}}(\omega)$ , we have

$$\underline{\underline{\mathbf{K}}}_L(\omega) = \begin{bmatrix} \underline{\underline{\epsilon}}(\omega) & \underline{\underline{\xi}}(\omega) \\ \underline{\underline{\zeta}}(\omega) & \underline{\underline{\mu}}(\omega) \end{bmatrix}. \quad (6.107)$$

The exclusively nonlinear contribution  $\underline{\mathbf{N}}_{NL}(\underline{r}, \omega)$  arises under the simultaneous stimulation of an ensemble of  $M > 1$  fields  $\underline{\mathbf{F}}(\underline{r}, \omega_m)$ , ( $m = 1, 2, \dots, M$ ). At the frequency  $\omega = \omega_{NL}$ , the  $j$ th component of  $\underline{\mathbf{N}}_{NL}(\underline{r}, \omega_{NL})$  may be expressed as

$$[\underline{\mathbf{N}}_{NL}(\underline{r}, \omega_{NL})]_j = \sum_{j_1=1}^6 \sum_{j_2=1}^6 \dots \sum_{j_M=1}^6 \left\{ \chi_{j_1 j_2 \dots j_M}^{NL}(\omega_{NL}; \mathcal{W}) \prod_{n=1}^M [\underline{\mathbf{F}}(\underline{r}, \omega_n)]_{j_n} \right\}, \quad (j \in [1, 6]), \quad (6.108)$$

with the constitutive properties being encapsulated by the nonlinear susceptibility tensor  $\chi_{j_1 j_2 \dots j_M}^{NL}(\omega_{NL}; \mathcal{W})$ . The set of angular frequencies  $\mathcal{W} = \{ \omega_1, \omega_2, \dots, \omega_M \}$ , wherein it is possible for two (or more) elements of  $\mathcal{W}$  to be the same. The angular frequency  $\omega_{NL}$  is determined by the elements of  $\mathcal{W}$  according to the sum

$$\omega_{NL} = \sum_{n=1}^M a_n \omega_n, \quad a_n = \pm 1, \quad (6.109)$$

on the understanding that if  $a_n = -1$ , then  $[\underline{\mathbf{F}}(\underline{r}, \omega_n)]_{j_n}$  in Eq. (6.108) is to be replaced by  $[\underline{\mathbf{F}}(\underline{r}, \omega_n)]_{j_n}^*$ . Thus, electromagnetic fields oscillating at angular frequency  $\omega_{NL}$  arise as a consequence of launching electromagnetic fields oscillating at angular frequencies  $\omega_m \in \mathcal{W}$  in the nonlinear material.

The constitutive relation (6.108) accommodates a vast range of nonlinear dielectric, magnetic and magnetoelectric properties [82–84], including a host of frequency-mixing processes [80, 85].

### 6.5.1 Nonlinearity of Quantum Electrodynamics Vacuum

Classically, vacuum (or free space) is regarded as a linear medium (not a material) which is characterized by the permittivity scalar  $\epsilon_0$  and permeability scalar  $\mu_0$ . As outlined in Section 6.4, when subjected to a gravitational field, the electromagnetic properties of classical vacuum are effectively the same as those of a linear bianisotropic material. We now depart from this classical viewpoint in order to present

an example of nonlinearity which is of fundamental significance: vacuum is electromagnetically nonlinear within the realm of quantum electrodynamics (QED) [2].

Suppose QED vacuum is subjected to a quasistatic magnetic field  $\underline{B}_{\text{qs}}(\underline{r}) = B_{\text{qs}}(\underline{r}) \hat{\underline{u}}$ , directed along the unit vector  $\hat{\underline{u}}$ . If the magnetic field is sufficiently strong, then the constitutive relations characterizing QED vacuum can be linearized, as follows. For definiteness, let us consider the case of optical fields  $\underline{\tilde{Z}}_{\text{opt}}(\underline{r}, t)$  ( $Z = E, B, D, H$ ) in the time domain. Provided that  $|\underline{\tilde{B}}_{\text{opt}}(\underline{r}, t)| \ll |\underline{B}_{\text{qs}}(\underline{r})| \forall \underline{r}$ , the optical fields are governed by the source-free Maxwell postulates represented as

$$\left. \begin{aligned} \nabla \times \underline{\tilde{E}}_{\text{opt}}(\underline{r}, t) + \frac{\partial}{\partial t} \underline{\tilde{B}}_{\text{opt}}(\underline{r}, t) &= \underline{0} \\ \nabla \times \underline{\tilde{H}}_{\text{opt}}(\underline{r}, t) - \frac{\partial}{\partial t} \underline{\tilde{D}}_{\text{opt}}(\underline{r}, t) &= \underline{0} \\ \nabla \bullet \underline{\tilde{D}}_{\text{opt}}(\underline{r}, t) &= 0 \\ \nabla \bullet \underline{\tilde{B}}_{\text{opt}}(\underline{r}, t) &= 0 \end{aligned} \right\}. \quad (6.110)$$

According to the QED theory—which involves implementing the Heisenberg–Euler effective Lagrangian of the electromagnetic field [86, 87]—the optical fields appearing in Eqs. (6.110) satisfy the Boys–Post constitutive equations [88]

$$\left. \begin{aligned} \underline{\tilde{D}}_{\text{opt}}(\underline{r}, t) &= \underline{\epsilon}_{\text{QV}}(\underline{r}) \bullet \underline{\tilde{E}}_{\text{opt}}(\underline{r}, t) \\ \underline{\tilde{H}}_{\text{opt}}(\underline{r}, t) &= \underline{\mu}_{\text{QV}}^{-1}(\underline{r}) \bullet \underline{\tilde{B}}_{\text{opt}}(\underline{r}, t) \end{aligned} \right\}. \quad (6.111)$$

Here the permittivity and inverse permeability dyadics are both of the uniaxial type, that is,

$$\underline{\epsilon}_{\text{QV}}(\underline{r}) = \epsilon_0 \left\{ \left[ 1 - \frac{8}{\mu_0} \Theta_{\text{QV}} B_{\text{qs}}^2(\underline{r}) \right] \underline{\underline{I}} + \frac{28}{\mu_0} \Theta_{\text{QV}} B_{\text{qs}}^2(\underline{r}) \hat{\underline{u}} \hat{\underline{u}} \right\}, \quad (6.112)$$

$$\underline{\mu}_{\text{QV}}^{-1}(\underline{r}) = \frac{1}{\mu_0} \left\{ \left[ 1 - \frac{8}{\mu_0} \Theta_{\text{QV}} B_{\text{qs}}^2(\underline{r}) \right] \underline{\underline{I}} - \frac{16}{\mu_0} \Theta_{\text{QV}} B_{\text{qs}}^2(\underline{r}) \hat{\underline{u}} \hat{\underline{u}} \right\}, \quad (6.113)$$

wherein the scalar parameter

$$\Theta_{\text{QV}} = \frac{q_{\text{el}}^4 \hbar}{45(4\pi\epsilon_0)^2 m_{\text{el}}^4 c_0^7} = 8.3229 \times 10^{-32} \text{ kg}^{-1} \text{ m s}^2, \quad (6.114)$$

with the electronic charge  $q_{\text{el}} = 1.6022 \times 10^{-19}$  C, the electronic mass  $m_{\text{el}} = 9.1096 \times 10^{-31}$  kg, and the reduced Planck constant  $\hbar = 1.0546 \times 10^{-34}$  J s.

Thus, the optical properties of QED vacuum are equivalent to those of a spatiotemporally local, spatially nonhomogeneous, uniaxial dielectric–magnetic material. However, the degree of anisotropy exhibited by QED vacuum is exceedingly small, even for the largest values  $|\underline{B}_{qs}(\underline{r})|$  that can be practicably achieved in the laboratory, as may be inferred from the tiny value of  $\Theta_{QV}$  given in Eq. (6.114). Accordingly, a direct measurement of QED vacuum anisotropy poses formidable challenges to experimentalists [89, 90].

However, the electromagnetic properties of QED vacuum may be accessible to experiment by indirect means, via a material analogue that is electromagnetically equivalent to QED vacuum subject to an affine transformation of the spatial coordinates. That is, under the affine transformation

$$\underline{r} \mapsto \underline{r}' \equiv \underline{\underline{J}} \bullet \underline{r}, \quad (6.115)$$

where the transformation dyadic

$$\underline{\underline{J}} = \beta_1 \left[ \frac{I}{\underline{r}} - \frac{1}{|\underline{B}_{qs}(\underline{r})|^2} \underline{B}_{qs}(\underline{r}) \underline{B}_{qs}(\underline{r}) \right] + \beta_2 \underline{B}_{qs}(\underline{r}) \underline{B}_{qs}(\underline{r}), \quad (6.116)$$

the uniaxial dielectric–magnetic nature of QED vacuum may be preserved but the degree of anisotropy may be greatly exaggerated provided that appropriate values are selected for the two scalar parameters  $\beta_1$  and  $\beta_2$ . Indeed, such a material analogue may be conceived as a HCM, with an inverse homogenization procedure [78] yielding appropriate values for  $\beta_1$  and  $\beta_2$  [91].

Parenthetically, notice that if one sets  $\hbar = 0$ , then the constitutive relations of QED vacuum (6.111) reduce to those of classical vacuum (6.100) for which the quasistatic magnetic field has no influence on the optical fields.

## 6.6 CLOSING REMARKS

A survey of the mathematical framework for characterizing the electromagnetic properties of materials, in terms of constitutive relations and dyadics, is presented in this chapter. Constraints and specializations of the constitutive dyadics are discussed for linear materials. The classifications of isotropy, anisotropy, and bianisotropy are defined and illustrated for both spatially homogeneous and spatially nonhomogeneous materials. A brief general overview of nonlinearity, within the setting of bianisotropic materials, is provided too. This mathematical framework is essential to our understanding of materials and crucial to future technological developments. Furthermore, fundamental physical studies of scenarios in special and general relativity, and in QED, may be facilitated by exploiting electromagnetic constitutive relations to construct material analogues.

## REFERENCES

- [1] J. Z. Buchwald, *From Maxwell to Microphysics: Aspects of Electromagnetic Theory in the Last Quarter of the Nineteenth Century* (University of Chicago Press, Chicago, IL, 1985).
- [2] J. D. Jackson, *Classical Electrodynamics*, 3rd ed. (John Wiley & Sons, Inc., New York, 1999).
- [3] M. Bornatici and O. Maj, “The effective polarization and magnetization fields in terms of charge-current densities,” *Phys. Scr.* **73**, 160–163 (2006).
- [4] A. Lakhtakia, “Covariances and invariances of the Maxwell postulates,” in *Advanced Electromagnetism: Foundations, Theory and Applications*, edited by T. W. Barrett and D. M. Grimes (World Scientific, Singapore, 1995), pp. 390–410.
- [5] T. G. Mackay and A. Lakhtakia, *Electromagnetic Anisotropy and Bianisotropy: A Field Guide* (World Scientific, Singapore, 2010).
- [6] W. S. Weiglhofer, “Constitutive characterization of simple and complex mediums,” in *Introduction to Complex Mediums for Optics and Electromagnetics*, edited by W. S. Weiglhofer and A. Lakhtakia (SPIE Press, Bellingham, WA, 2003), pp. 27–61.
- [7] S. Ponti, C. Oldano, and M. Becchi, “Bloch wave approach to the optics of crystals,” *Phys. Rev. E* **64**, 021704 (2001).
- [8] G. B. Arfken and H. J. Weber, *Mathematical Methods for Physicists*, 4th ed. (Academic Press, London, 1995).
- [9] J. A. Kong, *Electromagnetic Wave Theory* (John Wiley & Sons, New York, 1986).
- [10] W. S. Weiglhofer, “A perspective on bianisotropy and *Bianisotropics '97*,” *Int. J. Appl. Electromagn. Mech.* **9**, 93–101 (1998).
- [11] J. S. Toll, “Causality and the dispersion relation: logical foundations,” *Phys. Rev.* **104**, 1760–1770 (1956).
- [12] J. Hilgevoord, *Dispersion Relations and Causal Descriptions* (North-Holland, Amsterdam, 1962).
- [13] E. J. Post, *Formal Structure of Electromagnetics* (Dover Press, New York, 1997).
- [14] C. F. Bohren and D. R. Huffman, *Absorption and Scattering of Light by Small Particles* (John Wiley & Sons Inc., New York, 1983).
- [15] L. Ward, *The Optical Constants of Bulk Materials and Films*, 2nd ed. (Institute of Physics, Bristol, 2000).
- [16] L. Onsager, “Reciprocal relations in irreversible processes. I,” *Phys. Rev.* **37**, 405–426 (1931).
- [17] L. Onsager, “Reciprocal relations in irreversible processes. II,” *Phys. Rev.* **38**, 2265–2279 (1931).
- [18] H. B. G. Casimir, “On Onsager's principle of microscopic reversibility,” *Rev. Mod. Phys.* **17**, 343–350 (1945).
- [19] C. Altman and K. Suchy, *Reciprocity, Spatial Mapping and Time Reversal in Electromagnetics* (Kluwer Academic Publishers, Dordrecht, 1991).
- [20] A. Lakhtakia and R. A. Depine, “On Onsager relations and linear electromagnetic materials,” *Int. J. Electron. Commun. (AEÜ)* **59**, 101–104 (2005).
- [21] A. Lakhtakia, “On the genesis of Post constraint in modern electromagnetism,” *Optik* **115**, 151–158 (2004).

- [22] A. Lakhtakia and W. S. Weiglhofer, “Lorentz covariance, Occam’s razor, and a constraint on linear constitutive relations,” *Phys. Lett. A* **213**, 107–111 (1996). Corrections: **222**, 459 (1996).
- [23] A. Lakhtakia and W. S. Weiglhofer, “Constraint on linear, spatiotemporally nonlocal, spatiotemporally nonhomogeneous constitutive relations,” *Int. J. Infrared Millim Waves* **17**, 1867–1878 (1996).
- [24] O. L. de Lange and R. E. Raab, “Post’s constraint for electromagnetic constitutive relations,” *J. Opt. A: Pure Appl. Opt.* **3**, L23–L26 (2001).
- [25] F. W. Hehl, Y. N. Obukhov, J.-P. Rivera, and H. Schmid, “Relativistic analysis of magnetoelectric crystals: extracting a new 4-dimensional  $P$  odd and  $T$  odd pseudoscalar from  $\text{Cr}_2\text{O}_3$  data,” *Phys. Lett. A* **372**, 1141–1146 (2007).
- [26] A. Lakhtakia, “Remarks on the current status of the Post constraint,” *Optik* **120**, 422–424 (2009).
- [27] V. H. Rumsey, “Reaction concept in electromagnetic theory,” *Phys. Rev.* **94**, 1483–1491 (1954). Corrections: **95**, 1705 (1954).
- [28] C. M. Krowne, “Electromagnetic theorems for complex anisotropic media,” *IEEE Trans. Antennas Propagat.* **32**, 1224–1230 (1984).
- [29] H. C. Chen, *Theory of Electromagnetic Waves* (McGraw–Hill, New York, 1983).
- [30] W. S. Weiglhofer and A. Lakhtakia, “On causality requirements for material media,” *Arch Elektron Übertrag* **50**, 389–391 (1996).
- [31] S. M. Barnett, “Resolution of the Abraham–Minkowski dilemma,” *Phys. Rev. Lett.* **104** 070401 (2010).
- [32] E. L. Tan, “Reduced conditions for the constitutive parameters of lossy bi–anisotropic media,” *Microw. Opt. Technol. Lett.* **41**, 133–135 (2004).
- [33] S. A. Ramakrishna and T. M. Grzegorczyk, *Physics and Applications of Negative Refractive Index Materials* (CRC Press, Boca Raton, 2008).
- [34] R. A. Depine and A. Lakhtakia, “A new condition to identify isotropic dielectric-magnetic materials displaying negative phase velocity,” *Microw. Opt. Technol. Lett.* **41**, 315–316 (2004).
- [35] A. Lakhtakia, *Beltrami Fields in Chiral Media* (World Scientific, Singapore, 1994).
- [36] A. Lakhtakia (ed.), *Selected Papers on Natural Optical Activity* (SPIE Optical Engineering Press, Bellingham, WA, 1990).
- [37] M. Born and E. Wolf, *Principles of Optics*, 7th (expanded) ed. (Cambridge University Press, Cambridge, 1999).
- [38] T. G. Mackay and W. S. Weiglhofer, “Homogenization of biaxial composite materials: dissipative anisotropic properties,” *J. Opt. A: Pure Appl. Opt.* **2**, 426–432 (2000).
- [39] J. F. Nye, *Physical Properties of Crystals* (Oxford University Press, Oxford, 1985).
- [40] N. W. Ashcroft and N. D. Mermin, *Solid State Physics* (Saunders, Philadelphia, PA, 1976).
- [41] L. B. Felsen and N. Marcuvitz, *Radiation and Scattering of Waves* (IEEE Press, Piscataway, NJ, 1994).
- [42] W. S. Weiglhofer, “A flavour of constitutive relations: the linear regime,” in *Advances in Electromagnetics of Complex Media and Metamaterials*, edited by S. Zouhdi, A. Sihvola, and M. Arsalane (Kluwer, Dordrecht, 2003), pp. 61–80.

- [43] B. Lax and K. J. Button, *Microwave Ferrites and Ferrimagnetics* (McGraw-Hill, New York, 1962).
- [44] T. H. O'Dell, *The Electrodynamics of Magneto-Electric Media* (North-Holland, Amsterdam, 1970).
- [45] H. Schmid, "Magnetolectric effects in insulating magnetic materials," in *Introduction to Complex Mediums for Optics and Electromagnetics*, edited by W. S. Weiglhofer and A. Lakhtakia (SPIE Press, Bellingham, WA, 2003), pp. 167–195.
- [46] T. G. Mackay, "Linear and nonlinear homogenized composite media as metamaterials," *Electromagnetics* **25**, 461–481 (2005).
- [47] T. G. Mackay and A. Lakhtakia, "Negative refraction, negative phase velocity, and counterposition in bianisotropic materials and metamaterials," *Phys. Rev. B* **79**, 235121 (2009).
- [48] W. Schleich and M. O. Scully, "General relativity and modern optics," in *New Trends in Atomic Physics*, edited by G. Grynpberg and R. Stora (Elsevier, Amsterdam, 1984), pp. 995–1124.
- [49] T. G. Mackay and W. S. Weiglhofer, "A review of homogenization studies for biaxial bianisotropic materials," in *Advances in Electromagnetics of Complex Media and Metamaterials*, edited by S. Zouhdi, A. Sihvola, and M. Arsalane (Kluwer, Dordrecht, 2003), pp. 211–228.
- [50] A. Lakhtakia and W. S. Weiglhofer, "Electromagnetic waves in a material with simultaneous mirror-conjugated and racemic chirality characteristics," *Electromagnetics* **20**, 481–488 (2000).
- [51] G. Gorodetsky, R. M. Hornreich, and B. M. Wanklyn, "Statistical mechanics and critical behavior of the magnetoelectric effect in  $\text{GdVO}_4$ ," *Phys. Rev. B* **8**, 2263–2267 (1973).
- [52] A. H. Cooke, S. J. Swithenby, and M. R. Wells, "Magnetolectric measurements on holmium phosphate,  $\text{HoPO}_4$ ," *Int. J. Magnetism* **4**, 309–312 (1973).
- [53] J. C. Bose, "On the rotation of plane of polarization of electric waves by a twisted structure," *Proc. R. Soc. Lond.* **63**, 146–152 (1898).
- [54] K. W. Whites and C. Y. Chung, "Composite uniaxial bianisotropic chiral materials characterization: comparison of prediction and measured scattering," *J. Electromag. Waves Appl.* **11**, 371–394 (1997).
- [55] N. Engheta, D. L. Jaggard, and M. W. Kowarz, "Electromagnetic waves in Faraday chiral media," *IEEE Trans. Antennas Propagat.* **40**, 367–374 (1992).
- [56] R. E. Collin, *Foundations for Microwave Engineering* (McGraw-Hill, New York, 1966).
- [57] W. S. Weiglhofer, A. Lakhtakia, and B. Michel, "On the constitutive parameters of a chiroferrite composite medium," *Microw. Opt. Technol. Lett.* **18**, 342–345 (1998).
- [58] W. S. Weiglhofer and T. G. Mackay, "Numerical studies of the constitutive parameters of a chiroplasma composite medium," *Arch. Elektr. Übertrag.* **54**, 259–265 (2000).
- [59] W. S. Weiglhofer and A. Lakhtakia, "The correct constitutive relations of chiroplasmas and chiroferrites," *Microw. Opt. Technol. Lett.* **17**, 405–408 (1998).
- [60] T. G. Mackay, A. Lakhtakia, and W. S. Weiglhofer, "Ellipsoidal topology, orientation diversity and correlation length in bianisotropic composite media," *Arch. Elektr. Übertrag.* **55**, 243–251 (2001).
- [61] A. Serdyukov, I. Semchenko, S. Tretyakov, and A. Sihvola, *Electromagnetics of Bi-Anisotropic Materials* (Gordon and Breach, Amsterdam, 2001).

- [62] M. M. I. Saadoun and N. Engheta, “A reciprocal phase shifter using novel pseudochiral or omega medium,” *Microw. Opt. Technol. Lett.* **5**, 184–188 (1992).
- [63] X. Chen, B.-I. Wu, J. A. Kong, and T. M. Grzegorczyk, “Retrieval of the effective constitutive parameters of bianisotropic materials,” *Phys. Rev. E* **71**, 046610 (2005). Corrections: **73**, 019905(E) (2006).
- [64] D. Censor, “Electrodynamics, topsy–turvy special relativity, and generalized Minkowski constitutive relations for linear and nonlinear systems,” *Prog. Electromagn. Res.* **18**, 261–284 (1998).
- [65] S. Chandrasekhar, *Liquid Crystals*, 2nd ed. (Cambridge University Press, Cambridge, 1992).
- [66] P. G. de Gennes and J. A. Prost, *The Physics of Liquid Crystals*, 2nd ed. (Clarendon Press, Oxford, 1993).
- [67] I. Abdulhalim, “Light propagation along the helix of chiral smectics and twisted nematics,” *Opt. Commun.* **64**, 443–448 (1987).
- [68] V. C. Venugopal and A. Lakhtakia, “Sculptured thin films: conception, optical properties and applications,” in *Electromagnetic Fields in Unconventional Materials and Structures*, edited by O. N. Singh and A. Lakhtakia (John Wiley & Sons, New York, 2000), pp. 151–216.
- [69] A. Lakhtakia and R. Messier, *Sculptured Thin Films: Nanoengineered Morphology and Optics* (SPIE Press, Bellingham, WA, 2005).
- [70] A. Lakhtakia and W. S. Weiglhofer, “On light propagation in helicoidal bianisotropic mediums,” *Proc. R. Soc. Lond. A* **448**, 419–437 (1995). Corrections: **454**, 3275 (1998).
- [71] R. d’Inverno, *Introducing Einstein’s Relativity* (Clarendon Press, Oxford, 1992).
- [72] L. D. Landau and E. M. Lifshitz, *The Classical Theory of Fields* (Clarendon Press, Oxford, 1975), Section 90.
- [73] G. V. Skrotskii, “The influence of gravitation on the propagation of light,” *Soviet Phys.–Dokl.* **2**, 226–229 (1957).
- [74] J. Plébanski, “Electromagnetic waves in gravitational fields,” *Phys. Rev.* **118**, 1396–1408 (1960).
- [75] A. Lakhtakia and T. G. Mackay, “Towards gravitationally assisted negative refraction of light by vacuum,” *J. Phys. A: Math. Gen.* **37**, L505–L510 (2004). Corrections: **37**, 12093 (2004).
- [76] T. G. Mackay and A. Lakhtakia, “Towards a metamaterial simulation of a spinning cosmic string,” *Phys. Lett. A* **374**, 2305–2308 (2010).
- [77] T. G. Mackay and A. Lakhtakia, “Towards a realization of Schwarzschild-(anti-)de Sitter spacetime as a particulate metamaterial,” *Phys. Rev. B* **83**, 195424 (2011).
- [78] T. G. Mackay and A. Lakhtakia, “Determination of constitutive and morphological parameters of columnar thin films by inverse homogenization,” *J. Nanophoton.* **4**, 041535 (2010).
- [79] N. Bloembergen, *Nonlinear Optics*, 4th ed. (World Scientific, Singapore, 1996).
- [80] R. W. Boyd, *Nonlinear Optics*, 3rd ed. (Academic Press, London, 2008).
- [81] A. Lakhtakia and W. S. Weiglhofer, “Maxwell Garnett formalism for weakly nonlinear, bianisotropic, dilute, particulate composite media,” *Int. J. Electron.* **87**, 1401–1408 (2000).

- [82] S. Kielich and A. Piekarz, “Frequency– and spatially variable electric and magnetic polarizations induced in nonlinear media by electromagnetic fields,” *Acta Physica Polon.* **29**, 875–898 (1966).
- [83] P. W. Atkins and L. D. Barron, “Quantum field theory of optical birefringence phenomena I. Linear and nonlinear optical rotation,” *Proc. R. Soc. Lond. A* **304**, 303–317 (1968).
- [84] W. S. Weiglhofer and A. Lakhtakia, “Mediation of nonlinear polarization by the magnetic field in a composite medium with a chiral component,” *Microw. Opt. Technol. Lett.* **13**, 285–287 (1996).
- [85] T. Kobayashi, “Introduction to nonlinear optical materials,” *Nonlin. Opt.* **1**, 91–117 (1991).
- [86] W. Heisenberg and H. Euler, “Folgerungen aus der Diracschen Theorie des Positrons,” *Z Phys.* **98**, 714–732 (1936).
- [87] J. Schwinger, “On gauge invariance and vacuum polarization,” *Phys. Rev.* **82**, 664–679 (1951).
- [88] S. L. Adler, “Photon splitting and photon dispersion in a strong magnetic field,” *Ann. Phys. (NY)* **67**, 599–647 (1971).
- [89] E. Iacopini and E. Zavattini, “Experimental method to detect the vacuum birefringence induced by a magnetic field,” *Phys. Lett. B* **85**, 151–154 (1979).
- [90] E. Zavattini, G. Zavattini, G. Ruoso, E. Polacco, E. Milotti, M. Karuza, U. Gastaldi, G. Di Domenico, F. Della Valle, R. Cimino, et al., “Experimental observation of optical rotation generated in vacuum by a magnetic field,” *Phys. Rev. Lett.* **96**, 110406 (2006). See also: Editorial Note, *Phys. Rev. Lett.* **99**, 129901 (2007).
- [91] T. G. Mackay and A. Lakhtakia, “Towards an experimental realization of affinely transformed linearized quantum electrodynamics vacuum via inverse homogenization,” *J. Opt. Soc. Amer. B* **29**, 1680–1684 (2012).



---

# 7

---

## SURFACE AND CAVITY NANOPHOTONICS

MOHAMED BABIKER

*Department of Physics, University of York, York, UK*

### 7.1 INTRODUCTION

The interfaces separating dissimilar materials in contact have played crucial roles in many physical phenomena over a wide range of length scales and have led to the realization of a number of important applications. Not surprisingly, therefore, nanophysics—the physics of nanomaterials—would be dominated by the presence of surfaces. The subject of nanophysics spans a broad range of phenomena far beyond the remit of this chapter, which is narrowly focused on surface nanophotonics. We define the nanophysics of concern in this chapter as the area dealing with quantum processes involving photons, both virtual and real, which are influenced by the nanoscale environment and their interaction with matter in the vicinity of the interfaces. The realization that the presence of matter at the nanoscale near a surface leads to observable changes of its basic properties has been known for a considerable time.

Purcell [1] was the first to suggest that the emission rate of an excited emitter should be modified or even completely suppressed when the emitter is placed inside a cavity [2, 3]. Quantum theory would describe the modification of the de-excitation phenomenon as follows: Let the emitter-field combined state be an initial excited state, denoted by  $|i, \{0\}\rangle$ , with  $i$  indicating an upper energy state of the emitter of energy  $W_i$ , whereas  $|\{0\}\rangle$  represents the vacuum field state with zero photons in the cavity. The final state is  $|f; Q\rangle$ , in which the emitter state is changed to a lower

energy state  $f$  of energy  $W_f$  and a single mode  $|Q\rangle$  of frequency  $\omega_Q$  has been emitted. Here, we set up the formalism which describes the de-excitation process and detail the underlying principles and the main results of this striking phenomenon. Recent advances have shown that the emitter position and its characteristics such as dipole orientation can be experimentally determined with considerable accuracy [4–10] and it is possible to *in situ* control single quantum systems such as atoms, molecules, and quantum wells [11].

It is clear, however, that, in addition to the changes of de-excitation rates, the physics involving surfaces and cavities involves many other phenomena depending on the materials forming the cavity and the surface geometry. Furthermore, structured surfaces, in principle, of any required shape, can now be realized using lithographic and deposition techniques [12] and remarkable advances have recently been made in detection techniques.

Of special interest are the surface photonic effects involving quantum correlations. Here, a system of emitters interacts with each other via the cavity fields which conform to the type and surface geometry. The simplest correlations arise between two identical emitters. If one emitter is excited and the other in its ground state, the two-emitter system can either be in one of two possible quantum pair states, either a symmetric or an antisymmetric state, and such pair states are identified as two of Bell states [13]. The effects of the surface on pair correlations have been shown to lead to further enhancements and suppressions of the emission process [14–17].

The single surface is the simplest cavity. Here, real space is divided by a planar boundary along one direction. Two or more planar surfaces generate an open or closed cavity. The most widely discussed open cavities that are created using two planar surfaces are the parallel plates cavity and when two planes form a wedge of a given opening angle [18–20]. Open and closed cylindrical cavities have also been discussed [21] and finally a thin metallic or dielectric film can form a nanocavity [22, 23]. If such a film is sandwiched between two thick dielectric slabs, we have symmetric and asymmetric cavities. Quantum emitters localized inside, on the same side or on opposite sides of the film, experience cavity effects, including pair correlations.

There are other cavities of great variety, so we must restrict our attention to the simplest situations in which the formalism is manageable. In particular, we will focus on cavities formed by the intersection of the planar surfaces of the same material in contact with vacuum, or a dielectric where quantum systems are localized. We are concerned with quantum effects of contemporary relevance, namely the one-center system and the two-center correlations. Besides its significance as a quantum effect in its own right, the process involving two-center correlations is of relevance to quantum gates in quantum computing [13] and the involvement of surfaces has been identified as of practical significance for scalable quantum computing. It is well known that in a space free from boundaries a pair of identical electric dipole emitters one of which is excited would discharge the excitation in a manner dependent on the relative dipole orientations and their separation apart, and when the emitters are at close proximity, the de-excitation process becomes either superradiant or subradiant. The proximity of the system to surfaces adds further complexity, with possibilities of increased superradiance and subradiance.

This chapter begins with a brief outline of field quantization in general and moves on to consider the de-excitation process for a number of representative cavities. It also deals with correlation effects in the presence of cavities and the Dicke-type phenomena [24] that would arise in this context.

## 7.2 BASIC FORMALISM

### 7.2.1 Hamiltonian and Essential States

Formally, in general, the quantum mechanical description of the processes mentioned above begins with the Hamiltonian which we write as follows:

$$\hat{H} = \hat{H}_a + \hat{H}_f + \hat{H}_{\text{int}}, \quad (7.1)$$

where  $\hat{H}_a$  is the unperturbed Hamiltonian of the two-level system such that

$$\hat{H}_a |i\rangle = W_i |i\rangle; \quad \langle i|j\rangle = \delta_{ij}; \quad (i,j = 1, 2). \quad (7.2)$$

The two-level model is the simplest model for the atom, molecule, or quantum dot, but it is known to be suitable for the description of a number of processes, most notably the emission and absorption of quanta. The field states, however, require quantization before the effects of the interaction can be properly evaluated. The quantized form of the electric field can be written as follows:

$$\hat{\mathbf{E}}(\mathbf{r}, t) = \sum_Q \{ \mathbf{F}(\mathbf{r}, t, Q) \hat{a}_Q + h.c. \}, \quad (7.3)$$

where *h.c.* stands for “Hermitian conjugate”;  $\mathbf{F}(\mathbf{r}, t, Q)$  is the electric field distribution function of the mode  $Q$  and  $\hat{a}_Q$  is the boson annihilation operator of the mode satisfying boson commutation rules. The main requirement to be satisfied by the electric field function for the mode  $Q$  is that the electromagnetic field energy is normalized such that

$$\epsilon_0 \epsilon \int_V \mathbf{F}(\mathbf{r}, t, Q) \cdot \mathbf{F}^*(\mathbf{r}, t, Q) dV = \frac{1}{2} \hbar \omega_Q, \quad (7.4)$$

where  $V$  is a cavity quantization volume. Finally, the interaction Hamiltonian  $\hat{H}_{\text{int}}$  is defined by

$$\hat{H}_{\text{int}} = -\hat{\boldsymbol{\mu}} \cdot \hat{\mathbf{E}}(\mathbf{r}, t), \quad (7.5)$$

where  $\hat{\boldsymbol{\mu}}$  is the dipole moment vector operator of the atom such that the matrix elements between the two atomic states are given by

$$\langle 1 | \hat{\boldsymbol{\mu}} | 2 \rangle = \boldsymbol{\mu}; \quad \langle i | \hat{\boldsymbol{\mu}} | i \rangle = 0; \quad i = 1, 2. \quad (7.6)$$

In general, the de-excitation rate of a dipole-active emitter accompanied by photon emission is given by a standard result of time-dependent perturbation theory known as the Fermi golden rule formula [25]. The Fermi golden rule formula for the photon emission rate  $\Gamma$  can be written as

$$\Gamma = \frac{2\pi}{\hbar^2} \sum_Q \left| \langle i; \{0\} | \hat{H}_{\text{int}} | f; \{Q\} \rangle \right|^2 \delta [\omega_0 - \omega(Q)], \quad (7.7)$$

where  $\omega_0 = (W_i - W_f)/\hbar$ . Perturbation theory also predicts the existence of an energy shift  $\Delta^{(i)}(z)$  for a quantum system at distance  $z$  from the planar surface. This is given by

$$\Delta^{(i)}(z) = \sum_{j \neq i} \sum_Q \left\{ \frac{|\langle i; \{0\} | \hat{H}_{\text{int}} | j, Q \rangle|^2}{W_i - W_j - \hbar\omega(Q)} \right\} - R_c, \quad (7.8)$$

where  $R_c$  is a counter-term representing the shift in unbounded space.

For an emitter in unbounded space,  $R_c = 0$ , and the mode functions  $F(\mathbf{r}, t, Q)$  are plane waves in three-dimensional space. There are two wave polarizations with unit vectors  $\tilde{\mathbf{e}}_\eta$  with  $\eta = 1, 2$ . In this case,  $Q$  stands for  $(\mathbf{k}, \eta)$ , where  $\mathbf{k}$  is the wavevector which is orthogonal to both  $\tilde{\mathbf{e}}_1$  and  $\tilde{\mathbf{e}}_2$ . The dispersion relation is  $k = \omega\sqrt{\epsilon}/c$ . The mode functions are

$$F(\mathbf{r}, t, \mathbf{k}, \eta) = i \left( \frac{\hbar\omega}{2\epsilon\epsilon_0 V} \right)^{1/2} \tilde{\mathbf{e}}_\eta e^{i(\mathbf{k}\cdot\mathbf{r} - \omega t)}. \quad (7.9)$$

The evaluation of the emission rate in unbounded space, denoted by  $\Gamma_0$ , leads to the well-known result

$$\Gamma_0 = \frac{\omega_0^3 \mu^2 S(\omega_0)}{3\hbar\pi\epsilon_0 c^3} \sqrt{\epsilon(\omega_0)}, \quad (7.10)$$

where  $S(\omega_0)$  is a factor representing the local field correction for an emitter localized within the dielectric. There are several forms of  $S(\omega_0)$  in the literature, but here we shall adopt the Glauber–Lewinstein’s expression [26].

$$S(\omega_0) = \left( \frac{3}{2\epsilon(\omega_0) + 1} \right)^2 \quad (7.11)$$

In free space vacuum  $S = 1$ .

For a cavity, the field states are the normal modes which conform to the presence of interfaces and the topology of the space which forms the cavity. The spectrum of the allowed frequencies is also a function of the cavity nature, shape, and dimension. It follows that the emission rate as well as the energy shift would be modified when the emitter is placed inside the cavity.

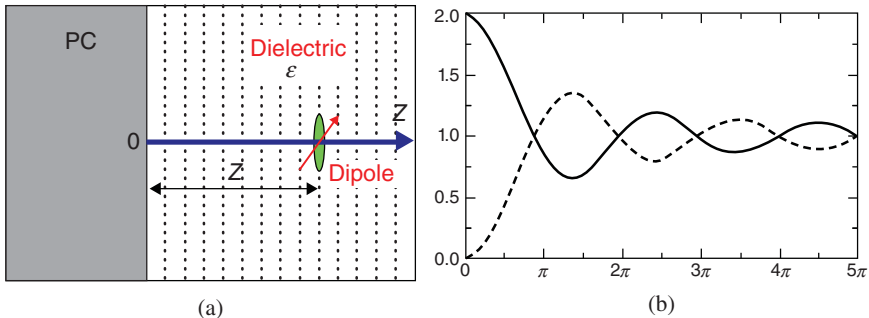


**FIGURE 7.1** (a) Schematic representation of a dipole emitter at distance  $z$  from a planar perfect conductor (PC) surface. (b) The variation of the emission rate (in units of  $\Gamma_0$ ) with distance (in units of  $k_0 z$ ), with the full (dashed) curve representing the case of the dipole perpendicular (parallel) to the surface.

### 7.2.2 Single Interface—the Simplest Open Cavity

The simplest cavity is formed by a single planar surface as shown in Figure 7.1a separating two different media, namely a dielectric half-space  $z > 0$  of dielectric constant  $\epsilon$  in contact with another (here taken as a perfect conductor) occupying the half space  $z < 0$ . An excited dipole emitter (identified as a dipole) positioned at a distance  $z$  from the surface would discharge its excitation energy at a rate that depends on its location near the surface, experiencing either an enhanced rate (superradiance) or a diminished rate (subradiance). These markedly different types of behavior depend not just on the position, but also on the orientation of the transition dipole moment relative to the surface. The outline of the physics describing these features, are as follows.

The electromagnetic modes for the scenario in Figure 7.1a can now be discussed with reference to the general scheme described above. The perfect conductor is taken to exclude all electromagnetic fields from its interior, and so Maxwell's equations demand that at the surface  $z = 0$  the tangential components of the electric and magnetic field vectors must vanish identically everywhere on the surface. In that case, the modes  $Q$  are identified with the states  $|Q\rangle \equiv |\{\mathbf{k}_{||}, k_z, \eta\}\rangle$  and the quantized electric field operator can be written as

$$\hat{E}(\mathbf{r}, t) = \int d^2\mathbf{k}_{||} \int_0^\infty dk_z \left\{ \mathbf{F}_s(\mathbf{k}_{||}, k_z; \mathbf{r}, t) \hat{a}_s + \mathbf{F}_p(\mathbf{k}_{||}, k_z; \mathbf{r}, t) \hat{a}_p + h.c. \right\}, \quad (7.12)$$

where  $\mathbf{F}_s$  and  $\mathbf{F}_p$  are the mode functions for s- and p-polarizations corresponding to index  $\eta = s, p$ . The explicit forms of these mode functions are as follows:

$$\mathbf{F}_s(\mathbf{k}_{||}, k_z; \mathbf{r}, t) = A_s (\hat{\mathbf{k}}_{||} \times \hat{\mathbf{z}}) \sin(k_z z) e^{i(\mathbf{k}_{||} \cdot \mathbf{r}_{||} - \omega t)}, \quad (7.13)$$

$$\mathbf{F}_p(\mathbf{k}_{||}, k_z; \mathbf{r}, t) = A_p \left\{ \hat{\mathbf{k}}_{||} \left( \frac{ik_z}{\omega} \right) \sin(k_z z) - \hat{\mathbf{z}} \left( \frac{k_{||}}{\omega} \right) \cos(k_z z) \right\} e^{i(\mathbf{k}_{||} \cdot \mathbf{r}_{||} - \omega t)}, \quad (7.14)$$

where  $A_s$  and  $A_p$  are overall energy normalization factors emerging from the application of the condition in Eq. (7.4).

As for the unbounded space case, the de-excitation of the emitter accompanied by quantum emission is described by the rate of emission  $\Gamma$  and derives from the Fermi golden rule formula

$$\Gamma = \frac{2\pi}{\hbar^2} \sum_{\eta} \int d^2 k_{||} \int_0^{\infty} dk_z \left| \langle i; \{0\} | \hat{H}_{\text{int}} | f; \{k_{||}, k_z, \eta\} \rangle \right|^2 \delta [\omega_0 - \omega(k_{||}, k_z)], \quad (7.15)$$

where  $\omega_0 = (W_i - W_f)/\hbar$ . Perturbation theory also predicts the existence of a level energy shift  $\Delta^{(i)}(z)$ , of level  $i$  for a quantum system at a distance  $z$  from the planar surface. This is given by

$$\Delta^{(i)}(z) = \sum_{j \neq i} \sum_{(\eta=s,p)} \int_0^{\infty} dk_z \int d^2 k_{||} \left\{ \frac{|\langle i; \{0\} | \hat{H}_{\text{int}} | j; \{k_{||}, k_z, \eta\} \rangle|^2}{W_i - W_j - \hbar \omega(k_{||}, k_z)} \right\} - R_c, \quad (7.16)$$

where, as above,  $\hat{H}_{\text{int}} = -\hat{\mu} \cdot \hat{E}(\mathbf{R}, t)$  is the interaction Hamiltonian with  $\hat{\mu}$  the electric dipole moment operator and  $\hat{E}(\mathbf{R}, t)$  is the electric field vector at the position of the dipole. Here, the counter term  $R_c$  is defined formally as the shift in unbounded space. The field states are the normal modes which conform to the presence of the interface. Clearly the emission rate as well as the energy shift is bound to be modified when the emitter is placed near the surface.

For a dipole oriented parallel to the surface the de-excitation rate is denoted  $\Gamma_{||}$  and is found to have the functional form

$$\begin{aligned} \Gamma_{||} &= \Gamma_0 \left\{ 1 - \frac{3}{2} \left( \frac{\sin(2k_0 z)}{(2k_0 z)} + \frac{\cos(2k_0 z)}{(2k_0 z)^2} - \frac{\sin(2k_0 z)}{(2k_0 z)^3} \right) \right\} \\ &= \frac{1}{3} \Gamma_0 \{ J_2(2k_0 z) - 2J_0(2k_0 z) \}, \end{aligned} \quad (7.17)$$

where  $J_0$  and  $J_2$  are Bessel functions and  $\Gamma_0$  is the de-excitation rate for the dipole emitter in the absence of the surface, given by Eq. (7.10) and  $k_0 = \omega_0 \sqrt{\epsilon}/c$ , when the dipole vector is normal to the surface the de-excitation rate is

$$\Gamma_{||} = \Gamma_0 \left\{ 1 - 3 \left( \frac{\cos(2k_0 z)}{(2k_0 z)^2} - \frac{\sin(2k_0 z)}{(2k_0 z)^3} \right) \right\} = \Gamma_0 \{ 1 + J_2(2k_0 z) + J_0(2k_0 z) \}. \quad (7.18)$$

Figure 7.1b shows the variation of the de-excitation rates in Eqs. (7.17) and (7.18) as functions of  $k_0 z$ . Note that in the limit of large distances  $z$ , both de-excitation rates

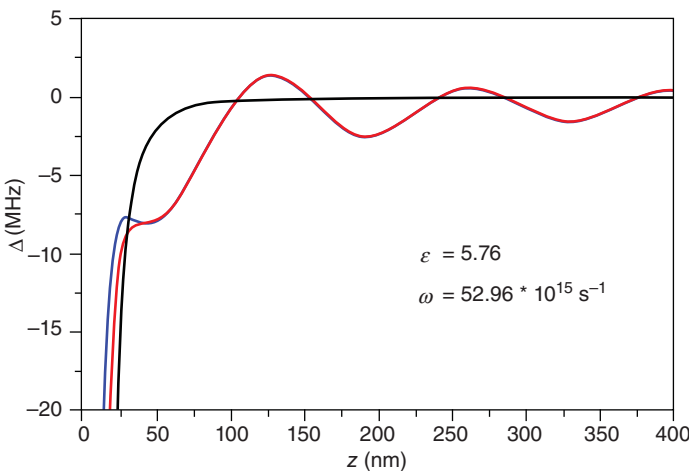


**FIGURE 7.2** Variation of the energy shift with the position of the dipole emitter  $z$  from a planar dielectric surface. The red curve represents the excited state shift and the blue curve the ground state, while the black represents the pure van der Waal's potential. (For a color version of this figure, see the color plate section.)

tend to the free space value  $\Gamma_0$ . On the other hand, in the limit of small  $z$  the upper curve tends to  $2\Gamma_0$  and the lower curve tends to zero rate. This is the origin of the phenomena of superradiance and subradiance which are experienced by radiating atoms in the vicinity of the surface.

Figure 7.2 shows the variation of the energy shift  $\Delta$ , Eq. (7.8), with the distance  $z$  from the surface. The formal expressions leading to Figure 7.2 emerge from complicated evaluations and the reader is referred to the literature for details [22]. The plots in Figure 7.2 have been evaluated for a specific transition of a Rb atom in the vicinity of the surface of a material with dielectric constant  $\epsilon = 5.76$ . Clearly for small distances both shifts tend to the van der Waal's potential, while for large  $z$  both energy shifts tend to the same value.

The modifications of the de-excitation rate are more amenable to experimental detection than the level shifts, so in the rest of this chapter we shall confine attention to de-excitation and the signature of correlations in the context of cooperative emission.

### 7.3 DIPOLE EMITTER NEAR EDGE

#### 7.3.1 Normal Modes

The next cavity offering more confinement, but still an open cavity is the one made of two planar boundaries intersecting at a right angle, as schematically shown in Figure 7.3.

A dipole emitter is assumed to be localized in the dielectric medium at the general point  $(x, y)$  on the plane  $z = 0$ . We shall assume that this plane is where this and other emitters are localized and that the surfaces are those due to a perfect conductor. Then,

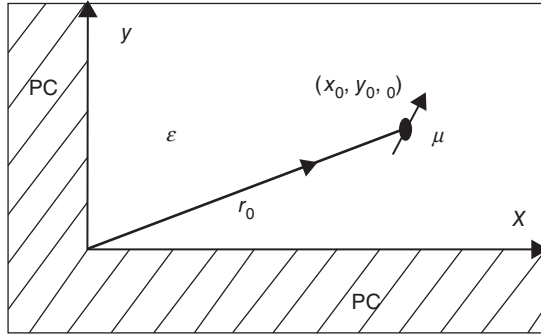


**FIGURE 7.3** The region of space forming a right-angle open cavity where a dielectric occupying the region  $x > 0, y > 0$  smoothly joins the conducting surfaces, denoted by PC. Emitters are localized in the dielectric region such as the one shown at the point  $(x_0, y_0, 0)$ .

the quantized modes are those satisfying the electromagnetic boundary conditions everywhere on the two conductor surfaces. The boundary conditions are

$$E_x(y = 0) = 0 = E_z(y = 0) \text{ and } E_y(x = 0) = 0 = E_z(x = 0). \quad (7.19)$$

The quantized modes must also satisfy transversality, namely that  $\nabla \cdot \mathbf{E} = 0$ . There are two types of mode, namely transverse electric (TE) and transverse magnetic (TM). We have [20]

$$\mathbf{F}^{\text{TE}}(\mathbf{r}, t) = \left( \frac{\epsilon \epsilon_0 \hbar \omega}{\pi^3} \right)^{1/2} \left\{ \frac{k_y}{k} \cos(k_x x) \sin(k_y y) \hat{\mathbf{x}} - \frac{k_x}{k} \sin(k_x x) \cos(k_y y) \hat{\mathbf{y}} \right\} e^{ik_z z - i\omega t}, \quad (7.20)$$

$$\mathbf{F}^{\text{TM}}(\mathbf{r}, t) = \left( \frac{\epsilon \epsilon_0 \hbar \omega}{\pi^3} \right)^{1/2} \left\{ \frac{k_z}{k} \left[ \frac{k_x}{k} \cos(k_x x) \sin(k_y y) \hat{\mathbf{x}} + \frac{k_y}{k} \sin(k_x x) \cos(k_y y) \hat{\mathbf{y}} \right] - i \sin(k_x x) \sin(k_y y) \hat{\mathbf{z}} \right\} e^{ik_z z - i\omega t}. \quad (7.21)$$

The quantized field is now formally given by

$$\mathbf{E}(x, y, t) = \sum_{\eta=\text{TE,TM}} \int d^3 k \left\{ \mathbf{F}^\eta(\mathbf{k}, x, y, t) \hat{a}(\mathbf{k}, \eta) + h.c. \right\}, \quad (7.22)$$

where  $\hat{a}(\mathbf{k}, \xi)$  are annihilation operators for the mode of wavevector  $\mathbf{k}$  and polarization  $\eta$  conforming to the commutation relation

$$[\hat{a}(\mathbf{k}, \eta), \hat{a}^\dagger(\mathbf{k}', \eta')] = \delta_{\eta\eta'} \delta(\mathbf{k} - \mathbf{k'}). \quad (7.23)$$

The quantized magnetic field is such that  $-i\omega\mathbf{B}'' = \nabla \times \mathbf{E}''$  using Eqs. (7.20) and (7.21) which further satisfy the energy normalization condition, namely that the field Hamiltonian reduces to the canonical form

$$\frac{1}{2}\epsilon_0 \int d^3r \left\{ \epsilon E^2 + c^2 \mathbf{B}^2 \right\} = \frac{1}{2} \sum_{\eta} \int d^3k \hbar\omega(\mathbf{k},\eta) \left\{ \hat{a}(\mathbf{k},\eta) \hat{a}^\dagger(\mathbf{k},\eta) + \hat{a}^\dagger(\mathbf{k},\eta) \hat{a}(\mathbf{k},\eta) \right\}. \quad (7.24)$$

With the mode functions defined as in Eqs. (7.20) and (7.21), the quantized field is formally given by Eq. (7.22) and this allows investigation of the influence of the quantized fields in this open cavity on the properties of emitters localized in the vicinity.

### 7.3.2 Single-Emitter De-excitation Rate

For a single emitter situated at the general point  $(x, y)$  on the  $z$ -plane, the de-excitation rate follows again using the Fermi golden rule. As aforementioned, the emitter is represented by a two-level system of the excited state  $|2\rangle$  and the ground state  $|1\rangle$  of energy separation  $\hbar\omega_0$ . The field state  $|\{\mathbf{k}, \xi\}\rangle$  now contains one field mode of energy  $\hbar\omega(\mathbf{k}, \eta)$ , and  $|\{0\}\rangle$  is the corresponding vacuum state. We have

$$\Gamma(x, y) = \frac{2\pi}{\hbar^2} \sum_{\eta} \int d^3k |\langle 2; \{0\} | \boldsymbol{\mu} \cdot \mathbf{E}(x, y) | 1; \{\mathbf{k}, \eta\} \rangle|^2 \delta[\omega_0 - \omega(k, \eta)], \quad (7.25)$$

where  $\mathbf{E}(x, y)$  is the quantized electric field, defined in Eqs. (7.20)–(7.24). The evaluations can be done analytically for an arbitrary dipole orientation, but the details will not be presented here.

The physics of the situation is best explored for special cases in which the dipole moment is oriented in high symmetry directions. This will allow us to draw conclusions when making a comparison of the situation in the open cavity with that in unbounded space. Dipole orientations can in principle be selected in a desired direction by optical means, simply sending a light pulse with the desired polarization.

### 7.3.3 Dipole Moment Normal to the $z$ -Plane.

When the emitter is localized at the general point  $(x, y)$  on the  $z = 0$  plane with its dipole moment vector pointing along the  $z$ -axis we have [19, 20]

$$\Gamma^{(z)}(x, y) = \frac{\mu^2 \omega_0^3}{3\epsilon_0 \pi \hbar c^3} U(x, y)|_{k_0} \quad (7.26)$$

The function  $U(x, y)$  is given by the following integral over the solid angle in  $k$ -space

$$\begin{aligned} U(x, y) &= \frac{3}{8\pi} \int d\Omega_k \left( 1 - \tilde{k}_z^2 \right) [1 - \cos(2\mathbf{k} \cdot \mathbf{x}) - \cos(2\mathbf{k} \cdot \mathbf{y}) - \cos(2\mathbf{k} \cdot \{\mathbf{x} + \mathbf{y}\})] \\ &= 1 - G_{zz}(2\mathbf{x}) - G_{zz}(2\mathbf{y}) - G_{zz}(2[\mathbf{x} + \mathbf{y}]), \end{aligned} \quad (7.27)$$

where  $\mathbf{x} = x\hat{\mathbf{x}}$  and tildes denote unit vectors. The integration in Eq. (7.27) can be done analytically in terms of the diagonal terms of the dyadic function  $G_{ij}(\mathbf{R})$  defined as

$$G_{ij}(\mathbf{R}) = (\delta_{ij} - \tilde{R}_i \tilde{R}_j) \frac{\sin(\omega_0 R/c)}{(\omega_0 R/c)} + (\delta_{ij} - 3\tilde{R}_i \tilde{R}_j) \left\{ \frac{\cos(\omega_0 R/c)}{(\omega_0 R/c)^2} - \frac{\sin(\omega_0 R/c)}{(\omega_0 R/c)^3} \right\}. \quad (7.28)$$

The final result is

$$\Gamma^{(z)} = \Gamma_0 \{ 1 - G_{zz}(2\mathbf{x}) - G_{zz}(2\mathbf{y}) - G_{zz}(2[\mathbf{x} + \mathbf{y}]) \}, \quad (7.29)$$

where  $\Gamma_0$  is the de-excitation rate in an unbounded dielectric including local field corrections, given by Eq. (7.10). Note that  $\epsilon$  is the dielectric constant of the material filling the region of the open cavity in which the emitter is located. The results for a dipole oriented along the  $z$ -axis are shown in Figure 7.4a which displays the spatial distribution of the ratio  $\Gamma^{(z)}/\Gamma_0$  in the  $z = 0$  plane of the right-angle open cavity. Distances are measured in units of the reduced wavelength  $\tilde{\chi} = 1/k = c/(\sqrt{\epsilon}\omega_0)$ .

It can be seen that there are regions of enhanced de-excitation rate (superradiance) and diminished rates (subradiance).

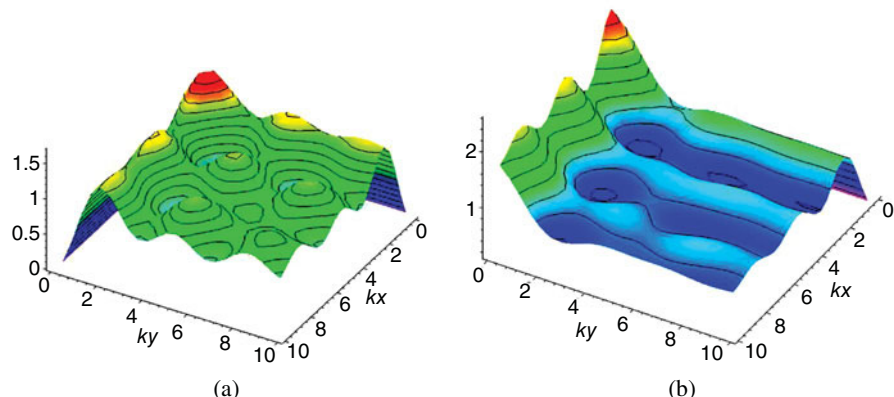


**FIGURE 7.4** (a) Spatial distribution of  $\Gamma^{(z)}/\Gamma_0$ , the relative de-excitation rate on the  $z = 0$  plane of the right-angle cavity. The dipole moment is oriented in the  $z$ -direction, that is, parallel to both surfaces. The color code is such that from blue to red is equivalent to from minimum to maximum. (b) Spatial distribution of  $\Gamma^y/\Gamma_0$ , the de-excitation rate in the  $z = 0$  plane of the open right-angle cavity. The dipole moment is oriented along the  $y$ -direction, that is, normal to one of the surfaces. The color code is such that from magenta to red is equivalent to from minimum to maximum. See the text for further details. (For a color version of this figure, see the color plate section.)

### 7.3.4 Dipole Along the y-Axis

A similar evaluation along the lines followed in the previous section can now be done for the case in which the dipole moment is taken along the  $y$ -axis. The details will not be presented here and we simply display the result in Figure 7.4b. Here the spatial variation is no longer symmetrical, with the maxima of the de-excitation rate now larger than those in Figure 7.4a and are located near the boundary normal to the direction of the dipole.

## 7.4 QUANTUM CORRELATIONS

The simplest quantum system displaying correlations consists a pair of such emitters. In unbounded space, the de-excitation rate shows superradiance and subradiance phenomena akin to those displayed in Figure 7.1b, depending on the relative positions of the emitters and their dipole orientations. As for the de-excitation of a single emitter, discussed in the previous sections, pair correlation effects would be dependent on the nature of the modes available. We expect the correlations to be modified when the two emitters are located within the open cavity discussed here.

We assume that the emitters are localized at the positions  $\mathbf{r}_1$  and  $\mathbf{r}_2$  in the dielectric region, as shown in Figure 7.5. Each emitter, as before, is represented as a two-level system of the ground state  $|g_i\rangle$  of energy  $W_g$  and the excited state  $|e_i\rangle$  of energy  $W_i$ , so that the energy difference is  $W_i - W_g = \hbar\omega_0$ . Since the emitters are identical, the ground state has energy  $2W_g$  and is simply written as

$$|g\rangle = |g_1 g_2\rangle. \quad (7.30)$$

There are two quantum states which span the degenerate energy eigenvalue  $W_g + W_e = W_g + \hbar\omega_0$  and are either the symmetric (+) or the antisymmetric (-) state:

$$|e_{\pm}\rangle = \frac{1}{\sqrt{2}} \{ |e_1 g_2\rangle \pm |e_2 g_1\rangle \}. \quad (7.31)$$

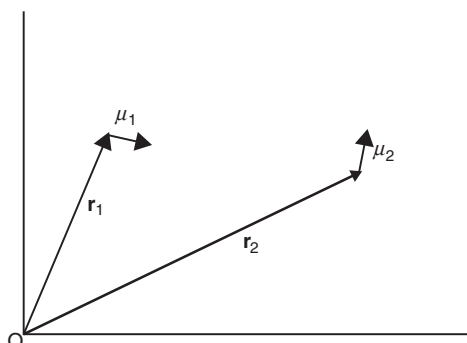


**FIGURE 7.5** Schematic showing a pair of dipole emitters interacting via and with the quantum field inside a right-angle wedge cavity.

The energy separation between  $|e_{\pm}\rangle$  and the ground state  $|g\rangle$  is again  $\hbar\omega_0$ . It is important to note at the outset that the  $|e_{\pm}\rangle$  states given in Eq. (7.31) are two of the well-known Bell states exhibiting quantum entanglement [13].

The two emitters interact with the quantized electromagnetic fields in the open cavity so that the interaction Hamiltonian is formally given by

$$\hat{H}_{\text{int}} = \hat{H}'(\mathbf{r}_1) + \hat{H}'(\mathbf{r}_2) \text{ where } \hat{H}'(\mathbf{r}_i) = -\hat{\mu}_i \cdot \mathbf{E}(\mathbf{r}_i), \quad (7.32)$$

where  $\hat{\mu}_i, i = 1, 2$ , stands for the dipole moment vector operator of the emitter  $i$ . The quantized electric field in the open cavity is described in Eqs. (7.20)–(7.23) and the evaluation turns out to be a little cumbersome, albeit formally carried out along the lines followed for the single emitter de-excitation rate. It turns out that the de-excitation process is different for the two excited states and it is found to be given by

$$\Gamma_{\pm} = \frac{1}{2} \left\{ \Gamma(\mathbf{r}_1) + \Gamma(\mathbf{r}_2) \right\} + \sum_{\alpha, \beta} \mu_{\alpha} \Gamma_{\alpha\beta}(\mathbf{r}_1, \mathbf{r}_2) \mu_{\beta}, \quad (7.33)$$

where  $\mu_{\alpha}$  and  $\mu_{\beta}$  are Cartesian components of the dipole moment matrix element;  $\Gamma(\mathbf{r}_1)$  and  $\Gamma(\mathbf{r}_2)$  are the de-excitation rates of individual emitters at their location, each of which conforms with the results shown in the previous section, so that the expression  $\frac{1}{2} \left\{ \Gamma(\mathbf{r}_1) + \Gamma(\mathbf{r}_2) \right\}$  appearing in Eq. (7.33) involves individual contributions which depend on the location and dipole orientation of the respective emitters. The last term involving the summation over Cartesian components in Eq. (7.33) includes the functions  $\Gamma_{\alpha\beta}(\mathbf{r}_1, \mathbf{r}_2)$ , which depend on the emitter positions within the open cavity. The details are not presented here and can be found in the literature [20]. The contribution of this term to the de-excitation rate is in excess of the isolated rates. It embodies the correlation effects and depends on positions as well as the relative dipole orientations. We write

$$\Gamma = \sum_{\alpha, \beta} \mu_{\alpha} \Gamma_{\alpha\beta}(\mathbf{r}_1, \mathbf{r}_2) \mu_{\beta}. \quad (7.34)$$

To illustrate the variation of this across the open cavity, we can conveniently fix the position of one of the emitters and vary the position of the second, while fixing both dipole orientations.

Figure 7.6a shows the variation of  $\Gamma$  across the  $z$ -plane when one of the emitters, designated by a cross ( $X$ ) is fixed in position at the point  $(x_1, y_1) = (\hat{x}, \hat{x})$ , where  $\hat{x} = k_0^{-1} = c/(\sqrt{\epsilon}\omega_0)$  is the reduced transition wavelength. The second emitter has varying positions within this plane of the open cavity. Here both dipoles are oriented parallel to the  $y$ -axis.

Clearly regions where the color code indicates high values are those where the two emitters are at close proximity. There are regions where the correlation is very small and is even negative, as shown by the darker color. As expected, the region with the

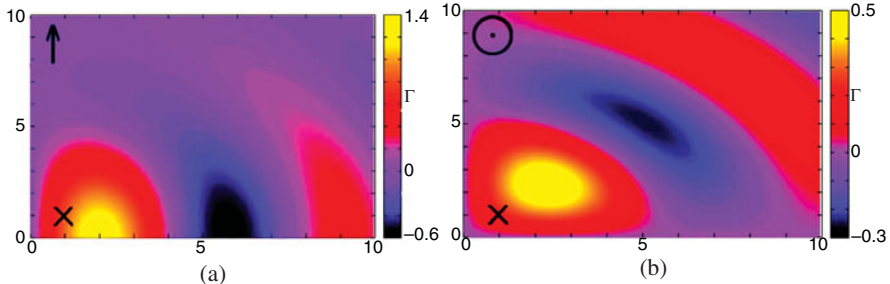


**FIGURE 7.6** Spatial distribution of the pair correlation term  $\Gamma$  defined by Eq. (7.34) in the  $z = 0$  plane of the right-angle cavity. One of the emitters is fixed at the point  $(x_1, y_1) = (\hat{x}, \hat{x})$ , shown by the cross, while the position of the second emitter is varied across the  $z$ -plane. (a) Both dipoles are parallel to the  $y$ -axis, shown by the arrow. (b) Both dipoles are parallel to the  $z$ -axis, indicated by the dot inside a circle. (For a color version of this figure, see the color plate section.)

largest values is where there are maximum cavity effects, namely closest to the edge where the surfaces intersect.

Figure 7.6a differs from Figure 7.6b in that in the latter the dipole orientation is along the  $z$ -axis, that is, parallel to both surfaces. The position of the fixed emitter is again taken as  $(x_1, y_1) = (\hat{x}, \hat{x})$  and the second emitter position varies across the plane of the cavity.

## 7.5 ENTANGLEMENT

The cases we have highlighted so far are (i) a single excited emitter discharging its excitation in the open cavity and (ii) two emitters cooperatively partaking in the de-excitation process in the open cavity. The work points to the existence of an interesting quantum phenomenon in which the open cavity mode at the excitation frequency is said to be entangled with the quantum system, but in a manner strongly dependent on the emitter positions and the dipole orientation. The concept of entanglement appears to be rather strange in the context of a real quantum system and a cavity as a macroscopic object.

In the case of a perfect conductor half-space it has been pointed out [22] that the de-excitation process for a single two-level system localized at a distance  $z$  from the planar surface is equivalent to that of a pair of two-level systems in unbounded space (one real and another fictitious) separated by a distance of  $2z$ , but with the dipole moment of the fictitious two-level system electrically inverted, as in the image. It has been verified by explicit evaluations that the de-excitation rate for a single emitter in this case involves the emitter/cavity ground state

$$|g\rangle = |g g_I\rangle, \quad (7.35)$$

where  $g(g_I)$  and  $e(e_I)$  designate the ground state of the real (fictitious) and excited state of the real (fictitious) two-level systems, respectively. It turns out, however, that the excited state of the entangled system is only the symmetric (+) Bell state:

$$|e_+\rangle = \frac{1}{\sqrt{2}} \{ |eg_I\rangle + |e_Ig\rangle \}. \quad (7.36)$$

The results for the single emitter/half-space open cavity confirm that the de-excitation process involves an entanglement between the two-level system and its image in the conductor. In reality, however, the image is equivalent to an induced electric charge distribution on the surface of the conductor, involving what is essentially a classical concept in a quantum scenario.

The results presented in Figures 7.6a and 7.6b for a single two-level emitter in the case of an open cavity formed by two orthogonal planar surfaces indicate that entanglement is indeed present between the real two-level system and a number of fictitious two-level systems forming the set of images. It is easy to verify that there are three images one in each surface as follows: (a) an upright image at distance  $2y$  perpendicular to the  $x$ -axis, (b) a second inverted image at a distance  $2x$  perpendicular to the  $y$ -axis, and (c) a third inverted image at a distance  $2\sqrt{x^2 + y^2}$  across the diagonal passing through the intersection point. The de-excitation rate clearly exhibits entanglement showing enhancement and suppression regions, as would be the case for a system of four real emitters in free space separated by the distances indicated above.

The evaluation of the de-excitation rate discussed here is based on the construction of the cavity mode that satisfies the electromagnetic boundary conditions at the surfaces. An alternative method is to evaluate the cooperative emission rate of the four emitters shown in Figure 7.7 where the system's lowest energy state is such that each of the four emitters occupies its own ground state, so that we have

$$|g\rangle = |gg_{I1}g_{I2}g_{I3}\rangle. \quad (7.37)$$

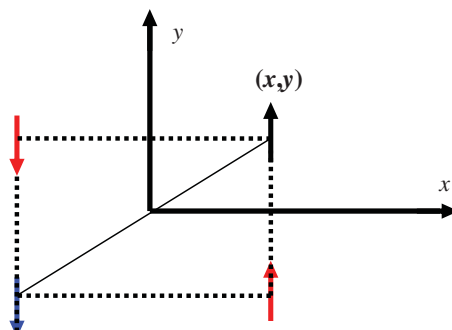


**FIGURE 7.7** A schematic drawing showing the real emitter localized at the point  $(x, y)$  and its three images in the two surfaces of the open cavity. For simplicity, we have chosen the dipole orientation along  $y$ .

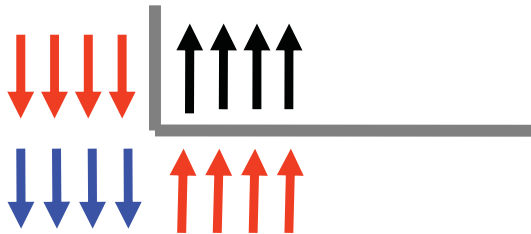


**FIGURE 7.8** A schematic drawing showing four real emitters and their set of images in the two surfaces of the right-angle cavity. For simplicity we have chosen the dipole orientation along the  $y$ -axis.

The excited state would clearly be a symmetric linear combinations of four terms in which one of the emitters is excited. We have

$$|e_+\rangle = \frac{1}{2} \{ |eg_{I1}g_{I2}g_{I3}\rangle + |ge_{I1}g_{I2}g_{I3}\rangle + |gg_{I1}e_{I2}g_{I3}\rangle + |gg_{I1}g_{I2}e_{I3}\rangle \}, \quad (7.38)$$

where  $e$  and  $g$  designate the ground and excited states of the real emitter, whereas  $g_{Ii}$  and  $e_{Ii}$  stand for the ground and excited states of the  $i$ th image, respectively.

When there are two real emitters, we then have six images, three for each emitter, as shown in Figure 7.7 in addition to the two real emitters. The ground and excited states are direct generalizations of Eqs. (7.37) and (7.38). This argument can be extended to any number of real emitters, as shown in Figure 7.8 where there are four real emitters near the edge of the right-angle cavity.

## 7.6 WEDGE CAVITIES

The open cavities we have so far considered, namely a single planar surface and two surfaces at right angles, are the simplest in terms of analysis. Both are, in fact, special cases of a general wedge cavity with a varying wedge angle [19, 20]. The planar single surface corresponds to a wedge angle equal to  $\pi$ , while the right-angle cavity corresponds to a wedge opening angle of  $\pi/2$ .

Fortunately, even the general case of an arbitrary opening angle wedge is amenable to analysis although it is understandably more analytically complex than the special cases discussed so far.

The wedge cavity of an opening angle  $\Phi_0$  is schematically represented in Figure 7.9, where two planar surfaces intersect at a line taken as the spine of the wedge along the  $z$ -axis. The shaded region is assumed to be homogeneous and it is convenient to continue to consider the simplest case of a perfect conductor. Dipole emitters are localized in the dielectric region close to the edge. Figure 7.9 shows a single emitter localized at the point  $R = (r_{\parallel}, \Phi, 0)$  in cylindrical coordinates, where  $r_{\parallel}$  is the in-plane polar coordinate in the  $x$ - $y$  plane and the polar angle  $\Phi$  is in the range  $(0, \Phi_0)$ . The analog of Figure 7.7 for an obtuse angle is shown in Figure 7.10,

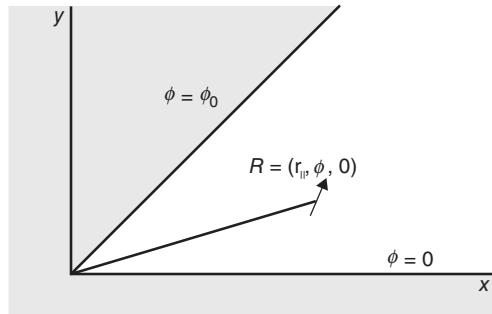


**FIGURE 7.9** A schematic drawing showing the wedge cavity formed by the intersection of two planar surfaces at an opening angle  $\Phi_0$ . Dipole emitters are localized as shown within the dielectric region (unshaded) at close proximity to the cavity edge.

which illustrates the way one constructs the positions and sense of the images of the real emitter localized within the dielectric wedge cavity. A necessary guide is that one must obtain a closed system of emitter and images. The de-excitation rate in this case can be interpreted as a cooperative effect between the real dipole and its five images in the wedge cavity.

The de-excitation rate for a single dipole emitter can be evaluated once the electromagnetic fields are expressed in terms of field quanta satisfying electromagnetic boundary conditions at the wedge interfaces. For perfectly conducting boundaries, the field modes emerge as either transverse electric TE, for which  $E_z = 0$  or transverse magnetic TM for which  $B_z = 0$ . Using cylindrical coordinates we write

$$E(r_{\parallel}, \Phi, z, t) = \sum_{\eta=1,2,n} \int dk_z \int d^2k_{\parallel} \left( \mathbf{F}_{(k_{\parallel}, k_z, n)}^{(\eta)}(\mathbf{r}_{\parallel}, z, t) a_{\eta}(k_{\parallel}, k_z, n) + h.c. \right) \quad (7.39)$$

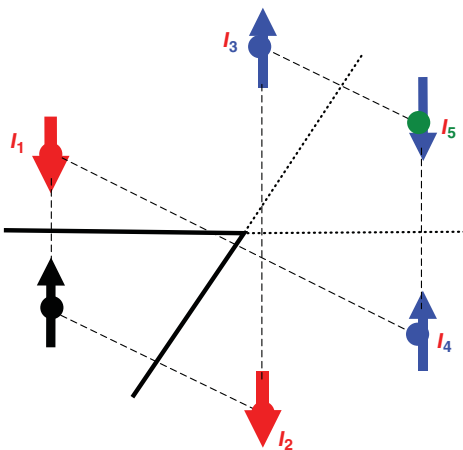


**FIGURE 7.10** Images of a single dipole in a wedge with acute opening angle. Here there are five images: two first-order images ( $I_1$  and  $I_2$ ) and three second-order images ( $I_3$  to  $I_5$ ).

where  $\mathbf{k}_{\parallel}$  is a two-dimensional wavevector in the  $x$ - $y$  plane. The operator  $a_{\eta}(k_{\parallel}, k_z, n)$  and its Hermitian conjugate are annihilation and creation operators for the quanta of the mode of polarization  $\eta$  which becomes TE for when  $\eta = 1$ , or TM, when  $\eta = 2$ . The vector functions  $\mathbf{F}_{(k_{\parallel}, k_z, n)}^{\eta}(\mathbf{r}_{\parallel}, z, t)$  are the mode spatial distribution functions. The procedure leading to the evaluation of these functions is the same as for other geometries. The main requirements are again that they should satisfy the energy normalization condition as well as the electromagnetic boundary conditions at the wedge surfaces [19]. For TE modes ( $\eta = 1$ ), we have

$$\mathbf{F}_{k_{\parallel}, k_z, n}^{(1)}(\mathbf{r}_{\parallel}, z, t) = C_{k_{\parallel}, k_z, n}^{(1)} \left\{ \begin{array}{l} J_m(k_{\parallel}, r_{\parallel})(n\pi/\Phi_0) \sin(n\pi\Phi/\Phi_0) \tilde{\mathbf{r}}_{\parallel} \\ - \frac{\partial J_m(k_{\parallel}, r_{\parallel})}{\partial r_{\parallel}} \cos(n\pi\Phi/\Phi_0) \tilde{\Phi} \end{array} \right\} e^{i(k_z z - \omega(k_{\parallel}, n)t)}, \quad (7.40)$$

where  $J_m(k_{\parallel}, r_{\parallel})$  is the Bessel function of order  $m$ , with  $m = n\pi/\Phi_0$  and tildes here denote unit vectors. For TM modes ( $\eta = 2$ ), we have

$$\mathbf{F}_{k_{\parallel}, k_z, n}^{(2)}(\mathbf{r}_{\parallel}, z, t) = C_{k_{\parallel}, k_z, n} \left\{ \begin{array}{l} \xi(k_{\parallel}) \frac{\partial J_m(k_{\parallel}, r_{\parallel})}{\partial r_{\parallel}} \sin(n\pi\Phi/\Phi_0) \tilde{\mathbf{r}}_{\parallel} \\ + \xi(k_{\parallel}) J_m(k_{\parallel}, r_{\parallel})(n\pi\Phi_0) \cos(n\pi\Phi/\Phi_0) \tilde{\Phi} / r_{\parallel} \\ + \left( c^2 k_{\parallel}^2 / \omega^2 \sqrt{\epsilon} \right) J_m(k_{\parallel}, r_{\parallel}) \sin(n\pi\Phi/\Phi_0) \tilde{z} \end{array} \right\} e^{i(k_z z - \omega(k_{\parallel}, n)t)}, \quad (7.41)$$

where

$$\xi(k_{\parallel}) = \left( 1 - \frac{c^2 k_{\parallel}^2}{\epsilon \omega^2} \right) \quad (7.42)$$

Note that the quantized fields so derived apply to all opening angles in the range  $\Phi_0 = (0, 2\pi)$ .

For obtuse angles, such as  $3\pi/4$ , the system becomes that of an emitter embedded in a bulk dielectric near and outside a metallic protrusion of wedge shape. In the limit of  $\Phi_0$  close to  $2\pi$  we have an emitter localized near the edge of a metallic sheet. It should be emphasized that the formalism, outlined above, is applicable to all these cases. It is possible to examine the manner in which the de-excitation rate distribution for emitters localized in the  $x$ - $y$  plane evolves with changing opening angle between the two extreme cases mentioned above. Illustrative results, as displayed in Figures 7.11a and 7.11b, are in the form of color-coded graphs in which the rate is enhanced in certain regions (regions of superradiance) and suppressed in other regions (regions of subradiance).

In Figures 7.11a and 7.11b we should note in particular the marked change in behavior when the dipole orientation is switched from parallel (along the  $z$ -axis) and

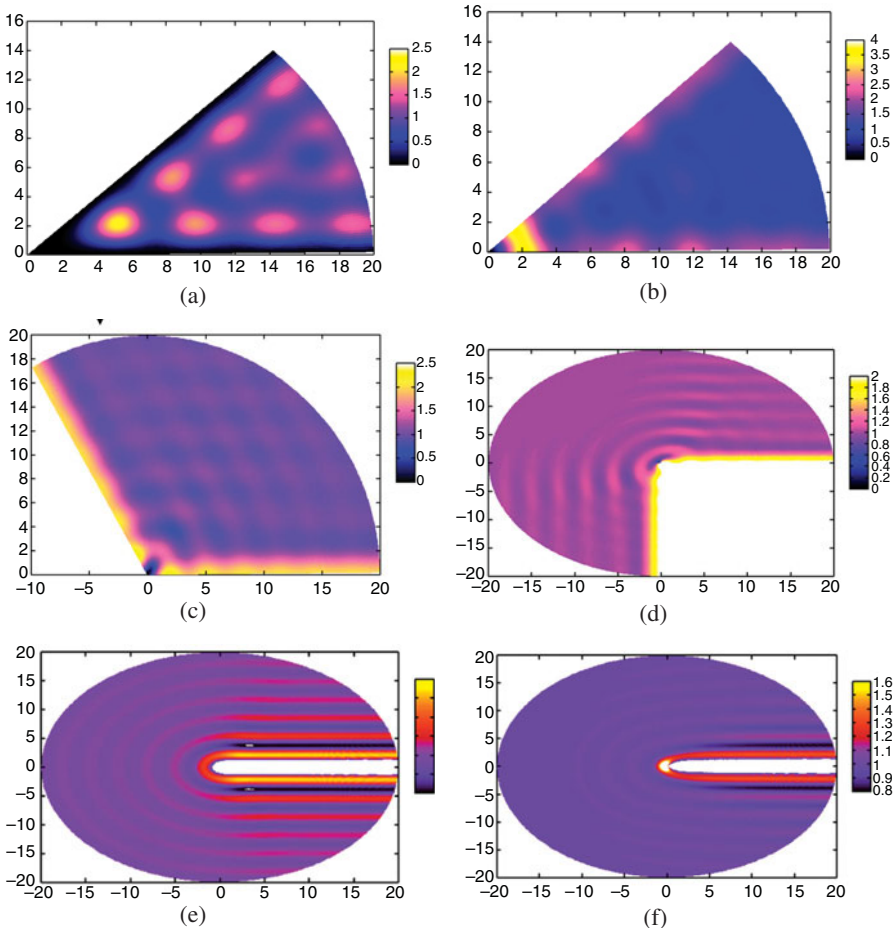


**FIGURE 7.11** De-excitation rates in units of  $\Gamma_0$  for dipole moments localized in the  $x$ - $y$  plane near the wedge edge in a wedge with an opening angle of  $\Phi_0 = \pi/4$  (dipole parallel to plane) (a); with an opening angle of  $\Phi_0 = \pi/4$  (dipole perpendicular to the plane) (b); with an opening angle  $\Phi_0 = 3\pi/4$  (c) (note the tendency to the planar surface case (attained when  $\Phi_0 = \pi$ ) as the opening angle increases); with an opening angle of  $\Phi_0 = 3\pi/2$  (d), but dipole moments are oriented in the direction of increasing  $\Phi$ ; with an opening angle of  $\Phi_0 \approx 2\pi$  (e), but dipole moments are oriented in the direction of increasing  $\Phi$ ; with an opening angle of  $\Phi_0 \approx 2\pi$  (f), but the dipole moments are oriented in the  $z$ -direction. Distances along the horizontal ( $x$ -axis) and vertical ( $y$ -axis) are in units of  $\lambda$ , the reduced transition wavelength. (For a color version of this figure, see the color plate section.)

perpendicular (in the  $x$ - $y$  plane). Note also that in the parallel polarization case the region nearest to the wedge tip is a region of high suppression. Excited emitters situated in this region, in principle, preserve their state of excitation indefinitely. If an emitter which is situated in these dark regions suddenly made to change its state of polarization (for example by optical means) from parallel to perpendicular, the emitter should be de-excited and in certain positions the de-excitation process is enhanced. As we explain in the concluding section, we envisaged that this *in situ* control of de-excitation from subradiant to superradiant could be useful in quantum information processing. Figure 7.11c shows the change in the distribution as the opening angle increases to  $3\pi/4$  and we note the tendency of the distribution to increasingly resemble that near a planar surface.

We should also highlight the interesting extreme case of the system we have defined, namely the case in which the angle  $\Phi_0$  increases beyond the planar surface attained when  $\Phi_0 = \pi$  and ultimately becomes approximately equal to  $2\pi$ . Figure 7.11d displays the de-excitation rate in units of  $\Gamma_0$  in a wedge with an opening angle of  $\Phi_0 = 3\pi/2$  for dipole moments oriented in the direction of increasing  $\Phi$ . The ultimate case is when the opening angle is nearly  $2\pi$ . In this limit the dipole emitter is near a metallic sheet half-plane occupying half the  $x$ - $z$  plane, with the rest of the space occupied by the dielectric. It is seen from Figure 7.11e that the rate varies symmetrically round the line of termination (the  $z$ -axis) for all excited emitters localized in the dielectric in the vicinity of the edge. A change in the polarization modifies the edge of rate distribution markedly, as in Figure 7.11f with considerable enhancement experienced in the vicinity of the termination line. This limit of the general treatment is a convenient route to tackle the problem of the dipole decay near the termination line of a metallic half plane, which would be of interest in its own right, with applications extending, beyond the current interest in quantum information to near field spectroscopy and microscopy.

## 7.7 CONCLUSIONS

In this chapter, we have explored some particular aspects of the photonics of quantum systems in the vicinity of interfaces of some simple structures. We have been concerned with structures possessing only one and two surfaces forming an open cavity. Although the geometry appears seemingly uncomplicated, we have shown that these scenarios do indeed adequately serve to reveal much of the essential physics for excited dipole emitters discharging their excitations at nanoscale distances from the structure surfaces. We have shown that the analysis of the de-excitation process in the case of a single emitter is relatively straightforward, but turns out to be quite complex when we considered correlations involving two or more emitters cooperatively partaking in the emission process near the surfaces. Quantum correlations are important for the realization of scalable architectures for quantum computing, and the properties of quantum systems inside cavities, near cavity surfaces, and within photonic crystals have been highlighted as constituting promising scenarios in that context [27–43].

We have outlined a general framework that quantifies the de-excitation rate for polarizable dipolar emitters embedded in a wedge-shaped dielectric surrounded by high conductivity metal. The treatment is general in the sense that it is capable of predicting de-excitation rate distributions for the case of a wedge of an arbitrary angle  $\Phi_0$  and we have highlighted the significance of the results in the limit of  $\Phi_0$  close to  $2\pi$ , corresponding to dipole decay near the termination line of a metallic half-plane.

The essential features of the physics behind the effect of surfaces on de-excitation rates have been clarified first for a single emitter localized within distances which are multiples of the reduced transition wavelength  $\tilde{\lambda}$ . Here we have found that the de-excitation of dipoles localized in the space close to surface experiences significant changes. The effect, which we have studied here using the concepts involving emission of quantized modes satisfying the boundary conditions at the various surfaces, can also be explained as arising from a cooperative emission process involving the real emitter and its images. Thus even for a single emitter the process involves quantum correlation, as though it is between real dipole emitters. However, in practice, it has been shown in the case of a single emitter and its image, only the symmetric excited state contributes when the image is replaced by a real emitter, with an appropriate set of image dipole orientations. The results can thus be regarded as an entanglement of the real emitter with its set of images, or equivalently, an entanglement of the real emitter with the surfaces forming the cavity. We have also seen that a pair of two identical emitters sharing the excitation also experiences a modified rate, depending on their relative positions and dipole orientations. For a right-angle cavity, the number of two-level systems is multiplied by four when localized within the open cavity. It should be clear from this observation that the scenario can be generalized to any number of emitters as, for example, the case of four real emitters with dipoles all parallel to the  $y$ -axis, as shown in Figure 7.8. The cooperative rate will now involve quantum states that are direct generalizations of Eqs. (7.35) and (7.36). We envisage that an ordered system of emitters as, for example, in a periodic array, would show evidence of periodicity and the system behavior can be controlled by optical manipulation of individual emitters as explained earlier.

The right-angle cavity is one of the simplest and it is in fact a special case of wedge cavities with a varying wedge angle. The correlations for the general case of a wedge of an arbitrary angle involve multiple images for each emitter. For example in the case of a  $\pi/3$  opening angle, there are five images for each emitter and the correlations would be modified in accordance with the degree of confinement of the open cavity.

The prospect of the applicability of the work presented here to the area of quantum information processing rests in the suggestion that the de-excitation rate of dipole emitters near the narrow end of the wedge can be controlled optically from totally dark to superradiant by a change of dipole orientation.

The two-body and multibody quantum correlations for systems localized in the same environment are envisaged to be important for the realization of two-bit quantum gates [13]. It would be interesting also to find out how transfer of excitation between such emitters is influenced by their proximity to the narrow end of material wedges. The experimental realization of such a system is not expected to pose difficulties

since any desired shape made with a variety of different materials can now be created, thanks to advances in material preparation at the nanoscale using modern deposition techniques and lithography. These advances, coupled with parallel advances in the detection of atomic and molecular position to nanometer accuracy, should make the predictions described above amenable to direct experimental investigation.

## ACKNOWLEDGMENTS

Much of the work presented in this chapter was carried out in collaboration with a number of colleagues and former doctorate students. I am particularly grateful to Drs. M. Al-Amri, G. Banyard, C. R. Bennett, G. Juzeliunas, and S. Skipsey.

## REFERENCES

- [1] E. M. Purcell, “Spontaneous transition probabilities in radio-frequency spectroscopy,” *Phys. Rev.* **69**, 681 (1946).
- [2] S. Haroche, “Cavity quantum electrodynamics,” in *Les Houches, Fundamental Systems in Quantum Optics*, LIII, edited by J. Dalibard, J. M. Raimond, and J. Zinn-Justin (Elsevier Science Publishers, BV, 1992), p. 263.
- [3] E. A. Hinds, “Cavity quantum electrodynamics,” *Adv. At. Mol. Opt. Phys.* **28**, 237 (1991).
- [4] J. Michaelis, C. Hettish, M. Mlynek, and V. Sandoghdar, “Optical microscopy using a single-molecule light source,” *Nature* **405**, 325 (2000).
- [5] A. Beveratos, R. Brouri, T. Cacoin, J. Ph. Poizat, and P. Grangier, “Nonclassical radiation from diamond nanocrystals,” *Phys. Rev. A* **64**, 061802(R) (2001).
- [6] C. Hettich, C. Schmitt, J. Zitzmann, S. Kühn, I. Gerhardt, and V. Sandoghdar, “Nanometer resolution and coherent optical dipole coupling of two individual molecules,” *Science* **298**, 385 (2002).
- [7] T. Kalkbrenner, M. Ramstein, J. Mlynek, and V. Sandoghdar, “A single gold particle as a probe for apertureless scanning near-field optical microscopy,” *J. Microsc.* **202**, 72 (2001).
- [8] G. Colas des Francs, C. Girard, and A. Dereux, “Theory of near-field optical imaging with a single molecule as light source,” *J. Chem. Phys.* **117**, 4659 (2002).
- [9] S. Kühn, C. Hettich, C. Schmitt, J.-Ph. Poizat, and V. Sandoghdar, “Diamond colour centres as a nanoscopic light source for scanning near-field optical microscopy,” *J. Microsc.* **202**, 2 (2001).
- [10] S. Götzinger, L. de, S. Menezes, A. Mazzei, S. Kühn, V. Sandoghdar, and O. Benson, “Controlled photon transfer between two individual nanoemitters via shared high- $Q$  modes of a microsphere resonator,” *Nano Lett.* **6**, 1151 (2006).
- [11] C. Toninelli, Y. Delley, T. Stöferle, A. Renn, S. Götzinger, and V. Sandoghdar, “A scanning microcavity for *in situ* control of single-molecule emission,” *Appl. Phys. Lett.* **97**, 021107 (2010).
- [12] C. Welch and J. Burgoyne, “Vacuum challenges and solutions,” *Physics World* **19**, 21 (2006).

- [13] S. M. Barnett, *Quantum Information* (Oxford University Press, New York, 2009).
- [14] M. Babiker, “Super-radiance near conductor and plasma surfaces,” *J. Phys. A* **9**, 799 (1976).
- [15] M. Al-Amri and M. Babiker, “Quantum correlations across a metallic screen,” *Phys. Rev. A* **67**, 043820 (2003).
- [16] D. Meschede, “Radiating atoms in confined space: from spontaneous emission to micro-masers,” *Phys. Rep.* **211**, 201 (1992).
- [17] M. Babiker, “ID image-molecular quantum states in layered media,” *J. Phys. Condens. Matter* **5**, 2137 (1993).
- [18] P. W. Milonni and P. L. Knight, “Spontaneous emission between mirrors,” *Opt. Commun.* **9**, 119 (1973).
- [19] S. C. Skipsey, M. Al-Amri, M. Babiker, and G. Juzeliunas, “Controllable spontaneous decay at material wedges,” *Phys. Rev. A* **73**, 011803 (2006).
- [20] S. C. Skipsey, G. Juzeliunas, M. Al-Amri, and M. Babiker, “Dipole de-excitation near orthogonal conductor surfaces,” *Optics Commun.* **254**, 262–270 (2005).
- [21] G. Banyard, C. R. Bennett, and M. Babiker, “Enhancement of energy relaxation rates near metal-coated dielectric cylinders,” *Opt. Commun.* **207**, 195 (2002).
- [22] M. Al-Amri and M. Babiker, “Quantum frequency shifts of qubits in heterostructures,” *Phys. Rev. A* **69**, 065801 (2004).
- [23] C. R. Bennett, M. Babiker, and J. B. Kirk, “Spontaneous emission and cooperative effects near a thin metallic film,” *J. Mod. Optics* **49**, 269 (2002).
- [24] R. H. Dicke, “Coherence in spontaneous radiation processes,” *Phys. Rev.* **93**, 99 (1954).
- [25] A. I. M. Rae, *Quantum Mechanics*, 5th ed. (IOP Publications, Bristol, 2007).
- [26] R. J. Glauber and M. Lewenstein, “Quantum optics of dielectric media,” *Phys. Rev. A* **43**, 467 (1991).
- [27] J. I. Cirac, P. Zoller, H. J. Kimble, and H. Mabucci, “Quantum state transfer and entanglement distribution among distant nodes in a quantum network,” *Phys. Rev. Lett.* **92**, 127902 (2004).
- [28] H. J. Kimble, “The quantum internet,” *Nature* **453**, 1023 (2008).
- [29] K. J. Vahala, “Optical microcavities,” *Nature* **424**, 839 (2003).
- [30] B. Lev, K. Srinivasan, P. Barclay, O. Painter, and H. Mabuchi, “Feasibility of detecting single atoms using photonic bandgap cavities,” *Nanotechnology* **15**, S556 (2004).
- [31] B. Dayan, A. S. Parkins, T. Aoki, E. Ostby, K. J. Vahala, and H. J. Kimble, “A photon turnstile dynamically regulated by one atom,” *Science* **319**, 1062 (2008).
- [32] G. Lepert, M. Trupke, M. J. Hartmann, M. B. Plenio, and E. A. Hinds, “Arrays of waveguide-coupled optical cavities that interact strongly with atoms,” *New J. Phys.* **13**, 113002 (2011).
- [33] L. M. Duan and H. J. Kimble, “Scalable photonic quantum computation through cavity-assisted interactions,” *Phys. Rev. Lett.* **92**, 127902 (2004).
- [34] J. T. Shen and S. Fan, “Coherent single photon transport in one-dimensional waveguides coupled with superconducting quantum bits,” *Phys. Rev. Lett.* **95**, 213001 (2005).
- [35] F. Le Kien, S. D. Gupta, K. P. Nayak, and K. Hakuta, “Nanofiber-mediated radiative transfer between two distant atoms,” *Phys. Rev. A* **72**, 063815 (2005).
- [36] D. Dzsotjan, A. S. Sorensen, and M. Fleischhauer, “Quantum emitters coupled to surface plasmons of a nanowire.” *Phys. Rev. B* **82**, 075427 (2010).

- [37] F. Le Kien and K. Hakuta, “Cooperative enhancement of channeling of emission from atoms into a nanofiber,” *Phys. Rev. A* **77**, 013801 (2008).
- [38] D. E. Chang, L. Jiang, A. V. Goshkov, and H. J. Kimble, “Cavity QED with atomic mirrors,” *New J. Phys.* **14**, 063003 (2012).
- [39] H. Zoubi and H. Ritsch, “Optical properties of collective excitations for an atomic chain with vacancies,” *New J. Phys.* **12**, 103014 (2010).
- [40] D. E. Chang, A. S. Sorensen, E. A. Demler, and M. D. Lukin, “A single-photon transistor using nano-scale surface plasmons,” *Nat. Phys.* **3**, 807 (2007).
- [41] Y. Chang, X. R. Gong, and C. P. Sun, “Multiatomic mirror for perfect reflection of single photons in a wide band of frequency,” *Phys. Rev. A* **83**, 013825 (2011).
- [42] J. K. Asboth, H. Ritsch, and P. Domokos, “Optomechanical coupling in a one-dimensional optical lattice,” *Phys. Rev. A* **77**, 063424 (2008).
- [43] S.-B. Zheng, “Virtual-photon-induced quantum phase gates for two distant atoms trapped in separate cavities,” *Appl. Phys. Lett.* **94**, 154101 (2009).



---

# 8

---

## QUANTUM ELECTRODYNAMICS

A. SALAM

*Department of Chemistry, Wake Forest University, Winston-Salem, NC, USA*

### 8.1 INTRODUCTION

While the first serious articulation of the concept of electromagnetic radiation having particle-like characteristics can be traced back to Newton's corpuscular theory of light, it was not until 1926 that the term "photon" was first introduced into the lexicon by the American chemist Gilbert N. Lewis [1]. This was necessitated in large part by the reappearance of the idea of the light particle as a result of Planck's quantum hypothesis in 1900, and Einstein's novel explanation and understanding of the photoelectric effect in 1905, as well as his radical work on relativity theory, along with that of Planck on the thermodynamics of radiation. While these advances preceded the subsequent development and application of the new quantum theory, the latter continued to help further propel and establish the notion of light quanta, especially to the interpretation and calculation of atomic spectra, and confirming the validity of microscopic conservation of energy and momentum in the Compton effect, where a quantum of light is scattered by a stationary electron [2].

It required Dirac's genius, however, to take the next step in quantizing the electromagnetic field [3], from which light quanta or photons emerged naturally as a consequence. In the process this gave rise to the first quantum field theory, which, at the time, for radiation interacting with slowly moving, bound electrons was called *Quantum Electrodynamics* (QED) [4]. This formulation finally enabled the wave and particle pictures of electromagnetic radiation to be successfully reconciled. Subsequent research was preoccupied with extending the treatment of matter to ever higher energies and to speeds approaching that of light as in the work of Jordan,

---

*Photonics: Scientific Foundations, Technology and Applications, Volume I*, First Edition.

Edited by David L. Andrews.

© 2015 John Wiley & Sons, Inc. Published 2015 by John Wiley & Sons, Inc.

Pauli, and Heisenberg [5, 6] first by employing relativistic quantum mechanics, and the later telling contributions of Schwinger, Tomonaga, Feynman, and Dyson [4, 7] which culminated in the establishment of the fully covariant form of QED theory and the renormalization program. This last advance enabled a number of key physical quantities to be computed such as the anomalous magnetic moment of the electron [8], spontaneous emission rates [3], and Bethe's non-relativistic calculation of the Lamb shift in atomic hydrogen [9]. These initial successes inspired confidence in the theory and highlighted the necessity of properly including radiative effects. Agreement between theory and experiment has remained singularly impressive, with recent values for the electronic  $g$ -factor, for example, in units of Bohr magnetons given by  $g(\text{theory}) = 2.00231930436558$  [10] and  $g(\text{expt}) = 2.00231930436146$  [11, 12]. With the discovery of the laser soon thereafter taking the field of spectroscopy to unprecedented levels of precision, as well as giving rise to numerous new linear and nonlinear optical phenomena, quantum field theoretic treatments and descriptions in terms of photons became ever more popular and widespread, and increased in importance. This continues to the present day.

The range of applicability of QED is not only limited to interaction of electromagnetic radiation with matter. Coupling between matter can also be treated successfully using the techniques of quantized radiation field theory since fundamentally, inter-particle interactions of the type manifested by atomic and molecular species are electromagnetic in origin. Perhaps the most celebrated example is provided by the Casimir–Polder dispersion potential between neutral non-polar systems [13], whose long-range behavior exhibits inverse seventh power interparticle distance dependence. This is attributed to retardation effects, which weakens the coupling relative to the inverse sixth power law obtained by London, who made the approximation that signals propagate instantaneously between centers.

The case mentioned immediately above serves to highlight important differences that can arise when adopting the so-called semiclassical approach compared to the fully quantum mechanical theory of radiation–matter interaction such as QED. In the former method only the material system obeys quantum mechanical laws with the electromagnetic field taken to be a classical external perturbation [14]. While the use of semiclassical methods is commonplace, most certainly due to its conceptual, formal, and actual computational simplicity relative to QED, in many cases yielding identical results to the latter, it often produces incorrect results and inferior physical insight, particularly in applications that require an explanation and understanding in terms of photons. A few well-known examples will be used in what follows to illustrate the power of a fully quantum mechanical description of light–matter interaction over semiclassical ones. These applications will come from atomic, molecular, optical, and chemical physics, where the non-relativistic form of QED has been applied most fruitfully.

This version of the theory can be obtained on making the approximation that the velocity of the particles is significantly less than that of light, and assuming their mass to be constant. The molecular QED Hamiltonian operator for the total system composed of radiation and matter in mutual interaction can also be derived from first principles starting from the classical Lagrangian function for a slowly moving

charged particle coupled to electromagnetic radiation. This is the approach taken in Section 8.2, which outlines the fundamentals of the theory. The treatment holds for non-conservation of photon number. The number of charged particles, on the other hand, remains constant, thereby excluding electron-positron creation-destruction processes. Hence, there is strict conservation of charge and mass. The theory is therefore readily applicable to non-relativistic charged particles such as bound electrons interacting with the electromagnetic field, with energy and not matter being exchanged between these two sub-systems. The remainder of this chapter is then devoted to photonic applications, beginning with the elementary processes of single-photon absorption, and stimulated and spontaneous emission, and computation of Einstein A and B coefficients. A presentation of two-photon processes—absorption and emission of light, both from different and identical beams, as well as linear scattering of light—both elastic and inelastic varieties, follows this. Additional nonlinear optical processes are considered next, with sum-frequency generation spectroscopy being used as a representative example. A brief survey of other important multiphoton light-scattering phenomena will also be given, such as optical rotation and circular dichroism, and their laser-induced analogs, magnetic circular dichroism, and second- and third-harmonic generation. While all of the above-mentioned examples involve the creation and destruction of real photons, this is not the only type of light quantum permitted by the theory. The other is the virtual photon, identical in all respects to their real counterparts except that they are absorbed very soon after their creation, and thus avoid detection. Even though the theory fundamentally makes no distinction between these two types of photons, the ascribed labels prove convenient in further helping to categorize and organize processes. Thus, virtual photons feature in the explanation of the manifestation of interparticle forces and in their evaluation. Two basic applications will be covered which illustrate single- and double-virtual photon exchange between two bodies, by which interaction between them is mediated. In the former case, resonance energy transfer will serve as the example of choice, while the van der Waals dispersion energy shift will be used to illustrate two virtual photon exchange. Finally, intermolecular forces modified by external radiation will be presented. As a topic of much recent theoretical and experimental interest, this application involves participation by both real and virtual photons. A brief summary and outlook then concludes the chapter.

## 8.2 MOLECULAR QED: PRINCIPLE OF MINIMAL ELECTROMAGNETIC COUPLING

A common starting point in the rigorous quantum mechanical solution of a problem involving the interaction of photons with non-relativistic matter is the Hamiltonian operator for the total system composed of the material particles—atoms and molecules, the electromagnetic field, and their mutual interaction. One fundamental way to arrive at such an operator form is to write the classical Lagrangian function for the coupling of a charged particle, say an electron of charge  $-e$ , mass  $m$  to a radiation field described by a scalar and vector potential  $\phi(\vec{r})$  and  $\vec{a}(\vec{r})$  respectively.

Defining  $\vec{q}_\alpha$  to be the generalized coordinate of the charged particle  $\alpha$ , along with its generalized velocity  $\dot{\vec{q}}_\alpha = \frac{d\vec{q}_\alpha}{dt}$ , a suitable Lagrangian is [15]

$$\begin{aligned} L = & \sum_{\alpha} \frac{1}{2} m_\alpha \dot{\vec{q}}_\alpha^2 - V(\vec{q}_\alpha) + \frac{\epsilon_0}{2} \int \left\{ \dot{\vec{a}}^2(\vec{r}) - c^2 (\nabla \times \vec{a}(\vec{r}))^2 \right\} d^3\vec{r} + \int \vec{j}(\vec{r}) \cdot \vec{a}(\vec{r}) d^3\vec{r} \\ & - \int \rho(\vec{r}) \phi(\vec{r}) d^3\vec{r}, \end{aligned} \quad (8.1)$$

a sum of particle, field, and interaction terms, where  $V(\vec{q}_\alpha)$  is the potential energy operator. Appearing in the interaction term of Eq. (8.1) are the charge and current density  $\rho(\vec{r})$  and  $\vec{j}(\vec{r})$ , respectively. Introduction of  $\phi(\vec{r})$  and  $\vec{a}(\vec{r})$  and re-expressing Maxwell's equations in terms of these quantities guarantee flexibility in the choice of gauge function that maybe chosen, thereby ensuring that the microscopic electric and magnetic field vectors,  $\vec{e}(\vec{r})$  and  $\vec{b}(\vec{r})$ , remain invariant [16]. A gauge that confers special advantages in the construction of the theory is the one in which  $\text{div } \vec{a}(\vec{r}) = 0$ , known as the Coulomb, radiation or transverse gauge. Decomposing any vector field into its parallel and perpendicular components via application of Helmholtz's theorem and substituting for the electromagnetic potentials and fields in Maxwell's equations, it is found that the Coulombic and solenoidal fields are completely decoupled:  $\vec{e}^\parallel = -\nabla\phi$  and  $\vec{e}^\perp = -\vec{a}$ . Thus  $\phi(\vec{r})$  satisfies Poisson's equation and  $\vec{a}(\vec{r})$  the wave equation with transverse current  $\vec{j}^\perp(\vec{r})$ , as its source. As a consequence, the interaction term in Eq. (8.1) therefore simplifies to  $\int \vec{j}^\perp(\vec{r}) \cdot \vec{a}(\vec{r}) d^3\vec{r}$ .

That the Lagrangian (Eq. 8.1) with modified Coulomb gauge interaction term constitutes an acceptable function depends on whether or not it leads to the correct equations of motion. Invoking Hamilton's principle, and applying the calculus of variations yields the Euler-Lagrange equations [17]

$$\frac{d}{dt} \frac{\partial L}{\partial \dot{q}_\alpha} - \frac{\partial L}{\partial q_\alpha} = 0, \quad \alpha = 1, 2, \dots, N, \quad (8.2)$$

for a system of particles with  $N$  degrees of freedom. For the electromagnetic field, an analogous relation ensues but with an additional term that accounts for spatial variation of the continuous field variable. It is found that for the particles the Lagrangian gives rise to Newton's equations of motion with extra Lorentz force law terms describing the coupling of charged particles to the transverse radiation field, while the vector potential satisfies the inhomogeneous wave equation with transverse current as its source, thereby confirming the initial choice of the Lagrangian. From inspection of the Lagrangian it is seen that the dynamical variables are the coordinates and velocities of the particles,  $\vec{q}_\alpha$  and  $\dot{\vec{q}}_\alpha$ , and of the field,  $\vec{a}(\vec{r})$  and  $\dot{\vec{a}}(\vec{r})$ , respectively. The next step in the development involves the evaluation of particle and field canonical momenta,  $\vec{p}_\alpha = \partial L / \partial \dot{\vec{q}}_\alpha$ , and  $\vec{\Pi}(\vec{r}) = \partial L / \partial \dot{\vec{a}}(\vec{r})$ , and the construction of the Hamiltonian function via

$$H = \sum_{\alpha} \vec{p}_\alpha \cdot \dot{\vec{q}}_\alpha + \int \vec{\Pi}(\vec{r}) \cdot \dot{\vec{a}}(\vec{r}) d^3\vec{r} - L, \quad (8.3)$$

after eliminating the velocities in favor of the momenta. The resulting Hamiltonian is called the minimal-coupling Hamiltonian, and is given explicitly by [15, 18–22]

$$H^{\min} = \sum_{\alpha} \frac{1}{2m_{\alpha}} \{ \vec{p}_{\alpha} - e_{\alpha} \vec{a}(\vec{q}_{\alpha}) \}^2 + V(\vec{q}) + \frac{1}{2\epsilon_0} \int \{ \vec{\Pi}^2(\vec{r}) + \epsilon_0^2 c^2 (\nabla \times \vec{a}(\vec{r}))^2 \} d^3 \vec{r}. \quad (8.4)$$

To facilitate application of Eq. (8.4) to atomic and molecular systems, the charged particles  $\alpha$  are grouped into aggregates  $\xi$  constituting a bound framework, and a sum taken over species  $\xi$  yields a many-body Hamiltonian. Note that  $V(\vec{q})$  in Eq. (8.4) is composed of both intramolecular and intermolecular contributions. Electronic and nuclear degrees of freedom are separated at this point and the latter are taken to be stationary. This approximation is easily justified on comparing the mass of the electron to that of the nuclear particles. It is clearly unnecessarily restrictive if vibrational effects are to be examined or the dynamics of chemical and biological reactions are to be studied, but can be readily relaxed [23].

The final step involves promotion of the classical variables to their quantum mechanical operator form [24], thereby yielding the quantum electrodynamical minimal-coupling Hamiltonian for the interaction of matter with electromagnetic radiation. The particle and field operators satisfy the equal-time commutation relations

$$[q_{i(\alpha)}(\xi), p_{j(\beta)}(\zeta)] = i\hbar \delta_{ij} \delta_{\alpha\beta} \delta_{\xi\zeta} \quad (8.5)$$

and

$$[a_i(\vec{r}), \Pi_j(\vec{r}')] = i\hbar \delta_{ij}^{\perp}(\vec{r} - \vec{r}'), \quad (8.6)$$

respectively, where  $\delta_{ij}^{\perp}(\vec{r})$  is the transverse delta-function dyadic, and  $i$  and  $j$  denote Cartesian tensor components in a space-fixed frame of reference, with the Einstein summation convention being adopted for repeated indices. The procedure described above is formally known as canonical quantization and, as a means for going from classical to quantum mechanics, is widespread. It is worth pointing out that the familiar ' $\vec{p} \cdot \vec{a}$ ' and ' $\vec{a}^2$ ' interaction terms associated with the minimal-coupling Hamiltonian (Eq. 8.4) follow on expanding the first term. Moreover, it is evident that including the radiation field at the outset in the classical Lagrangian will necessarily entail its quantization once the Hamiltonian operator form is arrived at. The electromagnetic field contribution is given by the last term in Eq. (8.4) and is written in canonical form. On using the definition  $\vec{b}(\vec{r}) = \nabla \times \vec{a}(\vec{r})$  and the relation  $\vec{\Pi}(\vec{r}) = -\epsilon_0 \vec{e}^{\perp}(\vec{r})$  in minimal-coupling, the radiation field Hamiltonian in this framework may be re-expressed in terms of microscopic transverse electric and magnetic fields as

$$H_{\text{rad}}^{\min} = \frac{\epsilon_0}{2} \int \{ \vec{e}^{\perp 2}(\vec{r}) + c^2 \vec{b}^2(\vec{r}) \} d^3 \vec{r}. \quad (8.7)$$

Of historical note is that Born, Heisenberg ,and Jordan [25] realized in 1926 that a mode description of classical electromagnetic radiation confined to a fixed volume  $V$  is equivalent to a mechanically oscillating system. This led Dirac [3] to quantize the free radiation field in the following year by expressing it in terms of a collection of non-interacting harmonic oscillator Hamiltonians,

$$H_{\text{rad}} = \sum_{\vec{k}, \lambda} \frac{1}{2} \left\{ p_{\vec{k}}^{(\lambda)2} + m\omega^2 q_{\vec{k}}^{(\lambda)2} \right\}, \quad (8.8)$$

one for each mode  $(\vec{k}, \lambda)$  of the radiation field, where  $\vec{k}$  symbolizes the direction of propagation or wavevector, and  $\lambda$  is the polarization index. To facilitate quantization, Dirac worked in the occupation number representation and introduced the bosonic lowering and raising operators,  $a^{(\lambda)}(\vec{k})$  and  $a^{\dagger(\lambda)}(\vec{k})$ , which depend on the canonically conjugate dynamical variables and, respectively, decrease and increase by one the number of particles of light of mode  $(\vec{k}, \lambda)$ —the photons. Hence, Eq. (8.8) could be rewritten in quantum mechanical form as

$$H_{\text{rad}} = \sum_{\vec{k}, \lambda} \{ a^{\dagger(\lambda)}(\vec{k}) a^{(\lambda)}(\vec{k}) + \frac{1}{2} \} \hbar\omega, \quad (8.9)$$

where  $\omega = ck$  is the circular frequency and  $a^{(\lambda)}(\vec{k})$  and  $a^{\dagger(\lambda)}(\vec{k})$  obey the commutator relation

$$[a^{(\lambda)}(\vec{k}), a^{\dagger(\lambda')}(\vec{k}')] = \delta_{\lambda\lambda'} \delta_{\vec{k}\vec{k}'}, \quad (8.10)$$

all other combinations vanishing. The factor  $a^\dagger a$  is the number operator, whose expectation value gives the number of quanta present. Hence, in this second quantized formalism, the eigenvalue spectrum of the quantized electromagnetic field is easily seen to be  $(n + \frac{1}{2})\hbar\omega$ ,  $n = 0, 1, 2, \dots$ , where  $n$  designates the number of photons. Each annihilation and creation operator acts on a number state of the field, which is represented by the ket  $|n(\vec{k}, \lambda)\rangle$ , as follows:

$$a^{(\lambda)}(\vec{k})|n(\vec{k}, \lambda)\rangle = \begin{cases} 0, & n = 0 \\ n^{1/2}|(n-1)(\vec{k}, \lambda)\rangle, & n = 1, 2, \dots \end{cases} \quad (8.11a)$$

$$a^{\dagger(\lambda)}(\vec{k})|n(\vec{k}, \lambda)\rangle = (n+1)^{1/2}|(n+1)(\vec{k}, \lambda)\rangle, \quad n = 0, 1, 2, \dots \quad (8.11b)$$

It is readily apparent that the field state in which  $n = 0$  for all radiation modes corresponds to the electromagnetic vacuum. Even though there is a complete absence of photons, the field still possesses energy,  $\frac{1}{2}\hbar\omega$  per mode. A photon cannot be annihilated in this state, but it can be created via action of the  $a^\dagger$  operator. This emission process ultimately gives rise to a number of observable phenomena that obviously

require quantization of the electromagnetic field for their proper explanation and computation, and are collectively attributed to vacuum field fluctuations and zero-point energy [26]. A few of these manifestations will be examined in the sections to follow.

The Maxwell field operators may be expanded as a mode sum in terms of  $a$  and  $a^\dagger$  as in

$$\vec{e}^\perp(\vec{r}) = i \sum_{\vec{k}, \lambda} \left( \frac{\hbar c k}{2\epsilon_0 V} \right)^{1/2} [\vec{e}^{(\lambda)}(\vec{k}) a^{(\lambda)}(\vec{k}) e^{i\vec{k}\cdot\vec{r}} - \overline{\vec{e}}^{(\lambda)}(\vec{k}) a^{\dagger(\lambda)}(\vec{k}) e^{-i\vec{k}\cdot\vec{r}}] \quad (8.12)$$

and

$$\vec{b}(\vec{r}) = i \sum_{\vec{k}, \lambda} \left( \frac{\hbar k}{2\epsilon_0 c V} \right)^{1/2} [\vec{b}^{(\lambda)}(\vec{k}) a^{(\lambda)}(\vec{k}) e^{i\vec{k}\cdot\vec{r}} - \overline{\vec{b}}^{(\lambda)}(\vec{k}) a^{\dagger(\lambda)}(\vec{k}) e^{-i\vec{k}\cdot\vec{r}}], \quad (8.13)$$

where  $\vec{e}^{(\lambda)}(\vec{k})$  and  $\vec{b}^{(\lambda)}(\vec{k}) = \hat{k} \times \vec{e}^{(\lambda)}(\vec{k})$  are complex unit electric and magnetic polarization vectors and the overbar signifies the complex conjugate quantity. Quantization occurs in a box of volume  $V$ , which limits the allowed values of the wavevector in each of the three spatial directions to a triple of integers and applies to two modes of the vector field, the third component being the direction of propagation itself. The operators (Eqs. 8.12 and 8.13) are normalized to reproduce the correct electromagnetic field energy.

In principle, the quantum electrodynamical minimal-coupling Hamiltonian (Eq. 8.4) can be employed to solve any problem involving the interaction of electromagnetic radiation with matter, as well as situations involving coupling between atoms and molecules, as is frequently done so in solid-state physics. In practice, however, in many cases its adoption proves to be difficult. This is because of the appearance of particle momentum and vector potential operators in the interaction terms, along with the presence of the cumbersome static interparticle Coulomb term when the application involves two or more material bodies. An alternative Hamiltonian, one that offers many advantages when employed, and is now more often the preferred option, is the multipolar coupling Hamiltonian. This may also be constructed on its own right from first principles, beginning with an appropriate classical Lagrangian. Alternatively, the minimal-coupling Hamiltonian may be transformed. This is outlined in the next section.

### 8.3 MULTIPOLAR HAMILTONIAN

Conversion of the minimal-coupling Hamiltonian to its more widely applicable multipolar form may be accomplished by application of a quantum canonical transformation to the former [24]. Under this transformation, the Heisenberg operator equations of motion and commutator relations for the canonically conjugate dynamical variables remain unaltered. Formally, this is analogous to the situation in classical

mechanics [17], where a dynamical system described by a Hamiltonian function is subject to a contact transformation. In this case, Hamilton's canonical equations and the Poisson bracket do not change. A transformation that can be employed between two operators to affect the change  $\text{min} \rightarrow \text{mult}$  is of the form

$$H^{\text{mult}} = e^{iS} H^{\text{min}} e^{-iS}. \quad (8.14)$$

The specific choice of generating function  $S$  that carries this out [12, 27–30] is when

$$S = \frac{1}{\hbar} \int \vec{p}^\perp(\vec{r}) \cdot \vec{a}(\vec{r}) d^3\vec{r}, \quad (8.15)$$

where  $\vec{p}^\perp(\vec{r})$  is the transverse electric polarization field. On introducing a reference point  $\vec{R}_\xi$  associated with centre  $\xi$ , about which an electric multipole moment expansion can be made, this field is defined as [28]

$$\vec{p}^\perp(\vec{r}) = \sum_{\alpha, \xi} e_\alpha (\vec{q}_\alpha(\xi) - \vec{R}_\xi) \int_0^1 \delta(\vec{r} - \vec{R}_\xi - \lambda(\vec{q}_\alpha(\xi) - \vec{R}_\xi)) d\lambda. \quad (8.16)$$

It is interesting to note that since  $S$  is a function of the generalized coordinates only, they remain invariant, with only the canonically conjugate particle and field momenta being transformed. The transformed variables are given by

$$\vec{p}_\alpha^{\text{mult}}(\xi) = \vec{p}_\alpha^{\text{min}}(\xi) + e\vec{a}(\vec{q}_\alpha(\xi)) - \int \vec{n}_\alpha(\xi; \vec{r}) \times \vec{b}(\vec{r}) d^3\vec{r}, \quad (8.17)$$

and

$$\vec{\Pi}^{\text{mult}}(\vec{r}) = \vec{\Pi}^{\text{min}}(\vec{r}) - \vec{p}^\perp(\vec{r}), \quad (8.18)$$

where  $\vec{n}_\alpha(\xi; \vec{r})$  is the vector field

$$\vec{n}_\alpha(\xi; \vec{r}) = -e(\vec{q}_\alpha(\xi) - \vec{R}_\xi) \int_0^1 \lambda \delta(\vec{r} - \vec{R}_\xi - \lambda(\vec{q}_\alpha(\xi) - \vec{R}_\xi)) d\lambda. \quad (8.19)$$

Substituting for the new dynamical variables into the minimal-coupling Hamiltonian (Eq. 8.4) yields the multipolar form [15, 18–22, 27, 29, 30]

$$\begin{aligned} H^{\text{mult}} &= \sum_\xi \left[ \frac{1}{2m} \sum_\alpha \left\{ \vec{p}_\alpha(\xi) + \int \vec{n}_\alpha(\xi; \vec{r}) \times \vec{b}(\vec{r}) d^3\vec{r} \right\}^2 + V(\xi) \right] \\ &\quad + \frac{1}{2\epsilon_0} \int \left\{ \left[ \vec{\Pi}(\vec{r}) + \vec{p}^\perp(\vec{r}) \right]^2 + \epsilon_0^2 c^2 (\nabla \times \vec{a}(\vec{r}))^2 \right\} d^3\vec{r} + \sum_{\xi < \zeta} V_{\text{inter}}(\xi, \zeta), \end{aligned} \quad (8.20)$$

where the Coulomb potential has been decomposed into intramolecular and intermolecular contributions, with the latter one given by the last term in Eq. (8.20). Inspection of the multipolar Hamiltonian reveals that there is a term which is proportional to  $\vec{p}^{\perp 2}(\vec{r})$ , and which is composed of intramolecular and intermolecular terms. It is remarkable that the intermolecular part exactly cancels the intermolecular Coulomb potential term  $\sum_{\xi < \zeta} V_{\text{inter}}(\xi, \zeta)$ , leaving behind an intramolecular transverse polarization squared contribution [19]. On employing Eqs. (8.17) and (8.18), the multipolar Hamiltonian (Eq. 8.20) becomes

$$H^{\text{mult}} = H_{\text{mol}}^{\text{mult}} + H_{\text{rad}}^{\text{mult}} + H_{\text{int}}^{\text{mult}} + \frac{1}{2\epsilon_0} \int \sum_{\xi} |\vec{p}^{\perp}(\xi; \vec{r})|^2 d^3\vec{r}, \quad (8.21)$$

where the first three individual terms are the familiar molecular Hamiltonian,

$$H_{\text{mol}}^{\text{mult}} = \sum_{\xi} \left\{ \frac{1}{2m} \sum_{\alpha} \vec{p}_{\alpha}^2(\xi) + V(\xi) \right\}, \quad (8.22)$$

the Hamiltonian for the radiation field,

$$H_{\text{rad}}^{\text{mult}} = \frac{1}{2\epsilon_0} \int \{ \vec{d}^{\perp 2}(\vec{r}) + \epsilon_0^2 c^2 \vec{b}^2(\vec{r}) \} d^3\vec{r}, \quad (8.23)$$

and that for the radiation-molecule coupling Hamiltonian,

$$\begin{aligned} H_{\text{int}}^{\text{mult}} = & -\epsilon_0^{-1} \int \vec{p}(r) \cdot \vec{d}^{\perp}(\vec{r}) d^3\vec{r} - \int \vec{m}(\vec{r}) \cdot \vec{b}(\vec{r}) d^3\vec{r} \\ & + \frac{1}{2} \int o_{ij}(\vec{r}, \vec{r}') b_i(\vec{r}) b_j(\vec{r}') d^3\vec{r} d^3\vec{r}'. \end{aligned} \quad (8.24)$$

It is interesting to note the presence of the transverse displacement field,  $\vec{d}^{\perp}(\vec{r})$ , in the last two expressions. This is a direct consequence of the multipolar formalism, where from relation (8.18) it is seen that the canonically conjugate field momentum,  $\vec{\Pi}^{\text{mult}}(\vec{r}) = -\epsilon_0 \vec{e}^{\perp}(\vec{r}) - \vec{p}^{\perp}(\vec{r}) = -\vec{d}^{\perp}(\vec{r})$ , and whose mode expansion is

$$\vec{d}^{\perp}(\vec{r}) = i \sum_{\vec{k}, \lambda} \left( \frac{\hbar c k \epsilon_0}{2V} \right)^{1/2} [\vec{e}^{(\lambda)}(\vec{k}) a^{(\lambda)}(\vec{k}) e^{i\vec{k} \cdot \vec{r}} - \vec{e}^{(\lambda)*}(\vec{k}) a^{(\lambda)*}(\vec{k}) e^{-i\vec{k} \cdot \vec{r}}]. \quad (8.25)$$

Rather than the electromagnetic potentials, the multipolar Hamiltonian is expressed entirely in terms of Maxwell fields. The magnetization,  $\vec{m}(\vec{r})$ , and

diamagnetization,  $o_{ij}(\vec{r}, \vec{r}')$ , fields appearing in the interaction Hamiltonian (Eq. 8.24) are defined as

$$\vec{m}(\vec{r}) = \frac{1}{2m} \sum_{\xi, \alpha} \{ \vec{n}_\alpha(\xi; \vec{r}) \times \vec{p}_\alpha(\xi) - \vec{p}_\alpha(\xi) \times \vec{n}_\alpha(\xi; \vec{r}) \} \quad (8.26)$$

and

$$o_{ij}(\vec{r}, \vec{r}') = \sum_{\xi, \zeta} \frac{1}{m} \epsilon_{ikl} \epsilon_{jml} n_k(\xi; \vec{r}) n_m(\zeta; \vec{r}'), \quad (8.27)$$

respectively. It is convenient to expand the electric polarization, magnetization, and diamagnetization fields in a Taylor series about  $\vec{R}_\xi$  and retain the first few terms. The interaction Hamiltonian (Eq. 8.24) then becomes

$$\begin{aligned} H_{\text{int}}^{\text{mult}}(\xi) = & -\epsilon_0^{-1} \vec{\mu}(\xi) \cdot \vec{d}^\perp(\vec{R}_\xi) - \epsilon_0^{-1} Q_{ij}(\xi) \nabla_j d_i^\perp(\vec{R}_\xi) - \vec{m}(\xi) \cdot \vec{b}(\vec{R}_\xi) \\ & + \frac{e^2}{8m} \sum_\alpha \{ (\vec{q}_\alpha(\xi) - \vec{R}_\xi) \times \vec{b}(\vec{R}_\xi) \}^2 + \dots, \end{aligned} \quad (8.28)$$

a sum of familiar electric dipole, electric quadrupole, magnetic dipole, and lowest order diamagnetic coupling terms. From inspection of  $H_{\text{int}}^{\text{mult}}$  it is seen that atoms and molecules couple directly to the electromagnetic fields through their molecular multipole moments. Interaction between particles occurs exclusively through the exchange of transverse photons, which propagate at the speed of light and are properly retarded since the Maxwell fields  $\vec{d}^\perp(\vec{r})$  and  $\vec{b}(\vec{r})$  are strictly causal. All static interparticle interaction terms have been eliminated. Individual or collective contributions due to specific multipole moment terms are easily identified and extracted.

The contribution to  $H^{\text{mult}}$  arising from the one-center transverse electric polarization, the last term written in Eq. (8.21), does not depend on the electromagnetic field and so can be ignored in the calculation of most radiative processes. For interactions involving self-energy corrections, however, such as the Lamb shift [9, 19, 31], it must be retained.

A brief outline was given above of how the multipolar Hamiltonian could be obtained from the minimal-coupling one by performing a canonical transformation. This is not the only way of deriving  $H^{\text{mult}}$ . Another approach is to modify the minimal-coupling Lagrangian (Eq. 8.1) so as to obtain an equivalent Lagrangian,  $L^{\text{mult}}$ , by adding to the former the time derivative of a function of the coordinates and the time only [12, 32, 33]. Such an addition leaves the Euler-Lagrange equations of motion invariant. It can be shown [19, 22] that the function,  $f$ , and the generator,  $S$ , used in the canonical transformation are related via  $f = -\hbar S$ . Hence, from Eq. (8.15)

$$L^{\text{mult}} = L^{\text{min}} - \frac{d}{dt} \int \vec{p}^\perp(\vec{r}) \cdot \vec{a}(\vec{r}) d^3 \vec{r}. \quad (8.29)$$

By carrying out the canonical quantization procedure, the multipolar Hamiltonian is evaluated via

$$H^{\text{mult}} = \sum_{\xi,\alpha} \vec{p}_\alpha(\xi) \cdot \vec{q}_\alpha(\xi) + \int \vec{\Pi}(\vec{r}) \cdot \vec{a}(\vec{r}) d^3r - L^{\text{mult}}, \quad (8.30)$$

yielding Eq. (8.20).

For the sake of completeness, it should be pointed out that the transformation from minimal to multipolar-coupling frameworks may also be achieved by effecting a gauge transformation on  $L^{\text{min}}$  when the scalar and vector potential are written in line integral form in the Coulomb gauge. Altering the curve changes the polarization and magnetization fields in a particular way that generates an equivalent multipolar Lagrangian. Further details may be found in References 34–36.

In addition to the texts already cited on the subject, there are other notable books that treat foundational aspects of the quantum theory of radiation–matter interaction [37–41], as well as a number of comprehensive review articles [42–48], many of which also deal with applications.

The quantum mechanical solution of the interacting radiation–matter system, described in either minimal- or multipolar-coupling versions of the theory, represents a formidable problem. A standard method of solution makes use of the fact that the non-relativistic coupling between electrons and photons is small compared to the magnitude of Coulomb fields present within atoms and molecules. Hence, the interaction Hamiltonian is taken to be a small perturbation on the system, and the total Hamiltonian is divided according to

$$H = H_0 + H_{\text{int}}, \quad (8.31)$$

where the unperturbed Hamiltonian,  $H_0$ , is a sum of molecular and radiation field terms

$$H_0 = H_{\text{mol}}^{\text{min/mult}} + H_{\text{rad}}^{\text{min/mult}}, \quad (8.32)$$

and the interaction Hamiltonians in minimal- and multipolar-coupling schemes are given by

$$H_{\text{int}}^{\text{min}} = \frac{e}{m} \sum_{\xi,\alpha} \vec{p}_\alpha(\xi) \cdot \vec{a}(\vec{q}_\alpha(\xi)) + \frac{e^2}{2m} \sum_{\xi,\alpha} \vec{a}^2(\vec{q}_\alpha(\xi)) + V_{\text{inter}}, \quad (8.33)$$

and Eq. (8.24), respectively, remembering to add the final term on the right-hand side of Eq. (8.21) to Eq. (8.24) when computing self-energy corrections. It is important to note that if  $H_{\text{int}}$  vanishes the unperturbed Hamiltonian is separable. Its eigenfunctions are a product of wavefunctions for the non-interacting molecular and radiation field subsystems. The former are assumed known from quantum chemistry and denoted by a ket containing an appropriate label (quantum number) such as  $|m\rangle$  for an atom or molecule in electronic state with quantum number  $m$ . As mentioned earlier, number

states are used to quantify the number of photons of a particular mode in the free radiation field via the ket  $|n(\vec{k}, \lambda) >$ . The total energy is therefore given by the sum of the component eigenenergies,  $E_m + n\hbar ck$ . Thus, the eigenvalue solution to the unperturbed problem is

$$H_0|m>|n(\vec{k}, \lambda) > = (E_m + n\hbar ck)|m>|n(\vec{k}, \lambda) >, \quad (8.34)$$

and hence the unperturbed molecule-field product state  $|m; n(\vec{k}, \lambda) >$  may be employed as base states for the solution of the perturbed Hamiltonian (Eq. 8.31).

The dynamics are governed by the time-dependent Schrödinger equation

$$i\hbar \frac{\partial}{\partial t}|\Psi(t)> = H|\Psi(t)>, \quad (8.35)$$

in which the total system wavefunction,  $\Psi(t)$ , is taken to be time-dependent, as is characteristic of the Schrödinger picture. Since it is the effect of the interaction Hamiltonian on the system that is of interest, it is convenient to isolate this contribution via the introduction of an appropriate time evolution operator,  $U(t_f, t_i)$ , which acts on the state of the system at initial time  $t_i$ ,  $|\Psi(t_i)>$ , giving the wavefunction at time  $t$ ,  $|\Psi(t)> = U(t, t_i)|\Psi(t_i)>$ . A power series solution for  $U(t_f, t_i)$  in terms of  $H_{\text{int}}$  is then generated, from which the probability amplitude for a process occurring between initial state  $|i>$  at  $t_i$  to the final time  $t_f$  when the system is in state  $|f>$  and is induced by the perturbation is readily evaluated as

$$\begin{aligned} M_{fi} = & \langle f | H_{\text{int}} | i \rangle + \sum_I \frac{\langle f | H_{\text{int}} | I \rangle \langle I | H_{\text{int}} | i \rangle}{E_i - E_I} \\ & + \sum_{I, II} \frac{\langle f | H_{\text{int}} | II \rangle \langle II | H_{\text{int}} | I \rangle \langle I | H_{\text{int}} | i \rangle}{(E_i - E_I)(E_i - E_{II})} + \dots \end{aligned} \quad (8.36)$$

a sum of first-, second-, ..., order terms in the perturbation operator [24, 49], where at the initial time,  $U(t_i, t_i)$  is taken to be unity. Quantum mechanical observables then readily follow from application of Eq. (8.36). Diagrams depicting the time-ordered sequence of photon absorption and emission events and the time evolution of the material system facilitate the evaluation of a specific contribution to the matrix element. These are modified forms [50] of the diagrams introduced by Feynman to represent the total system propagator [51, 52]. Examples of time-ordered diagrams will be given in the applications to follow, and their advantage as a book-keeping device will become apparent when higher-order processes are considered.

It should be mentioned that an alternate visual depiction of electron–photon couplings exists. Known as the state sequence representation [53], it has the advantage that all possible time-orderings are contained in one diagram. In addition, seemingly different physical processes can be described by a state sequence figure possessing identical features and structural components, thereby providing useful insight into the underlying inter-relatedness of a variety of phenomena. A formal mathematical

scheme has been devised that allows the state sequence diagram to be drawn for any particular radiation–molecule or intermolecular process that involves distinct or indistinguishable photon creation and destruction events for prescribed initial and final system states. Permutational calculus coupled with formal linkage rules enable individual paths to be traced in space and time so that the evolution of the system from  $|i\rangle$  to  $|f\rangle$  via appropriate intermediate states may be followed allowing the complete diagram to be sketched. A single path corresponds to one time-ordered diagram and a unique term in the contribution to the probability amplitude obtained from time-dependent perturbation theory. The method has been successfully applied to a number of different processes including linear absorption, emission and scattering of light, second-harmonic generation [53], energy transfer and pooling [54–56], the Casimir–Polder potential [57], and its modification by external radiation [58], being especially beneficial for the treatment of higher-order processes for which the number of time-ordered diagrams is frequently large. Identical results are of course obtained no matter which pictorial representation is employed in any particular computation. In what follows, only the more familiar time-ordered diagram methodology will be used to illustrate processes of interest, while the reader interested in the state sequence approach may consult the references cited in this paragraph for further details of the latter representation.

Development of the theory thus far has been in the Schrödinger representation of quantum mechanics in which the operators are time-independent and the states evolve in time. Molecular QED has, however, also been formulated in the Heisenberg picture [59, 60]. Now the state vectors are stationary and the operators are dependent on time. The time evolution is evaluated by solving the Heisenberg operator equation of motion for the dynamical variable. Due to formal equivalence of this viewpoint with the Hamiltonian description of classical mechanics, the Heisenberg picture is often used to study a variety of processes associated with the QED Maxwell fields, including observables such as the electromagnetic energy density and Poynting vector [61], and intermolecular energy shifts via response theory [62–64]. Identical results are of course obtained for any physical quantity computed in either the Schrödinger or Heisenberg representations since the two pictures are related via a unitary transformation [24]. It is also worth noting that in the Heisenberg treatment of molecular QED, the physical picture is one in which electron and photon wavefields interact, and the techniques of second quantization are employed to describe their coupling in terms of a many-particle occupation number representation, in the process highlighting the duality of wave and particle viewpoints.

## 8.4 ONE-PHOTON ABSORPTION

Perhaps the most elementary process involving the interaction of radiation with matter is the absorption of a single photon by an atom or molecule. A rigorous description is furnished by the molecular QED approach and is detailed below, serving as a useful introductory application of the theory, upon which more sophisticated processes are ultimately based.

Consider a sample of  $N$  identical non-interacting atoms or molecules, all initially in their ground electronic state  $|E_0\rangle$  in the presence of a single mode laser. From Eq. (8.21), after neglecting the transverse polarization term, the total Hamiltonian for such a system is given by

$$H = \sum_{\xi=1}^N H_{\text{mol}}(\xi) + H_{\text{rad}} + \sum_{\xi=1}^N H_{\text{int}}(\xi), \quad (8.37)$$

a sum of familiar molecule, field, and interaction Hamiltonians, each term of which was given explicitly in the previous section, either in the minimal-coupling or in the multipolar scheme. On making the long-wavelength approximation, in which there is no spatial variation of the vector potential over the dimensions of each absorber, it is sufficient to retain the first term in the multipolar Hamiltonian (Eq. 8.28), namely the electric dipole contribution,

$$H_{\text{int}}(\xi) = -\epsilon_0^{-1} \vec{\mu}(\xi) \cdot \vec{d}^\perp(\vec{R}_\xi), \quad (8.38)$$

where  $\vec{R}_\xi$  denotes the position vector of body  $\xi$ . On employing a number state representation for the radiation field, if each entity absorbs a single photon of mode  $(\vec{k}, \lambda)$  from the incident beam containing  $n$  photons and is subsequently excited to the electronic state  $|E_m\rangle$  with energy  $E_m$ , then the initial and final total system states are written as

$$|i\rangle = |n(\vec{k}, \lambda)\rangle \prod_{\xi=1}^N |E_0\rangle \quad (8.39a)$$

and

$$|f\rangle = |(n-1)(\vec{k}, \lambda)\rangle |E_m(\xi)\rangle \prod_{\zeta \neq \xi}^N |E_0(\zeta)\rangle, \quad (8.39b)$$

respectively. Overall, energy is conserved subject to the Bohr frequency condition  $E_m - E_0 \approx \hbar\omega$ . The time-ordered diagram shown in Figure 8.1 may be used to illustrate this fundamental process. Time progresses upward. The solid line denotes the electronic state of the atom or molecule. The dashed line denotes the photon, with only changes in the state of the radiation field being shown or written. Coupling between matter and field occurs at the intersection of dashed and solid lines via  $H_{\text{int}}$ , and is known as an interaction vertex. In this linear optical process, the matrix element is given by the first-order term in Eq. (8.36)

$$M_f(\xi) = \langle f | H_{\text{int}} | i \rangle = \langle (n-1)(\vec{k}, \lambda) | E_m | -\epsilon_0^{-1} \vec{\mu}(\xi) \cdot \vec{d}^\perp(\vec{R}_\xi) | E_0 \rangle | n(\vec{k}, \lambda) \rangle, \quad (8.40)$$

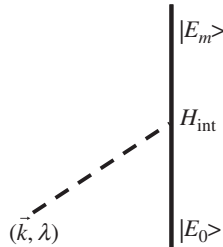


**FIGURE 8.1** Time-ordered diagram representing one-photon absorption.

where it has been assumed that absorption of the photon is equally likely at any of the absorbing species. Hence on using the expansion for the transverse electric displacement field (Eq. 8.25) and the operator relation (Eq. 8.11a), the matrix element is

$$M_f(\xi) = -i \left( \frac{n\hbar ck}{2\epsilon_0 V} \right)^{1/2} \vec{e}^{(\lambda)}(\vec{k}) \cdot \vec{\mu}^{m0}(\xi) e^{i\vec{k} \cdot \vec{R}_\xi}, \quad (8.41)$$

where the transition electric dipole moment is  $\vec{\mu}^{m0}(\xi) = \langle E_m | \vec{\mu}(\xi) | E_0 \rangle$ . The transition rate is given by the Fermi golden rule,

$$\Gamma = \frac{2\pi\rho_f}{\hbar} |M_f(\xi)|^2, \quad (8.42)$$

which is applicable to transitions occurring between a discrete state and a continuum, with  $\rho_f$  the density of final states. In the present case, the final state is  $N$ -fold degenerate. Summing over the rate for each individual absorption event yields the total rate

$$\Gamma = \frac{2\pi\rho_f}{\hbar} \left( \frac{n\hbar ck}{2\epsilon_0 V} \right) \sum_{\xi=1}^N |\vec{e}^{(\lambda)}(\vec{k}) \cdot \vec{\mu}^{m0}(\xi)|^2, \quad (8.43)$$

which holds for atoms or molecules in a fixed orientation relative to the field polarization. For species in the fluid phase, where random orientations feature, rotational averaging gives the isotropic rate formula

$$\langle \Gamma \rangle = \left( \frac{2\pi N \rho_f}{3\hbar} \right) \left( \frac{n\hbar ck}{2\epsilon_0 V} \right) |\vec{\mu}^{m0}|^2, \quad (8.44)$$

with the angular brackets denoting the averaged quantity. It is straightforward to express the rate (Eq. 8.44) in terms of the Einstein  $B$  coefficient. Recognizing that the energy of the radiation field in the interval  $\Delta\omega$  is  $\rho_f \hbar \Delta\omega n \hbar \omega$ , or alternatively in terms

of the radiant energy density per unit frequency interval  $J(\omega)$ ,  $\rho_f = J(\omega)V/2\pi n\hbar^2\omega$ , Eq. (8.44) becomes

$$\langle \Gamma \rangle = NBJ(\omega), \quad (8.45)$$

where

$$B = \frac{1}{6\epsilon_0\hbar^2} |\vec{\mu}^{m0}|^2. \quad (8.46)$$

## 8.5 EMISSION OF LIGHT: SPONTANEOUS AND STIMULATED PROCESSES

The second fundamental radiation-matter process, which together with single-photon absorption forms the basis by which all other spectroscopic and particle-particle interactions can be understood, is emission of radiation. This is of two types: spontaneous and induced. The former requires the quantum theory of radiation for its proper description and computation. The second phenomenon is the basis of laser light. Both are examined below.

Consider an atom or molecule, initially in some excited electronic state  $|m\rangle$ , with energy  $E_m$ . It is well known that such an entity will decay to the ground state  $|0\rangle$ , with energy  $E_0$ , by either the spontaneous or stimulated emission of a photon. In the former case the emitted radiation possesses arbitrary polarization and propagation direction, which for convenience are specified by the mode label  $(\vec{k}, \lambda)$ . Hence, the initial and final radiation-matter states are

$$|i\rangle = |E_m; 0\rangle \quad (8.47a)$$

and

$$|f\rangle = |E_0; 1(\vec{k}, \lambda)\rangle, \quad (8.47b)$$

where the ket  $|0\rangle$  denotes the state of the radiation field which contains no photons, corresponding to the electromagnetic vacuum, bearing in mind that this coupling is never actually switched off at any time. Diagrammatically, spontaneous emission can be pictured as in Figure 8.2. Remaining within the electric dipole approximation through use of the coupling Hamiltonian (Eq. 8.38), along with the use of Eq. (8.25) and the result for the action of the photon creation operator on a number state of the field (Eq. 8.11b), the first-order matrix element is found to be

$$M_{fi}^{(1)} = \langle 1(\vec{k}, \lambda); E_0 | -\epsilon_0^{-1} \vec{\mu} \cdot \vec{d}^\perp(\vec{R}) | E_m; 0 \rangle = i \left( \frac{\hbar c k}{2\epsilon_0 V} \right)^{1/2} \vec{e}^{(\lambda)}(\vec{k}) \cdot \vec{\mu}^{0m} e^{-i\vec{k} \cdot \vec{R}}. \quad (8.48)$$

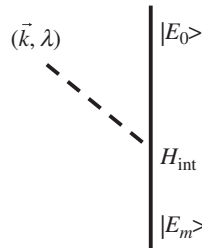


**FIGURE 8.2** Spontaneous emission of a photon from an excited atom.

With the density of final states for emission into a cone of solid angle  $d\Omega$  centered around the wavevector  $\hat{k}$  and given the polarization  $\lambda$  expressed as  $\rho_f = k^2 d\Omega V / (2\pi)^3 \hbar c$ , the total spontaneous emission rate after substituting Eq. (8.48) and  $\rho_f$  into the Fermi golden rule (Eq. 8.42) is

$$\langle \Gamma \rangle = \frac{k^3}{3\pi\epsilon_0\hbar} |\vec{\mu}^{0m}|^2, \quad (8.49)$$

for isotropic atoms, where summation over the two polarizations and integration over all spherical angles has been carried out. From the rate (Eq. 8.49), the Einstein  $A$  coefficient is readily seen to be

$$A = \frac{2k^3}{3\epsilon_0\hbar} |\vec{\mu}^{0m}|^2. \quad (8.50)$$

It is important to note that the spontaneous emission rate,  $\Gamma$ , and the radiative lifetime,  $\tau$ , are related via  $\Gamma\tau = 1$ . Thus, the vacuum electromagnetic field, whose quantization gives rise to zero-point energy of  $\frac{1}{2}\hbar\omega$  per mode, produces observable effects, in this case a measurable spontaneous emission rate. Further, the rate above applies to matter in free space. If the total system resides in a cavity [65], the rate differs considerably due to changes in the field energy density and its mode structure.

In the case of stimulated emission, action of an applied electromagnetic field of a particular mode induces emission of a photon with identical polarization and direction of propagation by an excited atom or molecule, which undergoes a downward transition, possibly to the lowest electronic level. Figure 8.2 may be used to illustrate the effect, bearing in mind that the laser contains  $n$  photons of mode  $(\vec{k}, \lambda)$ . Hence, the initial and final states (Eq. 8.47) are modified to read

$$|i\rangle = |E_m; n(\vec{k}, \lambda)\rangle, \quad (8.51a)$$

and

$$|f\rangle = |E_0; (n+1)(\vec{k}, \lambda)\rangle, \quad (8.51b)$$

for coherent emission with the atom populating the ground electronic state finally. Energy conservation is given by  $E_{m0} \approx \hbar\omega$ . First-order perturbation theory yields the matrix element

$$M_{fi} = i \left( \frac{(n+1)\hbar\omega}{2\varepsilon_0 V} \right)^{1/2} \vec{e}^{(\lambda)}(\vec{k}) \cdot \vec{\mu}^{0m} e^{-i\vec{k} \cdot \vec{R}}, \quad (8.52)$$

from which the isotropic transition rate is easily found to be

$$\langle \Gamma \rangle = \left( \frac{2\pi N \rho_f}{3\hbar} \right) \left( \frac{(n+1)\hbar\omega}{2\varepsilon_0 V} \right) |\vec{\mu}^{m0}|^2, \quad (8.53)$$

which can also be expressed in terms of the Einstein  $B$  coefficient (Eq. 8.46) via Eq. (8.45). Stimulated emission is clearly evident on account of the factor  $n+1$ . Obviously, the spontaneous emission rate is recovered on letting  $n \rightarrow 0$  in Eq. (8.53). For large  $n$ , the contribution from induced emission is larger than that arising from the spontaneous term. When a system subject to irradiation is at equilibrium, the rates of upward and downward transitions are of course equal.

## 8.6 LINEAR LIGHT-SCATTERING: THE KRAMERS-HEISENBERG DISPERSION FORMULA

Having examined in the two previous sections the absorption and emission of light, respectively, it is now possible to treat the processes that simultaneously involve both of these types of photonic events. One of the most elementary is the scattering of light, of which two of the best-known examples include Rayleigh scattering and the Raman effect. Before going on to study these phenomena, a general expression is obtained for light scattering by an atom—the Kramers–Heisenberg dispersion formula [66, 67].

Consider an atom initially in the electronic state  $|p\rangle$ , absorbing a photon from a radiation field containing  $n$  photons of mode  $(\vec{k}, \lambda)$  and emitting a photon of mode  $(\vec{k}', \lambda')$  and ending up in the electronic state  $|q\rangle$ . Therefore, the initial and final total system states are, respectively,

$$|i\rangle = |p; n(\vec{k}, \lambda) \rangle \quad (8.54a)$$

and

$$|f\rangle = |q; (n-1)(\vec{k}, \lambda), 1(\vec{k}', \lambda') \rangle. \quad (8.54b)$$

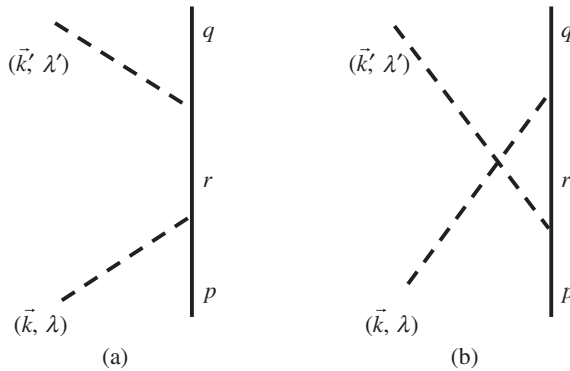


**FIGURE 8.3** Linear scattering of light.

Two diagrams can be sketched to represent the scattering, as shown in Figure 8.3, reflecting the different ordering in time of the photon absorption and emission events. Energy is conserved only between the initial and final states according to

$$E_p + \hbar c k = E_q + \hbar c k'. \quad (8.55)$$

Linear light scattering is a second-order process as seen by the two interaction vertices in Figure 8.3. Hence, second-order time-dependent perturbation theory is required for the computation of the matrix element,

$$M_{fi}^{(2)} = \sum_I \frac{< f | H_{\text{int}} | I > < I | H_{\text{int}} | i >}{E_i - E_f}, \quad (8.56)$$

where the summation is executed over all intermediate states that connect  $|i\rangle$  to  $|f\rangle$ . From Figure 8.3, these are easily seen to be

$$|I_a\rangle = |E_r; (n-1)(\vec{k}, \lambda)\rangle \quad (8.57a)$$

and

$$|I_b\rangle = |E_r; n(\vec{k}, \lambda), 1(\vec{k}', \lambda')\rangle, \quad (8.57b)$$

the first of these corresponding to the case in which a photon of mode  $(\vec{k}, \lambda)$  is absorbed first and the atom is excited to the intermediate state  $|r\rangle$  as illustrated in part (a), while  $|I_b\rangle$  represents the other possible time-ordering in which the photon of mode  $(\vec{k}', \lambda')$  is emitted first followed by absorption of the  $(\vec{k}, \lambda)$  photon, with the atom going through the same intermediate state  $|r\rangle$ . There is no conservation of energy condition applied to the intermediate states, their manifestation occurring through processes that are termed *virtual*, and can be rationalized on the basis of the

time-energy uncertainty relation. Working within the electric dipole approximation, the matrix element is readily evaluated using Eqs. (8.56) and (8.38), together with states (Eqs. 8.54 and 8.57). Using the density of final states for emission of the  $(\vec{k}', \lambda')$  photon in a solid angle  $d\Omega'$  around  $\hat{k}'$  and employing the Fermi golden rule, the differential scattering cross-section is found to be

$$\frac{d\sigma}{d\Omega'} = \frac{kk'^3}{16\pi^2\epsilon_0^2} \left| \sum_r \left\{ \frac{(\vec{\mu}^{qr} \cdot \vec{\bar{e}}')(\vec{\mu}^{rp} \cdot \vec{e})}{E_{rp} - \hbar ck} + \frac{(\vec{\mu}^{qr} \cdot \vec{e})(\vec{\mu}^{rp} \cdot \vec{\bar{e}}')}{E_{rp} + \hbar ck'} \right\} \right|^2, \quad (8.58)$$

which is the Kramers–Heisenberg dispersion formula [68]. In terms of the irradiance,  $I$ , Eq. (8.58) can be written as

$$I(\vec{k}') = \frac{d\Gamma}{d\Omega'} \hbar ck' = \frac{Ik'^4}{16\pi^2\epsilon_0^2} \bar{e}'_l e'_j e'_k \bar{e}_l \alpha_{ij}^{qp}(\omega, -\omega') \bar{\alpha}_{kl}^{qp}(\omega, -\omega'), \quad (8.59)$$

where the second-rank tensor  $\alpha_{ij}^{qp}(\omega, -\omega')$  is defined as

$$\alpha_{ij}^{qp}(\omega, -\omega') = \sum_r \left\{ \frac{\mu_i^{qr} \mu_j^{rp}}{E_{rp} - \hbar\omega} + \frac{\mu_j^{qr} \mu_i^{rp}}{E_{rp} + \hbar\omega'} \right\}. \quad (8.60)$$

The result (Eq. 8.58) is now applied to two cases. In the first, the absorbed and scattered photons are identical in energy and the atom remains in the same state. This corresponds to Rayleigh scattering. In the second case, which gives rise to the Raman effect, the scattering is inelastic and the atom changes the state.

Consider a sample of identical ground state atoms  $\xi$  undergoing elastic scattering of radiation, for which  $|\vec{k}| = |\vec{k}'|$ , represented by the initial and final states, respectively,

$$|i\rangle = |n(\vec{k}, \lambda)\rangle \prod_\xi |0(\xi)\rangle \quad (8.61a)$$

and

$$|f\rangle = |(n-1)(\vec{k}, \lambda), 1(\vec{k}', \lambda')\rangle \prod_\xi |0(\xi)\rangle. \quad (8.61b)$$

In the electric dipole approximation the matrix element is

$$M_f = - \left( \frac{\hbar ck}{2\epsilon_0 V} \right) n^{1/2} \bar{e}'_l e'_j \alpha_{ij}^{00}(\omega, -\omega) \sum_\xi e^{i(\vec{k}-\vec{k}') \cdot \vec{R}_\xi}, \quad (8.62)$$

where  $\alpha_{ij}^{00}(\omega, -\omega)$  is the ground state dynamic polarizability. In the so-called forward scattering,  $\vec{k} = \vec{k}'$ , the phase factor in Eq. (8.62) is unity and the scattering is independent of the position of the particles, being simply  $N$  times the single atom matrix element. Hence, forward scattering is coherent and the intensity varies as the square of the number of atoms,

$$I(\vec{k}') = \frac{N^2 k'^4}{16\pi^2 \epsilon_0^2} \bar{e}'_i e'_j e'_k \bar{e}_l \alpha_{ij}^{00}(\omega, -\omega) \bar{\alpha}_{kl}^{00}(\omega, -\omega). \quad (8.63)$$

For  $\vec{k} \neq \vec{k}'$ , corresponding to non-forward scattering, Eq. (8.62) depends on the positions of atoms forming the assembly. For low particle density and atoms distributed randomly in space, the scattered intensity is  $N$  times the single atom scattered intensity and is said to be incoherent. It is given by expression (8.63) divided by  $N$ ,

$$I(\vec{k}') = \frac{N k^4}{16\pi^2 \epsilon_0^2} |\bar{e} \cdot \bar{e}'|^2 |\alpha(\omega)|^2, \quad (8.64)$$

where  $\alpha(\omega)$  is the atomic polarizability, and the intensity is dependent upon the incident and scattered beam polarization. Regardless of whether scattering is forward or non-forward, the characteristic  $\omega^4$  dependence of Rayleigh scattering is found.

Because dynamic molecular polarizability is orientation dependent, the matrix element for Rayleigh scattering by a collection of molecules is of the form

$$M_{fi} = - \left( \frac{\hbar c k}{2\epsilon_0 V} \right) n^{1/2} \bar{e}'_i e_j \sum_{\xi} \alpha_{ij}^{00}(\omega, -\omega; \xi) e^{i(\vec{k}-\vec{k}') \cdot \vec{R}_{\xi}}, \quad (8.65)$$

in contrast to expression (8.62). Thus, the modulus square produces two- as well as one-center terms. For non-forward scattering, the two-center contributions vanish when averaging over all relative intersite separation distances, leaving only one-center terms to contribute to the scattered intensity, as in

$$I(\vec{k}') = \frac{N k^4}{16\pi^2 \epsilon_0^2} \bar{e}'_i e'_j e'_k \bar{e}_l < \alpha_{ij}^{00}(\omega, -\omega) \bar{\alpha}_{kl}^{00}(\omega, -\omega) >, \quad (8.66)$$

where the angular brackets indicate an average over ground state dynamic molecular polarizabilities. Unlike the case for atoms, for linearly polarized incident beam, the polarization of radiation scattered by randomly oriented molecules is no longer confined to the  $\bar{e}\hat{k}'$ -plane and is depolarized.

When the frequency of the emitted photon differs from that of the incident beam, and the initial and final particle states are not identical, the scattering process is known as the Raman effect [69]. The difference in frequency  $\omega' - \omega$  usually corresponds to characteristic vibrational and rotational frequencies associated with the scattering center.

In order to treat molecular vibrational Raman scattering, it is advantageous to invoke the Born–Oppenheimer approximation and separate the electronic and nuclear degrees of freedom. Let the wavefunction of an electron in a state with quantum number  $s$  be  $\psi_s(q, Q)$ , where  $q$  denotes the set of electronic coordinates and the parameter  $Q$  the normal coordinates of the nuclei. Thus,  $\psi_s(q, Q)$ , is known for fixed values of  $Q$ . Let the vibrational wavefunction for an oscillator in the  $v$ th level of electronic state  $s$  at nuclear coordinate  $Q_k$  be given by  $\phi_{sv}(Q_k)$ , the total wavefunction being a product of electronic and nuclear wavefunctions,  $\psi_s(q, Q)\phi_{sv}(Q)$ . If the molecule changes its vibrational state from  $v \rightarrow w$  but remains in the electronic ground state  $|0\rangle$ , as in vibrational Raman scattering, the initial and final states can be written, respectively, as

$$|i\rangle = |\psi_0(q, Q)\rangle > |\phi_{0v}(Q)\rangle > \quad (8.67a)$$

and

$$|f\rangle = |\psi_0(q, Q)\rangle > |\phi_{0w}(Q)\rangle >. \quad (8.67b)$$

From Eq. (8.59), the scattered intensity is

$$I(\vec{k}') = \frac{NIk'^4}{16\pi^2\varepsilon_0^2} \bar{e}'_i e'_j e'_k \bar{e}_l \alpha_{ij}^{0w,0v}(\omega, -\omega') \bar{\alpha}_{kl}^{0w,0v}(\omega, -\omega'), \quad (8.68)$$

where the tensor  $\alpha_{ij}^{0w,0v}$  is defined as

$$\begin{aligned} \alpha_{ij}^{0w,0v}(\omega, -\omega') = & \sum_{r,x} \left\{ \frac{\langle \phi_{0w} | \langle \psi_0 | \mu_i | \psi_r \rangle | \phi_{rx} \rangle \langle \phi_{rx} | \langle \psi_r | \mu_j | \psi_0 \rangle | \phi_{0v} \rangle}{E_{r0} + \varepsilon_{rx,0v} - \hbar\omega} \right. \\ & \left. + \frac{\langle \phi_{0w} | \langle \psi_0 | \mu_j | \psi_r \rangle | \phi_{rx} \rangle \langle \phi_{rx} | \langle \psi_r | \mu_i | \psi_0 \rangle | \phi_{0v} \rangle}{E_{r0} + \varepsilon_{rx,0v} + \hbar\omega'} \right\}, \end{aligned} \quad (8.69)$$

where  $E_{r0}$  and  $\varepsilon_{rx,0v}$  refer to differences in electronic and vibrational energy, respectively. The result (Eq. 8.68) holds for both resonant and non-resonant Raman scattering, though the tensor (Eq. 8.69) may be simplified in the latter case on account of  $|E_{r0} - \hbar\omega| \gg 0$ . For randomly oriented molecules, a variety of depolarization and reversal ratios may be evaluated, as given in Section 6.5 of Reference 19.

As for other processes involving spectroscopic transitions, whether they are observable or not ultimately depends on the derivation of pertinent selection rules. For electric dipole coupling, for instance, the matrix element between two states,  $\langle f | \vec{\mu} | i \rangle$ , vanishes unless the direct product of the irreducible representations of  $|i\rangle$ ,  $|f\rangle$ , and  $\vec{\mu}$  spans the totally symmetric representation of the group. In general, therefore, transitions that are infrared active are Raman inactive, and vice versa.

## 8.7 CHIROPTICAL EFFECTS

In all of the applications considered thus far it has been sufficient to work within the electric dipole approximation. This is easily justified on the grounds that this is the leading term for the coupling of a neutral species to electromagnetic radiation, in general giving the dominant contribution to the probability amplitude. Hence the succeeding terms in  $H_{\text{int}}$  (Eq. 8.28) such as the magnetic dipole and electric quadrupole contributions, for example, are commonly neglected, being a factor of the fine structure constant smaller in magnitude than  $\mu$ . For many situations, however, the electric dipole approximation is inadequate, and higher-order multipole moments must be accounted for. One important class of problems where this is the case are those involving the interaction of light with chiral molecules. Such species possess the property of handedness, namely that their mirror image forms are non-superposable. A characteristic feature of this type of structure is the absence of an improper rotation axis. A consequence of the reduced symmetry is the relaxation of spectroscopic selection rules, with higher multipole moment transitions now allowed. These compounds exhibit optical activity and their fundamental interactions with light have given rise to a number of key chiroptical techniques such as optical rotation, circular dichroism, and circular differential Rayleigh and Raman scattering, which are routinely used in the determination of chemical and biochemical structures.

When radiation traverses a chiral medium, the angle of the plane of polarization,  $\theta$ , undergoes rotation. Taking the optically active substance to be transparent to absorption, optical rotation may be understood in terms of forward scattering in which the state of the molecule remains the same with only the polarization index of radiation changing. A two-state model may therefore be adopted with

$$|i\rangle = |n(\vec{k}, \alpha)\rangle, \quad (8.70a)$$

and

$$|f\rangle = |(n - 1)(\vec{k}, \alpha), 1(\vec{k}, \beta)\rangle, \quad (8.70b)$$

corresponding to an initial state where there are  $n$  photons of wavevector  $\vec{k}$  and polarization in a state “ $\alpha$ ”, and finally  $n - 1$  of such photons together with one with a polarization state “ $\beta$ ”. Coupling between these states is weak and occurs via virtual transitions. Solution of the time-dependent  $2 \times 2$  eigenvalue problem yields

$$|\Psi(t)\rangle = \{\cos(M_{fi}t/\hbar)|\alpha\rangle - \sin(M_{fi}t/\hbar)|\beta\rangle\}e^{-iEt/\hbar}, \quad (8.71)$$

for the state of the forward scattered beam, with  $E$  the photon energy. For small clockwise rotation in the dilute medium approximation,

$$\theta = n^{-1/2} \frac{M_{fi}l}{\hbar c}, \quad (8.72)$$

where the path length,  $l = ct$ . To leading (second) order, the matrix element for a fluid sample undergoing transitions between states (Eq. 8.70) in the electric and magnetic dipole approximation is

$$M_{fi} = \left( \frac{2\hbar^2 ck^2}{3\varepsilon_0 V} \right) n^{1/2} \sum_r i \frac{\text{Im} \vec{\mu}^{0r} \cdot \vec{m}^{r0}}{(\hbar ck)^2 - E_{r0}^2}, \quad (8.73)$$

where  $\sum_r |r\rangle$  is a complete set of virtual molecular states. Inserting Eq. (8.73) in (8.72) and defining the specific rotation,  $\phi$  as the rotation per unit path length of sample yields the Rosenfeld–Condon formula [70]

$$\phi = -\frac{2\eta\hbar k^2}{3\varepsilon_0} \sum_r \text{Im} \frac{\vec{\mu}^{0r} \cdot \vec{m}^{r0}}{(\hbar ck)^2 - E_{r0}^2}, \quad (8.74)$$

noting that for real wavefunctions  $\vec{\mu}^{0r}$  is pure real and  $\vec{m}^{r0}$  is pure imaginary, and  $\eta$  is the number of optically active molecules per unit volume of the sample. The dependence of  $\phi$  on  $\omega = ck$  of the incident light is known as optical rotatory dispersion. Chirality of the sample is manifest by appearance of the pseudoscalar  $\vec{\mu}^{0r} \cdot \vec{m}^{r0}$ , which changes sign when one enantiomer is replaced by its mirror-image form.

The difference in absorption of left ( $L$ )- and right ( $R$ )-circularly polarized light by a chiral molecule is known as circular dichroism. It may also be computed using the methods of molecular QED [71]. Let an optically active molecule, initially in the ground electronic state, absorb a single, circularly polarized photon and be excited to the electronic state  $|m\rangle$ . Thus,

$$|i\rangle = |E_0; n(\vec{k}, L/R)\rangle, \quad (8.75a)$$

and

$$|f\rangle = |E_m; (n-1)(\vec{k}, L/R)\rangle, \quad (8.75b)$$

with  $E_{m0} \approx \hbar ck$ . Retaining only the electric and magnetic dipole coupling terms from Eq. (8.28) since the electric dipole–quadrupole contribution to circular dichroism is zero for an isotropic sample, the matrix element is evaluated to be

$$M_{fi}^{(L/R)} = -i \left( \frac{n\hbar ck}{2\varepsilon_0 V} \right)^{1/2} e_i^{(L/R)}(\vec{k}) \left[ \mu_i^{0m} \mp \frac{i}{c} m_i^{m0} \right], \quad (8.76)$$

for the molecule positioned at the origin, the upper and lower signs referring to  $L$  and  $R$  circular polarizations, respectively, whose unit electric polarization vector is

$\vec{e}^{(L/R)}(\vec{k})$ . From the Fermi golden rule, the difference in absorption rates for the two forms of light is easily evaluated to be

$$\langle \Gamma^{(L)} \rangle - \langle \Gamma^{(R)} \rangle = -i \left( \frac{8\pi N}{3\hbar c} \right) \left( \frac{n\hbar ck}{2\varepsilon_0 V} \right) \rho_f \vec{\mu}^{0m} \cdot \vec{m}^{m0}, \quad (8.77)$$

where  $N$  is the number of absorbers, and the contribution dependent upon the square of the transition electric or magnetic dipole moment is independent of the handedness of the incident beam, and clearly vanishes, leaving behind the interference term between these two moments. The result (Eq. 8.77) is also directly proportional to the scalar product of  $\vec{\mu}^{0m}$  and  $\vec{m}^{m0}$  which is of opposite sign for enantiomers.

Achiral molecules also exhibit circular dichroism. This occurs in the presence of a static magnetic field and is known as magnetic circular dichroism [72]. The effect arises from the interference of the first-order matrix element for the electric dipole allowed absorption of a single circularly polarized photon and the second-order contribution where a magnetic field,  $\vec{B}$ , is also applied. For randomly oriented molecules, the circular differential absorption rate is

$$\langle \Gamma^{(L)} \rangle - \langle \Gamma^{(R)} \rangle = \left( \frac{4\pi N}{3\hbar} \right) \left( \frac{n\hbar ck}{2\varepsilon_0 V} \right) \rho_f (\vec{B} \cdot \vec{k}) \varepsilon_{\lambda\mu\nu} \mu_\lambda^{m0} \text{Im} \sum_r \left\{ \frac{\mu_\mu^{mr} \bar{m}_v^{r0}}{E_{r0}} + \frac{\bar{m}_v^{mr} \mu_\mu^{r0}}{E_{r0} - \hbar ck} \right\} \quad (8.78)$$

with a  $|m\rangle \leftarrow |0\rangle$  transition taking place in the achiral species. Circular dichroism vanishes when the magnetic field is perpendicular to the direction of propagation of the incident radiation and is a maximum when these two vectors are parallel to one another.

Irradiation of achiral molecules by an intense beam of circularly polarized light can also result in optical rotation and circular dichroism. The former is a coherent four-photon process in which circularly polarized light is scattered but otherwise unchanged, and a second collinear plane-polarized beam changes its polarization state. It corresponds to the process

$$|E_0; n_1(\vec{k}, L), (n_2 - 1)(\vec{k}_2, \alpha), 1(\vec{k}_2, \beta) \rangle \leftarrow |E_0; n_1(\vec{k}_1, L), n_2(\vec{k}_2, \alpha) \rangle. \quad (8.79)$$

Laser-induced circular dichroism is described as

$$|E_m; n_1(\vec{k}_1, L), (n_2 - 1)(\vec{k}_2, L/R) \rangle \leftarrow |E_0; n_1(\vec{k}_1, L), n_2(\vec{k}_2, L/R) \rangle, \quad (8.80)$$

and corresponds to a three-photon process in which the probe beam ( $\vec{k}_2, L/R$ ) is resonant with the transition  $m \leftarrow 0$ , in the achiral molecule, and chirality is induced by the non-resonant circularly polarized laser ( $\vec{k}_2, L$ ). The phenomenon arises from interference of one- and three-photon amplitudes. Further details of these two effects may be found in Chapter 9 of Reference 19.

Chiral molecules also scatter circularly polarized light at different rates, as exemplified by circular differential Rayleigh and Raman processes. As for other chiroptical effects, theory is developed by including higher multipole moment terms, with a non-vanishing contribution arising from electric quadrupole coupling, in a systematic extension of the method [73] outlined in Section 8.6. For non-forward Rayleigh scattering, with the initial and final states

$$|i\rangle = |E_0; n(\vec{k}, L/R)\rangle, \quad (8.81a)$$

and

$$|f\rangle = |E_0; (n-1)(\vec{k}, L/R), 1(\vec{k}', \lambda)\rangle, \quad (8.81b)$$

respectively, and circular differential effects arise from interference between pure electric dipole and mixed electric-magnetic dipole and electric dipole-quadrupole amplitudes. The former contribution to the differential elastic scattered intensity for an isotropic system is

$$\begin{aligned} I(L \rightarrow \lambda) - I(R \rightarrow \lambda) = & -\frac{I_0 k^4}{240\pi^2 \epsilon_0^2 c} \text{Im}[(1 - 3|\hat{k} \cdot \vec{e}^{(\lambda)}|^2)\alpha_{\lambda\lambda}(\omega)\bar{G}_{\mu\mu}(\omega) \\ & + (7 - |\hat{k} \cdot \vec{e}^{(\lambda)}|^2)\alpha_{\lambda\mu}(\omega)\bar{G}_{\lambda\mu}(\omega) \\ & - 5(\hat{k} \cdot \hat{k}')\{\alpha_{\lambda\lambda}(\omega)G_{\mu\mu}(\omega) - \alpha_{\lambda\mu}(\omega)G_{\lambda\mu}(\omega)\}], \end{aligned} \quad (8.82)$$

where  $I_0$  is the power per unit area of the incident beam and  $G_{ij}(\omega)$  is the dynamic mixed electric-magnetic dipole polarizability. The analogous electric quadrupole-dependent contribution is

$$I(L \rightarrow \lambda) - I(R \rightarrow \lambda) = -\frac{I_0 k^5}{240\pi^2 \epsilon_0^2} (1 - 3|\hat{k} \cdot \vec{e}^{(\lambda)}|^2 - 3(\hat{k} \cdot \hat{k}'))\epsilon_{\lambda\nu\pi}\alpha_{\lambda\mu}(\omega)A_{\nu\pi\mu}(\omega), \quad (8.83)$$

where  $A_{ijk}(\omega)$  is the frequency-dependent mixed electric dipole-quadrupole polarizability tensor. The differential intensities (Eqs. 8.82 and 8.83) are about one-thousandth that of the total Rayleigh intensity (Eq. 8.63). Raman scattering by chiral molecules follows in a straightforward manner as presented in the previous section.

In addition to optical activity occurring at one center, chiral discriminatory effects can also manifest in two or more bodies, which may or may not be coupled intermolecularly. Optical rotation, circular dichroism, as well as Rayleigh and Raman scattering have all been evaluated in the so-called two-group model, where two achiral functional groups or chromophores are well separated, with chirality arising from their relative placement and orientation. Frequently the electric dipole approximation

is sufficient to describe transitions taking place within each center. For two identical functional groups, the rotationally averaged circular differential absorption rate is

$$\langle \Delta\Gamma(\pm) \rangle = \pm \frac{J(\omega)}{2\varepsilon_0\hbar^2} \left( \frac{\cos kR}{kR} - \frac{\sin kR}{k^2 R^2} \right) [\vec{\mu}^{m0}(A) \times \vec{\mu}^{m0}(B)] \cdot \hat{R}, \quad (8.84)$$

for the two stationary states  $\frac{1}{\sqrt{2}} \{ |E_m^A, E_0^B \rangle \pm |E_0^A, E_m^B \rangle \}$  and where  $J(\omega)$  is the radiant energy density per unit frequency interval of the incident radiation. Thus, the circular dichroism is equal and opposite for the symmetric and anti-symmetric states.

Optical activity can also be induced in an achiral species via intermolecular coupling with a chiral body in close proximity. Circular dichroism or circularly polarized luminescence occurs at a frequency characteristic of a transition in the achiral molecule with the chiral entity being transparent. Electric dipole transitions take place in the achiral species while both electric and magnetic dipole ones occur to leading order in the chiral body. Interference between first- and third-order terms (in the absence and presence of interparticle coupling) yields circular dichroism transition rates [74]. With continuing technological advances being made in the generation of coherent sources of laser light, new chiroptical spectroscopies have been proposed and developed, especially those involving nonlinear optics [75].

## 8.8 TWO-PHOTON ABSORPTION

Relative to scattering of light perhaps a more fundamental second-order radiation-molecule process is two-photon absorption of light. This is directly amenable to measurement with the wide availability of tunable lasers [76]. It is useful to give the general theory for absorption from two different beams before specializing to the more common case of two-photon absorption from the same beam.

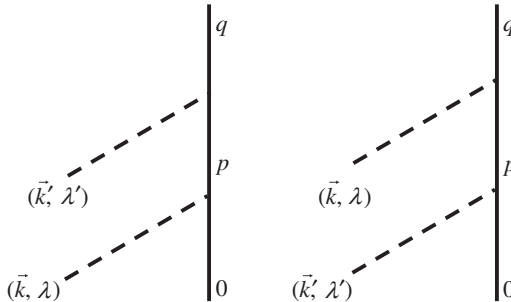
Consider an atom or molecule initially in the ground electronic state  $|0\rangle$  being excited to the electronic state  $|q\rangle$  by absorbing two photons, one of mode  $(\vec{k}, \lambda)$  and the other of mode  $(\vec{k}', \lambda')$  from two different lasers containing  $n(\vec{k}, \lambda)$  and  $n'(\vec{k}', \lambda')$  photons, respectively. The initial and final states are then

$$|i\rangle = |E_0; n(\vec{k}, \lambda), n'(\vec{k}', \lambda') \rangle \quad (8.85a)$$

and

$$|f\rangle = |E_q; (n-1)(\vec{k}, \lambda), (n'-1)(\vec{k}', \lambda') \rangle, \quad (8.85b)$$

respectively. The process may be represented by the two time-ordered diagrams of Figure 8.4, corresponding to the situation in which a photon of mode  $(\vec{k}, \lambda)$  is absorbed before or after that of mode  $(\vec{k}', \lambda')$ .  $|p\rangle$  is an intermediate level of the particle and which is taken to be non-resonant with respect to the energy associated with one-photon absorption. Hence, there are two possible virtual states that need to

**FIGURE 8.4** Two-photon absorption from two different beams.

be accounted for. Staying within the electric dipole approximation, using Eqs. (8.38) and (8.56) yields the matrix element

$$M_{fi} = \left( \frac{n\hbar ck}{2\varepsilon_0 V} \right)^{1/2} \left( \frac{n'\hbar ck'}{2\varepsilon_0 V} \right)^{1/2} e_i^{(\lambda')}(\vec{k}') e_j^{(\lambda)}(\vec{k}) \alpha_{ij}^{q0}(\omega, \omega'), \quad (8.86)$$

where  $e_i^{(\lambda')}(\vec{k}')$  and  $e_j^{(\lambda)}(\vec{k})$  denote the polarizations of the two distinct photon modes, and the tensor  $\alpha_{ij}^{q0}(\omega, -\omega')$  is given by Eq. (8.60). Analogous to Eq. (8.45), the absorption rate for a randomly oriented sample of  $N$  absorbing bodies may be written as

$$\langle \Gamma \rangle = N \bar{J}_1(\omega) \bar{I}_2 B^{(2)}, \quad (8.87)$$

where  $\bar{J}_1(\omega)$  is the mean intensity of the laser of frequency  $\omega$ , and  $\bar{I}_2 = \langle n' \rangle \hbar c^2 k'/V$  is the mean irradiance of the second beam, and the factor  $B^{(2)}$  is found to be

$$B^{(2)} = \frac{1}{120\hbar^2\varepsilon_0^2 c} [A \alpha_{\lambda\lambda}^{q0}(\omega, \omega') \bar{\alpha}_{\mu\mu}^{q0}(\omega, \omega') + B \alpha_{\lambda\mu}^{q0}(\omega, \omega') \bar{\alpha}_{\lambda\mu}^{q0}(\omega, \omega') + C \alpha_{\lambda\mu}^{q0}(\omega, \omega') \bar{\alpha}_{\mu\lambda}^{q0}(\omega, \omega')]. \quad (8.88)$$

In Eq. (8.88), Greek subscripts denote Cartesian tensor components in the molecule-fixed frame of reference, and as a result of fourth-rank tensor averaging and contraction,

$$A = 4|\vec{e} \cdot \vec{e}'|^2 - 1 - |\vec{e} \cdot \vec{e}''|^2; \quad B = -|\vec{e} \cdot \vec{e}'|^2 + 4 - |\vec{e} \cdot \vec{e}''|^2; \\ C = -|\vec{e} \cdot \vec{e}'|^2 - 1 + 4|\vec{e} \cdot \vec{e}''|^2; \quad (8.89)$$

noting that  $\vec{e} \cdot \vec{e}'$  and  $\vec{e} \cdot \vec{e}''$  are equal only for linear polarizations.

From the above, it is straightforward to obtain results when two identical photons are absorbed from the same beam, characterized by  $n(\vec{k}, \lambda)$ . Then, the states (Eq. 8.85) become

$$|i\rangle = |E_0; n(\vec{k}, \lambda)\rangle \quad (8.90a)$$

and

$$|f\rangle = |E_q; (n-2)(\vec{k}, \lambda)\rangle. \quad (8.90b)$$

Now only one graph and one type of intermediate state contributes to the matrix element, which from Eq. (8.86) is easily seen to be

$$M_{fi} = \left( \frac{\hbar ck}{4\epsilon_0 V} \right) [n(n-1)]^{1/2} e_i^{(\lambda)}(\vec{k}) e_j^{(\lambda)}(\vec{k}) \alpha_{ij}^{q0}(\omega, \omega), \quad (8.91)$$

where a factor of one-half has been introduced on account of  $i,j$ -index symmetry. Evaluating the isotropic transition rate for  $N$  molecules via the Fermi golden rule results in an expression similar to Eq. (8.87),

$$\langle \Gamma \rangle = NJ(\omega) \bar{I} g^{(2)} B^{(2)}, \quad (8.92)$$

where the new two-photon  $B$ -coefficient is given by

$$B^{(2)} = \frac{1}{240\hbar^2 \epsilon_0^2 c} [(2|\vec{e} \cdot \vec{e}|^2 - 1) \alpha_{\lambda\lambda}^{q0}(\omega, \omega) \bar{\alpha}_{\mu\mu}^{q0}(\omega, \omega) - (|\vec{e} \cdot \vec{e}|^2 - 3) \alpha_{\lambda\mu}^{q0}(\omega, \omega) \bar{\alpha}_{\lambda\mu}^{q0}(\omega, \omega)], \quad (8.93)$$

on using the  $\lambda,\mu$ -index symmetry property of the  $\alpha$ -tensor, and the degree of second-order coherence is given by the two-photon correlation factor  $g^{(2)} = \langle n(n-1) \rangle / \langle n \rangle^2$ . Two-photon transitions are allowed between the states of the same parity.

The process opposite to the absorption of two photons from two different lasers, namely spontaneous two-photon emission, may be calculated in a manner similar to that described earlier. Normally in such calculations it is assumed that the emission does not take place via one-photon processes. Analogously to stimulated emission, two-photon stimulated emission can also occur. If a laser of frequency  $\omega'$  irradiates a molecule undergoing two-photon emission at energy  $E_{m0}$  with  $\omega' < \omega_{m0}$  then an extra contribution to the transition rate arises from stimulated emission of a photon with energy  $\hbar ck'$  with the same mode characteristics as the stimulating beam, as well as the spontaneous emission of a photon with frequency  $\omega_{m0} - \omega'$  and any polarization and direction of propagation. The matrix element is easily computed to be

$$M_{fi} = \left( \frac{\hbar ck}{2\epsilon_0 V} \right)^{1/2} \left( \frac{n' \hbar ck'}{2\epsilon_0 V} \right)^{1/2} \bar{e}_i \bar{e}'_j \alpha_{ji}^{m0}(\omega, \omega'), \quad (8.94)$$

from which the Fermi golden rule transition rate for all possible relative orientations of the particle with respect to the applied laser field is found to be

$$\langle \Gamma \rangle = \frac{I' \omega^3}{18\pi \epsilon_0^2 \hbar c^4} \alpha_{\lambda\mu}^{m0}(\omega, \omega') \bar{\alpha}_{\lambda\mu}^{m0}(\omega, \omega'), \quad (8.95)$$

exhibiting  $\omega^3$  dependence on frequency.

## 8.9 NONLINEAR LIGHT-SCATTERING: SUM-FREQUENCY AND HARMONIC GENERATION

While the field of quantum optics is mature, it continues to develop both experimentally and in the prediction of novel phenomena, going beyond multiphoton absorption and emission processes and linear light scattering, to include nonlinear light scattering applications [14, 39, 40, 75]. A couple of these are described in this section such as sum-frequency generation and second- and third-harmonic generation, upon which more esoteric processes are typically based.

Consider an optically active molecule in the ground electronic state subject to two incident monochromatic laser fields with occupation number  $n$  photons of mode  $(\vec{k}, \lambda)$  and  $n'$  photons of mode  $(\vec{k}', \lambda')$ . Sum-frequency generation corresponds to the situation in which the molecule absorbs a single photon from each beam and emits a single photon at the sum frequency, whose mode is  $(\vec{k}_s, \lambda_s)$ , and remains in the ground state. Energy is conserved according to  $\hbar\omega_s = \hbar(\omega + \omega')$ . A signal is manifested from this type of spectroscopy only if the scattering medium is isotropic and non-centrosymmetric. It was first proposed by Giordmaine [77] and affords a means by which the structure of chiral liquids may be interrogated and the handedness of the solution determined. Intensities have been successfully recorded for 1,1'-bi-2-naphthol and limonene [78, 79]. The initial and final states are therefore written, respectively, as

$$|i\rangle = |E_0; n(\vec{k}, \lambda), n'(\vec{k}', \lambda')\rangle \quad (8.96a)$$

and

$$|f\rangle = |E_0; (n-1)(\vec{k}, \lambda), (n'-1)(\vec{k}', \lambda'), 1(\vec{k}_s, \lambda_s)\rangle. \quad (8.96b)$$

The matrix element is evaluated using third-order time-dependent perturbation theory together with the aid of six time-ordered diagrams, one of which is shown in Figure 8.5, in which  $|p\rangle$  and  $|q\rangle$  denote intermediate electronic states of the scattering entity. Even though linear light scattering by chiral molecules requires electric and magnetic dipoles, and electric quadrupole coupling terms to leading order for a proper description, it is sufficient to remain within the electric dipole approximation to treat

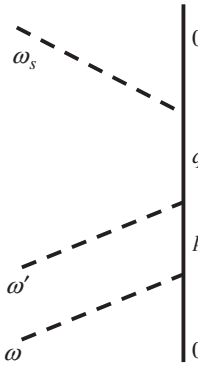


**FIGURE 8.5** One of six diagrams contributing to sum-frequency generation.

this three-photon process. For coherent forward scattering by  $N$  centers, the matrix element is [80–83],

$$M_{fi} = -iN \left( \frac{\hbar c}{2\epsilon_0 V} \right)^{3/2} (kk'k_s)^{1/2} (nn')^{1/2} e_i^{(\lambda)}(\vec{k}) e_j^{(\lambda')}(\vec{k}') \bar{e}_k^{(\lambda_s)}(\vec{k}_s) \beta_{ijk}, \quad (8.97)$$

where  $\beta_{ijk}$  is the first molecular hyperpolarizability tensor

$$\beta_{ijk} = \sum_{p,q} \left\{ \begin{array}{l} \frac{\mu_k^{0q} \mu_j^{qp} \mu_i^{p0}}{(E_{p0} - \hbar\omega)(E_{q0} - \hbar\omega - \hbar\omega')} + \frac{\mu_k^{0q} \mu_i^{qp} \mu_j^{p0}}{(E_{p0} - \hbar\omega')(E_{q0} - \hbar\omega - \hbar\omega')} \\ + \frac{\mu_j^{0q} \mu_k^{qp} \mu_i^{p0}}{(E_{p0} - \hbar\omega)(E_{q0} - \hbar\omega + \hbar\omega_s)} + \frac{\mu_i^{0q} \mu_k^{qp} \mu_j^{p0}}{(E_{p0} - \hbar\omega')(E_{q0} - \hbar\omega' + \hbar\omega_s)} \\ + \frac{\mu_j^{0q} \mu_i^{qp} \mu_k^{p0}}{(E_{p0} + \hbar\omega_s)(E_{q0} - \hbar\omega + \hbar\omega_s)} + \frac{\mu_i^{0q} \mu_j^{qp} \mu_k^{p0}}{(E_{p0} + \hbar\omega_s)(E_{q0} - \hbar\omega' + \hbar\omega_s)} \end{array} \right\}, \quad (8.98)$$

and which vanishes for centrosymmetric species.

In terms of the incident beam irradiances  $I$  and  $I'$ , the integrated intensity for emission at the sum-frequency in a cone centered around  $\hat{k}_s$  is then

$$I^{sfg} = \hbar c k_s \frac{d\Gamma}{d\Omega} = \frac{II' k_s^4 N^2}{32\pi^2 \epsilon_0^3 c} |e_i^{(\lambda)}(\vec{k}) e_j^{(\lambda')}(\vec{k}') \bar{e}_k^{(\lambda_s)}(\vec{k}_s) < \beta_{ijk} >|^2, \quad (8.99)$$

where  $< \beta_{ijk} >$  denotes an orientational average of the response tensor (Eq. 8.98). An expression for difference-frequency generation is easily obtained on replacing  $\omega'$  by

$-\omega'$  in Eq. (8.99). The result (Eq. 8.99) is proportional to the square of the number of scatterers and to the fourth power of the sum-frequency and is linearly dependent on  $I$  and  $I'$ . In addition to the signal intensity applicable to isotropic molecules, theory has also been developed for molecules that are partially oriented, aligned within thin films, or adsorbed on a surface [40, 80], the presence of an interface clearly resulting in the breakdown of spatial inversion symmetry. Further work included studying the effect of a static electric field on a chiral liquid undergoing sum-frequency generation, with measurements being reported on 1,1'-bi-2-naphthol dissolved in tetrahydrofuran solution [84]. Interestingly, the cross-term between static field-free and field-dependent contributions enables the absolute configuration and chirality of a solution of optically active molecules to be determined since it depends on a parity-odd seventh-rank observable quantity [83]. Both the coherent and incoherent integrated signal intensities are directly proportional to the strength of the dc field.

A noteworthy special case of sum-frequency generation occurs when the frequencies of the two incoming beams are identical, namely  $\omega = \omega'$ . The resulting process is the well-known second-harmonic generation, with emission occurring at  $\omega_s = 2\omega$  [85, 86]. Since the two absorbed photons are identical, only three diagrams of the type shown in Figure 8.5 contribute to the matrix element, which from Eq. (8.97) is easily found to be

$$M_{fi} = -\frac{i}{2}N \left( \frac{\hbar ck}{\epsilon_0 V} \right)^{3/2} [n(n-1)]^{1/2} e_i^{(\lambda)}(\vec{k}) e_j^{(\lambda)}(\vec{k}) \bar{e}_k^{(\lambda_s)}(\vec{k}_s) \beta_{ijk}, \quad (8.100)$$

with Eq. (8.98) modified appropriately to give the pertinent response tensor  $\beta_{ijk}$ . Making proper allowance for photon statistics, the harmonic intensity is readily obtained from Eq. (8.100) as

$$I^{shg} = \frac{\bar{I}^2 k^4 N^2 g^{(2)}}{2\pi^2 \epsilon_0^3 c} |e_i e_j \bar{e}_k^s < \beta_{ijk} >|^2. \quad (8.101)$$

Employing the relations between the components of the hyperpolarizability tensor in the lab and molecule fixed frames,  $< \beta_{ijk} > = \frac{1}{6} \epsilon_{ijk} \epsilon_{\lambda\mu\nu} \beta_{\lambda\mu\nu}$ , and noting that  $e_i e_j$  is symmetric while  $\epsilon_{ijk}$  is antisymmetric to interchange of indices  $i$  and  $j$ , leads to the well-known result that the second-harmonic intensity arising from an isotropic source is zero. The vanishing of the intensity occurs for all multipole orders for coherent generation of even harmonics in free molecules [85].

Second-harmonic generation in free molecules is allowed if the spatial isotropy is broken. This can occur by application of a static electric field [87], with the radiant intensity given by

$$I = \frac{E^2 \bar{I}^2 g^{(2)} k^4 N^2}{450 \pi^2 \epsilon_0^3 c} |\{3(\vec{e}' \cdot \vec{e})(\vec{e} \cdot \hat{E}) - (\vec{e}' \cdot \hat{E})(\vec{e} \cdot \vec{e})\} \chi_{\lambda\lambda\mu\mu} - \{(\vec{e}' \cdot \vec{e})(\vec{e} \cdot \hat{E}) - 2(\vec{e}' \cdot \hat{E})(\vec{e} \cdot \vec{e})\} \chi_{\lambda\mu\mu\lambda}|^2, \quad (8.102)$$

where  $\chi_{\lambda\mu\nu\pi}$  is a 24-term  $\mu\nu$ -symmetric response tensor, and the static electric field  $\vec{E} = E\hat{E}$  has the magnitude  $E$  and the direction indicated by the unit vector  $\hat{E}$ . Clearly Eq. (8.102) vanishes when  $\hat{E} \parallel \hat{k}$  since  $\vec{e}$  and  $\vec{e}'$  are then perpendicular to  $\hat{k}$ . Even though hyper-Rayleigh second-harmonic generation and electric field-induced second-harmonic generation are both independently symmetry allowed in any liquid, the incoherent cross-term between these processes is zero for mutually perpendicular incident, emitted, and dc fields [83].

Third-harmonic generation in a gaseous sample is allowed. This fourth-order process arises when three photons of frequency  $\omega$  are absorbed, and one at frequency  $3\omega$  is emitted. The coherent forward scattered intensity is

$$I = \frac{81\bar{I}^3 g^{(3)} k^4 N^2}{64\pi^2 \epsilon_0^4 c^2} |\vec{e}'_i e_j e_k e_l < \gamma_{ijkl} >|^2, \quad (8.103)$$

where  $g^{(3)} = < n(n-1)(n-2) > / < n >^3$  is the degree of third-order coherence and  $\gamma_{ijkl}$  is a fourth-rank hyperpolarizability tensor that is symmetric in  $j$ ,  $k$ , and  $l$ . For randomly oriented molecules the intensity is found to be

$$I = \frac{81\bar{I}^3 g^{(3)} k^4 N^2}{1600\pi^2 \epsilon_0^4 c^2} |\vec{e} \cdot \vec{e}|^2 |\vec{e} \cdot \vec{e}'|^2 |\gamma_{\lambda\lambda\mu\mu}|^2, \quad (8.104)$$

from which it is seen that the polarization of the harmonic is in the same direction as the polarization of the incoming radiation when the latter is linearly polarized.

Numerous other nonlinear and quantum optical processes such as four-, five-, ... wave mixing, hyper-Rayleigh and Raman scattering, and Kerr effect have been successfully treated using quantized radiation field methods and may be found in specific texts on the subject [14, 39, 40, 88, 89].

## 8.10 RESONANCE ENERGY TRANSFER

All of the processes considered thus far have either involved the absorption or emission, or a combination thereof, of real photons. These, however, are not the only types of photons permitted by the theory. As stated in Section 8.1, virtual photons are also allowed and are rationalized using time-energy uncertainty relations. This type of photon is used in molecular QED theory to understand the origin and manifestation of interparticle forces, as well as in self-energy corrections, as is done in quantum field theory when coupling between elementary particles is being computed.

Two fundamental intermolecular interactions will be examined. They bring to the fore the characteristic features associated with mediation of forces between bodies by virtual photon exchange. These include resonance energy transfer, to be examined briefly below, with other aspects being considered in the chapter by Andrews, Bradshaw, and Scholes, followed by van der Waals dispersion interactions, which will be studied in the next section.

A particularly insightful example of coupling between a pair of atoms, molecules, chromophores, or other such functional units that occurs via the exchange of a single virtual photon is the resonant transfer of excitation energy. In this situation, an initially electronically and/or vibrationally excited species, A, located at  $\vec{R}_A$ , transfers its energy resonantly to a neighboring species B, positioned at  $\vec{R}_B$ , which then becomes excited after initially being in its lowest level, with A decaying to the ground state. This has been a much studied problem in the field of QED, dating back to an early calculation by Fermi [42], and further investigation by numerous other workers since then [90–101]. This longstanding and ongoing interest in resonance energy transfer is due to the crucial role it plays when it comes to tackling fundamental issues associated with violation or otherwise of Einstein causality of the propagated signal, to questions related to state specification and preparation of quantum mechanical systems, to the burgeoning field of quantum information theory, and more recently to applications of energy transfer to chemical, physical, and biological systems such as in the light-harvesting complex of the photosynthetic unit, and other antennae structures, dendrimers, photovoltaics, and organic light-emitting diodes, to give but a few examples [97, 101].

The matrix element and transfer rate are readily calculable using molecular QED techniques. With the donor species initially in the excited state  $|m\rangle$ , the initial and final states of the total system are written, respectively, as

$$|i\rangle = |E_m^A, E_0^B \rangle \quad (8.105a)$$

and

$$|f\rangle = |E_0^A, E_m^B \rangle, \quad (8.105b)$$

with no photons (real or virtual) present before or after transfer. For electric dipole-dipole exchange, two time-ordered diagrams, depicted in Figure 8.6, contribute to

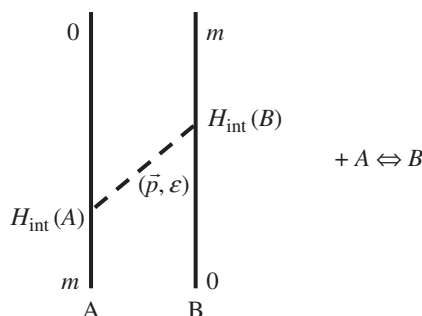


**FIGURE 8.6** Time-ordered diagrams for resonance energy transfer.

the matrix element. Employing second-order perturbation theory and standard calculational techniques yields, for the matrix element, the expression

$$M_{fi} = \mu_i^{0m}(A)\mu_j^{m0}(B)V_{ij}(k_{m0}, \vec{R}), \quad (8.106)$$

where the internuclear separation distance vector,  $\vec{R} = \vec{R}_B - \vec{R}_A$ , and  $V_{ij}(k, \vec{R})$  is the retarded resonant dipole-dipole exchange tensor

$$V_{ij}(k, \vec{R}) = \frac{1}{4\pi\epsilon_0 R^3}[(\delta_{ij} - 3\hat{R}_i\hat{R}_j)(1 - ikR) - (\delta_{ij} - \hat{R}_i\hat{R}_j)k^2 R^2]e^{ikR}. \quad (8.107)$$

Inspection of Eq. (8.107) reveals that the commonly used  $R^{-3}$  static ( $\omega = 0$ ) dipolar coupling follows on making the near-zone approximation  $kR \ll 1$ . Interestingly, at very long-range ( $kR \gg 1$ )  $V_{ij}(k, \vec{R})$  exhibits inverse separation distance dependence, with photon exchange being exclusively transverse in nature. From the last two formulae the Fermi golden rule transition rate is easily obtainable. For completely randomly oriented donor and acceptor species, as occurs in a fluid medium, the transfer rate is

$$\langle \Gamma \rangle = \frac{\rho_f}{36\pi\hbar\epsilon_0^2 R^6} |\vec{\mu}^{0m}(A)|^2 |\vec{\mu}^{m0}(B)|^2 [k_{m0}^4 R^4 + k_{m0}^2 R^2 + 3], \quad (8.108)$$

and which holds for all  $R$  outside the region of overlap of electronic charge clouds. When charge distributions overlap, Dexter theory [102] may be employed to compute the stronger direct- and exchange-type force terms.

The result (Eq. 8.108) provides an all encompassing formula for long-range transfer of energy, incorporating two distinct mechanisms at its asymptotic limits. These correspond to the widely used  $R^{-6}$ -dependent Förster rate law [103] in which near-zone migration of energy is understood as radiationless, arising from static coupling between centers, to transfer in the far zone which is radiative and displays inverse square separation distance dependence. At this extreme, exchange of energy is viewed as arising from emission of a photon by the excited donor followed by its capture by the unexcited acceptor moiety with the propagated photon acquiring ever more real character as  $R \rightarrow \infty$ . Hence, molecular QED provides a unified theory of resonant transfer of energy and a description in terms of virtual photon exchange.

Even though the presentation given above has been confined to migration of energy between two units in a vacuum, theory has been developed to take into account the effects of a medium [104, 105]. One way this has been done is via the introduction of medium-dressed photons that arise on quantizing the bath. The latter subsystem is composed of entities comprising the surrounding environment, their interaction with the radiation field, and the electromagnetic field itself. The resulting particle is the polariton, which mediates transfer in the medium instead of a photon, which

propagates in vacuum [106, 107]. With local field factors also correctly accounted for, the transfer tensor in a medium may be written in terms of Eq. (8.107) as

$$V_{ij}^{\text{med}}(k, \vec{R}) = \frac{1}{n^2} \left( \frac{n^2 + 2}{3} \right)^2 V_{ij}(nk, \vec{R}), \quad (8.109)$$

where  $n$  is the complex refractive index of the medium at a frequency corresponding to the resonant transfer of energy. This has the consequence of modifying the transfer rate by a scale factor, with dispersion and attenuation effects accounted for. Another approach is to solve explicitly for the Maxwell fields as they traverse a medium with dielectric and/or magnetic properties via the introduction of complex electric permittivity, magnetic permeability, and refractive index, and evaluate the appropriate matrix element directly from the operator forms of the fields [108, 109]. Typically, enhancement of the rate in a medium is small. Yet another method is to take a microscopic approach and calculate the change in transfer rate due to the presence of a third-, fourth-, ... body, which mediates exchange between the pair, these additional particles constituting the medium in the limit of very large particle number [54, 56, 110, 111].

## 8.11 VAN DER WAALS DISPERSION ENERGY

A second example illustrating the role of virtual photons in mediating forces between particles, and which is of historical significance, is the calculation of the van der Waals dispersion interaction using field theoretic techniques by Casimir and Polder in 1948 [13]. Although their technically demanding computation was carried out in the minimal-coupling framework of QED, their result may be obtained a little more straightforwardly using the multipolar version of the theory. Recall that in this formalism, molecules couple directly to the Maxwell fields via their molecular multipole moments and the interaction is properly retarded since all static intermolecular coupling terms have been eliminated. For two neutral, electric dipole polarizable atoms or molecules  $A$  and  $B$  in their ground electronic states, the initial and final states are given by

$$|i\rangle = |f\rangle = |E_0^A, E_0^B\rangle, \quad (8.110)$$

with no photons present, either real or virtual. Hence the dispersion force is another phenomenon that may be attributed to zero-point energy and fluctuations associated with the vacuum electromagnetic field. In the multipolar coupling scheme, the dispersion force is viewed as arising from two virtual photon exchange. A representative time-ordered diagram depicting the interaction is shown in Figure 8.7. Evidently, to leading order fourth-order time-dependent perturbation theory is necessary to evaluate the energy shift, with 24 diagrams contributing in total. These are reduced in number by a half since both virtual photon polarizations and momenta are summed,

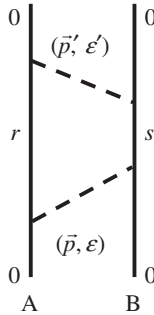


**FIGURE 8.7** One of 24 diagrams contributing to Casimir–Polder energy shift.

rendering them ultimately indistinguishable. An oft-repeated calculation leads to the Casimir–Polder dispersion potential energy formula [13, 15, 19, 21, 22, 26, 57, 112]

$$\Delta E = -\frac{\hbar c}{16\pi^3 \epsilon_0^2} \int_0^\infty du u^6 e^{-2uR} \alpha(A; iu) \alpha(B; iu) \left[ \frac{1}{u^2 R^2} + \frac{2}{u^3 R^3} + \frac{5}{u^4 R^4} + \frac{6}{u^5 R^5} + \frac{3}{u^6 R^6} \right], \quad (8.111)$$

which applies to all interparticle separation distances  $R$  between randomly oriented  $A$  and  $B$ , and is written in terms of the polarizability  $\alpha(\xi; iu)$  of body  $\xi = A, B$  at imaginary frequency  $\omega = icu$ ,

$$\alpha(\xi; iu) = \frac{2}{3} \sum_i \frac{|\vec{\mu}^{0r}(\xi)|^2 E_{i0}}{E_{i0}^2 + (\hbar cu)^2}. \quad (8.112)$$

Asymptotic limits at the extremes of separation follow readily from result Eq. (8.111). In the far-zone  $kR \gg 1$ , and the polarizabilities may be taken to be static ( $\omega \rightarrow 0$ ) and the  $u$ -integral carried out to yield the familiar  $R^{-7}$  dependence of the Casimir–Polder dispersion potential,

$$\Delta E_{FZ} = -\frac{23\hbar c}{64\pi^3 \epsilon_0^2 R^7} \alpha(A; 0) \alpha(B; 0). \quad (8.113)$$

At short separations, but still outside the overlap region,  $kR \ll 1$  and it is sufficient to retain the dominant  $R^{-6}$ -dependent term in Eq. (8.111) and approximate  $e^{-2uR}$  by unity. Integration results in the familiar London dispersion energy [113]

$$\Delta E_{NZ} = -\frac{1}{24\pi^2 \epsilon_0^2 R^6} \sum_{r,s} \frac{|\vec{\mu}^{0r}(A)|^2 |\vec{\mu}^{s0}(B)|^2}{E_{r0} + E_{s0}}, \quad (8.114)$$

and which is identical to the form obtained using semiclassical theory in which coupling between the pair is viewed as being static in origin. That the interaction energy weakens by a factor of  $R^{-1}$  at long-range relative to its near-zone counterpart is due to the effects of retardation, with correlation between the dipolar fluctuations in charge distribution at each center occurring at the speed of light, rather than instantaneously.

The van der Waals dispersion potential has been recalculated using a number of differing physical viewpoints within the framework of molecular QED in the multipolar coupling scheme. These include response theory [60, 62, 63], and coupling of induced multipole moments [114] as well as simplification of the computation via introduction and employment of an effective two-photon interaction Hamiltonian [115]. Subsequent work has involved the calculation of dispersion energy shifts between one ground and one excited molecule [116] and between two excited species [117], as well as contributions to the dispersion force arising from higher multipole moment terms, of particular interest being the discriminatory energy shift between two chiral molecules [64, 118, 119]. Theory has also been developed to treat three- and many-body retarded dispersion forces [120], extending familiar semiclassical results of Axilrod and Teller, and Muto [121].

## 8.12 RADIATION-INDUCED INTERP ARTICLE FORCES

A particularly interesting phenomenon from the viewpoint of molecular QED is the influence of an external radiation field on the coupling of two or more atoms or molecules. Both real and virtual photons are therefore involved in this application, with the most common manifestation being the modification of the dispersion force by an intense laser. Thirunamachandran was the first to predict such an effect in 1980 [122]. He evaluated the change in the van der Waals dispersion energy shift caused by the action of an applied electromagnetic field using perturbation theory within the molecular QED formalism. Prior to this proposal, experimental work had been confined to cooling and trapping single particles in an intense beam of laser light, most notably in the pioneering work of Ashkin [123]. Continuing progress in laser technology eventually led to the realization that two or more particles attracted and then situated in the high intensity focal point region couple to one another, and to the demonstration and measurement of so-called optical binding forces, as first carried out by Burns, Fournier, and Golovchenko [124], and then verified and extended by other experimental groups [125–127]. Possibilities therefore arise for utilizing these optomechanical forces in nano-electromechanical applications and devices, especially as a result of nanoparticle aggregation and particle array formation. Specifics may be found in a few recent review articles [128–130], the last two of which also cover theoretical approaches, and examine the consequences of using broadband or coherent state throughput radiation and other forms of structured light [131] such as beams of the Laguerre–Gaussian type. In what follows, the change in energy shift between a pair of neutral, polarizable molecules in their ground electronic states induced by radiation described by a number state is evaluated using

diagrammatic perturbation theory techniques, in keeping with the approach employed thus far.

For molecules  $A$  and  $B$ , located at  $\vec{R}_A$  and  $\vec{R}_B$ , respectively, with  $\vec{R} = \vec{R}_B - \vec{R}_A$ , subject to an intense beam of laser light of mode  $(\vec{k}, \lambda)$  the initial and final system states are given by

$$|i\rangle = |f\rangle = |E_0^A, E_0^B; n(\vec{k}, \lambda)\rangle. \quad (8.115)$$

Remaining within the electric dipole approximation, the total Hamiltonian for the two bodies and radiation field in mutual interaction is given by

$$H = \sum_{\xi=A,B} H_{\text{mol}}(\xi) + H_{\text{rad}} - \epsilon_0^{-1} \sum_{\xi=A,B} \vec{\mu}(\xi) \cdot \vec{d}^\perp(\vec{R}_\xi). \quad (8.116)$$

Since the dependence of the energy shift on  $R$  is of interest, interaction of radiation with either  $A$  or  $B$  in the absence of interparticle coupling, corresponding to a dynamic Stark shift, is ignored. Hence, the leading term is of fourth order and involves the scattering of a real photon and the exchange of a virtual photon of mode  $(\vec{p}, \epsilon)$  between the pair. For absorption and emission of a  $(\vec{k}, \lambda)$ -photon at different centers, 48 time-ordered diagrams have to be summed over in order to obtain the change in interaction energy. One of these is shown in Figure 8.8.

The energy shift for a pair of oriented molecules in a fixed orientation relative to the direction of propagation of the incoming beam is given by [58, 122, 132]

$$\Delta E^d = \frac{N\hbar ck}{\epsilon_0 V} \alpha_{jl}(A; k) \alpha_{ik}(B; k) \bar{e}_i^{(j)}(\vec{k}) e_j^{(i)}(\vec{k}) \text{Re}V_{kl}(k, \vec{R}) \cos(\vec{k} \cdot \vec{R}), \quad (8.117)$$

where  $\alpha_{ij}(\xi; k)$  is the dynamic electric dipole polarizability of species  $\xi = A, B$  and  $\text{Re}V_{ij}(k, \vec{R})$  is the real part of the retarded resonant electric dipole-dipole coupling tensor (Eq. 8.107). The contribution above is often known as the “dynamic” ( $d$ ) term

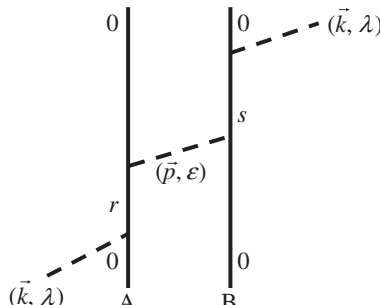


**FIGURE 8.8** One of 48 diagrams contributing to dynamic radiation-induced intermolecular energy shift.

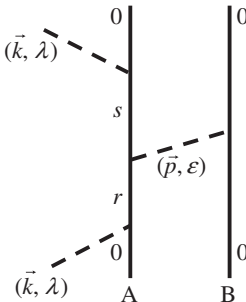


**FIGURE 8.9** One of 48 diagrams contributing to static radiation-modified inter-particle interaction energy.

since a real and finite amount of energy is exchanged between the pair. If one or both species is polar, there is another term contributing to the field-modified interaction energy. Coupling between the pair still exists, but now scattering of the real photon takes place at the same center, either at  $A$  or at  $B$ . One of the 48 contributing graphs is shown in Figure 8.9. Because in this instance virtual photon exchange involves no net transfer of energy, this contribution is termed the “static” ( $s$ ) one. It is found to be [58, 133]

$$\Delta E^s = \frac{N\hbar ck}{2\varepsilon_0 V} e_i^{(\lambda)}(\vec{k}) e_j^{(\lambda)}(\vec{k}) [\beta_{ijk}(A; k) \mu_l^{00}(B) + \mu_l^{00}(A) \beta_{ijk}(B; k)] V_{kl}(0, \vec{R}), \quad (8.118)$$

where  $\beta_{ijk}(\xi; k)$  is the hyperpolarizability tensor, and  $V_{ij}(0, \vec{R})$  is the static electric dipolar coupling tensor. Note that expression (8.118) vanishes for centrosymmetric molecules. The total change in energy shift is therefore given by the sum of  $\Delta E^d$  and  $\Delta E^s$ . Performing the molecular average results in  $\Delta E^s = 0$ . Carrying out both the molecular average and the pair orientational average on  $\Delta E^d$  yields

$$\begin{aligned} <\Delta E^d> = & -\frac{N\hbar ck}{8\pi\varepsilon_0^2 R^3 V} \alpha(A; k) \alpha(B; k) \left[ kR \sin 2kR + 2 \cos 2kR - 5 \frac{\sin 2kR}{kR} \right. \\ & \left. - 6 \frac{\cos 2kR}{k^2 R^2} + 3 \frac{\sin 2kR}{k^3 R^3} \right], \end{aligned} \quad (8.119)$$

and which applies for isotropic  $A$  and  $B$ , and for all directions of  $\vec{R}$  relative to  $\vec{k}$ . The result is seen to be proportional to the intensity of the incident radiation,  $I = N\hbar c^2 k / V$ , and to the polarizability of each molecule. It is independent of the polarization characteristics of the beam. At short range, the energy shift exhibits an inverse dependence on  $R$ , which can become significant for the situation in which there are a large number of molecular pairs in close proximity, as opposed to the London dispersion energy, which has the more rapid  $R^{-6}$  fall-off. In the far zone, the interaction energy (Eq. 8.119) has a modulated inverse square dependence. Interesting

topological features of the potential energy landscape, such as regions of maxima and minima, other islands of stability, and conditions that lead to particle array formation, have been examined, and details may be found in References 129, 130, and 134.

Finally, it should be mentioned that the results for static and dynamic contributions to the field-induced energy shift have been evaluated using the method of fluctuating electric dipole moments [119, 132–136]. In this picture, the applied electric field induces an electric moment at each centre, which interact via the dipole-dipole coupling tensor. Interaction energies are obtained on taking expectation values over molecular ground electronic states, and a state of the radiation field containing  $N$  photons of mode  $(\vec{k}, \lambda)$ . As expected, identical results ensue. This method was found to be advantageous when accounting for the effects of higher molecular multipole moments, as for example in the case of optical binding forces between chiral molecules [135], and when treating the effects of three and many bodies in the presence of an applied field and the resulting change in interaction energy [136].

### 8.13 SUMMARY AND OUTLOOK

In this chapter, the theory of QED has been outlined, with special emphasis placed on the coupling of radiation with non-relativistic matter. This version of the theory, formulated in the Coulomb gauge, is ideally suited to treat the interaction of electromagnetic fields with atoms and molecules, whose electrons are bound and move slowly relative to the speed of light. Its characteristic feature is that both the radiation field and the system of material particles are subject to the postulates of quantum mechanics. As a consequence, photons emerge automatically as quantized particles of light on describing the Maxwell fields as a collection of independent mechanical oscillators. Construction of the theory is carried out via the familiar techniques of canonical quantization applied to the interaction of a charged particle with the radiation field. This is achieved by starting with the total classical Lagrangian function for the material particle, the electromagnetic field, and their mutual interaction, and culminates in the QED Hamiltonian operator for the total many-body system. While the resulting minimal-coupling Hamiltonian can and has been applied successfully to solve problems involving the coupling of electrons and photons, it suffers from a couple of drawbacks which often limits its use. These include the explicit appearance of momentum and vector potential operators in the interaction term, along with static interparticle coupling terms. A more widely adopted alternative QED Hamiltonian, obtained via transformation of the minimal-coupling one, in which instantaneous interatomic interactions have been eliminated, and coupling between radiation and matter occurs via the interaction of electric and magnetic multipole moments with causal Maxwell field operators, and named the multipolar Hamiltonian, has also been presented, and is clearly better suited to applications in theoretical chemistry and atomic, molecular, and optical physics.

A number of fundamental linear radiation-molecule processes were then discussed. These included one-photon absorption, spontaneous and stimulated emission, Rayleigh and Raman scattering, as well as examples of chiroptical spectroscopies

such as circular dichroism, its magnetic field-induced analog, and optical rotation. Nonlinear optical processes such as two-photon absorption, sum-frequency generation, and second- and third-harmonic generation were also delineated. These and other types of optical phenomena are readily interpretable in terms of the elementary processes of absorption and emission of the requisite number of real photons in concert with changes in energy of the associated material particles, as represented by the initial and final state specification of the system, and any possible intermediate states that link the two. One common method of solution of the QED Hamiltonian applied to a particular problem is via time-dependent perturbation theory together with the aid of Feynman-like diagrams by separating the total Hamiltonian into unperturbed and perturbed parts, with the latter composed of the interaction Hamiltonian. Probability amplitudes are then evaluated, from which quantum mechanical observable quantities are then obtained. While this diagrammatic approach has been stressed in the coverage presented, and is characteristic of the Schrödinger picture, computational advantages and additional insight often accrue by working in the Heisenberg picture, especially when evaluating intermolecular processes or properties associated with electromagnetic radiation, for example.

Within the limits of the time-energy uncertainty principle, theory allows for the creation and destruction of so-called *virtual* photons, which are undetectable by definition. This type of particle is used to explain self-interactions, as manifest in the Lamb shift, for instance, as well as in the renormalization of the charge and mass of the electron. Exchange of one or more virtual photons between two or more bodies is used to understand the origin of interparticle forces. Two well-known examples, which serve to highlight the accurate treatment of, as well as the superior physical insight afforded by QED, were presented, namely the resonant transfer of energy, and the van der Waals dispersion potential. Because signals are transmitted at the correct speed of light in QED, the familiar semiclassical expressions for the two mentioned intermolecular effects are valid only in the near-zone regime, where electromagnetic influences propagate instantaneously. Retardation modifies the functional form of the transfer rate or dispersion energy shift, which now holds for all separation distances outside overlap of electronic charge distributions and extends out to infinity. Semiclassical results follow on taking the short-range asymptotic limit of the QED expression.

While QED and its non-relativistic version now rest on solid theoretical foundations, corroborated where possible by experiments in which unprecedented levels of agreement have been achieved, there remains much work to be done. Continuing efforts to develop theory for condensed phases, extended systems and accounting for the effects of an environment have occupied the attention of many workers, advancing the successful treatment of electron-photon interactions in vacuum. These forays have included interparticle forces in metals, dielectrics, semiconductors, and insulator materials for systems adopting a variety of geometrical configurations, possibly at vanishing or non-zero temperatures, as manifest, for instance, in a number of Casimir effects, where the Lifshitz theory, the Drude model, and the proximity force approximation have all been placed under greater scrutiny, as well as investigating the effects of an electric and/or magnetic dielectric medium on absorptive and emissive

processes, and the mediation of interparticle forces. Another fruitful avenue of research is to apply many of the general theoretical results obtained via QED techniques to specific chemical and physical systems. This is now possible and is beginning to take place by taking advantage of the considerable advances that have been made in computational electronic structure theory which have enabled high quality wavefunctions to be evaluated using a number of post-Hartree–Fock methods that include a high-level of electron correlation effects, or by employing density functional theory to calculate ground and excited electronic state properties. Finally, there is still plenty of room to employ and apply QED theory for predictive purposes, by proposing new phenomena, especially within the realm of photonics, thereby ensuring QED remains relevant to current and future generations of researchers working in chemical physics.

## REFERENCES

- [1] G. N. Lewis, “The conservation of photons,” *Nature (London)* **118**, 874–875 (1926).
- [2] A. Pais, *Subtle Is the Lord* (Oxford University Press, Clarendon, 1982).
- [3] P. A. M. Dirac, “The quantum theory of the emission and absorption of radiation,” *Proc. Roy. Soc. Lond. A* **114**, 243–265 (1927).
- [4] J. S. Schwinger (ed.), *Selected Papers on Quantum Electrodynamics* (Dover, New York, 1958).
- [5] P. Jordan and W. Pauli, “Zur Quantenelektrodynamik Ladungsfreier Felder,” *Z. Phys.* **47**, 151–173 (1928).
- [6] W. Heisenberg and W. Pauli, “Zur Quantendynamik der Wellenfelder,” *Z. Phys.* **56**, 1–61 (1929); “Zur Quantentheorie der Wellenfelder. II,” *Z. Phys.* **59**, 168–190 (1930).
- [7] S. S. Schweber, *QED and the Men Who Made It* (Princeton University Press, Princeton, 1994).
- [8] J. S. Schwinger, “On quantum-electrodynamics and the magnetic moment of the electron,” *Phys. Rev.* **73**, 416 (1948).
- [9] H. A. Bethe, “The electromagnetic shift of energy levels,” *Phys. Rev.* **72**, 339–341 (1947).
- [10] T. Aoyama, M. Hayakawa, T. Kinoshita, and M. Nio, “Revised value of the eighth-order contribution to the electron g-2,” *Phys. Rev. Lett.* **99**, 110406 1–4 (2007).
- [11] D. Hanneke, S. Fogwell, and G. Gabrielse, “New measurement of the electron magnetic moment and the fine structure constant,” *Phys. Rev. Lett.* **100**, 120801 1–4 (2008).
- [12] M. Babiker, E. A. Power, and T. Thirunamachandran, “On a generalization of the Power-Zienau-Woolley transformation in quantum electrodynamics and atomic field equations,” *Proc. Roy. Soc. Lond. A* **338**, 235–249 (1974).
- [13] H. B. G. Casimir and D. Polder, “The influence of retardation on the London-van der Waals forces,” *Phys. Rev.* **73**, 360–372 (1948).
- [14] G. Grynberg, A. Aspect, and C. Fabre, *Introduction to Quantum Optics* (Cambridge University Press, Cambridge, 2010).
- [15] E. A. Power, *Introductory Quantum Electrodynamics* (Longmans, London, 1964).
- [16] J. D. Jackson, *Classical Electrodynamics* (John Wiley & Sons, Inc., New York, 1975).

- [17] H. Goldstein, *Classical Mechanics* (Addison-Wesley, Reading, MA, 1980).
- [18] W. P. Healy, *Non-relativistic Quantum Electrodynamics* (Academic Press, London, 1982).
- [19] D. P. Craig and T. Thirunamachandran, *Molecular Quantum Electrodynamics* (Academic Press, London, 1984).
- [20] C. Cohen-Tannoudji, J. DuPont-Roc, and G. Grynberg, *Photons & Atoms* (John Wiley & Sons, Inc., New York, 1989).
- [21] G. Compagno, R. Passante, and F. Persico, *Atom-Field Interactions and Dressed Atoms* (Cambridge University Press, Cambridge, 1995).
- [22] A. Salam, *Molecular Quantum Electrodynamics* (John Wiley & Sons, Inc., New Jersey, 2010).
- [23] D. Masiello, E. Deumens, and Y. Öhrn, “On the canonical formulation of electrodynamics and wave mechanics,” *Adv. Quant. Chem.* **49**, 249–297 (2005).
- [24] P. A. M. Dirac, *The Principles of Quantum Mechanics* (Clarendon, Oxford, 1958).
- [25] M. Born, W. Heisenberg, and P. Jordan, “Zur Quantenmechanik II.,” *Z. Phys.* **35**, 557–615 (1926).
- [26] P. W. Milonni, *The Quantum Vacuum* (Academic Press, San Diego, 1994).
- [27] E. A. Power and S. Zienau, “Coulomb gauge in non-relativistic quantum electrodynamics and the shape of spectral lines,” *Phil. Trans. Roy. Soc. Lond. A* **251**, 427–454 (1959).
- [28] R. G. Woolley, “Molecular quantum electrodynamics,” *Proc. Roy. Soc. Lond. A* **321**, 557–572 (1971).
- [29] E. A. Power, “A review of canonical transformations as they affect multiphoton processes,” in *Multiphoton Processes*, edited by J. H. Eberly and P. Lambropoulos (John Wiley & Sons, New York, 1978), pp. 11–46.
- [30] E. A. Power and T. Thirunamachandran, “The multipolar Hamiltonian in radiation theory,” *Proc. Roy. Soc. Lond. A* **372**, 265–273 (1980).
- [31] E. A. Power, “Zero-point energy and the lamb shift,” *Am. J. Phys.* **34**, 516–518 (1966).
- [32] M. Göppert-Mayer, “Über Elementarakte mit Zwei Quantensprüngen,” *Ann. Phys. Leipzig* **9**, 273–294 (1931).
- [33] E. A. Power and T. Thirunamachandran, “On the nature of the Hamiltonian for the interaction of radiation with atoms and molecules:  $\left(\frac{e}{mc}\right) p \cdot A, -\mu \cdot E$ , and all that,” *Am. J. Phys.* **46**, 370–378 (1978).
- [34] R. G. Woolley and J. E. Cordle, “On the gauge invariance of the Schrödinger equation,” *Chem. Phys. Lett.* **22**, 411–413 (1973).
- [35] W. P. Healy, “Line integral Lagrangians for the electromagnetic field interacting with charged particles,” *Phys. Rev. A* **19**, 2353–2359 (1979).
- [36] R. G. Woolley, “Gauge invariant wave mechanics and the Power-Zienau-Woolley transformation,” *J. Phys. A: Math. Gen.* **13**, 2795–2806 (1980).
- [37] W. Heitler, *The Quantum Theory of Radiation* (Clarendon, Oxford, 1954).
- [38] R. Loudon, *The Quantum Theory of Light* (Oxford University Press, Oxford, 2000).
- [39] S. Mukamel, *Principles of Nonlinear Optical Spectroscopy* (Oxford University Press, New York, 1995).
- [40] D. L. Andrews and P. Alcock, *Optical Harmonics in Molecular Systems* (Wiley-VCH, Weinheim, 2002).

- [41] L. D. Barron, *Molecular Light Scattering and Optical Activity* (Cambridge University Press, Cambridge, 2004).
- [42] E. Fermi, “Quantum theory of radiation,” *Rev. Mod. Phys.* **4**, 87–132 (1932).
- [43] R. G. Woolley, “The electrodynamics of atoms and molecules,” *Adv. Chem. Phys.* **33**, 153–233 (1975).
- [44] P. W. Milonni, “Semi-classical and quantum electrodynamical approaches in non-relativistic radiation theory,” *Phys. Rep.* **25**, 1–81 (1976).
- [45] D. P. Craig and T. Thirunamachandran, “Radiation-molecule interactions in chemical physics,” *Adv. Quant. Chem.* **16**, 97–160 (1982).
- [46] D. P. Craig and T. Thirunamachandran, “Radiation-molecule and molecule-molecule interactions. A unified viewpoint from quantum electrodynamics,” *Acc. Chem. Res.* **19**, 10–16 (1986).
- [47] D. L. Andrews, D. P. Craig, and T. Thirunamachandran, “Molecular quantum electrodynamics in chemical physics,” *Int. Rev. Phys. Chem.* **8**, 339–383 (1989).
- [48] G. Compagno, G. M. Palma, R. Passante, and F. Persico, “Atoms dressed and partially dressed by the zero-point fluctuations of the electromagnetic field,” *J. Phys. B: At. Mol. Opt. Phys.* **28**, 1105–1158 (1995).
- [49] J. M. Ziman, *Elements of Advanced Quantum Theory* (Cambridge University Press, Cambridge, 1969).
- [50] J. F. Ward, “Calculation of nonlinear optical susceptibilities using diagrammatic perturbation theory,” *Rev. Mod. Phys.* **37**, 1–18 (1965).
- [51] R. P. Feynman, “Space-time approach to non-relativistic quantum mechanics,” *Rev. Mod. Phys.* **20**, 367–387 (1948).
- [52] R. P. Feynman, “Space-time approach to quantum electrodynamics,” *Phys. Rev.* **76**, 769–789 (1949).
- [53] R. D. Jenkins, D. L. Andrews, and L. C. Dávila-Romero, “A new diagrammatic methodology for non-relativistic quantum electrodynamics,” *J. Phys. B: At. Mol. Opt. Phys.* **35**, 445–468 (2002).
- [54] R. D. Jenkins and D. L. Andrews, “Three-centre systems for energy pooling: quantum electrodynamical theory,” *J. Phys. Chem. A* **102**, 10834–10842 (1998).
- [55] G. J. Daniels and D. L. Andrews, “The electronic influence of a third-body on resonance energy transfer,” *J. Chem. Phys.* **116**, 6701–6712 (2002).
- [56] R. D. Jenkins and D. L. Andrews, “Multichromophore excitons and resonance energy transfer: molecular quantum electrodynamics,” *J. Chem. Phys.* **118**, 3470–3479 (2003).
- [57] B. W. Alligood and A. Salam, “On the application of state sequence diagrams to the calculation of the Casimir-Polder potential,” *Mol. Phys.* **105**, 395–404 (2007).
- [58] D. S. Bradshaw and D. L. Andrews, “Optically induced forces and torques: interactions between nanoparticles in a laser beam,” *Phys. Rev. A* **72**, 033816 1–14 (2005).
- [59] E. A. Power and T. Thirunamachandran, “Quantum electrodynamics with non-relativistic sources. I. Transformation to the multipolar formalism for second-quantized electron and Maxwell interacting fields,” *Phys. Rev. A* **28**, 2649–2662 (1983).
- [60] A. Salam, “Molecular quantum electrodynamics in the Heisenberg picture: a field theoretic viewpoint,” *Int. Rev. Phys. Chem.* **27**, 405–448 (2008).
- [61] E. A. Power and T. Thirunamachandran, “Quantum electrodynamics with non-relativistic sources. IV. Poynting vector, energy densities and other quadratic operators of the electromagnetic field,” *Phys. Rev. A* **45**, 54–63 (1992).

- [62] E. A. Power and T. Thirunamachandran, “Quantum electrodynamics with non-relativistic sources. III. Intermolecular interactions,” *Phys. Rev. A* **28**, 2671–2675 (1983).
- [63] T. Thirunamachandran, “Vacuum fluctuations and intermolecular interactions,” *Phys. Scripta* **T21**, 123–128 (1988).
- [64] J. K. Jenkins, A. Salam, and T. Thirunamachandran, “Retarded dispersion interaction energies between chiral molecules,” *Phys. Rev. A* **50**, 4767–4777 (1994).
- [65] P. R. Berman, *Cavity Quantum Electrodynamics* (Academic Press, Boston, MA, 1994).
- [66] H. A. Kramers and W. Heisenberg, “Über die Streuung von Strahlung Durch Atome,” *Z. Phys.* **31**, 681–708 (1925).
- [67] P. A. M. Dirac, “The quantum theory of dispersion,” *Proc. Roy. Soc. Lond. A* **114**, 710–728 (1927).
- [68] W. P. Healy, “A generalization of the Kramers-Heisenberg dispersion formula,” *Phys. Rev. A* **16**, 1568–1574 (1977).
- [69] C. V. Raman and K. S. Krishnan, “A new type of secondary radiation,” *Nature (London)* **121**, 501–502 (1928).
- [70] E. A. Power and T. Thirunamachandran, “Optical activity as a two-state process,” *J. Chem. Phys.* **55**, 5322–5328 (1971).
- [71] E. A. Power and T. Thirunamachandran, “Circular dichroism: a general theory based on quantum electrodynamics,” *J. Chem. Phys.* **60**, 3695–3701 (1974).
- [72] W. P. Healy, “The multipole Hamiltonian and magnetic circular dichroism,” *J. Chem. Phys.* **64**, 3111–3117 (1976).
- [73] D. L. Andrews, “Rayleigh and Raman optical activity: an analysis of the dependence on scattering angle,” *J. Chem. Phys.* **72**, 4141–4144 (1980).
- [74] D. P. Craig, E. A. Power, and T. Thirunamachandran, “The dynamic terms in induced circular dichroism,” *Proc. Roy. Soc. Lond. A* **348**, 19–38 (1976).
- [75] P. Fischer and F. Hache, “Nonlinear optical spectroscopy of chiral molecules,” *Chirality* **17**, 421–437 (2005).
- [76] W. M. McClain, “Two-photon molecular spectroscopy,” *Acc. Chem. Res.* **7**, 129–135 (1974).
- [77] J. A. Giordmaine, “Nonlinear optical properties of liquids,” *Phys. Rev.* **138 A**, 1599–1606 (1965).
- [78] M. A. Belkin, S. H. Han, X. Wei, and Y. R. Shen, “Sum-frequency generation in chiral liquids near electronic resonance,” *Phys. Rev. Lett.* **87**, 113001 1–4 (2001).
- [79] P. Fischer, K. Beckwitt, F. W. Wise, and A. C. Albrecht, “The chiral specificity of sum-frequency generation in solutions,” *Chem. Phys. Lett.* **352**, 463–468 (2002).
- [80] D. L. Andrews and I. D. Hands, “Sum frequency generation from partially ordered media and interfaces: a polarization analysis,” *J. Phys. B: At. Mol. Opt. Phys.* **31**, 2809–2824 (1998).
- [81] S. Cheon and M. Cho, “Circularly polarized infrared and visible sum-frequency generation spectroscopy: vibrational optical activity measurement,” *Phys. Rev. A* **71**, 013808 1–8 (2005).
- [82] O. Roslyk and S. Mukamel, “A unified description of sum-frequency generation, parametric down conversion and two-photon fluorescence,” *Mol. Phys.* **107**, 265–280 (2009).
- [83] P. Fischer and A. Salam, “Molecular QED of coherent and incoherent sum-frequency and second-harmonic generation in chiral liquids in the presence of a static electric field,” *Mol. Phys.* **108**, 1857–1868 (2010).

- [84] P. Fischer, A. D. Buckingham, K. Beckwitt, D. S. Wiersma, and F. A. Wise, “New electro-optic effect: sum-frequency generation from optically active liquids in the presence of a dc electric field,” *Phys. Rev. Lett.* **91**, 173901 1–4 (2003).
- [85] D. L. Andrews, “Harmonic generation in free molecules,” *J. Phys. B: At. Mol. Opt. Phys.* **13**, 4091–4099 (1980).
- [86] D. L. Andrews, “Molecular theory of harmonic generation,” *Adv. Chem. Phys.* **85**, 545–606 (1993).
- [87] Y. T. Lam and T. Thirunamachandran, “DC-induced second-harmonic generation by chiral molecules,” *J. Chem. Phys.* **77**, 3810–3814 (1982).
- [88] L. Mandel and E. Wolf, *Optical Coherence and Quantum Optics* (Cambridge University Press, Cambridge, 1995).
- [89] N. Bloembergen, *Nonlinear Optics* (Benjamin, New York, 1965).
- [90] R. R. McLone and E. A. Power, “On the interaction between two identical neutral dipole systems, one in the excited state and the other in the ground state,” *Mathematika* **11**, 91–94 (1964).
- [91] J. S. Avery, “Resonance energy transfer and spontaneous photon emission,” *Proc. Phys. Soc. London A* **88**, 1–8 (1966).
- [92] D. L. Andrews and B. S. Sherborne, “Resonant excitation transfer: a quantum electrodynamical study,” *J. Chem. Phys.* **86**, 4011–4017 (1987).
- [93] A. K. Biswas, G. Compagno, G. M. Palma, R. Passante, and F. Persico, “Virtual photons and causality in the dynamics of a pair of two-level atoms,” *Phys. Rev. A* **42**, 4291–4301 (1990).
- [94] D. P. Craig and T. Thirunamachandran, “An analysis of models for resonant transfer of excitation using quantum electrodynamics,” *Chem. Phys.* **167**, 229–240 (1992).
- [95] E. A. Power and T. Thirunamachandran, “Analysis of the causal behaviour in energy transfer between atoms,” *Phys. Rev. A* **56**, 3395–3408 (1997).
- [96] D. L. Andrews and A. A. Demidov (eds.), *Resonance Energy Transfer* (John Wiley & Sons, Ltd., Chichester, 1999).
- [97] G. D. Scholes, “Long-range resonance energy transfer in molecular systems,” *Ann. Rev. Phys. Chem.* **54**, 57–87 (2003).
- [98] G. J. Daniels, R. D. Jenkins, D. S. Bradshaw, and D. L. Andrews, “Resonance energy transfer: the unified theory revisited,” *J. Chem. Phys.* **119**, 2264–2274 (2003).
- [99] A. Salam, “A general formula for the rate of resonant transfer of energy between two electric multipole moments of arbitrary order using molecular quantum electrodynamics,” *J. Chem. Phys.* **122**, 044112 1–12 (2005).
- [100] V. May and O. Kühn, *Charge and Energy Transfer Dynamics in Molecular Systems* (Wiley-VCH, Weinheim, 2011).
- [101] G. D. Scholes, “Energy transfer from Förster-Dexter theory to quantum coherent light-harvesting,” *Int. Rev. Phys. Chem.* **30**, 49–77 (2011).
- [102] D. L. Dexter, “A theory of sensitized luminescence in solids,” *J. Chem. Phys.* **21**, 836–850 (1953).
- [103] T. Förster, “Zwischenmolekulare Energiewanderung und Fluoreszenz,” *Ann. Phys.* **6**, 55–75 (1948).
- [104] M. Agranovitch and A. Maradudin, *Electronic Excitation Energy Transfer in Condensed Matter* (North-Holland, Amsterdam, 1982).

- [105] J. Knoester and S. Mukamel, “Intermolecular forces, spontaneous emission, and superradiance in a dielectric medium: polariton-mediated interactions,” *Phys. Rev. A* **40**, 7065–7080 (1989).
- [106] G. Juzeliunas and D. L. Andrews, “Quantum electrodynamics of resonant energy transfer in condensed matter,” *Phys. Rev. B* **49**, 8751–8763 (1994).
- [107] G. Juzeliunas and D. L. Andrews, “Quantum electrodynamics of resonance energy transfer,” *Adv. Chem. Phys.* **112**, 357–410 (2000).
- [108] J. J. Rodriguez and A. Salam, “Influence of medium chirality on electric dipole-dipole resonance energy transfer,” *Chem. Phys. Lett.* **498**, 67–70 (2010).
- [109] J. J. Rodriguez and A. Salam, “Effect of medium chirality on the rate of resonance energy transfer,” *J. Phys. Chem. B* **115**, 5183–5190 (2011).
- [110] D. P. Craig and T. Thirunamachandran, “Third-body mediation of resonance coupling between identical molecules,” *Chem. Phys.* **135**, 37–48 (1989).
- [111] A. Salam, “Mediation of resonance energy transfer by a third molecule,” *J. Chem. Phys.* **136**, 014509 1–5 (2012).
- [112] J. F. Babb, “Casimir effects in atomic, molecular, and optical physics,” *Adv. At. Mol. Opt. Phys.* **59**, 1–20 (2010).
- [113] F. London, “The general theory of molecular forces,” *Trans. Faraday Soc.* **33**, 8–26 (1937).
- [114] E. A. Power and T. Thirunamachandran, “Casimir-Polder potential as an interaction between induced dipoles,” *Phys. Rev. A* **48**, 4761–4763 (1993).
- [115] D. P. Craig and E. A. Power, “The asymptotic Casimir-Polder potential from second-order perturbation theory and its generalization for anisotropic polarizabilities,” *Int. J. Quant. Chem.* **3**, 903–911 (1969).
- [116] E. A. Power and T. Thirunamachandran, “Dispersion forces between molecules with one or both molecules excited,” *Phys. Rev. A* **51**, 3660–3666 (1995).
- [117] E. A. Power and T. Thirunamachandran, “Quantum electrodynamics with non-relativistic sources. V. Electromagnetic field correlations and intermolecular interactions between molecules in either ground or excited states,” *Phys. Rev. A* **47**, 2539–2551 (1993).
- [118] C. Mavroyannis and M. J. Stephen, “Dispersion forces,” *Mol. Phys.* **5**, 629–638 (1962).
- [119] D. P. Craig and T. Thirunamachandran, “New approaches to chiral discrimination in coupling between molecules,” *Theo. Chem. Acc.* **102**, 112–120 (1999).
- [120] E. A. Power and T. Thirunamachandran, “The non-additive dispersion energies for N-molecules: a quantum electrodynamical theory,” *Proc. Roy. Soc. Lond. A* **401**, 267–279 (1985).
- [121] B. M. Axilrod and E. Teller, “Interaction of the van der Waals type between three atoms,” *J. Chem. Phys.* **11**, 299–300 (1943).
- [122] T. Thirunamachandran, “Intermolecular interactions in the presence of an intense radiation field,” *Mol. Phys.* **40**, 393–399 (1980).
- [123] A. Ashkin, “Acceleration and trapping of particles by radiation pressure,” *Phys. Rev. Lett.* **24**, 156–159 (1970).
- [124] M. M. Burns, J.-M. Fournier, and J. A. Golovchenko, “Optical binding,” *Phys. Rev. Lett.* **63**, 1233–1236 (1989).

- [125] T. M. Grzegorczyk, B. A. Kemp, and J. A. Kong, “Trapping and binding of an arbitrary number of cylindrical particles in an in-plane electromagnetic field,” *J. Opt. Soc. Am. A* **23**, 2324–2330 (2006).
- [126] N. K. Metzger, E. M. Wright, W. Sibbett, and K. Dholakia, “Visualization of optical binding of microparticles using a femtosecond fiber optical trap,” *Opt. Exp.* **14**, 3677–3687 (2006).
- [127] F. Chen, G. L. Klimchitskaya, V. M. Mostepanenko, and U. Mohideen, “Demonstration of optically modulated dispersion forces,” *Opt. Exp.* **15**, 4823–4829 (2007).
- [128] K. Dholakia, P. Reece, and M. Gu, “Optical micromanipulation,” *Chem. Soc. Rev.* **37**, 42–55 (2008).
- [129] T. Czimár, L. C. Dávila-Romero, K. Dholakia, and D. L. Andrews, “Multiple optical trapping and binding: new routes to self-assembly,” *J. Phys. B: At. Mol. Opt. Phys.* **43**, 102001 1–25 (2010).
- [130] A. Salam, “Molecular quantum electrodynamics of radiation-induced intermolecular forces,” *Adv. Quant. Chem.* **62**, 1–34 (2011).
- [131] D. L. Andrews (ed.), *Structured Light and Its Applications* (Elsevier, Burlington, MA, 2008).
- [132] A. Salam, “Intermolecular interactions in a radiation field via the method of induced moments,” *Phys. Rev. A* **73**, 013406 1–8 (2006).
- [133] A. Salam, “Two alternative derivations of the static contribution to the radiation-induced intermolecular energy shift,” *Phys. Rev. A* **76**, 043805 1–5 (2007).
- [134] J. Rodriguez, L. C. Dávila-Romero, and D. L. Andrews, “Optical binding in nanoparticle assembly: potential energy landscapes,” *Phys. Rev. A* **78**, 043805 1–7 (2008).
- [135] A. Salam, “On the effect of a radiation field in modifying the intermolecular interaction between two chiral molecules,” *J. Chem. Phys.* **124**, 014302 1–6 (2006).
- [136] L. C. Dávila-Romero and D. L. Andrews, “A retarded coupling approach to intermolecular interactions,” *J. Phys. B: At. Mol. Opt. Phys.* **42**, 085403 1–10 (2009).



---

# 9

---

## MULTIPHOTON PROCESSES

ANGUS J. BAIN

*Department of Physics and Astronomy, University College London, London, UK*

### 9.1 INTRODUCTION

This chapter provides an introduction to the fundamental physics governing the simultaneous absorption of two or more photons by molecules. Multiphoton absorption has been at the forefront of scientific research for close to five decades, first as a spectroscopic tool providing new and complimentary information on molecular structure and dynamics to conventional (single-photon) techniques. More recently, multiphoton absorption has found widespread application at the interface between the physical and life sciences through its ability to provide inherent confocal resolution in fluorescence microscopy, allowing the investigation of complex biological samples and the study of molecular interactions in live cells.

Multiphoton absorption processes are examples of nonlinear optical phenomena [1–4]. Nonlinear optics covers a wide range of intensity-dependent optical processes where the applied electromagnetic (EM) fields are of sufficient intensity to modify the intrinsic (linear) optical properties of a medium (e.g., refractive index, birefringence, absorption coefficient). These interactions also give rise to the mixing of optical fields and the generation of new optical frequencies via second harmonic generation [5], sum and difference frequency generation [6], four-wave mixing [7], and super continuum generation [8]. Self-action effects where an EM wave modifies the optical properties of the medium through which it is propagating lead to phenomena such as self-focusing [9] and self-phase modulation [10]. The interplay between self-phase modulation and material dispersion is exploited in long low-loss optical fiber

communications via the formation of optical solitons [11]. Soliton formation through the interaction of self-phase modulation, self-focusing, and material dispersion is exploited in Kerr lens mode locking of femtosecond Ti:sapphire lasers [12, 13]. The development of the broadly tunable femtosecond Ti:sapphire laser has played a pivotal role in driving new applications of two- and multiphoton fluorescence in the life sciences [14].

All multiphoton processes depend on the intensity of the interacting fields. At very high optical field strengths where the interaction between the field and the medium can no longer be treated as a perturbation, in that the applied optical fields are of a similar or greater magnitude to those that bind the participating electrons, effects such as extreme/high harmonic generation [15], multiple ionization [16], and plasma production [17] are observed. For photon fluxes up to  $10^{35}$  photons  $\text{cm}^{-2} \text{ s}^{-1}$ , perturbation theory is applicable [18]. The diffraction-limited focal spot of a 100-mW, 76-MHz, 100-fs mode-locked Ti:sapphire laser at 800 nm using a 1.2-NA microscope objective yields a photon flux of  $6 \times 10^{31}$  photons  $\text{cm}^{-2} \text{ s}^{-1}$  and for focused nanosecond dye lasers used for wavelength-dependent two-photon excitation typical photon fluxes are on the order of  $10^{28}$  photons  $\text{cm}^{-2} \text{ s}^{-1}$  [19]. Both are therefore well within the perturbative regime. Perturbative nonlinear optical phenomena can be classified as either dissipative or parametric processes [7, 20], the former involving a net energy exchange between the applied optical field(s) and the medium. Multiphoton absorption phenomena are wholly dissipative processes; parametric nonlinear optical phenomena have been extensively reviewed by a number of authors [7, 20, 21].

Following an introduction to the nonlinear optical responses/susceptibilities that govern multiphoton absorption, we will cover fundamental aspects of molecular two-photon absorption in liquids and gases. Applications of two- and multiphoton absorption in molecular imaging, the investigation of molecular order, and motion and studies of resonance energy transfer will also be discussed.

### 9.1.1 Historical Perspective

Two-photon absorption is the simplest and most widely exploited multiphoton process. In its most fundamental form it is the process whereby two photons with frequency  $\nu$  are simultaneously absorbed by a quantum system in a transition between an initial (ground) state and an (allowed) excited state with an energy separation of  $2h\nu$ . Three decades separate the publication of the theoretical foundation of two-photon absorption in 1931 by Maria Göppert-Mayer [22] and its experimental realization in an  $\text{Eu}^{2+}$ -doped  $\text{CaF}$  crystal by Kaiser and Garrett in 1961 [23]. The experiments of Kaiser and Garrett were a rapid exploitation of the coherent pulsed output of the ruby laser developed by Maiman in 1960 [24]. In the ruby laser, oscillation is restricted to two lines at 692.7 and 694.5 nm and the ability to investigate two-photon absorption spectra needed a tunable laser source. Early experiments combined a pulsed ruby laser and the spectrally filtered output of a Xe flash lamp to achieve two-color two-photon absorption of molecular crystals [25] and liquids [26–28]. This approach

suffered from low resolution (about 100 cm<sup>-1</sup>) and had limited tuning. High resolution two-photon spectra required the development of tunable visible laser sources. To this end Bergman and Jortner [29, 30] utilized a dye laser pumped by the second harmonic output of a Q-switched ruby laser to obtain the two-photon fluorescence excitation spectrum of anthracene in a solution. Improvements in dye laser technology involving N<sub>2</sub> laser pumping of a Hänsch type dye laser [31] were used by Hochstrasser and co-workers to obtain high resolution spectra of biphenyl, benzene, and naphthalene crystals [32–34]. Two-photon absorption of gas-phase molecules was first demonstrated for benzene by Hochstrasser and co-workers in 1974 [35] followed by nitric oxide [36]. The expansion in two-photon spectroscopy from this point was rapid with the development of techniques for non-fluorescent species involving, for example, multiphoton ionization [37–39] and the exploitation of the two-photon resonant contribution to three-wave mixing [20, 40]. Two-photon absorption from dual counter-propagating beams yielded sub-Doppler resolution in gas-phase two-photon absorption [41, 42], allowing the hitherto unobserved rovibronic structure of polyatomic molecules to be investigated [43]. Scientific interest in molecular two-photon absorption was initially focused on exploiting the fundamental differences in the selection rules for single- and two-photon absorption (see below), allowing the identification and characterization of new and hitherto inaccessible (dipole forbidden) electronic transitions in molecules. Developments in molecular two-photon spectroscopy up to 1997 have been reviewed in detail by McClain [44], Friedrich and McClain [45], Goodman and Rava [46], Birge [47], Lin et al. [16], and Callis [48].

Improvements in the tunability and peak power of mode-locked lasers in the 1970s and 1980s led to rapid advances in the fields of nonlinear optics and nonlinear spectroscopy. These were paralleled by the development of molecules and materials with enhanced nonlinear optical responses together with new laser gain media. In 1986, the broad near-infrared laser gain properties of titanium sapphire (Ti:sapphire) were investigated by Moulton [49] shortly followed by the first demonstration of continuous-wave laser oscillation [50]. The broad lasing bandwidth of Ti:sapphire heralded the possibility of tunable femtosecond laser oscillation. Active mode-locking of continuous-wave Ti:sapphire lasers yielding stable 150 fs pulse trains was demonstrated in 1991 by Curley et al. [51]. Sub-100-fs Ti:sapphire oscillation using passive mode-locking was achieved in 1991 by Keane and co-workers [52] and Spinelli et al. [12]. Stable femtosecond continuous-wave passive mode-locking in Ti:sapphire was shown to arise from the intensity-dependent refractive index and termed Kerr lens mode-locking [13], a patent for the Kerr lens mode-locking technique was subsequently assigned to Coherent [12]. At this time the recently developed two-photon scanning fluorescence microscope [53] had utilized two-photon fluorescence excited by a non-tunable (630-nm) colliding pulse mode-locked (CPM) dye laser [54] limiting its practical application. Replacement of the CPM laser by a femtosecond Ti:sapphire laser transformed two-photon microscopy; near-infrared two-photon excitation yielded visible fluorescence in a wide range of fluorescent dyes and the then newly emerging fluorescent proteins [55, 56]. The first commercial two-photon microscope was marketed by BioRad in 1996. Research activity involving two- and

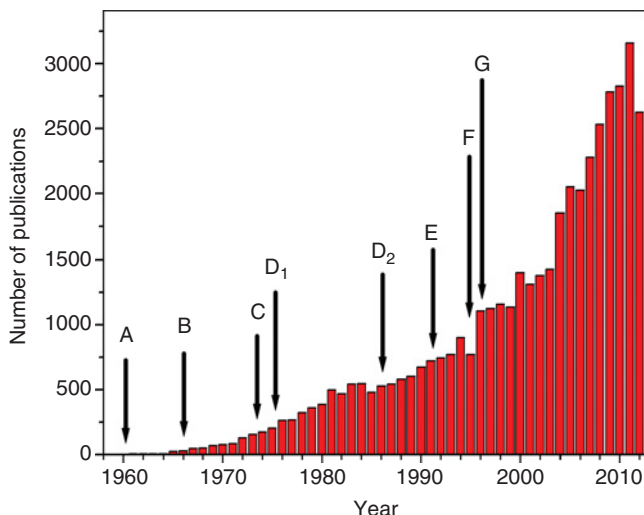


**FIGURE 9.1** The results of a search (Scopus) for journal and conference articles between 1962 and 2012 that contain the terms two-photon or multiphoton in their title, abstract, or full bibliographic record. Milestones along the timeline are as follows: (A) The development of the ruby laser by Mainman in 1960, (B) the first observation of molecular two-photon excited fluorescence in 1966, (C) nanosecond tunable dye lasers used to obtain the first two-photon fluorescent excitation spectra in liquids by Jortner et al. in 1972 and gases by Hochstrasser et al. in 1973, (D<sub>1</sub>) the development of both narrow bandwidth and sub-picosecond dye lasers from the 1970s to 1980s, (D<sub>2</sub>) Ti:sapphire laser first demonstrated by Moulton in 1986, (E) development of two-photon laser scanning microscopy using modelocked dye lasers by Denk et al. in 1990 and the demonstration of about 60–150-fs Ti:sapphire pulse widths using active mode-locking by Ferguson et al. and passive mode-locking by Spence et al. and Spinelli and Negus in 1991, (F) US patent for Kerr lens mode-locking issued to Coherent (Negus and Spinelli) in 1992, and (G) the development of enhanced green fluorescent protein (EGFP) by the Tsein laboratory in 1995, and the first commercial two-photon confocal microscope launched by BioRad in 1996.

multiphoton processes has seen a marked increase over the past 20 years as can be seen from Figure 9.1.

## 9.2 MOLECULAR TWO-PHOTON ABSORPTION: BASIC PRINCIPLES

In simple terms two-photon absorption can be thought of as two instantaneously consecutive single-photon transitions that take place via a set of “virtual” intermediate states. Virtual states are those which can be coupled (allowed) by single-photon electric dipole transitions to the ground and excited states. In its current usage molecular two-photon absorption generally involves the absorption of red to near-infrared photons, wavelengths for which there are no single-photon electronic transitions. The virtual states are thus strongly off-resonance and as a result their contributions to the

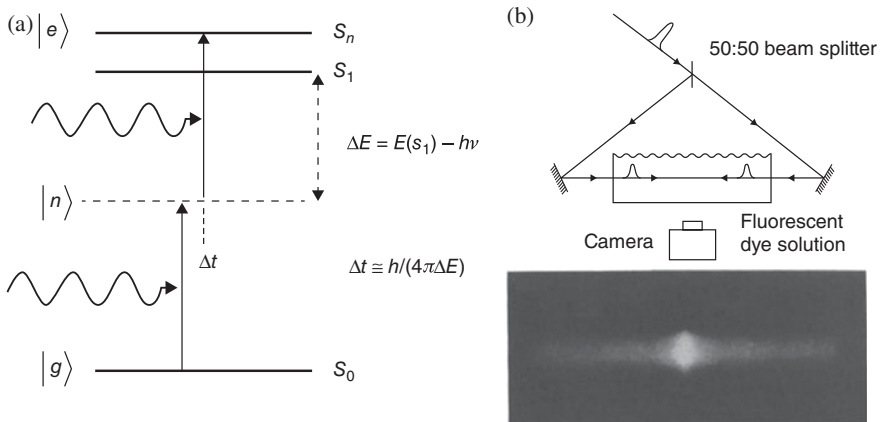


**FIGURE 9.2** (a) Pictorial representation of molecular two-photon absorption between the molecular ground state  $|g\rangle$  and the excited state  $|e\rangle$  via a virtual state  $|n\rangle$ . The virtual state has a lifetime  $\Delta t$  determined by the uncertainty principle. For two-photon absorption to occur the time difference between the two photons must be on or below  $\Delta t$ . The value of  $\Delta t$  is given by the difference between the photon energy and the nearest (single-photon) resonant state which for an 800-nm photon is on the order of 0.21 fs. (b) Two-photon fluorescence laser pulse autocorrelation: the output of a mode-locked laser is split and the two counter propagating pulse trains are recombined in a cell containing a two-photon fluorescing dye. The fluorescence signal is maximized in the region where the laser pulses are temporally overlapped the photographic image can be analyzed to yield an intensity versus distance (time) distribution proportional to  $1 + 2G^{(2)}(\tau)$ .

nonlinear polarization exist on a time scale  $\Delta t$  that is governed by the uncertainty principle,

$$\Delta t \approx \hbar/2\Delta E, \quad (9.1)$$

with

$$\Delta E = E_n - h\nu. \quad (9.2)$$

Here,  $E_n$  is the energy of the virtual state and  $h\nu$  is the incident photon energy (Fig. 9.2a). The nearest electronic state that in principle could act as a virtual state would be the first excited (singlet) state with a transition energy corresponding to photons in the visible to ultraviolet regions. The energy gap  $\Delta E$  is therefore on the order of  $h\nu$ ; for a typical two-photon excitation wavelength of 800 nm, these considerations yield a value for  $\Delta t$  of  $2.1 \times 10^{-16}$  s (0.21 fs). This is less than the oscillation period for light at 800 nm. Thus for two-photon absorption to occur a favorable quantum mechanical transition probability must also be combined by the effectively instantaneous interaction of both photons with the molecule. The probability of two photons interacting with a molecule simultaneously is therefore dependent on the intensity of the light source employed together with the statistical nature of its

short-time intensity distribution [57]. Two-photon-induced fluorescence was routinely used as a means of determining the second-order autocorrelation function of mode-locked (picosecond) laser pulses [58, 59] as depicted in Figure 9.2b. Two-photon absorption can be regarded as a dissipative third-order nonlinear process [1, 20]; the fundamental Physics of third-order nonlinear optics and two-photon absorption are covered in the sections 9.2.1 and 9.2.2.

### 9.2.1 The Nonlinear Optical Polarization

From Maxwell's constitutive relations [1, 3], the electric displacement  $\bar{D}$  induced by an EM field  $\bar{E}$  is given by

$$\bar{D} = \epsilon \epsilon_0 \bar{E} = \epsilon_0 (1 + \chi) \bar{E}, \quad (9.3)$$

where  $\epsilon$  signifies a dimensionless *relative* dielectric constant. The susceptibility  $\chi$  represents the response of the medium to the applied field giving rise to an induced polarization  $\bar{P}$ ,

$$\bar{P} = \epsilon_0 \chi \bar{E}. \quad (9.4)$$

With the low electric field strengths provided by conventional light sources, the response of the medium to the applied field is linear. For the higher electric fields present in intense lasers, the induced polarization contains additional terms,

$$\bar{P} = \epsilon_0 \chi \bar{E} + \sum_{N \geq 2} \chi^{(N)} (\bar{E})^N. \quad (9.5)$$

The nonlinear susceptibilities  $\chi^{(N)}$  depend on fundamental material properties and intrinsic symmetry [1]. In the simple case of a monochromatic wave of angular frequency  $\omega$  and wavevector  $\bar{k}$ ,  $\bar{E}$  has the following form:

$$\bar{E}(r, t) = \frac{\bar{E}_\omega}{2} \exp[i(\omega t - \bar{k} \cdot \bar{r})] + \frac{\bar{E}_\omega^*}{2} \exp[-i(\omega t - \bar{k} \cdot \bar{r})]. \quad (9.6)$$

Substituting Eq. (9.4) into Eq. (9.3) yields

$$\bar{P} = \epsilon_0 \chi \bar{E}(r, t) + P_{NL}. \quad (9.7)$$

Here,  $P_{NL}$  is the nonlinear polarization induced by  $\bar{E}(r, t)$  which is given by

$$P_{NL} = \sum_{N \geq 2} \chi^{(N)}(\omega') \frac{1}{2^N} (\bar{E}(\omega) \exp[i(\omega t - \bar{k} \cdot \bar{r})] + \bar{E}(\omega)^* \exp[-i(\omega t - \bar{k} \cdot \bar{r})])^N. \quad (9.8)$$

The  $\omega'$  dependence of  $\chi^{(N)}$  arises from different frequencies ( $\omega'$ ) that originate from the products of the Fourier components of the powers of  $\bar{E}(r, t)$  given in Eq. (9.6). Using  $P_{NL}$  as the source term in Maxwell's equations leads to the nonlinear

wave equation from which the nonlinear optical interactions arising from the various susceptibilities can be described. From Maxwell's third equation, we have [3]

$$\nabla \times \bar{H} = \sigma \bar{E} + \frac{\partial \bar{D}}{\partial t}. \quad (9.9)$$

For a nonlinear response, the electric displacement becomes

$$\bar{D} = \epsilon \epsilon_0 \bar{E} + P_{\text{NL}}. \quad (9.10)$$

Substitution of Eq. (9.10) into Eq. (9.9) gives

$$\nabla \times \bar{H} = \sigma \bar{E} + \epsilon \epsilon_0 \frac{\partial \bar{E}}{\partial t} + \frac{\partial P_{\text{NL}}}{\partial t}. \quad (9.11)$$

From Maxwell's equations, we have

$$\nabla^2 \bar{E} = \mu \mu_0 \frac{\partial}{\partial t} (\nabla \times \bar{H}), \quad (9.12)$$

where  $\mu$  is a relative magnetic permeability, and  $\mu_0$  the vacuum value. Combining Eqs. (9.11) and (9.12) yields

$$\nabla^2 \bar{E} = \mu \mu_0 \frac{\partial}{\partial t} \left( \sigma \bar{E} + \epsilon \epsilon_0 \frac{\partial \bar{E}}{\partial t} + \frac{\partial P_{\text{NL}}}{\partial t} \right). \quad (9.13)$$

For a dielectric medium that is lossless at  $\omega$  the conductivity  $\sigma$  is zero, and provided that  $P_{\text{NL}}$  is much smaller than the linear polarization, then the solutions to

$$\nabla^2 \bar{E} = \mu \mu_0 \epsilon \epsilon_0 \frac{\partial^2 \bar{E}}{\partial t^2} + \mu \mu_0 \frac{\partial^2 P_{\text{NL}}}{\partial t^2} \quad (9.14)$$

will have the same form as in Eq. (9.6) in that the waves generated by the nonlinear polarization are superimposed on those of the linear solution of Eq. (9.14) when  $P_{\text{NL}} = 0$ . For interactions in which  $\omega \neq \omega'$ , phase matching considerations come into play as the generated waves at  $\omega'$  do not propagate with the same spatial phase as that of the driving fields that give rise to  $P_{\text{NL}}$ . Thus, over a finite interaction length, destructive interference will occur and the nonlinear interaction will be greatly reduced [1, 3]. Symmetry considerations impose restrictions on the nonlinear interactions that are allowed. In addition to phase mismatching constraints, nonlinear optical interactions are governed by material symmetry. If we consider the first two terms in  $P_{\text{NL}}$  remembering that  $P_{\text{NL}}$  is a vector quantity as are the electric fields involved in the two products, we can write the second- and third-order nonlinear polarizations, respectively, as

$$\bar{P}_i^{(2)} = c_2 \chi_{ijk}^{(2)} \bar{E}_j \bar{E}_k \quad (9.15)$$

and

$$\bar{P}_i^{(3)} = c_3 \chi_{ijkl}^{(3)} \bar{E}_j \bar{E}_k \bar{E}_l, \quad (9.16)$$

where  $i$  is the component of the nonlinear polarization ( $x$ ,  $y$ , or  $z$ ) and  $j$ ,  $k$ , and  $l$  are the polarization components ( $x$ ,  $y$ , or  $z$ ) of the input fields. In a medium with inversion symmetry, the  $\chi^{(N)}$  will be invariant to inversion of the co-ordinate system (i.e.,  $(x, y, z) \rightarrow (-x, -y, -z)$ ), whilst the polarization components of  $P_{\text{NL}}$ , and the input fields all change sign, giving

$$-\bar{P}_i^{(2)} = c_2 \chi_{ijk}^{(2)} (-\bar{E}_j) (-\bar{E}_k) \quad (9.17)$$

and

$$-\bar{P}_i^{(3)} = c_3 \chi_{ijkl}^{(3)} (-\bar{E}_j) (-\bar{E}_k) (-\bar{E}_l). \quad (9.18)$$

Equating Eqs. (9.15)–(9.18), we have

$$\bar{P}_i^{(2)} = c_2 \chi_{ijk}^{(2)} \bar{E}_j \bar{E}_k \quad -\bar{P}_i^{(2)} = c_2 \chi_{ijk}^{(2)} \bar{E}_j \bar{E}_k, \quad (9.19)$$

$$-\bar{P}_i^{(3)} = -c_3 \chi_{ijkl}^{(3)} \bar{E}_j \bar{E}_k \bar{E}_l \quad \bar{P}_i^{(3)} = c_3 \chi_{ijkl}^{(3)} \bar{E}_j \bar{E}_k \bar{E}_l. \quad (9.20)$$

From Eq. (9.19),  $\bar{P}_i^{(2)} = -\bar{P}_i^{(2)}$  which means that  $\chi_{ijk}^{(2)}$  is necessarily zero. No such restriction is placed on  $\chi_{ijkl}^{(3)}$ . Irrespective of phase matching considerations, second-order nonlinear optical phenomena require a non-centrosymmetric medium and third-order nonlinear optical phenomena are in principle allowed in all media. Third harmonic generation arising from the Fourier combination of  $\omega' = \omega + \omega + \omega$  is possible but is restricted by the phase matching consideration that requires  $k_{3\omega} = 3k_\omega$ , and the relationship between the wavevector and the refractive index  $n$  is given by

$$k_\omega = \frac{\omega n_\omega}{c}. \quad (9.21)$$

Third harmonic generation requires

$$3k_\omega = \frac{3\omega n_\omega}{c} = k_{3\omega} = \frac{3\omega n_{3\omega}}{c} \Rightarrow n_\omega = n_{3\omega}. \quad (9.22)$$

Due to material dispersion, the difference between  $n_\omega$  and  $n_{3\omega}$  is substantial and third harmonic generation efficiencies are generally low [60]. The most commonly observed third-order nonlinear optical effect that is observed with a single driving frequency is the intensity-dependent refractive index  $n_2$  [61–65]. The combination

of fields in Eq. (9.16) that give rise to a nonlinear polarization oscillating at  $\omega$  is given by

$$\bar{P}_i^{(3)}(\omega) = \frac{3}{4} \chi_{ijkl}^{(3)} \bar{E}_j^* \bar{E}_k^* \bar{E}_l^* \frac{1}{2} \exp \left[ i \left( \omega t - \bar{k} \cdot \bar{r} \right) \right] + cc. \quad (9.23)$$

By convention, a summation over all the field polarization components  $j$ ,  $k$ , and  $l$  is implicit [1, 3]. For simplicity, let us take  $i=j=k=l=x$ . The electric displacement arising from this polarization is thus

$$\bar{D} = \epsilon \epsilon_0 \left( \frac{\bar{E}_x}{2} \exp \left[ i \left( \omega t - \bar{k} \cdot \bar{r} \right) \right] + cc \right) + \frac{3}{4} \chi_{xxxx}^{(3)} \left| \bar{E}_x \right|^2 \left( \frac{\bar{E}_x}{2} \exp \left[ i \left( \omega t - \bar{k} \cdot \bar{r} \right) \right] + cc \right). \quad (9.24)$$

Rearranging leads to

$$\bar{D} = \epsilon \epsilon_0 \left( \frac{\bar{E}_x}{2} \exp \left[ i \left( \omega t - \bar{k} \cdot \bar{r} \right) \right] + cc \right) \left( 1 + \frac{3}{4 \epsilon \epsilon_0} \chi_{xxxx}^{(3)} \left| \bar{E}_x \right|^2 \right). \quad (9.25)$$

The effective dielectric constant for the medium is thus

$$\epsilon_{EFF} = \epsilon \left( 1 + \frac{3}{4} \frac{\chi_{xxxx}^{(3)}}{\epsilon \epsilon_0} \left| \bar{E}_x \right|^2 \right). \quad (9.26)$$

The refractive index of the medium thus becomes

$$n = n_0 \left( 1 + \frac{3}{4} \frac{\chi_{xxxx}^{(3)}}{\epsilon \epsilon_0} \left| \bar{E}_x \right|^2 \right)^{\frac{1}{2}}, \quad (9.27)$$

where  $n_0$  is the linear refractive ( $\sqrt{\epsilon}$ ) index of the medium. Provided the change in refractive index is small, Eq. (9.27) can be written as

$$n = n_0 \left( 1 + \frac{3}{8} \frac{\chi_{xxxx}^{(3)}}{\epsilon \epsilon_0} \left| \bar{E}_x \right|^2 \right). \quad (9.28)$$

Given that the relationship between  $|E|^2$  and the intensity  $I$  of the applied optical field

$$\left| \bar{E}_x \right|^2 = 2I_x \left( \frac{\mu \mu_0}{\epsilon \epsilon_0} \right)^{\frac{1}{2}}, \quad (9.29)$$

the refractive index is given by

$$n = n_0 + \frac{3}{4} \frac{\chi_{xxxx}^{(3)}}{n_0 \epsilon_0} \left( \frac{\mu \mu_0}{\epsilon \epsilon_0} \right)^{\frac{1}{2}} I_x. \quad (9.30)$$

The intensity-dependent index of refraction  $n_2$  is thus

$$n_2 = \frac{3}{4} \left( \frac{\mu \mu_0}{\epsilon \epsilon_0} \right)^{\frac{1}{2}} \frac{\chi_{xxxx}^{(3)}}{n_0 \epsilon_0}. \quad (9.31)$$

In a wholly analogous manner to single-photon absorption, the imaginary part of  $n_2$  is responsible for two-photon absorption.

### 9.2.2 The Two-Photon Absorption Cross-Section

The rate of energy exchange per unit volume  $W$ , between a light wave with electric field  $\bar{E}$ , and a medium is given by the cycle-averaged scalar product

$$\frac{dW}{dt} = \left\langle \bar{E} \cdot \frac{d\bar{P}}{dt} \right\rangle, \quad (9.32)$$

where  $\bar{P}$  is the polarization induced in the medium by  $\bar{E}$ . Following Yariv [3] and substituting Eqs. (9.6) and (9.23) and expressing the third-order susceptibility in terms of real and imaginary components gives

$$\begin{aligned} \frac{dW}{dt} = & \frac{3}{4} \chi_{xxxx}^{(3)} \left| \bar{E}_x \right|^2 \left\langle \left( i\omega \frac{\bar{E}_x^2}{4} \exp \left[ 2i(\omega t - \bar{k} \cdot \bar{r}) \right] (\text{Re} \chi_{xxxx}^{(3)} - i\text{Im} \chi_{xxxx}^{(3)}) \right. \right. \\ & + i\omega \frac{\bar{E}_x \bar{E}_x^*}{4} (\text{Re} \chi_{xxxx}^{(3)} - i\text{Im} \chi_{xxxx}^{(3)}) - i\omega \frac{\bar{E}_x \bar{E}_x^*}{4} (\text{Re} \chi_{xxxx}^{(3)} + i\text{Im} \chi_{xxxx}^{(3)}) \\ & \left. \left. - i\omega \frac{\bar{E}_x^{*2}}{4} \exp \left[ -2i(\omega t - \bar{k} \cdot \bar{r}) \right] (\text{Re} \chi_{xxxx}^{(3)} + i\text{Im} \chi_{xxxx}^{(3)}) \right) \right\rangle \end{aligned} \quad (9.33)$$

All the terms containing the real components of  $\chi^{(3)}$  vanish in the cycle average giving

$$\frac{dW}{dt} = \frac{3}{8} \left| \bar{E}_x \right|^4 \omega \text{Im} \chi_{xxxx}^{(3)}. \quad (9.34)$$

Substituting Eq. (9.29) in Eq. (9.34), we have

$$\frac{dW}{dt} = \frac{3\omega}{2} \left( \frac{\mu\mu_0}{\epsilon\epsilon_0} \right) \text{Im}\chi_{xxxx}^{(3)} I_x^2. \quad (9.35)$$

The two-photon absorption cross-section  $\sigma_\omega^{(2)}$  is defined in terms of the photon absorption rate equation

$$\frac{dn_p}{dt} = \sigma_\omega^{(2)} N_{GS} \frac{I_x^2}{\hbar^2\omega^2}, \quad (9.36)$$

where  $n_p$  is the photon number,  $N_{GS}$  is the ground state population of absorbing species, and  $I/\hbar\omega$  is the photon flux

$$\frac{dW}{dt} = \sigma_\omega^{(2)} N_{GS} \frac{I_x^2}{\hbar\omega}. \quad (9.37)$$

The two-photon cross-section in units of  $m^4$  s per photon is thus

$$\sigma_\omega^{(2)} = \frac{3\hbar\omega^2\mu\mu_0}{2N_{GS}\epsilon\epsilon_0} \text{Im}\chi_{xxxx}^{(3)} = \frac{3\hbar\omega^2}{2N_{GS}c^2\epsilon^2\epsilon_0^2} \text{Im}\chi_{xxxx}^{(3)}, \quad (9.38)$$

where  $\chi^{(3)}$  has the SI units of  $m^2 V^{-2}$  and  $\sigma_\omega^{(2)}$   $m^4$   $s^{-1}$  per photon. Two-photon cross-sections are generally quoted in units of  $cm^4$  s per photon or in Göppert Mayer (GM) units, where  $1\text{ GM} = 10^{-50}\text{ cm}^4\text{ s}$  per photon [28]. In fluorescent species, two-photon absorption cross-sections are often quoted as the product of  $\sigma_\omega^{(2)}$  and the quantum yield of fluorescence of the molecule. This product  $\sigma_\omega^{(2)}\phi$  is termed the two-photon action cross-section. Two-photon action cross-sections of both intrinsic and synthetic fluorophores are shown in Table 9.1. In recent years, there has been considerable effort directed toward the design and synthesis of molecules with significantly enhanced two-photon cross-sections [64–72]. Two-photon action cross-sections as large as 12,000 GM have been achieved [72]. Research in this area has been driven by the large degree of potential applications of two-photon absorbing materials including optical power limiting [73,74], microfabrication [75,76], biological imaging [53], and three-dimensional data storage [75, 77, 78], comprehensive reviews of work in this active area have been produced by Blanchard-Desce et al. [79] and Anderson and co-workers [80]. Fundamental limitations to two-photon cross-sections and third-order nonlinear susceptibilities have been discussed by Kuzyk [81] and Samoc [82].

### 9.3 MOLECULAR TWO-PHOTON FLUORESCENCE

In quantum mechanical terms, the cross-section for the absorption of two photons of polarizations  $\alpha$  and  $\beta$  between states  $|g\rangle$  and  $|e\rangle$  is proportional to the squared modulus

**TABLE 9.1** Two-photon action cross-sections of common fluorophores

|   | $\sigma^{(2)}\phi$ (GM) | Excitation wavelength $\lambda$ (nm) |
|---|-------------------------|--------------------------------------|
| Extrinsic (synthetic) fluorophores        |                         |                                      |
| Rhodamine B                               | 153.00                  | 800                                  |
| Fluorescein                               | 37.33                   | 770–790                              |
| Alexa 488                                 | 97.94                   | 691                                  |
| Coumarin 307                              | 12                      | 700                                  |
| Intrinsic fluorophores                    |                         |                                      |
| Green fluorescent protein (GFP) wild type | 6.43                    | 800                                  |
| Enhanced GFP (EGFP)                       | 76.30                   | 880                                  |
| NADH                                      | $6.9 \times 10^{-2}$    | 720                                  |
| Folic acid                                | $7.161 \times 10^{-3}$  | 700                                  |
| Retinol                                   | $6.8 \times 10^{-2}$    | 700                                  |

The data given is a subset of an extensive compilation of the wavelength dependence of the two-photon action cross-sections of extrinsic and intrinsic fluorophores by the Developmental Resource for Biophysical Imaging Opto-Electronics (DRBIO) at Cornell University (W. Webb and co-workers): [http://www.drbio.cornell.edu/cross\\_sections.html](http://www.drbio.cornell.edu/cross_sections.html)

of the tensor  $W_{\alpha\beta}^{e \rightarrow e}$  defined by a sum of single-photon electric dipole transition moments  $\langle g | \mu | n \rangle \langle n | \mu | e \rangle$  involving the intermediate (virtual) states  $|n\rangle$  [83],

$$\left| W_{\alpha\beta}^{g \rightarrow e} \right|^2 = \left| \sum_n \left( \frac{\alpha \cdot \langle g | \mu | n \rangle \langle n | \mu | e \rangle \cdot \beta}{\nu_n - \nu_\alpha + i\Gamma_n} + \frac{\beta \cdot \langle g | \mu | n \rangle \langle n | \mu | e \rangle \cdot \alpha}{\nu_n - \nu_\beta + i\Gamma_n} \right) \right|^2, \quad (9.39)$$

where  $\nu_n$  and  $\Gamma_n$  are the transition frequency and homogeneous line-width of each  $|n\rangle$ , respectively. For identical photons with the same polarization ( $\alpha = \beta = \hat{e}$ ), Eq. (9.39) becomes

$$\left| W^{g \rightarrow e} (\hat{e}) \right|^2 \propto \left| \hat{e} \cdot \left[ \sum_n \left( \frac{\langle g | \mu | n \rangle \langle n | \mu | e \rangle}{\nu_n - \nu_\alpha + i\Gamma_n} \right) \right] \cdot \hat{e} \right|^2. \quad (9.40)$$

The selection rules for two-photon absorption are determined by the products of single-photon matrix elements  $\langle g | \mu | n \rangle \langle n | \mu | e \rangle$ . For single-photon electric dipole transitions a change in parity  $+ \leftrightarrow -$  must take place [84] and where the molecule possesses a center of symmetry a change in *g/u* electronic symmetry ( $g \leftrightarrow u, u \leftrightarrow g$ ) is required. For two-photon absorption the corresponding selection rules are thus  $+ \leftrightarrow +, - \leftrightarrow -, g \leftrightarrow g, u \leftrightarrow u$ . The differences in selection rules between single- and two-photon absorption are analogous to those between infrared and Raman spectroscopy. Two-photon absorption allows spectroscopic access to excited states largely inaccessible to one-photon spectroscopy and hidden *g* symmetry electronic states have been discovered [26, 85–89]. In molecules of lower symmetry, the

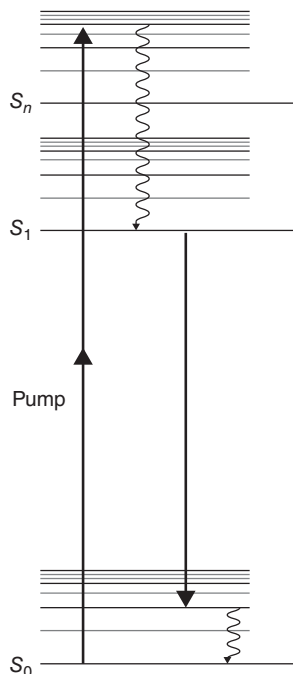


**FIGURE 9.3** A Jablonski diagram indicating the excitation and relaxation pathways that lead to two-photon excited fluorescence. Excitation occurs from the molecular ground state  $S_0$  to an excited singlet state  $S_n$ . This is followed by rapid ( $\tau_{IC}$  sub-picosecond) internal conversion and collisional relaxation to lower vibrational levels of  $S_1$ . Spontaneous emission (nanoseconds) takes place to high vibrational levels of the ground state with fast ( $\tau_R$  sub-picosecond) collisional relaxation returning molecules to the initially populated levels.

differences between one- and two-photon electronic transitions are more subtle, and the selection rules forbidding certain transitions can be relaxed by the coupling of electronic and vibrational degrees of freedom (vibronic coupling). Vibronic coupling and other perturbations make different contributions to one- and two-photon electronic spectra and the study of two-photon spectra in aromatic molecules and polyenes has proved most fruitful in investigating these phenomena. Comprehensive reviews of this research have been provided by Goodman and Rava [46] and Hollas [90]. Two- and multiphoton absorption in freely rotating molecules will be discussed in Section 9.3.3.

A simplified picture (Fig. 9.3) of molecular two-photon absorption and spontaneous emission using sub-picosecond laser pulses for a solvated population of molecules is shown in the Jablonski diagram. Initial excitation from low-lying vibrational levels in the molecular electronic ground state ( $S_0$ ) takes place via the simultaneous absorption of two (non-resonant) near-infrared photons (see Section 9.2). The initially excited state ( $S_n$ ) undergoes rapid (sub-picosecond) internal conversion and vibrational relaxation in collisions with surrounding solvent molecules leading

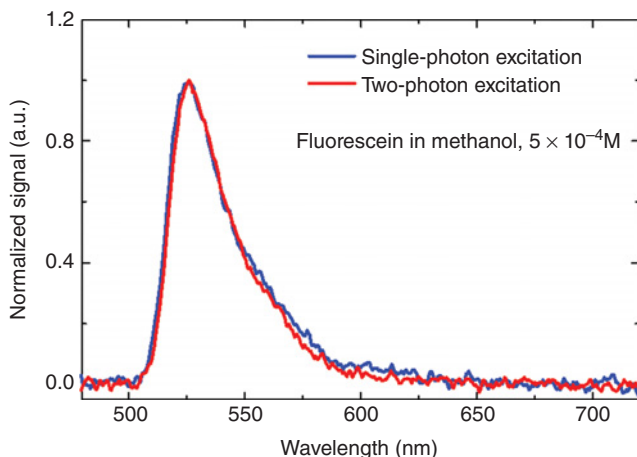


**FIGURE 9.4** Steady-state fluorescence spectra of fluorescein obtained using single-photon excitation at 500 nm and two-photon excitation at 800 nm. Although the two-photon transition energy is higher, 3.1 eV versus 2.48 eV, fast relaxation within the excited state manifold leads to the rapid population of the same low-lying vibrational levels in  $S_1$  as shown by the equivalence of the emission spectra. (For a color version of this figure, see the color plate section.)

to the population of lower vibrational levels in  $S_1$ . In the absence of external perturbations, the population in  $S_1$  decays by spontaneous emission (about  $10^{-9}$  s) to upper vibrational levels of  $S_0$  consistent with the Franck–Condon principle. Solvent deactivation of the vibrationally hot ground state population is correspondingly rapid. The fluorescence induced by molecular two-photon excitation in general originates from the same levels that are accessed by single-photon excitation (see Fig. 9.4); here, excitation is directly into high vibrational levels of  $S_1$  with rapid solvent-mediated vibrational relaxation prior to fluorescence.

### 9.3.1 Polarization Dependence of Two-Photon Absorption

In addition to the intensity-dependent transition probability, the excitation of two-photon fluorescence differs from single-photon excitation in that the absorption probability is intrinsically polarization dependent. A fundamental property of single-photon transitions in an isotropic medium is that the transition probability is independent of the polarization of the incident light [91]. However, for two-photon absorption, the transition does not involve a simple dipolar rearrangement of electronic charge density but depends on a sum of products of all the allowed single-photon electric dipole transition moments between the ground, virtual, and final states. In simple terms, the “first” photon can be thought of as selecting an oriented (virtual) molecular array with which the “second” photon interacts. The polarization dependence of molecular two-photon absorption was first investigated in azulene by Peticolas and co-workers in 1965 [92]. A theoretical treatment of polarized two-photon absorption in benzene was presented by Honig et al. in 1967 [93]. Monson and McClain’s experimental and

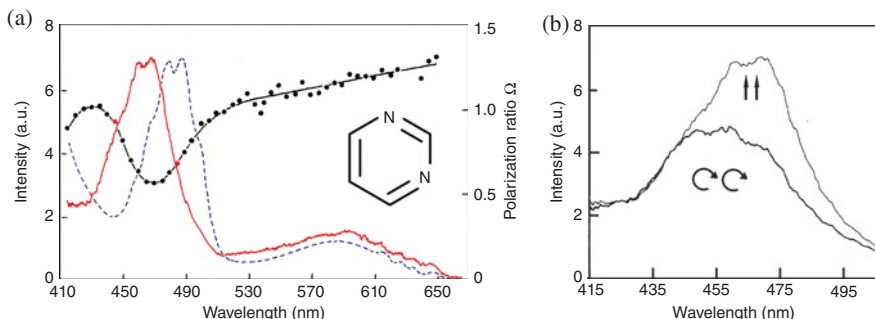


**FIGURE 9.5** (a) The two-photon excitation spectrum of pyrimidine in a 0.7M *n*-hexane solution at room temperature (----) and the one-photon absorption spectrum (—) is plotted at one half of the actual transition energy. The two-photon polarization ratios  $\Omega$  across the two-photon absorption spectrum are also shown (—•—•—). (b) Comparison of the two-photon fluorescence excitation spectra for linear and circularly polarized light in the region of the overlapping  $B_2(\pi\pi^*)$  and  $A_2(n\pi^*)$  two-photon transitions. Adapted from Reference 96.

theoretical work on polarized two-photon absorption in randomly oriented molecules showed how the combination of linear and circularly polarized photons could be used to determine the symmetry of the participating electronic states [27, 28, 94]. Drucker and McClain [95] introduced the concept of the two-photon polarization ratio—the transition probability/cross-section ratio for circular to linear polarization  $\Omega = \sigma^{(2)}(\text{circ})/\sigma^{(2)}(\text{lin})$ . These studies adopted a Cartesian tensor formalism which was extended by Nascimento [19] who expressed the polarization dependence of the participating transitions via a direction cosine formalism with the orientational average between the laboratory and molecular frames calculated via the connecting Euler rotation [91]. This work confirmed earlier theoretical predictions and predicted additional symmetry–polarization relationships. The utility of combining linear and circular polarization in two-photon absorption spectroscopy are clearly demonstrated in the study of pyrimidine by Callis et al. [96], in which the measurement of linear and circularly polarized two-photon excited fluorescence spectra and the measurement of  $\Omega$  revealed the hitherto unobserved  $A_2(\pi\pi^*) \leftarrow A_g$  transition (see Fig. 9.5). The importance of polarization measurements in determining the states involved in two-photon absorption [19, 27, 28, 48, 94–108] and higher order (multiphoton) transitions [109–115] is well established, providing information on fundamental photophysics, molecular structure, solvation symmetry, and protein secondary structure.

In this chapter, we will adopt a spherical tensor formalism for two-photon absorption [116]; following Wan and Johnson [117], the two-photon orientation-dependent transition probability for two identical photons (i.e.,  $\alpha = \beta = \hat{e}$ ) can be expressed as

$$A(\Omega) = |\hat{e} \cdot \underline{S} \cdot \hat{e}|^2, \quad (9.41)$$

$$S \propto \sum_n \left( \frac{\langle g | \mu | n \rangle \langle n | \mu | e \rangle}{\nu_n - \nu_\alpha + i\Gamma_n} \right), \quad (9.42)$$

where  $\hat{e}$  is the polarization vector of the light and  $\underline{S}$  is a second rank tensor describing the angular properties of the two-photon transition;  $\hat{e}$  and  $\underline{S}$  are defined by the laboratory frame angles  $\Omega(\alpha\beta\gamma)$ . For the absorption of two identical photons, Eq. (9.41) can be written as

$$A(\Omega) = |\underline{T} \cdot \underline{S}|^2. \quad (9.43)$$

The polarization tensor  $\underline{T}$  is given by the direct product of the two polarization vectors

$$\underline{T} = (\hat{e} \otimes \hat{e}) = \sum_{l,m} T_m^l (\text{Lab}). \quad (9.44)$$

Expressing  $\underline{S}$  and  $\underline{T}$  as spherical tensors, the scalar product in Eq. (9.44) becomes

$$\underline{T} \cdot \underline{S} = \sum_{l,m} T_m^l (\text{Lab}) S_{-m}^l (\text{Lab}) (-1)^m. \quad (9.45)$$

The transition tensor  $\underline{S}$  is determined by molecular frame quantities (i.e., the products of the single-photon molecular transition dipole matrix elements in Eq. (9.45)). However, the scalar product in Eq. (9.44) is expressed in the laboratory frame, where the components of  $\underline{T}$  are determined by the excitation polarization vectors. The components of  $\underline{S}$  in the laboratory frame are obtained by an Euler rotation  $D(\Omega_{LM})$  that connects the laboratory and molecular reference frames [91],

$$S_{-m}^l (\text{Lab}) = \sum_n S_n^l (\text{Mol}) D_{n-m}^l (\Omega_{LM}). \quad (9.46)$$

Substituting into Eq. (9.45) yields

$$\underline{T} \cdot \underline{S} = \sum_{l,m,n} T_m^l (\text{Lab}) D_{n-m}^l (\Omega_{LM}) S_n^l (\text{Mol}) (-1)^m. \quad (9.47)$$

The transition probability is thus

$$A(\Omega) = \left| \sum_{l,m,n} T_m^l (\text{Lab}) D_{n-m}^l (\Omega_{LM}) S_n^l (\text{Mol}) (-1)^m \right|^2, \quad (9.48)$$

$$\begin{aligned} A(\Omega) = & \sum_{l,l',m,m',n,n'} T_m^l (\text{Lab}) T_{m'}^{l'} (\text{Lab})^* D_{n-m}^l (\Omega_{LM}) D_{n'-m'}^{l'} (\Omega_{LM})^* \\ & \times S_n^l (\text{Mol}) S_{n'}^{l'} (\text{Mol})^* (-1)^{m+m'}. \end{aligned} \quad (9.49)$$

After some manipulation and the contraction of rotation matrix elements [91], the transition probability becomes

$$A(\Omega) = \sum_{K,Q,N} A_{NQ}^K D_{-N-Q}^K(\Omega_{LM}), \quad (9.50)$$

where

$$A_{QN}^K = (2K+1)(-1)^N \sum_{l,l',m,m',n,n'} \left[ \begin{pmatrix} l & l' & K \\ m & -m' & -Q \end{pmatrix} \begin{pmatrix} l & l' & K \\ -n & n' & -N \end{pmatrix} \right. \\ \times T_m^l(\text{Lab}) T_{-m'}^{l'}(\text{Lab}) S_n^l(\text{Mol}) S_{-n'}^{l'}(\text{Mol}) \left. \right]. \quad (9.51)$$

The laboratory frame tensor components for linear and circularly polarized photons (from Eq. (9.44)) are given by

$$e_0^1 \otimes e_0^1 = \frac{1}{\sqrt{3}} \left( \sqrt{2} T_0^2(\text{Lab}) - T_0^0(\text{Lab}) \right), \quad (9.52)$$

$$e_1^1 \otimes e_1^1 = T_2^2(\text{Lab}). \quad (9.53)$$

The linearly and circularly polarized laboratory frame tensor products are, respectively,

$$\frac{2T_0^2(\text{Lab}) T_0^2(\text{Lab}) + T_0^0(\text{Lab}) T_0^0(\text{Lab}) - 2\sqrt{2}T_0^2(\text{Lab}) T_0^0(\text{Lab})}{3} \quad (9.54)$$

and

$$T_2^2(\text{Lab}) T_{-2}^2(\text{Lab}). \quad (9.55)$$

For linear and circularly polarized excitation there is an overall (laboratory) axis of cylindrical symmetry and  $Q = 0$  in both Eqs. (9.54) and (9.55). It should be noted however that these laboratory-fixed axes are not equivalent and are determined by the polarization vector and the direction of propagation of the exciting radiation field for linearly and circularly polarized excitation, respectively (see Fig. 9.6). From the  $3j$  symbols in Eq. (9.51) and with reference to Eqs. (9.52) and (9.53), it can be seen that the excited state is characterized by tensors of rank  $K = 0, 2$ , and  $4$  ( $A_{00}^0, A_{N0}^2$ , and  $A_{N0}^4$ ). Unlike single-photon excitation, the relative values of these moments depend not only on the excitation polarization but also on the structure of the molecular frame transition tensor  $S$ . The relationship between the Cartesian and spherical components of a second rank tensor can be calculated using standard angular momentum

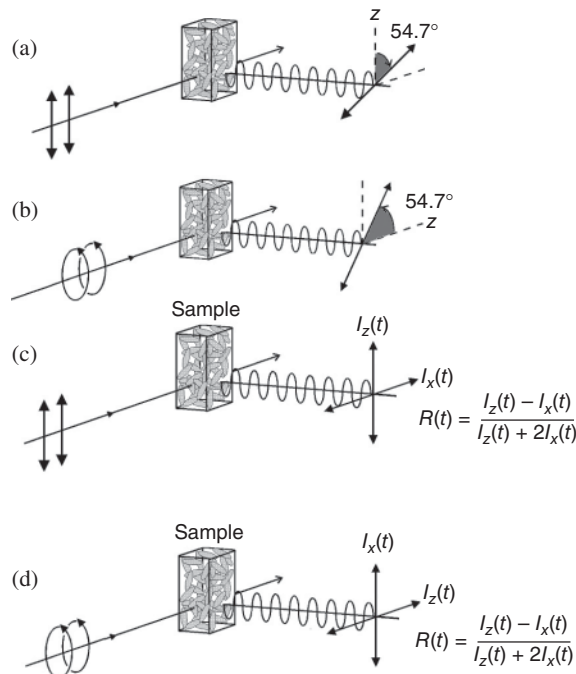


**FIGURE 9.6** Excitation–detection geometries for the determination of the transition strength for (a) linearly polarized and (b) circularly polarized two-photon excitation. Fluorescence intensity measurements are made at magic-angle polarization settings with respect to the quantization (symmetry) axis for the two polarizations. Alternatively, the fluorescence intensity can be constructed from  $I_V(t) + 2I_H(t)$  and  $2I_V(t) + I_H(t)$  measurements for linear and circular polarizations, respectively. (c) Excitation–detection geometry for fluorescence anisotropy measurements following linearly polarized two-photon excitation.

methods [118] and the coupling coefficients can be expressed in the following matrix form:

$$\begin{bmatrix} S_0^0 \\ S_{-2}^2 \\ S_{-1}^2 \\ S_0^2 \\ S_1^2 \\ S_2^2 \end{bmatrix} = \begin{bmatrix} -\frac{1}{\sqrt{3}} & 0 & 0 & 0 & -\frac{1}{\sqrt{3}} & 0 & 0 & 0 & -\frac{1}{\sqrt{3}} \\ \frac{1}{2} & \frac{-i}{2} & 0 & \frac{-i}{2} & \frac{1}{2} & 0 & 0 & 0 & 0 \\ 0 & 0 & \frac{1}{2} & 0 & 0 & \frac{-i}{2} & \frac{1}{2} & \frac{-i}{2} & 0 \\ -\frac{1}{\sqrt{6}} & 0 & 0 & 0 & -\frac{1}{\sqrt{6}} & 0 & 0 & 0 & \sqrt{\frac{2}{3}} \\ 0 & 0 & -\frac{1}{2} & 0 & 0 & -\frac{i}{2} & -\frac{1}{2} & -\frac{i}{2} & 0 \\ \frac{1}{2} & \frac{i}{2} & 0 & \frac{i}{2} & -\frac{1}{2} & 0 & 0 & 0 & 0 \end{bmatrix} \times \begin{bmatrix} S_{XX} \\ S_{XY} \\ S_{XZ} \\ S_{YX} \\ S_{YY} \\ S_{YZ} \\ S_{ZX} \\ S_{ZY} \\ S_{ZZ} \end{bmatrix}. \quad (9.56)$$

The difference between the laboratory frame polarization tensors is reflected in the degree to which linear and circularly polarized two-photon absorption “sample” the molecular fixed transition moments. The two-photon absorption cross-sections for linear and circularly polarized excitation are proportional to the scalar component  $A_{00}^0$  of  $|T \cdot S|^2$

$$A_{00}^0(\text{lin}) = \frac{(T_0^2(\text{Lab}))^2}{5} \sum_n (-1)^{2-n} S_n^2(\text{Mol}) S_{-n}^2(\text{Mol}) + (T_0^0(\text{Lab}))^2 (S_0^0(\text{Mol}))^2, \quad (9.57)$$

$$A_{00}^0(\text{circ}) = \frac{T_2^2(\text{Lab}) T_{-2}^2(\text{Lab})}{5} \sum_n (-1)^{2-n} S_n^2(\text{Mol}) S_{-n}^2(\text{Mol}). \quad (9.58)$$

Expressing the laboratory frame polarization tensors in Cartesian form (Eq. (9.56)), the ratio of circularly polarized to linearly polarized two-photon cross-sections is given by

$$\Omega = \frac{A_{00}^0(\text{circ})}{A_{00}^0(\text{Lin})} = \frac{3(T_{XY})^2 \sum_n (-1)^{2-n} S_n^2(\text{Mol}) S_{-n}^2(\text{Mol})}{(T_{ZZ})^2 \left[ 5(S_0^0(\text{Mol}))^2 + 2 \sum_n (-1)^{2-n} S_n^2(\text{Mol}) S_{-n}^2(\text{Mol}) \right]}. \quad (9.59)$$

The polarization tensors  $T_{XY}$  and  $T_{ZZ}$  have equal magnitude and the ratio  $\Omega$  is simply

$$\Omega = \frac{3 \sum_n (-1)^{2-n} S_n^2(\text{Mol}) S_{-n}^2(\text{Mol})}{5(S_0^0(\text{Mol}))^2 + 2 \sum_n (-1)^{2-n} S_n^2(\text{Mol}) S_{-n}^2(\text{Mol})}. \quad (9.60)$$

Linear and circularly polarized two-photon transitions show different sensitivities to the molecular frame tensor components. For planar aromatic molecules, the two-photon transition is dominated by transition moments in the plane of the molecule. If we consider a planar molecule for which there are no molecule frame Z components,  $\Omega$  is given by

$$\Omega = \frac{(S_{XX} + S_{YY})^2 + 3(S_{XX} - S_{YY})^2 + 3(S_{XY} + S_{YX})^2}{4(S_{XX} + S_{YY})^2 + 2(S_{XX} - S_{YY})^2 + 2(S_{XY} + S_{YX})^2}. \quad (9.61)$$

For the absorption of two identical photons,  $S_{AB} = S_{BA}$ , and Eq. (9.61) simplifies [117]

$$\Omega = \frac{(S_{XX} + S_{YY})^2 + 3(S_{XX} - S_{YY})^2 + 12(S_{XY})^2}{4(S_{XX} + S_{YY})^2 + 2(S_{XX} - S_{YY})^2 + 8(S_{XY})^2}. \quad (9.62)$$

Normalizing with respect to  $S_{XX}$ , we have

$$\Omega = \frac{(1+S)^2 + 3(1-S)^2 + 12D^2}{4(1+S)^2 + 2(1-S)^2 + 8D^2}. \quad (9.63)$$

In terms of the  $\delta F$ ,  $\delta G$ , and  $\delta H$  tensor parameters of Monson and McClain [28], the absorption polarization ratio becomes

$$\begin{aligned} \Omega &= \frac{-\delta F + 3\delta G'}{\delta F + 2\delta G'}, \\ \delta F &= C(1-S)^2, \\ \delta G' &= W[(1+S)^2 + (1-S)^2 + 4D^2], \end{aligned} \quad (9.64)$$

where  $W$  is a constant of proportionality.

Excitation of diagonal tensor elements corresponds to two parallel transition moments, which requires simultaneous action by the applied electric field twice along a single symmetry axis. Conversely, the preparation of off-diagonal terms requires simultaneous action by the applied electric field along two orthogonal axes. These considerations imply that the former is favored for linearly polarized excitation and the latter for circular polarization. This is borne out by the relative weighting of the diagonal and off-diagonal elements in the circular and linear polarization elements in Eq. (9.62). For a transition tensor with  $S = 1$ , the weighting of off-diagonal to diagonal elements in circularly polarized excitation is 3:1, whereas for linear polarization, the weighting of diagonal to off-diagonal elements is 2:1. Transitions into non-totally symmetric upper states have only mixed Cartesian elements in the transition tensor ( $S_{XX} = S_{YY} = 0$ ) and  $\Omega = 1.5$ , conversely in transitions to totally symmetric excited states diagonal elements are dominant [96] and a lower value of  $\Omega$  results. The two-photon absorption of pyrimidine shows a significant dip and rise in  $\Omega$  across the main absorption feature at 415–495 nm (Fig. 9.5). Callis et al. [96] show that this arises from transitions to the totally symmetric  $A_2(n\pi^*)$  and non-symmetric  $B_2(\pi\pi^*)$  states. For a single element diagonal transition tensor,  $S = D = 0$  and  $\Omega = 2/3$ . With no off-diagonal elements ( $D = 0$ ), values for  $\Omega$  can vary from 3/2 ( $S = -1$ ) to 1/4 ( $S = 1$ ) as shown in Figure 9.7. The relative absorption strengths for linear and circularly polarized two-photon absorption can be determined from the integrated fluorescence intensity for the relevant excitation polarization,

$$\Omega = I_{\text{ABS}}^C / I_{\text{ABS}}^L = \int I_{\text{F}}^C(t) dt / \int I_{\text{F}}^L(t) dt. \quad (9.65)$$

The total fluorescence intensity can be obtained from a “magic-angle” polarization measurement at 54.7° to the symmetry axis (axis of cylindrical symmetry for the transition). Measurement of fluorescence intensity and anisotropy data in linearly and circularly polarized, two-photon excited fluorescence necessarily requires different experimental arrangements [117, 119]. In particular, two “magic-angle” configurations are required for fluorescence lifetime and absorption anisotropy experiments

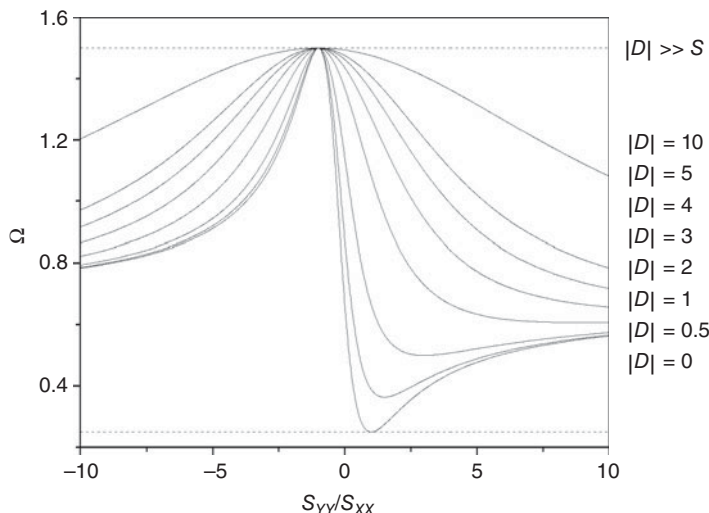


**FIGURE 9.7** Variation in the absorption ratio  $\Omega$  as a function of  $S$  and  $D$ . For a single element transition tensor  $S = D = 0$  and  $\Omega = 2/3$ . The limits of  $\Omega$  vary between 0.25 ( $S = 1$ ,  $|D| = 0$ ) and 1.5 ( $|D| \leq 1$ ).

[103] (Fig. 9.6). An alternative approach applicable to non-fluorescent materials using polarized Z-scan measurements has recently been demonstrated by Vivas and co-workers [107]. Polarization-dependent studies of two-photon absorption have until recently been wholly concerned with isotropically oriented samples. In a novel advance Hochstrasser and co-workers employed polarized single- and two-photon fluorescence excitation of surface-attached single rhodamine B molecules—an interaction where the isotropic laboratory–molecular frame orientation averaging does not exist [120]. Here, circularly polarized excitation provided equivalent photoselection in the plane parallel to the surface ( $X$ - $Y$ ) while retaining sensitivity to out-of-plane molecular orientations ( $Z$ ). Consequentially the intensity histogram of single molecule emitters was used to obtain the out-of-plane orientational distribution function of the population.

### 9.3.2 Two-Photon Excited Fluorescence

Fluorescence arising from two-photon absorption is generally spectrally and temporally identical to that arising from single-photon absorption, as in both cases, emission takes place from the lowest excited singlet state as discussed earlier. The fluorescence anisotropy arising from single- and two-photon excitation can however be markedly different highlighting the distinct photoselection mechanisms that operate in each process. Fluorescence anisotropy is an important experimental tool yielding information on molecular re-orientation [121–124], activated barrier crossing [125], the local environment of fluorescent probes [126, 127], and resonant energy transfer [128–130],

with two-photon excitation now complimenting single-photon techniques in many of these fields [117, 131–133]. A sound understanding of polarized two-photon photo-selection is therefore essential.

The intensity of fluorescence of polarization  $i$  emitted by an excited population of molecules at time  $t$  following short pulsed excitation is given by

$$I_i(t) \propto N(t) \int A(\Omega, t) B_i(\Omega) d\Omega, \quad (9.66)$$

where  $N(t)$  is the population at time  $t$ ,  $A(\Omega, t)$  is the orientational distribution function of the molecular axes in laboratory frame, and  $B_i(\Omega)$  is the detection probability for fluorescence of polarization  $i$ . For spontaneous emission,  $B_i(\Omega)$  is constructed from the scalar product of laboratory frame spherical polarization vectors  $T_q^1$  and molecular frame transition dipole moments  $\mu_n^1$  in an analogous manner to Eqs. (9.44)–(9.46),

$$B(\Omega) = \sum_{q,q'n,n'} \left( T_q^1 \mu_n^1 (-1)^q D_{-qn}^1(\Omega) \right) \left( T_{q'}^1 \mu_{n'}^1 (-1)^{q'} D_{-q'n'}^1(\Omega) \right)^* \quad (9.67)$$

yielding

$$B(\Omega) = \sum_{q,q'n,n'} T_q^1 T_{-q'}^1 \mu_n^1 (-1)^{q+1} \mu_{-n'}^1 (-1)^{q'+1} (-1)^{q'-n'} D_{-qn}^1(\Omega) D_{q'-n'}^1(\Omega). \quad (9.68)$$

Contracting the rotation matrices yields

$$\begin{aligned} B(\Omega) &= \sum_{K,q,q'n,n'} T_q^1 T_{-q'}^1 \mu_n^1 \mu_{-n'}^1 (-1)^{q-q'+Q-N} \\ &\times (2K+1) \begin{pmatrix} 1 & 1 & K \\ -q & q' & Q \end{pmatrix} \begin{pmatrix} 1 & 1 & K \\ n & -n' & N \end{pmatrix} D_{-Q-N}^K(\Omega). \end{aligned} \quad (9.69)$$

From the  $3j$  symbols  $Q = q - q'$  and  $N = n' - n$ ,  $B(\Omega)$  becomes

$$B(\Omega) = \sum_{K,N,Q} B_{NQ}^K D_{-N-Q}^K(\Omega), \quad (9.70)$$

where

$$B_{-Q-N}^K = \sum_{q,q',n,n'} (-1)^N T_q^1 T_{-q'}^1 \mu_n^1 \mu_{-n'}^1 (2K+1) \begin{pmatrix} 1 & 1 & K \\ n & -n' & N \end{pmatrix} \begin{pmatrix} 1 & 1 & K \\ -q & q' & Q \end{pmatrix}. \quad (9.71)$$

The fluorescence intensity for polarization  $i$  is

$$I_i(t) \propto N(t) \sum_{K,Q,N} A_{N'Q'}^{K'}(\Omega, t) B_{NQ}^K(\hat{i}) \int D_{NQ}^K(\Omega) D_{-N-Q}^K(\Omega) d\Omega. \quad (9.72)$$

Using standard rotation matrix orthogonality [91], this becomes

$$I_i(t) \propto N(t) \sum_{K,Q,N} \frac{8\pi^2}{2K+1} (-1)^{N-Q} A_{NQ}^K(\Omega, t) B_{-N-Q}^K(i). \quad (9.73)$$

In two-photon excitation with both linearly and circularly polarized excitation, we have a laboratory frame axis of cylindrical symmetry (see Fig. 9.6) and only moments with  $Q = 0$  are prepared. Consequently only  $B_{0N}^K$  terms have a non-zero orientation average, from the properties of the  $3j$  symbols in Eq. (9.71) only moments of rank  $K = 0$  and 2 are allowed. For  $Z$  and  $X$  polarized emissions, the polarization tensors are given by

$$e_Z e_Z^* = T_0^1 T_0^1, \quad (9.74)$$

$$e_X e_X^* = \frac{-1}{\sqrt{2}} (T_1^1 - T_{-1}^1) \frac{-1}{\sqrt{2}} (-T_1^1 + T_{-1}^1) = \frac{-1}{2} (T_1^1 T_1^1 - 2T_1^1 T_{-1}^1 + T_{-1}^1 T_{-1}^1). \quad (9.75)$$

The cylindrically symmetric component of Eq. (9.75) is  $T_1^1 T_{-1}^1$ ; for  $Z$  and  $X$  detection polarizations, the  $B_{0N}^K$  terms are thus

$$B_{0-N}^K(Z) = T_0^1 T_0^1 (2K+1) \begin{pmatrix} 1 & 1 & K \\ 0 & 0 & 0 \end{pmatrix} \sum_{n,n'} (-1)^N \mu_n^1 \mu_{-n'}^1 \begin{pmatrix} 1 & 1 & K \\ n & -n' & N \end{pmatrix}, \quad (9.76)$$

$$B_{0-N}^K(X) = T_1^1 T_{-1}^1 (2K+1) \begin{pmatrix} 1 & -1 & K \\ 1 & -1 & 0 \end{pmatrix} \sum_{n,n'} (-1)^N \mu_n^1 \mu_{-n'}^1 \begin{pmatrix} 1 & -1 & K \\ n & -n' & N \end{pmatrix}. \quad (9.77)$$

The polarization tensor products are related by  $T_0^1 T_0^1 = -T_1^1 T_{-1}^1 = -1$ , and the  $B_{00}^0$  terms are given by

$$B_{00}^0(Z) = B_{00}^0(X) = \frac{1}{3} \sum_n \mu_n^1 \mu_{-n}^1 (-1)^{1-n}. \quad (9.78)$$

The  $B_{0-N}^2$  terms are given by

$$B_{0-N}^K(Z) = \frac{10}{\sqrt{30}} \sum_{n,n'} (-1)^N \mu_n^1 \mu_{-n'}^1 \begin{pmatrix} 1 & 1 & 2 \\ n & -n' & N \end{pmatrix} = -2B_{0-N}^K(X). \quad (9.79)$$

The fluorescence anisotropy  $R(t)$  is constructed from the  $Z$  and  $X$  polarized emission intensities

$$R(t) = \frac{I_Z(t) - I_X(t)}{I_Z(t) + 2I_X(t)} = \frac{\sum_{K,N} (-1)^N \frac{A_{N0}^K(\Omega,t)}{2K+1} (B_{0-N}^K(Z) - B_{0-N}^K(X))}{\sum_{K,N} (-1)^N \frac{A_{N0}^K(\Omega,t)}{2K+1} (B_{0-N}^K(Z) + 2B_{0-N}^K(X))}. \quad (9.80)$$

From Eqs. (9.78) and (9.79), the anisotropy becomes

$$R(t) = \frac{\frac{1}{10} \sum_N (-1)^N A_{N0}^2(\Omega,t) B_{0-N}^2(Z)}{A_{00}^0(\Omega,t) B_{00}^0(Z)}. \quad (9.81)$$

Using Eq. (9.56) to express the molecular frame transition dipole products in Cartesian form, we have

$$\begin{aligned} B_{00}^0(Z) &= B_{00}^0(X) = \frac{1}{3} (\mu_x^2 + \mu_y^2 + \mu_z^2) \\ B_{00}^2(Z) &= \frac{1}{3} [2\mu_z^2 - (\mu_x^2 + \mu_y^2)] = -2B_{00}^2(X) \\ B_{0\pm 2}^2(Z) &= \frac{1}{\sqrt{6}} [\mu_x^2 - \mu_y^2 \mp 2i\mu_x\mu_y] = -2B_{0\pm 2}^2(X) \\ B_{0\pm 1}^2(Z) &= \mp \frac{2}{\sqrt{6}} \mu_z [\mu_x \pm i\mu_y] = -2B_{0\pm 1}^2(X). \end{aligned} \quad (9.82)$$

Similar relations have been derived by Zannoni [134]. For a planar transition,  $\mu_z = 0$  and  $B_{0\pm 1}^2$  terms are zero. Substituting Eq. (9.82) into Eq. (9.81) yields

$$R(t) = \frac{3}{10} \left[ \frac{A_{00}^2(\Omega,t)}{3} \left[ -(\mu_x^2 + \mu_y^2) \right] + \frac{(A_{02}^2(\Omega,t) + A_{0-2}^2(\Omega,t)) [\mu_x^2 - \mu_y^2]}{\sqrt{6}} \right. \\ \left. - \frac{(A_{02}^2(\Omega,t) - A_{0-2}^2(\Omega,t)) [2i\mu_x\mu_y]}{\sqrt{6}} \right] \left[ A_{00}^0(\Omega,t) (\mu_x^2 + \mu_y^2) \right]^{-1}. \quad (9.83)$$

Measurement of the  $Z$  and  $X$  polarized fluorescence intensities prior to the onset of orientational relaxation of the molecular distribution yields the initial fluorescence anisotropy  $R(0)$ . This provides complimentary information to  $\Omega$  as to the structure of the two-photon transition tensor [103, 117, 132, 133, 135, 136]. The variation in the initial (or collision free) fluorescence anisotropy with excitation polarization in both single- and two-photon excited fluorescence can be used to probe the degrees of alignment in ordered systems [118, 137–140].

Substituting the  $A_{0N}^K$  expressions (obtained from Eqs. (9.51), (9.56), and (9.83)) for linear and circularly polarized excitation as measured in Figure 9.6, the initial

anisotropies for linear and circularly polarized two-photon excitation after some manipulation are

$$R_L(0) = \frac{1}{7} \left[ 1 + \frac{9(1-S^2)(\cos^2 \theta_M - \sin^2 \theta_M) + 4(1+S)D \sin \theta_M \cos \theta_M}{2(1+S^2) + (1-S^2) + 4D^2} \right], \quad (9.84)$$

$$R_C(0) = \frac{1}{7} \left[ \frac{(1+S)^2 + 3[(1-S)^2 + 4D^2] - 6 \left[ (\cos^2 \theta_M - \sin^2 \theta_M)(1-S^2) + 4D(1+S) \sin \theta_M \cos \theta_M \right]}{(1+S)^2 + 3(1-S)^2 + 12D^2} \right], \quad (9.85)$$

where  $\theta_M$  is the angle made by the emission transition dipole with respect to  $X$  in the plane of the molecule and  $S$  and  $D$  are the  $S_{YY}$  and  $S_{XY}$  ( $= S_{YX}$ ) transition tensor components normalized to  $S_{XX}$  as in Eq. (9.63), respectively. For a diagonal single-element transition, tensor  $R_L(0)$  is given by

$$R_L(0) = \frac{1}{7} [1 + 3(\cos^2 \theta_M - \sin^2 \theta_M)] = \frac{4}{7} \left[ \frac{3 \cos^2 \theta_M - 1}{2} \right]. \quad (9.86)$$

When  $\theta_M = 0$ ,  $R_L(0)$  is maximized at 4/7, the initial fluorescence anisotropy for single-photon absorption shows an identical dependence on  $\theta_M$  (where  $X$  defines the direction of the absorption transition moment) with a maximum value of 2/5 when  $\theta_M = 0$ . The variation in  $R_L(0)$  and  $R_C(0)$  with the structure of the transition tensor has been discussed at length by Callis [135] and Johnson and Wan [117, 136].

The contribution of the  $A_{0N}^2(\Omega, t)$  excited state moments to the fluorescence anisotropy is the same irrespective of the excitation process; however, the initial  $A_{0N}^2(\Omega, 0)$  values will differ between single- and two-photon excitation due to the difference between the space and molecule frame fixed orientational photoselection in the two processes. A comparison between the time-resolved fluorescence anisotropy decays of rhodamine 6G for linearly polarized single- and two-photon excitation is shown in Figure 9.8. Both decays are well described by single exponential orientational relaxation times of 2.72 ns and 2.77 ns, respectively, and have initial anisotropies close to the 2/5 and 4/7 limits (0.35 and 0.52, respectively). The  $S_0 \rightarrow S_1$  emission transition dipole moment in rhodamine 6G is oriented along the long molecular axis of the xanthene ring [141, 142], and the similarity of the fluorescence anisotropy decays and the values of the initial anisotropies are consistent with the principal axis of the transition tensor lying along this axis with  $S \approx 1 > D$ . A more complex transition tensor coupled with bi-exponential orientational dynamics is provided by perylene, studied initially by Pauls et al. [132], with a later study by Johansson and co-workers comparing single- and two-photon fluorescence anisotropy decays [133]. These were found to be well described by the same correlation times. The differing contribution of diagonal and off-diagonal terms to  $R_L$  and  $R_C$ , as seen for example by Eqs. (9.84) and (9.85), makes a comparison between linearly and circularly polarized anisotropy decays an additional route to determining the structure of

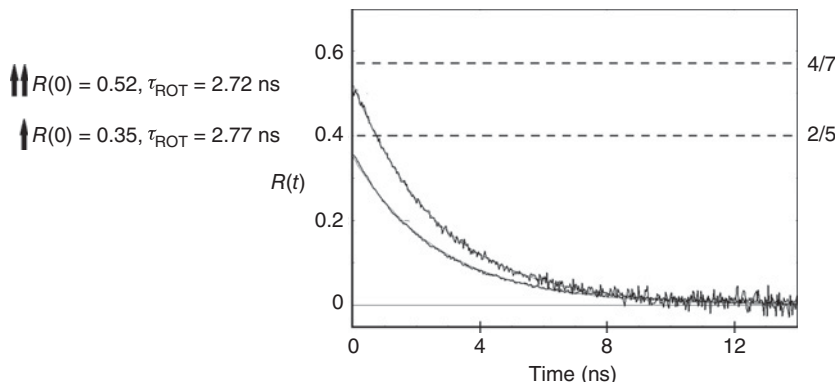


**FIGURE 9.8** A comparison between single- and two- photon excited fluorescence anisotropy decays recorded in our laboratory for rhodamine 6G in ethylene glycol, the initial anisotropies for both processes are close to the theoretical maxima (dashed lines) for excitation from an isotropic ground state and (in the case of the two-photon excited population) a diagonal transition tensor dominated by  $S_{XX}$ .

the transition tensor [117]. Although single- and two-photon anisotropy decays probe the same orientational dynamics, two-photon excitation leads to the creation of more highly ordered arrays of molecular orientations in the laboratory frame; this gives rise not only to increased values of the fluorescence anisotropy but also to the creation of moments of rank  $K = 4$  (i.e.,  $A_{0N}^4$ ), which are forbidden from contributing to spontaneous emission observables [143]. Measurement of these “hidden” degrees of molecular order created by two-photon excitation is possible via the interaction with a third photon and measurement of a vector quantity such as the resulting (altered) fluorescence anisotropy [143, 144]. Using this approach Bain and co-workers have used polarized stimulated emission depletion to measure the  $K = 4$  orientational relaxation dynamics of two-photon excited rhodamine 6G [144]. The measurement of higher order correlation functions for molecular motion in condensed phases is an attractive proposition as this affords a test of fundamental theories of molecular relaxation [145]. Third-order pump-probe [146] and fluorescence anisotropy measurements [121–124] are restricted to  $K = 2$  relaxation dynamics. A number of pump-probe techniques have been developed which access odd rank correlation functions in non-centrosymmetric molecules; terahertz-field-induced second-harmonic generation [147] provides a direct measurement of  $K = 1$  reorientation, whilst six-wave mixing is sensitive to both  $K = 1$  and  $K = 3$  relaxation [148]. Two-photon excitation coupled with a suitable probe (e.g., STED) provides a non-symmetry restricted means of accessing the  $K = 4$  dynamics of a fluorescent probe.

### 9.3.3 Two- and Multiphoton Absorption in Free Rotors

In the gas phase, the time between molecular collisions is in general long compared to that for free rotation. Consequently the molecular angular momentum  $J$  and its

laboratory frame projection  $M$  are good quantum numbers and the classical treatment of molecular photoselection and fluorescence anisotropy above does not hold. A treatment of the linear and circular polarization dependence of two-photon absorption in diatomic molecules was first developed by Bray and Hochstrasser [149], and subsequent work by McClain and Harris [83] and Dixon and co-workers [113] considered two- and three-photon absorption in symmetric rotors, respectively. These approaches while allowing an interpretation of the linear and circular polarization dependence of the observed line strengths did not extend to the properties of the excited state that was created by the nonlinear absorption process. Orientational photoselection in rotationally resolved two- and multiphoton excitation was first developed by Bain and McCaffery [150]. In freely rotating molecules, orientational photoselection is described in terms of the  $M$  state population distribution prepared as a result of polarized photoselection. This is conveniently handled in terms of a spherical tensor (state multipole) expansion of the excited state density matrix [116, 150–153]. The excited state density matrix elements for non-resonant two-photon excitation from ground-state rovibronic level  $|J''M''\rangle$  of a diatomic molecule to an excited rovibronic level  $|J\rangle$  with two co-propagating photons of frequency  $\nu$  is given by

$$\begin{aligned} {}^{JJ}\rho_{M_1 M_2} \propto & \left| \sum_{n, M'''} \left( \frac{\langle J''M'' | \vec{e} \cdot \vec{d} | n \rangle \langle n | e \cdot \mu | JM_1 \rangle}{\nu_n - \nu + i\Gamma_n} + \frac{\langle J''M'' | \vec{e} \cdot \vec{d} | n \rangle \langle n | \vec{e} \cdot \vec{d} | JM_1 \rangle}{\nu_n - \nu + i\Gamma_n} \right) \right. \\ & \times \left. \left( \frac{\langle J''M'' | \vec{e} \cdot \vec{d} | n \rangle^* \langle n | \vec{e} \cdot \vec{d} | JM_2 \rangle^*}{\nu_n - \nu - i\Gamma_n} + \frac{\langle J''M'' | \vec{e} \cdot \vec{d} | n \rangle^* \langle n | \vec{e} \cdot \vec{d} | JM_2 \rangle^*}{\nu_n - \nu - i\Gamma_n} \right)^2 \right|. \end{aligned} \quad (9.87)$$

The resonant frequencies and linewidths of the intermediate (virtual) states  $|n\rangle$  are  $\nu_n$  and  $\Gamma_n$ , respectively, and the summation extends over the intermediate states and the  $M''$  quantum numbers of the ground state rotational level  $J''$ . If the excitation frequency  $\nu$  is well detuned from  $\nu_n$ , the intermediate levels do not develop in time. The tensor density matrix elements or state multipoles of the excited state are defined by [150–153]

$${}^{JJ}\rho_Q^K = \sum_{M_1, M_2} (-1)^{J-M_1} (2K+1) \begin{pmatrix} J & J & K \\ M_1 & -M_2 & Q \end{pmatrix} {}^{JJ}\rho_{M_1 M_2}. \quad (9.88)$$

Substitution of Eq. (9.87) into Eq. (9.88) and application of the Wigner–Eckart theorem yields a lengthy expression in terms of the reduced matrix elements of the allowed transitions [153]. The excited state is characterized by well-defined values of the state multipoles where the tensorial rank  $K$  ranges from zero to four; in the case of circularly polarized excitation, both even- and odd-order rank multipoles are created. Although with opposing circular polarizations of the same frequency, the excited state is characterized by even-order moments as is found for linearly polarized excitation. This is in contrast to the circularly polarized photoselection of fluorescent probes in condensed phases where the ‘effective excitation and observation’ of all rotational branches have opposing (or zero) contributions to  $K = 1$  and  $K = 3$  observables.

In rotationally resolved two-photon absorption, it was found that for transitions in which the change in rotational quantum number  $\Delta J = \pm 2$  (the *R* and *S* branches) the expressions for the relative values of the state multipoles were considerably simplified, on contracting the summations over 5-3j symbols [154].

$$\begin{aligned} {}^{JJ}\rho_Q^K(q_A, q_A) \propto & \sqrt{5} \left\{ \begin{matrix} 1 & 1 & 2 \\ J'' & J & J' \end{matrix} \right\} \sum_{a_2} (-1)^{J+J'+q_A} (2a_2 + 1) (2K + 1)^{\frac{1}{2}} \\ & \times \left\{ \begin{matrix} 2 & 1 & a_2 \\ J' & J & J'' \end{matrix} \right\} \left\{ \begin{matrix} a_2 & 1 & K \\ J & J & J'' \end{matrix} \right\} \left( \begin{matrix} 2 & 1 & a_2 \\ -2q_A & q_A & q_A \end{matrix} \right) \left( \begin{matrix} a_2 & 1 & K \\ q_A & q_A & Q \end{matrix} \right), \end{aligned} \quad (9.89)$$

where  $q_A$  denotes the polarization component of the photon ( $q_A = 0$ , linear  $q_A = +1$  or  $-1$  circular) and  $J'$  is the rotational quantum number of the single virtual level ( $J' = J''+1$  or  $J'' - 1$ ). For linearly polarized excitation in the case of transitions dominated by pure *Q* steps, that is,  $J = J' = J''$ , Eq. (9.89) becomes

$$\begin{aligned} {}^{JJ}\rho_Q^K(q_A, q_A) \propto & \sqrt{5} \left\{ \begin{matrix} 1 & 1 & 2 \\ J & J & J \end{matrix} \right\} \sum_{a_2} (-1)^{J+J'} (2a_2 + 1) (2K + 1)^{\frac{1}{2}} \\ & \times \left\{ \begin{matrix} 2 & 1 & a_2 \\ J & J & J \end{matrix} \right\} \left\{ \begin{matrix} a_2 & 1 & K \\ J & J & J \end{matrix} \right\} \left( \begin{matrix} 2 & 1 & a_2 \\ 0 & 0 & 0 \end{matrix} \right) \left( \begin{matrix} a_2 & 1 & K \\ 0 & 0 & Q \end{matrix} \right). \end{aligned} \quad (9.90)$$

The degree of circular polarization *C*, linear polarization *P*, and anisotropy *R* in rotationally resolved fluorescence to a final rotational level  $J'''$  are given by [150, 153]

$$\begin{aligned} P = & -3 \left( \frac{{}^{JJ}\rho_0^2}{{}^{JJ}\rho_0^0} \right) \frac{\left\{ \begin{matrix} 1 & 1 & 2 \\ J & J & J''' \end{matrix} \right\}}{\left\{ \begin{matrix} 1 & 1 & 0 \\ J & J & J''' \end{matrix} \right\}} \left[ \sqrt{8} - \left( \frac{{}^{JJ}\rho_0^2}{{}^{JJ}\rho_0^0} \right) \frac{\left\{ \begin{matrix} 1 & 1 & 2 \\ J & J & J''' \end{matrix} \right\}}{\left\{ \begin{matrix} 1 & 1 & 0 \\ J & J & J''' \end{matrix} \right\}} \right]^{-1} \\ R = & \frac{2P}{3-P} \end{aligned} \quad (9.91)$$

$$C = - \left( \frac{{}^{JJ}\rho_0^2}{{}^{JJ}\rho_0^0} \right) \frac{\left\{ \begin{matrix} 1 & 1 & 1 \\ J & J & J''' \end{matrix} \right\}}{\left\{ \begin{matrix} 1 & 1 & 0 \\ J & J & J''' \end{matrix} \right\}} \left[ \sqrt{\frac{2}{3}} - \sqrt{\frac{1}{3}} \left( \frac{{}^{JJ}\rho_0^2}{{}^{JJ}\rho_0^0} \right) \frac{\left\{ \begin{matrix} 1 & 1 & 2 \\ J & J & J''' \end{matrix} \right\}}{\left\{ \begin{matrix} 1 & 1 & 0 \\ J & J & J''' \end{matrix} \right\}} \right]^{-1}$$

Substitution of the specific values of the  ${}^{JJ}\rho_Q^K$  obtained by this analysis into Eq. (9.91) leads to fluorescence anisotropies significantly higher than the single-photon values for *C* and *P* (and *R*). The degree of circular polarization *C* tends to

a value of  $-7/8$  for  $(P\uparrow P\uparrow) R\downarrow$  and  $(R\uparrow R\uparrow) P\downarrow$  and  $+7/8$  for  $(P\uparrow P\uparrow) P\downarrow$  and  $(R\uparrow R\uparrow) R\downarrow$ , the highest values of  $C$  obtained for single-photon excited fluorescence in the high  $J$  limit are  $+5/7$  ( $R\uparrow R\downarrow$  and  $P\uparrow P\downarrow$ ) and  $-5/7$  ( $P\uparrow R\downarrow$  and  $R\uparrow P\downarrow$ ). The degree of linear polarization  $P$  for near resonant two-photon excitation dominated by the  $Q\uparrow Q\uparrow$  path is also high tending to  $+2/3$  in the high- $J$  limit. The above analysis was further applied to multiphoton absorption, in the case where  $\Delta J = \pm n$ ,  $n$  being the number of photons absorbed the state multipoles. In this limit the state multipoles characterizing the final state are determined by  $n$  effective single-photon transitions via  $(n - 1)$  “virtual multipoles.”

Two-photon and multiphoton excitation routes that have a wholly angular momentum-based polarization dependence rather than a potentially complex and unknown dependence on the excitation pathway are ideally suited as a means of probing the alignment of molecular populations in molecular dynamics studies [119]. The determination of molecular alignment parameters using rotationally resolved polarized two-photon excitation and ionization-based detection is now a well-established tool in state-selected molecular dynamics [155–159].

#### 9.4 APPLICATIONS AND FUTURE PROSPECTS

Two-photon excitation techniques now find widespread application in the biological sciences, perhaps the most significant contribution two-photon excited fluorescence has made to date is in fluorescence microscopy. Prior to the invention and commercial realization of the two-photon microscope, depth resolution in fluorescence microscopy was achieved using the confocal microscope [160], the principles of which are illustrated in Figure 9.9. Fluorescence is excited via single-photon absorption using a continuous wave laser (typically an argon ion laser line), and this is scanned in the  $X-Y$  plane to build up an image of the sample. However, a considerable degree of fluorescence is generated both above and below the focal plane and, if allowed to reach the detector, will cause blurring of the final image. In a confocal microscope, a pinhole is introduced in front of the detector in a position that prevents emission from above and below the focal plane of the sample when the focal plane of illumination and detection are the same. The drawbacks are that large regions of the sample outside the region of interest are excited; this carries a significant risk of damage (particularly for studies of live cells) arising from heat deposition and photochemical reactions. In addition, the presence of the confocal pinhole results in reduced collection efficiency with a subsequent increase in data collection time. In two-photon fluorescence, excitation is restricted to the waist region of the laser focus [14] and excitation of fluorescence outside the Rayleigh range of the laser focus is significantly reduced. The spatial differences between the two- and single-photon excitation are clearly illustrated in Figure 9.10.

Two-photon excitation is ideally suited for scanning fluorescence microscopy, allowing confocal resolution with a significant reduction in the drawbacks outlined above. The use of near-infrared wavelengths in two-photon excitation as opposed

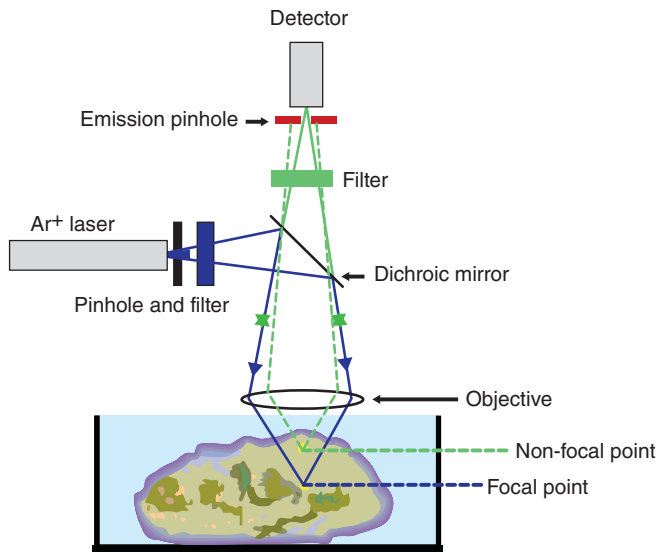


**FIGURE 9.9** Principles of the confocal fluorescence microscope; single-photon excited fluorescence occurs along the entire beam path; however, the insertion of a pinhole in the focal plane of the objective ensures that fluorescence from outside the focal point of the laser (dashed line) is prevented from reaching the detector. The laser is scanned in the  $x$ - $y$  plane to build up an image of the sample for a given depth. Translation of the sample in the  $z$ -direction allows images (optical sections) to be recorded as a function of depth.

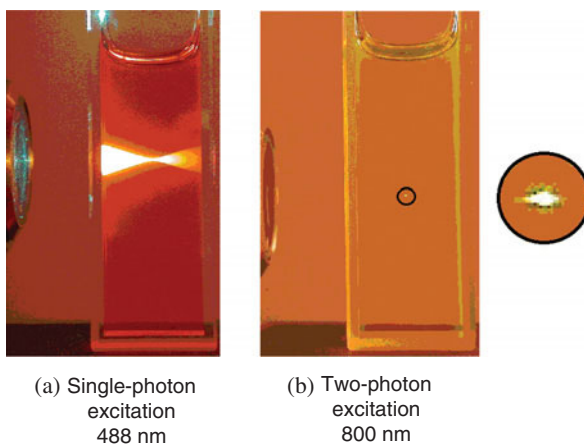


**FIGURE 9.10** A direct comparison between the spatial dependence of two- and single-photon absorption from a fluorescent probe in an isotropic solution contained in a cuvette and viewed at  $90^\circ$  to the excitation direction. (a) Single-photon excitation at 488 nm produces fluorescence throughout the sample, whereas (b) the restriction of two-photon fluorescence (excited at 800 nm) to the Rayleigh range around the laser focus is clearly evident. The photographs were provided courtesy of Dr. Mireille Blanchard-Desce (CNRS Bordeaux).

to visible and ultra-violet wavelengths in single-photon excitation is in itself less detrimental to studies of living cells. In tissues better penetration is afforded due to lower scattering losses and (single-photon) absorption by endogenous molecules. The so-called biological window between 700 and 1200 nm coincides with the two-photon absorption bands of many fluorescent probes. A two-photon scanning microscope thus provides near confocal resolution with increased fluorescence collection efficiency and a reduction in sample damage. The principles of operation of a two-photon microscope and an example of deep (1 mm) tissue imaging in a live heart are presented in Figure 9.11.

Two-photon microscopy has been coupled with time-resolved single-photon counting detection to enable two-photon fluorescence lifetime imaging microscopy (FLIM). Förster resonance energy transfer (FRET) studies using two-photon FLIM with fluorescent protein pairs have proved a highly effective tool in cell biophysics research [130, 161, 162]. While there has been considerable activity in this field, there has until recently been little research directed toward understanding the fundamental nature of two-photon absorption process in fluorescent proteins and their optimization for multiphoton excitation. Drobizhev and co-workers have undertaken a detailed and systematic study of two-photon absorption across a wide range of fluorescent proteins [163–165]; a new model for vibronic coupling in red fluorescent proteins and an investigation of the mechanisms operating in photobleaching have been reported [166, 167]. The utility of employing two-photon excitation in the study of FRET between fluorescent protein pairs has recently been demonstrated by Masters et al. [168]. It is clear that research into the fundamental nature of two- and multiphoton excitations in, and the photophysics of, fluorescent proteins will be an area of increasing activity and interest.

## 9.5 CONCLUSIONS

Research into multiphoton absorption in molecules was initially driven by the excitement of investigating a hitherto unobservable physical phenomenon. The development of two-photon absorption as a widely applicable measurement technique in molecular and chemical physics advanced rapidly, and polarized two- and multiphoton excitation techniques after nearly three decades still find wide application in the study of molecular dynamics. With the development of near-infrared tunable femtosecond lasers, the study and exploitation of two- and multiphoton absorption became possible with significantly lower energy laser pulses. These advances ushered in new applications—most notably the two-photon confocal fluorescence microscope. The drive to incorporate spectroscopic techniques into fluorescence microscopy to probe molecular interactions and dynamics in living cells and tissue and the need to develop new and improved fluorescent proteins have in turn led to renewed interest into the fundamental nature of multiphoton absorption and photophysics. After 50 years, the field has advanced to a point where there is real synergy between fundamental research and practical applications.

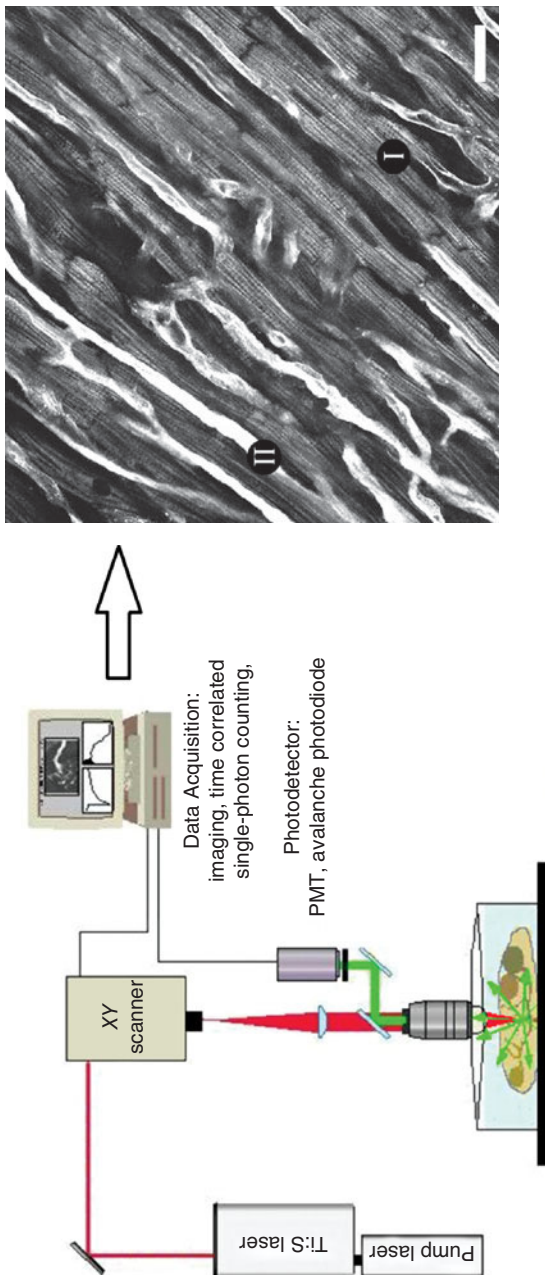


**FIGURE 9.11** (a) Principles of operation of a two-photon fluorescence microscope system, two-photon excitation within the sample is achieved using the output of a Ti:sapphire laser. This is scanned in the  $x-y$  plane to produce an image of a section of the sample. (b) Two-photon microscopy of an isolated, perfused mouse heart using a Zeiss 510 NLO microscope. Cardiomyocyte cells are revealed by the striated (mitochondrial) fluorescence of the metabolic cofactor NAD(P)H (I). Endothelial cells (II) stained by the voltage-sensitive dye ANEPPS lie beneath the cardiomyocytes. Scale bar 20  $\mu\text{m}$ . Image courtesy of Sean M. Davidson, The Hatter Cardiovascular Institute (UCL).

## ACKNOWLEDGMENTS

My introduction to two-photon absorption and third-order nonlinear optics began during my D. Phil research with Tony McCaffery at the University of Sussex and continued during a postdoctoral fellowship with the late Robin Hochstrasser at the University of Pennsylvania. I am indeed grateful to both Tony and Robin for their good-humored supervision and for many interesting discussions over the years. I am happy to acknowledge the contribution of my research group, some of whose work is cited in this chapter. I have endeavored to provide within the practical limitations of a chapter as comprehensive a review of the fundamental physics and coverage of the development and application of two- and multiphoton absorption as possible. I would also like to thank Tom Blacker for careful proofreading of the manuscript.

## REFERENCES

- [1] P. Butcher and D. Cotter, *The Elements of Nonlinear Optics* (Cambridge University Press, Cambridge, 1990).
- [2] Y. R. Shen, *The Principles of Nonlinear Optics* (John Wiley & Sons, London, 2002).
- [3] A. Yariv, *Optical Electronics* (Oxford University Press, Oxford, 1990).
- [4] R. Boyd, *Nonlinear Optics*, 3rd ed. (Academic Press, London, 2008).
- [5] M. Bass, P. A. Franken, A. E. Hill, C. W. Peters, and G. Weinrich, “Optical mixing,” *Phys. Rev. Lett.* **8**, 18 (1962).
- [6] R. C. Miller and A. Savage, “Harmonic generation and mixing of CaWO<sub>4</sub>: Nd<sup>3+</sup> and ruby pulsed laser beams in piezoelectric crystals,” *Phys. Rev.* **128**, 2175–2179 (1962).
- [7] J. F. Reintjes, *Nonlinear Optical Parametric Processes in Liquids and Gases* (Academic Press, New York, 1984).
- [8] R. R. Alfano (ed.), *The Supercontinuum Laser Source*, 2nd ed. (Springer, New York, 2006).
- [9] Y. R. Shen, “Self-focusing: Experimental,” *Prog. Quantum Electron.* **4**, 1–34 (1975).
- [10] G. P. Agrawal, *Nonlinear Fibre Optics*, 1st ed. (Academic Press, New York, 1989).
- [11] A. Barthelemy, S. Maneuf, and C. Froehly, “Propagation soliton et auto-confinement de faisceaux laser par non linearité optique de kerr,” *Opt. Commun.* **55**, 201–206 (1985).
- [12] D. K. Negus and L. Spinelli, “Mode-locked laser using non-linear self-focusing element,” US Patent No. 5,097,471A, 1992.
- [13] L. Spinelli, N. Couillaud, N. Goldblatt, and D. K. Negus, “Starting and generation of sub-100 fs pulses in Ti:sapphire by self focusing,” in Conference on Lasers and Electro-optics, 1991, Washington, DC, CPDP7, Optical Society of America.
- [14] B. Larijani and A. J. Bain, “Single and two-photon fluorescence in biology,” in *Chemical Biology: Techniques and Applications*, edited by B. Larijani, C. A. Rosser, and R. Woscholski (John Wiley & Sons, Inc., Hoboken, 2006).
- [15] J. G. Eden, “High-order harmonic generation and other intense optical field-matter interactions: review of recent experimental and theoretical advances,” *Prog. Quantum Electron.* **28**, 197–246 (2004).
- [16] S. H. Lin, Y. Fujimura, H. J. Neusser, and E. W. Schlag, *Multiphoton Spectroscopy of Molecules* (Academic Press, London, 1984).

- [17] P. Mulser, R. Sigel, and S. Witkowski, “Plasma production by laser,” *Phys. Rep.* **6**, 187–239 (1973).
- [18] P. Lambropoulos, “Topics on multiphoton processes in atoms,” *Adv. At. Mol. Phys.* **12**, 87–164 (1976).
- [19] M. A. C. Nascimento, “The polarization dependence of two-photon absorption rates for randomly oriented molecules,” *Chem. Phys.* **74**, 51–66 (1983).
- [20] B. Dick, R. M. Hochstrasser, and H. P. Trommsdorff, *Non-linear Properties of Organic Molecules and Crystals*, edited by D. S. Chemla and J. Zyss (Academic Press, London, 1987), pp. 167–170.
- [21] M. D. Levenson and S. S. Kano, *Introduction to Nonlinear Laser Spectroscopy*, 2nd ed. (Academic Press, London, 1988).
- [22] M. Göppert-Mayer, “Über elementarakte mit zwei quantensprüngen,” *Ann. Phys.* **401**, 273–294 (1931).
- [23] W. Kaiser and C. G. B. Garrett, “Two-photon excitation in CaF<sub>2</sub>:Eu<sup>2+</sup>,” *Phys. Rev. Lett.* **7**, 229–231 (1961).
- [24] T. H. Maiman, “Stimulated optical radiation in ruby,” *Nature* **187**, 493–494 (1960).
- [25] D. Fröhlich and H. Mahr, “Two-photon spectroscopy in anthracene,” *Phys. Rev. Lett.* **16**, 895–987 (1966).
- [26] K. B. Eisenthal, M. W. Dowley, and W. L. Peticolas, “Two-photon spectrum of a liquid,” *Phys. Rev. Lett.* **20**, 93–95 (1968).
- [27] P. R. Monson and W. M. McClain, “Polarization dependence of the two-photon absorption of tumbling molecules with application to liquid 1-chloronaphthalene and benzene,” *J. Chem. Phys.* **53**, 29–37 (1970).
- [28] P. R. Monson and W. M. McClain, “Complete polarization study of the two-photon absorption of liquid 1-chloronaphthalene,” *J. Chem. Phys.* **56**, 4817–4825 (1972).
- [29] A. Bergman and J. Jortner, “Two-photon spectroscopy utilizing dye lasers,” *Chem. Phys. Lett.* **15**, 309–315 (1972).
- [30] A. Bergman and J. Jortner, “Two-photon absorption spectra of crystalline naphthalene and of the naphthalene molecule in solution,” *Chem. Phys. Lett.* **26**, 323–326 (1974).
- [31] T. W. Hänsch, “Repetitively pulsed tunable dye laser for high resolution spectroscopy,” *Appl. Opt.* **11**, 895–898 (1972).
- [32] R. M. Hochstrasser, H. N. Sung, and J. E. Wessel, “High resolution two-photon excitation spectra,” *J. Chem. Phys.* **58**, 4694–4695 (1973).
- [33] R. M. Hochstrasser, H. N. Sung, and J. E. Wessel, “Moderate-resolution study of the two-photon spectrum of the <sup>1</sup>B<sub>2u</sub> state of benzene-*h*<sub>6</sub> and benzene-*d*<sub>6</sub>,” *Chem. Phys. Lett.* **24**, 7–10 (1974).
- [34] R. M. Hochstrasser, H. N. Sung, and J. E. Wessel, “Moderate-resolution two-photon spectrum of the naphthalene crystal and naphthalene in durene,” *Chem. Phys. Lett.* **24**, 168–171 (1974).
- [35] R. M. Hochstrasser, J. E. Wessel, and H. N. Sung, “Two-photon excitation spectrum of benzene in the gas phase and the crystal,” *J. Chem. Phys.* **60**, 317–318 (1974).
- [36] R. G. Bray, R. M. Hochstrasser, and J. E. Wessel, “Continuously tunable two-photon excitation of individual rotational levels of the A<sup>2</sup>σ<sup>+</sup> state of nitric oxide,” *Chem. Phys. Lett.* **27**, 167–171 (1974).

- [37] P. M. Johnson, “Multiphoton ionization spectroscopy: a new state of benzene,” *J. Chem. Phys.* **62**, 4562–4563 (1975).
- [38] P. M. Johnson, “The multiphoton ionization spectrum of *trans*-1,3-butadiene,” *J. Chem. Phys.* **64**, 4638–4644 (1976).
- [39] P. M. Johnson and C. E. Otis, “Molecular multiphoton spectroscopy with ionization detection,” *Ann. Rev. Phys. Chem.* **32**, 139–157 (1981).
- [40] R. M. Hochstrasser, G. R. Meredith, and H. P. Trommsdorff, “Two-photon spectra of gases by three-wave mixing,” *Chem. Phys. Lett.* **53**, 423–428 (1978).
- [41] F. Biraben, B. Cagnac, and G. Grynberg, “Experimental evidence of two-photon transition without Doppler broadening,” *Phys. Rev. Lett.* **32**, 643–645 (1974).
- [42] J. P. Woerdman, “Doppler-free two-photon transitions of the sodium molecule,” *Chem. Phys. Lett.* **43**, 279–282 (1976).
- [43] E. Riedle, H. J. Neusser, and E. W. Schlag, “Electronic spectra of polyatomic molecules with resolved individual rotational transitions: benzene,” *J. Chem. Phys.* **75**, 4231–4240 (1981).
- [44] W. M. McClain, “Two-photon molecular spectroscopy,” *Acc. Chem. Res.* **7**, 129–135 (1974).
- [45] D. M. Friedrich and W. M. McClain, “Two-photon molecular electronic spectroscopy,” *Annu. Rev. Phys. Chem.* **31**, 559–577 (1980).
- [46] L. Goodman and R. P. Rava, “Two-photon spectra of aromatic molecules,” *Acc. Chem. Res.* **17**, 250–257 (1984).
- [47] R. R. Birge, “Two-photon spectroscopy of protein-bound chromophores,” *Acc. Chem. Res.* **19**, 138–146 (1986).
- [48] P. R. Callis, “Two-photon-induced fluorescence,” *Ann. Rev. Phys. Chem.* **48**, 271–297 (1997).
- [49] P. F. Moulton, “Spectroscopic and laser characteristics of Ti:Al<sub>2</sub>O<sub>3</sub>,” *J. Opt. Soc. Am. B* **3**, 125–133 (1986).
- [50] P. Albers, E. Stark, and G. Huber, “Continuous-wave laser operation and quantum efficiency of titanium-doped sapphire,” *J. Opt. Soc. Am. B* **3**, 134–139 (1986).
- [51] P. F. Curley and A. I. Ferguson, “Actively mode-locked Ti:sapphire laser producing transform-limited pulses of 150-fs duration,” *Opt. Lett.* **16**, 1016–1018 (1991).
- [52] D. E. Spence, P. N. Kean, and W. Sibbett, “60-fsec Pulse generation from a self-mode-locked Ti:sapphire laser,” *Opt. Lett.* **16**, 42–44 (1991).
- [53] W. Denk, J. H. Strickler, and W. W. Webb, “Two-photon laser scanning fluorescence microscopy,” *Science* **248**, 73–76 (1990).
- [54] R. L. Fork, B. I. Greene, and C. V. Shank, “Generation of optical pulses shorter than 0.1 psec by colliding pulse mode locking,” *Appl. Phys. Lett.* **38**, 671–672 (1981).
- [55] M. Chalfie, Y. Tu, G. Euskirchen, W. W. Ward, and D. C. Prasher, “Green fluorescent protein as a marker for gene expression,” *Science* **263**, 802–805 (1994).
- [56] R. Heim, A. B. Cubitt, and R. Y. Tsien, “Improved green fluorescence,” *Nature* **373**, 663–664 (1995).
- [57] R. Loudon, *The Quantum Theory of Light* (Oxford University Press, Oxford, 1983).
- [58] J. A. Giordmaine, P. M. Rentzepis, S. L. Shapiro, and K. W. Wecht, “Two-photon excitation of fluorescence by picosecond light pulses,” *Appl. Phys. Lett.* **11**, 216–218 (1967).

- [59] J. R. Klauder, M. A. Duguay, J. A. Giordmaine, and S. L. Shapiro, "Correlation effects in the display of picosecond pulses by two-photon techniques," *Appl. Phys. Lett.* **13**, 174–176 (1968).
- [60] P. D. Maker and R. W. Terhune, "Study of optical effects due to an induced polarization third order in the electric field strength," *Phys. Rev.* **137**, A801–A818 (1965).
- [61] R. W. Hellwarth, A. Owyong, and N. George, "Origin of the nonlinear refractive index of liquid  $\text{CCl}_4$ ," *Phys. Rev. A* **4**, 2342–2347 (1971).
- [62] J. H. Marburger, "Self-focusing: theory," *Prog. Quantum Electron.* **4**, 35–110 (1975).
- [63] P. P. Ho and R. R. Alfano, "Optical kerr effect in liquids," *Phys. Rev. A* **20**, 2170–2187 (1979).
- [64] G. S. He, J. D. Bhawalkar, C. F. Zhao, and P. N. Prasad, "Optical limiting effect in a two-photon absorption dye doped solid matrix," *Appl. Phys. Lett.* **67**, 2433–2435 (1995).
- [65] J. E. Ehrlich, X. L. Xu, I.-Y. S. Lee, X.-Y. Hu, H. Röckel, S. R. Marder, and J. W. Perry, "Two-photon absorption and broadband optical limiting with bis-donor stilbenes," *Opt. Lett.* **22**, 1843–1845 (1997).
- [66] G. S. He, L. Yuan, N. Cheng, J. D. Bhawalkar, P. N. Prasad, L. L. Brott, S. J. Clarson, and B. A. Reinhardt, "Nonlinear optical properties of a new chromophore," *J. Opt. Soc. Am. B* **14**, 1079–1087 (1997).
- [67] M. Albota, D. Beljonne, J.-L. Bredas, J. E. Ehrlich, J.-Y. Fu, A. A. Heikal, S. E. Hess, T. Kogej, M. D. Levin, S. R. Marder, et al., "Design of organic molecules with large two-photon absorption cross sections," *Science* **281**, 1653–1656 (1998).
- [68] A. Abbotto, L. Beverina, R. Bozio, S. Bradamante, C. Ferrante, G. A. Pagani, and R. Signorini, "Push-pull organic chromophores for frequency-upconverted lasing," *Adv. Mater.* **12**, 1963–1967 (2000).
- [69] O. Mongin, L. Porrès, C. Katan, T. Pons, J. Mertz, and M. Blanchard-Desce, "Synthesis and two-photon absorption of highly soluble three-branched fluorenylene-vinylene derivatives," *Tetrahedron Lett.* **44**, 8121–8125 (2003).
- [70] L. Porrès, O. Mongin, C. Katan, M. Charlot, B. K. G. Bhatthula, V. Jouikov, T. Pons, J. Mertz, and M. Blanchard-Desce, "Two-photon absorption and fluorescence with quadrupolar and branched chromophores—effect of structure and branching," *J. Non-linear Opt. Phys. Mater.* **13**, 451–460 (2004).
- [71] O. Mongin, L. Porrès, M. Charlot, C. Katan, and M. Blanchard-Desce, "Synthesis, fluorescence, and two-photon absorption of a series of elongated rodlike and banana-shaped quadrupolar fluorophores: a comprehensive study of structure–property relationships," *Chem. Eur. J.* **13**, 1481–1498 (2007).
- [72] C. Katan, S. Tretiak, M. H. V. Werts, A. J. Bain, R. J. Marsh, N. Leonczek, N. Nicolaou, E. Badaeva, O. Mongin, and M. Blanchard-Desce, "Two-photon transitions in quadrupolar and branched chromophores: experiment and theory," *J. Phys. Chem. B* **111**, 9468–9483 (2007).
- [73] M. Charlot, N. Izard, O. Mongin, D. Riehl, and M. Blanchard-Desce, "Optical limiting with soluble two-photon absorbing quadrupoles: structure–property relationships," *Chem. Phys. Lett.* **417**, 297–302 (2006).
- [74] N. S. Makarov, M. Drobizhev, and A. Rebane, "Two-photon absorption standards in the 550–1600 nm excitation wavelength range," *Opt. Exp.* **16**, 4029–4047 (2008).
- [75] B. H. Cumpston, S. P. Ananthavel, S. Barlow, D. L. Dyer, J. E. Ehrlich, L. L. Erskine, A. A. Heikal, S. M. Kuebler, I.-Y. S. Lee, D. McCord-Maughton, et al., "Two-photon

- polymerization initiators for three-dimensional optical data storage and microfabrication," *Nature* **398**, 51–54 (1999).
- [76] W. Zhou, S. M. Kuebler, K. L. Braun, T. Yu, J. K. Cammack, C. K. Ober, J. W. Perry, and S. R. Marder, "An efficient two-photon-generated photoacid applied to positive-tone 3d microfabrication," *Science* **296**, 1106–1109 (2002).
- [77] D. A. Parthenopoulos and P. M. Rentzepis, "Three-dimensional optical storage memory," *Science* **245**, 843–845 (1989).
- [78] S. Kawata and Y. Kawata, "Three-dimensional optical data storage using photochromic materials," *Chem. Rev.* **100**, 1777–1788 (2000).
- [79] F. Terenziani, C. Katan, E. Badaeva, S. Tretiak, and M. Blanchard-Desce, "Enhanced two-photon absorption of organic chromophores: theoretical and experimental assessments," *Adv. Mater.* **20**, 4641–4678 (2008).
- [80] M. Pawlicki, H. A. Collins, R. G. Denning, and H. L. Anderson, "Two-photon absorption and the design of two-photon dyes," *Angew. Chem. Int. Ed.* **48**, 3244–3266 (2009).
- [81] M. G. Kuzyk, J. Pérez-Moreno, and S. Shafei, "Sum rules and scaling in nonlinear optics," *Phys. Rep.* **529**, 297–398 (2013).
- [82] M. Samoć, "Third-order nonlinear optical materials: practical issues and theoretical challenges," *J. Mol. Model.* **17**, 2183–2189 (2011).
- [83] W. M. McClain and R. A. Harris, "Two-photon molecular spectroscopy in liquids and gases," in *Excited States*, edited by E. C. Lim (Academic Press, New York, 1977), pp. 1–56.
- [84] P. W. Atkins and R. S. Friedman, *Molecular Quantum Mechanics*, 3rd ed. (Oxford University Press, Oxford, 1999).
- [85] P. M. Johnson, "The multiphoton ionization spectrum of benzene," *J. Chem. Phys.* **64**, 4143–4148 (1976).
- [86] T. M. Stachelek, T. A. Pazoha, W. M. McClain, and R. P. Drucker, "Detection and assignment of the 'phantom' photochemical singlet of *trans*-stilbene by two-photon excitation," *J. Chem. Phys.* **66**, 4540–4543 (1977).
- [87] M. F. Granville, G. R. Holtom, B. E. Kohler, R. L. Christensen, and K. L.D'Amico, "Experimental confirmation of the dipole forbidden character of the lowest excited singlet state in 1,3,5,7-octatetraene," *J. Chem. Phys.* **70**, 593–594 (1979).
- [88] B. Dick and G. Hohlneicher, "Two-photon spectroscopy of dipole-forbidden transitions: the low-lying singlet states of anthracene," *Chem. Phys. Lett.* **83**, 615–621 (1981).
- [89] B. Dick and G. Hohlneicher, "Two-photon spectroscopy of the low-lying singlet states of naphthalene and acenaphthene," *Chem. Phys. Lett.* **84**, 471–478 (1981).
- [90] J. M. Hollas, "Progress in electronic spectroscopy of large molecules," *J. Chem. Soc. Faraday Trans.* **94**, 1527–1540 (1998).
- [91] D. M. Brink and G. R. Satchler, *Angular Momentum*, 3rd ed. (Oxford University Press, Oxford, 1994).
- [92] W. L. Peticolas, R. Norris, and K. E. Rieckhoff, "Polarization effects in the two-photon excitation of anthracene fluorescence," *J. Chem. Phys.* **42**, 4164–4169 (1965).
- [93] B. Honig, J. Jortner, and A. Szöke, "Theoretical studies of two-photon absorption processes. i. molecular benzene," *J. Chem. Phys.* **46**, 2714–2727 (1967).
- [94] W. M. McClain, "Excited state symmetry assignment through polarized two-photon absorption studies of fluids," *J. Chem. Phys.* **55**, 2789–2796 (1971).

- [95] R. P. Drucker and W. M. McClain, "Dye laser two-photon excitation study of several  $O,O'$ -bridged biphenyls," *J. Chem. Phys.* **61**, 2616–2619 (1974).
- [96] P. R. Callis, T. W. Scott, and A. C. Albrecht, "Polarized two-photon fluorescence excitation studies of pyrimidine," *J. Chem. Phys.* **75**, 5640–5646 (1981).
- [97] J. M. Hollas, B. J. Langham, H. Musa, and T. Ridley, "The  $\tilde{A}^1A_1$ - $\tilde{X}^1A_1$  two-photon fluorescence excitation spectrum of 1,2-difluorobenzene," *J. Mol. Spec.* **97**, 405–419 (1983).
- [98] J. M. Hollas, H. Musa, and T. Ridley, "The  $\tilde{A}^1B_2$ - $\tilde{X}^1A_1$  two-photon fluorescence excitation spectrum of 1,3-difluorobenzene," *J. Mol. Spec.* **98**, 125–137 (1983).
- [99] M. J. Wirth, A. C. Koskelo, and C. E. Mohler, "Study of solvation symmetry by two-photon polarization measurements," *J. Phys. Chem.* **87**, 4395–4400 (1983).
- [100] C. E. Mohler and M. J. Wirth, "Solvent perturbations on the excited state symmetry of randomly oriented molecules by two-photon absorption," *J. Chem. Phys.* **88**, 7369–7375 (1988).
- [101] A. A. Rehms and P. R. Callis, "Resolution of  $L_a$  and  $L_b$  bands in methyl indoles by two-photon spectroscopy," *Chem. Phys. Lett.* **140**, 83–89 (1987).
- [102] D. Scherer, R. Dörfler, A. Feldner, T. Vogtmann, M. Schwoerer, U. Lawrentz, W. Grahn, and C. Lambert, "Two-photon states in squaraine monomers and oligomers," *Chem. Phys.* **279**, 179–207 (2002).
- [103] R. J. Marsh, N. D. Leonczek, D. A. Armoogum, L. Porrès, O. M. Mongin , M. H. Blanchard-Desce, and A. J. Bain, "Stimulated emission depletion dynamics in push-push polyenes," *Proc. SPIE* **5510** (2004).
- [104] D. Wanapun, R. D. Wampler, N. J. Begue, and G. J. Simpson, "Polarization-dependent two-photon absorption for the determination of protein secondary structure: a theoretical study," *Chem. Phys. Lett.* **455**, 6–12 (2008).
- [105] Elles, C. G., Rivera, C. A., Zhang, Y., Pieniazek, P. A., and Bradforth, S. E., "Electronic structure of liquid water from polarization-dependent two-photon absorption spectroscopy," *J. Chem. Phys.* **130**, 084501 (2009).
- [106] N. Amit and G. Debabrata, "Polarization induced control of single and two-photon fluorescence," *J. Chem. Phys.* **132**, 154508 (2010).
- [107] M. G. Vivas, D. L. Silva, L. De Boni, Y. Bretonniere, C. Andraud, F. Laibe-Darbour, J.-C. Mulate, R. Zaleśny, W. Bartkowiak, S. Canuto et al., "Revealing the electronic and molecular structure of randomly oriented molecules by polarized two-photon spectroscopy," *J. Phys. Chem. Lett.* **4**, 1753–1759 (2013).
- [108] M. G. Vivas, C. Diaz, L. Echevarria, C. R. Mendonca, F. E. Hernández, and L. De Boni, "Two-photon circular-linear dichroism of perylene in solution: a theoretical-experimental study," *J. Phys. Chem. B* **117**, 2742–2747 (2013).
- [109] W. M. McClain, "Polarization dependence of three-photon phenomena for randomly oriented molecules," *J. Chem. Phys.* **57**, 2264–2272 (1972).
- [110] D. L. Andrews and W. A. Ghoul, "Polarization studies in multiphoton absorption spectroscopy," *J. Chem. Phys.* **75**, 530–538 (1981).
- [111] D. L. Andrews, "The theory of double-beam three-photon absorption," *J. Chem. Phys.* **77**, 2831–2835 (1982).
- [112] D. L. Andrews, "The theory of double-beam three-photon absorption. ii. polarization ratio analysis," *J. Chem. Phys.* **78**, 1731–1734 (1983).

- [113] R. N. Dixon, J. M. Bayley, and M. N. R. Ashfold, "The rotational structure of three-photon resonances of polyatomic molecules," *Chem. Phys.* **84**, 21–34 (1984).
- [114] J. M. Leeder and D. L. Andrews, "A molecular theory for two-photon and three-photon fluorescence polarization," *J. Chem. Phys.* **134**, 094503 (2011).
- [115] D. L. Andrews, "Symmetry characterization in molecular multiphoton spectroscopy," *Spectrochim. Acta A: Mol. Spec.* **46**, 871–885 (1990).
- [116] D. A. Case, G. M. McClelland, and D. R. Herschbach, "Angular momentum polarization in molecular collisions: classical and quantum theory for measurements using resonance fluorescence," *Mol. Phys.* **35**, 541–573 (1978).
- [117] C. Wan and C. K. Johnson, "Time-resolved anisotropic two-photon spectroscopy," *Chem. Phys.* **179**, 513–531 (1994).
- [118] R. N. Zare, *Angular Momentum—Understanding Spatial Aspects in Chemistry and Physics* (John Wiley & Sons, New York, 1988).
- [119] A. J. Bain and A. J. McCaffery, "On the measurement of molecular anisotropies using laser techniques. III. Detection of the higher multipoles," *J. Chem. Phys.* **83**, 2641–2645 (1985).
- [120] M. A. Bopp, Y. Jia, G. Haran, E. A. Morlino, and R. M. Hochstrasser, "Single-molecule spectroscopy with 27 fs pulses: time-resolved experiments and direct imaging of orientational distributions," *Appl. Phys. Lett.* **73**, 7–9 (1998).
- [121] T. Tao, "Time-dependent fluorescence depolarization and Brownian rotational diffusion coefficients of macromolecules," *Biopolymers* **8**, 609–632 (1969).
- [122] M. J. Sanders and M. J. Wirth, "Evidence for solvation structural dependence of rotational diffusion anisotropy," *Chem. Phys. Lett.* **101**, 361–366 (1983).
- [123] L. X.-Q. Chen, R. A. Engh, and G. R. Fleming, "Reorientation of tryptophan and simple peptides: onset of internal flexibility and comparison with molecular dynamics simulation," *J. Phys. Chem.* **92**, 4811–4816 (1988).
- [124] J. Szubiakowski, A. Balter, W. Nowak, A. Kowalczyk, K. Wiśniewski, and M. Wierzbowska, "Anisotropic reorientation of perylene and 3,9-dibromoperylene in glycerol: fluorescence anisotropy decay and quantum-mechanical study," *Chem. Phys.* **208**, 283–296 (1996).
- [125] T. S. Blacker, R. J. Marsh, M. R. Duchen, and A. J. Bain, "Activated barrier crossing dynamics in the non-radiative decay of NADH and NADPH," *Chem. Phys.* **422**, 184–194 (2013).
- [126] N. Chadborn, J. Bryant, A. J. Bain, and P. O'Shea, "Ligand-dependent conformational equilibria of serum albumin revealed by tryptophan fluorescence quenching," *Biophys. J.* **76**, 2198–2207 (1999).
- [127] C. W. Ko, Z. Wei, R. J. Marsh, D. A. Armoogum, N. Nicolaou, A. J. Bain, A. Zhou, and L. Ying, "Probing nanosecond motions of plasminogen activator inhibitor-1 by time-resolved fluorescence anisotropy," *Mol. Biosyst.* **5**, 1025 (2009).
- [128] R. M. Hochstrasser and D. K. Negus, "Picosecond fluorescence decay of tryptophans in myoglobin," *Proc. Natl. Acad. Sci.* **81**, 4399–4403 (1984).
- [129] F. Huang, S. Rajagopalan, G. Settanni, R. J. Marsh, D. A. Armoogum, N. Nicolaou, A. J. Bain, E. Lerner, E. Haas, L. Ying, et al., "Multiple conformations of full-length p53 detected with single-molecule fluorescence resonance energy transfer," *Proc. Natl. Acad. Sci.* **106**, 20758–20763 (2009).

- [130] T. A. Masters, V. Calleja, D. A. Armoogum, R. J. Marsh, C. J. Applebee, M. Laguerre, A. J. Bain, and B. Larijani, “Regulation of 3-phosphoinositide-dependent protein kinase 1 activity by homodimerization in live cells,” *Sci. Signal.* **3**, ra78 (2010).
- [131] S.-Y. Chen and B. W. Van der Meer, “Theory of two-photon induced fluorescence anisotropy decay in membranes,” *Biophys. J.* **64**, 1567–1575 (1993).
- [132] S. W. Pauls, J. F. Hedstrom, and C. K. Johnson, “Rotational relaxation of perylene in *n*-alcohols and *n*-alkanes studied by two-photon-induced anisotropy decay,” *Chem. Phys.* **237**, 205–222 (1998).
- [133] L. Ryderfors, E. Mukhtar, and L. B.-Å. Johansson, “Excited-state symmetry and reorientation dynamics of perylenes in liquid solutions: time-resolved fluorescence depolarization studies using one- and two-photon excitation,” *J. Phys. Chem. A* **112**, 5794–5803 (2008).
- [134] C. Zannoni, “A Theory of fluorescence depolarization in membranes,” *Mol. Phys.* **42**, 1303–1320 (1981).
- [135] P. R. Callis, “The theory of two-photon-induced fluorescence anisotropy,” in *Topics in Fluorescence Spectroscopy*, edited by J. R. Lakowicz (Kluwer Academic Publishing, New York, 2002).
- [136] C. K. Johnson and C. Wan, “Anisotropy decays induced by two-photon excitation,” in *Topics in Fluorescence Spectroscopy*, edited by J. R. Lakowicz (Kluwer Academic Publishing, New York, 2002).
- [137] A. J. Bain and A. J. McCaffery, “On the measurement of molecular anisotropies using laser techniques. I. polarized laser fluorescence,” *J. Chem. Phys.* **83**, 2627–2631 (1985).
- [138] C. H. Greene and R. N. Zare, “Determination of Product population and alignment using laser-induced fluorescence,” *J. Chem. Phys.* **78**, 6741–6753 (1983).
- [139] A. C. Kummel, G. O. Sitz, and R. N. Zare, “Determination of population and alignment of the ground state using two-photon nonresonant excitation,” *J. Chem. Phys.* **85**, 6874–6897 (1986).
- [140] E. M. Monge, D. A. Armoogum, and A. J. Bain, “Single- and two-photon time-resolved polarized fluorescence studies of probe molecule dynamics in nematic liquid crystals,” *Proc. SPIE* **4797** (2002).
- [141] A. Penzkofer and J. Wiedmann, “Orientation of transition dipole moments of rhodamine 6g determined by excited state absorption,” *Opt. Commun.* **35**, 81–86 (1980).
- [142] F. López Arbeloa and V. Martínez Martínez, “Orientation of adsorbed dyes in the interlayer space of clays. 2 fluorescence polarization of rhodamine 6g in laponite films,” *Chem. Mater.* **18**, 1407–1416 (2006).
- [143] R. J. Marsh, D. A. Armoogum, and A. J. Bain, “Stimulated emission depletion of two-photon excited states,” *Chem. Phys. Lett.* **366**, 398–405 (2002).
- [144] A. J. Bain, R. J. Marsh, D. A. Armoogum, O. Mongin, L. Porrès, and M. Blanchard-Desce, “Time-resolved stimulated emission depletion in two-photon excited states,” *Biochem. Soc. Trans.* **31**, 1047–1051 (2003).
- [145] D. Laage and J. T. Hynes, “A molecular jump mechanism of water reorientation,” *Science* **311**, 832–835 (2006).
- [146] F. W. Deeg, J. J. Stankus, S. R. Greenfield, V. J. Newell, and M. D. Fayer, “Anisotropic reorientational relaxation of biphenyl: transient grating optical kerr effect measurements,” *J. Chem. Phys.* **90**, 6893–6902 (1989).

- [147] D. J. Cook, J. X. Chen, E. A. Morlino, and R. M. Hochstrasser, “Terahertz-field-induced second-harmonic generation measurements of liquid dynamics,” *Chem. Phys. Lett.* **309**, 221–228 (1999).
- [148] S. Lin, I. D. Hands, D. L. Andrews, and S. R. Meech, “Optically induced second harmonic generation by six-wave mixing: a novel probe of solute orientational dynamics,” *J. Phys. Chem. A* **103**, 3830–3836 (1999).
- [149] R. G. Bray and R. M. Hochstrasser, “Two-photon absorption by rotating diatomic molecules,” *Mol. Phys.* **31**, 1199–1211 (1976).
- [150] A. J. Bain and A. J. McCaffery, “Multipolar evolution in two- and n-photon excitation,” *Chem. Phys. Lett.* **108**, 275–282 (1984).
- [151] M. D. Rowe and A. J. McCaffery, “Transfer of state multipoles in excited  $A\ ^1\Sigma^+_u$   ${}^7\text{Li}_2$  following rotationally inelastic collisions with he: experiment and theory,” *Chem. Phys.* **43**, 35–54 (1979).
- [152] A. J. Bain and A. J. McCaffery, “Complete determination of the state multipoles of rotationally resolved polarized fluorescence using a single experimental geometry,” *J. Chem. Phys.* **80**, 5883 (1984).
- [153] A. J. Bain, “Polarised laser fluorescence studies of ground and excited state dynamics,” D. Phil. Thesis, University of Sussex (1984).
- [154] A. P. Yutsis, I. B. Levinson, V. V. Vanagas, and A. Sen, *Mathematical Apparatus of the Theory of Angular Momentum* (Israel Program for Scientific Translations, 1962).
- [155] S.-L. Cong, K.-L. Han, G.-Z. He, and N.-Q. Lou, “Determination of population, orientation and alignment of symmetric top molecule using laser-induced fluorescence,” *Chem. Phys.* **256**, 225–237 (2000).
- [156] S. Manzhos, C. Romanescu, H.-P. Loock, and J. G. Underwood, “Two-photon state selection and angular momentum polarization probed by velocity map imaging: application to h atom photofragment angular distributions from the photodissociation of two-photon state selected HCl and HBr,” *J. Chem. Phys.* **121**, 11802–11809 (2004).
- [157] A. J. Alexander, “Determination of the helicity of oriented photofragments,” *J. Chem. Phys.* **123**, 194312 (2005).
- [158] A. I. Chichinin, P. S. Shternin, N. Gödecke, S. Kauczok, C. Maul, O. S. Vasyutinskii, and K.-H. Gericke, “Intermediate state polarization in multiphoton ionization of HCl,” *J. Chem. Phys.* **125**, 034310 (2006).
- [159] P. S. Shternin, V. K. Ivanov, A. G. Suits, and O. S. Vasyutinskii, “The role of intermediate state polarization in determination of vector properties of the ground state using multiphoton excitation,” *Phys. Chem. Chem. Phys.* **8**, 2972 (2006).
- [160] M. Minsky, “Microscopy apparatus,” US Patent No. 3,013,467 A, 1961.
- [161] V. Calleja, S. Ameer-Beg, B. Vojnovic, R. Woscholski, J. Downward, and B. Larjani, “Monitoring conformational changes of proteins in cells by fluorescence lifetime imaging microscopy,” *Biochem. J.* **372**, 33–40 (2003).
- [162] R. D. Byrne, C. Applebee, D. L. Poccia, and B. Larjani, “Dynamics of PLC $\gamma$  and src family kinase 1 interactions during nuclear envelope formation Revealed by FRET-FLIM,” *PLoS ONE* **7**(7), e40669 (2012).
- [163] M. Drobizhev, N. S. Makarov, T. Hughes, and A. Rebane, “Resonance enhancement of two-photon absorption in fluorescent proteins,” *J. Phys. Chem. B* **111**, 14051–14054 (2007).

- [164] M. Drobizhev, S. Tillo, N. S. Makarov, T. E. Hughes, and A. Rebane, “Absolute two-photon absorption spectra and two-photon brightness of orange and red fluorescent proteins,” *J. Phys. Chem. B* **113**, 855–859 (2009).
- [165] M. Drobizhev, N. S. Makarov, S. E. Tillo, T. E. Hughes, and A. Rebane, “Two-photon absorption properties of fluorescent proteins,” *Nat. Methods* **8**, 393–399 (2011).
- [166] M. Drobizhev, N. S. Makarov, S. E. Tillo, T. E. Hughes, and A. Rebane, “Describing two-photon absorptivity of fluorescent proteins with a new vibronic coupling mechanism,” *J. Phys. Chem. B* **116**, 1736–1744 (2012).
- [167] M. Drobizhev, T. E. Hughes, Y. Stepanenko, P. Wnuk, K. O’Donnell, J. N. Scott, P. R. Callis, A. Mikhaylov, L. Dokken, and A. Rebane, “Primary role of the chromophore bond length alternation in reversible photoconversion of red fluorescence proteins,” *Sci. Rep.* **2**, 688 (2012).
- [168] T. A. Masters, R. J. Marsh, D. A. Armoogum, N. Nicolaou, B. Larjani, and A. J. Bain, “Restricted state selection in fluorescent protein förster resonance energy transfer,” *J. Am. Chem. Soc.* **135**, 7883–7890 (2013).

---

# 10

---

## ORBITAL ANGULAR MOMENTUM

EMMA WISNIEWSKI-BARKER AND MILES J. PADGETT

*School of Physics and Astronomy, University of Glasgow, SUPA, Glasgow, UK*

### 10.1 HISTORICAL INTRODUCTION

For more than a century, scientists have known that light carries momentum. In 1909, Poynting stated that circularly polarized light, should have angular momentum of  $\sigma\hbar$  per photon, where  $\hbar$  is Plank's constant,  $h$ , divided by  $2\pi$  and  $\sigma = \pm 1$  for right- and left-circularly polarized light, respectively [1]. This angular momentum became known as spin angular momentum (SAM). Poynting reasoned that the effects of SAM were very small and would be extremely difficult to detect experimentally, but in 1936 Beth performed an experiment in which he observed the physical effects of SAM. Beth suspended a waveplate from a quartz fiber, and as the circularly polarized light passed through the waveplate, the handedness of the light was switched. The quartz fiber gave a low friction suspension so that the angular momentum transferred from the light to the waveplate by the reversal of the handedness of the circular polarization caused the waveplate to rotate [2].

While the physical effects of angular momentum can be difficult to see (although not impossible), it is simple to determine the interactions between light and atoms. The angular momentum of an atom is changed by  $\pm\hbar$  when it emits a circularly polarized photon [3]; however, a higher order transition, such as a quadrupole transition, results in an angular momentum transfer of a higher integer multiple of  $\hbar$ . Circularly polarized light, and thus SAM, alone cannot account for this; therefore, another type of angular momentum is required. In 1932, Darwin (the grandson of the famous evolutionary scientist) described how a photon emitted a short distance from the center of mass of an atom would provide the additional angular momentum

---

*Photonics: Scientific Foundations, Technology and Applications, Volume I*, First Edition.

Edited by David L. Andrews.

© 2015 John Wiley & Sons, Inc. Published 2015 by John Wiley & Sons, Inc.

needed for higher order transitions [4]. This angular momentum eventually became known as orbital angular momentum (OAM). In 1992, Allen et al. released a seminal article that described OAM as a natural property of light beams with helical phase fronts and noted that these beams could be generated quite easily in the laboratory [3]. OAM-carrying beams often take the form of (but not limited to) Laguerre-Gaussian (LG) beams, with amplitude distributions,  $\text{LG}_{pl}$  described as

$$\begin{aligned} \text{LG}_{pl} = & \sqrt{\frac{2p!}{\pi(p+|l|)!}} \frac{1}{w(z)} \left[ \frac{r\sqrt{2}}{w(z)} \right]^{|l|} \exp \left[ \frac{-r^2}{w^2(z)} \right] L_p^{|l|} \left( \frac{2r^2}{w^2(z)} \right) \exp [il\theta] \\ & \exp \left[ \frac{ik_0 r^2 z}{2(z62 + z_R^2)} \right] \exp \left[ -i(2p + |l| + 1) \tan^{-1} \left( \frac{z}{z_R} \right) \right], \end{aligned} \quad (10.1)$$

where  $r$  is the radius,  $w(z) = w(0)[(z^2 + z_R^2)/z_R^2]^{1/2}$  with  $w(0)$  as the beam waist,  $z_R$  as the Rayleigh range, and  $(2p + |l| + 1) \tan^{-1}(z/z_R)$  as the Gouy phase [5].  $L_p^{|l|}$  is a Laguerre polynomial that is a result of

$$L_p^{|l|}(x) = (-1)^{|l|} \frac{d^{|l|}}{dx^{|l|}} L_{p+|l|}(x), \quad (10.2)$$

where  $l$  is the azimuthal index resulting in OAM of  $L = l\hbar$  per photon, as shown in Figure 10.1, and  $p$  is the number of radial nodes in the intensity distribution. The

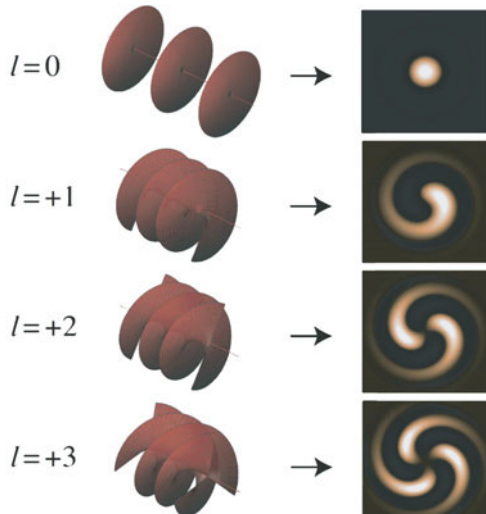


**FIGURE 10.1** Interfering a helical phase front and a plane wave results in spoked fringes. Using beams with slightly different radii of curvature turns normal spoked fringes into the beautiful spiral fringes shown here for  $l = 0$  through  $l = +3$ .

simplest OAM beam has a phase in the transverse plane of  $\phi(\theta) = l\theta$ , where  $\theta$  is the angular coordinate and  $l$  is any integer. Allen et al. derived that all light beams with helical phase fronts described by  $e^{il\theta}$  have an OAM of  $l\hbar$  per photon [3]. This value for the OAM is consistent with a simple geometrical argument based on the helical phase fronts. The local momentum flow is directed along a normal to the phase fronts. For helical phase fronts, this implies that the local momentum flow is not directed in the global direction of beam propagation, rather than it is skewed to the beam axis by an angle  $\beta = l/k_0 r$  [6, 7], where  $k_0 = 2\pi/\lambda$  is the wavenumber and  $\lambda$  is the wavelength of light. Associating a linear momentum of  $\hbar k$  along this direction gives an azimuthal component to the momentum of

$$p = \frac{\hbar k_0 l \lambda}{2\pi r} \quad (10.3)$$

per photon and results in an angular momentum along the beam axis of  $l\hbar$  [8].

One ubiquitous feature of beams with helical phase fronts is that they have a phase singularity running down their center, which is an intensity null surrounded by a  $2\pi l$  phase change [9]. The mathematical similarity between helically phased beams and superfluid vortices led to these phase singularities being named optical vortices [10]. These optical vortices do not carry any angular momentum themselves, as they are points of zero energy; all angular momenta in the beam come from the field surrounding the singularity.

In the 1970s, there were two important developments in the study of phase singularities. First, Nye and Berry investigated phase singularities in ultrasound waves in order to model radio wave echoes off arctic ice sheets [11]. Second, Vaughan and Willets created a phase singularity in a laser beam by combining high order Hermite–Gaussian (HG) modes [12], which are the solutions of the paraxial wave equation in Cartesian coordinates. The handedness of these singularity-carrying beams was studied by breaking the cylindrical symmetry of an output beam of a laser [13] and through the recognition of a bistable helical phase [14, 15]. These developments culminated in the realization of the importance of LG modes, which are the solutions of the paraxial wave equation in cylindrical coordinates, as described by D’Alessandro and Oppo [16]. Helical phase fronts are not unique to LG beams; Bessel beams [17], Mathieu beams [18], and Ince–Gaussian beams [19] also have helical phase fronts. All beams with helical phase fronts give rise to spiral interference fringes when interfered with a plane wave with a slightly different radius of curvature [20–22], shown in Figure 10.1.

OAM can lead to quite simple descriptions of situations that are rotationally symmetric or contain singularities. One instance where OAM is useful in understanding a broad concept is the angular uncertainty relationship. Similar to the more widely recognized Heisenberg uncertainty relationship, an uncertainty relationship for angular momentum can be described quite simply. If a beam did not have an angular restriction from an aperture, the full cyclic nature of the azimuthal phase could be observed and would result in no uncertainty in the OAM and a single-valued OAM state. However, light restricted to a certain azimuthal range by an aperture is described by

a spread of OAM states [23]. The relation between the width of the aperture and the spread of OAM values has been studied extensively [24–27] and is an example of an uncertainty relationship. For apertures of width  $\Delta\theta$ , the spread in OAM states,  $\Delta L$ , is described by the angular uncertainty relationship:

$$\Delta\theta\Delta L \geq \frac{1}{2}\hbar|1 - 2\pi P(\theta)|, \quad (10.4)$$

where  $P(\theta)$  is the angular probability density of the boundary of the angular range and takes the periodicity of the angle into account [25]. For a narrow Gaussian aperture, this relationship simplifies to  $\Delta\theta\Delta L > \hbar/2$ .

## 10.2 CREATING BEAMS WITH OAM

There are many ways to create beams that have OAM. One of the earliest methods of creating OAM-carrying beams is to use a pair of cylindrical lenses that transform a HG beam to an LG beam. This kind of mode transformation was the method used by Allen et al. in 1992 [3]. HG and LG modes are both complete sets, which means that a mode of either set can be described as a superposition of modes of the other. As the beam is focused in the cylindrical lens pair, it acquires an additional Gouy phase determined by the orientation and mode indices of the HG mode used, which will cause the HG mode to rephase into a specific LG mode [28]. There are two varieties of cylindrical lens mode converters, both of which are shown in Figure 10.2; a  $\pi/2$  converter will transform HG modes into LG modes when there is a beam waist midway between the cylindrical lenses, whereas a  $\pi$  converter will transform any mode of collimated light into its own mirror image. In this way, a  $\pi$  converter is optically equivalent to a Dove prism [29]. These  $\pi$  and  $\pi/2$  mode converters are mathematically analogous to polarization-converting half-wave plates and quarter-wave plates, respectively.

Instead of using cylindrical lenses to convert between HG and LG modes, spiral phase plates can be used to change plane waves into helically phased waves. Spiral phase plates are transmissive plates that increase in thickness with azimuthal angle with a discontinuity step of one wavelength, such that a plane wave passing through

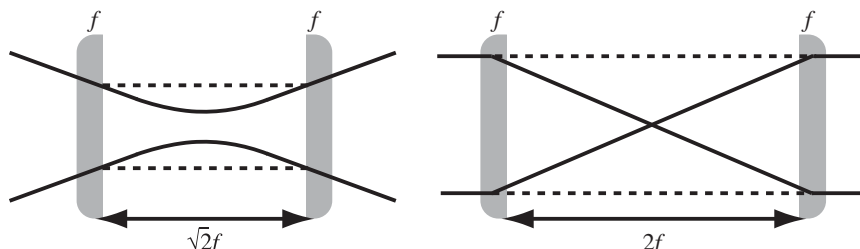


**FIGURE 10.2**  $\pi/2$  converters (*left*) switch between HG and LG modes, whereas  $\pi$  converters (*right*) switch modes to their mirror images.

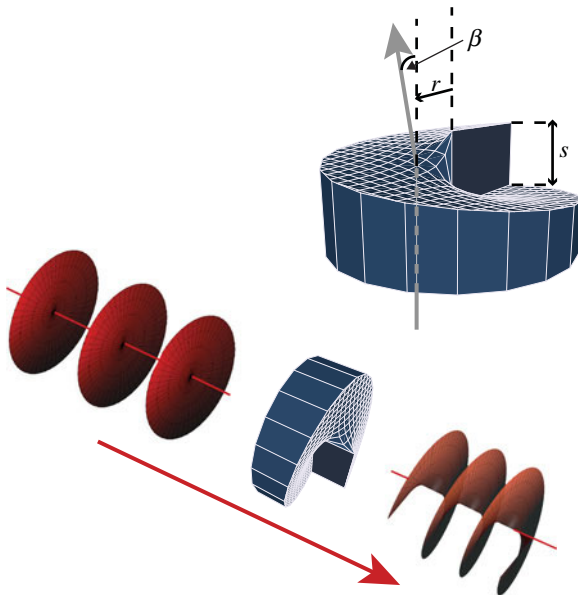


**FIGURE 10.3** A plane wave gains a helical phase front when shone through a spiral phase plate with a skew angle  $\beta$  at a distance  $r$  from the center and a step height  $s$ .

the spiral phase plate exits with a helical phase front. An example of this is shown in Figure 10.3. The required step height,  $s$ , of a spiral phase plate for light with a wavelength of  $\lambda$  is

$$s = \frac{l\lambda}{(n - 1)}, \quad (10.5)$$

where  $n$  is the refractive index of the medium from which the plate is made. Applying Snell's law leads to the angular change in the transmitted ray, or skew angle, being  $\beta = l/k_0 r$ , as stated previously.

The required level of precision of the spiral phase plate's thickness is very difficult to obtain for light beams, and so to circumvent these difficulties, Beijersbergen et al. placed a spiral phase plate in a fluid bath. The temperature of the bath was tuned to achieve the proper index of refraction and thus the difference in thickness, or step height, for a certain wavelength [30]. More recently, micro-fabrication techniques have allowed for direct construction of millimeter wave [7] and optical spiral phase plates [31,32]. However, individual physical spiral phase plates have to be constructed for each wavelength of light being investigated, due to the relation of the wavelength to the necessary thickness of the spiral phase plate.

Holographic alternatives to physical spiral phase plates are created through the use of diffractive optical elements (DOEs). Holograms can be used to shape a beam's intensity or phase. The advantage of phase-only holograms is that nearly

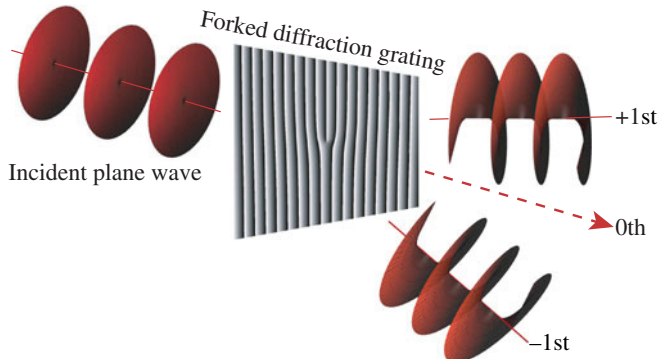


**FIGURE 10.4** Plane waves gain a helical phase front when shone through a forked diffraction grating, resulting in 1st and -1st order diffracted beams. The +1st and -1st order diffracted beams are shown here with  $l = +1$  and  $-1$ , respectively.

all the incident light can be directed with the desired phase profile into the first diffracted order. By adding the desired phase profile modulo  $2\pi$  to a linear phase ramp, any phase profile can be generated in the first diffracted order, as shown in Figure 10.4. In the case of a helical beam, this hologram is a diffraction grating with an  $l$ -pronged dislocation at the center [33–35], as shown in Figure 10.4. Spatial light modulators (SLMs) have been developed and refined over the past decade and have greatly increased the ease with which holograms can be implemented. Spatial light modulators use liquid crystal controlled by a video interface on a computer to act as holograms that can be easily changed in real time. SLMs have become widely used due to the ease of creating and changing the displayed hologram in real time, the circumvention of the manufacturing problems associated with making spiral phase plates, and their ability to work for a wide range of wavelengths within the visible spectrum.

As an alternative to diffractive optics, OAM-carrying beams can be made with Q-plates, which are birefringent liquid crystal plates with spatially varying optical axes [36, 37]. Q-plates have an azimuthal spatial dependence and thus are able to transform between spin and orbital angular momenta by taking a circularly polarized beam and adding an azimuthally dependent phase that gives the transmitted beam a helical phase. This process also makes Q-plates useful for creating entanglement between spin and orbital angular momenta [38].

Phase singularities can also occur naturally, without the use of spiral phase plates, DOEs, or Q-plates. Simply interfering three or more plane wave components of similar intensity results in many vortices in any field cross-section [39, 40]. A common example of this is laser speckle, where each black speck is an optical vortex [41].

While the previously described methods of obtaining helically phased beams all use spatially coherent light, spatial and temporal coherence are not fundamental requirements for creating OAM. The description of a helical phase front implies a coherence of phase across the beam; however, it is possible to illuminate a spiral phase plate or forked diffraction grating with a spatially incoherent source. If light

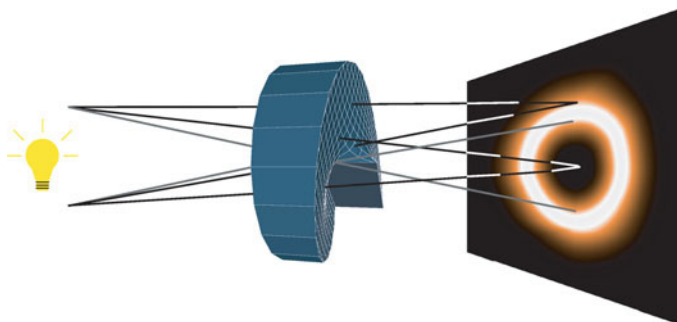


**FIGURE 10.5** A spiral phase plate illuminated by incoherent light produces an incoherent vortex in the far field.

rays are projected through the center of a spiral phase plate at small radii, as shown in Figure 10.5, incoherent vortices are generated in the far field; their time-averaged intensity is not zero [42]. Therefore, a vortex beam can be used to determine spatial coherence. A vortex beam with zero on-axis intensity implies spatial coherence, whereas nonzero on-axis intensity indicates spatial incoherence.

One can see by comparing the energy, momentum, and angular momentum of a photon that linear momentum per unit energy is inversely proportional to phase velocity and that angular momentum is inversely proportional to frequency. These relationships are not exclusive to light waves but do in fact apply to all forms of waves. It follows, then, that orbital angular momentum is not only a property of light. Early rotational Doppler shift studies were conducted at millimeter wave frequencies, as experiments at these wavelengths were easier to align [7, 43]. Radio waves carrying OAM have also been proposed for applications in astronomy and radio frequency communications, using arrays of antennae for detection [44]. Coherent arrays of detectors or emitters act on longer wavelengths much like a spatial light modulator does for optical frequencies. A synchotron, or cyclical particle accelerator, along with the correct diffractive optics results in an X-ray vortex, which could be used for determining molecular structure in X-ray diffraction [45]. OAM can also be created in electron beams. Putting a spiral phase plate into an electron microscope can increase edge detection in low-contrast imaging [46], which has led to a new holographic reconstruction technique in a transmission electron microscope (TEM) [47].

### 10.3 MICRO-MANIPULATION THROUGH THE USE OF OAM

OAM has been observed in several experiments and has even become a method of manipulating physical objects. One way of using the orbital OAM of light to manipulate particles was discovered through the development of optical tweezers. Optical tweezers use highly focused laser radiation to trap and move micron-sized dielectric particles [48], which are often made of glass, silica, or polystyrene. Introducing OAM-carrying beams with the use of SLMs allows us to expand the functionality of optical tweezers, enabling them to act as optical spanners [49]. Optical spanners

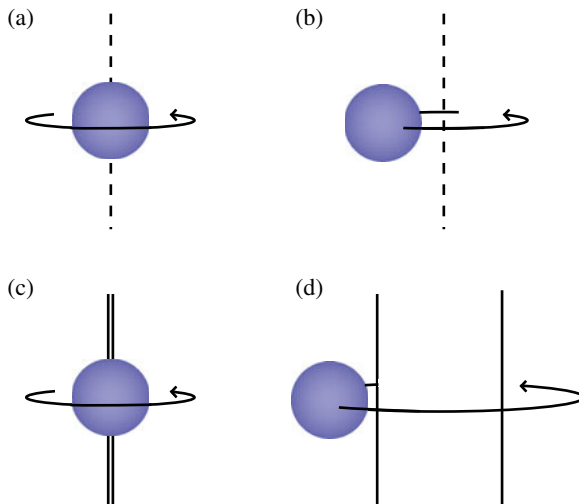


**FIGURE 10.6** Different rotation conditions for spin and orbital angular momentum. SAM makes the particle spin about its own axis (a), whereas OAM orbits the particle about the beam axis (b). For a beam much smaller than the particle, SAM and OAM will both make the particle spin in the same way (c). For a large beam, OAM will make the particle orbit the beam (d).

work in a very similar way to optical tweezers, with the added capability to rotate the trapped object. For example, for a beam with  $l = 1$  and  $\sigma = \pm 1$ , when the sign of the SAM is positive, the particle will spin. When the sign of the SAM is negative, the particle will stop [50]. If the center of mass of the particle is on the beam axis, then SAM and OAM will both spin the particle about its axis, although they can be in the same or in opposite directions. If the center of mass is off-axis, SAM and OAM will act differently, with the SAM spinning the particle about its own axis and the OAM spinning the particle in an orbit [51]. SAM is intrinsic, as its rotation is independent of the choice of axis used to calculate it. OAM is said to be quasi-intrinsic when the center of mass is on-axis, because in that case it spins about both its axis and the beam axis, which happens to be the same. However, when the center of mass is off-axis, it is said to be extrinsic, or dependent upon the axis about which it is calculated [51]. These situations are illustrated in Figure 10.6.

As the phase of an OAM-carrying beam changes with the spatial position in the beam, mechanical effects of SAM and OAM depend on the size of the beam with respect to the size of the particle. If the beam size is larger than the particle size, then a beam carrying SAM will make the particle spin about its own axis and one carrying OAM will make the particle rotate around the beam. If the beam size is much smaller than the particle size, SAM and OAM will both make the particle spin the same way, as a rotation around a beam of that size does not move the particle and instead just spins it as if the beam were the rotation axis, also shown in Figure 10.6.

When light with SAM and/or OAM is spinning a particle of radius  $r$ , the light can exert a maximum torque of the order  $\hbar k_0 r$  on the particle [52]. This torque can be used to create micromachines for the manipulation of particles. The sign of the total

angular momentum (SAM and OAM added together) determines the direction of the particles rotation [53]. One benefit of using angular momentum as a micromachine is that the “axle” is optical and hence will never wear out. One of the most common type of micromachines is the micropump, which can be made by an array of beams with OAM that causes a circulation of microparticles. The fluid flows through the array and carries other particles with it [54]. Another way to design a micropump using angular momentum is to transfer SAM to two birefringent particles to spin them in opposite directions. This leads to a flow along the channel between them [55].

SAM and OAM interact with cold atoms in distinct ways. Circular polarization and SAM play a role in atomic selection rules, whereas OAM does not, as a helical phase front is locally indistinguishable from an inclined phase front. However, absorption of a photon from a plane wave by a gas will lead to isotropic spontaneous emission with the atoms or molecules recoiling away from the incident light. For a helically phased beam with a force acting at any distance from the beam axis, there will be a torque continually acting on the center of mass of the atom such that the repeated recoil will guide the atom in a spiral [56]. As the atoms travel around the beam axis, this torque is seen as a manifestation of the rotational Doppler shift [57], described later. The annular intensity of a helically phased beam with the region of darkness in the center allows for blue-detuned atom trapping, where there is a force attracting the particles to the center of the beam [58]. This blue-detuned atom trapping acts in a similar fashion to optical tweezers for low index particles.

## 10.4 BEAM TRANSFORMATIONS

SAM and OAM are usually separable, as they are typically independent when traveling through a transparent, homogeneous medium with no spatially dependent optical properties. However, transfer of SAM to OAM can happen in such a medium if a Gaussian beam [59] or a circularly polarized vortex beam [60] is tightly focused through a high numerical-aperture lens. This occurs in the optical spanners described above. Although SAM and OAM can interchange in this way, the mechanisms for transferring SAM and OAM are not the same. SAM affects particles that are birefringent. Given the right conditions, birefringent materials change circular polarization to linear polarization, causing the SAM to change and therefore the birefringent particle to spin [61]. Birefringence does not affect helical phase fronts and thus does not interact with the OAM at all. Astigmatism, however, does change the helical phase front, which means that it affects the OAM of the beam, while leaving polarization and SAM unchanged.

There are two basic types of transformations. The first type of transformation is a coordinate transformation, which is equivalent to a rotation of the state about the optical axis and results in no change in angular momentum. For polarization, this type of rotation about the optical axis could arise from optical activity, Faraday-type effects, or a phase difference between the circularly polarized states. Optically active materials do not alter the OAM state of the transmitted light [62, 63]. Image rotation is the equivalent transformation for an OAM-carrying beam to that of optical activity for an SAM-carrying beam [64]. This second type of transformation is a rephasing of

linear states. This rephasing of the linear states does change the angular momentum, which for polarization comes from birefringence. For OAM, the rotation of the state manifests as a rotation about the optical axis of the mode or the superposition of modes. This rotation corresponds to a changing in phase between positive and negative OAM states. The equivalence between the rotation of polarization and the rotation of an image has been used recently to investigate photon drag [65].

Photon drag was studied in depth experimentally by Jones in the 1970s. He called it Fresnel or aether drag, and he showed that light passing through a moving medium would be dragged either longitudinally or transversely by the medium [66]. In addition, he showed that the polarization of light through a spinning disk could be rotated by a small angle,  $\Delta\theta_{\text{pol}}$ , which is defined as

$$\Delta\theta_{\text{pol}} = \Omega \left( n_g - \frac{1}{n_\phi} \right) \frac{L}{c}, \quad (10.6)$$

where  $\Omega$  is the angular velocity of the medium,  $L$  is its length, and  $n_g$  and  $n_\phi$  are, respectively, the group and phase refractive indices of the light in the medium [67]. Recent experimental work by Franke-Arnold et al. has shown that a spinning disk drags the image through the same rotation angle as the polarization [65],

$$\Delta\theta_{\text{pol}} = \Delta\theta_{\text{image}} = \Omega \left( n_g - \frac{1}{n_\phi} \right) \frac{L}{c}. \quad (10.7)$$

In other words, photon drag has the same effect on spin and orbital angular momenta. The equivalent rotation of polarization and image is shown in Figure 10.7.

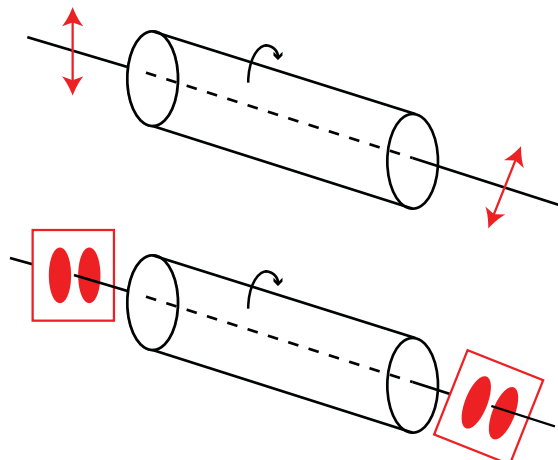


**FIGURE 10.7** Equivalent dragging of polarization (top) and transmitted image (bottom) through a rotating medium.

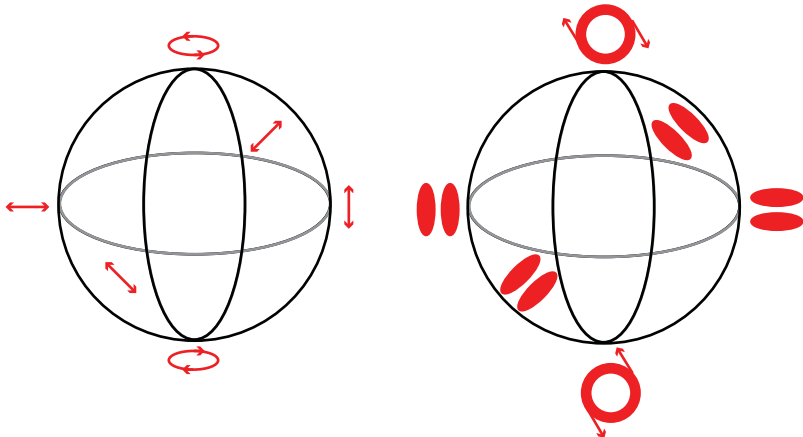


**FIGURE 10.8** Poincaré sphere for polarization (left) and the analogous Bloch sphere for OAM (right).

As mentioned above, HG and LG modes are both complete sets, and any mode in one set can be made by a superposition of modes in the other set. Polarization is a useful analogy for the transformation between HG and LG modes. A Poincaré sphere shows how right- and left-circularly polarized states can be combined to form linearly polarized states, as shown in Figure 10.8. Any two-dimensional space can be described by an analogous Bloch sphere [68, 69]. A generalized two-state system in the OAM basis,  $|\mathbf{a}\rangle$ , can be written as:

$$|\mathbf{a}\rangle = \cos\left(\frac{\theta_a}{2}\right)|l\rangle + e^{i\phi_a} \sin\left(\frac{\theta_a}{2}\right)|-l\rangle, \quad (10.8)$$

where  $\mathbf{a} = (\sin(\theta_a)\cos(\phi_a), \sin(\theta_a)\sin(\phi_a), \cos(\theta_a))$  is a vector with longitude  $0 \leq \phi_a \leq 2\pi$  and latitude  $0 \leq \theta_a \leq \pi$ . On the Bloch sphere, the longitudinal position,  $\phi$ , gives the orientation of the mode superposition. Figure 10.8 shows both the Poincaré sphere for polarization and the analogous Bloch sphere for OAM.

It is well known that light emitted from a moving source undergoes a frequency shift, a concept known as the Doppler shift. This effect was seen by Garetz in the 1970s for rotation between a detector and a source of circularly polarized light. Garetz showed this effect by spinning one half-wave plate with respect to another half-wave plate, showing that the polarization state was rotated at twice the rotational speed of the waveplate, and measuring the corresponding frequency shift [70, 71]. There is a similar effect for a helically phased beam [57, 72]. The single rotation of a helically phased beam changes the field by  $l$  cycles, and this can be easily implemented by rotating Dove prisms or cylindrical lenses [43]. When light has both SAM spin and OAM, a single rotation of the beam about the beam axis changes the phase by  $(l + \sigma)$  cycles and the frequency by  $\Delta\omega = J\Omega$  [73], which is proportional to the total angular momentum of light. The beam cross-section has an  $(l + \sigma)$ -fold rotation symmetry.

SAM and OAM act similarly when being rotated about the beam axis, so the total angular momentum is the important parameter.

## 10.5 MEASURING BEAMS WITH OAM

We have discussed how to create a beam having nonzero OAM, how to observe the physical effects of OAM, how to manipulate OAM, and how to transform between different modes and between SAM and OAM. We have yet to discuss how to measure OAM. Sometimes it is not enough to simply know that a beam has a helical phase front; there are situations where we want to quantify the OAM. There are many ways to measure OAM. First is through the use of forked diffraction gratings. As we have discussed previously, to generate an OAM-carrying beam, one can use the collimated output of a single mode fiber to illuminate a forked diffraction grating and get a vortex beam in the far field [33], as shown in Figure 10.4. If, instead, one wants to measure a beam with OAM, this process can be reversed. A vortex beam incident on a forked grating will result in a fundamental Gaussian beam only if the OAM of the incoming beam is opposite to that of the diffraction grating. By scanning the diffraction grating through all possible OAM states and detecting which state corresponds to a detected photon after a single mode fiber, the mode of the incident photon can be deduced [74]. This method works with low levels of light down to single photons. However, when working with single photons, the efficiency of the detection system is only  $1/N$ , where  $N$  is the number of states to be assessed, and so for effective detection of the OAM mode, many photons must be prepared in the same state.

Another method for measuring OAM is to interfere the unknown helically phased beam with a plane wave. The resulting fringes are spiral in nature, and the number of forked fringes matches the  $l$  of the beam [20], shown in Figure 10.1. Interference can be used to determine OAM for a diffraction pattern from any aperture as well. For single and double slits, there is a displacement due to the helical phase front that is perpendicular to the slit direction and leads to a sharp bend in the otherwise straight fringes. The direction of the bend depends on the handedness of the helicity [74, 75]. More complicated diffraction patterns can also be used to measure OAM. One interesting case is when an LG beam is diffracted through a triangular aperture. The result is an array of  $(l+1)(l+2)/2$  spots in a triangular configuration, set at a right angle to the aperture's orientation, with the sign of  $l$  determining the direction of the orientation [76]. All of these interferometric methods allow for the measure of both the magnitude and the sign of the OAM. However, these approaches require many photons, and thus cannot measure the  $l$  of single photons.

The rotational frequency shift that was discussed previously can also be used to measure OAM, where each value of  $l$  results in a frequency sideband [77]. However, in low light it is difficult to measure both the frequency and the beam rotation. If a fixed rotation is used, a static,  $l$ -dependent phase shift is created [78]. Dove prisms can be used to make an image rotation, and this has been built into Mach-Zehnder [79] and Sagnac [24] interferometers. This rotational frequency shift method can be used to measure the OAM or the total angular momentum [80]. This method requires

$N - 1$  interferometers to measure  $N$  states, which limits this technique to measuring a small number of states.

A recently-developed method for measuring OAM is through the use of mode sorters. The azimuthal position of the input beam is transformed into a transverse position in the output beam [81, 82]. This takes a helically phased beam and turns it into a transverse phase gradient. The reformatting introduces a phase aberration, but it can be corrected in the output plane. Spatial light modulators have been used to create a system that both reformats the image and also corrects the phase. A lens then focuses the input modes to separate lateral positions, where they can be detected using a detector array [83]. This method is less technically demanding than interferometric approaches and can measure the  $l$  of single photons [84], and although not perfect, it is more efficient than other common techniques.

## 10.6 OAM IN CLASSICAL IMAGING

OAM measurement methods can be used in imaging by placing a forked hologram in the Fourier plane of the object [35, 85]. This technique is especially useful for contrast enhancement in optical microscopy. When the phase mask corresponds to a spiral phase plate, the point spread function of the microscope is changed into a helically phased ring, and the phase edges appear as bright lines, a process that is referred to as unidirectional edge enhancement. This technique has been used at the single-photon level in ghost imaging [86], which we will describe later. Varying the technique slightly results in spiral interferometry, where spiral fringes replace the common circular fringes. This allows for the recovery of information that is usually lost by the up/down degeneracy of traditional interferometric techniques. Beyond forked holograms, the same technique can be used in phase contrast and dark field microscopy. A spatial light modulator can be used instead of having separate phase masks for each imaging modality [87].

Apart from being used in a microscope, OAM can also be exploited in telescopes for the detection of off-axis light. The phase discontinuity caused by a spiral phase plate placed within a telescope blocks on-axis light and allows for fainter off-axis light to be detected [88]. This has proven interesting to astronomers, who hope to attenuate bright stars in order to look for nearby planets whose light would otherwise be eclipsed by the star [89, 90].

## 10.7 OAM IN NONLINEAR AND QUANTUM OPTICS

Optical vortices in nonlinear materials are often studied within a Kerr medium. A Kerr medium is one in which the refractive index changes with the intensity of the incident light [91], a third-order nonlinear interaction. If the increase in intensity increases the refractive index, the transmitted beam will self-focus. Conversely, if the increase in intensity decreases the refractive index, the transmitted beam will self-defocus as it passes through the medium. In this situation, a beam carrying OAM, which has an

annular intensity, will create a path of high refractive-index material that can guide a second beam through the Kerr medium [92].

Another category of nonlinear processes is second-order nonlinear interactions, where two low-frequency waves,  $\omega_1$  and  $\omega_2$ , exchange energy with  $\omega_3$ , a higher frequency wave [91]. Energy conservation requires the frequencies to be related by  $\omega_1 + \omega_2 = \omega_3$  and momentum conservation requires the momenta to be related by  $\mathbf{k}_1 + \mathbf{k}_2 = \mathbf{k}_3$ , where  $\mathbf{k}_1$ ,  $\mathbf{k}_2$ , and  $\mathbf{k}_3$  are the momentum vectors of the three waves and  $|\mathbf{k}| = \omega n(\omega)/c$ . The conservation of momentum is much more complicated than energy conservation, because the refractive index,  $n(\omega)$ , is a function of the frequency,  $\omega$ . The various approaches to modify  $n(\omega)$  include temperature and angle tuning of the crystal, and these lead to different phase-matching conditions. For example, type I phase matching is where the medium is such that the refractive indices of all three waves are the same.

A specific example of second-order nonlinear interactions is parametric down-conversion, where the energy from one high-frequency wave is transferred to two lower-frequency waves. This process is only partially constrained in that the frequencies of  $\omega_1$  and  $\omega_2$  can vary, so long as they sum to give  $\omega_3$ , the frequency of the starting wave [93]. The two emitted beams are each spatially incoherent, whilst being phase conjugate with respect to each other, leading to quantum entanglement of the spatial modes [79, 94]. The measurement of one photon in a particular basis collapses the two-photon state and, because of entanglement, immediately gives knowledge about the same basis for the other photon, regardless of the photons' spatial separation.

OAM can be used for the encoding of both classical and quantum information [76]. OAM is potentially useful in quantum cryptography, as it gives access to an unbounded number of states, in contrast to the two states associated with SAM, thus greatly increasing the amount of information that can be transmitted on each photon [95, 96]. Other quantum phenomena explored with OAM-carrying light include hyperentanglement, multiple variables including OAM are entangled simultaneously [97], and hybrid entanglement, where there is entanglement between OAM and a different variable [38, 98].

OAM can be used in various tests of quantum mechanics. As discussed earlier, a Poincaré sphere equivalent exists for OAM, and by drawing direct analogy with polarization, it is possible to formulate a Bell-type argument for OAM that discounts the local hidden-variable theory [99]. Violation of the Bell inequality has been shown for the case where the phase filter is nonlocal with respect to the object [86]. In a different type of test of quantum mechanics using wedge-shaped apertures and forked holograms, it has also been shown that the EPR paradox also applies to OAM and angular position [100].

With possibilities for carrying an unbounded state space, OAM presents itself as an extremely useful tool to increase information capacity in quantum information. However, a drawback to using OAM is that the decomposition of an OAM-carrying beam into its eigenstates depends on both its transverse and angular alignment. Because it is an extended beam, the phase fronts and the OAM spectrum are sensitive to atmospheric turbulence [100–102]. Despite these sensitivities, OAM multiplexing has recently been shown to result in very high data rates [103].

## 10.8 CONCLUSIONS

OAM has helped scientists think differently about light and has led to a number of discoveries both on the microscopic and macroscopic level. It has proven useful for applications in micromanipulation, imaging, and communication systems. Knowledge and study of OAM has increased with the development of spatial light modulators, which have allowed increased control over both the phase and intensity of light. OAM has also allowed for new demonstrations of quantum entanglement, and the multidimensional OAM basis set has led to higher numbers of states for encoding of information. In the 20 years since Allen et al. published the groundbreaking paper on OAM, we have learned much about OAM, but there is no doubt that there are more areas to explore.

## REFERENCES

- [1] J. Poynting, “The wave motion of a revolving shaft, and a suggestion as to the angular momentum in a beam of circularly polarised light,” *Proc. R. Soc. Lond., A* **82**, 560–567 (1909).
- [2] R. Beth, “Mechanical detection and measurement of the angular momentum of light,” *Phy. Rev.* **50**, 115–125 (1936).
- [3] L. Allen, M. Beijersbergen, R. Spreeuw, and J. Woerdman, “Orbital angular momentum of light and the transformation of laguerre-gaussian laser modes,” *Phy. Rev. A* **45**, 8185–8189 (1992).
- [4] C. G. Darwin, “Notes on the theory of radiation,” *Proc. R. Soc. Lond., A* **136**, 36–52 (1932).
- [5] L. Allen, M. J. Padgett, and M. Babiker, “The orbital angular momentum of light,” *Prog. Opt.* **39**, 291–372 (1999).
- [6] M. J. Padgett and L. Allen, “The poynting vector in laguerre-gaussian laser modes,” *Opt. Commun.* **121**, 36–40 (1995).
- [7] G. A. Turnbull, D. A. Robertson, G. M. Smith, L. Allen, and M. J. Padgett, “Generation of free-space laguerre-gaussian modes at millimetre-wave frequencies by use of a spiral phaseplate,” *Opt. Commun.* **127**(4–6), 183–188 (1996).
- [8] J. Leach, S. Keen, M. J. Padgett, C. Saunter, and G. D. Love, “Direct measurement of the skew angle of the poynting vector in a helically phased beam,” *Opt. Exp.* **14**, 11919–11924 (2006).
- [9] M. Berry, J. Nye, and F. Wright, “The elliptic umbilic diffraction catastrophe,” *Phil. Trans. R. Soc. Lond.* **291**, 453–484 (1979).
- [10] P. Coullet, G. Gil, and F. Rocca, “Optical vortices,” *Opt. Commun.* **73**, 403–408 (1989).
- [11] J. F. Nye and M. Berry, “Dislocations in wave trains,” *Proc. R. Soc. Lond., A* **336**, 165–190 (1974).
- [12] J. M. Vaughan and D. Willetts, “Interference properties of a light-beam having a helical wave surface,” *Opt. Commun.* **30**, 263–267 (1979).
- [13] L. A. Lugiato, F. Prati, L. M. Narducci, and G.-L. Oppo, “Spontaneous breaking of the cylindrical symmetry in lasers,” *Opt. Commun.* **69**, 387–392 (1989).

- [14] C. Tamm, “Frequency locking of 2 transverse optical modes of a laser,” *Phys. Rev. A* **38**, 5960–5963 (1988).
- [15] C. Tamm and C. Weiss, “Bistability and optical switching of spatial patterns in a laser,” *J. Opt. Soc. Am. B* **7**, 1034–1038 (1990).
- [16] G. D’Alessandro and G.-L. Oppo, “Gauss-laguerre modes: a sensible basis for laser dynamics,” *Opt. Commun.* **88**, 130–136 (1992).
- [17] D. McGloin and K. Dholakia, “Bessel beam: diffraction in a new light, contemporary,” *Physics* **46**, 15–28 (2005).
- [18] J. C. Gutierrez-Vega, M. D. Iturbe-Castillo, and S. Chavez-Cerda, “Alternative formulation for invariant optical fields: Mathieu beams,” *Opt. Lett.* **25**, 1493–1495 (2000).
- [19] M. A. Bandres and J. C. Gutierrez-Vega, “Ince-Gaussian beams,” *Opt. Lett.* **29**, 144–146 (2004).
- [20] M. Harris, C. A. Hill, and J. M. Vaughan, “Optical helices and spiral interference fringes,” *Opt. Commun.* **106**, 161–166 (1994).
- [21] M. J. Padgett, J. Arlt, N. Simpson, and L. Allen, “An experiment to observe the intensity and phase structure of laguerre-gaussian laser modes,” *Am. J. Phys.* **64**, 77–82 (1996).
- [22] M. S. Soskin, V. N. Gorshkov, M. V. Vasnetsov, J. T. Malos, and N. R. Heckenberg, “Topological charge and angular momentum of light beams carrying optical vortices,” *Phys. Rev. A* **56**, 4064–4075 (1997).
- [23] G. W. Forbes and M. A. Alonso, “Measures of spread for periodic distributions and the associated uncertainty relations,” *Am. J. Phys.* **69**, 340–347 (2001).
- [24] E. Yao, S. Franke-Arnold, J. Courtial, M. J. Padgett, and S. M. Barnett, “Observation of quantum entanglement using spatial light modulators,” *Opt. Exp.* **14**(26), 13089–13094 (2006).
- [25] S. Franke-Arnold, S. M. Barnett, E. Yao, J. Leach, J. Courtial, and M. Padgett, “Uncertainty principle for angular position and angular momentum,” *New J. Phys.* **6**, 1–8 (2004).
- [26] G. W. Forbes and M. A. Alonso, “Consistent analogs of the Fourier uncertainty relation,” *Am. J. Phys.* **69**, 1091 (2001).
- [27] J. Řeháček, Z. Bouchal, R. Čelechovský, Z. Hradil, and L. L. Sánchez-Soto, “Experimental test of uncertainty relations for quantum mechanics on a circle,” *Phys. Rev. A* **77**, 13 (2008).
- [28] M. Beijersbergen, L. Allen, H. van der Veen, and J. Woerdman, “Astigmatic laser mode converters and transfer of orbital angular momentum,” *Opt. Commun.* **96**, 123–132 (1993).
- [29] N. González, G. Molina-Terriza, and J. P. Torres, “How a dove prism transforms the orbital angular momentum of a light beam,” *Opt. Exp.* **14**(20), 9093–9102 (2006).
- [30] M. W. Beijersbergen, R. P. C. Coerwinkel, M. Kristensen, and J. P. Woerdman, “Helical-wavefront laser beams produced with a spiral phaseplate,” *Opt. Commun.* **112**(5–6), 321–327 (1994).
- [31] S. S. R. Oemrawsingh, J. A. W. van Houwelingen, E. R. Eliel, J. P. Woerdman, E. J. K. Versteegen, J. G. Kloosterboer, and G. W. Hooft, “Production and characterization of spiral phase plates for optical wavelengths,” *Appl. Opt.* **43**(3), 688–694 (2004).
- [32] K. Sueda, G. Miyaji, N. Miyanaga, and M. Nakatsuka, “Laguerre-Gaussian beam generated with a multilevel spiral phase plate for high intensity laser pulses,” *Opt. Exp.* **12**(15), 3548–3553 (2004).

- [33] V. Y. Bazhenov, M. V. Vasnetsov, and M. S. Soskin, “Laser-beams with screw dislocations in their wave-fronts,” *JETP Lett.* **52**(8), 429–431 (1990).
- [34] V. Y. Bazhenov, M. S. Soskin, and M. V. Vasnetsov, “Screw dislocations in light wave-fronts,” *J. Mod. Opt.* **39**, 985–990 (1992).
- [35] N. R. Heckenberg, R. McDuff, C. P. Smith, H. Rubinsztein-Dunlop, and M. J. Wegener, “Laser beams with phase singularities,” *Opt. Quant. Electron.* **24**(9), S951–S962 (1992).
- [36] L. Marrucci, C. Manzo, and D. Paparo, “Optical spin-to-orbital angular momentum conversion in inhomogeneous anisotropic media,” *Phys. Rev. Lett.* **96**, 163905 (2006).
- [37] L. Marrucci, E. Karimi, S. Slussarenko, B. Piccirillo, E. Santamato, E. Nagali, and F. Sciarrino, “Spin-to-orbital conversion of the angular momentum of light and its classical and quantum applications,” *J. Opt.* **13**, 064001 (2011).
- [38] E. Nagali, L. Sansoni, F. Sciarrino, F. De Martini, L. Marrucci, B. Piccirillo, E. Karimi, and E. Santamato, “Optimal quantum cloning of orbital angular momentum photon qubits through Hong-Ou-Mandel coalescence,” *Nat. Photon.* **3**(12), 720–723 (2009).
- [39] J. Masajada and B. Dubik, “Optical vortex generation by three plane wave interference,” *Opt. Commun.* **198**(1–3), 21–27 (2001).
- [40] K. O’Holleran, M. J. Padgett, and M. R. Dennis, “Topology of optical vortex lines formed by the interference of three, four, and five plane waves,” *Opt. Exp.* **14**(7), 3039–3044 (2006).
- [41] J. F. Nye, *Natural Focusing and Fine Structure of Light: Caustics and Wave Dislocations*. Taylor & Francis, 1999).
- [42] G. A. Swartzlander and R. I. Hernandez-Aranda, “Optical rankine vortex and anomalous circulation of light,” *Phys. Rev. Lett.* **99**(16), (2007).
- [43] J. Courtial, K. Dholakia, D. A. Robertson, L. Allen, and M. J. Padgett, “Measurement of the rotational frequency shift imparted to a rotating light beam possessing orbital angular momentum,” *Phys. Rev. Lett.* **80**(15), 3217–3219 (1998).
- [44] B. Thidé, H. Then, J. Sjoholm, K. Palmer, J. Bergman, T. D. Carozzi, Y. N. Istomin, N. H. Ibragimov, and R. Khamitova, “Utilization of photon orbital angular momentum in the low-frequency radio domain,” *Phys. Rev. Lett.* **99**(8), 1–4 (2007).
- [45] S. Sasaki and I. McNulty, “Proposal for generating brilliant x-ray beams carrying orbital angular momentum,” *Phys. Rev. Lett.* **100**(12), (2008).
- [46] M. Uchida and A. Tonomura, “Generation of electron beams carrying orbital angular momentum,” *Nature* **464**, 737–739 (2010).
- [47] J. Verbeeck, H. Tian, and P. Schattschneider, “Production and application of electron vortex beams,” *Nature* **467**, 301–304 (2010).
- [48] H. He, M. E. J. Friese, N. R. Heckenberg, and H. Rubinsztein-Dunlop, “Direct observation of transfer of angular momentum to absorptive particles from a laser beam with a phase singularity,” *Phys. Rev. Lett.* **75**(5), 826–829 (1995).
- [49] M. Padgett and L. Allen, “Optical tweezers and spanners,” *Phy. World* **10**(9), 35–38 (1997).
- [50] N. B. Simpson, K. Dholakia, L. Allen, and M. J. Padgett, “Mechanical equivalence of spin and orbital angular momentum of light: an optical spanner,” *Opt. Lett.* **22**(1), 52–54 (1997).
- [51] A. T. O’Neil, I. MacVicar, L. Allen, and M. J. Padgett, “Intrinsic and extrinsic nature of the orbital angular momentum of a light beam,” *Phys. Rev. Lett.* **88**(5), 053601 (2002).

- [52] J. Courtial and M. J. Padgett, “Limit to the orbital angular momentum per unit energy in a light beam that can be focussed onto a small particle,” *Opt. Commun.* **173**, 269–274 (2000).
- [53] M. E. J. Friese, H. Rubinsztein-Dunlop, J. Gold, P. Hagberg, and D. Hanstorp, “Optically driven micromachine elements,” *Appl. Phys. Lett.* **78**(4), 547–549 (2001).
- [54] K. Ladavac and D. Grier, “Microoptomechanical pumps assembled and driven by holographic optical vortex arrays,” *Opt. Exp.* **12**(6), 1144–1149 (2004).
- [55] J. Leach, H. Mushfique, R. Di Leonardo, M. Padgett, and J. M. Cooper, “An optically driven pump for microfluidics,” *Lab Chip* **6**(6), 735–739 (2006).
- [56] M. Babiker, W. L. Power, and L. Allen, “Light-induced torque on moving atoms,” *Phys. Rev. Lett.* **73**(9), 1239–1242 (1994).
- [57] L. Allen, M. Babiker, and W. L. Power, “Azimuthal doppler-shift in light-beams with orbital angular-momentum,” *Opt. Commun.* **112**(3–4), 141–144 (1994).
- [58] T. Kuga, Y. Torii, N. Shiokawa, T. Hirano, Y. Shimizu, and H. Sasada, “Novel optical trap of atoms with a doughnut beam,” *Phys. Rev. Lett.* **78**(25), 4713–4716 (1997).
- [59] T. A. Nieminen, A. B. Stilgoe, N. R. Heckenberg, and H. Rubinsztein-Dunlop, “Angular momentum of a strongly focused gaussian beam,” *J. Opt. A* **10**(11), (2008).
- [60] Y. Zhao, J. S. Edgar, G. D. M. Jeffries, D. McGloin, and D. T. Chiu, “Spin-to-orbital angular momentum of a strongly focused optical beam,” *Phys. Rev. Lett.* **99**, 073901 (2007).
- [61] M. E. J. Friese, T. A. Nieminen, N. R. Heckenberg, and H. Rubinsztein-Dunlop, “Optical alignment and spinning of laser-trapped microscopic particles,” *Nature* **394**(6691), 348–350 (1998).
- [62] D. L. Andrews, L. C. D. Romero, and M. Babiker, “On optical vortex interactions with chiral matter,” *Opt. Commun.* **237**(1–3), 133–139 (2004).
- [63] F. Araoka, T. Verbiest, K. Clays, and A. Persoons, “Interactions of twisted light with chiral molecules: an experimental investigation,” *Phys. Rev. A* **71**(5), 055401 (2005).
- [64] L. Allen and M. Padgett, “Equivalent geometric transformations for spin and orbital angular momentum of light,” *J. Mod. Opt.* **54**(4), 487–491 (2007).
- [65] S. Franke-Arnold, G. Gibson, R. W. Boyd, and M. J. Padgett, “Rotary photon drag enhanced by a slow-light medium,” *Science* **333**, 65–67 (2011).
- [66] R. Jones, “‘fresnel aether drag’ in a transversely moving medium,” *Proc. R. Soc. Lond., A.* **328**, 337–352 (1972).
- [67] R. V. Jones, “Rotary ‘aether drag’,” *Proc. R. Soc. Lond., A* **349**, 423–439 (1976).
- [68] M. J. Padgett and J. Courtial, “Poincare-sphere equivalent for light beams containing orbital angular momentum,” *Opt. Lett.* **24**(7), 430–432 (1999).
- [69] E. J. Galvez, P. R. Crawford, H. I. Sztul, M. J. Pysher, P. J. Haglin, and R. E. Williams, “Geometric phase associated with mode transformations of optical beams bearing orbital angular momentum,” *Phys. Rev. Lett.* **90**(20), 203901 (2003).
- [70] B. A. Garetz and A. S., “Variable frequency-shifting of circularly polarized laser-radiation via a rotating half-wave retardation plate,” *Opt. Commun.* **31**(1), 1–3 (1979).
- [71] B. A. Garetz, “Angular dopper efect,” *J. Opt. Soc. Am.* **71**(5), 609–611 (1981).
- [72] I. V. Basistiy, V. V. Slyusar, M. S. Soskin, M. V. Vasnetsov, and A. Y. Bekshaev, “Manifestation of the rotational Doppler efect by use of an off-axis optical vortex beam,” *Opt. Lett.* **28**(14), 1185–1187 (2003).

- [73] G. Nienhuis, “Doppler efect induced by rotating lenses,” *Opt. Commun.* **132**, 8–14 (1996).
- [74] D. Ghai, P. Senthilkumaran, and R. S. Sirohi, “Single-slit difraction of an optical beam with phase singularity,” *Opt. Lasers Eng.* **47**(1), 123–126 (2009).
- [75] H. I. Sztul and R. R. Alfano, “Double-slit interference with Laguerre-Gaussian beams,” *Opt. Lett.* **31**(7), 999–1001 (2006).
- [76] J. M. Hickmann, E. J. S. Fonseca, W. C. Soares, and S. Chávez-Cerda, “Unveiling a truncated optical lattice associated with a triangular aperture using light’s orbital angular momentum,” *Phys. Rev. Lett.* **105**, 053904 (2010).
- [77] J. Courtial, D. A. Robertson, and K. Dholakia, “Rotational frequency shift of a light beam,” *Phys. Rev. Lett.* **81**(22), 4828–4830 (1998).
- [78] G. Molina-Terriza, J. P. Torres, and L. Torner, “Management of the angular momentum of light: preparation of photons in multidimensional vector states of angular momentum,” *Phys. Rev. Lett.* **88**(1), 013601 (2002).
- [79] A. Mair, A. Vaziri, G. Weihs, and A. Zeilinger, “Entanglement of the orbital angular momentum states of photons,” *Nature* **412**(6844), 313–316 (2001).
- [80] S. N. Khonina, V. V. Kotlyar, R. V. Skidanov, V. A. Soifer, P. Laakkonen, and J. Tu-runen, “Gauss-Laguerre modes with different indices in prescribed diffraction orders of a diffractive phase element,” *Opt. Commun.* **175**(4–6), 301–308 (2000).
- [81] O. Bryngdahl, “Geometrical transformations in optics,” *J. Opt. Soc. Am.* **64**, 1092–1099 (1974).
- [82] W. J. Hossack, A. M. Darling, and A. Dahdouh, “Coordinate transformations with multiple computer-generated optical-elements,” *J. Mod. Opt.* **34**(9), 1235–1250 (1987).
- [83] G. C. G. Berkhout, M. P. J. Lavery, J. Courtial, M. W. Beijersbergen, and M. J. Padgett, “Efficient sorting of orbital angular momentum states of light,” *Phys. Rev. Lett.* **105**(15), 153601 (2010).
- [84] M. P. J. Lavery, D. J. Robertson, G. C. G. Berkhout, G. D. Love, M. J. Padgett, and J. Courtial, “Refractive elements for the measurement of the orbital angular momentum of a single photon,” *Opt. Exp.* **20**(3), 2110–2115 (2012).
- [85] L. Torner, J. P. Torres, and S. Carrasco, “Digital spiral imaging,” *Opt. Exp.* **13**(3), 873–881 (2005).
- [86] B. Jack, J. Leach, J. Romero, S. Franke-Arnold, M. Ritsch-Marte, S. M. Barnett, and M. J. Padgett, “Holographic ghost imaging and the violation of a bell inequality,” *Phys. Rev. Lett.* **103**(8), 083602 (2009).
- [87] S. Furhapter, A. Jesacher, S. Bernet, and M. Ritsch-Marte, “Spiral phase contrast imaging in microscopy,” *Opt. Exp.* **13**(3), 689–694 (2005).
- [88] G. A. Swartzlander, “Peering into darkness with a vortex spatial filter,” *Opt. Lett.* **26**(8), 497–499 (2001).
- [89] J. H. Lee, G. Foo, E. G. Johnson, and G. A. Swartzlander, “Experimental verification of an optical vortex coronagraph,” *Phys. Rev. Lett.* **97**(5), (2006).
- [90] G. Swartzlander, E. Ford, R. Abdul-Malik, L. Close, M. Peters, D. Palacios, and D. Wilson, “Astronomical demonstration of an optical vortex coronagraph,” *Opt. Exp.* **16**(14), 10200–10207 (2008).
- [91] A. M. Yao and M. J. Padgett, “Orbital angular momentum: origins, behavior and applications,” *Adv. Opt. Photon.* **3**, 161–204 (2011).

- [92] G. A. Swartzlander and C. T. Law, “Optical vortex solitons observed in Kerr nonlinear media,” *Phys. Rev. Lett.* **69**(17), 2503–2506 (1992).
- [93] J. Arlt, K. Dholakia, L. Allen, and M. J. Padgett, “Parametric down-conversion for light beams possessing orbital angular momentum,” *Phys. Rev. A* **59**(5), 3950–3952 (1999).
- [94] R. Ghosh and L. Mandel, “Observation of nonclassical effects in the interference of two photons,” *Phys. Rev. Lett.* **59**(17), 1903–1905 (1987).
- [95] A. Vaziri, G. Weihs, and A. Zeilinger, “Experimental two-photon, three-dimensional entanglement for quantum communication,” *Phys. Rev. Lett.* **89**(24), 4 (2002).
- [96] G. Molina-Terriza, A. Vaziri, J. Řeháček, Z. Hradil, and A. Zeilinger, “Triggered qutrits for quantum communication protocols,” *Phys. Rev. Lett.* **92**(16), 167903 (2004).
- [97] J. T. Barreiro, N. K. Langford, N. A. Peters, and P. G. Kwiat, “Generation of hyper-entangled photon pairs,” *Phys. Rev. Lett.* **95**, 260501 (2005).
- [98] E. Karimi, J. Leach, S. Slussarenko, B. Piccirillo, L. Marrucci, L. Chen, W. She, S. Franke-Arnold, M. Padgett, and E. Santamato, “Spin-orbit hybrid entanglement of photons and quantum contextuality,” *Phys. Rev. A* **82**, 022115 (2010).
- [99] J. Leach, B. Jack, J. Romero, M. Ritsch-Marte, R. W. Boyd, A. K. Jha, S. M. Barnett, S. Franke-Arnold, and M. J. Padgett, “Violation of a bell inequality in two-dimensional orbital angular momentum state-spaces,” *Opt. Exp.* **17**(10), 8287–8293 (2009).
- [100] J. Leach, B. Jack, J. Romero, A. K. Jha, A. M. Yao, S. Franke-Arnold, D. G. Ireland, R. W. Boyd, S. M. Barnett, and M. J. Padgett, “Quantum correlations in optical angle-orbital angular momentum variables,” *Science* **329**, 662–665 (2010).
- [101] J. Romero, J. Leach, B. Jack, M. R. Dennis, S. Franke-Arnold, S. M. Barnett, and M. Padgett, “Entangled optical vortex links,” *Phys. Rev. Lett.* **106**, 100407 (2011).
- [102] V. D. Salakhutdinov, E. R. Eliel, and W. Löfller, “Full-field quantum correlations of spatially entangled photons,” *Phys. Rev. Lett.* **108**, 173604 (2012).
- [103] S. Barreiro and J. W. R. Tabosa, “Generation of light carrying orbital angular momentum via induced coherence grating in cold atoms,” *Phys. Rev. Lett.* **90**(13), (2003).

---

# 11

---

## INTRODUCTION TO HELICITY AND ELECTROMAGNETIC DUALITY TRANSFORMATIONS IN OPTICS

IVAN FERNANDEZ-CORBATON AND GABRIEL MOLINA-TERRIZA

*Department of Physics and Astronomy, Macquarie University, Sydney, Australia*

### 11.1 INTRODUCTION

The scientific laws that we use to understand natural phenomena typically stem from the conservation of a few fundamental quantities like electric charge, energy, or angular momentum. There is an intimate connection between conserved quantities and the symmetries of the system under study. For this reason, symmetries, both continuous and discrete, are a powerful tool for studying nature. According to Noether's celebrated theorem [1], any continuous symmetry of a system gives rise to a conserved quantity in the dynamic equations. In modern algebraic terms we say that when a system is invariant under the continuous transformation generated by a given operator, the observable represented by that operator is a conserved quantity. For example, rotational and translational invariances are associated with the conservation of angular momentum and linear momentum because, as transformations, rotations are generated by the components of angular momentum and translations are generated by the components of linear momentum. Conversely, conserved quantities always indicate the presence of a symmetry of the system. For example, angular momentum is conserved by spherically symmetric systems. A spherically symmetric system has the property of being identical to any rotated version of itself. We then say that such a system is invariant under rotations. Identifying symmetric patterns

---

*Photonics: Scientific Foundations, Technology and Applications, Volume I*, First Edition.

Edited by David L. Andrews.

© 2015 John Wiley & Sons, Inc. Published 2015 by John Wiley & Sons, Inc.

in natural systems and their related conserved quantities is therefore essential in the most areas of science. Geometrical symmetries, such as the above-mentioned spherical symmetry, are not always easily identifiable, but it is even more challenging to ascertain symmetries which do not have a geometrical origin.

In this chapter we will present a detailed introduction to a fundamental non-geometrical symmetry of electromagnetic fields: electromagnetic duality. This symmetry appears in free-space Maxwell equations which remain invariant under the exchange of electric and magnetic fields  $\mathbf{E} \rightarrow \mathbf{H}$  and  $\mathbf{H} \rightarrow -\mathbf{E}$ . More generally, they also remain invariant under certain parametric combinations of the electric and magnetic vector fields of which the exchange referred to before is a particular case. This continuous symmetry is called electromagnetic duality. The conserved quantity related to electromagnetic duality is the optical helicity. An introduction to electromagnetic duality can be found in most books in electrodynamics and electromagnetism, even though the connection with helicity is usually lacking. The extension of the connection between helicity and duality to material systems turns this relationship into a powerful tool for the study of light–matter interactions. Our aim in this chapter is to present a detailed account of the fundamental properties of both electromagnetic duality and optical helicity and how to use and measure them in photonics experiments. We start by presenting a formalism which is seldom used in electromagnetism and photonics, but that constitutes the mathematical framework for this chapter.

## 11.2 SYMMETRIES AND OPERATORS

The paradigm that we will follow in this chapter is the use of symmetries and conserved quantities for the study of electromagnetic problems. We will focus on classical Maxwell fields. Symmetry operations like rotations and translations are linear transformations that apply to the fields. Similarly, we model the light–matter interactions as linear transformations of the free space fields. Nonlinear interactions are out of the scope of this chapter, but can be treated in a similar manner. We will work in regions of space which are absent of free charges and currents, thus the fields themselves will always be transverse. These ideas are best formalized using the mathematical setting of Hilbert spaces. Therefore, we will make extensive use of the concepts and tools associated with a vector space endowed with an inner product, that is, a Hilbert space and the linear operators acting within that vector space.

The vector space we consider is the space of transverse solutions of Maxwell's equations, or transverse Maxwell fields, which we call  $\mathbb{M}$ . A linear operator within  $\mathbb{M}$  takes one of its vectors, a transverse Maxwell field, and transforms it into another vector of the space, still a transverse solution of Maxwell's equations. We are interested in transformations of the fields such as time translation, spatial translations and rotations, etc. These transformations are operators acting within  $\mathbb{M}$ . Such continuous operations are generated by hermitian operators, also acting within  $\mathbb{M}$ , which are associated with properties of the fields. For instance, energy generates time translations, the components of linear momentum generate spatial translations and the

components of angular momentum generate spatial rotations. A hermitian operator  $O$  generates a continuous transformation  $T(\theta)$  by means of

$$T(\theta) = \exp(-i\theta O) = \sum_n \frac{(-i\theta O)^n}{n!}. \quad (11.1)$$

As an example of the use of this kind of formalism in classical Maxwell fields, the interested reader can see Section 21 of Reference 2, where it is applied to angular momentum and its generated transformation, spatial rotations. The fact that  $\mathbb{M}$  has an inner product allows us to speak of hermitian operators. It also allows us to construct orthonormal basis into which any transverse Maxwell field can be expanded. The basis vectors can be chosen to be transverse fields which are simultaneous eigenvectors of four commuting hermitian operators.

The consideration of the set of orthonormal functions, the hermitian operators associated with the fundamental quantities of the field and the transformations that these operators generate, allows to study electromagnetic problems using Maxwell fields together with the powerful framework of symmetries and conserved quantities. When the electromagnetic equations of a given system are invariant under the transformations generated by a given hermitian operator, the property of the field associated with that operator is a constant of the motion. Conversely, if the system does not possess that symmetry, we know that the associated property can, in general, change during evolution. The effect of the symmetry of the system is quite strong: it must preserve the eigenvectors and eigenvalues of the operator generating the symmetry, thus offering an adequate basis of vectors to solve the electromagnetic problem. As it will be seen, this is a simple yet insightful approach to electromagnetic problems. In this approach, we only use properties of the electromagnetic field which are associated with a hermitian operator in  $\mathbb{M}$ . Only then can we consider their associated symmetry. In this context one can write the operators for the angular momentum  $\mathbf{J}$ , the linear momentum  $\mathbf{P}$ , the energy  $H$ , and, as we will discuss more in detail later on, the helicity  $\Lambda$  in different representations. In the most commonly used representation, the expressions corresponding to these operators are

$$\begin{aligned} H &= i \frac{\partial}{\partial t}, \\ \mathbf{P} &= -i\nabla, \\ \mathbf{J} &= \mathbf{L} + \mathbf{S}, \\ \Lambda &= \frac{\mathbf{J} \cdot \mathbf{P}}{|\mathbf{P}|}. \end{aligned} \quad (11.2)$$

$\mathbf{L}$  and  $\mathbf{S}$  are typically understood as the orbital angular momentum and the spin angular momentum, respectively, and they can be expressed as

$$\mathbf{L} = -i\mathbf{r} \times \nabla \quad (11.3)$$

$$S_{nm}^k = -ie_{knm}, \quad (11.4)$$

where the  $k$ th component of the vector  $\mathbf{S}$ ,  $S^k$ , is a matrix of indexes  $nm$  defined using the totally antisymmetric tensor  $\epsilon_{knm}$  with  $\epsilon_{123} = 1$ . Note however that the operators  $\mathbf{L}$  and  $\mathbf{S}$  are not operators in  $\mathbb{M}$ , because they break the transversality of the fields [3, 4, B<sub>1.2</sub>] . On the other hand, all the operators in (11.2) are well behaved in this sense and can operate within the set  $\mathbb{M}$  of solutions of free-space Maxwell equations.

In our notation we use capital letters like  $J_z$  and  $P_x$  to denote operators, and lower case letters like  $j_z$  (or  $n$ ) and  $k_x$  to denote their eigenvalues. When we speak of a field having a “sharp” or “well-defined” value for an operator, we mean that the field is an eigenvector of that operator with eigenvalue equal to its “sharp” value. In the text, names like “helicity” or “third component of angular momentum” refer to the operators unless it is clear from the context that this is not the case. Also, all calculations in this chapter assume a time harmonic decomposition of the fields with an  $\exp(-i\omega t)$  dependence.

Finally, we would like to repeat that the main context of this chapter is that of classical Maxwell fields. Nevertheless, the approach here taken, which is based on the study of symmetries, is general and often used in Quantum Mechanics and other areas of modern Physics.

### 11.3 ELECTROMAGNETIC DUALITY

In this context, we now embark on the study of the electromagnetic duality symmetry. Electromagnetic duality is a transformation where the roles of electric and magnetic fields are mixed. Mathematically, the duality transformation of electromagnetic fields is expressed as

$$\begin{aligned}\mathbf{E} &\rightarrow \mathbf{E}_\theta = \cos(\theta)\mathbf{E} - \sin(\theta)\mathbf{H}, \\ \mathbf{H} &\rightarrow \mathbf{H}_\theta = \sin(\theta)\mathbf{E} + \cos(\theta)\mathbf{H}.\end{aligned}\tag{11.5}$$

The typical exchange transformation,  $\mathbf{E} \rightarrow \mathbf{H}$  and  $\mathbf{H} \rightarrow -\mathbf{E}$ , is recovered by setting  $\theta = -\frac{\pi}{2}$ . In the absence of charges and currents, Eq. (11.5) is a symmetry of Maxwell’s equations: if the electromagnetic field  $(\mathbf{E}, \mathbf{H})$  is a solution of the free-space Maxwell equations, then the field  $(\mathbf{E}_\theta, \mathbf{H}_\theta)$  is also a solution. In 1965, Calkin [5] showed that helicity was the conserved quantity related to such symmetry. With the notation of the last section, if we think of duality as an operator in  $\mathbb{M}$  which depends on  $\theta$ , like  $T(\theta)$  in (11.1), the hermitian operator which plays the role of the generator  $O$  in Eq. (11.1) is the helicity.

Helicity is defined [6, Chapter 8.4.1] as the projection of the total angular momentum  $\mathbf{J}$  onto the linear momentum direction  $\mathbf{P}/|\mathbf{P}|$ , that is,  $\Lambda = \mathbf{J} \cdot \mathbf{P}/|\mathbf{P}|$ . In the case of the electromagnetic field the eigenvalues of helicity are  $\pm 1$ . It is possible to intuitively understand the meaning of helicity when considering the wave function of the particle in the momentum representation, that is, as a superposition of plane waves. In this representation, helicity is related to the handedness of the polarization of each and every plane wave. Only when all the plane waves have the same handedness with respect to their momentum, the helicity of the particle is well defined. This is

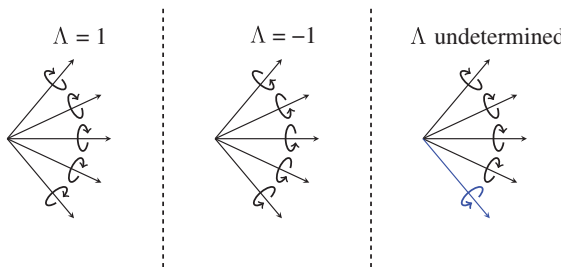


**FIGURE 11.1** A field composed by the superposition of five plane waves is an eigenstate of helicity with eigenvalue equal to one if all the plane waves have left-handedness (left panel), equal to minus one if they all have right-handedness (central panel) and it is not an eigenstate of helicity if some plane waves have a handedness and others have the opposite (right panel). (For a color version of this figure, see the color plate section.)

illustrated in Figure 11.1. Note that polarization in momentum space and polarization in real space are not the same concept.

What Calkin showed is that, as an operator, helicity generates duality transformations in the same way that linear momentum generates translations and angular momentum generates rotations. Since that seminal work, the role of helicity as the generator of duality symmetry transformations for the free-space Maxwell's equations has been reported several times [7–10]. Other related works, also in free space, include dual-symmetric Lagrangians [11–13] and optical chirality [14, 15].

In 1968, Zwanzinger [16] extended this free-space invariance and conservation law to a material quantum field theory with both electric and magnetic charges. The symmetry studied by Zwanzinger has not been experimentally confirmed due to the lack of experimental evidence of magnetic charges.

In this chapter we will show that in photonics experiments, the concepts of helicity and duality are still relevant. The key to understand this is that duality can be restored for the macroscopic Maxwell's equations for material systems characterized by electric permittivities and magnetic permeabilities. The restoration condition for a system composed of different isotropic and homogeneous domains depends only on the materials and is independent of the shapes of the domains. When the system is dual, the helicity of the light interacting with it is preserved.

This geometrical independence of helicity in material systems turns the relationship between helicity and duality into a simple and powerful tool for the practical study of light–matter interactions using symmetries and conserved quantities [17]. This tool has provided insight in nanophotonics [18–20], optical activity [21], and metamaterials [22, 23].

The practical applicability of our ideas is enabled by a fact of crucial importance: measurement and preparation of light beams with well-defined helicity can be done with very simple optical elements. Armed with this tool, we can experimentally investigate helicity transformations in focused light fields interacting with different scatterers.

Let us first explain more in detail how the relation between helicity and duality is derived and how to use the operator formalism in this context.

## 11.4 OPTICAL HELICITY AND ELECTROMAGNETIC DUALITY SYMMETRY

In our derivations, we will use a harmonic decomposition of the fields and assume an  $\exp(-i\omega t)$  dependency with the angular frequency  $\omega$ . Additionally, we will work in the representation of space-dependent vectorial fields, also known as the real representation. This setting is different from those in References 5 and 16, and, although the final result is not new, the derivation in this section sets the stage for the study of the piecewise homogeneous and isotropic case.

The expression of the helicity operator for monochromatic fields in the real representation can be obtained directly from the definition of helicity:

$$\Lambda = \frac{\mathbf{J} \cdot \mathbf{P}}{|\mathbf{P}|} = \frac{(\mathbf{S} + \mathbf{L}) \cdot \mathbf{P}}{|\mathbf{P}|} = \frac{\mathbf{S} \cdot \mathbf{P}}{|\mathbf{P}|} = \frac{\nabla \times}{k}, \quad (11.6)$$

where  $\mathbf{S}$  and  $\mathbf{L}$  are, respectively, the spin and orbital angular momentum operators, the third equality follows from the orthogonality of  $\mathbf{L} = \mathbf{r} \times \mathbf{P}$  and  $\mathbf{P}$ , and the last one is valid in the real representation because  $\mathbf{S} \cdot \mathbf{P} = \nabla \times$  [24, Expr. XIII.93] and  $|\mathbf{P}|$  is equal to the wavenumber  $k$  for monochromatic fields.

Related to the different settings mentioned above, a clarification regarding different definitions of helicity is in order before we start. In Reference 5, helicity appears as an operator in the Fock space representation and in Reference 16 as an integral involving the electric and magnetic fields and potentials operators. Both of these definitions have since then appeared in the literature several times. Here are the two expressions in a slightly different notation from that of the original references:

$$\Lambda = \hbar \int d\mathbf{k} \left( a_{\mathbf{k}+}^\dagger a_{\mathbf{k}+} - a_{\mathbf{k}-}^\dagger a_{\mathbf{k}-} \right), \quad (11.7)$$

where the Fock space operators  $(a_{\mathbf{k}\pm}^\dagger, a_{\mathbf{k}\pm})$  create and annihilate photons of definite momentum  $\mathbf{k}$  and helicity  $\pm$ . And

$$\Lambda = \frac{1}{2} \int d\mathbf{r} (\hat{\mathbf{A}}(\mathbf{r}) \cdot \hat{\mathbf{H}}(\mathbf{r}) - \hat{\mathbf{C}}(\mathbf{r}) \cdot \hat{\mathbf{E}}(\mathbf{r})), \quad (11.8)$$

where  $(\hat{\mathbf{E}}, \hat{\mathbf{H}})$  are the electric and magnetic field operators and  $(\hat{\mathbf{C}}, \hat{\mathbf{A}})$  the electric and magnetic potential operators [16].

All of the expressions (11.6)–(11.8) generate the same fundamental symmetry transformation, albeit in different representation spaces.

We start the derivation by setting convenient units of  $\epsilon_0 = \mu_0 = 1$  for the vacuum electric and magnetic constants (thus  $c = 1$  and  $k = \omega$ ). We can then use (11.6) to write the free-space Maxwell equations as

$$\begin{aligned} \nabla \times \mathbf{E} &= i\omega \mathbf{H} \Rightarrow \mathbf{H} = -i\Lambda \mathbf{E} \\ \nabla \times \mathbf{H} &= -i\omega \mathbf{E} \Rightarrow \mathbf{E} = i\Lambda \mathbf{H}. \end{aligned} \quad (11.9)$$

Equations (11.9) already reveal that  $\Lambda$  is an operator that transforms electric fields into magnetic fields and vice versa. Note that invariance under duality transformation can be interpreted as equivalence between electric and magnetic responses. In the same way that angular momentum generates rotation matrices [2], let us use  $\Lambda$  as the generator of a continuous transformation parametrized by the real number  $\theta$ :  $D(\theta) = \exp(i\theta\Lambda)$ . To obtain an explicit expression for the transformation that  $D(\theta)$  performs on the fields, we start by showing that  $\Lambda^2$  is the identity operator for Maxwell fields.

$$\Lambda^2 \mathbf{E} = \Lambda \left( \frac{\mathbf{H}}{-i} \right) = \mathbf{E}, \quad \Lambda^2 \mathbf{H} = \Lambda \left( \frac{\mathbf{E}}{i} \right) = \mathbf{H}, \quad (11.10)$$

where the equalities in each equation follow from (11.9). Since (11.10) is valid for all  $\mathbf{E}$  and  $\mathbf{H}$ , we conclude that  $\Lambda^2 = I$  for Maxwell fields. Using that  $\Lambda^2 = I$  and the Taylor expansion of the exponential, the continuous transformation generated by helicity can be written:

$$D(\theta) = \exp(i\theta\Lambda) = \cos(\theta)I + i \sin(\theta)\Lambda. \quad (11.11)$$

The application of  $D(\theta)$  to both electric and magnetic fields reads

$$\begin{aligned} \mathbf{E}_\theta &= (\cos(\theta)I + i \sin(\theta)\Lambda) \mathbf{E}, \\ \mathbf{H}_\theta &= (\cos(\theta)I + i \sin(\theta)\Lambda) \mathbf{H}, \end{aligned} \quad (11.12)$$

which, after using (11.9) again, becomes the well-known [25, Chapter 6.11] duality transformation of electromagnetic fields written in (11.5).

## 11.5 DUALITY SYMMETRY IN PIECEWISE HOMOGENEOUS AND ISOTROPIC MEDIA

We will now show that the duality symmetry can be restored in the macroscopic Maxwell's equations independently of the shapes of the material domains involved. The macroscopic Maxwell equations are valid whenever the electric and magnetic fields are averaged over many of the atoms or molecules composing the materials. In this way, for most situations, the electromagnetic properties of the materials are determined only by the electric permittivities  $\epsilon$  and magnetic permeabilities  $\mu$ .

We consider an inhomogeneous medium  $\Omega$  composed of several material domains with arbitrary geometry. We assume that each domain  $i$  is homogeneous and isotropic and fully characterized by its electric  $\epsilon_i$  and magnetic  $\mu_i$  constants (we again use  $\epsilon_0 = \mu_0 = 1$ ). In each domain, the constitutive relations are  $\mathbf{B} = \mu_i \mathbf{H}$ ,  $\mathbf{D} = \epsilon_i \mathbf{E}$ , and the curl equations for monochromatic fields read

$$\nabla \times \mathbf{H} = -i\omega \mathbf{D} = -i\omega \epsilon_i \mathbf{E}, \quad \nabla \times \mathbf{E} = i\omega \mathbf{B} = i\omega \mu_i \mathbf{H}. \quad (11.13)$$

Using  $\Lambda = (1/k)\nabla \times$  from (11.6) and  $\omega = k_0 = k/\sqrt{\epsilon_i\mu_i}$ , we obtain

$$\Lambda \mathbf{H} = -i\sqrt{\frac{\epsilon_i}{\mu_i}}\mathbf{E}, \quad \Lambda \mathbf{E} = i\sqrt{\frac{\mu_i}{\epsilon_i}}\mathbf{H}. \quad (11.14)$$

Note that to arrive at this result, the fact that the wavenumber in each medium is  $k = k_0\sqrt{\epsilon_i\mu_i}$  has to be used in the expression of the helicity operator. With this change, we are able to obtain the formal expression of the helicity operator for a material medium. Now, we can normalize the electric field in (11.14) by  $\mathbf{E} \rightarrow \sqrt{\frac{\epsilon_i}{\mu_i}}\mathbf{E}$  to show that we can recover the exact form of Maxwell's equations in free space (11.9). Clearly, the normalization can only be done when all the different materials have the same ratio  $\frac{\epsilon_i}{\mu_i} = \alpha \forall i$ . When the normalization is possible, the electromagnetic field equations on the whole medium  $\Omega$  are invariant under the duality transformations of (11.5).

The remaining question is what happens at the interfaces between the different domains, where the material constants are discontinuous. We now examine the boundary conditions in  $\Omega$ . At the interfaces between media, the electromagnetic boundary conditions impose the following restrictions on the fields:

$$\begin{aligned} \hat{\mathbf{n}} \times (\mathbf{E}_1 - \mathbf{E}_2) &= 0, & \hat{\mathbf{n}} \times (\mathbf{H}_1 - \mathbf{H}_2) &= \mathbf{K}, \\ \hat{\mathbf{n}} \cdot (\mathbf{D}_1 - \mathbf{D}_2) &= \sigma, & \hat{\mathbf{n}} \cdot (\mathbf{B}_1 - \mathbf{B}_2) &= 0, \end{aligned} \quad (11.15)$$

where  $\mathbf{K}$  is the surface current density,  $\sigma$  the charge density, and  $\hat{\mathbf{n}}$  the unit vector perpendicular to the interface. The boundary conditions can be seen as applying point to point to a differential surface area at the interface between the two media [26, Chapter 2.8]. Let us choose a particular point  $\mathbf{r}$  on the interface. Assuming no free charges, that is,  $\mathbf{K} = 0$  and  $\sigma = 0$ , Eqs. (11.15) may be interpreted as a linear transformation applied to the fields at one medium which results in the fields at the other medium. Using (11.15) and the constitutive relations, the transformation equation reads

$$\begin{bmatrix} \mathbf{E}_2(\mathbf{r}) \\ \mathbf{H}_2(\mathbf{r}) \end{bmatrix} = \begin{bmatrix} 1 & 0 & 0 & 0 & 0 & 0 \\ 0 & 1 & 0 & 0 & 0 & 0 \\ 0 & 0 & \frac{\epsilon_1}{\epsilon_2} & 0 & 0 & 0 \\ 0 & 0 & 0 & 1 & 0 & 0 \\ 0 & 0 & 0 & 0 & 1 & 0 \\ 0 & 0 & 0 & 0 & 0 & \frac{\mu_1}{\mu_2} \end{bmatrix} \begin{bmatrix} \mathbf{E}_1(\mathbf{r}) \\ \mathbf{H}_1(\mathbf{r}) \end{bmatrix}, \quad (11.16)$$

where we have oriented our reference axis so that  $\hat{\mathbf{n}} = \hat{\mathbf{z}}$ .

On the other hand, the duality transformation (11.5) may also be written in matrix form:

$$\begin{bmatrix} \mathbf{E}_\theta \\ \mathbf{H}_\theta \end{bmatrix} = \begin{bmatrix} I \cos(\theta) & -I \sin(\theta) \\ I \sin(\theta) & I \cos(\theta) \end{bmatrix} \begin{bmatrix} \mathbf{E} \\ \mathbf{H} \end{bmatrix} = U(\theta) \begin{bmatrix} \mathbf{E} \\ \mathbf{H} \end{bmatrix}, \quad (11.17)$$

where  $I$  is the  $3 \times 3$  identity matrix. It is a trivial exercise to check that the transformation matrix of (11.16) commutes with  $U(\theta)$  if and only if  $\epsilon_1/\mu_1 = \epsilon_2/\mu_2$ . In such case, the fields in each of the two media can be transformed as in (11.5) while still meeting the boundary conditions at point  $\mathbf{r}$ . We can now vary  $\mathbf{r}$  to cover all the points of the interface and repeat the same argument: the fact that  $U(\theta)$  does not depend on the spatial coordinates allows to reorient the reference axis as needed to follow the shape of the interface between two media. The derivation is hence independent of the shape of the interface, and we may say that the boundary conditions are invariant under duality transformations when  $\epsilon_1/\mu_1 = \epsilon_2/\mu_2$ . The above derivations show that both the equations and the boundary conditions in  $\Omega$  are invariant under (11.5) when  $\frac{\epsilon_i}{\mu_i} = \alpha \forall$  domain  $i$ . As a conclusion, we can state that independently of the shapes of each domain, a piecewise homogeneous and isotropic system has an electromagnetic response that is invariant under duality transformations if and only if all the materials have the same ratio of electric and magnetic constants:

$$\frac{\epsilon_i}{\mu_i} = \alpha \forall \text{ domain } i. \quad (11.18)$$

In this case, since helicity is the generator of duality transformations, the system preserves the helicity of light interacting with it.

Our results are in agreement with Bialynicki-Birula's wave equation for photons propagating in a linear, time-independent, isotropic, and inhomogeneous medium. In Section 2 of Reference 27, he shows that the two helicities of the photon are only coupled through the gradient of  $\sqrt{\frac{\mu(\mathbf{r})}{\epsilon(\mathbf{r})}}$ .

In the same review [Section 11 of Reference 27], the author discusses the conservation of helicity in arbitrarily curved spacetime. This notable fact is related to the equivalence of the free space Maxwell's equations on an arbitrary spacetime geometry and the macroscopic equations on a flat spacetime occupied by an anisotropic medium. This equivalence is fundamental in transformation optics [Section 4 of Reference 28], the theoretical basis for metamaterials. Not all anisotropic media represent spacetime geometries, there is a necessary and sufficient condition for it [Section 4 of Reference 28]: The electric permittivity and magnetic permeability tensors must be equal to each other and equal to a certain function of the spacetime metric  $\epsilon^{ij} = \mu^{ij} = f(g^{ij})$  [Section 4 of Reference 28]. At this point, the possible relationship with our results is apparent through the condition  $\epsilon^{ij} = \mu^{ij}$  and the conservation of helicity discovered by Bialynicki-Birula. Extending the proof in this section to interfaces between anisotropic media could lead to new insights.

Relation (11.18) is often referred to as surface impedance matching condition. It has already been explored in scattering from spheres [29] and in the context of

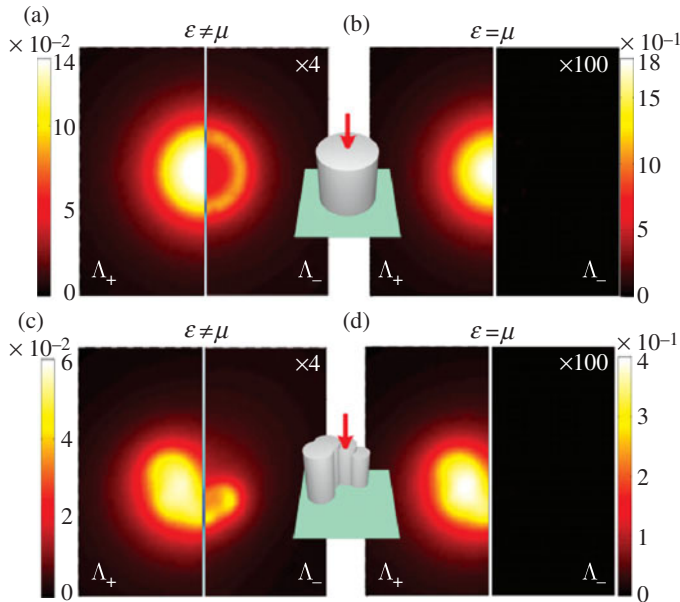


**FIGURE 11.2** Impact of the different symmetries on the field scattered by two dielectric structures. The upper row shows the scattered intensity for a symmetric cylinder and the lower row for a panflute like shape without any rotational, translational or spatial inversion symmetry. The length and diameter of the cylinder are 200 nm. The panflute is made of cylinders of different lengths and diameters, the longest one is 200 nm long and the total panflute's width is around 200 nm. In (a) and (c) the structures have  $\epsilon = 2.25$ ,  $\mu = 1$ , while in (b) and (d) we enforced duality symmetry by setting  $\epsilon = \mu = \epsilon_{\text{glass}} = 2.25$ . The incident field is a plane wave of well defined helicity equal to 1, momentum vector pointing to the positive  $z$  axis and a wavelength of 633 nm. Its electric field is  $(\hat{x} + i\hat{y})/\sqrt{2} \exp(kz - \omega t)$ . The left half side of each subfigure corresponds to the scattered field with helicity equal to the incident plane wave  $\Lambda_+$ ; the right half is for the opposite helicity  $\Lambda_-$ . The calculation plane is perpendicular to the  $z$  axis and 20 nm away from the surface of the scatterers opposite to the one where the incident field comes from. The calculation area is  $700 \times 700$  nm. For color scaling purposes, the right half side is multiplied by the factor in the upper right corner. The (lack of) cylindrical symmetry of the structures results in (non)-cylindrically symmetric field patterns, which is consistent with the geometry of each case. On the other hand, both scatterers behave identically with respect to conservation of helicity, which is seen to depend exclusively on the electromagnetic properties of the material. (For a color version of this figure, see the color plate section.)

plasmonic metamaterials [30]. The above derivation shows that these particular cases are part of a more general, geometry independent symmetry: electromagnetic duality.

The independence of helicity conservation from geometry is illustrated in Figure 11.2. We analyzed the helicity change for two different dielectric structures in free space: A circular cylinder, which is symmetric under rotations along its axis, and a curved pan-flute like structure without any rotational or translational symmetry. Two

versions of each structure were simulated, corresponding to two different materials: the first one would represent silica by setting  $\epsilon = \epsilon_{\text{glass}} = 2.25$  and  $\mu = \mu_{\text{glass}} = 1$ . In the second material we enforce duality (11.18), by setting  $\epsilon = \mu = \epsilon_{\text{glass}} = 2.25$ . The incident field is a circularly polarized plane wave (i.e., it has well defined helicity) propagating parallel to the axis of the cylinder and the curved surface of the pan-flute. The intensities of the two helicities ( $\pm$ ) are computed as  $|\mathbf{E} \pm i\mathbf{H}|^2$ . In Section 2.1 of Reference 27, it is shown that  $\mathbf{E} \pm i\mathbf{H}$  (with our choice of units) separates the two helicity components. Figure 11.2 shows that helicity is conserved independently of the spatial symmetries, whenever Eq. (11.18) is fulfilled, that is, under conditions of duality symmetry. On the other hand, conservation of angular momentum, resulting in cylindrical symmetry of the scattered fields, is only achieved in the case of the cylinder.

We would like to now turn our attention to some electromagnetic problems where the application of these concepts provides new insight and allows a simple and deep understanding.

## 11.6 APPLICATIONS OF THE FRAMEWORK

### 11.6.1 Spin to Orbit Angular Momentum Transfer

The conversion between spin and orbital angular momentum is widely used to explain phase singularities in numerical simulations of tightly focused fields [31–33], and in scattering experiments [34–36]. A detailed discussion of the SAM to OAM conversion can be found in Reference 37.

We will now use symmetries and conserved quantities arguments, particularly those related to  $J_z$  and  $\Lambda$ , to identify the actual physical reasons for those observations. We will demonstrate that the mechanism responsible for the presence of optical vortices in focused fields is totally different from the one responsible for the observation of optical vortices in scattering experiments. This, in our opinion, shows that the SAM-OAM formulation can be quite misleading: it assigns the same explanation to two distinct physical phenomena.

The analytical tools and methodology employed in this section allow a simple application of the ideas developed in the previous section to practical electromagnetic problems.

### 11.6.2 Bessel Beams with Well Defined Angular Momentum and Helicity

As already mentioned,  $J_z$  and  $\Lambda$  commute. For our analysis we will need a basis of transverse electromagnetic modes which are simultaneous eigenvectors of  $J_z$  and  $\Lambda$ . One such set of modes is a particular type of Bessel beams. Bessel beams have been thoroughly studied. See for instance the series of papers [38], [39], and [40].

A complete orthonormal basis for transverse electromagnetic fields consisting of Bessel beams with well defined third component of angular momentum  $J_z$  and helicity  $\Lambda$  can be constructed. These modes appear in Reference 3, although their relationship with helicity is not considered in that paper. In Reference 38, these type

of electromagnetic modes are obtained in a different way as linear combinations of other type of more commonly used Bessel beams, the transverse electric (TE) and transverse magnetic (TM) modes.

The real space expressions for this set of Bessel beams in cylindrical coordinates read as

$$\begin{aligned}\mathbf{C}_{mp_\rho}(\rho, \theta, z) &= \sqrt{\frac{p_\rho}{2\pi}} i^n \exp(i(p_z z + n\theta)) \\ &\left( \frac{i}{\sqrt{2}} \left( \left(1 + \frac{p_z}{k}\right) J_{n+1}(p_\rho \rho) \exp(i\theta) \hat{\mathbf{r}} + \left(1 - \frac{p_z}{k}\right) J_{n-1}(p_\rho \rho) \exp(-i\theta) \hat{\mathbf{l}} \right) - \frac{p_\rho}{k} J_n(p_\rho \rho) \hat{\mathbf{z}} \right), \\ \mathbf{D}_{mp_\rho}(\rho, \theta, z) &= \sqrt{\frac{p_\rho}{2\pi}} i^n \exp(i(p_z z + n\theta)) \\ &\left( \frac{i}{\sqrt{2}} \left( \left(1 - \frac{p_z}{k}\right) J_{n+1}(p_\rho \rho) \exp(i\theta) \hat{\mathbf{r}} + \left(1 + \frac{p_z}{k}\right) J_{n-1}(p_\rho \rho) \exp(-i\theta) \hat{\mathbf{l}} \right) + \frac{p_\rho}{k} J_n(p_\rho \rho) \hat{\mathbf{z}} \right),\end{aligned}\tag{11.19}$$

where a harmonic  $\exp(-iwt)$  dependence has been assumed and

$$\begin{aligned}p_\rho &= \sqrt{k_x^2 + k_y^2}, k^2 = p_\rho^2 + p_z^2, \\ \hat{\mathbf{l}} &= \frac{\hat{\mathbf{x}} + i\hat{\mathbf{y}}}{\sqrt{2}}, \hat{\mathbf{r}} = \frac{\hat{\mathbf{x}} - i\hat{\mathbf{y}}}{\sqrt{2}}.\end{aligned}$$

By construction, the two types of vector wave functions  $\mathbf{C}_{mp_\rho}$  and  $\mathbf{D}_{mp_\rho}$  have a sharp value of the  $z$  component of angular momentum  $J_z$  equal to  $m$  and a sharp value of helicity  $\Lambda$  equal to  $-1$  and  $+1$ , respectively. Additionally, they have well defined values for the energy  $H$  and the  $z$  component of the linear momentum  $P_z$  proportional to  $k$  and  $p_z$ , respectively. For a given value of  $k$ , a well defined value of  $P_z$  implies a well defined value of the transverse momentum  $P_\rho$  proportional to  $p_\rho$ . Modes (11.19) form a complete orthonormal basis of transverse electromagnetic fields when

$$k \in [0, \infty), \quad n \in [0, \pm 1, \pm 2, \dots], \quad p_\rho \in [0, \infty), \text{ and } \Lambda = \pm 1,\tag{11.20}$$

and both signs of  $p_z$  in  $p_z = \pm \sqrt{k^2 - p_\rho^2}$  are considered. In the following, the consideration of both signs of  $p_z$  is implicitly made.

### 11.6.3 Optical Vortices in Focusing

In order to study why optical vortices seem to appear in numerical studies of focalization of apparently vortex free beams [31–33], we analyze the aplanatic lens model [41], which is routinely used to study the effects of high numerical aperture lenses.

The action of an aplanatic lens preserves  $J_z$  and  $\Lambda$  [37]. The cylindrical symmetry of the model can be reasonably expected, but its invariance under duality transformations is “hidden” in the assumption that the lens transmission coefficients for the two polarization components, TE and TM, are identical and that there is no crosstalk between input and output TE and TM components. That this assumption implies duality symmetry (helicity conservation) is proved in Appendix A of Reference 18. The preservation of  $\Lambda$  by an aplanatic lens has been discussed in Reference 37 without using its relationship to electromagnetic duality.

Even though the model has both cylindrical and duality symmetries, the focalized beam is quite different from the input beam: some other symmetry must be broken. In this case, it is clear that we lack translational symmetry on the plane perpendicular to the optical axis of the lens. We know that the transverse momentum components  $P_x$  and  $P_y$  are the generators of that symmetry. We will now show that the differences between the input and focalized beams are due to changes in  $(k_x, k_y)$ . We will prove this point using the basis introduced in (11.19).

Let us take a collimated right circularly (RC) polarized Gaussian beam going through an aplanatic lens of high numerical aperture. The linear momentum components of a collimated beam are all almost totally aligned with the propagation direction  $z$ :  $p_z \approx k$ . Consequently, a collimated beam only has components with small transverse momentum value  $p_\rho$ . With respect to (11.19), in the limit when  $p_z \approx k$  ( $\frac{p_\rho}{k} \rightarrow 0$ ), both  $\mathbf{C}_{mp_\rho}$  and  $\mathbf{D}_{mp_\rho}$  approach pure RC and LC polarized modes, respectively. This can be easily seen by setting a  $\frac{p_\rho}{k} \rightarrow 0 \Rightarrow (p_z \approx k)$  in (11.19):

$$\mathbf{C}_{mp_\rho}(\rho, \theta, z) \approx \sqrt{\frac{p_\rho}{\pi}} i^{n+1} \exp(ip_z z) J_{n+1}(p_\rho \rho) \exp(i\theta(n+1)) \hat{\mathbf{r}}, \quad (11.21)$$

$$\mathbf{D}_{mp_\rho}(\rho, \theta, z) \approx \sqrt{\frac{p_\rho}{\pi}} i^{n+1} \exp(ip_z z) J_{n-1}(p_\rho \rho) \exp(i\theta(n-1)) \hat{\mathbf{l}}. \quad (11.22)$$

The other polarization components, the opposite circular and the longitudinal  $\hat{\mathbf{z}}$  component, are strongly attenuated in this regime. Importantly though, they are actually present: without them, the modes are not solutions of Maxwell’s equations, and cannot be consistently analyzed by means of the transformation properties of general electromagnetic fields.

From (11.21), and since the collimated input RC Gaussian beam does not have a phase singularity in its  $\hat{\mathbf{r}}$  dominant polarization, we can conclude that mostly  $C$  type modes with  $n = -1$  will exist in its expansion in the (11.19) basis:

$$\mathbf{E}_{\text{input}} = \int_0^\infty dp_\rho c_{-1,p_\rho}^{\text{input}} \mathbf{C}_{mp_\rho}, \quad (11.23)$$

where  $c_{-1,p_\rho}^{\text{input}}$  is only significant when  $\frac{p_\rho}{k} \rightarrow 0$ . Equation (11.23) defines a beam with a sharp value of  $J_z$ ,  $n = -1$ , and a sharp value of  $\Lambda$ ,  $\lambda = -1$ . As per the above discussion regarding symmetries, the output beam must also have sharp  $J_z$  and  $\Lambda$

values of  $n = -1$  and  $\lambda = -1$ . Focusing can hence only change the relative weight of  $p_\rho$  components. Intuitively, modes with higher transverse momentum are needed to expand the field after focusing.

$$\mathbf{E}_{\text{foc}} = \int_0^\infty dp_\rho c_{-1,p_\rho}^{\text{foc}} \mathbf{C}_{mp_\rho}, \quad (11.24)$$

this is in line the non-preservation of  $(k_x, k_y)$  due to broken transverse translational symmetry. The fact that the change is limited to  $p_\rho = \sqrt{k_x^2 + k_y^2}$  could have been foreseen: it stems from the cylindrical symmetry of the model.

Now, let's go back to Eq. (11.19) and check the spatial shape of  $\mathbf{C}_{mp_\rho}$  modes when  $m = -1$  and the condition  $\frac{p_\rho}{k} \rightarrow 0$  is not met:

$$\begin{aligned} \mathbf{C}_{mp_\rho}(\rho, \theta, z) = & -\sqrt{\frac{p_\rho}{2\pi}} i \exp(ip_z z) \left( \frac{i}{\sqrt{2}} \left( 1 + \frac{p_z}{k} \right) J_0(p_\rho \rho) \hat{\mathbf{r}} \right. \\ & \left. + \frac{i}{\sqrt{2}} \left( 1 - \frac{p_z}{k} \right) J_{-2}(p_\rho \rho) \exp(-i2\theta) \hat{\mathbf{l}} - \frac{p_\rho}{k} J_{-1}(p_\rho \rho) \exp(-i\theta) \hat{\mathbf{z}} \right). \end{aligned} \quad (11.25)$$

The  $\mathbf{C}_{mp_\rho}, \frac{p_\rho}{k} \rightarrow 0$  modes are almost purely right polarized, but when  $p_\rho$  increases, the terms multiplying  $\hat{\mathbf{l}}$  and  $\hat{\mathbf{z}}$  become significant. As it can be seen in (11.25), for  $m = -1$  these newly enhanced terms have phase singularities of orders minus two and minus one, respectively. Figure 11.3 shows the radial spatial profiles of the three

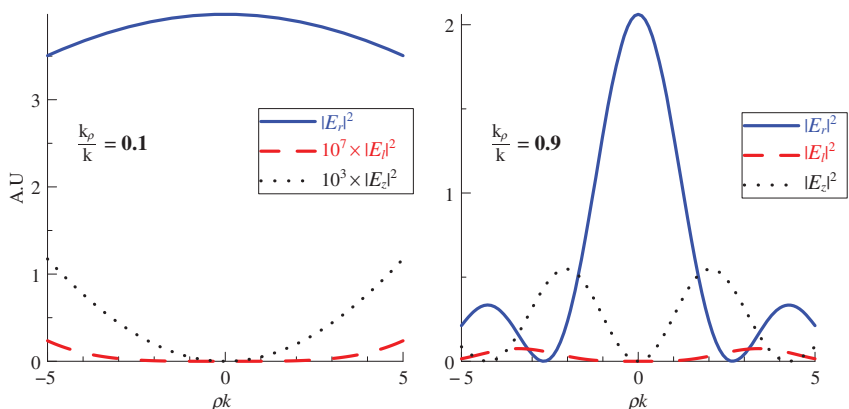


**FIGURE 11.3** Normalized field intensity for the right, left and longitudinal polarization components for two  $\mathbf{C}_{mp_\rho}$ ,  $n = -1$  modes, one with  $\frac{p_\rho}{k} = 0.1$  (left figure) and the other with  $\frac{p_\rho}{k} = 0.9$ . Note the scaling of the non-dominant polarization components on the  $\frac{p_\rho}{k} = 0.1$  case.

polarization components for two  $\mathbf{C}_{-1,p_\rho}(\rho, \theta, z)$  modes, one with  $\frac{p_\rho}{k} = 0.1$  and the other with  $\frac{p_\rho}{k} = 0.9$ . In the small  $p_\rho$  case (Fig. 11.3a), the dominant polarization component  $\hat{\mathbf{r}}$  is much stronger than the  $\hat{\mathbf{l}}$  and  $\hat{\mathbf{z}}$  components (which are nonetheless present). In the large  $p_\rho$  case (Fig. 11.3b), the relative weight between the intensity of the different polarizations has shifted significantly. The vortices of charge  $-1$  in  $\hat{\mathbf{z}}$  and charge  $-2$  in  $\hat{\mathbf{l}}$  (see Eq. 11.25) become relatively more important.

We argue that these are the optical vortices appearing in numerical simulations of focused beams are due to the inherent spatial properties of light modes with definite energy,  $P_z$ ,  $J_z$  and  $\Lambda$  propagating through a system that conserves energy,  $\Lambda$  and  $J_z$  while breaking transverse translational invariance. The lens shifts the weight distribution towards modes with larger  $p_\rho$  values and optical vortices already existing in the initially strongly attenuated polarization components of the input beam gain relative importance in the focalized beam.

For the theoretical study of optical vortices in focused beams, References 31 and 37 use solutions of the paraxial equation as the input modes, instead of using solutions of the full Maxwell equations as we have done. Since paraxial input modes do not have the attenuated phase singularities in the other polarization components because only a single polarization component is non zero, the appearance of optical vortices upon focusing was attributed to SAM to OAM conversion.

It is worth mentioning that  $\mathbf{J}$  can always be decomposed into two separately meaningful operators  $\hat{\mathbf{S}} = \Lambda \frac{\mathbf{P}}{|\mathbf{P}|}$  and  $\hat{\mathbf{L}} = \mathbf{J} - \hat{\mathbf{S}}$  such that  $\mathbf{J} = \hat{\mathbf{L}} + \hat{\mathbf{S}}$  [3, 24, 38, 42, 43]. However, these two operators are not angular momenta since they do not fulfill the correct commutation relationships, but their components might be used to analyze electromagnetic problems in a way similar to how we have used  $J_z$  and  $\Lambda$ . There is one important caveat though: loss of geometry independence. This is illustrated by the fact that the property associated with  $\Lambda P_z / |\mathbf{P}|$  is not preserved upon focusing. Helicity is conserved but, due to the lack of translational symmetry in the transverse plane,  $P_\rho$  changes, which implies that  $P_z$  changes. The fact that the lack of a “geometrical” symmetry breaks the conservation law corresponding to  $\Lambda P_z / |\mathbf{P}|$  indicates that the symmetry transformation generated by such “spin operator” is, in general, not independent of the geometry of the problem. In a recent work [44], it has been shown that the components of  $\hat{\mathbf{S}}$  are the generators of helicity and frequency dependent translations while the components of  $\hat{\mathbf{L}}$  generate commuting compositions of rotations and the transformations generated by  $\hat{\mathbf{S}}$ . Simultaneous eigenvectors of  $\hat{\mathbf{S}}$  and parity seem to have a role in the study of the interaction of light with chiral molecules.

#### 11.6.4 Optical Vortices in Scattering

The experimental observation of optical vortices in scattered fields has been reported in the literature [34–36]. In these papers, the observations are explained by means of spin to orbit angular momentum conversion during the interaction with the scatterer. Recently, similar observations have been analyzed in Reference 45 using symmetries

and conserved quantities. In line with the discussion of the last paper, we will show in this section that these experimental observations can be explained as a partial helicity change during the light-matter interaction due to the breaking of electromagnetic duality symmetry in the system. We will also argue that the helicity change is enhanced by physical effects which strongly break duality, beyond the inherent duality asymmetry of general planar multilayer structures.

We have already mentioned several times that helicity transforms independently of the geometry of the scatterer. In particular, it transforms independently of whether the considered system has cylindrical symmetry or not. Nevertheless, as seen below, a change in helicity is very clearly identifiable in the spatial patterns of the scattered fields when the system has cylindrical symmetry. Several of the experimental setups and input beams in the articles cited in this section have cylindrical symmetry and are similar to the system in Figure 11.4, which we will now analyze.

In Figure 11.4, we distinguish the preparation and measurement apparatus from the focusing and scattering part of the setup. In the preparation stage, a collimated Gaussian beam goes through a linear polarizer (LP) and quarter wave plate (QWP), which results in a beam with well defined values of  $J_z$  and  $\Lambda$  (see more details below). In the central part, the beam is focused onto a cylindrically symmetric target and the resulting scattered light is collected by another lens. The measurement part of the setup uses another QWP and LP to project light with different helicity depending on the setting of the LP (see more details below).

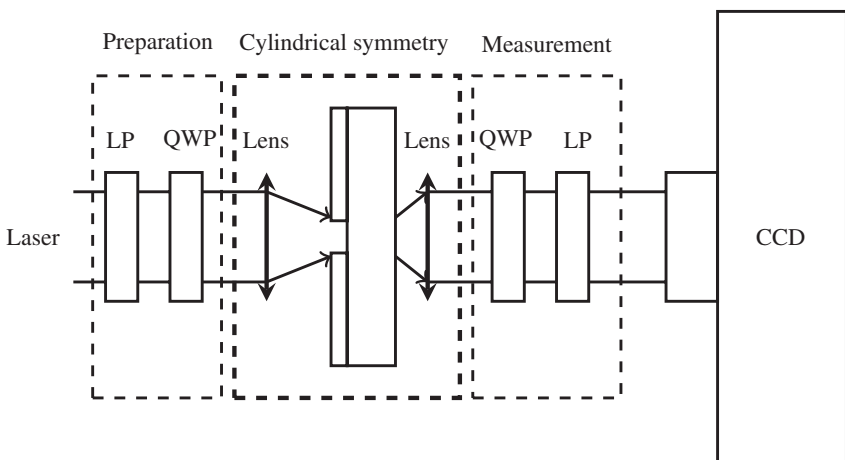


**FIGURE 11.4** Archetypal experimental setup. A collimated beam is circularly polarized by means of a linear polarizer (LP) and a quarter wave plate (QWP). After focusing, the beam interacts with a cylindrically symmetric target, in this example, a circular nano-aperture in a metallic film on a substrate. A portion of the scattered field is collected and collimated by a second lens, analyzed by a second set of QWP and LP, and its spatial profile is imaged into a Charged Couple Device (CCD) camera. The two orthogonal settings of the last LP allow the projection of the two collimated helicity modes (see the text for details).

At first sight, the central part is cylindrically symmetric but lacks translational symmetry in the transverse plane. We should hence expect conservation of  $J_z$  and, as in Section 11.6.3, non-conservation of  $P_\rho$ . Since the lenses preserve helicity, the behavior of the system with respect to  $\Lambda$  depends on whether the target sample meets condition (11.18). Let us assume that it does not meet such condition.

Let us imagine that, after the first LP and QWP, the input to the first lens is a predominantly RC polarized Gaussian beam. Assuming perfect optical elements, and using the same arguments as in Section 11.6.3, we can see that the input beam can be expanded using basis (11.19) into modes with  $\frac{p_\rho}{k} \rightarrow 0$  and sharp values of  $J_z$ ,  $n = -1$ , and of  $\Lambda$ ,  $\lambda = -1$ . The first lens will focus the beam into the sample without altering either  $J_z$  or  $\Lambda$ , then, since it is assumed that the sample does not meet (11.18), part of the light will change helicity upon interacting with the cylindrically symmetric target and, after collimation with the second lens, there will be two types of collimated modes, both with  $n = -1$ , but differing in the value of helicity. Schematically representing the actions of the lenses and the cylindrically symmetric scatterer as transformations of fields expanded in the basis (11.19) by coordinates  $c_{mp_\rho}$  and  $d_{mp_\rho}$ , we may summarize the whole sequence as

$$c_{-1, \frac{p_\rho}{k} \rightarrow 0} \xrightarrow{\text{Lens}} c_{-1, k_\rho} \xrightarrow{\text{Scattering}} (c_{-1, k_\rho}, d_{-1, k_\rho}) \xrightarrow{\text{Lens}} \left( c_{-1, \frac{p_\rho}{k} \rightarrow 0}, d_{-1, \frac{p_\rho}{k} \rightarrow 0} \right). \quad (11.26)$$

The corresponding modal expressions for the components of the two types of output modes are

$$\begin{aligned} \mathbf{C}_{-1, \frac{p_\rho}{k} \rightarrow 0}(\rho, \theta, z) &\approx \sqrt{\frac{p_\rho}{\pi}} i^2 \exp(ip_z z) J_0(p_\rho \rho) \hat{\mathbf{r}}, \\ \mathbf{D}_{-1, \frac{p_\rho}{k} \rightarrow 0}(\rho, \theta, z) &\approx \sqrt{\frac{p_\rho}{\pi}} i^2 \exp(ip_z z) J_{-2}(p_\rho \rho) \exp(-i2\theta) \hat{\mathbf{l}}. \end{aligned} \quad (11.27)$$

That is, a predominantly RC beam similar to the input, without any phase singularity in  $\hat{\mathbf{r}}$  and a predominantly LC vortex beam with a singularity of charge two in  $\hat{\mathbf{l}}$ . If we set the last LP to project the LC component of the output collimated beam, this vortex will appear in the CCD camera.

We argue that these are the vortices observed in the cylindrically symmetric scattering experiments of [34, Fig. 4], [35, Figs. 2(c)–(d)] and [36], and that the underlying reason for their appearance is that the electromagnetic duality symmetry is broken in those systems.

The samples used in References 34 and 35 consist of nano-apertures on metallic thin films. The breaking of duality in a general planar multilayer structure, and in particular when it includes a metal, is clear since the relative electric and magnetic constants of the system will not meet condition (11.18). Nevertheless, as shown in Reference 45, the effect due to the multilayer alone is typically small in terms of

helicity conversion. The reason why the helicity conversion is enhanced making it easily detectable, is that the nano-apertures allow for light to couple to the natural modes of the multilayer system, where duality is strongly broken. In a multilayer system, the natural modes are either TE or TM resonances. Since a mode with well defined helicity has equal contributions from TE and TM components (see Appendix A in Reference 18), a TE only or TM only resonance implies a strong breaking of electromagnetic duality. The interfaces between a metal and a dielectric allow the existence of surface plasmon polaritons of TM only character. As shown in Reference 45, the influence of these modes in the transmitted light is responsible for the experimentally detectable helicity change.

In Reference 36, optical vortices are observed upon propagation of light through a planar semiconductor microcavity, still a cylindrically symmetric system as noted in that work. In this case, duality is strongly broken in the multilayer itself by the energy splitting between TE and TM modes in the structure. This splitting is identified in that work as the enabler for SAM to OAM conversion.

References 34 and 35 contain also results for non-cylindrically symmetric setups. Even though their study using  $J_z$  is not as simple, we are confident that the generality of the methodology that we propose can lead to further physical insights. For instance, for the square nano-apertures studied in Reference 35, the same argumentation about the nano-aperture mediated coupling onto strong duality breaking multilayer natural modes applies.

### 11.6.5 Kerker Conditions

Consider the unusual scattering effects for magnetic spheres reported by Kerker [29]. One of them refers to the fact that a plane wave impinging on a vacuum embedded sphere with  $\frac{\epsilon}{\mu} = 1$  does not produce any backscattered field (at a  $180^\circ$  scattering angle). This effect, which has been referred to as an anomaly [46], can be easily understood using our results. Let us take as incident field a circularly polarized plane wave with momentum aligned along the  $z$  axis. Its angular momentum is also aligned with the  $z$  axis and, in natural units of  $\hbar = 1$ , equal to  $\pm 1$  depending on the handedness of the polarization. We now know (Eq. 11.18) that, based only on the properties of the materials, helicity has to be preserved in the interaction between the plane wave and a dual sphere. Let us now assume that there exist a component of backscattered field at  $180^\circ$ , that is, a plane wave whose linear momentum is the negative of the linear momentum of the incident plane wave. Recalling that  $\Lambda = \mathbf{J} \cdot \mathbf{P}/|\mathbf{P}|$ , we see that, to preserve helicity, the angular momentum of the backscattered plane wave must also change sign with respect to the angular momentum of the incident plane wave. But such change is impossible: the rotational symmetry of the sphere implies that angular momentum is preserved in all axes, in particular along the axes shared by the incident and the backscattered plane waves. As a consequence, the backscattering amplitude must be zero. Since this argument applies independently to both circular polarizations, the backscattering gain will be zero for any polarization of the incoming plane wave. What is sometimes referred to as the first Kerker condition is hereby explained. Interestingly, zero backscattering from dual objects has already been the

object of investigation by the radar community [47]: in these works, the connection between duality and helicity is not recognized.

In the same paper, Kerker finds that upon scattering off a vacuum embedded sphere with  $\frac{\epsilon}{\mu} = 1$ , the state of polarization of light is preserved independently of the scattering angle. The root cause of such interesting phenomenon is the simultaneous invariance of the system with respect to duality transformations, due to the materials, and any mirror operations through planes containing the origin of coordinates, due to the geometry. In the helicity basis, the  $2 \times 2$  scattering matrix between an incident and a scattered plane wave [48, Chapter 3] must be diagonal because of helicity preservation. Additionally, it must also preserve the linear polarizations parallel and perpendicular to the plane containing the two plane wave momentum vectors, because a mirror operation across such plane leaves the sphere and both momentum vectors invariant. Using then that helicity flips with mirror operations, it can be easily shown that all the  $2 \times 2$  scattering matrices are indeed diagonal and hence preserve the state of polarization between any pair of incident and scattered plane waves.

## 11.7 CONCLUSIONS

In this chapter, we have shown that the restoration of duality symmetry is possible for the macroscopic Maxwell's equations, even though the microscopic equations are rendered asymmetric by the empirical absence of magnetic charges. The restoration of the symmetry is independent of the geometry of the problem: a system made of piecewise isotropic and homogeneous domains of different materials characterized by electric and magnetic constants  $(\epsilon_i, \mu_i)$  is invariant under duality transformations if and only if  $\frac{\epsilon_i}{\mu_i} = \alpha \forall$  media  $i$ . This result is independent of the shapes of the domains. With this result, the known relationship between helicity and duality transformations, namely that the former is the generator of the latter, is turned into a simple and powerful tool for the practical study of light-matter interactions using symmetries and conserved quantities.

We are confident that the reader will find the analytical tools that we have explained here, mainly the use of duality symmetry and its related helicity conservation, useful in the treatment of problems in photonics and electromagnetism. In particular, we have shown how to apply it to some experiments and gain valuable insight with it. We have also shown how to use these concepts to explain some unusual scattering effects in a straightforward way. In Reference 18, it allowed to proof the inconsistency of the concept of optical spin to orbital angular momentum conversion in focusing and scattering, and to propose a substitute framework based on helicity. Another example where the use of the concept helicity is relevant is in the treatment of optical activity [21].

Our results may be useful in other fields. For example, they may prove important in the field of metamaterials and transformation optics [49], which is dramatically extending the range of wavelengths where effective electric and magnetic constants can be engineered. The transfer of helicity between light and matter remains an open line of research, which could have importance in the fields of plasmonics and

“spintronics” [50], where the control of the helicity of electrons is crucial. Finally, it can be seen that the same tools we have developed here can be successfully used to explain recently reported effects in electron beams [51]. This parallelism is an encouraging sign towards the possibility of simulating particle interactions on an optical table [52].

## REFERENCES

- [1] A. Noether, “Invariante variationsprobleme,” *Nachr. D. König. Gesellsch. D. Wiss. Zu Göttingen, Math-Phys.* 235–257 (1918).
- [2] M. E. Rose, *Elementary Theory of Angular Momentum* (Wiley, New York, 1957).
- [3] S. J. Van Enk and G. Nienhuis, “Commutation rules and eigenvalues of spin and orbital angular momentum of radiation fields,” *J. Mod. Opt.* **41**(5), 963–977 (1994).
- [4] C. Cohen-Tannoudji, J. Dupont-Roc, and G. Grynberg, *Photons and Atoms - Introduction to Quantum Electrodynamics* (Wiley, New York, 1989).
- [5] M. G. Calkin, “An invariance property of the free electromagnetic field,” *Am. J. Phys.*, **33**(11), 958 (1965).
- [6] W.-K. Tung, *Group Theory in Physics* (World Scientific, 1985).
- [7] S. Deser and C. Teitelboim, “Duality transformations of abelian and non-abelian gauge fields,” *Phys. Rev. D*, **13**(6), 1592–1597 (1976).
- [8] I. Salom, “Algebraic approach to the duality symmetry,” *arXiv:hep-th/0602282v1* (2006).
- [9] R. P. Cameron, S. M. Barnett, and A. M. Yao, “Optical helicity, optical spin and related quantities in electromagnetic theory,” *New J. Phys.* **14**(5), 053050 (2012).
- [10] S. M. Barnett, R. P. Cameron, and A. M. Yao, “Duplex symmetry and its relation to the conservation of optical helicity,” *Phys. Rev. A* **86**(1), 013845 (2012).
- [11] P. D. Drummond, “Dual symmetric lagrangians and conservation laws,” *Phys. Rev. A* **60**(5), R3331–R3334 (1999).
- [12] P. D. Drummond, “Dual-symmetric lagrangians in quantum electrodynamics: I. conservation laws and multipolar coupling,” *J. Phys. B* **39**(15), S573 (2006).
- [13] K. Y. Bliokh, A. Y. Bekshaev, and F. Nori, “Dual electromagnetism: helicity, spin, momentum and angular momentum,” *New J. Phys.* **15**(3), 033026 (2013).
- [14] K. Y. Bliokh and F. Nori, “Characterizing optical chirality,” *Phys. Rev. A* **83**(2), 021803 (2011).
- [15] M. M. Coles and D. L. Andrews, “Chirality and angular momentum in optical radiation,” *Phys. Rev. A* **85**(6), 063810 (2012).
- [16] D. Zwanziger, “Quantum field theory of particles with both electric and magnetic charges,” *Phys. Rev.* **176**, 1489–1495 (1968).
- [17] I. Fernandez-Corbaton, X. Zambrana-Puyalto, N. Tischler, X. Vidal, M. L. Juan, and G. Molina-Terriza, “Electromagnetic duality symmetry and helicity conservation for the macroscopic maxwells equations,” *Phys. Rev. Lett.* **111**(6), 060401 (2013).
- [18] I. Fernandez-Corbaton, X. Zambrana-Puyalto, and G. Molina-Terriza, “Helicity and angular momentum: a symmetry-based framework for the study of light-matter interactions,” *Phys. Rev. A* **86**(4), 042103 (2012).

- [19] X. Zambrana-Puyalto, I. Fernandez-Corbaton, M. L. Juan, X. Vidal, and G. Molina-Terriza, “Duality symmetry and kerker conditions,” *Opt. Lett.* **38**(11), 1857–1859 (2013).
- [20] X. Zambrana-Puyalto, X. Vidal, M. L. Juan, and G. Molina-Terriza, “Dual and anti-dual modes in dielectric spheres,” *Opt. Express* **21**(15), 17520–17530 (2013).
- [21] I. Fernandez-Corbaton, X. Vidal, N. Tischler, and G. Molina-Terriza, “Necessary symmetry conditions for the rotation of light,” *J. Chem. Phys.* **138**(21), 214311–214311–7 (2013).
- [22] I. Fernandez-Corbaton and G. Molina-Terriza, “Role of duality symmetry in transformation optics,” *Phys. Rev. B* **88**(8), 085111 (2013).
- [23] I. Fernandez-Corbaton, “Forward and backward helicity scattering coefficients for systems with discrete rotational symmetry,” *Opt. Express* **21**(24), 29885–29893 (2013).
- [24] A. Messiah, *Quantum Mechanics* (Dover, 1999).
- [25] J. D. Jackson, *Classical Electrodynamics* (John Wiley & Sons, 1998).
- [26] L. Novotny and B. Hecht, *Principles of Nano-Optics* (Cambridge University Press, 2006).
- [27] I. Bialynicki-Birula, “Photon wave function,” in *Progress in Optics*, edited by E. Wolf (Elsevier, 1996), Vol. 36, pp. 245–294.
- [28] U. Leonhardt and T. G. Philbin, “Transformation optics and the geometry of light,” *Prog. Opt.* **53**, 69–152 (2009).
- [29] M. Kerker, D. S. Wang, and C. L. Giles, “Electromagnetic scattering by magnetic spheres,” *J. Opt. Soc. Am.* **73**(6), 765–767 (1983).
- [30] J. W. Lee, M. A. Seo, J. Y. Sohn, Y. H. Ahn, D. S. Kim, S. C. Jeoung, C. Lienau, and Q.-H. Park, “Invisible plasmonic meta-materials through impedance matching to vacuum,” *Opt. Express* **13**(26), 10681–10687 (2005).
- [31] Y. Zhao, J. S. Edgar, G. D. M. Jeffries, D. McGloin, and D. T. Chi, “Spin-to-orbital angular momentum conversion in a strongly focused optical beam,” *Phys. Rev. Lett.* **99**, 073901 (2007).
- [32] T. A. Nieminen, A. B. Stilgoe, N. R. Heckenberg, and H. Rubinsztein-Dunlop, “Angular momentum of a strongly focused gaussian beam,” *J. Opt. A* **10**(11), 115005 (2008).
- [33] A. M. Yao and M. J. Padgett, “Orbital angular momentum: origins, behavior and applications,” *Adv. Opt. Photon.* **3**(2), 161–204 (2011).
- [34] Y. Gorodetski, N. Shitrit, I. Bretner, V. Kleiner, and E. Hasman, “Observation of optical spin symmetry breaking in nanoapertures,” *Nano Lett.* **9**(8), 3016–3019 (2009).
- [35] L. T. Vuong, A. J. L. Adam, J. M. Brok, P. C. M. Planken, and H. P. Urbach, “Electromagnetic spin-orbit interactions via scattering of subwavelength apertures,” *Phys. Rev. Lett.* **104**, 083903 (2010).
- [36] F. Manni, K. G. Lagoudakis, T. K. Paraïso, R. Cerna, Y. Léger, T. C. H. Liew, I. A. Shelykh, A. V. Kavokin, F. Morier-Genoud, and B. Deveaud-Plédran, “Spin-to-orbital angular momentum conversion in semiconductor microcavities,” *Phys. Rev. B* **83**, 241307 (2011).
- [37] K. Y. Bliokh, E. A. Ostrovskaya, M. A. Alonso, O. G. Rodríguez-Herrera, D. Lara, and C. Dainty, “Spin-to-orbital angular momentum conversion in focusing, scattering, and imaging systems,” *Opt. Express* **19**(27), 26132–26149 (2011).
- [38] R. Jáuregui and S. Hacyan, “Quantum-mechanical properties of Bessel beams,” *Phys. Rev. A* **71**, 033411 (2005).

- [39] R. Jáuregui, “Rotational effects of twisted light on atoms beyond the paraxial approximation,” *Phys. Rev. A* **70**, 033415 (2004).
- [40] S. Hacyan and R. Jáuregui, “A relativistic study of Bessel beams,” *J. Phys. B* **39**, 1669 (2006).
- [41] B. Richards and E. Wolf, “Electromagnetic diffraction in optical systems. II. Structure of the image field in an aplanatic system,” *Proc. R. Soc. London* **253**(1274), 358–379 (1959).
- [42] K. Y. Bliokh, M. Alonso, E. Ostrovskaya, and A. Aiello, “Angular momenta and spin-orbit interaction of nonparaxial light in free space,” *Phys. Rev. A* **82**(6), 063825 (2010).
- [43] I. Bialynicki-Birula and Z. Bialynicka-Birula, “Canonical separation of angular momentum of light into its orbital and spin parts,” *J. Opt.* **13**(6), 064014 (2011).
- [44] I. Fernandez-Corbaton, X. Zambrana-Puyalto, and G. Molina-Terriza, “On the transformations generated by the electromagnetic spin and orbital angular momentum operators,” *J. Opt. Soc. Am. B* **31**(9), 2136–2141 (2014).
- [45] I. Fernandez-Corbaton, X. Zambrana-Puyalto, N. Tischler, X. Vidal, M. L. Juan and G. Molina-Terriza, “Electromagnetic Duality Symmetry and Helicity Conservation for the Macroscopic Maxwell’s Equations,” *Phys. Rev. Lett.* **111**(6), 060401 (2013).
- [46] M. Nieto-Vesperinas, R. Gomez-Medina, and J. J. Saenz, “Angle-suppressed scattering and optical forces on submicrometer dielectric particles,” *J. Opt. Soc. Am. A* **28**(1), 54–60 (2011).
- [47] I. Lindell, A. Sihvola, P. Yla-Oijala, and H. Wallen, “Zero backscattering from self-dual objects of finite size,” *IEEE Trans. Antennas Propag.* **57**(9), 2725 –2731 (2009).
- [48] S. Weinberg, *The Quantum Theory of Fields (Volume 1)*, 1st ed. (Cambridge University Press, 1995).
- [49] H. Chen, C. T. Chan, and P. Sheng, “Transformation optics and metamaterials,” *Nature Mater.* **9**(5), 387–396 (2010).
- [50] S. O. Valenzuela and M. Tinkham, “Direct electronic measurement of the spin hall effect,” *Nature* **442**(7099), 176–179 (2006).
- [51] E. Karimi, L. Marrucci, V. Grillo, and E. Santamato, “Spin-to-orbital angular momentum conversion and spin-polarization filtering in electron beams,” *Phys. Rev. Lett.* **108**, 044801 (2012).
- [52] R. Gerritsma, G. Kirchmair, F. Zahringer, E. Solano, R. Blatt, and C. F. Roos, “Quantum simulation of the Dirac equation,” *Nature* **463**(7277), 68–71 (2010).

---

# 12

---

## SLOW AND FAST LIGHT

ROBERT W. BOYD<sup>1,2,3</sup> AND ZHIMIN SHI<sup>4</sup>

<sup>1</sup>*The Institute of Optics, University of Rochester, Rochester, NY, USA*

<sup>2</sup>*Department of Physics and Astronomy, University of Rochester, Rochester, NY, USA*

<sup>3</sup>*Department of Physics and School of Electrical Engineering and Computer Science, University of Ottawa, Ottawa, ON, Canada*

<sup>4</sup>*Department of Physics, University of South Florida, Tampa, FL, USA*

### 12.1 INTRODUCTION

The pursuit of understanding the propagation of light has fascinated generations of scientists as well as the general public. The speed of light in vacuum,  $c$ , is a very important physical quantity for many fundamentals of our living universe, including the special relativity, Maxwell's equations. Yet while one talks about the speed of light in a medium, extra attention is needed to what she/he means by the speed of light [1]. For a monochromatic light, that is, an electromagnetic plane wave at a single frequency, the speed of light is usually defined by how fast a constant phase plane propagates. Mathematically, the phase velocity  $v_p$  of light within a medium is given by

$$v_p = \frac{\omega}{k} = \frac{c}{n}, \quad (12.1)$$

where  $k$  and  $\omega$  are the wave number and the angular frequency of the monochromatic field within the medium, respectively, and  $n$  is known as the refractive index of the medium at frequency  $\omega$ , which describes the material response of the medium to light at this specific frequency. Thus, such a speed is referred to as the *phase velocity* of light.

---

*Photonics: Scientific Foundations, Technology and Applications, Volume I*, First Edition.

Edited by David L. Andrews.

© 2015 John Wiley & Sons, Inc. Published 2015 by John Wiley & Sons, Inc.

On the other hand, the propagation speed of a wave packet, for example, a light pulse, could be quite different from the phase velocity. A wave packet can be seen as a temporal–spatial constitution of a group of different frequency components. To the first-order approximation, the propagation of such a wave packet can be considered as the propagation of a point for which the phase relation among all spectral components is retained. Such speed is usually referred to as the *group* velocity of light which is given by

$$v_g = \frac{d\omega}{dk} = \frac{c}{n_g}, \quad (12.2)$$

where

$$n_g \equiv n + \omega dn/d\omega \quad (12.3)$$

is known as the group index of the medium at frequency  $\omega$ . “Slow light” indicates the situation when  $\omega dn/d\omega > 0$ , so the group index  $n_g$  is larger than  $n$ , and the group velocity  $v_g$  becomes smaller than the phase velocity  $v_p$ . On the other hand, “fast light” represents situations when  $\omega dn/d\omega$  is negative, but its absolute value is less than  $n$ ; the group velocity  $v_g$  becomes smaller than the phase velocity  $v_p$ . Note that  $\omega dn/d\omega$  can be equal to or even less than  $-n$ . In such cases, the group velocity becomes infinity or even negative, and such phenomena are also known as “stopped light” or “backward light”, respectively.

The recent surge of interest in controlling the group velocity of light propagation, which started in the late 1990s, is partly indebted to the latest technologies that enable the achievement of exotic group indices. Remarkably slow group velocities of light,  $17 \text{ ms}^{-1}$  and  $57 \text{ ms}^{-1}$ , have been experimentally observed in Bose–Einstein condensates (BEC) [2] and in room-temperature Ruby crystals [3], respectively. Such a broad class of science and technologies that can dramatically change the group index of a medium within certain wavelength range is known as “slow and fast light” [1, 4] or simply “slow light”.

## 12.2 MECHANISMS OF SLOW LIGHT

In the last decade, scientists have explored a vast amount of various approaches to achieve slow light, which typically fall into one of the two general categories: material slow light and structural slow light.

### 12.2.1 Material Slow Light

Material slow light (also known as “microscopic slow light”) refers to those processes in which the change of group index is mainly due to light–matter interactions at the atomic or molecular level, that is, the interaction of light with a homogeneous

medium. The optical property of a non-magnetic material is often described by the dielectric susceptibility  $\chi$ . Generally speaking,  $\chi$  is a complex function of frequency  $\omega$  and is related to the generalized complex refractive index  $\tilde{n}$  through the relation of  $\tilde{n}^2 = 1 + \chi$  or  $\tilde{n} \approx 1 + 0.5\chi$  when  $|\chi| \ll 1$ .

While material slow light only indicates exotic frequency dependence of the real part of the complex refractive index  $\tilde{n}$  (or  $\chi$ ), the real part  $n'$  and the imaginary part  $n''$  of the refractive index as two functions of frequency  $\omega$  actually are related through the following Kramers–Kronig relation [5, 6]:

$$n'(\omega) = \frac{1}{\pi} \mathcal{P} \int_{-\infty}^{\infty} \frac{n''(\omega')}{\omega' - \omega} d\omega', \quad (12.4)$$

$$n''(\omega) = -\frac{1}{\pi} \mathcal{P} \int_{-\infty}^{\infty} \frac{n'(\omega')}{\omega' - \omega} d\omega'. \quad (12.5)$$

Note that the Kramers–Kronig relation is the description of causality in the frequency domain. As a consequence, the real part of the refractive index typically has a rapid swing in the vicinity of an absorption or gain feature. For example, the gain coefficient, refractive index, and reduced group index of an unsaturated Lorentzian gain line [7, 8] as functions of the frequency detuning  $\nu' = \nu - \nu_0$  from the resonance center  $\nu_0$  are given by

$$g(\nu') = g_0 \frac{\gamma^2}{\nu'^2 + \gamma^2}, \quad (12.6)$$

$$n(\nu') = n(0) + \frac{g_0 c}{4\pi\nu_0} \frac{\gamma\nu'}{\nu'^2 + \gamma^2}, \quad (12.7)$$

$$n'_g(\nu') = \frac{cg_0\gamma}{4\pi} \frac{-\nu'^2 + \gamma^2}{(\nu'^2 + \gamma^2)^2}, \quad (12.8)$$

where  $g_0$  is the gain coefficient at the center frequency  $\nu_0$ , respectively,  $\gamma$  is the half width at half maximum (HWHM) linewidth, and  $n(0)$  is the background refractive index at the resonance center. Here  $n'_g \equiv n_g - n$  is defined as the reduced group index. The profile of  $g$ ,  $n$ , and  $n_g$  near a Lorentzian-shaped gain feature is shown in Figure 12.1, which shows that one can achieve slow light ( $n_g > n$ ) near the center of the resonance and fast light ( $n_g < n$ ) in the wings of the resonance.

While such absorption-induced-slow-light features can be found in naturally available materials, such as atomic vapors [9], semiconductors [10], a lot of efforts have been given to use nonlinear optical processes to create controllable slow light at specific frequency range of interest. Some examples of such controllable slow light include electromagnetically induced transparency (EIT) [2], coherent population oscillations (CPO) [3, 11–13], stimulated Raman scattering (SRS) [14], spectral hole burning [15], parametric amplification [16, 17].

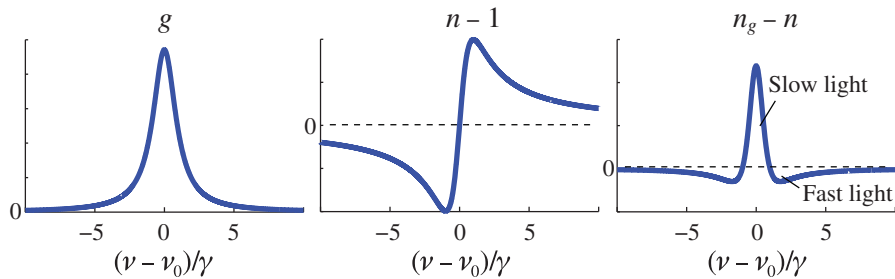


**FIGURE 12.1** Gain coefficient  $g$ , real part of refractive index  $n$  and group index  $n_g$  as functions of frequency detuning near a Lorentzian shape gain resonance.

### 12.2.2 Structural Slow Light

The second general category is “structural” (or “macroscopic”) slow light, which indicates that the manipulation of the “effective group velocity” of light in the medium is achieved through the interaction between light and the structural geometry of an element that is comparable or larger than the optical wavelength. A macroscopic slow-light element is typically not spatially homogeneous but has a structural geometry with characteristic feature size comparable to or much larger than the wavelength. In such cases, the slow-light effect is best described by the group delay of propagation through the entire element, or at least one period of the periodic structure as follows:

$$\tau_g = \frac{d\phi(\omega)}{d\omega}, \quad (12.9)$$

where  $\phi(\omega)$  is the phase of the complex transfer function  $\tilde{H}(\omega) = A(\omega) \exp[i\phi(\omega)]$ . Sometimes it is convenient to define the effective refractive index  $n_{\text{eff}}$  and effective group index  $n_{g,\text{eff}}$  by assuming that the medium is effectively homogeneous:

$$n_{\text{eff}}(\omega) = \frac{\phi(\omega)c}{\omega L}, \quad (12.10)$$

$$n_{g,\text{eff}} = n_{\text{eff}} + \omega \frac{dn_{\text{eff}}}{d\omega}, \quad (12.11)$$

where  $c$  is the speed of light in vacuum, and  $L$  is the length of the element or one period of the periodic structure.

For example, photonic crystal (PhC) structure has been particularly of interest for many on-chip applications. Figure 12.2a shows an example of a slab PhC single-line-defect waveguide [18]. The light is confined by index contrast in the  $z$ -direction and by the photonic crystal structures in the  $x-y$  plane. One advantage of PhC slow light is that the dispersive property can be highly controlled or designed through the geometry, rather than the material, of the structure. Here, Li et al. [18] suppressed the higher order dispersion of the PhC waveguide through fine-tuning the super-lattice

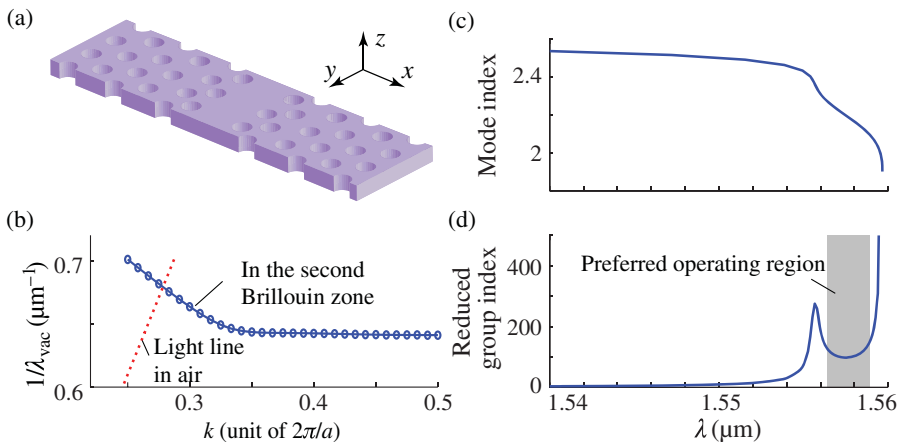


**FIGURE 12.2** (a) Schematics of a flat-band PhC line-defect waveguide [18]; (b) Dispersion relations of the fundamental guided Bloch modes of a PhC W1 waveguide; and corresponding effective mode index (c) and reduced group index  $n'_g$  (d) as functions of wavelength for such a waveguide structure.

geometry such that the group index exhibits a plateau near the desired working bandwidth (Fig. 12.2d).

Other structural slow light includes photonic bandgap structures [19–24], single and coupled ring resonators [25–27], fiber or waveguide grating structures [28].

## 12.3 PHYSICS WITH SLOW AND FAST LIGHT

### 12.3.1 Common Slow-Light Processes

It is clear from our discussion of the Kramers–Kronig relations in Section 2.1 that any rapid variation of the absorption coefficient of a material system will be accompanied by a rapid spectral variation of the refractive index. This variation will make a large contribution to the group index in accordance with the standard result

$$n_g = n + \omega dn/d\omega. \quad (12.12)$$

Most material mechanisms for slow light can be understood simply from this point of view. In this section we review some examples of this behavior.

#### 12.3.1.1 Slow Light Based on the Linear Response of Atomic Absorption Lines

One of the simplest laboratory procedures for observing an appreciable slowdown of the group velocity of light is to make use of the linear response of an isolated atomic resonance. Atomic vapors tend to possess well-separated absorption lines. The strongest of these lines can possess oscillator strengths with values approaching

unity and linewidths determined by Doppler broadening which is often of the order of magnitude of 1 GHz. Under these conditions, a simple order of magnitude calculation leads to the conclusion that the group index is of the order of 100.

Some simple variations of this idea can be implemented to achieve improved results. One such example is the work of Camacho et al. [9] who obtained enhanced group indices by working with the 852 nm  $6^2S_{1/2}$  to  $6^2P_{3/2}$  resonance of the cesium atom. These researchers tuned their laser to a frequency between the two hyperfine resonances associated with the 9.2 GHz splitting of the  $6^2S_{1/2}$  electronic ground state into  $F = 3$  and  $F = 4$  components. For this detuning, the slow-light contribution from the two resonances added, the group velocity dispersion of the two resonances tended to cancel, and absorption was minimized by tuning away from line center. They found that they could delay a 740 ps input pulse by up to 59 ns, corresponding to a delay of approximately 80 pulse widths. Tunability was achieved by adjusting the cesium temperature.

**12.3.1.2 Slow Light Based on EIT** EIT is a coherent nonlinear optical process [2]. It can be used to obtain much larger slow-light effects (much larger group indices) than can be obtained by isolated atomic resonances. The EIT process is often studied in the so-called  $\Lambda$  configuration. Typically the signal wave to be slowed is tuned close to the  $a \rightarrow b$  atomic transition, and a strong pump wave is tuned to the  $c \rightarrow b$  atomic transition. Here  $b$  is an excited state and  $a$  and  $c$  are low-lying states, perhaps different hyperfine levels of the electronic ground state. The presence of the strong pump field creates a narrow spectral hole in the otherwise broad  $a \rightarrow b$  optical transition. This dip can be extremely narrow, as its width depends on the relaxation rate between levels  $a$  and  $c$ , which for the case of hyperfine transitions can be very small. This narrow dip then gives rise to a large group index, which can be of the order of one million under proper transitions.

One of the early dramatic demonstrations of slow-light effects was that of Hau et al. (1999) [29] and made use of EIT effects in an ensemble of sodium atoms. The experiment was performed at very low temperature, very close to the transition temperature to a BEC. These workers were able to slow the group velocity of light to the extremely small value of  $17\text{ ms}^{-1}$  and showed that they could delay an optical pulse by as much as five pulse widths. Later work by Kash et al. [30] showed that nearly comparable results could be obtained in a warm atomic vapor. This crucial observation was extremely important as it removed the perceived restriction of needed to work in a Doppler-free regime or in a BEC in order to observe slow light.

**12.3.1.3 Slow Light Based on Stimulated Brillouin Scattering** Stimulated Brillouin Scattering (SBS) has proven to be a useful and versatile means for inducing slow-light effects. SBS is a pure gain process, that is, one of the waves (the Stokes wave) experiences amplification at the expense of the pump wave. The gain is largest when the Stokes and pump waves are detuned from one another by the acoustic resonance frequency of the medium, which is given by  $\Omega = 2\omega v n/c$ , where  $\omega$  is the pump-wave frequency,  $v$  is the velocity of sound in the material, and  $n$  is its refractive index. Conversely, an anti-Stokes wave will experience attenuation. Consequently,

the Stokes wave will experience a strong slow-light effect and the anti-Stokes wave will experience a fast-light effect. Slow light by means of SBS was discovered nearly simultaneously by Okawachi et al. [7] and by Gonzalez-Herraez et al. [31]. It is easy to show that the slow-light delay, defined here as the difference in transit times through a medium of length  $L$  for a resonant signal pulse in the presence and the absence of the pump wave, is given by

$$\Delta T_d = \frac{G}{\Gamma_B}, \quad (12.13)$$

where  $G = g_0 I_p L$  is the single-pass gain parameter, and  $\Gamma_B$  is the acoustic damping rate that determines the width of the Brillouin resonance. In their initial study, Okawachi et al. observed delays of as large as 20 ns for a 15-ns-long input pulse for a gain parameter of  $g = 11$ .

Much of the attraction of the use of SBS for slow light is that its properties are readily controllable. For example, Shi et al. [32] showed that they could control the shape of the SBS gain curve by using several overlapping gain lines. The central frequency of each gain lines was tuned through the use of a Mach-Zehnder modulator. These authors found that through use of a three overlapping gain lines they were able to achieve twice as much the delay as from a single gain line while obtaining a modulation bandwidth three-times as large and with good fidelity (i.e., with good eye-opening diagrams: the “0”s and “1”s were well separated). In a separate experiment, Zhu et al. [33] described an optical memory for a stream of data pulses based on the properties of SBS. Specifically, the information content is written into an acoustic excitation which can later be read out through the use of an intense read beam. Storage of 2-ns-long pulses for as long as 12 ns was reported.

**12.3.1.4 Slow Light Based on CPO** Slow light based on CPO is another broadly employed procedure for controlling the group velocity of light. In the CPO process, pump and probe beams detuned from one another by an amount  $\delta\omega$  co-propagate through a saturable absorbing medium. If the frequency difference  $\delta\omega$  is smaller than the inverse of the population decay time  $T_1$ , the ground state population is induced to oscillate with appreciable amplitude at the beat frequency  $\delta\omega$ . Detailed calculation [3] shows that these oscillations will lead to a decrease in the absorption over a frequency band of the order of  $\delta\omega$ . This narrow dip in absorption leads to a rapid swing in the real part of the refractive index, producing a large contribution to the group index. In their original paper, Bigelow et al. observed velocities as small as  $60 \text{ ms}^{-1}$  corresponding to a group index of  $5 \times 10^6$ . Many researches have made use of the CPO model and find that it is extremely useful in describing their experimental data.

Certain aspects of the CPO process can be understood intuitively by means of a model first formulated by Bassov and coworkers [34] for the case of a saturable gain medium with non-instantaneous response. Because of saturation, the leading edge of the pulse will experience more amplification than the trailing edge of the pulse. The peak of the pulse will thus tend to move to earlier times, that is, the pulse will show

“fast-light” effects. For the case of non-instantaneous saturable absorber, just the opposite happens and the system shows slow-light effects. The Basov model is useful in giving an intuitive picture for the origin of slow and fast light in non-instantaneous saturable materials. However, it does not readily provide quantitative predictions, because numerical methods must be used to determine how a pulse will propagate through such a material. An advantage of the CPO model is that it leads to simple analytic predictions for the properties of slow-light effect. For example, it is easy to show that under CPO conditions the group index is given by

$$n_g = \frac{1}{2} \alpha_0 T_1 c \frac{I/I_s}{(1 + I/I_s)^3}, \quad (12.14)$$

where  $\alpha_0$  is the unsaturated absorption coefficient of the material.

### 12.3.2 Superluminal and Backward Light

As noted above, the group index of a dispersive medium is given by

$$n_g = n + \omega dn/d\omega. \quad (12.15)$$

Under appropriate conditions (near the center for an absorption line, or in the wings for a gain line), the second contribution to  $n_g$  can become negative, and if this contribution is sufficiently large, the group index can become smaller than unity. Under these circumstances, the group velocity of light can exceed the vacuum speed of light [12, 35], which at first sight might seem inconsistent with the principle of causality. The resolution to this paradox is a bit subtle and has been discussed by several workers [1, 36]. In brief summary, the propagation of a light pulse cannot be described by a single velocity. Different definitions of velocity need to be introduced to describe different aspects of pulse propagation. In addition to the well-known phase velocity and group velocity, one sometimes needs to introduce the information velocity (the velocity at which information is transported through a system) and the front velocity (the velocity at which a sharp dislocation in the pulse propagates). It is surmised that the front velocity is equal to the information velocity and that in fact both of these are equal to the vacuum speed of light  $c$ . The rationale for this argument is that information is encoded at points of non-analyticity of the wavefront, and the broad frequency spectrum that accompanies these points will not experience the slow- or fast-light effects that tend to be confined to narrow frequency ranges.

There is an even more exotic phenomenon that can occur when the second contribution to  $n_g$  is negative and larger in magnitude than the first contribution. Under these circumstances the group index and also the group velocity become negative. Thus pulses propagate in a direction opposite to that of their propagation vector  $\mathbf{k}$ . This exotic behavior had been predicted theoretically by several workers [37] and was observed unambiguously by Gehring et al. [38]. Under these circumstances, the peak of a pulse exiting the medium exits before the peak of the incident pulse enters the medium. Also, the peak of the pulse moves in the backward direction within

the medium. Again, causality is preserved in this process, because this behavior can be observed only in the case of smooth pulses with “infinite support.” For example, a Gaussian pulse has wings that extend from  $-\infty$  to  $+\infty$ , and thus in a real sense the pulse is “everywhere” at all times, and there can be no concern with causality violation.

### 12.3.3 Kinetics Properties and Photon Drag

Because of the change in the group velocity when a pulse enters a dispersive medium, there is inherently a change in the pulse duration and hence in the energy density of the pulse. For example, when a pulse enters a slow-light medium, it will become spatially compressed and its energy density will increase. Exactly the opposite will happen when a pulse enters a fast-light medium. Here we describe the kinematics of this process. We will describe the consequence of this behavior on nonlinear optics in the following section.

It turns out that it is straightforward to derive Poynting’s Theorem for the case of a dispersive (homogeneous) medium [39–41]. One finds that the intensity (magnitude of the Poynting vector) is given by

$$S = \frac{1}{2}n\epsilon_0|E|^2 \quad (12.16)$$

and that the energy density is given by

$$u = \frac{1}{2}nn_g\epsilon_0|E|^2. \quad (12.17)$$

As usual, the group velocity is given by

$$v_g = c/n_g. \quad (12.18)$$

These results lead to the intuitively pleasing conclusion that

$$S = uv_g. \quad (12.19)$$

One should note that even though the energy density is enhanced in a material slow-light medium, the electric field strength is not enhanced. This fact has important consequences for the nonlinear optics of slow-light materials.

Dispersive media can also show enhanced photon drag effects. The transverse photon drag effect was measured by Jones in 1972 [42]. In his experiment, a glass slab of length  $L$  was translated in the transverse direction at a velocity  $v = 200 \text{ cm s}^{-1}$ . It was found that a beam of light incident on the slab was dragged in the transverse direction by a small but measurable amount of 6 nm. Theoretical work [43] showed that the transverse displacement is given by

$$\Delta x = (vL/c)(n_g - 1/n). \quad (12.20)$$

We thus see that photon drag effects can be increased enormously through the use of a slow-light medium.

Motivated by this conclusion, Franke-Arnold et al. [44] performed an experiment to observe a rotary photon drag effect. In their experiment, an elliptically shaped laser beam was transmitted through a rotating ruby rod. The ruby showed a very strong self-pumped slow-light effect (the group index was of the order of  $10^6$ ) as a result of the CPO mechanism mentioned above. It was found that the elliptical beam became rotated by several degrees in either the clockwise or the counter-clockwise direction depending on the direction of rotation of the ruby rod. A refinement of this experiment was reported more recently by Wisniewski-Barker et al. [45]. In this experiment, a dark line in the form of a topological defect was first impressed on the laser beam before it passed through the ruby. It was found that the dark line was rotated along with the rest of the elliptical beam. The fact that laser light was found in the regions that were originally dark and that “darkness” was found in the regions that were originally bright rules out other possible interpretations of the experiment of Franke-Arnold et al., such as certain simple forms of pulse reshaping.

Another topic of considerable interest is the question of the momentum carried by a photon in a material medium. As is well known, the momentum carried by a photon traveling in vacuum is

$$p_v = \hbar\omega/c. \quad (12.21)$$

The question is how to generalize this result for the case of a material medium. This question has been a topic of discussion for at least 100 years, and there is still some uncertainty as to the complete answer to this question. In fact, there are two competing theories to determine this momentum and each theory has arguments that tend to support it. We quote results for the case of a dispersive medium. The case of a non-dispersive medium can be treated simply by replacing the group index  $n_g$  by the refractive index  $n$  in all formulas.

The Abraham form assumes that the electromagnetic momentum density is given by

$$\mathbf{P} = \mathbf{E} \times \mathbf{H}/c^2. \quad (12.22)$$

A straightforward consequence of this assumption is that the momentum carried by a photon is given by [46, 47]

$$p_A = (\hbar\omega/c)(1/n_g). \quad (12.23)$$

It is commonly accepted that the Abraham momentum is associated with the kinetic (i.e., the “ $mv$ ”) momentum of the photon. It is also taken to be the momentum of the field itself (without the material response that is naturally associated with it). It is also the momentum that is deduced by the Einstein block (or Balazs block) argument.

The Minkowski form of the momentum assumes that

$$\mathbf{P} = \mathbf{D} \times \mathbf{B}. \quad (12.24)$$

Here there is some disagreement as to the momentum of the photon. Milonni and Boyd [47] deduce that

$$p_M = (\hbar\omega/c)(n^2 1/n_g), \quad (12.25)$$

whereas Barnett deduces that

$$p_M = (\hbar\omega/c)n. \quad (12.26)$$

We believe that there is no fundamental disagreement between these two treatments. We believe that the two sets of authors are simply following different conventions. And specifically, we are unaware of any situations in which the measurable predictions of the two formalisms are in disagreement. The Minkowski momentum is associated with the canonical momentum and corresponds to Planck's constant  $\hbar$  divided by the de Broglie wavelength for a massive particle. It is also the momentum that comes out of Fermi's Doppler-shift analysis.

### 12.3.4 Enhancement of Nonlinearity

**12.3.4.1 Slow Light and Enhancement of Optical Nonlinearities** There has been discussion in the scientific literature regarding the conditions under which slow-light effects can be used to enhance optical nonlinearities. Common sense might seem to suggest that nonlinear effects would be enhanced for any slow-light interaction, because the light spends more time interacting with the medium. But this argument is invalid. Nonlinear optical effects occur as a consequence of propagation effects and thus depend on the distance of nonlinear material through which the light travels. How long it takes light to travel through the medium is of no concern.

This issue has been analyzed by Boyd [48]. He finds that whether nonlinear effects are enhanced depends critically upon whether the slow light occurs because of a material resonance or a structural resonance. As we remarked earlier, in relation to Eq. (12.16), there is no (or little) enhancement in the electric field amplitude when a light wave enters a slow-light medium. The boundary conditions on Maxwell's equations dictate that any change in field amplitude will depend on the discontinuity in the refractive index, not the group index, and the discontinuity in the refractive index tends to lead to a very small effect. The situation is quite different when light enters a medium in which light is slowed down by a structural resonance, such as for a fiber Bragg grating (FBG). In this case there is an enhancement in the nonlinear optical response, which tends to scale as the square of the group index [49]. On the one hand, the field amplitude is increased inside the structure by one power of the group index because of the resonator nature of elements of the FBG. In addition, the effective pathlength through the structure is increased by another factor of the group index because of the tendency of light to circulate many times through the structure before being fully transmitted.

## 12.4 SOME APPLICATIONS OF SLOW AND FAST LIGHT

### 12.4.1 Optical Tunable Delay Lines

One of the most promising applications that use slow and fast light is optical tunable delay lines. Such capabilities allow dynamically adjusting the transit time of optical signal fields propagating through an slow-light medium, which is required for many applications in all-optical domain including buffering, signal processing, data traffic control, signal re-synchronization.

One of the most dominantly used media to carry optical signals today is optical fiber, which can be found today from transcontinental communication networks to super-computing centers. In optical fibers, SBS is one commonly used slow-light technique. Through the interaction between photons and acoustic phonons, a pump field at frequency  $\nu$  would give a narrow gain feature in the vicinity of the Stokes frequency  $\nu - \Omega_B$  and a narrow absorption feature in the vicinity of the anti-Stokes frequency  $\omega + \Omega_B$ . Here  $\Omega_B$  is the SBS Stokes frequency shift, which is approximately 10 GHz in optical fibers. The intrinsic linewidth of SBS process is typically of the order of a few tens of MHz. However, the SBS-induced complex refractive index profile is indeed the convolution of SBS intrinsic lineshape and the spectrum of the pump profile, that is,

$$\tilde{n}(\nu) = \frac{cg_0}{4\pi\nu} \frac{\gamma}{\nu + i\gamma} * P(\nu + \Omega_s), \quad (12.27)$$

where  $g_0$  is the SBS gain coefficient of the medium,  $\gamma$  is the SBS linewidth,  $P(\nu + \Omega_s)$  is the pump power spectrum, and  $\Omega_s$  is the SBS Stokes frequency shift of the medium.

By modifying the pump field spectrum using, for example, intensity modulation, phase modulation, or laser injection current modulation, SBS slow light with working bandwidth ranging from tens of MHz to tens of GHz has been achieved to accommodate different needs of signal bandwidth. Since the SBS Stokes frequency shift  $\Omega_s$  in optical fibers is approximately 10 GHz, the gain profile broadening becomes much more challenging when the signal bandwidth goes beyond  $2\Omega_s$  when the Stokes gain profile and the anti-Stokes absorption profile starts to overlap at the pump center frequency. This limit can be overcome by using multiple pump fields, in which the Stokes gain feature of one pump frequency compensates the anti-Stokes absorption feature of some other pump frequency. This scheme is demonstrated to achieve 20 GHz slow light using SBS in fiber [50].

For even larger bandwidth with sub-picosecond light pulses, stimulated Raman scattering (SRS) becomes a more suitable slow-light technique. The intrinsic linewidth of SRS in optical fibers is approximately a few THz, and 85% delay of 430 fs pulses has been demonstrated in optical fibers [51].

Besides the optical fiber, photonic integrated circuits (PICs) are playing more and more important rule in communication and signal processing. Both SBS and SRS slow light has been demonstrated in nano-wire optical waveguides on either chalcogenide [52] or silicon platforms [14].

Moreover, PIC is a convenient platform to realize structural slow light. Xia et al. demonstrated a compact optical buffer on silicon chip using up to 100 cascaded ring resonators and achieved 10 bits of delay at a data rate of 20 Gbps [53]. Baba et al. demonstrated a tunable delay line with a maximum delay of 40 ps for signals with a bandwidth of 1.4 THz using photonic crystal line defect waveguides [54].

### 12.4.2 Optical Memories

Besides tunable optical delay lines, an all-optical communication system or information processing system is also inevitably in need of memories in an all-optical fashion. The ability to completely halt the propagation of a light pulse is also known as “stopped light.” There have been a lot of designs and implementations of optical memories using the concept of “stopped light.” Particularly, the physics of “stopped light” using material slow light and structure slow light could be quite different.

In material slow light, the spatial extension of an optical pulse along the propagation direction is inversely proportional to the magnitude of the group index. For example, the longitudinal extension of an 1 ms optical pulse in vacuum is approximately 300 km. When such a pulse enters an EIT medium whose group index is  $10^7$ , the longitudinal extension of such a pulse is compressed by a factor of  $10^7$  and becomes 3 cm. Such dramatic spatial compression of the pulse greatly reduces the physical size of a slow-light-based optical memory. Meanwhile, material slow light typically indicates a strong interaction between the optical field and some other physical quantities, such as atomic coherence in an EIT medium. Moreover, such strong interaction can usually be controlled through additional optical control fields, that is, be turned on and off using a second beam.

We here describe a typical process of “stopped” light using material slow light. The slow-light medium is first prepared with the presence of a control field. As the signal field enters the medium, it interacts strongly with the medium and the information is partially transferred to the medium in some physical quantity. After the signal field completely enters the medium, the control field is turned off, which changes the interaction condition between the signal field and the medium. However, the information of the optical signal field is already partially present in the medium, which does not propagate, that is, the optical information is stored in the medium. After the desired “storage” time elapses, the “read-out” control field is turned back on, and the information stored in the medium is transferred back to a regenerated signal field. Such a “write” and “read” process stores the optical information to medium during the “storage” period, which constitutes an optical memory in analogue of the more familiar electronic memories.

An optical memory using EIT was first demonstrated by Liu et al. [55], in which an 11  $\mu$ s pulse is stored in ultracold EIT medium for 1 ms. Phillips et al. [56] separately demonstrated a similar EIT-based optical storage experiment with a delay time up to 200  $\mu$ s. Camacho et al. [57] demonstrated a system using four-wave mixing in hot atomic vapors. Their demonstration simultaneously generates two entangled read-out pulses, which can potentially serve for applications in quantum information science. Zhu et al. demonstrated an all-fiber optical memory based on SBS [33]. Their

demonstration can potentially work at any telecommunication wavelength, which makes it easy to be integrated with existing fiber-optic communication systems.

The “stopped” light using structural slow light works in a different way, in which light interacts more with the geometry of the medium rather than the material. Generally speaking, after the optical signal pulse enters the “device” regime, the properties of the device are tuned such that the light bounces back and forth, or “stays”, inside the device until the device is tuned again to release the signal field. Xu et al. demonstrated a stopped-light device consisting of two rings and two coupled waveguides on silicon-on-insulator platform [58]. The turning on and off of the device is realized through tuning the resonance wavelength of the ring resonators with respect to the signal field. Saito and Baba proposed a technique of stopping light pulses using a slow-light device based on photonic crystal coupled waveguide (PCCW). The stopping of light is realized through dynamically tuning the material index chirp in the PCCW and by adiabatically transforming slow-light pulses into stopped ones [59]. As the nanofabrication technique is advanced, integrated optical memory devices can have much better performance.

### 12.4.3 SLIDAR

Light detection and ranging (LIDAR) is employed in a wide variety of remote sensing applications, such as measuring atmospheric properties, detecting chemical and biological agents, vehicle surveillance, and aerial/bathymetric surveying. The key performance parameters of a LIDAR system include its transverse and longitudinal resolutions. Similar to imaging systems, the far-field transverse resolution of a LIDAR system depends on the aperture size of its emitter. Recently, multi-aperture systems are studied for various optical applications including high-performance telescopes and high-power lasers. Compared to a single large aperture, a multi-aperture system can achieve a larger effective aperture size, that is, fine far-field transverse resolution, without the need of heavy and slow opto-mechanical components.

Since the signals from different emitters need to be coherently combined in the far-field, a multi-aperture LIDAR requires precise optical phase control of every emitter’s output. Furthermore, a LIDAR working in a pulsed mode faces an additional challenge. When the beam is steered far off from the direction normal to the emitter array plane, the emitters at one side of the system become closer to the far-field target than those on the other side. Thus, the signal pulses sent from different emitters may no longer overlap in time when they reach the far field. Such a group delay mismatch will significantly degrade both the longitudinal and transverse resolutions of the system. Thus, it is crucial to dynamically correct the group delay mismatch such that the pulsed signals emitted from different channels are always aligned properly in time when they reach the far field.

Schweinsberg et al. have demonstrated a multi-aperture slow-light laser radar (SLIDAR) system. In their work, two independent tunable slow-light mechanisms, namely dispersive delay and SBS slow light [7], are incorporated to realize dynamic group delay synchronization while the system scans in two orthogonal directions. Furthermore, a heterodyne locking scheme is also used to control the optical phase of the output of each emitter to realize coherent beam combining at the far field.

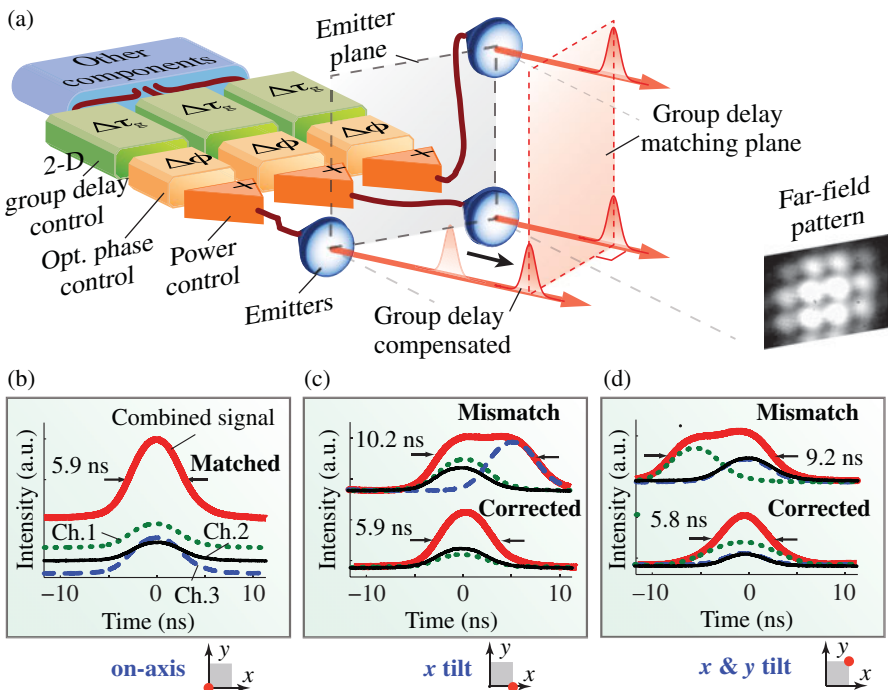


**FIGURE 12.3** (a) The schematics of a SLIDAR system capable of 2D beam steering; normalized time traces of the returned signal when the system is pointing on-axis (b), tilted in the  $x$ -direction (c), and tilted in both the  $x$ - and  $y$ -directions (d). (For a color version of this figure, see the color plate section.)

A schematic of the demonstrated 2D SLIDAR system is shown in Figure 12.3a, which uses three emitters arranged in a right-angle 2D pattern. Such an arrangement contains all of the conceptual difficulties of a multi-channel system.

The time traces of the returned signal are plotted in Figures 12.3b–12.3d when the system is pointing in the normal,  $x$ -tilted and  $x$ - and  $y$ -tilted directions, respectively. The thick red line is the combined signal, while the thin lines are the signal from three individual channels. It is clear that when the system is pointing at off-axis directions, the group delay mismatch will result in significant signal broadening, indicating serious degradation in both the longitudinal and transverse resolutions. When the 2D group delay control units are turned on, the group delay mismatch is compensated well and there is no pulse broadening in the returned signal.

Note that similar slow-light approaches have also been studied in the context of microwave photonics and synthetic aperture radar [60, 61].

#### 12.4.4 Interferometric Spectrometers

While many current applications of slow light focus on taking advantage of controllable group delay of optical pulses propagating through a slow-light medium, the

impact of the large dispersion inside a slow-light medium on the phase change of different frequency components of the optical fields has sometimes been overlooked.

Interferometric spectrometers refer to a large family of instrument that extract the spectral information of an given optical field through optical interference. Spectrometers with high spectral sensitivity are becoming more and more desired in applications such as metrology [62], optical sensing [63], quantum information processing [64], biomedical engineering [65].

One way to see this enhancement effect is to study the output of a Mach–Zehnder (M–Z) interferometer. When the optical path difference between the two routes through the M–Z interferometer is caused only by a medium with length  $L$  and refractive index  $n$ , the phase difference of the two beams passing through two different routes is given by

$$\Delta\phi = \frac{\omega}{c} nL, \quad (12.28)$$

where  $\omega$  is the optical frequency of the input light and  $c$  is the velocity of light in vacuum. The intensity transmission of such an M–Z interferometer is given by

$$T = \frac{1}{2}(1 + \cos \Delta\phi). \quad (12.29)$$

Note that  $\Delta\phi$  can further be a function of transverse coordinates and  $\Delta\phi$  appears also in the expressions for the transmission of many other types of interferometers.

For a spectroscopic interferometer, a change in frequency  $\omega$  will produce a change in the phase difference term  $\Delta\phi$ , which will consequently lead to a change in intensity and enables the detection of the frequency shift. Thus, the sensitivity of a spectroscopic interferometer can typically be described in terms of the quantity  $d\Delta\phi/d\omega$ , and an interferometer is especially sensitive to a shift in frequency if the value of  $d\Delta\phi/d\omega$  is large. Using Eq. (12.28), one can rewrite  $d\Delta\phi/d\omega$  as follows,

$$\frac{d\Delta\phi}{d\omega} = \frac{d}{d\omega} \left( \frac{\omega n L}{c} \right) = \frac{L}{c} \left( n + \omega \frac{dn}{d\omega} \right) = \frac{Ln_g}{c}, \quad (12.30)$$

where  $n_g \equiv n + \omega dn/d\omega$  is the group index.

Thus, one sees that the spectral sensitivity is proportional to the group index  $n_g$  of the medium that is inside the interferometer. For common interferometers in which non-dispersive media (or media with small dispersion) are used,  $n_g$  equals (or approximates) the phase index  $n$ , and therefore the dependence of spectral sensitivity on dispersion can often be neglected. However, if a slow-light medium with very large group index  $n_g$  is used, the spectral sensitivity of such an interferometer can be greatly enhanced.

The enhancement by using slow light has been experimentally demonstrated in a various interferometer constructions [10, 66, 67]. Similar concept has been extended to integrated arrayed waveguide gratings (AWGs) [68, 69] and other structures as well.

While slow light can greatly enhance the spectral resolution of an given interferometer construction, for a given required spectral sensitivity, a shorter path length can be used for a slow-light medium. The resulting reduction in the device size could be important in applications where space is limited or where high stability is required.

## 12.5 FUNDAMENTAL LIMITS ON SLOW LIGHT

### 12.5.1 Limits for Optical Delay Lines

While the magnitude of the group index of a medium is an important figure of merit for exploring the fundamentals of slow light, a more practical figure of merit for delay-line applications is how much time delay a slow-light element can provide as compared to the temporal duration of a signal pulse or of one data bit.

This thought can be quantified using the maximum fractional delay [70] (also known as the delay-bandwidth product [71]). One definition for the maximum fractional delay  $\overline{\Delta T}_{\max}$  is given by

$$\overline{\Delta T}_{\max} \equiv \frac{\Delta T_{\max}}{\Delta \tau} = 2\pi\Delta\nu\Delta T_{\max}, \quad (12.31)$$

where  $\Delta T_{\max}$  is the maximum achievable absolute delay,  $\Delta\tau = 1/(2\pi\Delta\nu)$  is the temporal duration of the pulse, and  $\Delta\nu$  is the signal bandwidth.

In practice, a practical slow-light medium typically has frequency-dependent gain and group index. These frequency dependencies can lead to pulse distortion and/or power level change [72], which can consequently deteriorate the quality of transmitted information.

To quantify the impact of pulse distortion and power level change, various criteria have been used based on different considerations.

One set of criteria is based on the physical origins of the various distortions, known as the gain distortion factor and phase distortion factor, respectively [73]. Since a practical medium cannot provide arbitrarily large gain to the signal, an additional criterion is often set on the maximum frequency-dependent amplitude gain within the bandwidth  $G_{\max}$ , such as 3.5, corresponding to a maximum power gain of less than 30 dB. While such criteria emphasize the physical origin of the distortion and provide a intuitive picture of whether a given gain profile is optimum or not, the magnitude of the two distortion factors are quite difficult to be measured. Thus, there are also other distortion factors that is more measurable and can be tested, such as the change of the full width at half maximum (FWHM) of the temporal duration of the signal pulse.

When individual pulse delay is studied, the group delay is usually defined in terms of the peak position of a single Gaussian pulse [32, 73–78]. In a real telecommunication system, however, data packets are comprised of varying sequences of “0” and “1” bits in designated time slots, and the peak positions of individual pulses often experience a pattern-dependent delay [79] due to inter-symbol interference (ISI) [80],

etc. Thus, an alternative way to determine the delay of a data packet through a slow-light medium is to define it in terms of the best-decision-time (BDT)  $t_{\text{opt}}$  in the eye diagram when highest data fidelity (i.e., lowest bit error rate (BER)) is achieved. Note that the eye diagram is also most open at  $t_{\text{opt}}$ ; this thought can be quantified using the eye-opening metric. Consequently, the BDT delay of a data packet can be determined by comparing the values of  $t_{\text{opt}}$  for propagation through the slow-light medium and through a reference medium. In such cases, it makes more sense to quantify the distortion in terms of system metrics, such as the eye-opening penalty EOP [32, 81] or the Q-factor penalty [79].

There have been various approaches to optimize the gain profile or dispersion of practical slow-light processes to maximize its fractional delay. Generally speaking, the approaches are often to create a flat-top gain profile or to create two separated absorption profiles with a transparent window in between. The achievable fractional delay is consequently limited by the amount of gain or absorption one can achieve. Typically, a fractional delay of approximately 2 is achievable using gain-induced slow light with maximum gain of approximately 30 dB, and fractional delay of hundreds can be achieved using double-absorption-line features in atomic vapors.

Alternatively, one can describe the limit in a more concise manner. For example, Miller [82] has given a limit, which relates the maximum achievable fractional delay  $\tau_g \Delta v$  of a device of size  $L$  with its average refractive index  $n_{\text{avg}}$  and its maximum variation of  $\Delta n$  over  $\Delta v$  near the center wavelength  $\lambda_0$  through the relation

$$\tau_g \Delta v \leq n_{\text{avg}} L \Delta n / (\sqrt{3} \lambda_0). \quad (12.32)$$

This expression sets a upper bound on the fractional delay for any 1D slow-light medium. And it is consistent with the criteria set in maximum gain. There have been proposals to overcome such a limit by using systems with higher dimensions, for example, by allowing different frequency components to propagate through spatially separated channels [83].

### 12.5.2 Limits for Interferometric Spectroscopy

While fractional delay is the primary figure of merit of slow-light media for delay-line applications, it is more convenient to use some other criteria that directly related to the need of spectroscopy when one quantifies the limit of slow light for spectroscopy applications. Typically, spectral resolution  $\delta v$  is one important figure of merit for any spectrometer.

Although different types of interferometers have very different geometrical construction, they actually share surprising similarity in the expression of spectral resolution in terms of the parameters such as length and group index of the medium [69, 84].

In ideal cases when the slow-light medium is transparent to input light, the spectral performance is typically given by

$$\delta v = \frac{c}{n_g L}, \quad (12.33)$$

where  $L$  is the length of the slow-light medium. One sees that in such ideal cases, the spectral resolution can be linearly enhanced by the magnitude of the group index  $n_g$ .

However, most practical slow-light media have associated gains and losses, and this eventually limits the finest spectral resolution that is achievable. In particular, when a lossy slow-light medium is used, the characteristic resolution of slow-light interferometers becomes

$$\delta\nu = \frac{c\alpha}{n_g}, \quad (12.34)$$

where  $\alpha$  is the loss coefficient of the slow-light medium.

Besides the spectral resolution, the number of resolving spectral lines within the working bandwidth is often another important criterion. Since both  $n_g$  and  $\alpha$  are often highly frequency dependent, one way to set a bound is to require that the spectral resolution should not vary by a certain amount (e.g., 10%) within the working bandwidth  $\Delta\nu$ . After that, one can use the quantity working finesse  $\mathcal{F}_w$  defined as follows:

$$\mathcal{F}_w \equiv \frac{\Delta\nu}{\delta\nu} = \frac{n_g \Delta\nu}{c\alpha}. \quad (12.35)$$

To increase the spectral resolution, one essentially needs to maximize  $n_g/\alpha$ . Meanwhile, the key to improve the working finesse  $\mathcal{F}_w$  is to optimize the gain–loss-ratio profile so it exhibits a plateau over which  $n_g/\alpha$  remains a constant.

## REFERENCES

- [1] P. W. Milonni, *Fast Light, Slow Light and Left-Handed Light* (Institute of Physics, Bristol and Philadelphia, 2005).
- [2] S. E. Harris and L. V. Hau, “Nonlinear optics at low light levels,” *Phys. Rev. Lett.* **82**, 4611–4614 (1999).
- [3] M. S. Bigelow, N. N. Lepeshkin, and R. W. Boyd, “Observation of ultraslow light propagation in a ruby crystal at room temperature,” *Phys. Rev. Lett.* **90**, 113903 (2003).
- [4] R. W. Boyd and D. J. Gauthier, “‘Slow’ and ‘fast’ light,” in *Progress in Optics*, edited by E. Wolf (Elsevier Science, Amsterdam, 2002), Vol. 43, pp. 497–530.
- [5] R. D. L. Kronig, “On the theory of dispersion of x-rays,” *J. Opt. Soc. Am.* **12**(6), 547–556 (1926).
- [6] H. Kramers, “La diffusion de la lumiere par les atomes,” *Atti Cong. Intern. Fisica, (Transactions of Volta Centenary Congress) Como* **2**, 545–557 (1927).
- [7] Y. Okawachi, M. S. Bigelow, J. E. Sharping, Z. Zhu, A. Schweinsberg, D. J. Gauthier, R. W. Boyd, and A. L. Gaeta, “Tunable all-optical delays via Brillouin slow light in an optical fiber,” *Phys. Rev. Lett.* **94**(15), 153902 (2005).
- [8] J. Sharping, Y. Okawachi, and A. Gaeta, “Wide bandwidth slow light using a Raman fiber amplifier,” *Opt. Express* **13**(16), 6092–6098 (2005).

- [9] R. M. Camacho, M. V. Pack, J. C. Howell, A. Schweinsberg, and R. W. Boyd, "Wide-bandwidth, tunable, multiple-pulse-width optical delays using slow light in Cesium vapor," *Phys. Rev. Lett.* **98**(15), 153601 (2007).
- [10] Z. Shi, R. W. Boyd, D. J. Gauthier, and C. C. Dudley, "Enhancing the spectral sensitivity of interferometers using slow-light media," *Opt. Lett.* **32**(8), 915–917 (2007).
- [11] P. Ku, C. Chang-Hasnain, and S. Chuang, "Variable semiconductor all-optical buffer," *Electron. Lett.* **38**, 1581–1583, (2002).
- [12] M. S. Bigelow, N. N. Lepeshkin, and R. W. Boyd, "Superluminal and slow light propagation in a room-temperature solid," *Science* **301**(5630), 200–202 (2003).
- [13] A. Schweinsberg, N. N. Lepeshkin, M. S. Bigelow, R. W. Boyd, and S. Jarabo, "Observation of superluminal and slow light propagation in erbium-doped optical fiber," *Europhys. Lett.* **73**, 218–224 (2006).
- [14] Y. Okawachi, M. A. Foster, J. E. Sharping, A. L. Gaeta, Q. Xu, and M. Lipson, "All-optical slow-light on a photonic chip," *Opt. Express* **14**, 2317–2322 (2006).
- [15] R. M. Camacho, M. V. Pack, and J. C. Howell, "Slow light with large fractional delays by spectral hole-burning in rubidium vapor," *Phys. Rev. A* **74**(3), 033801 (2006).
- [16] L. Yi, W. Hu, Y. Su, M. Gao, and L. Leng, "Design and system demonstration of a tunable slow-light delay line based on fiber parametric process," *IEEE Phot. Tech. Lett.* **18**, 2575–2577 (2006).
- [17] E. Shumakher, A. Willinger, R. Blit, D. Dahan, and G. Eisenstein, "Large tunable delay with low distortion of 10 Gbit/s data in a slow light system based on narrow band fiber parametric amplification," *Opt. Express* **14**(19), 8540–8545 (2006).
- [18] J. Li, T. P. White, L. O'Faolain, A. Gomez-Iglesias, and T. F. Krauss, "Systematic design of flat band slow light in photonic crystal waveguides," *Opt. Express* **16**(9), 6227–6232 (2008).
- [19] M. Soljačić, S. G. Johnson, S. Fan, M. Ibanescu, E. Ippen, and J. D. Joannopoulos, "Photonic-crystal slow-light enhancement of nonlinear phase sensitivity," *J. Opt. Soc. Amer. B* **19**, 2052–2059 (2002).
- [20] H. Gersen, T. J. Karle, R. J. P. Engelen, W. Bogaerts, J. P. Korterik, N. F. van Hulst, T. F. Krauss, and L. Kuipers, "Real-space observation of ultraslow light in photonic crystal waveguides," *Phys. Rev. Lett.* **94**, 073903 (2005).
- [21] Y. A. Vlasov, M. O'Boyle, H. F. Hamann, and S. J. McNab, "Active control of slow light on a chip with photonic crystal waveguides," *Nature* **438**(3), 65–69 (2005).
- [22] T. F. Krauss, "Slow light in photonic crystal waveguides," *J. Physics D: Appl. Phys.* **40**(9), 2666–2670 (2007).
- [23] T. Baba, "Slow light in photonics crystals," *Nature Photonics* **2**, 465–473 (2008).
- [24] S. P. Anderson, A. R. Shroff, and P. M. Fauchet, "Slow light with photonic crystals for on-chip optical interconnects," *Adv. Opt. Technol.* **2008**, 293531 (2008).
- [25] J. E. Heebner and R. W. Boyd, "Slow light with low dispersion and nonlinear enhancement in a lattice-shifted photonic crystal waveguide," *J. Mod. Opt.* **49**(14), 2629–2636 (2002).
- [26] A. Yariv, Y. Xu, R. K. Lee, and A. Scherer, "Coupled-resonator optical waveguide: a proposal and analysis," *Opt. Lett.* **24**(11), 711–713 (1999).
- [27] F. Xia, L. Sekaric, and Y. Vlasov, "Ultracompact optical buffers on a silicon chip," *Nature Photonics* **1**, 65–71 (2007).

- [28] D. Janner, G. Galzerano, G. D. Valle, P. Laporta, S. Longhi, and M. Belmonte, “Slow light in periodic superstructure Bragg gratings,” *Phys. Rev. E* **72**, 056605 (2005).
- [29] L. V. Hau, S. E. Harris, Z. Dutton, and C. H. Behroozi, “Light speed reduction to 17 metres per second in an ultracold atomic gas,” *Nature* **397**, 594–598 (1998).
- [30] M. M. Kash, V. A. Sautenkov, A. S. Zibrov, L. Hollberg, G. R. Welch, M. D. Lukin, Y. Rostovtsev, E. S. Fry, and M. O. Scully, “Ultraslow group velocity and enhanced nonlinear optical effects in a coherently driven hot atomic gas,” *Phys. Rev. Lett.* **82**, 5229–5232 (1999).
- [31] M. Herráez, K. Y. Song, and L. Thévenaz, “Optically controlled slow and fast light in optical fibers using stimulated Brillouin scattering,” *Appl. Phys. Lett.* **87**, 081113 (2005).
- [32] Z. Shi, R. Pant, Z. Zhu, M. D. Stenner, M. A. Neifeld, D. J. Gauthier, and R. W. Boyd, “Design of a tunable time-delay element using multiple gain lines for increased fractional delay with high data fidelity,” *Opt. Lett.* **32**(14), 1986–1988 (2007).
- [33] Z. Zhu, D. J. Gauthier, and R. W. Boyd, “Stored light in an optical fiber via stimulated Brillouin scattering,” *Science* **318**, 1748–1750 (2007).
- [34] N. G. Basov, R. V. Ambartsumyan, V. S. Zuev, P. G. Kryukov, and V. S. Letokhov, “Nonlinear amplification of light pulses,” *Sov. Phys. JETP* **23**, 16–22 (1966).
- [35] L. J. Wang, A. Kuzmich, and A. Dogariu, “Gain-assisted superluminal light propagation,” *Nature* **406**, 277–279 (2000).
- [36] R. Y. Chiao, “Superluminal (but causal) propagation of wave packets in transparent media with inverted atomic populations,” *Phys. Rev. A* **48**, R34–R37 (1993).
- [37] M. Ware, S. Glasgow, and J. Peatross, “Energy transport in linear dielectrics,” *Opt. Express* **9**, 519–532 (2001).
- [38] G. M. Gehring, A. Schweinsberg, C. Barsi, N. Kostinski, and R. W. Boyd, “Observation of backwards pulse propagation through a medium with a negative group velocity,” *Science* **312**, 895–897 (2006).
- [39] H. Haus, “Momentum, energy and power densities of {TEM} wave packet,” *Physica* **43**(1), 77–91 (1969).
- [40] P. W. Milonni, “Field quantization and radiative processes in dispersive dielectric media,” *J. Mod. Opt.* **42**(10), 1991–2004 (1995).
- [41] S. E. Harris, “Ponderomotive forces with slow light,” *Phys. Rev. Lett.* **85**, 4032–4035 (2000).
- [42] R. V. Jones, “Fresnel aether drag’ in a transversely moving medium,” *Proc. R. Soc. Lond. A.* **328**, 337–352 (1972).
- [43] M. Padgett, G. Whyte, J. Girkin, A. Wright, L. Allen, P. Öhberg, and S. M. Barnett, “Polarization and image rotation induced by a rotating dielectric rod: an optical angular momentum interpretation,” *Opt. Lett.* **31**, 2205–2207 (2006).
- [44] S. Franke-Arnold, G. Gibson, R. W. Boyd, and M. J. Padgett, “Rotary photon drag enhanced by a slow-light medium,” *Science* **333**, 65–67 (2011).
- [45] E. Wisniewski-Barker, G. Gibson, S. Franke-Arnold, Z. Shi, R. W. Boyd, and M. J. Padgett, “Evidence of slow-light effects from rotary drag of structured beams,” *New J. Phys.* **15**(8), 083020 (2013).
- [46] D. H. Bradshaw, Z. Shib, R. W. Boyd, and P. W. Milonni, “Electromagnetic momenta and forces in dispersive dielectric media,” *Opt. Commun.* **283**(5), 650–656 (2010).

- [47] P. W. Milonni and R. W. Boyd, "Momentum of light in a dielectric medium," *Adv. Opt. Photon.* **2**, 519–553 (2010).
- [48] R. W. Boyd, "Material slow light and structural slow light: similarities and differences for nonlinear optics [invited]," *J. Opt. Soc. Am. B* **28**, A38–A44 (2011).
- [49] N. A. R. Bhat and J. E. Sipe, "Optical pulse propagation in nonlinear photonic crystals," *Phys. Rev. E* **64**, 056604 (2001).
- [50] K. Y. Song and K. Hotate, "25 GHz bandwidth Brillouin slow light in optical fibers," *Opt. Lett.* **32**(3), 217–219 (2007).
- [51] J. Sharping, Y. Okawachi, and A. Gaeta, "Wide bandwidth slow light using a raman fiber amplifier," *Opt. Express* **13**, 6092–6098 (2005).
- [52] R. Pant, C. G. Poulton, D.-Y. Choi, H. Mcfarlane, S. Hile, E. Li, L. Thevenaz, B. Luther-Davies, S. J. Madden, and B. J. Eggleton, "On-chip stimulated brillouin scattering," *Opt. Express* **19**, 8285–8290 (2011).
- [53] F. Xia, L. Sekaric, and Y. Vlasov, "Ultracompact optical buffers on a silicon chip," *Nature Photonics* **1**, 65–71 (2007).
- [54] T. Baba, T. Kawaaski, H. Sasaki, J. Adachi, and D. Mori, "Large delay-bandwidth product and tuning of slow light pulse in photonic crystal coupled waveguide," *Opt. Express* **16**, 9245–9253 (2008).
- [55] C. Liu, Z. Dutton, C. H. Behroozi, and L. V. Hau, "Observation of coherent optical information storage in an atomic medium using halted light pulses," *Nature* **409**, 490–493 (2001).
- [56] D. F. Phillips, A. Fleischhauer, A. Mair, R. L. Walsworth, and M. D. Lukin, "Storage of light in atomic vapor," *Phys. Rev. Lett.* **86**, 783–786 (2001).
- [57] R. M. Camacho, P. K. Vudyasetu, and J. C. Howell, "Four-wave-mixing stopped light in hot atomic rubidium vapour," *Nature Photonics* **3**, 103–106 (2009).
- [58] Q. Xu, P. Dong, and L. Michal, "Breaking the delay-bandwidth limit in a photonic structure," *Nature Physics* **3**, 406–410 (2007).
- [59] Y. Saito and T. Baba, "Stopping of light by the dynamic tuning of photonic crystal slow light device," *Opt. Express* **18**, 17141–17153 (2010).
- [60] L. Gao, S. I. Herriot, and K. H. Wagner, "Sluggish light for radio-frequency true-time-delay applications with a large time-bandwidth product," *Opt. Lett.* **31**, 3360–3362 (2006).
- [61] A. Zadok, O. Raz, A. Eyal, and M. Tur, "Optically controlled low-distortion delay of Ghz-wide radio-frequency signals using slow light in fibers," *Photon. Technol. Lett., IEEE* **19**, 462–464 (2007).
- [62] O. P. Lay, S. Dubovitsky, R. D. Peters, J. P. Burger, S.-W. Ahn, W. H. Steier, H. R. Fetterman, and Y. Chang, "Mstar: a submicrometer absolute metrology system," *Opt. Lett.* **28**(11), 890–892 (2003).
- [63] Z. Xie and H. F. Taylor, "Fabry-Perot optical binary switch for aircraft applications," *Opt. Lett.* **31**(18), 2695–2697 (2006).
- [64] X.-F. Mo, B. Zhu, Z.-F. Han, Y.-Z. Gui, and G.-C. Guo, "Faraday-Michelson system for quantum cryptography," *Opt. Lett.* **30**(19), 2632–2634 (2005).
- [65] S. Sakadzic and L. V. Wang, "High-resolution ultrasound-modulated optical tomography in biological tissues," *Opt. Lett.* **29**(23), 2770–2772 (2004).
- [66] Z. Shi, R. W. Boyd, R. M. Camacho, P. K. Vudyasetu, and J. C. Howell, "Slow-light Fourier transform interferometer," *Phys. Rev. Lett.* **99**(24), 240801 (2007).

- [67] U. Bortolozzo, S. Residori, and J.-P. Huignard, "Slow-light birefringence and polarization interferometry," *Opt. Lett.* **35**, 2076–2078 (2010).
- [68] O. Matos, M. Calvo, P. Cheben, S. Janz, J. Rodrigo, D.-X. Xu, and A. Delage, "Arrayed waveguide grating based on group-index modification," *J. Lightwave Technol.* **24**, 1551–1557 (2006).
- [69] Z. Shi and R. W. Boyd, "Fundamental limits to slow-light arrayed-waveguide-grating spectrometers," *Opt. Express* **21**, 7793–7798 (2013).
- [70] R. W. Boyd, D. J. Gauthier, A. L. Gaeta, and A. E. Willner, "Maximum time delay achievable on propagation through a slow-light medium," *Phys. Rev. A* **71**(2), 023801 (2005).
- [71] R. Tucker, P. Ku, and C. Chang-Hasnain, "Delay–bandwidth product and storage density in slow-light optical buffers," *Electron. Lett.* **41**(4), 208–209 (2005).
- [72] R. W. Boyd and P. Narum, "Slow- and fast-light: fundamental limitations," *J. Mod. Opt.* **54**(16–17), 2403–2411 (2007).
- [73] M. D. Stenner, M. A. Neifeld, Z. Zhu, A. M. Dawes, and D. J. Gauthier, "Distortion management in slow-light pulse delay," *Opt. Express* **13**(25), 9995–10002 (2005).
- [74] A. Minardo, R. Bernini, and L. Zeni, "Low distortion Brillouin slow light in optical fibers using AM modulation," *Opt. Express* **14**(13), 5866–5876 (2006).
- [75] T. Schneider, M. Junker, K. Lauterbach, and R. Henker, "Distortion reduction in cascaded slow light delays," *Electron. Lett.* **42**, 1110–1111 (2006).
- [76] J. B. Khurgin, "Performance limits of delay lines based on optical amplifiers," *Opt. Lett.* **31**(7), 948–950 (2006).
- [77] A. Zadok, A. Eyal, and M. Tur, "Extended delay of broadband signals in stimulated Brillouin scattering slow light using synthesized pump chirp," *Opt. Express* **14**(19), 8498–8505 (2006).
- [78] Z. Lu, Y. Dong, and Q. Li, "Slow light in multi-line Brillouin gain spectrum," *Opt. Express* **15**(4), 1871–1877 (2007).
- [79] C. Yu, T. Luo, L. Zhang, and A. E. Willner, "Data pulse distortion induced by a slow-light tunable delay line in optical fiber," *Opt. Lett.* **32**(1), 20–22 (2007).
- [80] G. P. Agrawal, *Fiber-Optic Communication Systems*, 3rd ed. (John Wiley & Sons, New York, 2002), Chapter 4.
- [81] J. Downie, "Relationship of Q penalty to eye-closure penalty for NRZ and RZ signals with signal-dependent noise," *J. Lightwave Technol.* **23**, 2031–2038 (2005).
- [82] D. A. B. Miller, "Fundamental limit to linear one-dimensional slow light structures," *Phys. Rev. Lett.* **99**(20), 203903 (2007).
- [83] Z. Shi and R. W. Boyd, "Discretely tunable optical packet delays using channelized slow light," *Phys. Rev. A* **79**(1), 013805 (2009).
- [84] Z. Shi and R. W. Boyd, "Slow-light interferometry: practical limitations to spectroscopic performance," *J. Opt. Soc. Amer. B* **25**(12), C136–C143 (2008).



---

# 13

---

## ATTOSECOND PHYSICS: ATTOSECOND STREAKING SPECTROSCOPY OF ATOMS AND SOLIDS

UWE THUMM<sup>1</sup>, QING LIAO<sup>1</sup>, ELISABETH M. BOTHSCHAFTER<sup>2,3</sup>,  
FREDERIK SÜßMANN<sup>2,3</sup>, MATTHIAS F. KLING<sup>2,3</sup>, AND  
REINHARD KIENBERGER<sup>2,4</sup>

<sup>1</sup>*J.R. Macdonald Laboratory, Physics Department, Kansas-State University,  
Manhattan, KS, USA*

<sup>2</sup>*Max-Planck Institut für Quantenoptik, Garching, Germany*

<sup>3</sup>*Physik Department, Ludwig-Maximilians-Universität, Garching, Germany*

<sup>4</sup>*Physik Department, Technische Universität München, Garching, Germany*

### 13.1 INTRODUCTION

Irradiation of atoms and surfaces with ultrashort pulses of electromagnetic radiation leads to photoelectron emission if the incident light pulse has a short enough wavelength or has sufficient intensity (or both) [1, 2]. For pulse intensities sufficiently low to prevent multiphoton absorption, photoemission occurs provided that the photon energy is larger than the photoelectron's binding energy prior to photoabsorption,  $\hbar\omega > I_p$ . Photoelectron emission from metal surfaces was first analyzed by Albert Einstein in terms of light quanta, which we now call photons, and is commonly known as the photoelectric effect [3]. Even though the photoelectric effect can be elegantly interpreted within the corpuscular description of light, for strong fields it can be equally well described if the incident radiation is represented as a classical electromagnetic wave [4, 5]. With the emergence of lasers able to generate very intense light,

---

*Photonics: Scientific Foundations, Technology and Applications, Volume I*, First Edition.

Edited by David L. Andrews.

© 2015 John Wiley & Sons, Inc. Published 2015 by John Wiley & Sons, Inc.

it was soon shown that at sufficiently high intensities (routinely provided by modern laser systems) the condition  $\hbar\omega < I_p$  no longer precludes photoemission. Instead, the absorption of two or more photons can lead to photoemission, where a single photon would fail to provide the ionization energy  $I_p$  [6]. For more than a century, photoelectron spectroscopy has supplied information about the structure of atoms, molecules, and solid matter [1, 6, 7]. In conjunction with quantum theory, it was, and continues to be, instrumental in revealing the microscopic, electronic, and morphological properties of matter.

Starting in the 1990s, laser technology [8, 9] had advanced to provide intense pulses of light short enough to resolve the nuclear motion in molecules [10–15] in experiments using mutually delayed pulses. By varying the delay  $\tau$  between the first (pump) pulse and second (probe) pulse, stroboscopic pictures of the nuclear motion could be obtained by recording a movie-like stroboscopic sequence of events. Typically, these molecular (or atomic) movies were assembled in a destructive way: The pump pulse creates an excited state which, over a range of pump-probe delays, is stroboscopically imaged by dissociative ionization of the molecule (or ionization of the highly excited atom) by the ultrashort probe pulse, which destroys the particular sample under study. Typical lengths for the pump and probe pulses in such experiments are of the order of several femtoseconds ( $1 \text{ fs} = 10^{-15} \text{ seconds}$ ), short enough to resolve the rotational and vibrational motion of molecules as well as the largely classical, slow motion of highly excited Rydberg electron wave packets in atoms.

### 13.1.1 The Advent of Attosecond Physics

More recently, starting in the new millennium, advances in laser technology enabled attosecond pulses which opened the door to attosecond physics [10, 11, 16]. Attosecond physics includes (but is not limited to) a variety of phenomena that occur in strong laser fields. It is thus not surprising that the first attosecond light pulses were created by the interaction of strong laser fields with gaseous, atomic targets [10, 11]. One attosecond is staggeringly short,  $1 \text{ as} = 10^{-18} \text{ seconds}$ , and one attosecond compares to one second in the way one second compares to the age of the universe. The timescale is so short that light in vacuum, which moves at a speed of  $299,792,458 \text{ m s}^{-1}$ , travels only about  $0.3 \text{ nm}$  ( $1 \text{ nm} = 10^{-9} \text{ m}$ ) during 1 as. Attosecond physics is therefore intrinsically connected *not only* to an ultrashort timescale but also to very small length scales [16].

Modern laser technology currently provides table-top laser systems in state-of-the-art laboratories that generate short pulses in the near-infrared (NIR) spectral range with peak intensities reaching  $10^{22} \text{ W cm}^{-2}$ , corresponding to electric field strengths in the range of  $10^{14} \text{ V m}^{-1}$ . Such sources have not yet reached few-cycle pulse durations and have limited repetition rates in the sub-Hz range. The repetition rates of laser sources capable of exceeding peak intensities in the  $10^{14} \text{ W cm}^{-2}$  range, however, reach 10 kHz and higher [13]. Optical parametric chirped-pulse amplifier (OPCPA) lasers [14] have extended intense short-pulse generation to the mid-infrared and permit repetition rates in the 100 kHz range [15]. Laser pulses with intensities up to  $10^{15} \text{ W cm}^{-2}$ , in turn, are used to generate ultrashort radiation in the extreme

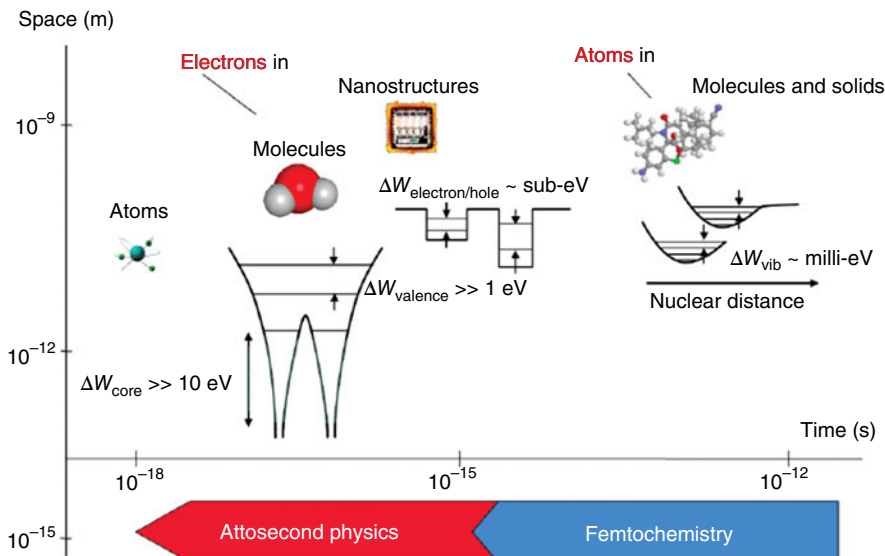


**FIGURE 13.1** Time and length scales for ultrafast processes. Adapted from Reference 16.

ultraviolet (XUV) and soft X-ray range with pulse lengths down to 70 as [16–18]. While such attosecond pulses enable unprecedented resolution in time, their spectral width is of the order of several electron volts (eV), and thus tends to compromise precise measurements in the energy domain.

Which particles move at the speeds corresponding to attosecond timescales? Nuclear motion in molecules happens on much longer timescales, well above the attosecond threshold. This is on the order of tens of femtoseconds, or slower (Fig. 13.1). The study of the formation and breaking of chemical bonds with (longer-duration) femtosecond laser fields has given rise to the field of Femtochemistry [9].

For phenomena that happen at the attosecond timescale, we must turn to particles that are much lighter than the protons and neutrons of the nucleus: electrons. Electrons balance the positive charge of the atomic cores, form the glue for chemical bonds, and are responsible for electric conduction in solids (to name only a few examples). As an electron weighs about 1/1836 of a proton [19], their motion can occur *much* faster than the motion of nuclei, and they can also react much faster to an external electromagnetic force. As an example, one roundtrip of an electron in the first Bohr orbit in atomic hydrogen takes about 152 as [16]. More generally, the energy spacing of the involved electronic levels,  $\Delta\epsilon$ , directly relates to the timescale of electron motion as shown in Figure 13.1 [16].

### 13.1.2 Ultrashort Laser Pulses Exert Well-Defined Electromagnetic Forces

Electrons (as charged particles) are susceptible to electric fields and can thus be driven by them. As electrons have very little mass, they can be driven at high frequencies,

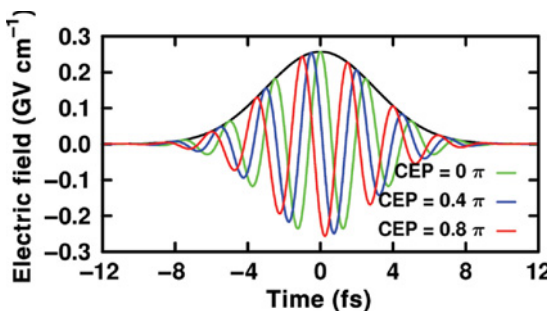


**FIGURE 13.2** Carrier–envelope phase (CEP) stable, few-cycle pulses at 800 nm. The electric fields for different CEP values are shown in color. The pulse envelope is indicated as a solid black line. Reproduced from Reference 27 with the permission of the PCCP Owner Societies. (For a color version of this figure, see the color plate section.)

orders of magnitude above the current gigahertz–terahertz rates ( $10^9$ – $10^{12}$  Hz) used in contemporary electronics. Advances in laser technology have allowed tailoring the lightwave’s electric field (in the optical spectral region) with sub-femtosecond precision [20]. If this well-defined force is used to control electron motion, petahertz (1 pHz =  $10^{15}$  Hz) lightwave electronics can be realized [21–23].

The electric field of a light pulse in the few-cycle domain may be described as

$$E(t) = E_0(t) \cos(\omega t + \phi_{\text{CEP}}) \quad (13.1)$$

with envelope  $E_0(t)$ , carrier frequency  $\omega$ , and the phase between the carrier wave and the envelope (carrier–envelope phase, CEP),  $\phi_{\text{CEP}}$ . Examples of few-cycle pulses with different CEP values are shown in Figure 13.2. To utilize the CEP as a control parameter, the electric field waveform of a few-cycle laser pulse can either be stabilized [24] or precisely measured for each laser shot [25, 26]. Light that is synthesized from ultra-broadband continua (spanning over more than one octave) permits *sculpting* of the electric field waveform with subcycle precision [20]. Such synthesized fields permit the control of electron dynamics on attosecond to femtosecond timescales.

The duration of such short pulses may be monitored with commercial dispersion-balanced autocorrelators or frequency-resolved optical gating (FROG) devices [28]. One of the most precise ways to determine the subcycle evolution of the electric field of an intense laser pulse relies on the attosecond streaking technique [29, 30], which will be introduced in Section 13.2.2.

### 13.1.3 Attosecond Light Pulses Through High Harmonic Generation

In most materials, electrons react so fast to external forces that their motion can be easily manipulated by a laser’s electromagnetic field. Driven electron motion is at the heart of high harmonic generation (HHG) and the creation of attosecond light pulses. HHG is most easily described by way of the three-step model [31]. Here, a strong laser field (strong enough to distort the Coulomb potential that binds an electron to an

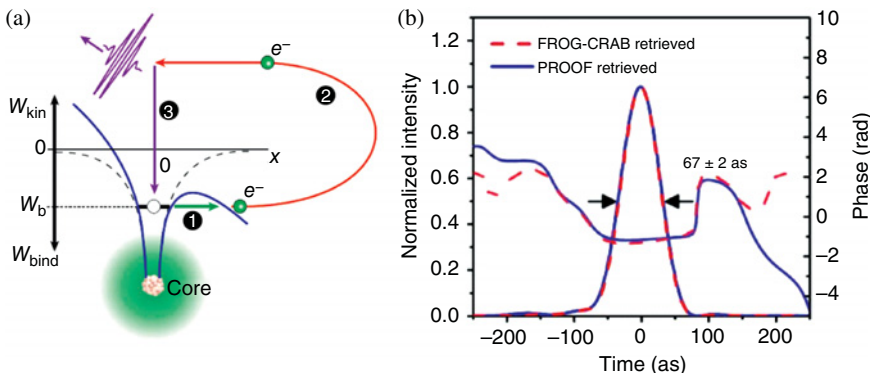


**FIGURE 13.3** (a) High harmonic generation process illustrated for an atom. Reprinted from Reference 48 with copyright permission of *Annual Reviews*. (b) Retrieved pulse duration (with two retrieval algorithms indicated in the legend, for details see Reference 18) of an isolated attosecond pulse spanning a spectral range from 55 to 130 eV. Reprinted from Reference 18 with copyright permission of *OSA*. (For a color version of this figure, see the color plate section.)

atom) results in tunnel ionization where an electron tunnels through a potential barrier (step 1). This electron is then accelerated in the field-dressed potential (step 2), and finally recollides with the core. This recollision results not only in the recombination of the electron with the atom, but also in the emission of high energy photons (step 3). These photons have energies that are multiples of the photon energy in the driving laser pulses, see Figure 13.3a. The highest energy photon that can be generated in this process is given by the classical cut-off formula

$$E_{\max} = 3.17U_p + I_p, \quad (13.2)$$

where  $I_p$  is the ionization potential of the atom and  $U_p$  is the ponderomotive potential given as the average, classical kinetic energy of an electron in the laser's electric field,

$$U_p = \frac{e^2 E_0^2}{4m_e \omega^2}, \quad (13.3)$$

with elementary charge  $e$ , electron mass  $m_e$ , and the peak electric field  $E_0$ .

The first step requires high electromagnetic field strength and therefore occurs at (or near) the peaks of the external electric field. This leads to a good synchronization between the external field and the “birth” time of the electron (when the electron is emitted into the continuum). In the case of optical fields, this synchronization occurs on a sub-femtosecond timescale. The three-step HHG process is repetitive and can occur near each peak of the driving laser field. Considering rare gas targets (or other targets with inversion symmetry) which are often used in HHG, this periodically driven electron rescattering process leads (for long driving pulses) to the emission of very distinct frequency combs with equidistant energy spacing  $\Delta E = 2\hbar\omega$  [32]. Attosecond light pulses are generated by selecting and superimposing a sufficiently

broad spectral range of (very) approximately constant spectral intensity in these combs, typically by sending the higher harmonic radiation through a thin metal foil. The generation of attosecond light pulses can be controlled by certain parameters of the driving laser field such as its polarization, frequency, waveform, envelope, and intensity, as well properties of the laser-target interaction (type of target, target density, laser caustic) [16, 33–36]. A wealth of research has been devoted to the production of attosecond pulses and the use of HHG as a spectroscopic tool to explore attosecond phenomena in atoms and molecules (cf. [37–41]). Using various techniques to limit HHG to below a single cycle of the driving pulse, the repetitive character can be interrupted, and isolated attosecond pulses can be generated [17, 24, 42–44]. These isolated pulses can be characterized by streaking measurements (see Section 13.2.2) and by making use of retrieval algorithms such as FROG-CRAB (Frequency-Resolved Optical Gating for Complete Reconstruction of Attosecond Bursts) [45, 46] or PROOF (Phase Retrieval by Omega Oscillation Filtering) [47]. The current record for the shortest, isolated attosecond pulses is 67 as [18], see Figure 13.3b, covering a spectral range from 55 to 130 eV.

### 13.1.4 Time-Resolving Basic Optoelectronic Phenomena on an Attosecond Scale

Advances in attosecond metrology enabled the resolution in time of photoionization processes on their natural time scale (tens of attoseconds) for valence electron motion in atoms [10, 49, 50] and solids [51, 52]. So far, this was mainly achieved through pump-probe experiments with intense, ultrashort NIR and XUV pulses of electromagnetic radiation. This ultrahigh time resolution allows for the unprecedented observation of an apparent time delay between the detection of multiple photoelectrons emitted by the same pulse of XUV photons but from different electronic levels of atoms and solids. Measured relative time delays for photoemission from different initial states are of the order of tens of attoseconds or less [52] and constitute accurate probes for the entirety of photoemission dynamics [51–55].

Time-resolved photoelectron emission experiments carried out by atomic, molecular, and optical (AMO) physics research groups have established “attosecond physics” as a promising research area [16, 48, 56–60]. Since the year 2007, attosecond physics has started to extend into solid-state physics, with the prospect of allowing the time-resolved observation of ultrafast electronic processes in metals [51, 52, 61], semiconductors, insulators [22, 23, 62, 63], and nanostructures [64–66]. Time-resolved photoemission experiments at the intrinsic time scales of the correlated dynamics of two electrons [67–71] or the collective motion of many electrons [61, 65, 72] promise unprecedentedly sensitive experimental tests of electronic phenomena in solids and novel nanodevices [73, 74]. The results of these tests will be relevant to lightwave electronics and the emerging field of nanophotonics [75].

In this chapter, we review the basic physics behind recent attosecond measurements of electronic dynamics in atoms, solid surfaces, and nanoparticles at a level accessible to a beginning physics graduate student. We will discuss time-resolved “dressed” (or “streaked”) photoemission and photoemission delay times based on the

comparison of calculated, time-resolved photoelectron spectra [4, 51, 61, 76–86] with recent experiments [51–53]. Examined on an attosecond timescale, photoemission from atoms is sensitive to details in the modeling, such as the electronic structure of the target and the photoemission dynamics. The interplay of experimental and theoretical investigations in the field of attosecond physics therefore allows for extremely sensitive tests which enhance our understanding of electronic and photonic dynamics in matter. As compared to gaseous targets, for solid targets the understanding of streaked photoelectron spectra is further complicated by the substrate dielectric response [61] and electron-propagation effects [4, 5, 77, 78] during the laser-assisted XUV excitation and emission processes. However, these “complications” could possibly offer a new approach for the time-resolved observation of collective (plasmon) excitations in large atoms, nanoparticles, and solids. As an added effect for attosecond time-resolved photoemission from nanometer-sized particles, the influence of local electric (and magnetic) field enhancements near the particle’s surface needs to be taken into account [75].

## 13.2 TIME-RESOLVED PHOTOEMISSION FROM ATOMS

### 13.2.1 Emission and Characterization of Photoelectron Wave Packets

Upon absorption of a photon, an atom may release a photoelectron. In this subsection, we describe this process for model atoms exposed to short pulses of XUV radiation (Fig. 13.4a). For simplicity, we only consider one spatial dimension. The generalization to three spatial dimensions, which more realistically account for the

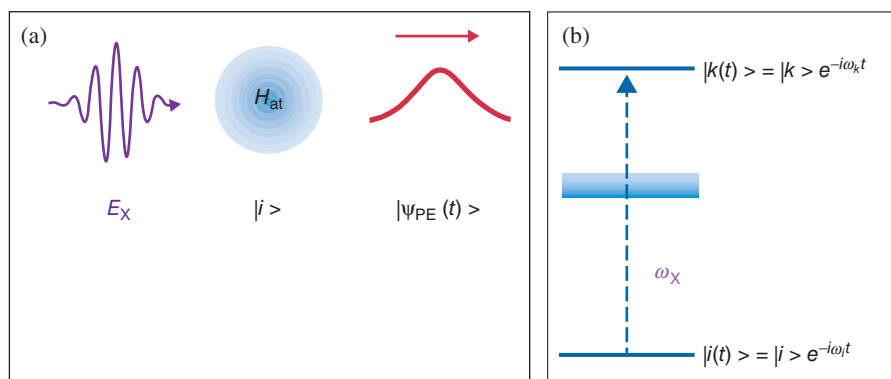


**FIGURE 13.4** (a) Basic scenario for atomic photoionization by an ultrashort XUV pulse. The electric XUV field,  $E_X$ , acts on an atom as described by the Hamiltonian  $H_{at}$  and generates a photoelectron wave packet  $|\Psi_{PE}(t)\rangle$ . (b) Schematic energy-level diagram. The absorption of one XUV photon results in electronic excitation from the bound atomic initial state  $|i\rangle$  with energy  $\omega_i$  to a superposition of unbound continuum states  $|k\rangle$  of energy  $\omega_k$ . At large distances between the photoelectron and the atom, this superposition forms  $|\Psi_{PE}(t)\rangle$ .

electronic structure and photoemission dynamics, is conceptually straightforward but technically more challenging.

We describe the model atom in terms of the atomic Hamilton operator  $H_{\text{at}}$  and assume that the atom is initially in a bound state,  $|i\rangle$ . Absorption of one XUV photon with energy  $\omega_X > I_p$  ionizes the atom by emitting an electron into a continuum state with energy  $\omega_k$  and momentum  $k$ . Here, and throughout this chapter, we use atomic units (a.u.), unless stated otherwise, for which  $\hbar = 1$ , elementary charge = 1, electron mass = 1, Bohr radius = 1,  $4\pi\epsilon_0 = 1$ . The initial bound and final continuum states of the active (photo)electron are given as solutions of the Schrödinger equation (SE),

$$H_{\text{at}} |i\rangle = \omega_i |i\rangle, \quad H_{\text{at}} |k\rangle = \omega_k |k\rangle. \quad (13.4)$$

Disregarding all bound states with the exception of  $|i\rangle$ , the general state of the atom after ionization is a superposition of the bound state and continuum states,

$$|\psi(t)\rangle = g(t)|i(t)\rangle + \int dk a_k(t)|k(t)\rangle. \quad (13.5)$$

Designating the electronic potential in the electric field,  $E_X(t)$ , of the XUV pulse as

$$V_X(t) = -zE_X(t) \propto z \int d\omega_X \tilde{E}_X(\omega_X) e^{-i\omega_X t}, \quad (13.6)$$

the time-dependent coefficients in (13.5) are obtained by solving the time-dependent Schrödinger equation (TDSE)

$$i\frac{d}{dt}|\psi(t)\rangle = [H_{\text{at}} + V_X(t)]|\psi(t)\rangle \quad (13.7)$$

subject to the initial conditions

$$g(-\infty) = 1, \quad a_k(-\infty) = 0. \quad (13.8)$$

Consistent with our assumption that just one XUV photon is absorbed, we treat the XUV pulse as a weak perturbation and neglect couplings between continuum states by the XUV field. This means that we assume

$$\langle k|V_X|k'\rangle \approx 0. \quad (13.9)$$

To first order in  $V_X$ , the expansion coefficients in (13.5) now follow as

$$g(t) = 1, \quad a_k(t) = -i \int_{-\infty}^t dt' \langle k(t')|V_X|i(t')\rangle. \quad (13.10)$$

The second term in (13.5) describes the photoelectron wave packet. For sufficiently large times after the interaction of the XUV pulse with the atom, the wave packet has moved far enough away from the atom so as to no longer overlap with the initial-state wavefunction. By combining the second term in Eqs. (13.5), (13.10), and (13.6), the photoelectron wave packet can be written as

$$|\psi_{\text{PE}}(t)\rangle \propto \int dk |k\rangle \langle k|z|i\rangle \tilde{E}_X(\omega_{ki}) e^{-i\omega_k t} \quad (13.11)$$

that is, in terms of the spectral profile of the XUV pulse,  $\tilde{E}_X$ , and the dipole matrix element,  $\langle k|z|i\rangle$ , with  $\omega_{ki} = \omega_k - \omega_i$ . Both factors are shown schematically in Figure 13.5. Owing to the limited range of the initial state in the configuration (and in momentum) representation, the dipole matrix element monotonously decreases at sufficiently large momenta,  $k$ . Assuming an XUV spectral pulse profile with a pronounced maximum at the momentum  $k_{\max}^X$ , the photoelectron wave packet has its strongest spectral component at the momentum  $k_{\max}$  close to and slightly red-shifted from  $k_{\max}^X$ .

In position representation, the photoelectron wavefunction can be written as

$$\psi_{\text{PE}}(z, t) \propto \int dk |A(k)| \exp(i[\arg\langle k|z|i\rangle + kz - \omega_k t]), \quad (13.12)$$

where the complex-valued expansion coefficients

$$A(k) = \langle k|z|i\rangle \tilde{E}_X(\omega_{ki}) \quad (13.13)$$

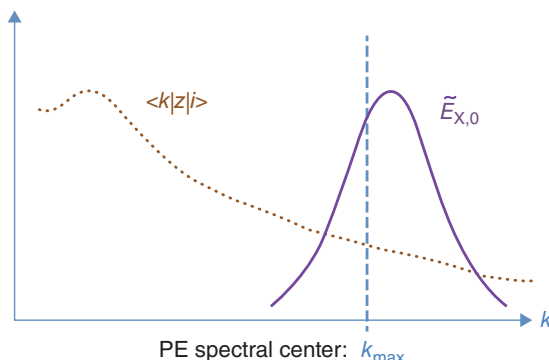


**FIGURE 13.5** Sketch of the determinants of a photoelectron wave packet, generated by XUV photoemission, as a function of the momentum  $k$ : dipole matrix element  $\langle k|z|i\rangle$  and envelope  $\tilde{E}_{X,0}(k)$  of the spectral profile of the XUV pulse electric field  $\tilde{E}_X(\omega_{ki})$ . The dominant spectral contribution to the photoelectron wave packet has the momentum  $k_{\max}$ .

are separated into their magnitude,  $|A(k)|$ , and phase,  $\arg(A) = \arg(\langle k | z | i \rangle)$ . Taylor expansion of the phase of the dipole matrix element around the dominant momentum component,

$$\arg \langle k | z | i \rangle = \arg \langle k_{\max} | z | i \rangle + \frac{d}{dk} \arg \langle k | z | i \rangle |_{k_{\max}} (k - k_{\max}) + \dots, \quad (13.14)$$

leads to the photoelectron probability density

$$|\psi_{\text{PE}}(z, t)|^2 \propto \left| \int dk |A(k)| \exp(i[k(z - z_X) - \omega_k t]) \right|^2, \quad (13.15)$$

where we define

$$z_X = -\frac{d}{dk} \arg \langle k | z | i \rangle |_{k_{\max}}. \quad (13.16)$$

The distance  $z_X$  can be thought of as the displacement of the photoelectron wave packet from a hypothetical reference wave packet with  $z_X = 0$ , while both wave packets propagate with the same group velocity,  $v_g = d\omega_k/dk|_{k_{\max}}$ , as illustrated in Figure 13.6.

The time the photoelectron would need to catch up with the reference wave packet (if the reference wave packet could hypothetically remain stationary in space) defines the time delay,

$$t_X = z_X/v_g = -\frac{d}{d\omega} \arg \langle k | z | i \rangle |_{k_{\max}}, \quad (13.17)$$

where we assume free-electron dispersion,  $\omega_k = k^2/2$ , in the last part of the equation. Such a time delay was first introduced within the context of particle scattering. It can be related to the width (in energy) of scattering resonances and is often referred to

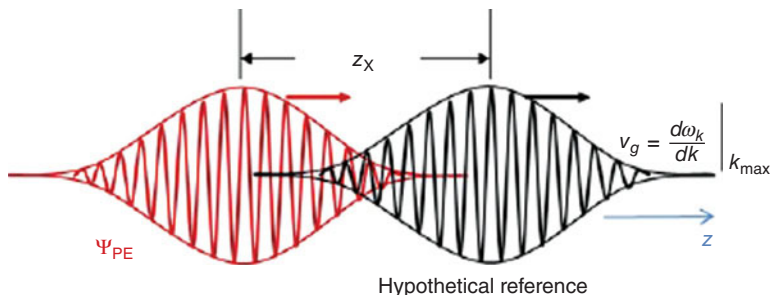


**FIGURE 13.6** Displacement of the photoelectron wave packet  $|\psi_{\text{PE}}(t)\rangle$ , relative to a fictitious reference wave packet. Both wave packets move with group velocity  $v_g$  to a photoelectron detector. A photoemission time delay can be defined as  $t_X = z_X/v_g$ . (For a color version of this figure, see the color plate section.)

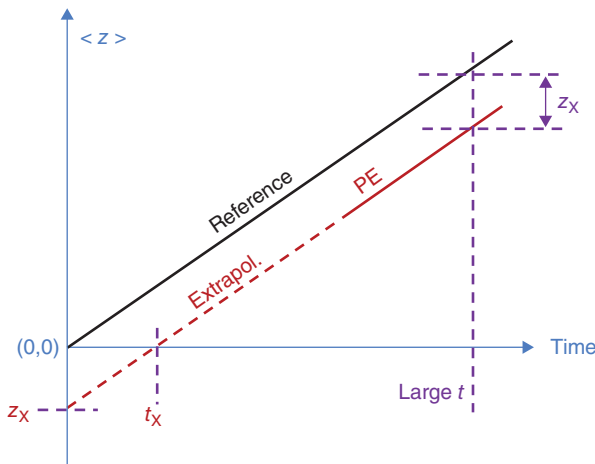


**FIGURE 13.7** Interpretation of the photoemission time delay  $t_X$ , as delayed photoemission, starting at the position  $z = 0$ . Long after the photoemission, the photoelectron is assumed to move freely and is displaced by  $z_X$  from a reference wave packet, and its position expectation value  $\langle z \rangle = \langle \Psi_{\text{PE}}(t) | z | \Psi_{\text{PE}}(t) \rangle$  is extrapolated to  $z = 0$ .

as the “Wigner time delay” [87–89]. Mostly within particle scattering investigations, several definitions of time delays and so-called “dwell times” were introduced in the past half century. (For a comprehensive review cf. Reference 90.) For photoemission, a back-of-the-envelope approximation for the delay time, based on order-of-magnitude estimates for atomic and XUV parameters, shows that  $t_X$  is within the attosecond time domain. For  $I_p = 10 \text{ eV}$  and  $\omega_X = 100 \text{ eV}$ ,  $k_{\max} \approx 2.6$  and  $v_g \approx 2.4$ . Taking the de Broglie wavelength,  $2\pi/k_{\max}$ , as an upper limit for  $z_X$  now results in the upper limit of 1 a.u. = 24 as for  $t_X$ .

The delay time,  $t_X$ , can also be viewed as a delayed start time of a photoelectron relative to a non-delayed reference photoelectron by comparing the position expectation values of both wave packets (Fig. 13.7) long after ionization [53, 79, 82, 83],

$$\langle z \rangle = \lim_{n \rightarrow \infty} \langle z \rangle^{\text{ref}} - z_X. \quad (13.18)$$

### 13.2.2 Influence of the IR Streaking Field on the Photoemission Process

Measurement of photoionization time delays requires a time reference. In theory, the time reference can be a reference wave packet, as discussed in Section 13.2.1. In practice, such a reference can be provided by simultaneously measuring photoemission from two energetically distinct initial states—of either the same target *or* two different targets—in the same streaked photoelectron spectrum. The energy mismatch of the two initial states needs to be large enough to be distinguishable in the photoelectron spectrum. For example, in order to measure time delays for photoionization

of target atoms  $A$  out of the bound state  $|A : i\rangle$ , with an admixture of a gas of reference atoms  $B$ , that are ionized out of the state  $|B : i\rangle$ , one would measure the *relative* time delay  $\Delta t_{X,A-B} = t_{X,B} - t_{X,A}$ . If the reference time delay  $t_{X,B}$ , is known, one can obtain  $t_{X,A}$ . By measuring the time difference relative only to a single reference, the contributions of  $t_{X,B}$  and  $t_{X,A}$  to the absolute time delays cancel. However, this lost information may be (to some extent) recovered by examining relative delays for different references and under different conditions, for example, with different XUV pulse parameters [80].

As the simple back-of-the-envelope example given in Section 13.2.1 has shown, photoionization time delays are of the order of attoseconds and therefore many orders of magnitude too short to be resolved with state-of-the-art electronics. Instead, yet another reference is needed. Such a reference is provided by employing a second pulse of electromagnetic radiation, typically in the IR spectral range, with a fixed, but variable time delay  $\tau$  relative to the center of the ionizing XUV pulse (Fig. 13.8). The IR field modulates the photoelectron energy, and XUV photoelectron energies obtained as a function of  $\tau$  are referred as “IR-streaked” photoemission spectra.

Recording XUV photoionization yields, assisted by delayed IR pulses, as a function of  $\tau$  generates streaked photoelectron spectra that effectively convert photoemission time delays into photoelectron energy shifts. Thus, relative photoemission delays can be obtained by analyzing the temporal shift (i.e., the phase shift  $\tau$ ) between two streaking traces in the photoelectron spectrum, as shown schematically in Figure 13.9a). Assuming, for the time being, that the IR-pulse intensities are small enough to prevent any distortion of the target’s electronic structure, photoelectron streaking can be analyzed classically by solving Newton’s equation,

$$\frac{dp}{dt} = F = -E_{\text{IR}}, \quad (13.19)$$

for the motion of a photoelectron that is released instantaneously at time  $\tau$  by the XUV pulse into the IR electric field  $E_{\text{IR}}(t)$  with the momentum

$$p_0 = \sqrt{2(\omega_X - \omega_i)}. \quad (13.20)$$

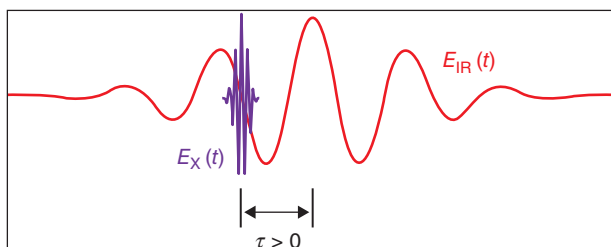


**FIGURE 13.8** Streaked photoelectron spectra are obtained by recording XUV photoemission spectra for a range of delays  $\tau$  between the centers of the XUV pulse and IR laser pulse.

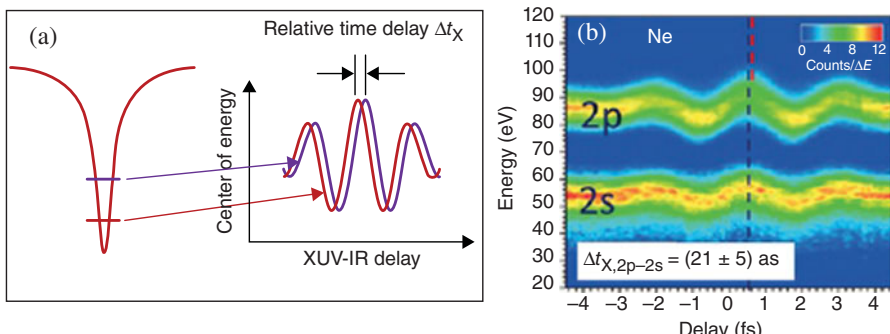


**FIGURE 13.9** (a) Illustration of the *relative* photoemission time delay,  $\Delta t_X$ , for photoionization from two energetically separate atomic levels. The two initial states yield energetically separated streaking traces in the photoelectron streaking spectrum.  $\Delta t_X$  is obtained from the phase difference between the centers of energy of the two traces. (b) Measured photoemission streaking spectrum for XUV photoionization of Ne. The *relative* photoemission time delay for emission out of 2s and 2p levels is determined as  $\Delta t_{X,2p-2s} = (21 \pm 5)$  fs. Adapted from Reference 53. (For a color version of this figure, see the color plate section.)

For the initial electron momentum (13.20), integration of (13.19) yields the momentum long after the emitted electron has been subjected to the IR pulse,

$$p(\infty) = p_0 - A_{\text{IR}}(\tau), \quad (13.21)$$

in terms of the IR-pulse vector potential,  $A_{\text{IR}}(\tau) = \int_{\tau}^{\infty} dt E_{\text{IR}}(t)$ . The photoelectron momentum and energy registered by a photoelectron detector thus oscillate 90° out of phase with the IR-laser vector potential as a function of the delay between the XUV and IR pulses. Figure 13.9b shows as an example a measurement of IR-streaked XUV photoemission from neon atoms with a measured relative photoemission delay of  $\Delta t_{X,2p-2s} = (21 \pm 5)$  fs [53].

In practice, appropriate peak intensities of the IR streaking field are limited. A lower limit is given by the need to clearly resolve streaking oscillations (i.e., by the energy resolution of the photoelectron detector). An upper limit is vaguely defined as the onset of distortions in the streaking spectra by the streaking IR field. The interpretation of streaked photoemission thus requires an understanding of the influence of the measurement itself (time to energy mapping in the IR field) on the measured observables: photoemission spectra and time delays. In the following subsections, we discuss this basic concern of quantum measurement. We will separately discuss effects that distortions of the *initial* and *final* quantum mechanical state of the active electron by the streaking electric field may have on photoemission spectra and time delays.

**13.2.2.1 Initial-State Perturbation** We examine the effect of a weak IR streaking field

$$E_{\text{IR}}(t) = E_{\text{IR},0} \cos(\omega_{\text{IR}} t + \phi_{\text{CEP}}) \quad (13.22)$$

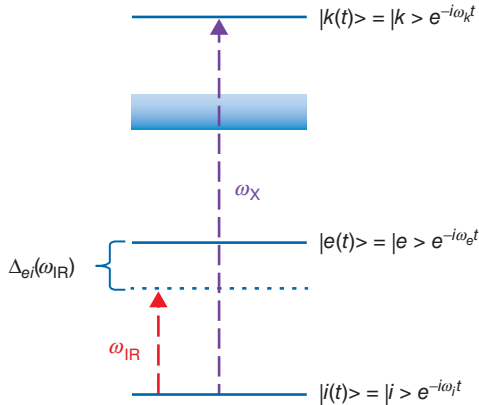


**FIGURE 13.10** Schematic energy level diagram for XUV photoionization of an atom by absorption of a single XUV photon with energy  $\omega_i$  in the presence of a streaking IR laser field of energy  $\omega_{\text{IR}}$ . The streaking field perturbs the initial state  $|i\rangle$  by coupling it to an excited state  $|e\rangle$  that is detuned from resonance by  $\Delta_{ei}(\omega_{\text{IR}})$ .

on streaked photoemission for model atoms with two bound, in which the excitation energy from a state  $|i\rangle$  to an excited state  $|e\rangle$  is detuned by the energy  $\Delta_{ei}(\omega_{\text{IR}})$  from the photon energy  $\omega_{\text{IR}}$  of the IR field (Fig. 13.10). The influence of the IR field on the initial state of the target results in replacing the unperturbed initial state  $|i\rangle$  in Figure 13.10 by the state

$$|\psi_i(t)\rangle = g(t)|i(t)\rangle + h(t)|e(t)\rangle. \quad (13.23)$$

For the initial condition  $g(-\infty) = 1, h(-\infty) = 0$ , the TDSE for the active electron, including intra-atomic forces, accounted for by the Hamiltonian  $H_{\text{at}}$  and the force the photoelectron experiences in the IR laser field (in dipole approximation),

$$i\frac{d}{dt}|\psi_i(t)\rangle = [H_{\text{at}} - zE_{\text{IR}}(t)]|\psi_i(t)\rangle \quad (13.24)$$

yields, to first order in  $E_{\text{IR}}$ ,

$$g(t) = 1, h(t) = iE_{\text{IR},0}\langle e|z|i\rangle \frac{\sin(\Delta_{ei}t/2)}{\Delta_{ei}} e^{i(\Delta_{ei}t/2 - \phi_{\text{CEP}})}. \quad (13.25)$$

Retracing the steps that lead to the photoelectron wave packet in Eq. (13.11), we see that the effect of the IR field on the photoelectron effectively amounts to replacing the dipole matrix element  $\langle k|z|i\rangle$  in (13.11) by

$$\langle k|z|i\rangle \left[ 1 + iE_{\text{IR},0} \frac{\langle k|z|e\rangle \langle e|z|i\rangle}{\langle k|z|i\rangle} \frac{\sin\Delta_{ei}}{\Delta_{ei}} e^{i(\Delta_{ei}/2 - \omega_{ei})\tau - i\phi_{\text{CEP}}} \right] = \langle k|z|i\rangle [1 + B], \quad (13.26)$$

where  $B$  is defined as the delay-dependent, complex-valued second term inside the second factor. Replacing the dipole matrix element in the XUV photoemission delay (13.17) with (13.26) and neglecting the influence of the IR field on both  $k_{\max}$  and  $v_g$  yields the photoemission delay

$$t_{X,IR} \approx t_X - \frac{Re(B)}{v_g} \frac{d}{dk} \arg \{ \langle k | z | e \rangle - \langle k | z | i \rangle \} |_{k_{\max}} \quad (13.27)$$

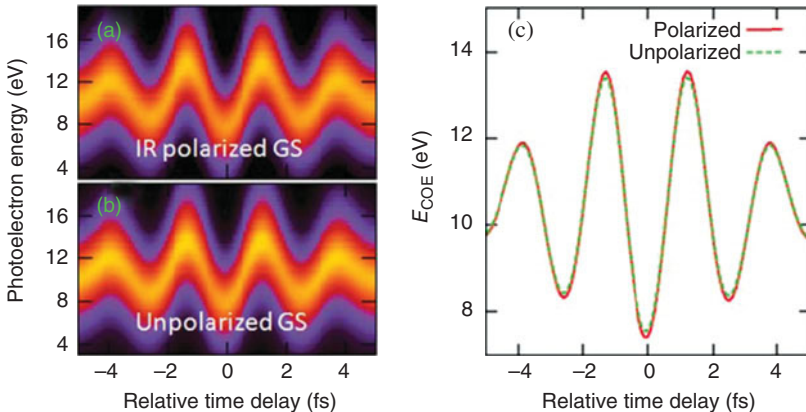
in which the IR electric field appears as an additive, linear perturbation (second term) to the unperturbed delay  $t_X$ . The IR-field-dependent term is largest at resonance, where  $\Delta_{ei} = 0$ . It oscillates with the XUV-IR delay so that within this perturbative analysis, (i.e., for sufficiently small  $E_{IR,0}$ ) the influence of the streaking field on the photoemission time delay tends to cancel (on average) over one IR period. The oscillation occurring with the delay is a result of measuring  $t_X$  and distorts the sinusoidal behavior of the streaking traces in the photoelectron spectra as predicted—without taking the streaking field into account—by Eq. (13.21). As an example of the signature of the initial-state perturbation on streaked photoemission spectra, Figure 13.11 shows numerical results obtained for one-dimensional, model hydrogen atoms in which the electron and nucleus interact via the soft-core Coulomb potential

$$V(x) = \frac{-1}{\sqrt{x^2 + a^2}}. \quad (13.28)$$

The parameter  $a$  is adjusted to the ionization energy of hydrogen atoms (13.6 eV). The calculation was performed with the following parameters: for the XUV pulses, a central energy of 25 eV and a pulse length of 200 as were used; for the streaking IR pulses, a wavelength of 800 nm at a peak intensity of  $2 \times 10^{12}$  W cm<sup>-2</sup> and a pulse length of 5 fs [80] were employed. For photoionization from the relatively strongly bound ground state, the streaking field's effect on both the photoelectron spectrum and the streaking trace's center of energy is very small (Fig. 13.11a–c). In contrast, for photoionization from the model atom's first excited state, the streaking field severely distorts the central energy and the sinusoidal shape of the unperturbed streaking trace (Fig. 13.11d–f).

**13.2.2.2 Final-State Interactions** In deriving the streaking momentum of the emitted photoelectron in Eq. (13.21), we assumed that the active electron is instantaneously released by the absorption of one XUV photon, and that the photoelectron continues to move classically *solely* under the influence of the electric field it experiences in the IR streaking pulse. All other forces, such as the interaction of the photoelectron with the residual ion, are excluded in this approach. The implementation of this idea—the sudden release of a photoelectron and subsequent disregard of all but the IR-laser field—within a quantum mechanical model is straightforward and referred to as “strong-field approximation (SFA)” (Fig. 13.12) [4, 80, 91]. The

## XUV photoemission from ground state



## XUV photoemission from first excited state

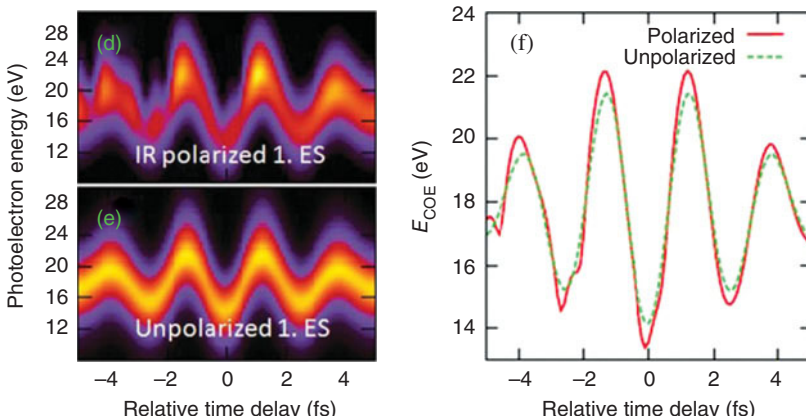


**FIGURE 13.11** The effect of initial-state perturbation (here referred to as “polarization”) by the IR streaking field on XUV photoemission from the ground state of an 1D model hydrogen atom for  $\hbar\omega_X = 25$  eV XUV pulses with a pulse length of 300 as. (a) Spectrogram including initial state polarization. (b) Spectrogram without initial state polarization. (c) Corresponding central energies  $E_{\text{COE}}(\tau)$  obtained as first moments in energy from the streaking traces. (d, e, f) Same as (a, b, c) for XUV photoionization from the first excited state of the model hydrogen atom. Adapted from Reference 80. (For a color version of this figure, see the color plate section.)

SFA takes advantage of the fact that the TDSE for the motion of an electron that is exposed solely to an oscillating electromagnetic field can be solved analytically. The corresponding closed-form solutions are the so-called Volkov states [6, 92]

$$|k(t)\rangle^{\text{Volkov}} = |k + A_{\text{IR}}(t)\rangle e^{i\Phi(t)}. \quad (13.29)$$

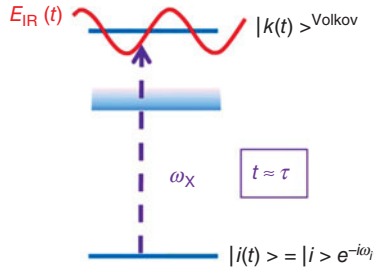


**FIGURE 13.12** Schematic energy level diagram for XUV photoemission at the specific XUV–IR delay  $\tau$ . In strong-field approximation, the final photoelectron state  $|k(t)\rangle^{\text{Volkov}}$  is modeled as an eigenstate of the photoelectron in the electric field,  $E_{\text{IR}}(t)$  of the IR laser field.

The Volkov phase

$$\Phi(t) = -\frac{1}{2} \int_0^t dt' [k^2 + 2kA_{\text{IR}}(t') + A_{\text{IR}}(t')^2] \quad (13.30)$$

includes three terms with a distinct physical meaning. The first term simply corresponds to the kinetic energy,  $k^2/2$ , of a free electron with momentum  $k$ . The second and third terms depend on the streaking field. The second term represents the energy shift that the active electron experiences due to the streaking field and explains the energy oscillations in photoelectron streaking spectra with  $kA_{\text{IR}}(\tau)$ . This is consistent with the classical derivation of the final photoelectron momentum in Eq. (13.21). The third (so-called “ponderomotive”) term is the energy associated with the photoelectron’s quiver motion in the streaking field and can be neglected for typical streaking field intensities.

The SFA allows photoemission streaking spectra to be easily modeled in quantum mechanical calculations by replacing the free final state of the photoelectron in Eq. (13.10),  $|k(t)\rangle$ , with the Volkov state (13.29) [4, 5, 80, 91]. Since the oscillatory behavior of the streaking traces is explained by the Volkov phase (13.30) alone, the question arises to what extent photoemission streaking spectra and time delays are affected by replacing the free-electron momentum eigenstate  $|k\rangle$ , in the phase  $\arg \langle k | z | i \rangle$  of the dipole matrix element in Eqs. (13.12) and (13.13) with the state  $|k + A_{\text{IR}}(\tau)\rangle$  corresponding to the electron’s kinematic momentum in the field. We seek an answer to this question by expanding the phase of the IR-field-dressed dipole matrix element in both,  $A_{\text{IR},0}$  and the momentum difference  $k - k_{\max}$ . Since  $k$ -independent terms do not change the photoelectron probability density (13.15), we do not keep these terms and obtain

$$\arg \langle k + A_{\text{IR}}(\tau) | z | i \rangle = -\{z_X + \Delta z_{\text{IR}}(\tau)\} k + O\left(A_{\text{IR},0}^2; [k - k_{\max}]^2\right), \quad (13.31)$$

with the definition

$$\Delta z_{\text{IR}}(\tau) = \frac{d^2}{dk^2} \arg \langle k | z | i \rangle \Big|_{k_{\max}} A_{\text{IR}}(\tau). \quad (13.32)$$

The presence of the streaking field thus adds the displacement  $\Delta z_{\text{IR}}$  to the IR-field-free displacement  $z_{\text{IR}}$  in Eq. (13.16) and Figure 13.6. Consequently, the IR field changes the field-free photoemission time delay  $t_X$  in Eq. (13.17) to

$$t_{X,\text{IR}}(\tau) = \frac{z_X + \Delta z_{\text{IR}}(\tau)}{v_g + A_{\text{IR}}(\tau)} = t_X + \Delta t_{\text{IR}}(\tau) + O\left(A_{\text{IR},0}^2\right), \quad (13.33)$$

with the first-order correction

$$\Delta t_{\text{IR}}(\tau) = \frac{\Delta z_X}{v_g} - t_X \frac{A_{\text{IR}}(\tau)}{v_g}. \quad (13.34)$$

The first term in the IR-field-induced temporal shift,  $\Delta t_{\text{IR}}$ , corresponds to the extra time the photoelectron needs to cover the displacement  $\Delta z_{\text{IR}}$  at the group velocity  $v_g$ . The second term accounts for the IR-laser-induced change of the group velocity in the denominator of Eq. (13.33).  $\Delta t_{\text{IR}}$  oscillates with the XUV–IR delay  $\tau$ , and vanishes in the average over one IR period (for sufficiently long IR pulses). Averaged over the IR-laser period, the change of the phase in (13.31),  $\Delta z_{\text{IR}}(\tau)k$ , due to a weak streaking field therefore does not affect relative photoemission time delays. IR-laser-induced changes in (13.31) can, however, modify the shape of the photoelectron dispersion wave packet in streaking traces; this is similar to the effect of initial-state distortions discussed above (cf. Fig. 13.11).

**13.2.2.3 Coulomb–Laser Interactions** For theoretical studies of streaked photo-electron spectra and photoemission time delays, the SFA is a convenient scheme thanks to a particularly simple representation of the photoelectron’s final state. The availability of a closed-form expression for the final-state wavefunction of the photoelectron facilitates photoemission calculations significantly. In addition, quantum-mechanical photoemission streaking calculations with Volkov final states yield streaking traces that follow, without distortion, the laser vector potential. This is in agreement with the simple classical result for the final photoelectron momentum, Eq. (13.21). In order to examine to what extent effects that are not accounted for in the SFA influence streaked photoemission spectra, we proceed by using the results of the SFA calculations as a reference [80].

An important shortcoming of the SFA is its complete neglect of the interaction between the emitted electron and the residual, positively charged ion. In order to include this interaction (i.e., both the influence of the streaking laser’s electric field and the residual ion’s Coulomb field) on the motion of the photoelectron, we seek an approximation for the full Coulomb–Volkov final-state wavefunction that goes beyond the SFA. For clarity and simplicity, we continue to illustrate our discussion with numerical results of a one-dimensional simulation of the photoionization process. For a single-active-electron description in full dimensionality, see Reference 93.

From the SFA analysis, we learned that the streaking of photoelectron energies in the IR-laser electric field is approximately represented by the phase of the final-state

wavefunction. Taking the SFA as a guide, we now write the final-state wavefunction as

$$\psi_k^{\text{EA}}(x, t) \sim e^{-ik^2 t/2 - iS^{\text{EA}}(x, t)} \quad (13.35)$$

and split the action function,  $S^{\text{EA}}$ , into two parts—the known action in the SFA,  $S^{\text{SFA}}$ , and a to-be-determined action,  $S^{\text{CL}}$ ,

$$S^{\text{EA}} = S^{\text{SFA}} + S^{\text{CL}}. \quad (13.36)$$

In order to determine  $S^{\text{CL}}$ , we apply the semiclassical eikonal approximation (EA) [6, 80, 93]. In the EA, the quantum mechanical wavefunction is written in the form of Eq. (13.35), and the action,  $S^{\text{EA}}$ , is determined classically by calculating the phase accumulation along classical electron trajectories  $x_{\text{free}}(x, t') = x + k(t - t')$  that start at position  $x$  at time  $t$ . For the motion of photoelectrons subjected to the potential of the residual ion,  $V_{\text{Ion}}(x)$ , and the laser electric field, the accumulated “Coulomb-laser (CL)” phase (13.36) is given by [80]

$$S^{\text{CL}}(x, t) = \int_t^\infty dt' \frac{\delta V_{\text{Ion}}[x_{\text{free}}(x, t')]}{\delta x_{\text{free}}} \Delta x(t') + O(A_{\text{IR},0}^2). \quad (13.37)$$

In classical mechanics (expressed in terms of action and angle variables), the negative time derivative of an action results in an energy [94]. Here, the time derivative of  $S^{\text{EA}}$  with (13.37) results in the expression

$$\begin{aligned} \delta E^{\text{EA}}(x, \tau) &= -\left. \frac{\delta S^{\text{EA}}(x, t)}{\delta t} \right|_\tau = -\left[ k + \frac{|V_{\text{Ion}}(x)|}{k} \right] A_{\text{IR}}(\tau) \\ &\quad + \int_{-\tau}^\infty dt \frac{\delta V_{\text{Ion}}[x'(t)]}{\delta x'} A_{\text{IR}}(t) \end{aligned} \quad (13.38)$$

for the energy shift in the IR streaking field. The first term in this formula is the familiar streaking shift in SFA,

$$\delta E^{\text{SFA}}(\tau) = -\left. \frac{\delta S^{\text{SFA}}(t)}{\delta t} \right|_\tau = -k A_{\text{IR}}(\tau). \quad (13.39)$$

The second and third terms include the combined interaction of the photoelectron with the laser and Coulomb fields. In our numerical applications for typical streaking parameters [80], we find that the third term can be neglected in comparison with the second term.

In order to reveal changes—relative to the SFA predictions—in the streaking amplitude and photoemission delay due to the simultaneous interaction of the emitted

photoelectron with the Coulomb and IR-laser fields, we fit local amplitude and delay functions,  $K(x)$  and  $\Delta t_X(x)$ , to the streaking shift (13.38),

$$\delta E^{\text{EA}}(x, \tau) = -K(x) A_{\text{IR}} [\tau - \Delta t_X(x)]. \quad (13.40)$$

Numerical tests for streaked photoemission from one-dimensional model hydrogen atoms with the soft-core Coulomb potential (13.28) [80] show dominant contributions to the local streaking shift at  $x = 0$  where the initial-state wavefunction is localized. Numerical results for the same target atom also show very close agreement between the EA and full TDSE solutions, while TDSE calculations deviate noticeably from results obtained in SFA.

Figures 13.13a and b show streaked photoemission spectra for an IR field with a peak intensity of  $2 \times 10^{12} \text{ W cm}^{-2}$ . Here, the XUV pulses have a pulse length of 300 as and central photon energies of 90 eV (Fig. 13.13a) and 25 eV (Fig. 13.13b). Figure 13.13c shows the corresponding centers of energy relative to the SFA shift (13.39). The centers of energy are evaluated as first moments of the streaking traces in Figures 13.13a and 13.13b, respectively. The two curves are shifted by 50 as. The deviation from the SFA results for  $\hbar\omega_X = 90 \text{ eV}$  are smaller than for 25 eV, as one

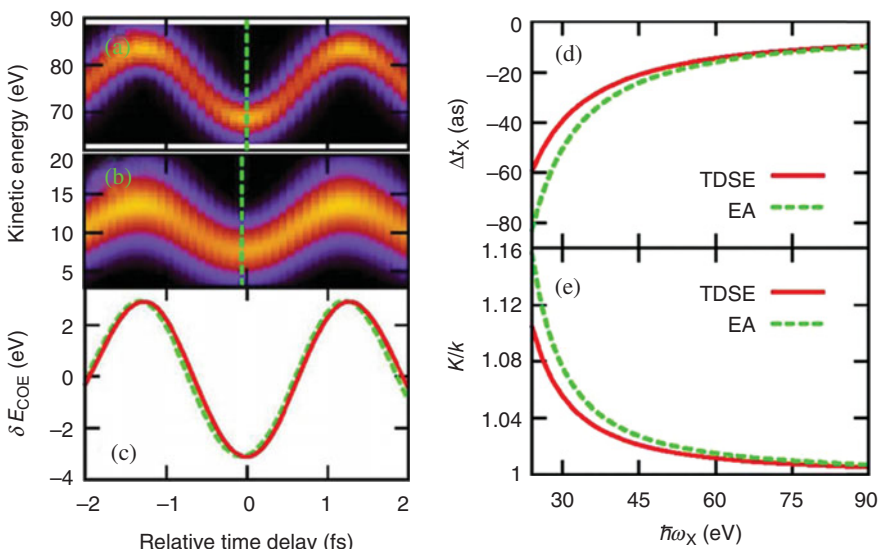


**FIGURE 13.13** Streaked photoemission from model hydrogen atoms. Results obtained by numerically solving the time-dependent Schrödinger equation (TDSE) for XUV pulses with (a)  $\hbar\omega_X = 90 \text{ eV}$  and (b)  $25 \text{ eV}$ . (c) Corresponding center-of-energy shifts  $\delta E_{\text{COE}}(\tau)$  for  $\hbar\omega_X = 90 \text{ eV}$  (solid line) and  $25 \text{ eV}$  (dashed line). To facilitate the identification of the temporal shifts  $\Delta t \times \delta E_{\text{COE}}(\tau, \hbar\omega_X = 90 \text{ eV})$  is normalized to the  $\hbar\omega_X = 25 \text{ eV}$  result. (d)  $\Delta t_X(x = 0)$  and (e) oscillation amplitude  $K(x = 0)$  in Eq. (13.40) relative to the strong-field approximation (SFA) for TDSE (full line) and eikonal-approximation (EA, dashed line) calculations. Adapted from Reference 80.

would expect in view of faster photoelectrons being affected less by their interaction with the residual ion.

In Figures 13.13d and e we compare the EA results with the TDSE results for XUV photon energies between 25 and 90 eV. Figure 13.13d compares the change in photoemission time delay relative to the SFA photoemission delay, obtained by fitting Eq. (13.40) and evaluated at  $x = 0$ , with the prediction of full TDSE calculations. Figure 13.13e shows the amplitude  $K(x = 0)$  in EA relative to the SFA streaking amplitude  $k$  obtained by fitting Eq. (13.40) to Eq. (13.38). The EA and TDSE results are in good agreement and converge, as expected, to the SFA results for higher photoelectron energies.

### 13.3 STREAKED PHOTOEMISSION FROM SOLIDS

#### 13.3.1 Principle and Setup for Fs to Sub-Fs Time-Resolved Experiments on Surfaces

NIR-dressed, attosecond XUV-photoemission spectroscopy, as described in the previous sections, can be used to investigate fs to sub-fs dynamics in solids. In order to apply this spectroscopic method to the study of surface-electron dynamics, special experimental conditions are necessary which are introduced here first. We then review some benchmark experimental results achieved with this method [52, 95, 96], which shall give a taste of the exciting insights into surface dynamics and spectroscopy that can be expected when investigating the ultrafast interaction of solid-state systems with attosecond light pulses.

The most direct access to electron dynamics in regions near a surface is granted by photoemission, since the typical escape depth (taken as the electron mean-free path (MFP),  $\lambda$ ) of photoelectrons excited by XUV photons is in the range of 5–10 Å, which corresponds to only two to three lattice constants [97]. Conceptually, the simplest way to resolve attosecond dynamics by photoemission would be to perform pump-probe measurements using attosecond XUV pulses for both triggering and probing excitations in the substrate as it is done in the femtosecond domain with UV two-photon photoemission (cf. [98]). However, this approach is so far stymied by the low intensities available from contemporary high harmonic (HH) light sources. Nevertheless, a high time resolution can be achieved by using the attosecond streaking technique, where single-photon photoionization is initiated by an XUV pulse in the presence of a strong NIR laser field. If the duration of the XUV-induced photoelectron wave packet becomes shorter than half the period of the dressing field ( $\sim 1.3$  fs for NIR pulses) the wave packet's energy is modified according to the vector potential of the dressing field at the instant of emission. This technique was introduced in Section 13.2.2 as a tool for characterizing light pulses and electronic dynamics with sub-fs time resolution.

The NIR-induced energy shift in streaked electron spectra is highly dependent on the time when the electrons enter the laser-dressed continuum. Therefore, relative photoemission time delays,  $\Delta t_X$ , between the release of photoelectrons from different

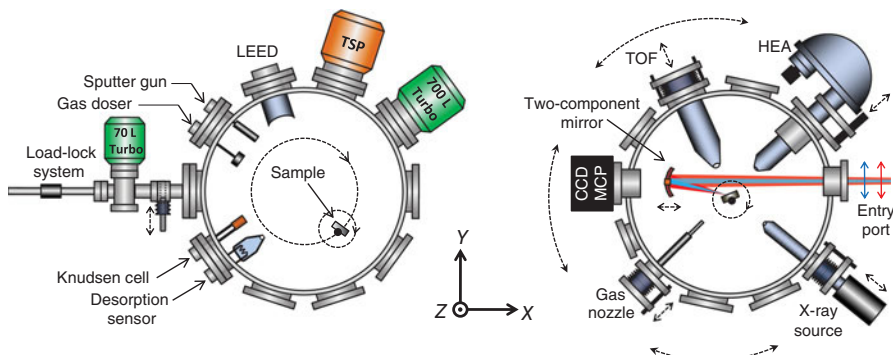


**FIGURE 13.14** Apparatus for attosecond photoemission experiments in UHV. The sample is transferred from ambient into the preparation chamber (left), where an atomically clean surface can be prepared under UHV conditions. The UHV conditions are achieved and maintained by combining standard turbomolecular pumps (Turbo) with liquid nitrogen-cooled titanium sublimation pumps (TSPs) and high temperature bake-out after each venting procedure. The quality of the surface preparation can be monitored with low-energy electron diffraction (LEED). Atomic mono- and multilayers of various materials can be evaporated onto the sample with a Knudsen cell and calibrated with a desorption sensor. The attosecond photoemission experiments are performed in a second UHV chamber (right), which is connected to the NIR–XUV beamline and incorporates two electron energy analyzers, a simple time-of-flight (TOF) electron spectrometer, and a hemispherical analyzer (HEA) for resolving the lateral momentum. The various degrees of freedom for the positioning of individual components are indicated by dashed arrows (from Reference 95 with copyright permission of Springer). A charge-coupled device (CCD) combined with a XUV-sensitive multichannel plate detector (MCP) allows for detection and optimization of the XUV beam profile before sending both the XUV and NIR beams on the two-component mirror.

electronic states in a solid can be resolved by varying the relative delay,  $\tau$ , between the NIR and XUV pulses, since any time delay in emission will be mapped in streaked photoemission spectra as a relative shift between the streaking traces along the NIR–XUV delay axis (cf. Section 13.2.2).

The typical experimental setup necessary for attosecond streaking measurements on solids as presented in Reference 95 is summarized in Figure 13.14: HH radiation is generated by exposing neon atoms to intense, waveform-controlled, few-cycle NIR laser pulses (violet beam). A thin metal filter spatially separates the low-divergence XUV radiation (blue beam) from the residual NIR light. The two collinear beams are reflected by a two-component mirror. The outer portion of this mirror is fixed and focuses the NIR pulses onto the sample while the inner part serves as a band-pass reflector in order to filter isolated sub-fs XUV pulses from the HH cutoff continuum. Moving the inner mirror back and forth changes the length of the pathway for the XUV pulses and therefore introduces a delay between the XUV and NIR pulses. This is made possible by a piezo-electric translation stage onto which the inner mirror is mounted. Both pulses are spatially and temporally overlapped on the sample surface positioned in the focus of the double mirror assembly [99]. The kinetic

energies of the XUV-induced photoelectrons emitted along the surface normal are analyzed by a TOF spectrometer as a function of the relative delay between the NIR and XUV pulses.

Due to the high surface sensitivity of XUV photoemission, the experiments must be performed under excellent ultrahigh vacuum (UHV) conditions (base pressure  $<10^{-10}$  mbar) to avoid the disrupting influence of adsorbed atomic impurities on the surface [100]. The end-station used for the experiments presented in the next section is divided into two segments. The first chamber accommodates several surface-science diagnostic tools such as a sputter gun, evaporators, a gas-dosing system, and a LEED system, which are necessary for preparing and characterizing atomically clean, single-crystal surfaces and well-defined adsorbate layers [97]. Sample transfer from the ambient into the UHV system is enabled by a load-lock system. The sample is mounted on a motorized, 360° rotatable XYZ manipulator. Full temperature control of the sample (in the range of  $\sim 10$ –2500 K) is provided by an integrated flow-cryostat (operated with liquid helium) and the combination of heating filaments with a variable sample potential up to  $\sim 1$  kV. The second chamber is connected to the NIR–XUV beamline and is dedicated to attosecond streaking experiments. It houses different electron analyzers (e.g., TOF or hemispherical energy analyzer, HEA) and the double-mirror assembly. A cross-sectional view of the UHV system is schematically depicted in Figure 13.14.

### 13.3.2 Photoemission Delay Measured for Tungsten Surfaces

In the case of multiple, distinct emission lines in the photoelectron spectrum, the attosecond streaking technique can be used to compare the characteristics of photoelectrons originating from the different states. For example, the photoelectron spectrum of a (110)-oriented tungsten surface obtained with attosecond XUV pulses (Fig. 13.15) shows two distinct peaks originating from 5d/6sp valence/conduction band (VB, CB) electrons and 4f/5p core levels. By employing the attosecond streaking technique, the relative timing of the photoelectron emission, the instant when they leave the surface, can be determined.

As is illustrated in Figure 13.16, photoelectrons leaving the surface at different instants are subjected to different phases of the streaking field. It is possible to extract an effective emergence time for the electrons using the waveform-controlled streaking field [30]. Here, we ignore the streaking field inside the solid which, due to the metal's optical properties, is weak [101]. As a result, the effective delay in photoemission can be reconstructed from the spectrograms.

A tungsten (110) surface was the sample used in the first proof-of-principle experiment [51]. From clean W(110), two nearly parallel spectrograms are observed that originate from different electronic bands, the 5d valence and 6sp conduction band, and the 4f/5p core level band, which are emitted with different kinetic energies (Fig. 13.17a). The large bandwidth of the excitation pulse does not allow separation of the 4f/5p, and the 5d/6sp intensities, respectively. However, due to their comparatively small ionization cross-sections and densities of states, the 5p and 6sp contributions are minor, and the spectra are dominated by 5d valence and 4f core

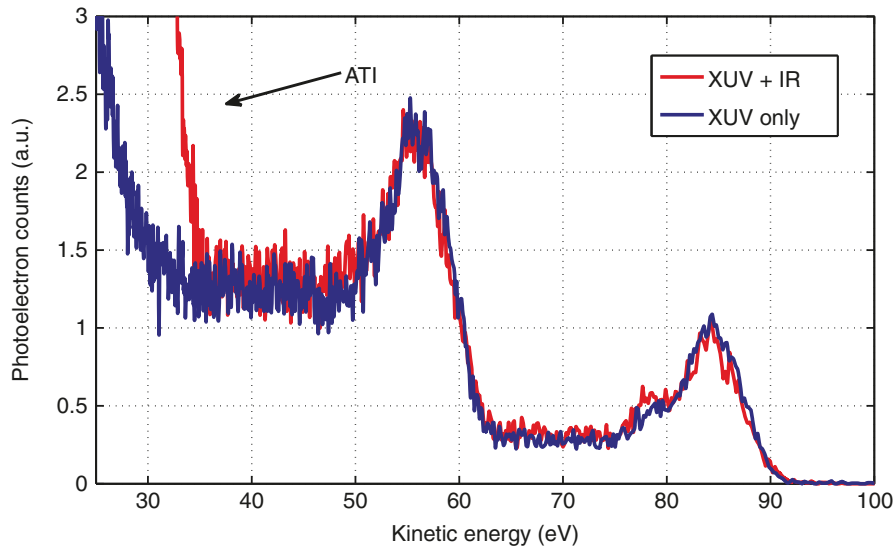


**FIGURE 13.15** Raw photoelectron spectra of tungsten (110) measured with (red curve) and without (blue curve) the presence of the probe NIR streaking field using 91 eV, XUV photons. The spectra show two distinct peaks originating from 5d/6sp valence and 4f/5p core levels at  $\sim 83$  and  $\sim 56$  eV, respectively. In the presence of the NIR probe field, there is an intense photoelectron signal below 35 eV induced by above threshold ionization (ATI). Each spectrum was obtained by integration over 60,000 laser pulses (from Reference 95 with permission of John Wiley & Sons). (For a color version of this figure, see the color plate section.)

emission lines. Both spectrograms show the change in electron energy corresponding to the evolution of the electric field of the NIR streaking pulse. Figure 13.17b shows a center-of-mass (COM) analysis of the spectrograms. For this analysis, the time-dependent COM of both emission lines were calculated in a global fit of the function:

$$\text{COM}(\tau) = ae^{-4 \ln(2) \frac{(\tau - t_0 - \Delta t_X)^2}{\text{FWHM}^2}} \sin(\omega\tau + \phi_{\text{CEP}} - \omega\Delta t_X) + \text{offset}, \quad (13.41)$$

where  $a$  and offset denote the respective streaking amplitudes and the time-independent positions of the emission lines, respectively.  $t_0$  and FWHM denote center and full width at half maximum of the Gaussian-shaped envelope of the streaking field, respectively, and  $\phi_{\text{CEP}}$  gives its carrier envelope offset phase. The relative photoemission delay  $\Delta t_X$  accounts for a temporal shift between the spectrograms of both emission lines. The fit results are shown as solid lines in Figure 13.17b, and a temporal shift in the streaking of  $\Delta t_X = 85 \pm 45$  as is extracted. This result is in good agreement with the initial study, where the valence electrons were found to be emitted approximately 100 as earlier than their tightly bound core-state counterparts [51].

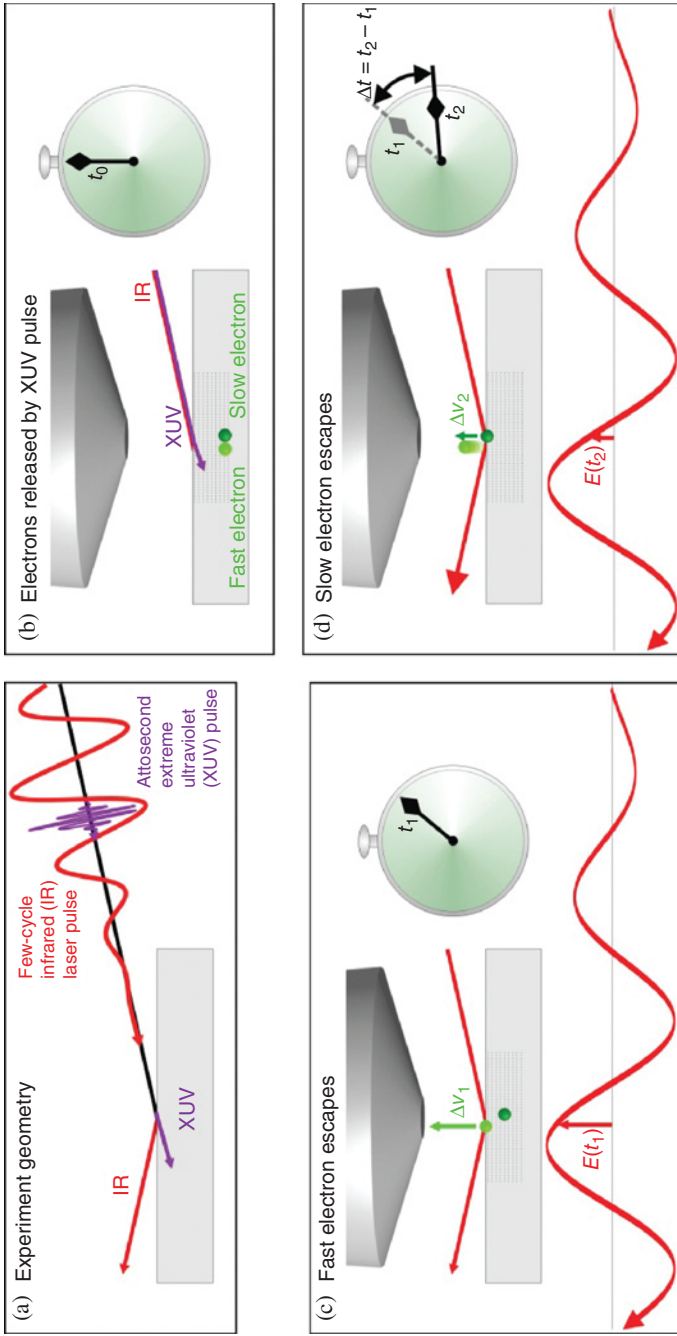


**FIGURE 13.16** Attosecond spectroscopy on solids: Electrons arriving at the surface at different instants are subjected to different phases of the streaking field outside the metal. In panel (a) an isolated attosecond XUV pulse and a delayed few-cycle waveform-controlled streaking field are incident on a solid surface. In panel (b), at time  $t_0$ , the XUV pulse is absorbed in the solid and two types of photoelectrons are born, for simplicity one photoelectron is called “slow,” the other “fast”. In panel (c), at time  $t_1$ , the fast electron has propagated to the surface and is now subjected to the strong streaking field, which modulates its outgoing kinetic energy which is dependent on the instant of release. In panel (d) at time  $t_2$ , the slow electron has reached the surface and feels the strong streaking field on the vacuum side; since it has emerged at a different time, the modulation of its kinetic energy will vary depending on the precise delay in emission. By evaluation of the full streaking spectrograms, collected as a function of relative delay between the attosecond XUV pulse and the streaking field, the delay in photoemission can be determined. Compared to streaking experiments at isolated particles, detailed models of electron localization, and electron and photon transport and interactions in the surface are necessary for the evaluation of such spectrograms correct: (from Reference 96 with permission of John Wiley & Sons).

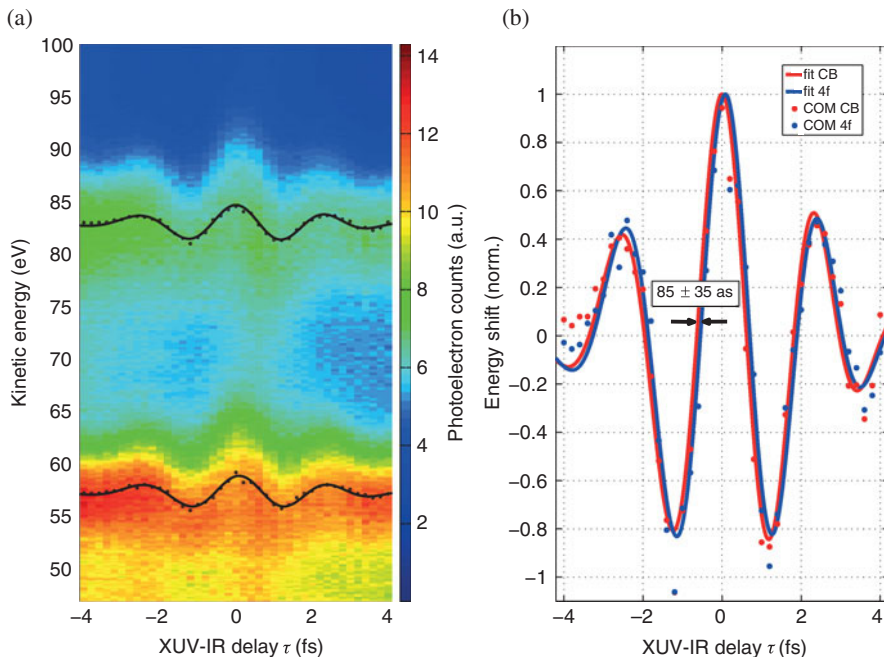


**FIGURE 13.17** (a) Raw attosecond streaking technique spectrogram of a tungsten (110) surface. Photoelectron intensities are given in arbitrary units. (b) Center-of-mass (COM) analysis of the spectrogram. The COM of both emission lines measured are given as dots, and a global fit to both COM traces is shown in solid lines (from Reference 96 with permission of John Wiley & Sons). (For a color version of this figure, see the color plate section.)

These results demonstrate the technical capability of measuring photon-induced electron release, electron transport through the topmost atomic layers of a solid sample, and emission into the vacuum in real time, with attosecond temporal resolution. Explaining the state-dependent differences of the emission dynamics seen in the streaking experiment is unfortunately a much more challenging task for metal surfaces than for gaseous targets [30].

### 13.3.3 Theoretical Modeling of Attosecond Photoemission from Tungsten

Four different theoretical approaches explaining the dynamics seen in this W(110) experiment have been put forward, all yielding delayed emission between the core and valence electrons varying from 42 to 110 as. The first theoretical approach by Cavalieri et al. [51] explained the delayed emission of the core electrons by different group velocities of the final states. Assuming the validity of the static band-structure picture, the authors showed that for the photon energy of the experiment (91 eV) the final-state bands of the valence electrons exhibit stronger dispersion than those of the core electrons. As a result, a smaller effective mass, larger group velocity, and

more rapid transport were extracted for the valence electrons, explaining the observed timing. As for the theoretical models discussed below, a critical point of this model was the application of the *static* band structure.

Considering this, in a second study Kazansky and Echenique have investigated the relative contributions of final- and initial-state effects on the observed dynamics [78]. In their revised quantum model, they treat core electrons as localized, and valence electrons as completely delocalized. Attenuation by inelastic scattering is taken into account in addition to electron–hole interaction for the inner-shell levels (but not for valence states). The streaking field inside the metal is set to zero. Pseudopotentials obtained for copper are used to model electron transport in tungsten. Calculations based on this one-dimensional theory also reproduce the experimentally obtained results quite well. Compared with the first approach, however, the relative magnitudes of final- and initial-state effects are reversed.

The authors show that different final state energies for core and valence emission contribute only 10 as to the net relative photoemission delay. To understand this, it must be remembered that the initial energies for valence and core states are different; therefore, their final kinetic energies will be different even if absorbing the same XUV photon. However, standardizing the final energy of core emission to match with that of valence band emission induces *only* 10 as to the relative delay mentioned above. As this factor is minor it is largely ignored, and the observed relative delay is attributed to the contrast in wavefunction localization between the core-level and valence-band states.

A third theoretical study by Lemell et al. models the attosecond streaking experiment within a classical electron-transport approach [77]. Quantum effects enter this classical calculation via a stochastic force  $F_{\text{stoc}}(t)$  containing elastic and inelastic scattering with tungsten cores as well as with conduction electrons. Other forces changing the electrons' momenta result from the NIR streaking field, which penetrates  $\sim$ 85 layers of the solid in their model, and from the potential barrier at the surface. Rather detailed assumptions are made concerning the properties of the various involved electronic states. The authors discriminate 5p and 4f core electrons and 5d and 6s valence electrons, and treat only the 6s band as delocalized. Elastic scattering cross-sections, used as input for the classical calculation, are calculated with the ELSEPA package [102]. Inelastic scattering cross-sections and angular distributions of inelastically scattered electrons are obtained from the momentum distribution and energy-dependent dielectric constant of tungsten. Two limiting cases are considered for the final states: (i) a free-particle dispersion relation and (ii) the group-velocity distribution (cf. supplementary material in [51]). Depending on these two alternatives, emission of the core electrons is found to be delayed from 42 as (case i) to 110 as (case ii). The authors point out, however, that the group-velocity distribution from Reference 79 had to be blue-shifted by 8 eV to obtain the maximum effect. For the limiting case (i), the larger emission depth of core electrons and inelastic scattering of valence electrons (which enter into the energy region of the core photoelectrons) are the main sources of the observed delay. This occurs as these electrons require additional time to escape, again due to inelastic scattering. These electrons are missing in the valence streaking trace, but are included in the core streaking trace. We note

that the authors address possible extensions of their model, particularly the inclusion of local field enhancements at the surface (due to plasmon excitation), which might affect emission and transport of localized and delocalized states differently (cf. Section 13.4).

Here, we will detail the fourth, quantum-mechanical study by Zhang and Thumm [4, 5], since the main characteristics of streaked photoemission from solid metal surfaces can be understood within a quantum mechanical, one-active-electron model that includes simplifying assumptions. Compared to Reference 78, the authors include the streaking field inside the solid. Solving Helmholtz' equation for the IR electric field, they calculate a skin depth ( $\sim 100 \text{ \AA}$ ) that is much larger than the electrons' MFP,  $\lambda$  ( $\sim 5 \text{ \AA}$ ). The precise value of the skin depth is then irrelevant, since photoelectrons originating at a distance from the surface of more than a few times  $\lambda$  do not contribute noticeably to the measured photocurrent. The interaction of the photoelectron with the streaking IR field is treated non-perturbatively, and the photoemission by the XUV pulse is treated in first-order perturbation theory. The initial states are assumed as fully localized core and fully delocalized valence electrons. Core-level photoelectrons from different lattice layers are added coherently to the photoemission yield. Within this model, the interference between photoelectron emissions from 4f core levels (that are localized in different lattice planes parallel to the surface) is the main source of the delay. For this relative delay between core-level and CB emission they obtain 110 as, a value compatible with the experiment.

Apart from restricting the electron dynamics to one active electron, simplifying assumptions in the model of Zhang and Thumm [4, 5] are included in their representation of (i) the initial state of the active electron, (ii) the propagation of the released photoelectron into the bulk and near the surface, and (iii) the final photoelectron states in terms of a modified Volkov wave (13.29). To further simplify the discussion and remain consistent with the numerical modeling [4, 76, 86, 91, 95, 103] of recently performed experiments on tungsten [51], platinum [104], rhenium [96], and magnesium [52] surfaces, they assume linearly polarized, grazingly incident XUV and IR pulses with electric field vectors that may be approximated as being perpendicular to the surface.

Due to the large XUV photon energy, XUV photoemission by one or several XUV photons can easily be distinguished in streaked photoelectron spectra. As for the description of photoelectron wave packets in Section 13.2, we therefore accurately model XUV photoabsorption in the first-order perturbation theory. The transition amplitude for absorption of a single XUV photon resulting in the emission of an electron from an initial Bloch state,  $|\Psi_{\vec{k}}(t)\rangle = |\Psi_{\vec{k}}\rangle e^{-i\epsilon_{\vec{k}}t}$ , with the crystal momentum  $\vec{k}$ , and energy  $\epsilon_{\vec{k}}$ , of a metal substrate to an IR-field-dressed final continuum state,  $|\Psi_f\rangle$ , is then given by [4, 5]

$$T_{\vec{k}} = -i \int_{-\infty}^{+\infty} dt \left\langle \Psi_f \left| \vec{r} \cdot \vec{E}_X(t + \tau) \right| \Psi_{\vec{k}} \right\rangle. \quad (13.42)$$

As mentioned earlier, the most elementary quantum-mechanical description of photoelectrons is achieved in the SFA, which represents the interaction of the photo-released electron with the IR streaking field by a Volkov final-state wavefunction (13.29). Including elastic and inelastic scattering of the photo-released electron before its emission from the surface (in terms of the damping factor  $e^{\kappa z}$ ), the final photoemission state is represented as a Volkov wave that is exponentially damped inside the surface [4, 5, 76],

$$\Psi_f(\vec{r}, t) = (2\pi)^{-3/2} e^{i[\vec{k}_f + \vec{A}_{IR}(t)] \cdot \vec{r} + i\Phi_{\vec{k}_f}(t)} [\Theta(z) - \Theta(-z) e^{\kappa z}], \quad (13.43)$$

with the Volkov phase (cf. Eq. 13.30)

$$\Phi_{\vec{k}_f}(t) = -\frac{1}{2} \int_0^t dt' \left[ \vec{k}_f + \vec{A}_{IR}(t') \right]^2 \quad (13.44)$$

and the unit step function  $\Theta(z)$ . In this model, all propagation effects that the electron encounters inside the substrate are included in the finite MFP  $\lambda = 1/(2\kappa)$  [2, 97]. Integration of (13.42) over all momenta  $\vec{k}$  in the first Brillouin zone [2] yields the photoemission probability

$$P(\vec{k}_f, \tau) = \int_{\vec{k} \in 1. BZ} d\vec{k} |\mathcal{T}_{\vec{k}}(\tau)|^2. \quad (13.45)$$

The initial state  $|\Psi_{\vec{k}}\rangle$  in (13.42) is composed of Bloch waves,  $|\Psi_{\vec{k}^-}\rangle$  and  $|\Psi_{\vec{k}^+}\rangle$ , for electrons moving with (crystal) momenta  $\vec{k}^{\pm} = (\vec{k}, \pm k_z)$  inside the solid toward and away from the surface, respectively, and a transmitted wave [4, 5, 76]. The transmitted wave decays exponentially into the vacuum ( $z > 0$ ) and is negligible in the applications discussed below. For photoemission from core levels, the Bloch waves are linear superpositions of tightly bound atomic levels,  $|\Psi_C\rangle$ , that are localized at the lattice points,  $\vec{R}_j$ , of the substrate. In an elementary approach, the atomic core levels can be approximated by closed-form expressions (e.g., screened hydrogenic wavefunctions), and adjusted to the core-level energies  $\epsilon_B$ , of the substrate,

$$\Psi_{\vec{k}}^{\pm}(\vec{r}, t) = e^{-i\epsilon_B t} \sum_j e^{i\vec{k}^{\pm} \cdot \vec{R}_j} \Psi_C(\vec{r} - \vec{R}_j). \quad (13.46)$$

Thus, the corresponding transition amplitude includes the interlayer interference effects, mentioned earlier, in terms of a coherent sum over contributions to the photocurrent from different substrate layers. The relevant layers are located within a distance equal to a small multiple of  $\lambda$  from the surface. In the numerical applications

shown below, we model  $|\Psi_C\rangle$  by adjusting hydrogenic ground-state orbitals to the core-level binding energy [4, 5].

In general, the representation of the initial states in terms of Bloch waves (13.46) can be applied to localized core levels and delocalized valence and conduction-band (CB) states of the substrate. Assuming fully delocalized CB states, an alternative and technically convenient approach consists in representing the substrate's CB with the so-called “jellium” approximation [97, 105]. In the jellium model, electronic motion in the initial states is regarded as free, while the active electron's motion (perpendicular to the surface) is described in terms of eigenfunctions

$$\Psi_{\vec{k}}(\vec{r}, z, t) \sim e^{-i\varepsilon_{\vec{k}}t} e^{-i\vec{k}\vec{r}} (e^{ik_z z} + R e^{-ik_z z}) \quad (13.47)$$

of the step potential  $U(x, y, z) = -U_0\Theta(z)$ , with  $U_0 = \varepsilon_F + WU$ , Fermi energy  $\varepsilon_F$ , work function  $W$ , and reflection coefficient  $R(U_0, k_z)$ . The photoemission yield in the jellium approximation is obtained by replacing the integrals in (13.45) with an integral over the Fermi volume (containing all initially occupied CB states).

### 13.3.4 Modeling of Photoemission Delays in Tungsten

XUV pulses can release electrons from either bound core levels or delocalized conduction band states of a metal surface. The released photoelectrons get exposed to (and “streaked”) by the same IR probe pulse used to generate the XUV pulse via harmonic generation [31, 55]. The two laser pulses are thus synchronized. By varying their delay,  $\tau$ , Cavalieri et al. [51] measured time-resolved, photoelectron kinetic energy distributions  $P(\varepsilon_f, \tau)$  and deduced a relative delay of  $110 \pm 70$  as between the detection of photoelectrons emitted from 4f core and CB levels of a W(110) surface by absorption of a single XUV photon (Fig. 13.18, left column; see also Figs. 13.15 and 13.17).

To compare model calculations [4, 5] with this streaking experiment, the IR and XUV pulses with Gaussian envelopes are assumed and the experimental parameters of Reference 51 for IR and XUV pulse lengths ( $\tau_{\text{IR}} = 6.5$  fs and  $\tau_X = 0.29$  fs (FWHM)), photon energies ( $\hbar\omega_{\text{IR}} = 1.7$  eV and  $\hbar\omega_X = 91$  eV), and IR peak intensity ( $2 \times 10^{12}$  W cm $^{-2}$ ) are used. For the W(110) surface, measured values for the work function and Fermi energy are 5.5 eV and  $\varepsilon_F = 4.5$  eV, respectively, and the lattice constant in direction perpendicular to the surface is 3.13 Å. Figures 13.18 and 13.19 show that the simulated modulation of the photoelectron kinetic energy agrees with the measurement. In order to find the relative photoemission delay between the two calculated spectra in the right column of Figure 13.18, it is important to compute the center of energies (first moments in energy) in the calculated spectra for the same spectral intervals for which the central energies were deduced from the measured spectra (Fig. 13.19). The relative photoemission delay  $\Delta t_{X,4f-\text{CB}}$  between the 4f-core level and the CB photoelectrons corresponds to the temporal shift between the two calculated centers of energy shown in Figure 13.19b. It agrees well with the experiment for an adjusted electron MFP of  $\lambda = 2.65$  Å [4, 5, 97].

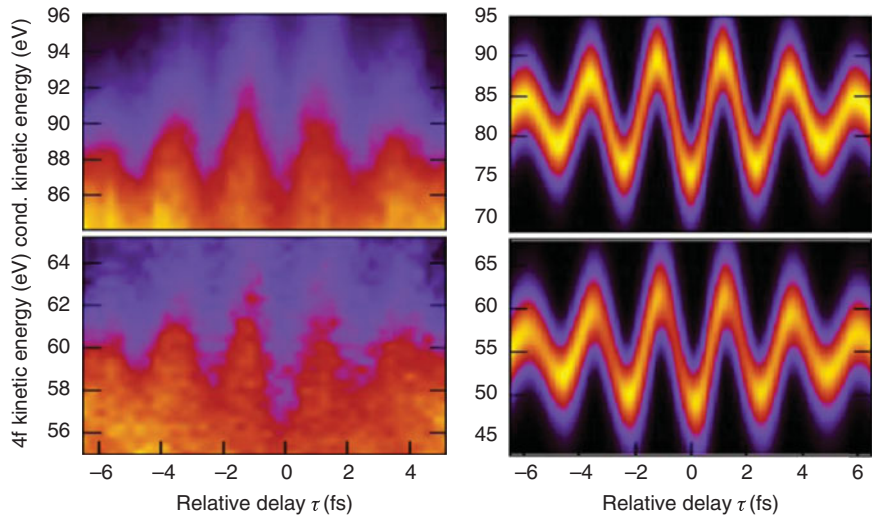


**FIGURE 13.18** Time-resolved, streaked photoelectron spectra for emission from the CB (top) and 4f-core levels (bottom) of a W(110) surface as a function of the delay between the XUV and IR pulses. Linear intensity scales. Experimental results of Cavalieri et al. [51] (left) in comparison with numerical simulations of Reference 4 (right). Reprinted with permissions of APS. (For a color version of this figure, see the color plate section.)

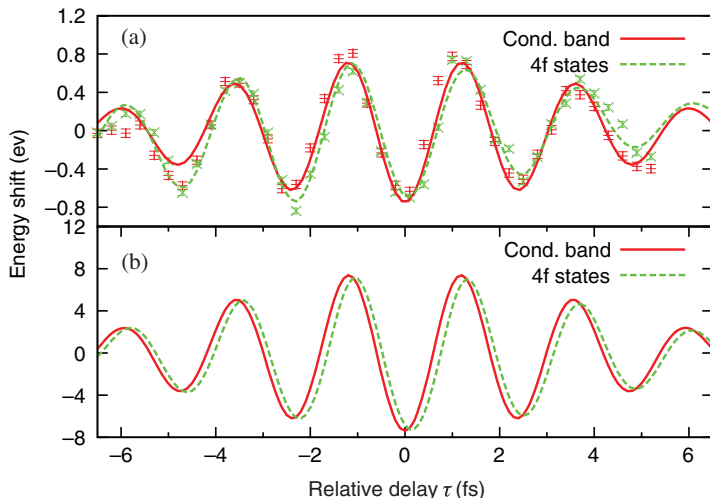


**FIGURE 13.19** Streaked electron spectra for photoemission from CB and 4f-core levels of a W(110) surface. (a) Measured center-of-energy shifts as a function of the delay between the XUV and IR pulses. The damped sinusoidal curves are fits to the raw experimental data (points with error bars) and are shifted by a relative photoemission time delay of  $110 \pm 70$  as. Adapted from Reference 51. (b) Calculated center-of-energy shifts showing a relative photoemission time delay of 110 as between the two groups of electrons. The central energy shifts for the 4f photoelectrons are multiplied by 2.5 in (a) and 1.1 in (b). Adapted from Reference 4.

### 13.3.5 Attosecond Photoemission from Rhenium Surfaces

The time delay measured in the first proof-of-principle experiment with  $\sim$ 300-as XUV pulses centered near 90 eV has a comparably large experimental uncertainty [51]. The accuracy with which such time shifts can be extracted from a streaking spectrogram depends mainly on the depth of the NIR-induced modulation in the photoelectron spectra, the energetic separation between the photoemission lines (whose emission timing should be analyzed), and the signal-to-noise (S/N) ratio of the photoelectron spectra. Experimentally, the modulation depth can be controlled by the NIR field intensity which, however, has to be restricted to much lower values compared to gas-phase experiments in order to avoid an excessive background signal due to above-threshold photoemission (ATP) electrons. ATP stems from the CB electrons of the solid and is generated by the absorption of multiple NIR photons from the streaking field. To enable an unambiguous analysis of the streaked electron distributions, this background should not overlap with the XUV-induced photoemission lines. In this respect, the use of higher XUV photon energies is beneficial.

Figure 13.20a shows the photoemission spectrum obtained from the (0001) surface of rhenium with  $\sim$ 350-as XUV pulses with a central photon energy of 125 eV. Two emission lines corresponding to the 4f and the CB states are well resolved, but are superimposed by a background originating from inelastically scattered XUV photoelectrons. This background (dashed line) has to be subtracted from the spectra prior to the analysis, which represents a further complication compared to gas-phase streaking experiments. A background-corrected spectrogram obtained with a  $4 \times 10^{11} \text{ W cm}^{-2}$  NIR dressing field is depicted in panel b. The results of the data evaluation are shown as crosses in panel c, along with a global fit of both traces to the same parameterized NIR waveform (shown as solid lines). A relative shift of 100 as of the 4f trace to positive NIR–XUV delays is clearly discernible and reveals the delayed emission of the 4f electrons with respect to the CB electrons.

### 13.3.6 Attosecond Photoemission from Magnesium Surfaces

Neppl et al. [52] measured the relative time delay in the emission of VB and core-level electrons from Mg(0001) surfaces. Mg as a test material is well suited to discern the possible effects of the delay in photoemission since the band structure for this material is “free-electron-like.” The influence of the group velocity of the photoelectron wave packet on the photoemission delay can thus be calculated and accounted for. Figure 13.21 shows the streaking spectrograms for both types of electrons. There is no measureable delay in the streaking traces. A simple estimation of the respective “travel time” using free-particle velocities and calculated penetration depths [52] shows that the vanishing time delay can be well accounted for by simply considering transport effects—hinting at a negligible contribution from other phenomena, such as initial-state effects.

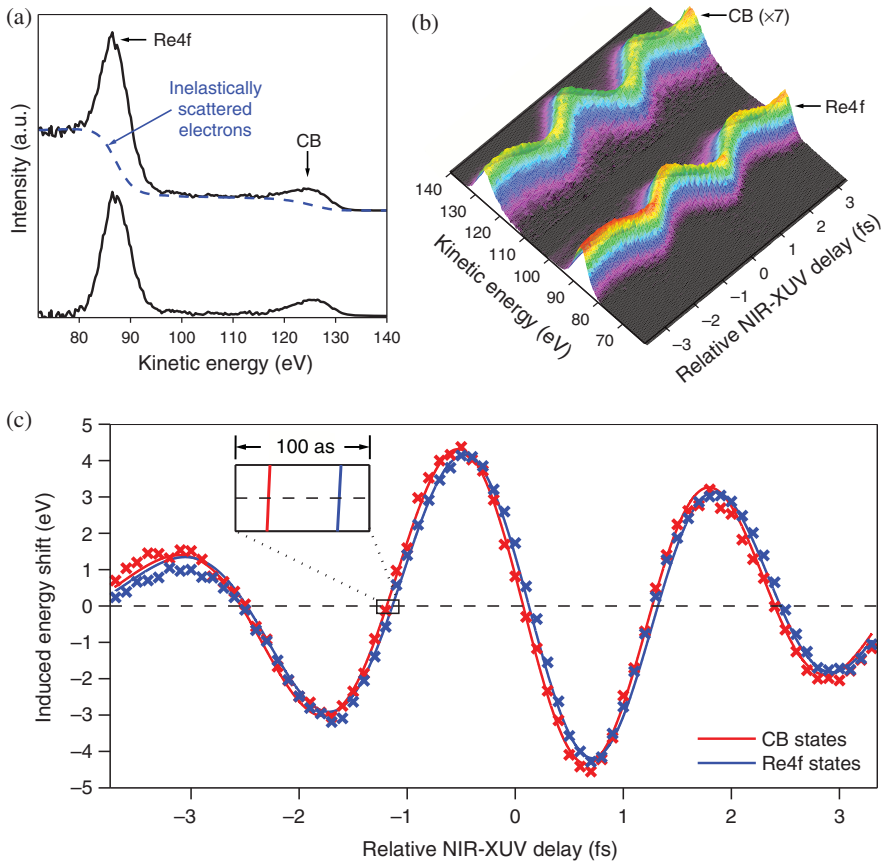


**FIGURE 13.20** Attosecond, time-resolved photoemission from the (0001) surface of rhenium. (a) Static photoelectron emission from rhenium (in the absence of the NIR streaking field) obtained with HH radiation filtered by a 6-eV (FWHM) bandwidth mirror centered near 125 eV. The background of inelastically scattered electrons (blue dashed line) is removed before the analysis. The full streaking spectrogram is shown in panel (b), with the CB intensity scaled by a factor of 7. The comparison of the first moments of the streaked electron distributions as a function of the NIR–XUV delay, shown in panel (c), reveals emission of the 4f photoelectrons from the metal surface delayed by 100 as compared to the photoelectrons released from the conduction-band states. (Adapted from Reference 96, with permission of John Wiley & Sons). (For a color version of this figure, see the color plate section.)

Numerical results for streaked photoemission from Mg(0001) are shown in Figure 13.22. The calculations were performed within a quantum mechanical model [103, 106] similar to the one discussed in Section 13.3.3, and with the IR laser and XUV parameters of the experiment [52]. In contrast to the model discussed in Section 13.3.3, the VB of Mg(0001) is modeled by a more realistic potential (the Chulkov potential [106, 107]). Additionally, the 2p-core level is represented by combining Chulkov and Yukawa potentials [78, 106]. These potentials reproduce the respective

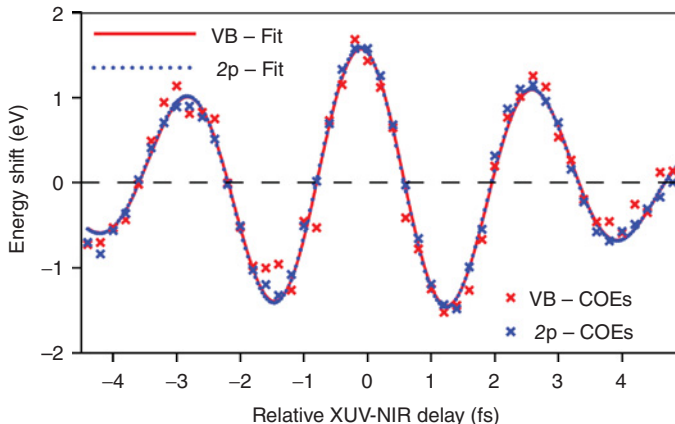


**FIGURE 13.21** Timing analysis of the VB and 2p core-level photoemission from Mg(0001). Calculated center-of-energies (COE) for the VB and 2p region of the spectrogram (depicted as crosses) are fitted to a pair of parameterized analytic functions describing the vector potential of the NIR streaking pulse. The absence of a relative shift between the fitted functions, shown as red solid line for the VB and blue dotted line for the 2p emission, provides evidence for a synchronous release of these electrons from the metal surface. Adapted from Reference 52. (For a color version of this figure, see the color plate section.)

band structures at the level of density-functional theory. The intensity of the NIR pulse is assumed to decay exponentially inside the solid with a skin depth of about one lattice constant  $\delta_L = 2 \text{ \AA}$  [78, 101]. The energy-dependent electron MFP is also taken into account in the calculations. Electron MFPs are adjusted to reproduce the measured XUV synchrotron photoemission spectrum for VB and vanishing relative photoemission delays for 2p-core level emission. The resultant MFP values are 5.0 Å for VB photoelectrons and 4 Å for 2p-core level photoelectrons, complying with previously published data [2, 52, 108].

Figure 13.22a shows the calculated streaking traces for core level and VB emission. The spectral profile of the photoelectron wave packet and its variation as a function of  $\tau$  shown in Figure 13.22a are, in general, determined by the spectral profile of the XUV pulse and the dipole matrix element, as detailed in Section 13.2. Surprisingly, the spectrograms exhibit distinct  $\tau$ -dependent dispersion. The 2p-core level photoelectron dispersion is found to be dominantly determined by the XUV pulse and robust against MFP variations. In contrast, the VB photoelectron dispersion is found to be determined by both the XUV pulse and the MFP-dependent dipole matrix element. The corresponding COE shifts in Figure 13.22b do not reveal any noticeable relative photoemission delay, in agreement with the experimental results given in Figure 13.21.

### 13.3.7 Toward Time Resolving Collective Electrons Dynamics: Probing Plasmon-Response Effects in Streaked Photoelectron Spectra

Under the correct conditions, the external electromagnetic field can excite modes of collective electron motion where the excited electrons oscillate in unison, so-called

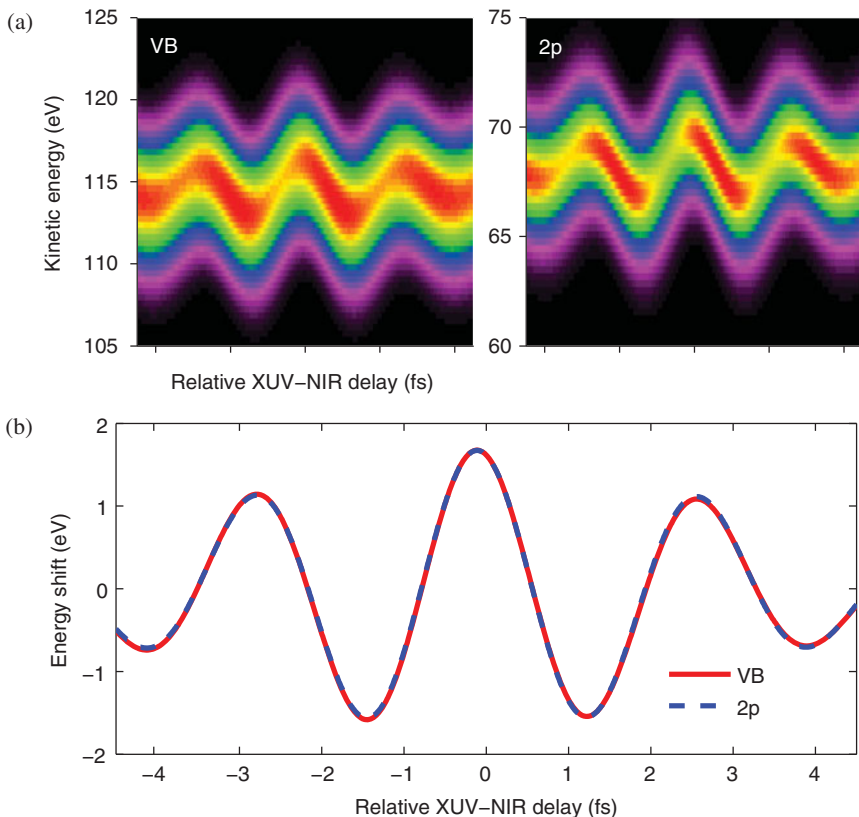


**FIGURE 13.22** (a) Calculated streaked photoemission spectrum for a Mg(0001) surface. The XUV-chirp rate is  $\beta = -2 \text{ fs}^{-2}$  and the NIR-field CEP is  $\phi = 1.22\pi$ . The MFPs are  $\lambda = 5.0 \text{ \AA}$  for VB photoelectron and  $\lambda = 4 \text{ \AA}$  for 2p-core level photoelectron. (b) Corresponding center-of-energy shift. The 2p-core level center-of-energy shift is multiplied by 1.09 for better comparison. Adapted from Reference 103. (For a color version of this figure, see the color plate section.)

plasmons. Plasmons can either be confined to a single nanoparticle (as localized surface plasmons, see Fig. 13.23a), or propagate along metal–dielectric interfaces (as surface plasmon polaritons, see Fig. 13.23b [109]). In both cases, energy from the external electromagnetic field can be localized below the diffraction limit—to nanometer scales [110]. Some of the spectral properties of plasmons in nanoparticles—as a function of particle size, shape, and dielectric properties—are reasonably well understood and can be predicted by solving the classical Maxwell equations, including quantum mechanical aspects by appropriate modeling of the particle’s dielectric response [111]. These dielectric properties are typically described in terms of phenomenological dielectric response functions that are adjusted to fit measured photoemission and absorption spectra [112, 113]. However, the subcycle dynamics of collective electronic excitations in strong laser fields (i.e., how such excitations are formed and how their phase coherence is lost) have not been directly measured, and the

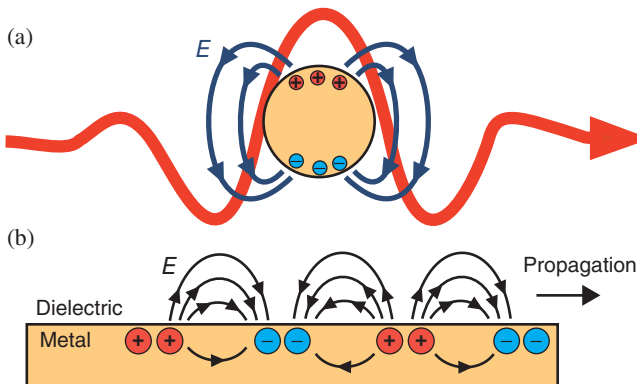


**FIGURE 13.23** Field configurations of (a) a localized surface plasmon of a metal nanosphere in an external light field and (b) a traveling surface plasmon polariton along a metal–dielectric interface. Adapted from Reference 109.

accurate modeling of the creation and decay of plasmons in nanostructures creates a formidable challenge to theory [109]. The field-free dephasing time of a nanolocalized plasmon is typically in the lower femtosecond domain across the plasmonic spectrum [75].

Photoelectron emission from a metal surface by a sub-femtosecond XUV pulse and the subsequent propagation of those electrons through and near the solid provokes a dielectric response in the substrate that acts back on the electron wave packet [61, 114–117] (Fig. 13.24). In an attempt to model this many-electron response, a combined classical and quantum mechanical model was suggested [61]. The classical part of this model assumed that the photoelectron moves as a classical particle at speed  $v_z$ , in a direction perpendicular to the surface, corresponding to the charge density

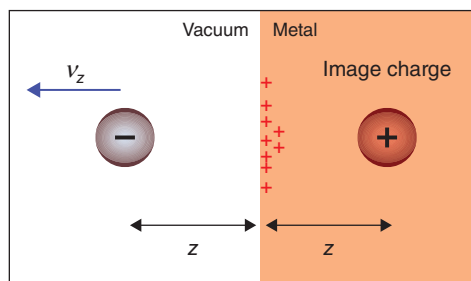


**FIGURE 13.24** A photoelectron held at distance  $z$  from the surface of a perfect conductor induces a redistribution of the electronic surface-charge density that exerts the same static force on the photoelectron as a fictitious positive image charge inside the substrate. For non-perfect conductors and moving photoelectrons, the self-interaction of the photoelectron deviates from the static image force due to the finite response time of surface and bulk plasmons.

$\varrho(\mathbf{r}, t) = \delta(\mathbf{r}_{\parallel})\delta(z - v_z t)$ . The response of the solid is described by the complex self-interaction potential

$$\Sigma(z, v_z) = \Sigma_r(z, v_z) + i\Sigma_i(z, v_z), \quad (13.48)$$

which converges for large distances from the surface to the classical image potential  $-\frac{1}{4z}$ . Its real part,  $\Sigma_r$ , represents an energy shift of the photoelectron by virtual excitations of bulk and surface plasmons and electron-hole pairs in the solid, while its imaginary part,  $\Sigma_i$ , accounts for a loss of photoelectron current due to the interaction between the photoelectron and collective modes of the substrate [61, 114]. The electronic self-interaction potential (13.48) is subsequently employed in the quantum-mechanical description of the photoemission process.

The solid is modeled as a wide slab in jellium approximation (see Section 13.3.3), and the time-independent SE is first solved numerically for the potential  $V_J(z) + \Sigma_r(z, 0)$ , with the smeared-out jellium step potential of width  $a$  at both sides of the solid–vacuum interface,  $V_J(z) = -\frac{U_0}{\{1+\exp(\frac{z}{a})\}}$ , and the static energy shift  $\Sigma_r(z, 0)$  [114]. This provides the initial bound slab eigenfunctions and their corresponding energies. The effect of the full dielectric response, (13.48), on the released photoelectron wave packet is then accounted for by numerically propagating the TDSE with the potential  $V_J(z) + \Sigma(z, v_z)$ , and the potentials for the active electron’s interaction with the XUV and IR pulses [61].

The self-interaction potential  $\Sigma(z, v_z)$  can be calculated based on phenomenological dielectric functions,  $\epsilon_B(\mathbf{k}, \omega)$  and  $\epsilon_S(\mathbf{k}, \omega)$ , that model bulk- and surface-plasmon and particle-hole excitations by the photoelectron in the bulk and at the surface [118, 119]. The calculation proceeds analytically by propagating the initial state of the bulk and surface plasmon quantum field,  $\Psi(t=0)$ , subject to the interaction  $H_{\text{int}} = \int d\mathbf{r} \varrho(\mathbf{r}, t) \Psi(\mathbf{r}, t=0)$  [120, 121]. This propagation calculation can be mostly carried out analytically and results in a lengthy expression [61] for  $\Sigma(t, v_z) = \frac{1}{2} \langle \Psi(t) | H_{\text{int}}(t) | \Psi(t) \rangle$  that depends on the bulk ( $\omega_B$ ) and surface plasmon frequencies ( $\omega_S = \omega_B/\sqrt{2}$ ). Figure 13.25 shows streaked photoemission spectra for an aluminum model surface with  $U_0 = 10.2$  eV,  $\omega_S = 0.378$ ,  $a = 1.4$  Å,  $\lambda = 5$  Å, and  $\delta_L = 0$ , and a 300-as XUV pulse centered at  $\hbar\omega_X = 40$  eV. The streaked spectrum shown in Figure 13.25a is calculated by solving the TDSE with the “dynamical” plasmon response  $\Sigma(z, v_z)$ . As a reference, Figure 13.25b shows the photoemission spectrum obtained using the “static” response  $\Sigma_r(z, 0)$  in the propagation calculation. The central energies for the two spectra are shifted by the streaking-time-delay difference  $\Delta t_{X,\text{wake}} = t_{X,\text{dyn}} - t_{X,\text{sta}} = 100$  as (Fig. 13.25c).

Streaking-delay differences  $\Delta t_{X,\text{wake}}$  are shown for different MFPs in Figure 13.26a and for different plasmon frequencies (i.e., electron densities) in Figure 13.26b as a function of  $\hbar\omega_X$ . Figure 13.26a shows results for the surface-plasmon frequency  $\omega_S = 0.378$  and Figure 13.26b for the MFP  $\lambda = 5$  Å. All other parameters are as in Figure 13.25. Increasing  $\lambda$  by a factor of two significantly increases  $\Delta t_{X,\text{wake}}$  for XUV photon energies  $\hbar\omega_X < 50$  eV, but has little influence at larger  $\omega_X$  (Fig. 13.26a).

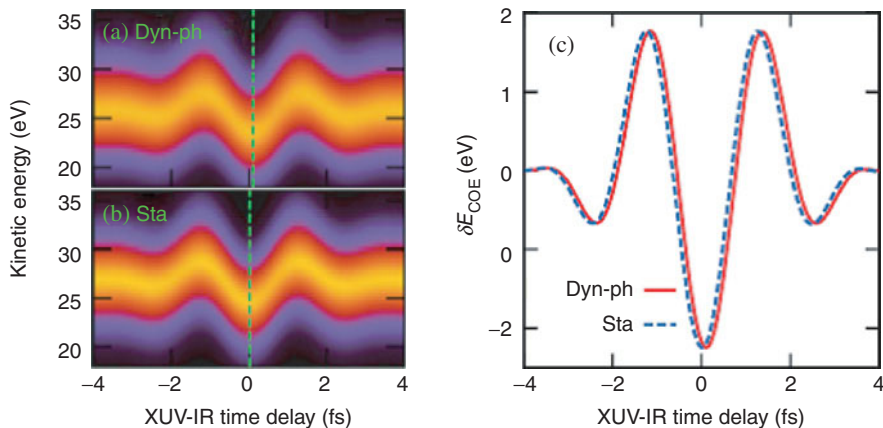


**FIGURE 13.25** Streaked photoelectron spectra as a function of the pump-probe delay for a model aluminum surface and  $\hbar\omega_X = 40$  eV, including (a) the dynamical plasmon response during the motion of the photoelectron and (b) the plasmon response in static (adiabatic) approximation, allowing the plasmon field an infinite time to adjust to the perturbation by a classical photoelectron at any given position. (c) Central energies of the spectra in (a) and (b) showing a streaking-time-delay difference of 100 as. Adapted from Reference 61.

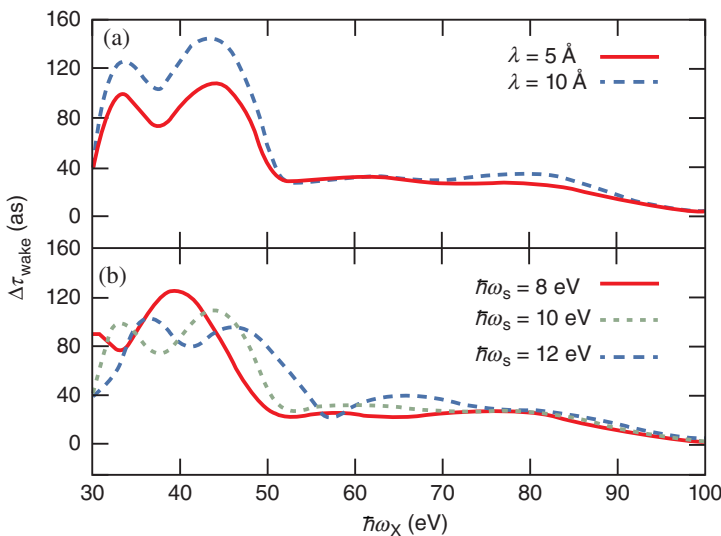


**FIGURE 13.26** Streaking-delay difference  $\Delta t_{X,\text{wake}}$ , induced by the non-adiabatic response of model substrates, as a function of the XUV photon energy for different (a) electron MFPs  $\lambda$ , and (b) surface plasmon frequencies  $\omega_s$ . Adapted from Reference 61.

The results shown in Figure 13.26 appear to be incompatible with the interpretation [51, 78] of the observed [51] delay between photoemission from core and conduction-band levels in tungsten in terms of the photoelectron's travel time in the solid,  $\lambda/\langle v_z \rangle$ . Decreasing  $\omega_S$  shifts the double-hump structure to lower  $\omega_X$  (lower photoelectron energies), as expected in view of the decreased thresholds for plasmon excitations (Fig. 13.26b).

## 13.4 ATTOSECOND STREAKING FROM NANOSTRUCTURES

The spatial homogeneity of the driving laser field is one of the key aspects in the attosecond streaking of atoms or surfaces [17, 30, 122]. Nanosystems, in contrast, can exhibit vast spatial variations of local field profiles especially in amplitude and phase. Nanoscopic effects such as field enhancement, resonant (plasmonic) oscillations, and coupling of multiple elements is dependent on material properties as well as shape and environment [113]. The spectral composition of the incident radiation gives a certain control over these effects. As nanofabrication technology progresses, ever-increasing control over these properties is gained. The result is custom or tailored materials which can be produced to respond in specific ways to external fields.

Based on theoretical work, in the following we discuss attosecond nanoplasmonic streaking and its application in the measurement of collective electron dynamics within nanostructures in external fields.

### 13.4.1 Instantaneous Versus Ponderomotive Streaking

The principle regimes for attosecond streaking from nanostructures were introduced by Stockman et al. [65] and will be discussed next for spherical metal nanoparticles. Here, we will follow the formalism and presentation in References 66 and 109. The experimental arrangement, depicted in Figure 13.27, is identical to streaking from gases or surfaces as discussed above. The main difference is that a nanostructure (here a single nanoparticle) is the target.

Electrons are emitted by an attosecond XUV pulse, which can be synchronized to a driving laser field in the optical region. On their way to the detector, the photoelectrons are accelerated by the near-field which results in an effective change in their kinetic energy. For more complex nanostructure geometries, the electric near-field may need to be evaluated using numerical computations such as the finite-difference time-domain (FDTD) method [123]. For spherical nanoparticles, Mie theory [124] can be employed. The inset in Figure 13.27 shows the maximum near-field of a Au nanoparticle resulting from the interaction of a few-cycle pulse at 800 nm with a 100 nm diameter gold nanosphere [66]. The enhancement of the near-field close the surface of the gold sphere is clearly visible and takes a dipolar shape. The spatial inhomogeneity of this near-field leads to substantial differences in the acceleration of the electrons as compared to streaking in gases or from planar surfaces.

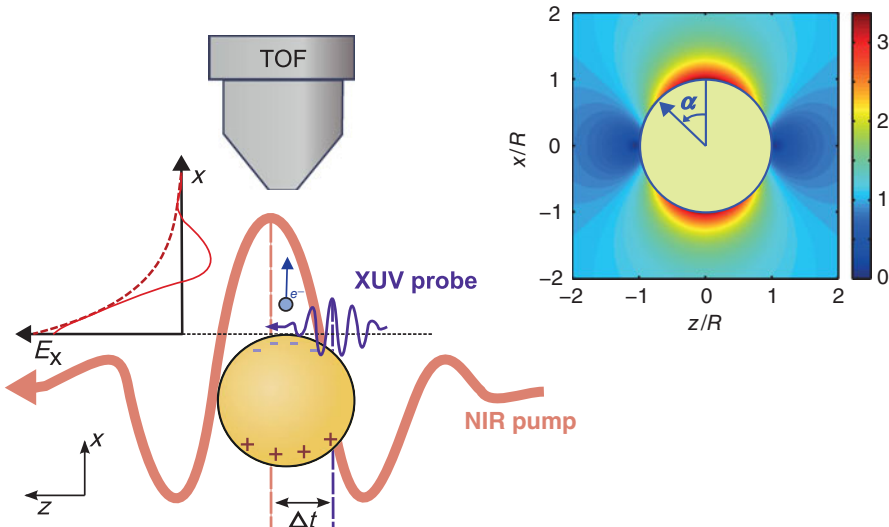


**FIGURE 13.27** Attosecond nanoplasmonic streaking principle illustrated for a spherical metal particle. An NIR pump pulse excites a localized surface plasmon in a metal nanoparticle, and a synchronized attosecond extreme-ultraviolet (XUV) pulse ejects photoelectrons. The field caused by the collective electron motion in the nanoparticle is imprinted in the kinetic energy of the electrons, which are measured by TOF spectroscopy. The inset shows the near-field around the nanoparticle as calculated by Mie theory in the  $y = 0$  plane through the center of the sphere [66]. Due to the symmetry of the plasmonic field in nanoparticles with diameters much smaller than the laser wavelength, the point of electron emission is uniquely defined by the angle  $\alpha$ . Reprinted from Reference 66 with copyright permission of APS. (For a color version of this figure, see the color plate section.)

The final drift velocity of a photoelectron emitted from a nanoparticle by an XUV pulse at time  $t_e$  with initial velocity  $\vec{v}_0$  can be obtained by integrating the electron's classical equation of motion

$$\vec{v}_f(t_e) = \vec{v}_0 - \int_{t_e}^{\infty} \vec{E}(\vec{r}, t) dt. \quad (13.49)$$

The initial velocity is determined by the spectrum of the attosecond XUV pulse and the material's work function. The kinetic energy of released electrons is then given by the difference between the photon energy and the local work function. It was shown that the evolution of plasmonic near-fields from many simple nanostructured surfaces into free space can be well approximated by an exponential function [125]. Introducing the spatial decay constant  $\chi$ , the decay of the field component perpendicular to the surface can be written as

$$E(x, t) = E_{pl}(t) \exp\left(-\frac{x(t)}{\chi}\right), \quad (13.50)$$

where it is assumed that the surface is normal to the  $x$ -axis and the electron is emitted in the  $x$ -direction (toward the TOF detector). Note that  $\chi$  is not a constant and depends on the emission position from the nanostructure (for a nanosphere given by the angle  $\alpha$  in Figure 13.27) and the emission angle of the electron trajectory. The change in the electron's drift velocity by acceleration in the near-field of the nanostructure is typically smaller than the initial velocity  $v_0$ . For example, an electron with  $E_{\text{kin}} = 100$  eV and a streaking amplitude of 10 eV experience a relative change in velocity of only  $\frac{(v_0 + \Delta_v)}{v_0} \approx 5\%$ . The electron's distance from the surface can thus be approximated by

$$x(t) \approx x_0 + v_0(t - t_e). \quad (13.51)$$

Inserting  $x(t)$  into Eq. (13.50) yields

$$E(x, t) = E_{\text{pl}}(t) \exp\left(\frac{-v_0(t - t_e)}{\chi}\right) = E_{\text{pl}}(t) \exp\left(\frac{-(t - t_e)}{\tau_s}\right), \quad (13.52)$$

where the spatial decay time is defined as  $\tau_s = \frac{\chi}{v_0}$ . Treating the plasmonic response as a damped, driven oscillator [113] results in an exponential decay of  $E_{\text{pl}}(t)$  after its excitation at  $t = 0$ , which may be described by

$$E_{\text{pl}}(t) = E_0 \cos(\omega t - \phi_{\text{CEP}}) \exp\left(\frac{-t}{\tau_{\text{pl}}}\right). \quad (13.53)$$

where  $E_0$  is the peak field amplitude,  $\phi_{\text{CEP}}$  the carrier-envelope phase of the plasmonic field, and  $\tau_{\text{pl}}$  the temporal decay constant. Inserting Eqs. (13.51), (13.52), and (13.53) into (13.49) yields

$$\Delta v(t_e) = v_0 - v_f(t_e) = - \int_{t_e}^{\infty} E_0 \exp\left(-\frac{t}{\tau_{\text{pl}}} - \frac{t - t_e}{\tau_s}\right) \cos(\omega t - \phi_{\text{CEP}}) dt. \quad (13.54)$$

With the simplifications made above, Eq. (13.54) can be integrated (for the result see [66]). Note that this equation only holds for probing the field *after* its excitation when the plasmon is decaying. The streaking amplitude will exhibit an exponential decay  $\exp(-t_e/\tau_{\text{pl}})$  which directly reflects the temporal decay of the near-field. The streaking regime can be characterized by the phase shift  $\Delta\phi_s$  between the waveform which is apparent in the streaking spectrogram and the local near-field oscillation (see Figure 13.28a),

$$\Delta\phi_s = \arctan\left(\frac{\tau_{\text{pl}}\tau_s\omega}{\tau_{\text{pl}} + \tau_s}\right). \quad (13.55)$$

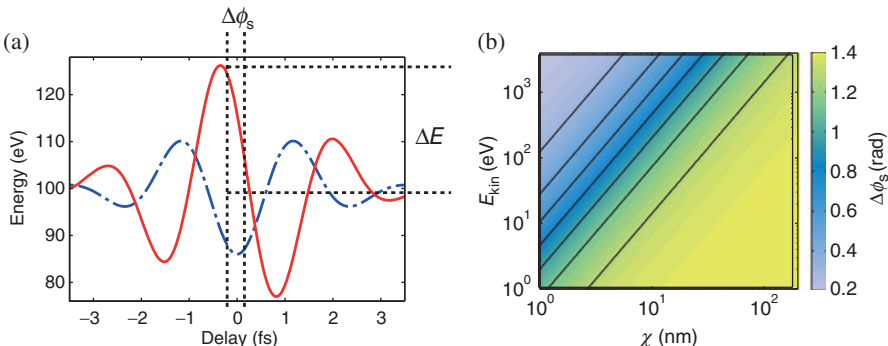


**FIGURE 13.28** (a) Phase shift  $\Delta\phi_s$  between the waveform apparent in the streaking spectrogram (red line) and the local near-field oscillation (blue dash-dotted line). (b) Phase shift  $\Delta\phi_s$  as a function of initial electron energy  $E_{\text{kin}}$  and spatial decay constant  $\chi$  for a fixed plasmonic decay constant of  $\tau_{\text{pl}} = 10$  fs and a laser wavelength of  $\lambda = 720$  nm [109]. The upper left corner ( $\Delta\phi_s$  close to zero) corresponds to the instantaneous streaking regime. The lower right corner ( $\Delta\phi_s$  close to  $\pi/2$ ) corresponds to the ponderomotive streaking regime. (For a color version of this figure, see the color plate section.)

If the plasmonic decay constant is much smaller than the spatial decay constant (due to the motion of the electron in the inhomogeneous field),  $\tau_{\text{pl}} \ll \tau_s$ , the phase shift can be reduced to  $\Delta\phi_s \approx \arctan(\tau_{\text{pl}}\omega)$ . In this case  $\Delta\phi_s$  is close to  $\pi/2$  for oscillating fields with a period shorter than its envelope ( $\omega^{-1} < \tau_{\text{pl}}$ , which is the case for few-cycle and longer fields). This regime resembles conventional streaking, where the streaking energy shift is proportional to the vector potential (see Section 13.2.2). It is referred to as the *ponderomotive regime*.

In the opposite limiting case where  $\tau_{\text{pl}} \ll \tau_s$  and  $\tau_s \ll (\omega^{-1})$ , the electron will leave the surface during a fraction of a half-cycle of the laser field. In this case the spatial decay time constant is small compared to both the temporal decay constant and the oscillation period. This results in a phase shift close to zero:  $\Delta\phi_s = \arctan(\tau_s\omega) \approx 0$ . The measured streaking waveform will thus directly reflect the electric field of the plasmonic oscillation. This regime is referred to as the *instantaneous regime*.

So far, we have not considered the interaction of near-field-accelerated electrons with the external driving laser field. “Fast” electrons, which leave the near-field within a fraction of an optical period (in the instantaneous regime), are only minimally accelerated by the near-field as compared to ponderomotive streaking in the surrounding external laser field. Under these conditions, the impact of the near-field is determined by its relative strength compared to the driving field, which is simply known as the field-enhancement factor (here denoted as  $Q$ ). The direct field-probing regime is therefore only achievable with sufficiently high  $Q$ , present in so-called “hot spots” (with enhancement factors of 2–4 orders of magnitude) [65]. The field enhancement factor and pattern around Au spheres remains similar to the one shown in Figure 13.27 ( $Q \approx 3$ ) even when decreasing the particle size. For such simple geometries, the instantaneous regime cannot be reached and the streaking amplitude is dominated by ponderomotive acceleration in the ambient laser field.

### 13.4.2 Modeling of the Attosecond Streaking from Metal Nanoparticles

To get more insight into the possible outcome of an attosecond nanoplasmonic streaking experiment, numerical simulations have been performed for rectangular Au antennas [64, 126] and spherical particles made of both Au [66, 126, 127] and Ag [128]. The key results from spherical Au particles will be outlined as an example, and special emphasis will be placed on the dependence of the streaking traces on the emission position of the electrons [66].

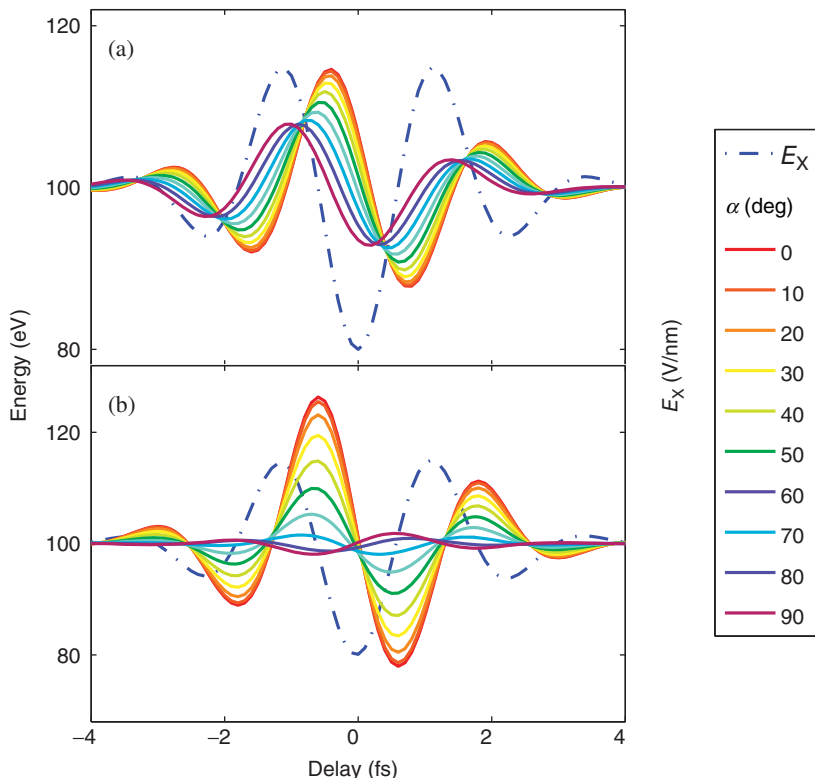
In the simulations contained in Reference 66, the equations of motion (13.49) were integrated for different emission times  $t_e$ , to obtain a complete streaking waveform. The laser field was assumed to have a Gaussian envelope of 5 fs (FWHM of the electric field), a center wavelength of  $\lambda = 720$  nm, and a peak intensity of  $1 \times 10^{12}$  W cm $^{-2}$ . The local field was calculated by Mie theory [124], where only the solution for the center wavelength was considered. This is well justified for sizes between 10 and 100 nm considered here. The kinetic energy of the electrons after their photoemission was fixed to  $E_{\text{kin}} = 100$  eV.

Figures 13.29a and b show simulated streaking curves for different emission positions, defined by the angle  $\alpha$  for two different gold spheres, with diameters  $d = 10$  nm and 100 nm, respectively. The driving field is depicted by the blue dashed-dotted line in all plots. For the 10-nm spheres, emission at the pole ( $\alpha = 0$ ) leads to a phase shift of about  $0.3 \pi$  with respect to the (negative) driving field. This indicates that the streaking process is in an intermediate regime. Emission at larger angles causes larger phase shifts. For a sphere diameter of 100 nm, the dependence on emission position is even stronger. Here, electrons emitted at the pole show a streaking waveform which is phase offset by  $\pi/2$  relative to the driving near-field (ponderomotive regime). Going to larger angles  $\alpha$ , the streaking amplitude decreases rapidly but only a minor phase shift occurs.

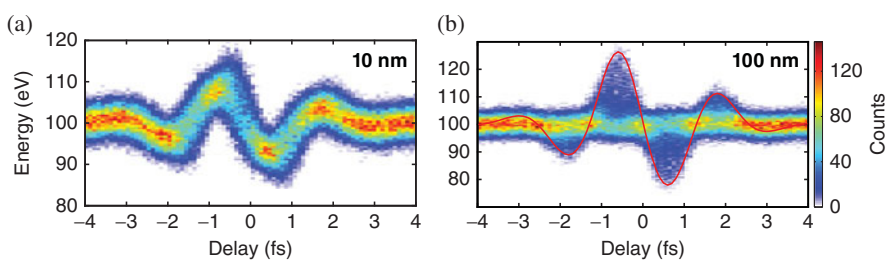
If an experiment does not allow for the discrimination of the emission position (such as with TOF spectroscopy, see Figure 13.27), the attosecond nanoplasmonic streaking spectrogram may contain contributions from all emission positions. The weighting of the contributions from different emission positions depends on the XUV absorption and photoemission. Since typical spot sizes of XUV foci for the photon energy considered here (around 100 eV) are in the micrometer range (much larger than the nanoparticle diameters considered), photoemission will take place over the entire illuminated side of the nanoparticle and, attenuated by the transmission through the material, also on its backside.

Figure 13.30 shows streaking spectrograms for 10 and 100 nm Au particles that have been computed via Monte-Carlo simulations [66]. The attosecond probe pulse was assigned a pulse length of 250 as, a spectrum centered at 105 eV, and a bandwidth of 7 eV. The emission was assumed to occur from a well-defined, narrow valence band.

The smaller Au sphere exhibits a streaking spectrogram with relatively high contrast and the contributions from different emission positions on the sphere cause a distortion of the waveform. As expected, the spectrogram for the 100-nm sphere is drastically different. The streaking features are blurred and the spectrogram has lost its waveform-like character. The findings are in good agreement with another



**FIGURE 13.29** Simulated streaking waveforms for electrons emitted at different positions (defined by the angle  $\alpha$  in Figure 13.27) on a Au sphere with a diameter of 10 nm (a) and 100 nm (b). The blue dash-dotted line indicates the driving field. Adapted from Reference 66 with copyright permission of APS. (For a color version of this figure, see the color plate section.)



**FIGURE 13.30** Simulated streaking spectrograms for 10 nm (a) and 100 nm (b) Au spheres. The red line shows the contribution of electrons emitted on axis with the laser polarization vector. Reprinted from Reference 66 with copyright permission of APS. (For a color version of this figure, see the color plate section.)

study on spherical gold particles [126], where the plasmon decay time was taken into account. In the considered case of a single TOF detector, the streaking spectrograms are not easy to interpret if the system is not well known. Nevertheless, major properties of the plasmonic oscillation can still be recovered. Inspecting Figures 13.29 and 13.30, the streaking curves of all trajectories exhibit a crossing at almost the same time for each half-cycle. This results in the characteristic periodic spots in the streaking spectrogram. From the period, one can directly deduce the frequency of the plasmonic oscillation as proposed by Borisov et al. [126]. Also, the envelope, and thus the lifetime, can be recovered from the spectrogram by analyzing the maximum streaking amplitudes at each delay step. Prell et al. proposed using photoelectron angular distributions measured by velocity-map imaging to reconstruct the dipole moment of Ag nanospheres [128].

Similar results were shown for coupled systems on a substrate [64], where the streaking process from the gap region of a coupled antenna was simulated. The results show that due to the high homogeneity of the field enhancement within the gap region, averaging over electron emission positions yields clear streaking spectrograms predominantly in the ponderomotive regime [64].

### 13.4.3 Attosecond Nanoplasmonic Microscopy

Combining the described nanoplasmonic streaking technique with ultrahigh, nanometer spatial resolution is highly desirable for measurements on surface-assembled nanostructures.

Stockman et al. proposed the combination of photoemission electron microscopy (PEEM) and attosecond nanoplasmonic streaking for the non-invasive, direct probing of nanoplasmonic fields with nanometer (spatial) and attosecond (temporal) resolution [65]. The principle of this technique is shown in Figure 13.31. A short, NIR

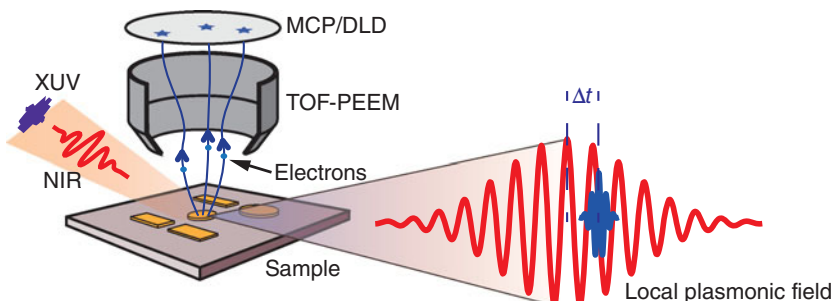


**FIGURE 13.31** Principle of the attosecond nanoplasmonic microscope (adapted from Reference 65). A short NIR pulse induces plasmonic oscillations which are probed by a time-delayed attosecond XUV pulse. The streaked photoelectrons are imaged with a time-of-flight PEEM (TOF-PEEM), where their TOF and position are detected by a microchannel plate (MCP)/delay-line detector. Streaking spectrograms for each image point can be measured by scanning the delay between the pump and probe pulses.

laser pulse excites the collective electron dynamics on a nanostructured surface, then a synchronized attosecond XUV pulse photoemits electrons from the surface. These electrons are then accelerated in the plasmonic near-fields as described in the last section. However, in contrast to conventional streaking spectroscopy, now the detector is a TOF-PEEM, which enables the imaging of photoelectrons from the sample surface with nanometer resolution [129]. By scanning the delay between the NIR pump and XUV probe pulses, a streaking spectrogram is obtained for each image point on the TOF-PEEM, representing a small volume on the sample surface.

The theoretical study by Stockman et al. included calculations for a rough silver surface with hot spots exhibiting field enhancement factors of  $Q = 30$  and a spatial extent of only a few nanometers [65]. These hot spots are so small that the electron escape time is much smaller than the plasmonic oscillation period. For this limiting case, a direct mapping of the near-fields in the instantaneous regime is possible.

Results of the calculations by Stockman et al. [65] are shown in Figure 13.32. An attosecond XUV pulse at 90 eV with a pulse duration of 170 as was employed. The XUV pulse is synchronized with a few-cycle optical field (5 fs in duration) for the excitation of the nanosystem, and both are focused onto the sample. Due to their large kinetic energy and short emission time, the XUV-emitted VB photoelectrons escape from the nanometer-sized regions of local electric field enhancement within a fraction of the oscillation period of the driven plasmonic field.

The spatial resolution is limited by the aberrations of the TOF-PEEM electron optics and experimental conditions (such as space-charge generation). Using UV excitation, Lin et al. reached 25-nm spatial resolution with a TOF-PEEM [129]. The application of attosecond XUV photoemission in TOF-PEEM and PEEM poses some challenges. These have been outlined in References 130 and 131, but even in those studies resolutions in the few-100-nanometer range have already been realized and will likely improve. The temporal resolution is determined by the duration of the attosecond pulse and the TOF of the photoelectrons through the local-field region. This can be on the order of a few hundred attoseconds. Figure 13.32 shows that streaking amplitudes of up to approximately 10 eV at an NIR intensity of  $1 \times 10^{10} \text{ W cm}^{-2}$  can be achieved for typical experimental parameters [65]. At this intensity of the driving NIR-laser pulse, the direct streaking of the electrons by the external NIR field can be neglected. These theoretical studies show that spatiotemporal measurements in the nanometer–attosecond range can be achieved. The full experimental implementation of the attosecond nanoplasmonic field microscope will thus mark an important advancement of attosecond photoelectron spectroscopy and its applications.

## 13.5 CONCLUSIONS

In this chapter, we reviewed the basic physics behind state-of-the-art investigations of ultrafast electronic dynamics in atoms, solid surfaces, and nanoparticles. We discussed how XUV photoelectron emission can, with the help of a streaking IR laser

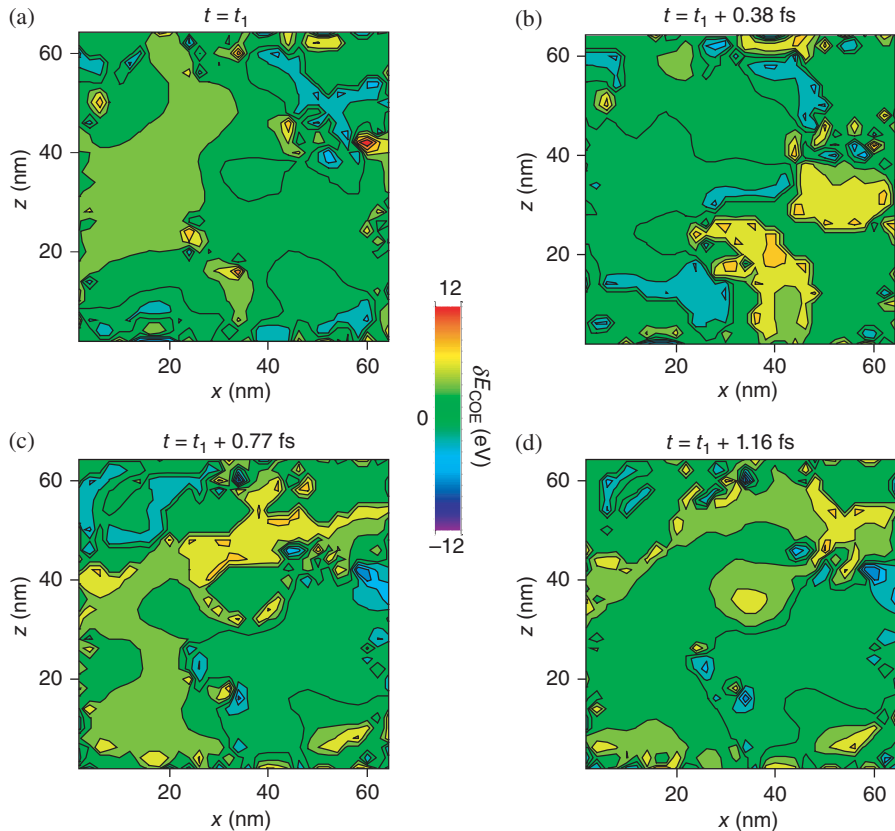


**FIGURE 13.32** Topographic color maps of the streaking energy shift  $\delta E_{\text{COE}}$ , of electrons emitted by an XUV pulse in the plane of this nanostructure. (a)–(d) Different times after excitation of the nanostructure by a 5.5-fs pulse at 800 nm. The time  $t_1$  corresponds to a time at which the near-field in the hotspot has reached a peak. Adapted from Reference 65 with copyright permission of *Nature*. (For a color version of this figure, see the color plate section.)

field, measure time differences between the emission of electrons from two different initial states at the time-scale of the motion of electrons in matter. We further analyzed the influence the streaking electric field has on the measured observables, XUV–IR-pulse-delay-dependent photoelectron energy distributions (photoelectron dispersion) and photoemission time delays, and provided simple examples to illustrate the effects of initial- and final-state distortions on streaked photoelectron spectra. We discussed recently measured streaking experiments for photoemission from metal surfaces in comparison with theoretical models. For streaked photoemission from nanoscale particles, we explained simulation results that reveal effects due to the significant local electric field enhancement at nanometer-sized “hot spots” near the nanoparticle surface.

Attosecond physics has been rapidly established over the past decade as a promising research direction, to a large part through novel, attosecond time-resolved laser-streaked XUV photoemission spectroscopy of atoms in the gas phase. More recently, over the past few years, attosecond physics has begun to branch out to more complex systems, holding promise to enable, with attosecond resolution in time and (tens of) nanometer spatial resolution, investigations of basic electronic process on (adsorbate-covered) solid surfaces, semiconductor interfaces, nanostructures, and large biomolecules.

The extension of attosecond science to include complex systems has the potential to promote the development of diagnostic tools for basic research with atomic-scale resolution in both, space and time, and to lead to novel devices for information processing, drug delivery, and imaging in medicine in material science.

## ACKNOWLEDGMENTS

We acknowledge countless contributions to the presented work by our coworkers and collaborators at JRML, KSU, MPQ, LMU, and TUM. This work was supported by the MPG and the DFG via the excellence cluster “Munich Center for Advanced Photonics (MAP)” and SPP1391. We acknowledge partial support by the NSF and the Division of Chemical Sciences, Office of Basic Energy Sciences, Office of Energy Research, U.S. Department of Energy.

## REFERENCES

- [1] H. Hertz, “Über einen Einfluss des ultravioletten Lichtes auf die electrische Entladung,” *Ann. Phys.* **267**, 983–1000 (1887).
- [2] S. Hüfner, *Photoelectron Spectroscopy: Principles and Applications*, 3rd ed. (Springer, Berlin; New York, 2003).
- [3] A. Einstein, “Über einen die Erzeugung und Verwandlung des Lichtes betreffenden heuristischen Gesichtspunkt [AdP 17, 132 (1905)],” *Ann. Phys.* **14**, 164–181 (1905).
- [4] C. H. Zhang and U. Thumm, “Attosecond photoelectron spectroscopy of metal surfaces,” *Phys. Rev. Lett.* **102**, 123601 (2009).
- [5] C. H. Zhang and U. Thumm, “Erratum: Attosecond photoelectron spectroscopy of metal surfaces [*Phys. Rev. Lett.* **102**, 123601 (2009)],” *Phys. Rev. Lett.* **103**, 239902 (2009).
- [6] B. H. Bransden and C. J. Joachain, *Physics of Atoms and Molecules*, 2nd ed. (Prentice Hall, Harlow, England; New York, 2003).
- [7] M. C. Desjonquères and D. Spanjaard, *Concepts in Surface Physics*, 2nd ed. (Springer, Berlin; New York, 1996).
- [8] J. Ullrich, A. Rudenko, and R. Moshammer, “Free-electron lasers: new avenues in molecular physics and photochemistry,” *Annu. Rev. Phys. Chem.* **63**, 635–660 (2012).
- [9] A. H. Zewail, “Femtochemistry: atomic-scale dynamics of the chemical bond,” *J. Phys. Chem. A* **104**, 5660–5694 (2000).

- [10] M. Hentschel, R. Kienberger, C. Spielmann, G. A. Raider, N. Milosevic, T. Brabec, P. Corkum, U. Heinzmann, M. Drescher, and F. Krausz, “Attosecond metrology,” *Nature* **414**, 509–513 (2001).
- [11] P. M. Paul, E. S. Toma, P. Breger, G. Mullot, F. Augé, P. Balcou, H. G. Muller, and P. Agostini, “Observation of a train of attosecond pulses from high harmonic generation,” *Science* **292**, 1689–1692 (2001).
- [12] V. Yanovsky, V. Chvykov, G. Kalinchenko, P. Rousseau, T. Planchon, T. Matsuoka, A. Maksimchuk, J. Nees, G. Cheriaux, G. Mourou, et al., “Ultra-high intensity-300-TW laser at 0.1 Hz repetition rate,” *Opt. Exp.* **16**, 2109–2114 (2008).
- [13] X. Zhang, E. Schneider, G. Taft, H. Kapteyn, M. Murnane, and S. Backus, “Multi-microjoule, MHz repetition rate Ti:sapphire ultrafast regenerative amplifier system,” *Opt. Exp.* **20**, 7015–7021 (2012).
- [14] A. Dubietis, R. Butkus, and A. P. Piskarskas, “Trends in chirped pulse optical parametric amplification,” *IEEE J. Sel. Top. Quant. Electr.* **12**, 163 (2006).
- [15] O. Chalus, P. K. Bates, M. Smolarski, and J. Biegert, “Mid-IR short-pulse OPCPA with micro-Joule energy at 100 kHz,” *Opt. Exp.* **17**, 3587–3594 (2009).
- [16] F. Krausz and M. Ivanov, “Attosecond physics,” *Rev. Mod. Phys.* **81**, 163–234 (2009).
- [17] E. Goulielmakis, M. Schultze, M. Hofstetter, V. S. Yakovlev, J. Gagnon, M. Uiberacker, A. L. Aquila, E. M. Gullikson, D. T. Attwood, R. Kienberger, et al., “Single-cycle nonlinear optics,” *Science* **320**, 1614–1617 (2008).
- [18] K. Zhao, Q. Zhang, M. Chini, Y. Wu, X. Wang, and Z. Chang, “Tailoring a 67 attosecond pulse through advantageous phase-mismatch,” *Opt. Lett.* **37**, 3891–3893 (2012).
- [19] “CODATA Value: proton-electron mass ratio.” *The NIST Reference on Constants, Units, and Uncertainty* (US National Institute of Standards and Technology, 2011). <http://physics.nist.gov/cgi-bin/cuu/Value?mpsme>
- [20] A. Wirth, M. T. Hassan, I. Grguras, J. Gagnon, A. Moulet, T. T. Luu, S. Pabst, R. Santra, Z. A. Alahmed, A. M. Azzeer, et al., “Synthesized light transients,” *Science* **334**, 195–200 (2011).
- [21] E. Goulielmakis, V. S. Yakovlev, A. L. Cavalieri, M. Uiberacker, V. Pervak, A. Apolonski, R. Kienberger, U. Kleineberg, and F. Krausz, “Attosecond control and measurement: lightwave electronics,” *Science* **317**, 769–775 (2007).
- [22] A. Schiffrin, T. Paasch-Colberg, N. Karpowicz, V. Apalkov, D. Gerster, S. Mühlbrandt, M. Korbman, J. Reichert, M. Schultze, S. Holzner, et al., “Optical-field-induced current in dielectrics,” *Nature* **493**, 70–74 (2013).
- [23] M. Schultze, E. M. Bothschafter, A. Sommer, S. Holzner, W. Schweinberger, M. Fiess, M. Hofstetter, R. Kienberger, V. Apalkov, V. S. Yakovlev, et al., “Controlling dielectrics with the electric field of light,” *Nature* **493**, 75–78 (2013).
- [24] A. Baltuska, T. Udem, M. Uiberacker, M. Hentschel, E. Goulielmakis, C. Gohle, R. Holzwarth, V. S. Yakovlev, A. Scrinzi, T. W. Hansch, et al., “Attosecond control of electronic processes by intense light fields,” *Nature* **421**, 611–615 (2003).
- [25] T. Rathje, N. G. Johnson, M. Möller, F. Süßmann, D. Adolph, M. Kübel, R. Kienberger, M. F. Kling, G. G. Paulus, and A. M. Sayler, “Review of attosecond resolved measurement and control via carrier-envelope phase tagging with above-threshold ionization,” *J. Phys. B* **45**, 074003 (2012).
- [26] T. Wittmann, B. Horvath, W. Helml, M. G. Schätzel, X. Gu, A. L. Cavalieri, G. G. Paulus, and R. Kienberger, “Single-shot carrier-envelope phase measurement of few-cycle laser pulses,” *Nat. Phys.* **5**, 357–362 (2009).

- [27] M. F. Kling, P. von den Hoff, I. Znakovskaya, and R. de Vivie-Riedle, “(Sub-) femtosecond control of molecular reactions via tailoring the electric field of light,” *Phys. Chem. Chem. Phys.* **15**, 9448–9467 (2013).
- [28] R. Trebino, *Frequency-Resolved Optical Gating: The Measurement of Ultrashort Laser Pulses* (Springer, 2002).
- [29] J. Itatani, F. Quere, G. L. Yudin, M. Y. Ivanov, F. Krausz, and P. B. Corkum, “Attosecond streak camera,” *Phys. Rev. Lett.* **88**, 173903 (2002).
- [30] R. Kienberger, E. Goulielmakis, M. Uiberacker, A. Baltuska, V. S. Yakovlev, F. Bammer, A. Scrinzi, T. Westerwalbesloh, U. Kleineberg, U. Heinzmann, et al., “Atomic transient recorder,” *Nature* **427**, 817–821 (2004).
- [31] P. B. Corkum, “Plasma perspective on strong-field multiphoton ionization,” *Phys. Rev. Lett.* **71**, 1994–1997 (1993).
- [32] M. Lewenstein, P. Balcou, M. Y. Ivanov, A. L’Huillier, and P. B. Corkum, “Theory of high-harmonic generation by low-frequency laser fields,” *Phys. Rev. A* **49**, 2117–2132 (1994).
- [33] G. Sansone, E. Benedetti, F. Calegari, C. Vozzi, L. Avaldi, R. Flammini, L. Poletto, P. Villoresi, C. Altucci, R. Velotta, et al., “Isolated single-cycle attosecond pulses,” *Science* **314**, 443–446 (2006).
- [34] I. J. Sola, E. Mevel, L. Elouga, E. Constant, V. Strelkov, L. Poletto, P. Villoresi, E. Benedetti, J. P. Caumes, S. Stagira, et al., “Controlling attosecond electron dynamics by phase-stabilized polarization gating.” *Nat. Phys.* **2**, 319–322 (2006).
- [35] H. Mashiko, S. Gilbertson, C. Li, S. D. Khan, M. M. Shakya, E. Moon, and Z. Chang, “Double optical gating of high-order harmonic generation with carrier-envelope phase stabilized lasers,” *Phys. Rev. Lett.* **100**, 103906 (2008).
- [36] T. Popmintchev, M.-C. Chen, P. Arpin, M. M. Murnane, and H. C. Kapteyn, “The attosecond nonlinear optics of bright coherent X-ray generation,” *Nat. Photon.* **4**, 822–832 (2010).
- [37] O. Smirnova, Y. Mairesse, S. Patchkovskii, N. Dudovich, D. Villeneuve, P. Corkum, and M. Y. Ivanov, “High harmonic interferometry of multi-electron dynamics in molecules,” *Nature* **460**, 972–977 (2009).
- [38] R. M. Lock, S. Ramakrishna, X. Zhou, H. C. Kapteyn, M. M. Murnane, and T. Seideman, “Extracting continuum electron dynamics from high harmonic emission from molecules,” *Phys. Rev. Lett.* **108**, 133901 (2012).
- [39] W. Li, X. Zhou, R. Lock, S. Patchkovskii, A. Stolow, H. C. Kapteyn, and M. M. Murnane, “Time-resolved dynamics in  $\text{N}_2\text{O}_4$  probed using high harmonic generation,” *Science* **322**, 1207–1211 (2008).
- [40] S. Haessler, J. Caillat, and P. Salieres, “Self-probing of molecules with high harmonic generation,” *J. Phys. B* **44**, 203001 (2011).
- [41] M. C. Kohler, T. Pfeifer, K. Z. Hatsagortsyan, and C. H. Keitel, “Frontiers of atomic high-harmonic generation,” in *Advances in Atomic, Molecular and Optical Physics*, edited by P. Berman, E. Arimondo, and C. Lin (Elsevier, 2012), Vol. 61, pp. 159–208.
- [42] F. Ferrari, F. Calegari, M. Lucchini, C. Vozzi, S. Stagira, G. Sansone, and M. Nisoli, “High-energy isolated attosecond pulses generated by above-saturation few-cycle fields,” *Nat. Photon.* **4** (2010).
- [43] A. L. Cavalieri, E. Goulielmakis, B. Horvath, W. Helml, M. Schultze, M. Fieß, V. Pervak, L. Veisz, V. S. Yakovlev, M. Uiberacker, et al., “Intense 1.5-cycle near

- infrared laser waveforms and their use for the generation of ultra-broadband soft-x-ray harmonic continua," *New J. Phys.* **9**, 242 (2007).
- [44] X. Feng, S. Gilbertson, H. Mashiko, H. Wang, S. D. Khan, M. Chini, Y. Wu, K. Zhao, and Z. Chang, "Generation of Isolated attosecond pulses with 20 to 28 femtosecond lasers," *Phys. Rev. Lett.* **103**, 183901 (2009).
- [45] Y. Mairesse and F. Quere, "Frequency-resolved optical gating for complete reconstruction of attosecond bursts," *Phys. Rev. A* **71**, 011401(R) (2005).
- [46] J. Gagnon, E. Goulielmakis, and V. S. Yakovlev, "The accurate FROG characterization of attosecond pulses from streaking measurements," *Appl. Phys. B* **92**, 25–32 (2008).
- [47] M. Chini, S. Gilbertson, S. D. Khan, and Z. Chang, "Characterizing ultrabroadband attosecond lasers," *Opt. Exp.* **18**, 13006–13016 (2010).
- [48] M. F. Kling and M. J. J. Vrakking, "Attosecond electron dynamics," *Annu. Rev. Phys. Chem.* **59**, 463–492 (2008).
- [49] P. B. Corkum and F. Krausz, "Attosecond science," *Nat. Phys.* **3**, 381–387 (2007).
- [50] E. Goulielmakis, Z. H. Loh, A. Wirth, R. Santra, N. Rohringer, V. S. Yakovlev, S. Zherebtsov, T. Pfeifer, A. M. Azzeer, M. F. Kling, et al., "Real-time observation of valence electron motion," *Nature* **466**, 739–743 (2010).
- [51] A. L. Cavalieri, N. Muller, T. Uphues, V. S. Yakovlev, A. Baltuska, B. Horvath, B. Schmidt, L. Blumel, R. Holzwarth, S. Hendel, et al., "Attosecond spectroscopy in condensed matter," *Nature* **449**, 1029–1032 (2007).
- [52] S. Neppl, R. Ernstorfer, E. M. Bothschafter, A. L. Cavalieri, D. Menzel, J. V. Barth, F. Krausz, R. Kienberger, and P. Feulner, "Attosecond time-resolved photoemission from core and valence states of magnesium," *Phys. Rev. Lett.* **109**, 087401 (2012).
- [53] M. Schultze, M. Fieß, N. Karpowicz, J. Gagnon, M. Korbman, M. Hofstetter, S. Neppl, A. L. Cavalieri, Y. Komninou, T. Mercouris, et al., "Delay in photoemission," *Science* **328**, 1658–1662 (2010).
- [54] K. Klünder, J. M. Dahlström, M. Gisselbrecht, T. Fordell, M. Swoboda, D. Guenot, P. Johnsson, J. Caillat, J. Mauritsson, A. Maquet, et al., "Probing single-photon ionization on the attosecond time scale," *Phys. Rev. Lett.* **106**, 143002 (2011).
- [55] J. M. Dahlstrom, A. L'Huillier, and A. Maquet, "Introduction to attosecond delays in photoionization," *J. Phys. B: Atom. Mol. Opt. Phys.* **45**, 183001 (2012).
- [56] T. Schultz and M. J. J. Vrakking, *Attosecond and XUV Spectroscopy* (John Wiley & Sons, 2013).
- [57] L. Gallmann, C. Cirelli, and U. Keller, "Attosecond science: recent highlights and future trends," *Annu. Rev. Phys. Chem.* **63**, 447–469 (2012).
- [58] A. Scrinzi, M. Y. Ivanov, R. Kienberger, and D. M. Villeneuve, "Attosecond physics," *J. Phys. B* **39**, R1–R37 (2006).
- [59] *Attosecond Physics: Attosecond Measurement and Control of Physical Systems* (Springer, 2013), Vol. 177.
- [60] Z. Chang, *Fundamentals of Attosecond Optics* (CRC Press, Taylor and Francis Group, 2011).
- [61] C. H. Zhang and U. Thumm, "Probing dielectric-response effects with attosecond time-resolved streaked photoelectron spectroscopy of metal surfaces," *Phys. Rev. A* **84**, 063403 (2011).

- [62] M. Gertsvolf, M. Spanner, D. M. Rayner, and P. B. Corkum, “Demonstration of attosecond ionization dynamics inside transparent solids,” *J. Phys. B* **43**, 131002 (2010).
- [63] A. V. Mitrofanov, A. J. Verhoef, E. E. Serebryannikov, J. Lumeau, L. Glebov, A. M. Zheltikov, and A. Baltuska, “Optical detection of attosecond ionization induced by a few-cycle laser field in a transparent dielectric material,” *Phys. Rev. Lett.* **106**, 147401 (2011).
- [64] E. Skopalova, D. Y. Lei, T. Witting, C. Arrell, F. Frank, Y. Sonnenaud, S. A. Maier, J. W. G. Tisch, and J. P. Marangos, “Numerical simulation of attosecond nanoplasmonic streaking,” *New J. Phys.* **13**, 083003 (2011).
- [65] M. I. Stockman, M. F. Kling, U. Kleineberg, and F. Krausz, “Attosecond nanoplasmonic-field microscope,” *Nat. Photon.* **1**, 539–544 (2007).
- [66] F. Süßmann and M. F. Kling, “Attosecond nanoplasmonic streaking of localized fields near metal nanospheres,” *Phys. Rev. B* **84**, 121406(R) (2011).
- [67] M. Drescher, M. Hentschel, R. Kienberger, M. Uiberacker, V. S. Yakovlev, A. Scrinzi, T. Westerwalbesloh, U. Kleineberg, U. Heinzmann, and F. Krausz, “Time-resolved atomic inner-shell spectroscopy,” *Nature* **419**, 803–807 (2002).
- [68] L. Miaja-Avila, G. Saathoff, S. Mathias, J. Yin, C. La-o-vorakiat, M. Bauer, M. Aeschlimann, M. M. Murnane, and H. C. Kapteyn, “Direct measurement of core-level relaxation dynamics on a surface-adsorbate system,” *Phys. Rev. Lett.* **101**, 046101 (2008).
- [69] L. R. Moore, M. A. Lysaght, J. S. Parker, H. W. van der Hart, and K. T. Taylor, “Time delay between photoemission from the 2p and 2s subshells of neon,” *Phys. Rev. A* **84**, 061404 (2011).
- [70] S. Nagele, R. Pazourek, J. Feist, and J. Burgdörfer, “Time shifts in photoemission from a fully correlated two-electron model system,” *Phys. Rev. A* **85**, 033401 (2012).
- [71] R. Pazourek, J. Feist, S. Nagele, and J. Burgdörfer, “Attosecond streaking of correlated two-electron transitions in helium,” *Phys. Rev. Lett.* **108**, 163001 (2012).
- [72] A. Kubo, K. Onda, H. Petek, Z. J. Sun, Y. S. Jung, and H. K. Kim, “Femtosecond imaging of surface plasmon dynamics in a nanostructured silver film,” *Nano Lett.* **5**, 1123–1127 (2005).
- [73] M. Sukharev and T. Seideman, “Phase and polarization control as a route to plasmonic nanodevices,” *Nano Lett.* **6**, 715–719 (2006).
- [74] F. Le, N. Z. Lwin, N. J. Halas, and P. Nordlander, “Plasmonic interactions between a metallic nanoshell and a thin metallic film,” *Phys. Rev. B* **76**, 165410 (2007).
- [75] M. I. Stockman, “Nanoplasmonics: the physics behind the applications,” *Phys. Today* **64**, 39–44 (2011).
- [76] C. H. Zhang and U. Thumm, “Laser-assisted photoemission from adsorbate-covered metal surfaces: time-resolved core-hole relaxation dynamics from sideband profiles,” *Phys. Rev. A* **80**, 032902 (2009).
- [77] C. Lemell, B. Solleder, K. Tokesi, and J. Burgdörfer, “Simulation of attosecond streaking of electrons emitted from a tungsten surface,” *Phys. Rev. A* **79**, 062901 (2009).
- [78] A. K. Kazansky and P. M. Echenique, “One-electron model for the electronic response of metal surfaces to subfemtosecond photoexcitation,” *Phys. Rev. Lett.* **102**, 177401 (2009).
- [79] A. S. Kheifets and I. A. Ivanov, “Delay in atomic photoionization,” *Phys. Rev. Lett.* **105**, 233002 (2010).

- [80] C. H. Zhang and U. Thumm, “Electron-ion interaction effects in attosecond time-resolved photoelectron spectra,” *Phys. Rev. A* **82**, 043405 (2010).
- [81] S. Nagele, R. Pazourek, J. Feist, K. Doblhoff-Dier, C. Lemell, K. Tokesi, and J. Burgdörfer, “Time-resolved photoemission by attosecond streaking: extraction of time information,” *J. Phys. B* **44**, 081001 (2011).
- [82] I. A. Ivanov, “Time delay in strong-field photoionization of a hydrogen atom,” *Phys. Rev. A* **83**, 023421 (2011).
- [83] C. H. Zhang and U. Thumm, “Streaking and Wigner time delays in photoemission from atoms and surfaces,” *Phys. Rev. A* **84**, 033401 (2011).
- [84] C. H. Zhang and U. Thumm, “Effect of wave-function localization on the time delay in photoemission from surfaces,” *Phys. Rev. A* **84**, 065403 (2011).
- [85] E. E. Krasovskii, “Attosecond spectroscopy of solids: streaking phase shift due to lattice scattering,” *Phys. Rev. B* **84**, 195106 (2011).
- [86] A. G. Borisov, D. Sanchez-Portal, A. K. Kazansky, and P. M. Echenique, “Resonant and nonresonant processes in attosecond streaking from metals,” *Phys. Rev. B* **87**, 121110(R) (2013).
- [87] L. Eisenbud, “Formal properties of nuclear collisions,” PhD thesis, Princeton University, 1948.
- [88] F. T. Smith, “Lifetime matrix in collision theory,” *Phys. Rev.* **118**, 349–356 (1960).
- [89] E. P. Wigner, “Lower limit for the energy derivative of the scattering phase shift,” *Phys. Rev.* **98**, 145–147 (1955).
- [90] C. A. A. de Carvalho and H. M. Nussenzveig, “Time delay,” *Phys. Rep.* **364**, 83 (2002).
- [91] J. C. Baggesen and L. B. Madsen, “Theory for time-resolved measurements of laser-induced electron emission from metal surfaces,” *Phys. Rev. A* **78**, 032903 (2008).
- [92] H. Friedrich, *Theoretical Atomic Physics*, 3rd ed. (Springer, Berlin, New York, 2005).
- [93] O. Smirnova, M. Spanner, and M. Ivanov, “Analytical solutions for strong field-driven atomic and molecular one- and two-electron continua and applications to strong-field problems,” *Phys. Rev. A* **77**, 033407 (2008).
- [94] H. Goldstein, C. P. Poole, and J. L. Safko, *Classical Mechanics*, 3rd ed. (Addison Wesley, San Francisco, 2002).
- [95] E. Bothschafter, S. Neppl, and R. Kienberger, “Few-femtosecond and attosecond electron dynamics at surfaces,” in *Progress in Ultrafast Intense Laser Science IX*, edited by K. Yamanouchi (Springer, 2013), pp. 183–211.
- [96] A. Cavalieri, F. Krausz, R. Ernstorfer, R. Kienberger, P. Feulner, J. Barth, and D. Menzel, “Attosecond time-resolved spectroscopy at surfaces,” in *Dynamics at Solid State Surfaces and Interfaces*, (John Wiley & Sons, 2010), pp. 537–553.
- [97] A. Zangwill, *Physics at surfaces* (Cambridge University Press, Cambridge Cambridgeshire, New York, 1988).
- [98] H. Petek and S. Ogawa, “Femtosecond time-resolved two-photon photoemission studies of electron dynamics in metals,” *Prog. Surf. Sci.* **56**, 239–310 (1997).
- [99] M. Drescher, M. Hentschel, R. Kienberger, G. Tempea, C. Spielmann, G. A. Raider, P. Corkum, and F. Krausz, “X-ray pulses approaching the attosecond frontier,” *Science* **291**, 1923–1927 (2001).
- [100] E. Magerl, S. Neppl, A. L. Cavalieri, E. M. Bothschafter, M. Stanislawski, T. Uphues, M. Hofstetter, U. Kleineberg, J. V. Barth, D. Menzel, et al., “A flexible apparatus for

- attosecond photoelectron spectroscopy of solids and surfaces,” *Rev. Sci. Instr.* **82**, 063104 (2011).
- [101] E. E. Krasovskii, V. M. Silkin, V. U. Nazarov, P. M. Echenique, and E. V. Chulkov, “Dielectric screening and band-structure effects in low-energy photoemission,” *Phys. Rev. B* **82**, 125102 (2010).
  - [102] F. Salvat, A. Jablonski, and C. J. Powell, “ELSEPA—Dirac partial-wave calculation of elastic scattering of electrons and positrons by atoms, positive ions and molecules,” *Comput. Phys. Commun.* **165**, 157–190 (2005).
  - [103] Q. Liao and U. Thumm, “Attosecond time-resolved photoelectron dispersion and photochemistry time delays,” *Phys. Rev. Lett.* **112**, 023602 (2014).
  - [104] L. Miaja-Avila, C. Lei, M. Aeschlimann, J. L. Gland, M. M. Murnane, H. C. Kapteyn, and G. Saathoff, “Laser-assisted photoelectric effect from surfaces,” *Phys. Rev. Lett.* **97**, 113604 (2006).
  - [105] U. Thumm, “Theory of fast ion surface collisions at grazing-incidence—emission of electrons due to capture and loss to the continuum,” *J. Phys. B* **25**, 421–435 (1992).
  - [106] Q. Liao and U. Thumm, “Initial-state, mean-free-path, and skin-depth dependence of attosecond time-resolved IR-streaked XUV photoemission from single-crystal magnesium,” *Phys. Rev. A* **89**, 033849 (2014).
  - [107] E. V. Chulkov, V. M. Silkin, and P. M. Echenique, “Image potential states on metal surfaces: binding energies and wave functions,” *Surf. Sci.* **437**, 330–352 (1999).
  - [108] S. Tanuma, C. J. Powell, and D. R. Penn, “Calculations of electron inelastic mean free paths. IX. Data for 41 elemental solids over the 50 eV to 30 keV range,” *Surf. Interface Anal.* **43**, 689–713 (2011).
  - [109] F. Süßmann, S. L. Stebbings, S. Zherebtsov, S. H. Chew, M. I. Stockman, E. Rühl, U. Kleineberg, T. Fennel, and M. F. Kling, “Attosecond electron dynamics in nanostructures,” in *Attosecond Physics*, edited by T. Schultz, and M. J. J. Vrakking (John Wiley & Sons, 2013).
  - [110] D. K. Gramov and S. I. Bozhevolnyi, “Plasmonics beyond the diffraction limit,” *Nat. Photon.* **4**, 83–91 (2010).
  - [111] C. Varin, C. Peltz, T. Brabec, and T. Fennel, “Attosecond plasma wave dynamics in laser-driven cluster nanoplasmas,” *Phys. Rev. Lett.* **108**, 175007 (2012).
  - [112] C. Bohren and D. R. Huffman, *Absorption and Scattering of Light by Small Particles* (John Wiley & Sons, New York, 1983).
  - [113] S. Maier, *Plasmonics: fundamentals and applications* (Springer, New York, 2007).
  - [114] P. Kürpick, U. Thumm, and U. Wille, “Resonance formation of hydrogenic levels in front of metal surfaces,” *Phys. Rev. A* **56**, 543–554 (1997).
  - [115] J. Ducreé, H. J. Andrä, and U. Thumm, “Neutralization of hyperthermal multiply charged ions at surfaces: comparison between the extended dynamical overbarrier model and experiment,” *Phys. Rev. A* **60**, 3029–3043 (1999).
  - [116] A. Schmitz, J. Shaw, H. S. Chakraborty, and U. Thumm, “Band-gap-confinement and image-state-recapture effects in the survival of anions scattered from metal surfaces,” *Phys. Rev. A* **81**, 042901 (2010).
  - [117] B. Obreshkov and U. Thumm, “H-formation in collisions of hydrogen atoms with an Al(100) surfaces,” *Phys. Rev. A* **87**, 022903 (2013).
  - [118] F. J. García de Abajo and P. M. Echenique, “Wake potential in the vicinity of a surface,” *Phys. Rev. B* **46**, 2663–2675 (1992).

- [119] F. J. García de Abajo and P. M. Echenique, “Surface wake in the random-phase approximation,” *Phys. Rev. B* **48**, 13399–13407 (1993).
- [120] J. I. Gersten and N. Tzoar, “Many-body formalism for photoemission studies,” *Phys. Rev. B* **8**, 5671–5683 (1973).
- [121] N. Tzoar and J. I. Gersten, “Calculation of many-body effects on energy-distribution curves in photoemission,” *Phys. Rev. B* **8**, 5684–5695 (1973).
- [122] E. Goulielmakis, M. Uiberacker, R. Kienberger, A. Baltuska, V. S. Yakovlev, A. Scrinzi, T. Westerwalbesloh, U. Kleineberg, U. Heinzmann, M. Drescher, et al., “Direct measurement of light waves,” *Science* **305**, 1267–1269 (2004).
- [123] A. Taflove and S. C. Hagness, *Computational Electrodynamics: the Finite-Difference Time-Domain Method*, 3rd ed. (Artech House, Boston, MA, 2005).
- [124] G. Mie, “Beiträge zur Optik trüber Medien, speziell kolloidaler Metallösungen,” *Ann. Phys.* **330**, 337–445 (1908).
- [125] S. Lal, N. K. Grady, G. P. Goodrich, and N. J. Halas, “Profiling the near field of a plasmonic nanoparticle with Raman-based molecular rulers,” *Nano Lett.* **6**, 2338–2343 (2006).
- [126] A. G. Borisov, P. M. Echenique, and A. K. Kazansky, “Attostreaking with metallic nano-objects,” *New J. Phys.* **14**, 023036 (2012).
- [127] F. Kelkensberg, A. F. Koenderink, and M. J. J. Vrakking, “Attosecond streaking in a nano-plasmonic field,” *New J. Phys.* **14**, 093034 (2012).
- [128] J. S. Prell, L. J. Borja, D. M. Neumark, and S. R. Leone, “Simulation of attosecond-resolved imaging of the plasmon electric field in metallic nanoparticles,” *Ann. Phys.* **525**, 151–161 (2013).
- [129] J. Lin, N. Weber, A. Wirth, S. H. Chew, M. Escher, M. Merkel, M. F. Kling, M. I. Stockman, F. Krausz, and U. Kleineberg, “Time of flight-photoemission electron microscope for ultrahigh spatiotemporal probing of nanoplasmionic optical fields,” *J. Phys. Cond. Mat.* **21**, 314005 (2009).
- [130] S. H. Chew, S. Süßmann, C. Späth, A. Wirth, J. Schmidt, S. Zherebtsov, A. Guggenmos, A. Oelsner, N. Weber, J. Kapaldo, et al., “Time-of-flight-photoelectron emission microscopy on plasmonic structures using attosecond extreme ultraviolet pulses,” *Appl. Phys. Lett.* **100**, 051904 (2012).
- [131] A. Mikkelsen, J. Schwenke, T. Fordell, G. Luo, K. Klünder, E. Hilner, N. Anttu, A. A. Zakharov, E. Lundgren, J. Mauritsson, et al., “Photoemission electron microscopy using extreme ultraviolet attosecond pulse trains,” *Rev. Sci. Instr.* **80**, 123703 (2009).



# INDEX

Note: Page number followed by f indicates figure only.

- Above-threshold photoemission (ATP)  
electrons, 418
- Abraham–Minkowski controversy, 9–10
- Abraham momentum, 372
- Abraham momentum density, 178
- Achiral molecules, irradiation of, 253
- Active material, 178
- Advanced LIGO, 157, 158
- Aether drag, 330
- Alice’s and Bob’s position observables, 126
- Amplitude-squeezed, 122
- Angular momentum, 16, 321
- Angular uncertainty relationship, orbital  
angular momentum and, 323–324
- Anisotropic materials, 180  
biaxial materials, 181–183  
gyrotropic materials, 183–186  
uniaxial materials, 180–181
- Annihilation operator, 137, 138
- Anti-Stokes wave, 368–369
- Arrayed waveguide gratings (AWGs), 378
- Astigmatism, 329
- Atomic ensembles, for squeezed light  
generation, 146–147
- Attosecond, 388
- Attosecond light pulses, 388  
generation of, 390–392
- Attosecond nanoplasmonic microscopy,  
431–432, 433f
- Attosecond physics, 388  
advent of, 388–389  
attosecond light pulses through HHG,  
390–392
- attosecond streaking from  
nanostructures, 425
- attosecond nanoplasmonic  
microscopy, 431–432, 433f
- instantaneous versus ponderomotive  
streaking, 425–428
- modeling of, 429–431
- electromagnetic forces by ultrashort  
laser pulses, 389–390

- Attosecond physics (*Continued*)
- streaked photoemission from solids
    - fs to sub-fs time-resolved
      - experiments on surfaces, 407–409
    - modeling of photoemission delay in tungsten, 416–417
  - photoemission delay measured for tungsten surfaces, 409–412
  - photoemission from magnesium surfaces, 417–420
  - photoemission from rhenium surfaces, 417
  - plasmon-response effects in, 420–425
  - theoretical models on, 412–416
- time-resolved photoemission from atoms
- emission and characterization of
    - photoelectron wave packets, 393–397
  - IR streaking field, influence of, 397–407
- time-resolving optoelectronic phenomena on attosecond scale, 392–393
- Attosecond streaking technique, 390, 407, 409
- Attosecond timescales, phenomena at, 389
- Azimuthal index, 322
- Backward light, 364
- Balanced homodyne detection, 136–138
- Basov model, 370
- Beam splitter model of loss, 135, 135f
- Beam splitter transformation, 133–134
- Beam transformations, 329–332
  - coordinate transformation, 329
  - rephasing of linear states, 329–330
- Bell inequality, violation of, 334
- Bell states, 216
- Bessel beams, 323, 351–352
- Bialynicki–Birula’s wave equation, 349
- Bianisotropic material
- Faraday chiral materials, 188–189
  - mirror-conjugated and racemic chiral materials, 187–188
  - motion-induced bianisotropy, 189–190
  - pseudochiral materials, 189
  - uniaxial and biaxial materials, 186–187
- Biaxially bianisotropic, 186
- Biaxial materials, 181–183
- Biisotropic material, 180
- Biphotons, 12
- Birefringent materials, 329
- BKS proposal, 97
- Black speck, 326
- Bloch sphere, 85, 87f
  - for OAM, 331, 331f
- Blue-detuned atom trapping, 329
- Bogoliubov transformation, 129
- Born–Oppenheimer approximation, 250
- Bose–Einstein condensates (BEC), 364
- Bose–Einstein statistics, 7
- Boys–Post constitutive relations, 171, 174
- Brillouin scattering, 147, 148
- Canonical momentum, 10
- Canonical quantization, 233
- Carrier–envelope phase (CEP), 390, 390f
- Casimir forces, 15
- Casimir–Polder dispersion potential energy formula, 265
- Cauchy integral formula, 172
- Causality, 171–173
- Cavity and circuit QED, 105–106
  - Jaynes–Cummings model, 106–108
  - Jaynes–Cummings model with decay, 109–110
    - strong coupling, 110–111
- Center-of-mass (COM) analysis of spectrograms, 410, 412f
- Chirality, 16
- Chiral nematic liquid crystals, 191
- Chiral sculptured thin films (CSTFs), 191–192
- Chiral smectic liquid crystals, 191
- Chiroptical effects, 251–255
- Cholesteric liquid crystals, *see* Chiral nematic liquid crystals
- Circular dichroism, 251–255
- Circular differential Rayleigh and Raman scattering, 251, 254
- Circularly polarized light, 321
- Circularly polarized luminescence, 255
- Classical field, quantum optics, 97
- Classical Maxwell fields, 342–344
- Classical optical state, 149

- Classical theory of coherence, 28–38  
     geometry of Young’s interference experiment, 29  
     in space-frequency domain, 34–38  
         complete spatial coherence, 37–38  
         cross-spectral density function, 34–35  
         degree of coherence, 35–37  
         stationary random function, 34  
     in space-time domain, 28–34  
         complete spatial coherence, 33–34  
         degree of coherence, 29–32  
         fluctuations in unison, 33  
     in structure determination of random media, 40–43
- Coherence, 18–19  
     classical theory of, 28–38  
         in space-frequency domain, 34–38  
         in space-time domain, 28–34  
     overview, 27–28  
     quantum theory of, 52–55
- Coherent arrays of detectors/emitters, 327
- Coherent drive, 90
- Coherent plane wave propagation, 41
- Coherent population oscillations (CPO), 365, 369–370
- Coherent-state fidelity, 153
- Coherent states, 80
- Colliding pulse mode-locked (CPM) dye laser, 281
- Complete spatial coherence  
     in space-frequency domain, 37–38  
     in space-time domain, 33–34
- Complete spectral coherence,  
     cross-spectrally pure field for, 39–40
- Conduction-band (CB) states, 416
- Confocal fluorescence microscope, 307, 308f
- Constitutive dyadics, 171  
     constraints, 171–175  
         causality, 171–173  
         Onsager relations, 173–174  
         Post constraint, 174–175  
     specializations, 175–178  
         dissipative, nondissipative, and active materials, 176–178  
         Lorentz reciprocity, 175–176
- Constitutive relations, 168–169
- Continuous-variable quantum information processing, 148. *See also* Squeezed light
- Continuous-variable quantum repeater, 158
- Continuous-variable quantum teleportation, 102–103, 152–154
- Coordinate transformation, 329
- Coulomb gauge, 232
- Coulomb-laser (CL) phase, 405
- CPO, *see* Coherent population oscillations (CPO)
- Cross-spectral density function (CSD function), 34–35
- Cross-spectral density matrix (CSD matrix), 36–37  
     equal-point, 47  
     two-point, 51–52
- Cross-spectrally pure field, 38–43  
     complete spectral coherence and, 39–40  
     conditions for, 38–39
- CSTFs, *see* Chiral sculptured thin films (CSTFs)
- Cyclical particle accelerator, 327
- Cylindrical lens mode converters, 324, 324f
- Data packets, in telecommunication system, 379
- De-excitation phenomenon, modification of, 205–206
- Degree of coherence  
     in space-frequency domain, 35–37  
     in space-time domain, 29–32
- Degree of polarization, 3
- Dehmelt, Hans, 94
- Dehmelt scheme, 94–95
- Delay-bandwidth product, 379
- Dexter theory, 263
- Dielectric–magnetic materials, 179
- Diffraction optical elements (DOEs), 325–326
- Dipole emitter near edge  
     dipole along  $y$ -axis, 215  
     dipole moment normal to  $z$ -plane, 213–214  
     normal modes, 211–213  
     single-emitter de-excitation rate, 213
- Dipole or quadrupole photons, 17

- Dispersion-balanced autocorrelators, 390  
 Dispersion curve, 8  
 Dispersive media, photon drag effects by, 371–372  
 Dissipation, in materials, 176, 178  
 Distances, measurements of, by single-mode squeezed light, 124  
 DOEs, *see* Diffractive optical elements (DOEs)  
 Doppler shift, 331  
 Dove prisms, 324, 332  
 Dressed or medium-dressed Photons, 8–9  
 Dressed states, 107–108  
 Duality symmetry, in piecewise homogeneous and isotropic media, 347–351  
 Duality transformation of electromagnetic fields, 344. *See also* Electromagnetic duality and optical helicity  
 Dual-rail single-photon qubits, 154  
 Dwell times, 397  
 Dynamic radiation-induced intermolecular energy shift, 267, 267f  
 Dyson expansion for master equation, 94
- Eikonal approximation (EA), 405  
 Einstein *A* coefficient, 245  
 Einstein *B* coefficient, 246  
 EIT, *see* Electromagnetically induced transparency (EIT)  
 Electric photon, 17  
 Electromagnetically induced transparency (EIT), 365, 368, 375  
 Electromagnetic duality and optical helicity, 342, 344–347  
     applications of framework  
         Bessel beams, 351–352  
         Kerker conditions, 358–359  
         optical vortices in focusing, 352–355  
         optical vortices in scattering, 355–358  
         spin to orbit angular momentum transfer, 351  
     duality symmetry in piecewise homogeneous and isotropic media, 347–351  
     symmetries and operators, 342–344  
 Electromagnetic energy equation, 5
- Electromagnetic theory of materials, 165  
     constitutive dyadics, 171  
     constraints, 171–175  
     specializations, 175–178  
     linear materials, 178–179  
         anisotropic materials, 180–186  
         bianisotropic material, 186–190  
         isotropic materials, 179–180  
         nonhomogeneous materials, 190–194  
     macroscopic viewpoint, 166  
         constitutive relations, 168–169  
         Maxwell postulates, 166–168  
         time/frequency domain, 169–171  
     nonlinear materials, 194–196  
         nonlinearity of quantum electrodynamics vacuum, 196  
         notation employed, 166
- Electron, 389–390  
 Electron beams, OAM in, 327  
 Emission of light, 244–246  
     spontaneous, 244–245, 245f  
     stimulated, 245–246  
 Energy spectrum, 107–108  
 Entangled photons, 12  
 Entanglement swapping, 154  
 Equal-point CSD matrix, 47  
 Equal-time correlation functions, 44  
 Euler–Lagrange equations, 232  
 Even Schrödinger kitten, 150, 151f  
 Ewald’s spheres of reflection, 42  
 Eye-opening penalty, 380
- Fabry-Perot cavity, 144  
 Fano factor, 97  
 Faraday chiral materials, 188–189  
 Fast electrons, 428  
 Fast light, 364  
 Femtochemistry, 389  
 Femtosecond Ti:sapphire laser, 280  
 Fermi golden rule formula, 208, 210  
 Ferroelectric crystals, 147  
 Few-cycle laser pulse, 390  
 Fiber Bragg grating (FBG), 378  
 Fiber or waveguide grating structures, 367  
 Field phasors, 170  
 Finite-difference time-domain (FDTD) method, 425  
 Fluctuations in unison, 33  
 Fluorescence, 14

- Fluorescence anisotropy, 299–304  
 Fock space operators, 346  
 Forked diffraction grating, for measuring OAM, 332  
 Forked holograms, 333  
 Förster energy transfer, 14  
 Förster resonance energy transfer (FRET) studies, 309  
 Forward scattering, 249  
 Franck–Condon principle, 291  
 Free charges, and bound charges, 166  
 Free rotors, two- and multiphoton absorption in, 304–307  
 Frequency-domain approach, to homodyne measurements, 139–141, 140f  
 Frequency-domain constitutive relations, 169–170  
 Frequency-resolved optical gating (FROG) devices, 390  
 Fresnel drag, 330  
 FROG-CRAB (Frequency-Resolved Optical Gating for Complete Reconstruction of Attosecond Bursts), 392  
 Front velocity, 370  
 Gain distortion factor, 379  
 GEO 600, Germany, 155  
 Geometrical symmetries, 341–342  
 Glauber coherence theory, 95–96  
 Glauber–Lewinstein’s expression, 208  
 Glauber’s theory of coherence, 80  
 Göppert Mayer (GM) units, 289  
 Gouy phase, 66, 322  
 Gravitational wave detection, application of squeezed light in, 154–157  
 Gravitational wave detectors, 155 squeezing in, 124  
 Gravitational waves (GWs), 154  
 Group index of dispersive medium, 370  
 Group velocity of light, 9, 364  
 GWs, *see* Gravitational waves (GWs)  
 Gyrofrequency, 184  
 Gyrotropic materials, 183–186  
 Hamiltonian and essential states, 207–208  
 Harmonic oscillator, quantum mechanics of, 78–80  
 Helically phased beams, 322f, 323  
 Helicoidal bianisotropic material, 192  
 Heralded photon, 12  
 Heralded single photons, 149  
 Hermite–Gaussian (HG) modes, 323, 331.  
*See also* Orbital angular momentum (OAM)  
 Hermite–Gauss (HG) modes, 67, 69  
 Hermitian operator, transformations generated by, 342–344  
 HG modes, *see* Hermite–Gauss (HG) modes  
 HHG, *see* High harmonic generation (HHG)  
 High harmonic generation (HHG), 390–392  
 Hilbert space, 123, 342  
 Hilbert transforms, 172  
 Holograms, 325 phase-only, 325–326  
 Homodyne and heterodyne detection, 99, 105 quantum state tomography and teleportation, 102–103 simple single-mode model, 99–101 squeezed light, 101–102  
 Homodyne tomography, 138–139  
 Homogenized composite materials (HCMs), 188  
 Hot spots, 428  
 Hybrid entanglement, 334  
 Hyperpolarizability tensor, 268  
 Image rotation, 329  
 Ince–Gaussian beams, 67, 323  
 Incoherent vortices, by spiral phase plate, 327, 327f  
 Induction fields, 167  
 Information velocity, 370  
 Instantaneous regime, 428  
 Intensity-dependent refractive index, 286, 288  
 Intensity fluctuations, 18–19  
 Interaction Hamiltonian, 238, 239  
 Interaction vertex, 242  
 Interferometric methods, for measuring OAM, 332  
 Interferometric spectrometers, 377–379, 380–381  
 Interferometry, 124  
 IR-streaked photoemission spectra, 398

- IR streaking field, influence of, on photoemission process, 397–399
- Coulomb–laser interactions, 404–407
- final-state interactions, 401–404
- initial-state perturbation, 399–401
- Isotropic chiral materials, 179–180
- Isotropic materials, 179–180
- dielectric–magnetic materials, 179
  - isotropic chiral materials, 179–180
- Jablonski diagram, 291
- Jaynes–Cummings Hamiltonian, 107
- Jaynes–Cummings model with decay, 109–110
- Jellium model, 416
- Kelley–Kleiner formula, 96, 103–104
- Kerker conditions, 358–359
- Kerr medium, 333
- effect of, on coherent state, 147, 148f
- Kramers–Heisenberg dispersion formula, 246–250
- Kramers–Kronig relations, 173, 365
- Laguerre–Gaussian (LG) beams, 322, 323.
- See also* Orbital angular momentum (OAM)
- Laguerre–Gauss (LG) modes, 65–69
- azimuthal phase, 66
  - forked amplitude diffraction grating for, 66
  - Lemon polarization pattern, 68
  - transverse phase maps for, 66
  - with unit-norm amplitudes, 68
- Laguerre polynomial, 322
- Lamb shift, 238
- Laser beam, phase singularities in, 323
- Laser-induced circular dichroism, 253
- Laser speckle, 326
- Laser technology, 387
- advances in, 388. *See also* Attosecond physics
  - starting of, 388
- Lemon polarization pattern, 68
- Lewis, Gilbert N., 229
- Light beams
- partially polarized, 45–46, 51–52
  - Poincaré modes of, 67–69
  - polarized light, 45–46
  - with spatially variable polarization, 61–73
  - spatial modes, 65–67
  - unpolarized, 45–46
- Light beams with helical phase fronts, 322f, 323
- Light detection and ranging (LIDAR), 376
- Light (photon) propagation
- directedness of, 10
  - equations for, 6
  - material medium and, 8–10
  - momentum, 9–10
  - spatial modes, 65–67
  - speed of, 8–9
- LIGO, United States, 155, 157
- Lindblad master equation, 89–90, 103
- Linear light scattering, 247, 247f. *See also* Quantum electrodynamics (QED)
- Linear materials, 178–179
- anisotropic materials, 180
  - biaxial materials, 181–183
  - gyrotropic materials, 183–186
  - uniaxial materials, 180–181
- bianisotropic material, 186
- Faraday chiral materials, 188–189
  - mirror-conjugated and racemic chiral materials, 187–188
  - motion-induced bianisotropy, 189–190
  - pseudochiral materials, 189
  - uniaxial and biaxial materials, 186–187
- isotropic materials, 179–180
- dielectric–magnetic materials, 179
  - isotropic chiral materials, 179–180
- nonhomogeneous materials, 190–191
- material analogues of curved spacetime, 193–194
  - periodically nonhomogeneous materials, 191–193
- Linear polarizer (LP), 356
- Linear transformations, 342
- Liquid crystals, 70
- L-lines, 72
- Localization, 11
- Local oscillator (LO), 136
- London dispersion energy, 265, 268
- Lorentz covariant, 190

- Lorentz force, 167  
 Lorentz reciprocity, 175–176
- Mach–Zehnder (M–Z) interferometer, 332, 378  
 Mach–Zehnder modulator, 369  
 Macroscopic fields, 166–167  
 Macroscopic slow light, *see* Structural slow light  
 Magic-angle configurations, 298  
 Magnetic circular dichroism, 253  
 Magnetic photon, 17  
 Magnetoelectric dyadics, 169  
 Mandel formula, 97  
 Markov approximation, 87  
 Master equation unravelings, 104–105  
 Material analogues of curved spacetime, 193–194  
 Material slow light, 364–365, 366f, 375.  
*See also* Slow and fast light  
 Material specializations, 177–178  
 Mathieu beams, 323  
 Maximum fractional delay, 379  
 Maxwell postulates, 166–168  
 MC function, *see* Mutual coherence function (MC function)  
 Mean-free path (MFP), electron, 407, 414, 420  
 Metric, 193  
 Michelson-type laser interferometer, 155  
 Micro-fabrication techniques, 325  
 Micromachines, 328–329  
 Micropump, 329  
 Microscopic slow light, *see* Material slow light  
 Mie theory, 425  
 Millimeter wave, 325, 327  
 Minimal-coupling Hamiltonian, 233  
 Minkowski momentum, 372–373  
 Mirror-conjugated and racemic characteristics, in bianisotropic material, 187–188  
 Mode sorters, use of, for measuring OAM, 333  
 Mollow spectrum, 92–93  
 Momentum carried by photon in material medium, 372–373  
 Momentum conservation, 334
- Momentum-squeezed vacuum state, Wigner function of, 122, 123f  
 Monochromatic field, 176–177  
 Monoclinic biaxial dielectric materials, 182  
 Motion-induced bianisotropy, 189–190  
 Multimode quadrature-entangled states, 158  
 Multiphoton absorption, 279. *See also* Multiphoton process  
 Multiphoton process, 279–280  
 applications and future prospects, 307–309  
 historical perspective, 280–281, 282f  
 molecular two-photon fluorescence, 289–292  
 applications and future prospects, 307–309  
 polarization dependence of two-photon absorption, 292–299  
 two- and multiphoton absorption in free rotors, 304–307  
 two-photon excited fluorescence, 299–304  
 two-photon absorption, 282  
 basic principles, 282–284  
 nonlinear optical polarization, 284–288  
 two-photon absorption cross-section, 288–289  
 Multi-photon resonance, 111  
 Multipolar coupling Hamiltonian, 235–241  
 Multipole emission, 17  
 Mutual coherence function (MC function), 30  
 M–Z interferometer, *see* Mach–Zehnder (M–Z) interferometer
- Nanophysics, 205  
 Newton’s equation, 398  
 No-cloning fidelity, 154  
 Noether’s celebrated theorem, 341  
 Nonclassical field, quantum optics, 97  
 Nonclassical optical states, 149  
 Nondissipative material, 177–178  
 Non-forward scattering, 249  
 Nonhomogeneous materials, 190–191  
 material analogues of curved spacetime, 193–194  
 periodically, 191–193  
 Nonlinear light scattering, 258–261

- Nonlinear materials, 194–196  
 Nonlinear optical effects, enhancement of, 373  
 Nonlinear optical polarization, 284–288  
 Nonlinear optics, 279  
 Nonlinear processes, OAM in, 333–334  
 Non-Lorentz reciprocal, 180, 183
- OAM**, *see* Orbital angular momentum (OAM)  
 OAM-carrying beams, 322  
 Occupation number, 6  
 “Odd Schrödinger kitten,” 151, 151f  
 One-photon absorption, 241–244  
 Onsager relations, 173–174  
 Open quantum systems, 87  
     Heisenberg picture, 87  
     model in 1D, 87–88  
     quantum Langevin equation and output field, 88–89  
 quantum jump, 93–94  
     Dehmelt scheme, 94–95  
     Dyson expansion for master equation, 94  
 quantum regression, 91  
     Hanbury Brown and Twiss photon bunching effect, 92  
     in manner of Lax, 91–92  
     Mollow spectrum, 92–93  
     solving master equation twice, 91  
 Schrödinger picture, 89  
     coherent drive, 90  
     Lindblad master equation, 89–90  
     Pauli master equation, 90
- Optical beam, through narrowband filter, 48  
 Optical binding forces, 266  
 Optical coherence, *see* Coherence  
 Optical eigenstates, 6–7  
 Optical fibers, 374  
     squeezing in, 147–148  
 Optical helicity, 342  
 Optical homodyne tomography, 138  
 Optical memories, 375–376  
 Optical parametric amplifier (OPA), squeezing in, 144–146, 145f  
 Optical parametric chirped-pulse amplifier (OPCPA) lasers, 388  
 Optical parametric oscillator/amplifier (OPO/OPA), 144
- Optical rotation, 251, 253, 254  
 Optical solitons, 280  
 Optical spanners, 327–329  
 Optical spiral phase plates, 325  
 Optical tunable delay lines, 374–375  
 Optical tweezers, 327  
 Optical vortices, 16, 323  
     in focusing, 352–355  
     in scattering, 355–358  
 Optic axes, 182  
 Optomechanical cavity, 157  
 Orbital angular momentum (OAM), 322–323, 351  
     and angular uncertainty relationship, 323–324  
     beams with, creation of, 324–327  
         cylindrical lenses, 324, 324f  
         diffractive optical elements, 325–326  
         Q-plates, 326  
         spiral phase plates, 324–325, 325f  
     beam transformations, 329–332  
     in classical imaging, 333  
     drawback of use of, 334  
     measuring of, 332  
         forked diffraction grating, use of, 332  
         interferometric methods, 332  
         mode sorters, use of, 333  
         rotational frequency shift method, 332–333  
     micro-manipulation through use of, 327–329  
     in nonlinear and quantum optics, 333–334
- Orthorhombic bianisotropic materials, 187  
 Orthorhombic biaxial dielectric material, 181
- Parametric amplification, 365  
 Parametric down-conversion, 143–146, 149, 334  
 Partially coherent light, 31, 51–52  
 Partially polarized light beam, 45–46, 51–52  
 Pauli master equation, 90  
 Pauli operators, 84–85  
 PCCW, *see* Photonic crystal coupled waveguide (PCCW)  
 Periodically nonhomogeneous materials, 191–193  
 Permittivity and permeability dyadics, 169

- Perturbation theory, 208  
 Perturbative nonlinear optical phenomena,  
   280  
 Petahertz lightwave electronics, 390  
*P* function, 82–83  
 Phase, 19–20  
 Phase distortion factor, 379  
 Phase singularities, 323  
 Phase-space displacement, implementation  
   of, 135, 135f  
 Phase squeezing, 122, 123f  
 Phase velocity, 8, 363  
 Photoelectric effect, 387  
 Photoelectron, 393  
 Photoelectron emission, 387  
 Photoelectron wave packets  
   emission and characterization of,  
   393–397  
 Photoemission electron microscopy  
   (PEEM), 431  
 Photon antibunching and single-photon  
   sources, 97–99  
 Photon blockade, 111  
 Photon bunching, 98  
 Photon bunching effect, of Hanbury Brown  
   and Twiss, 92  
 Photon counting, 95  
   classical and nonclassical fields, 97–99  
   Glauber coherence theory, 95–96  
   homodyne and heterodyne detection,  
   99–103  
   Kelley–Kleiner formula, 96  
   quantum trajectory theory, 103–105  
   shot noise and Fano factor, 96–97  
 Photon drag, 330, 330f, 371–372  
 Photonic bandgap structures, 367  
 Photonic crystal coupled waveguide  
   (PCCW), 376  
 Photonic crystal (PhC) structure, 366–367,  
   367f  
 Photonic integrated circuits (PICs),  
   374–375  
 Photon momentum, 5, 9–10  
   angular, 16  
 Photon number statistics, 130–132  
 Photons, 1, 387  
   Bose–Einstein statistics for, 7  
   categorization, 7  
   characteristics of, 2  
   coherence and fluctuations, 18–19  
   definition of, 1–2  
   dipole or quadrupole, 17  
   dressed or medium-dressed, 8–9  
   entangled, 12  
   heralded, 12  
   information in, 17–18  
   localization, 11  
   momentum, 5, 9–10  
   optical propagation, modes of, 3–5. *See also* Light (photon) propagation  
   polarization and, 3  
   overview, 1–2  
   phase, 19–20  
   quantum foundations, 5–6  
   quantum optics, development of, 6–7  
   superluminal, 9  
   virtual, *see* Virtual photons  
   wavefunction, 11–12  
 Photon wavefunction, 11–12  
 PICs, *see* Photonic integrated circuits  
   (PICs)  
 Plank’s constant, 321  
 Plasma frequency, 184  
 Plasmons, 421–422  
 Poincaré modes, 67–69  
   apparatus for creation, 70  
 Poincaré sphere, 62–64  
   for polarization, 331, 331f  
 Polaritons, 8–9, 263  
 Polarization, 3, 331  
   of light  
     in frequency domain, 47–50  
     in time and frequency domains, 50  
   matrix formulation of, 44–45  
   patterns produced by superposition, 72  
   space-time degree of, 50  
   spatially variable, 61–73  
     experimental approaches for, 69–70  
     overview, 61–62  
   states of, 62–65  
   statistical similarity and complete, 46–47  
   of stochastic beams, 43–50  
 Polarization-maintaining fiber, 148  
 Polarization singularities, 70–73  
   C-point, 71–72  
   L-line, 72  
   perturbations and, 72–73  
 Polarization-state map, for star pattern, 71

- Polarized light beam, 45–46  
 Ponderomotive regime, 428  
 Position-squeezed vacuum state, Wigner function of, 122, 123f  
 Post constraint, 174–175  
 Primitive fields, 167  
 Principle of causality, 171–172  
 Principle of minimal electromagnetic coupling, 231–235  
 PROOF (Phase Retrieval by Omega Oscillation Filtering), 392  
 Pseudochiral materials, 189  
 Purcell effect, 109
- Q-factor penalty, 380  
 $Q$  or Husimi function, 82  
 Q-plates, 326  
 Quadrature angle, 122  
 Quadrupole transition, 321  
 Quantum canonical transformation, 235  
 Quantum correlations, 215–217  
 Quantum cryptography, 334  
 Quantum electrodynamics (QED), 229–231  
     chiroptical effects, 251–255  
     emission of light, 244–246  
         spontaneous, 244–245, 245f  
         stimulated, 245–246  
     linear light scattering, 246–250  
     molecular, 231–235  
     multipolar coupling Hamiltonian, 235–241  
     nonlinear light-scattering, 258–261  
     one-photon absorption, 241–244  
     radiation-induced interparticle forces, 266–269  
     resonance energy transfer, 261–264  
     two-photon absorption, 255–258  
     van der Waals dispersion interactions, 264–266  
 Quantum electrodynamics (QED) vacuum, nonlinearity of, 196  
 Quantum harmonic oscillator, 121–122  
 Quantum information, application of  
     squeezed light in, 148–154, 157  
 “Quantum internet,” 158  
 Quantum jump, 93–95  
 Quantum Langevin equation, 88–89  
 Quantum mechanics, use of OAM in tests of, 334
- Quantum metrology, application of  
     squeezed light in, 154–157  
 Quantum-optical state engineering, 149–151  
 Quantum optics, 6–7, 77–78  
     cavity and circuit QED, 105–106  
         Jaynes–Cummings model, 106–108  
         Jaynes–Cummings model with decay, 109–110  
         strong coupling, 110–111  
     electric dipole interaction  
         classical drive, 86  
         Hamiltonian and coupling strength, 85–86  
     electromagnetic energy density in, 6–7  
     electromagnetic field, 80–81  
         energy density and photon flux, 81  
         expansion in 1D, 81  
     equations for light propagation in vacuum, 6  
 open systems, 87. *See also* Open quantum systems  
     Heisenberg picture, 87–89  
     quantum jump, 93–95  
     quantum regression, 91–93  
     Schrödinger picture, 89–90  
 phase-space representations of quantum state, 82  
 $P$  function, 82–83  
 $Q$  or Husimi function, 82  
 Wigner function, 83–84  
 photon counting, 95  
     classical and nonclassical fields, 97–99  
 Glauber coherence theory, 95–96  
 homodyne and heterodyne detection, 99–103  
 Kelley–Kleiner formula, 96  
 quantum trajectory theory, 103–105  
 shot noise and Fano factor, 96–97  
 quantum mechanics of harmonic oscillator, 78  
     energy spectrum and photon number, 79  
 Hamiltonian and observables, 78–79  
 rotation, displacement, and squeeze, 79–80  
 radiation Hamiltonian, 6  
 two-state system or qubit, 84

- Pauli operators, 84–85  
 rotations and Bloch sphere, 85  
 Quantum Rabi oscillation, 108  
 Quantum regression, 91–93  
 Quantum state tomography and teleportation, 102  
 Quantum teleportation protocol, 152, 152f.  
*See also* Continuous-variable quantum teleportation  
 Quantum trajectory theory, 103, 104  
 counts for photoemissive sources, 103–104  
 simulated detection records, 104–105  
 Quantum vacuum, 12–15  
 Casimir forces and, 15  
 fluctuation, 12–13  
 virtual photons and, 13–15  
 Quarter wave plate (QWP), 356
- Rabi frequency, 86  
 Rabi oscillation, 86  
 Racemic mixture, 180  
 Radiation Hamiltonian, 6  
 Radiation-induced interparticle forces, 266–269  
 Radio waves with OAM, 327  
 Raman effect, 248, 249–250. *See also* Quantum electrodynamics (QED)  
 Raman scattering, 147, 148  
 Rayleigh range, 322  
 Rayleigh scattering, 248–249. *See also* Quantum electrodynamics (QED)  
 Reference time delay, 398  
 Relative time delay, 398  
 Rephasing of linear states, 329–330  
 Resonance energy transfer, 14, 261–264  
 Right-angle cavity, 224. *See also* Surface and cavity nanophotonics  
 Right circularly (RC) polarized Gaussian beam, 353  
 Rosenfeld–Condon formula, 252  
 Rotational Doppler shift, 329  
 Rotational frequency shift method, for measuring OAM, 332–333  
 Rotations, in quantum optics, 85  
 Ruby crystals, 364
- Sagnac interferometer, 332  
 Sagnac-type interferometer, 148
- SAM, *see* Spin angular momentum (SAM)  
 SBS, *see* Stimulated Brillouin Scattering (SBS)  
 SBS Stokes frequency shift, 374  
 Schrödinger equation (SE), 394  
 Second-harmonic generation, 260–261  
 Second-order nonlinear interactions, 334  
 Self-action effects, 279  
 Self-phase modulation, 279  
 SFA, *see* Strong-field approximation (SFA)  
 Shot noise, 96–97  
 Simple single-mode model, homodyne/heterodyne detection, 99–101  
 Simplest open cavity, 209–211  
 Single and coupled ring resonators, 367  
 Single-atom cooperativity, 109  
 Single-mode squeezed light, 121–124  
 Single-photon counting modules (SPCMs), 150f  
 Singularity index, 71  
 SLM, *see* Spatial light modulator (SLM)  
 Slow and fast light, 363–364  
 applications of  
 interferometric spectrometers, 377–379  
 light detection and ranging, 376–377  
 optical memories, 375–376  
 optical tunable delay lines, 374–375  
 common slow-light processes, 367–370  
 and enhancement of optical nonlineairties, 373  
 fundamental limits on  
 for interferometric spectroscopy, 380–381  
 for optical delay lines, 379–380  
 kinetics properties and photon drag, 371–373  
 linear response of atomic absorption lines for, use of, 367–368  
 mechanisms of slow light, 364  
 material slow light, 364–365, 366f  
 structural slow light, 366–367  
 slow light based on CPO, 369–370  
 slow light based on EIT, 368  
 slow light based on SBS, 368–369  
 superluminal and backward light, 370–371

- Slow light, 9, 364. *See also* Slow and fast light
- Slow-light delay, 369
- Slow-light laser radar (SLIDAR) system, 376–377
- Snell’s law, 325
- Soliton formation, 280
- Space-time degree of polarization, 50
- Spatial light modulator (SLM), 69–70, 326, 333
- Spatially variable polarization, 61–73
- experimental approaches for, 69–70
  - overview, 61–62
  - Poincaré modes, 67–69
  - states of, 62–65
- Spatial nonlocality, 169
- SPDC, *see* Spontaneous parametric down-conversion (SPDC)
- Spectral hole burning, 365
- Spectral intensity law, 36
- Spectral polarization matrix (SP matrix), 47
- Spectrum analyzer, electronic, 141
- Speed of light
- in medium, 363–364. *See also* Slow and fast light
  - in vacuum, 363
- Spherically symmetric system, 341
- Spin angular momentum (SAM), 321, 328–329, 328f, 331–332, 351.
- See also* Orbital angular momentum (OAM)
- Spintronics, 360
- Spiral interferometry, 333
- Spiral phase plates, 324–325, 325f
- SP matrix, *see* Spectral polarization matrix (SP matrix)
- Spontaneous emission of radiation, 244–245, 245f
- Spontaneous parametric down-conversion (SPDC), 124, 127, 131, 149
- degenerate, 124, 124f
  - non-degenerate, 124f, 127
- Squeezed coherent states, 122, 123f, 124
- Squeezed light, 101–102, 121, 134–135
- detection of
  - balanced homodyne detection, 136–138
  - frequency-domain approach, 139–141
  - time-domain approach, 138–139
- preparation, 141–143
- in atomic ensembles, 146–147
  - in fibers, 147–148
  - via parametric down-conversion, 143–146
- in quantum information, 149
- continuous-variable quantum teleportation, 152–154
  - quantum-optical state engineering, 149–151
- in quantum metrology, 154–157
- single-mode, 121–124
  - two-mode, 125–127
- Squeezed optical states, 124
- Squeezed states, features of
- effect of losses, 135–136
  - photon number statistics, 130–132
  - single- and two-mode squeezing, interconversion between, 132–134
  - squeezed vacuum and squeezed light, 134–135
  - squeezing operator, 128–130
- Squeezed vacuum, 134–135
- Squeezing operator, 128
- single-mode squeezing, 128–129
  - two-mode squeezing, 129–130
- Squeezing parameter, 122, 128
- SRS, *see* Stimulated Raman scattering (SRS)
- Standard quantum limit (SQL), 123
- State sequence representation, 240–241
- Static electric dipolar coupling tensor, 268
- Static radiation-induced intermolecular energy shift, 268, 268f
- Stimulated Brillouin Scattering (SBS), 368–369, 374
- Stimulated emission of radiation, 245–246
- Stimulated Raman scattering (SRS), 365, 374
- Stochastic beams, polarization properties of, 43–50. *See also* Light beams
- complete polarization, 46–47
  - in frequency domain, 47–50
  - matrix formulation, 44–45
  - statistical similarity, 46–47
  - in time and frequency domains, 50
  - unpolarized, polarized, and partially polarized, 45–46
- Stokes parameters, 3

- Stokes wave, 368–369  
 Stopped light, 364, 375  
 Strong-field approximation (SFA), 401–403  
 Structural slow light, 366–367, 376. *See also* Slow and fast light  
 Structured light, 15–18  
     chirality and angular momentum, 16  
     complex modes, 15–16  
     information in photon, 17–18  
     multipole emission, 17  
     vector beams, 15–16  
 Sum-frequency generation, 258–260, 259f  
 Superluminal and backward light, 9, 370–371  
 Superluminal photons, 9  
 Surface and cavity nanophotonics, 205–207  
     dipole emitter near edge  
     dipole along  $y$ -axis, 215  
     dipole moment normal to  $z$ -plane, 213–214  
     normal modes, 211–213  
     single-emitter de-excitation rate, 213  
     entanglement, 217–219  
     Hamiltonian and essential states, 207–208  
     quantum correlations, 215–217  
     simplest open cavity, 209–211  
     wedge cavities, 219–223  
 Surface impedance matching condition, 349  
 Symmetries and operators, 342–344  
 Synchotron, 327  
 Table-top laser systems, 388  
 TAMA, Japan, 155  
 TDSE, *see* Time-dependent Schrödinger equation (TDSE)  
 Technical noises, and quantum noise, 139  
 Teleportation, 152. *See also* Continuous-variable quantum teleportation  
 Telescopes, OAM in, for detection of off-axis light, 333  
 Tellegen constitutive relations, 171  
 Temporal nonlocality, 169  
 Third-harmonic generation, 261, 286  
 Third-order nonlinear interaction, 333  
 Time-averaged Poynting vector, 178  
 Time delay, 396–397  
 Time-dependent Schrödinger equation (TDSE), 394, 402, 406–407  
 Time-domain constitutive relations, 169  
 Time-domain homodyne detection, 138–139  
 Time-of-flight PEEM (TOF-PEEM), 432  
 Time-ordered diagrams, 240–241  
     one-photon absorption, 242, 243f  
     for resonance energy transfer, 262, 262f  
 Time-resolved photoelectron emission experiments, 392  
 TMSV, *see* Two-mode squeezed vacuum (TMSV)  
 Total system propagator, 240  
 Transmission electron microscope (TEM), 327  
 Transverse Maxwell fields, 342  
 Triclinic biaxial dielectric materials, 182  
 Twin-beam state, *see* Two-mode squeezed vacuum (TMSV)  
 Two-level model, 207  
 Two-mode squeezed vacuum (TMSV), 125–127  
     heralded single photons by, 149  
     use of, 127  
     wavefunction of, 125–126  
 Two-photon absorption, 280. *See also* Multiphoton process  
     polarization dependence of, 292–299  
 Two-photon absorption cross-section, 288–289  
 Two-photon absorption of light, 255–258  
 Two-photon excited fluorescence, 299–304  
 Two-photon fluorescence lifetime imaging microscopy (FLIM), 309  
 Two-photon microscope, 309, 310f  
 Two-photon resonance, 111  
 Ultrahigh vacuum (UHV) conditions, 409  
 Ultrashort radiation in extreme ultraviolet (XUV) radiation, 388–389, 393–397  
 Ultrasound waves, phase singularities in, 323  
 Uncertainty principle, 122, 127, 154  
 Uniaxial anisotropic materials, 180–181  
 Uniaxial bianisotropic materials, 187  
 Unidirectional edge enhancement, 333  
 Unperturbed Hamiltonian, 239  
 Unpolarized light beam, 45–46

- Vacuum-field Rabi splitting, 110  
Vacuum fluctuation, 12–13  
Van der Waals dispersion interactions, 264–266  
Vector beams, 3, 15–16  
Vector space, 342  
VIRGO, Italy, 155  
Virtual, 247  
Virtual photon cloud, 14  
Virtual photons, 231, 261, 264, 270  
    in action, 13–14  
    definition of, 13  
    propagation of, 14–15  
Virtual states, 282  
Volkov states, 402  
Vortex beam, and spatial coherence, 327  
Wave packet, propagation speed of, 364  
Wedge cavities, 219–223  
Wigner function, 83–84, 122, 153  
    of single-oscillator states, 122, 123f  
Wigner time delay, 397  
X-ray vortex, 327

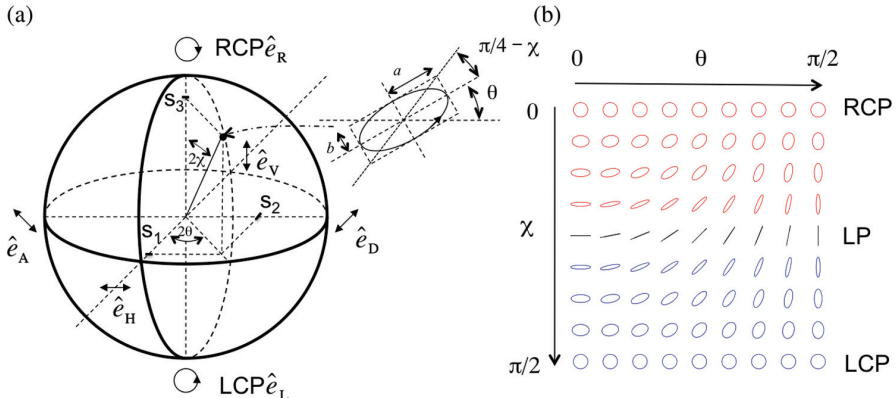


**FIGURE 3.1** (a) Poincaré sphere and (b) states of polarization as a function of the angles  $\chi$  and  $\theta$ . Right- and left-handed ellipses are colored red and blue, respectively.

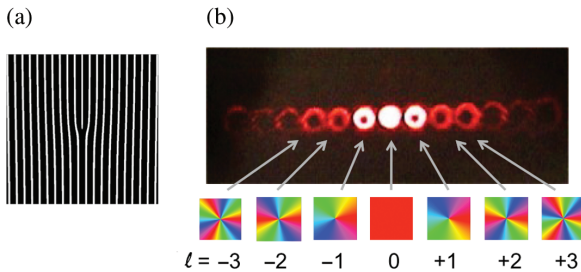


**FIGURE 3.3** (a) Forked amplitude diffraction grating used to produce LG modes in (b). Each order has a different topological phase, shown below in colored phase maps, where each color is a unique phase (modulo  $2\pi$ ).

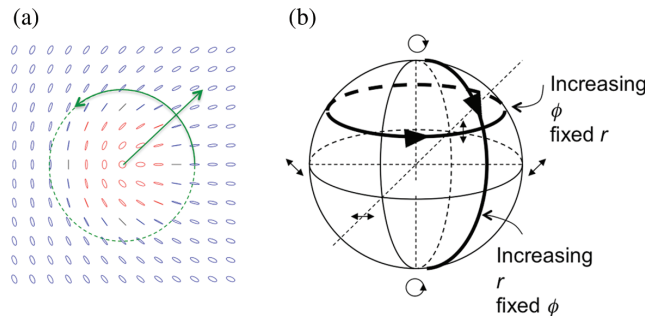
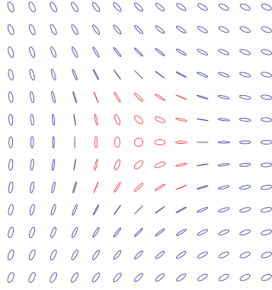


**FIGURE 3.4** (a) Lemon polarization pattern formed by a superposition of LG modes, one with topological charges 1 and 0, in opposite states of circular polarization. (b) Illustration of the mapping of the beam pattern onto the Poincaré sphere. Right- and left-handed ellipses are colored red and blue, respectively.

(a)



(b)

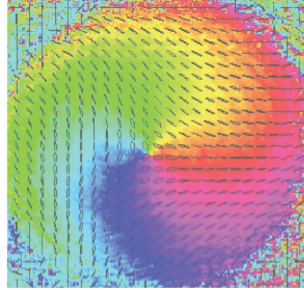
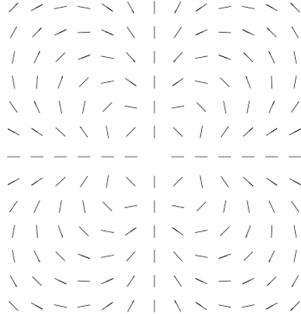


**FIGURE 3.6** (a) Polarization-state map for a star pattern, created by the superposition of LG modes with topological charges 1 and 0, in opposite circular polarization states, but the reverse combination as Figure 3.4. (b) Measured polarization field for the pattern corresponding to a star, taken with the setup of Figure 3.5. The color map is the phase of the Stokes field  $\sigma_{12}$ .

(a)



(b)

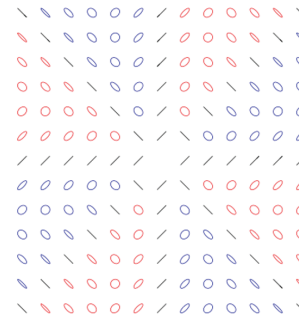
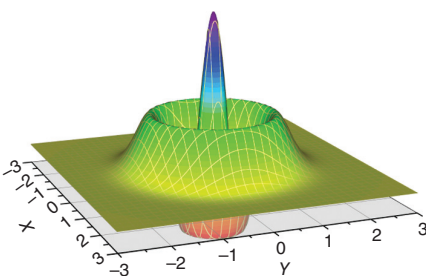
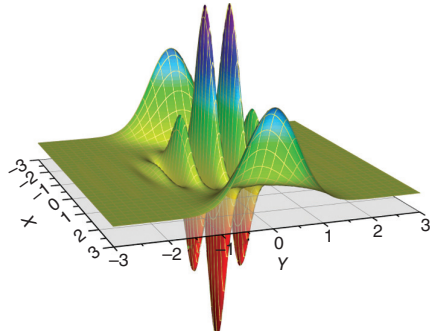


**FIGURE 3.7** (a) Polarization patterns produced by the superposition of  $LG_0^{+3}$  and  $LG_0^{-3}$  modes in circular polarization eigenstates. (b)  $LG_0^{+2}$  and  $LG_0^{-2}$  modes in linear polarization eigenstates. The central points are singular. Regions of right- and left-handed ellipticity are colored red and blue, respectively.



(a)



(b)

**FIGURE 4.2** Wigner functions for (a) the Fock state  $|2\rangle$  and (b) the coherent state superposition  $|3\rangle - |-3\rangle$ .

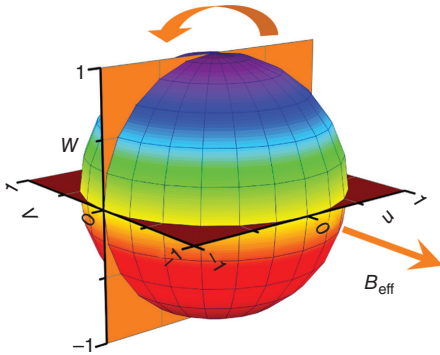


**FIGURE 4.3** The Bloch sphere: for on-resonance driving the precessing Bloch vector describes a circle in a plane parallel to the orange ( $u,w$ )-plane.

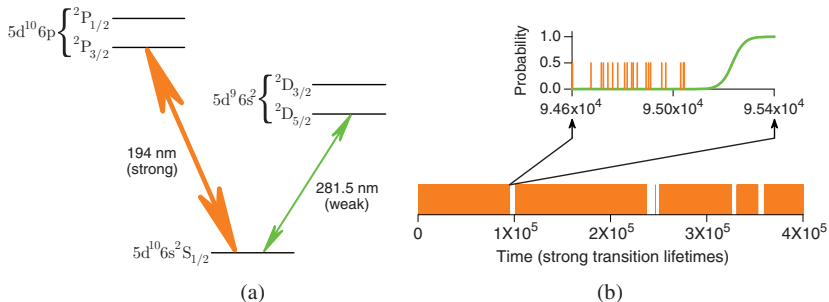


**FIGURE 4.6** (a) Level scheme used for the realization of quantum jumps in Mercury II [37]. (b) The probability to occupy the weak excited state evolves continuously (green curve) in a quantum trajectory simulation (Section 4.4.4.2).

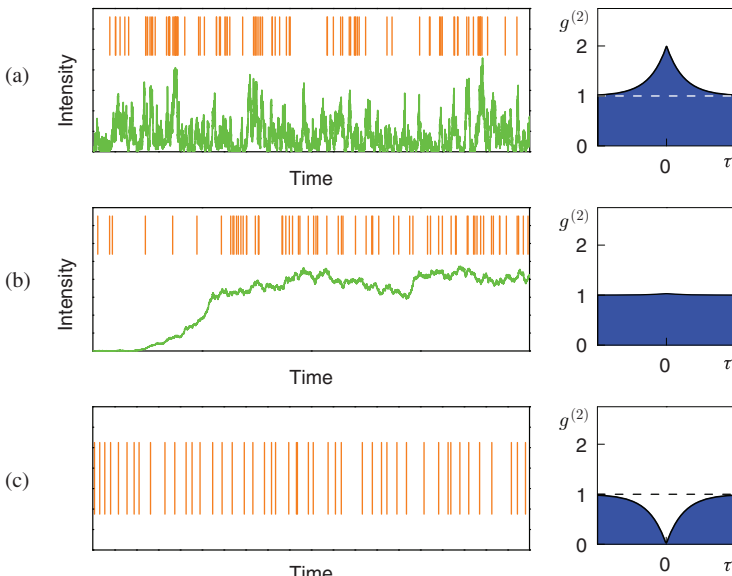


**FIGURE 4.7** Simulated photon counting sequences: (a) filtered thermal light, (b) laser turn-on, and (c) resonance fluorescence. Green curves plot the a priori rate of events (classical intensity); an event rate for resonance fluorescence must include back-action (Section 4.4.4.2).

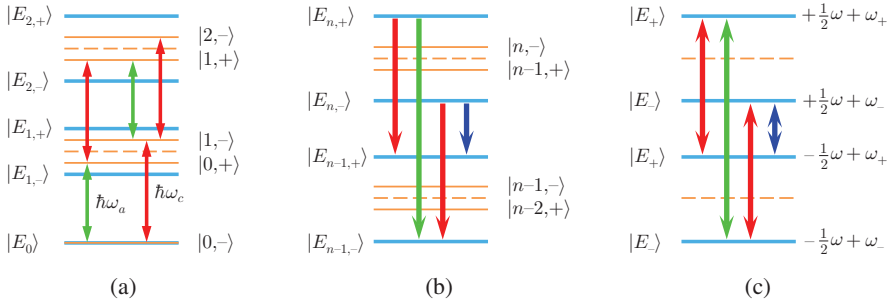


**FIGURE 4.11** Dressed state energies: (a) lower rungs of the Jaynes–Cummings ladder; (b) equally split doublets for  $n \gg 1$ ; (blue, red, green) transitions yield the (lower, center, upper) peaks of the Mollow spectrum (Section 4.3.3.4); (c) quasi-energies show the same transition frequencies as (b).

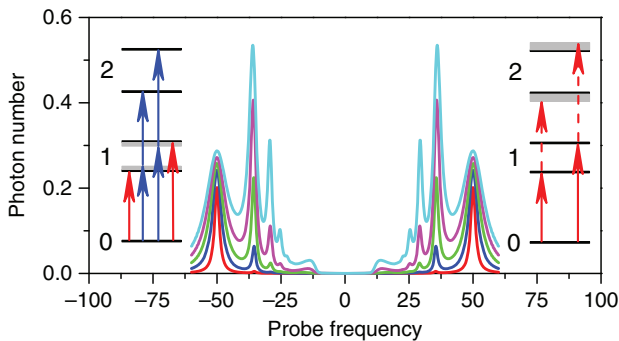


**FIGURE 4.12** Cavity photon number for increasing drive strength (red to cyan); for  $\omega_c = \omega_a$ ,  $\gamma/\kappa = 0$ , and  $g/\kappa = 50$ . One- and two-photon resonances are shown on the left and photon blockade on the right.

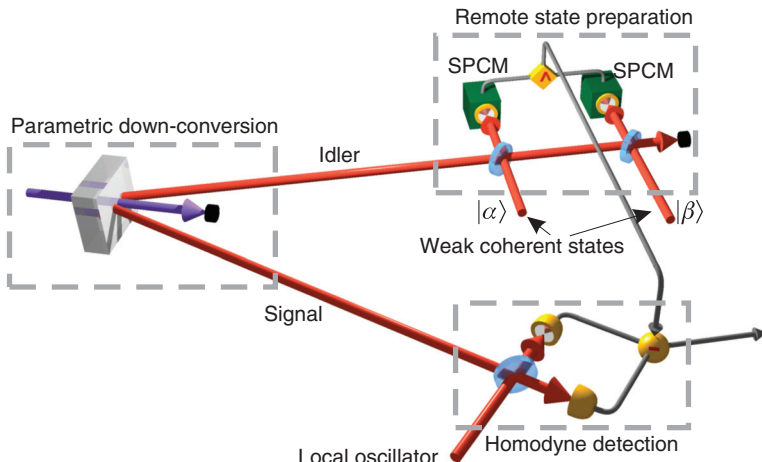


**FIGURE 5.15** Generating arbitrary superpositions of the zero-, one-, and two-photon states. The light in the idler channel of parametric down-conversion is brought into interference with two weak coherent states and subsequently detected by single-photon counting modules (SPCMs). A double “click” heralds the generation of the desired state in the signal channel.

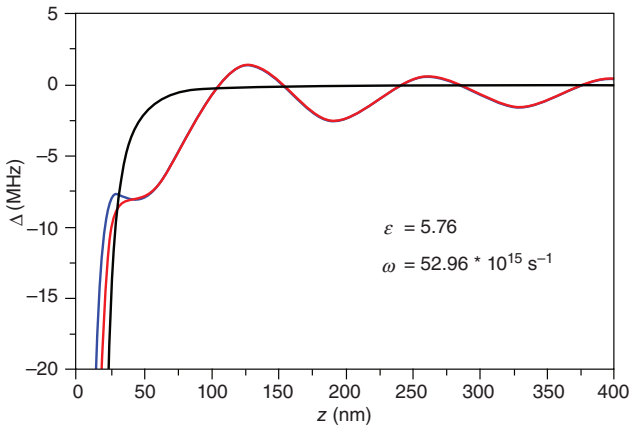


**FIGURE 7.2** Variation of the energy shift with the position of the dipole emitter  $z$  from a planar dielectric surface. The red curve represents the excited state shift and the blue curve the ground state, while the black represents the pure van der Waal's potential.

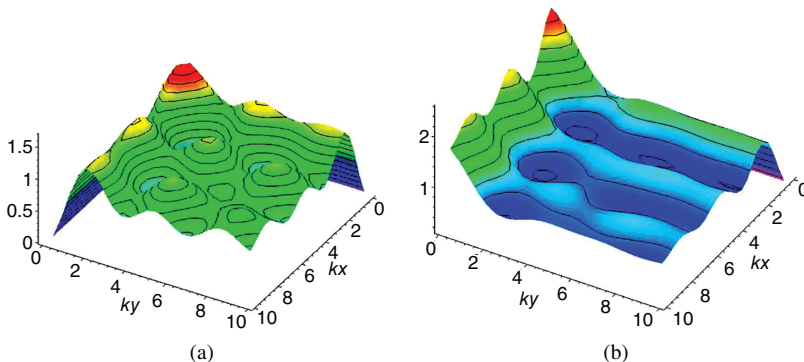


**FIGURE 7.4** (a) Spatial distribution of  $\Gamma^z/\Gamma_0$ , the relative de-excitation rate on the  $z = 0$  plane of the right-angle cavity. The dipole moment is oriented in the  $z$ -direction, that is, parallel to both surfaces. The color code is such that from blue to red is equivalent to from minimum to maximum. (b) Spatial distribution of  $\Gamma^y/\Gamma_0$ , the de-excitation rate in the  $z = 0$  plane of the open right-angle cavity. The dipole moment is oriented along the  $y$ -direction, that is, normal to one of the surfaces. The color code is such that from magenta to red is equivalent to from minimum to maximum. See the text for further details.

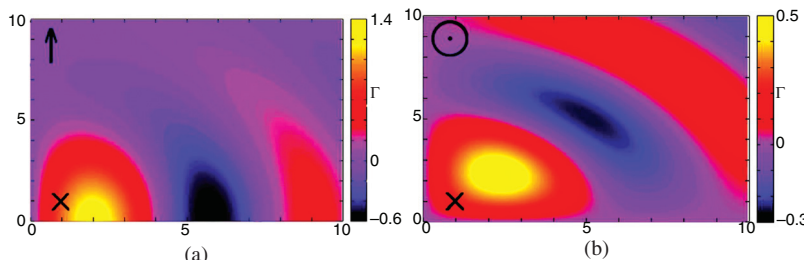


**FIGURE 7.6** Spatial distribution of the pair correlation term  $\Gamma$  defined by Eq. (7.34) in the  $z = 0$  plane of the right-angle cavity. One of the emitters is fixed at the point  $(x_1, y_1) = (\hat{x}, \hat{x})$ , shown by the cross, while the position of the second emitter is varied across the  $z$ -plane. (a) Both dipoles are parallel to the  $y$ -axis, shown by the arrow. (b) Both dipoles are parallel to the  $z$ -axis, indicated by the dot inside a circle.

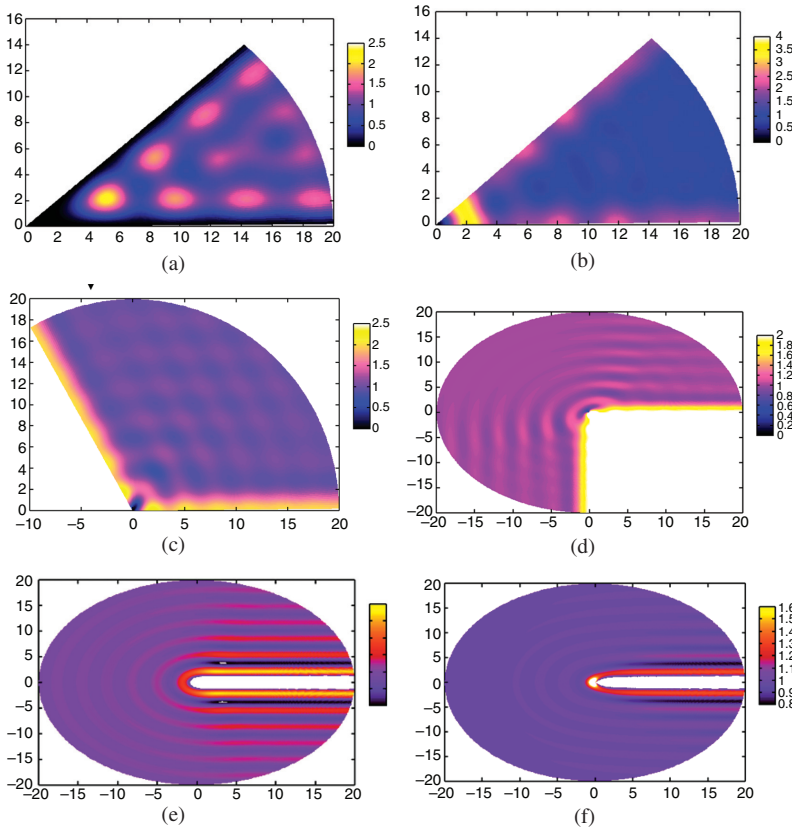


**FIGURE 7.11** De-excitation rates in units of  $\Gamma_0$  for dipole moments localized in the  $x$ - $y$  plane near the wedge edge in a wedge with an opening angle of  $\Phi_0 = \pi/4$  (dipole parallel to plane) (a); with an opening angle of  $\Phi_0 = \pi/4$  (dipole perpendicular to the plane) (b); with an opening angle  $\Phi_0 = 3\pi/4$  (c) (note the tendency to the planar surface case (attained when  $\Phi_0 = \pi$ ) as the opening angle increases); with an opening angle of  $\Phi_0 = 3\pi/2$  (d), but dipole moments are oriented in the direction of increasing  $\Phi$ ; with an opening angle of  $\Phi_0 \approx 2\pi$  (e), but dipole moments are oriented in the direction of increasing  $\Phi$ ; with an opening angle of  $\Phi_0 \approx 2\pi$  (f), but the dipole moments are oriented in the  $z$ -direction. Distances along the horizontal ( $x$ -axis) and vertical ( $y$ -axis) are in units of  $\lambda$ ; the reduced transition wavelength.

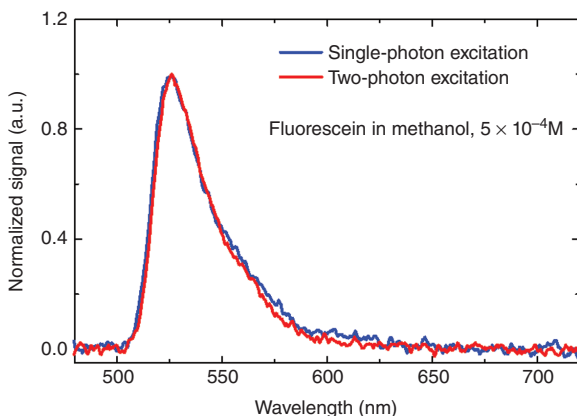


**FIGURE 9.4** Steady-state fluorescence spectra of fluorescein obtained using single-photon excitation at 500 nm and two-photon excitation at 800 nm. Although the two-photon transition energy is higher, 3.1 eV versus 2.48 eV, fast relaxation within the excited state manifold leads to the rapid population of the same low-lying vibrational levels in  $S_1$  as shown by the equivalence of the emission spectra.

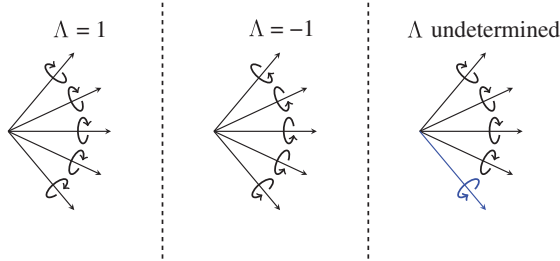


**FIGURE 11.1** A field composed by the superposition of five plane waves is an eigenstate of helicity with eigenvalue equal to one if all the plane waves have left-handedness (left panel), equal to minus one if they all have right-handedness (central panel) and it is not an eigenstate of helicity if some plane waves have a handedness and others have the opposite (right panel).

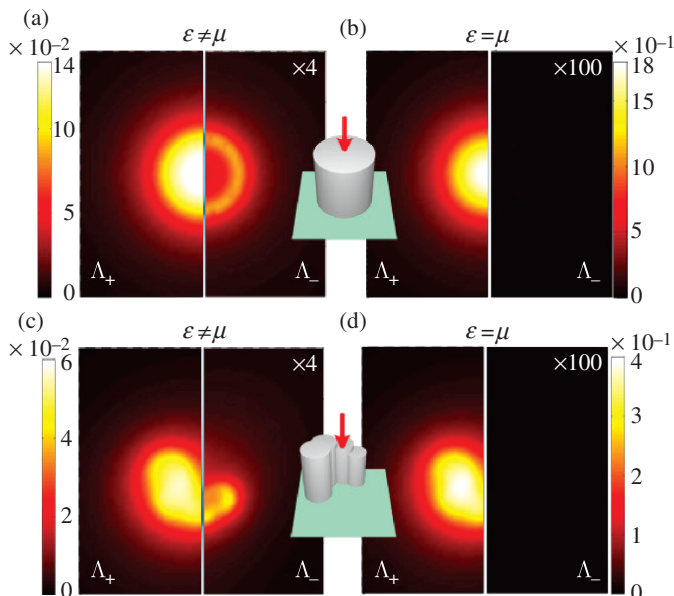


**FIGURE 11.2** Impact of the different symmetries on the field scattered by two dielectric structures. The upper row shows the scattered intensity for a symmetric cylinder and the lower row for a panflute like shape without any rotational, translational or spatial inversion symmetry. The length and diameter of the cylinder are 200 nm. The panflute is made of cylinders of different lengths and diameters, the longest one is 200 nm long and the total panflute's width is around 200 nm. In (a) and (c) the structures have  $\epsilon = 2.25$ ,  $\mu = 1$ , while in (b) and (d) we enforced duality symmetry by setting  $\epsilon = \mu = \epsilon_{\text{glass}} = 2.25$ . The incident field is a plane wave of well defined helicity equal to 1, momentum vector pointing to the positive  $z$  axis and a wavelength of 633 nm. Its electric field is  $(\hat{x} + i\hat{y})/\sqrt{2} \exp(kz - \omega t)$ . The left half side of each subfigure corresponds to the scattered field with helicity equal to the incident plane wave  $\Lambda_+$ ; the right half is for the opposite helicity  $\Lambda_-$ . The calculation plane is perpendicular to the  $z$  axis and 20 nm away from the surface of the scatterers opposite to the one where the incident field comes from. The calculation area is 700×700 nm. For color scaling purposes, the right half side is multiplied by the factor in the upper right corner. The (lack of) cylindrical symmetry of the structures results in (non)-cylindrically symmetric field patterns, which is consistent with the geometry of each case. On the other hand, both scatterers behave identically with respect to conservation of helicity, which is seen to depend exclusively on the electromagnetic properties of the material.

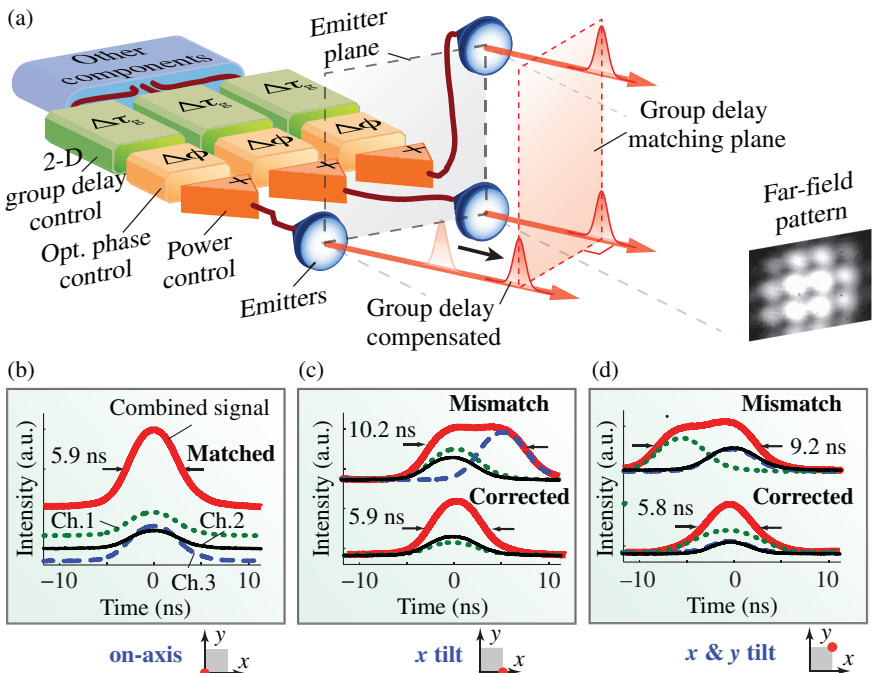


**FIGURE 12.3** (a) The schematics of a SLIDAR system capable of 2D beam steering; normalized time traces of the returned signal when the system is pointing on-axis (b), tilted in the  $x$ -direction (c), and tilted in both the  $x$ - and  $y$ -directions (d).

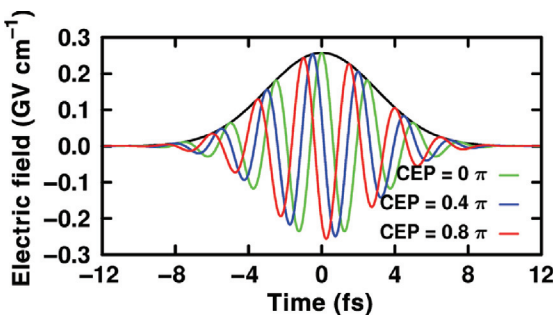


**FIGURE 13.2** Carrier-envelope phase (CEP) stable, few-cycle pulses at 800 nm. The electric fields for different CEP values are shown in color. The pulse envelope is indicated as a solid black line. Reproduced from Reference 27 with the permission of the PCCP Owner Societies.

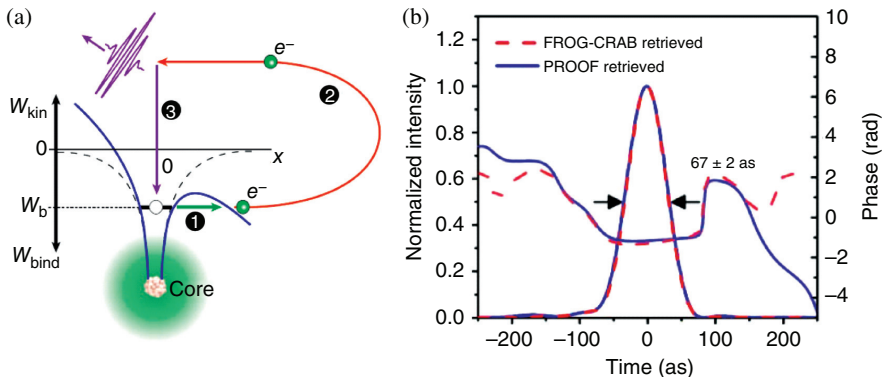


**FIGURE 13.3** (a) High harmonic generation process illustrated for an atom. Reprinted from Reference 48 with copyright permission of *Annual Reviews*. (b) Retrieved pulse duration (with two retrieval algorithms indicated in the legend, for details see Reference 18) of an isolated attosecond pulse spanning a spectral range from 55 to 130 eV. Reprinted from Reference 18 with copyright permission of OSA.

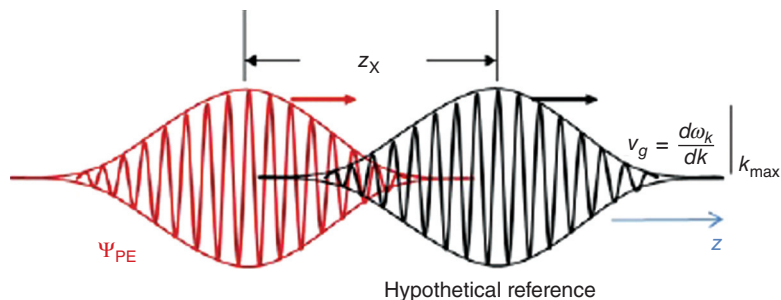


**FIGURE 13.6** Displacement of the photoelectron wave packet  $|\psi_{\text{PE}}(t)\rangle$ , relative to a fictitious reference wave packet. Both wave packets move with group velocity  $v_g$  to a photoelectron detector. A photoemission time delay can be defined as  $t_X = z_X/v_g$ .

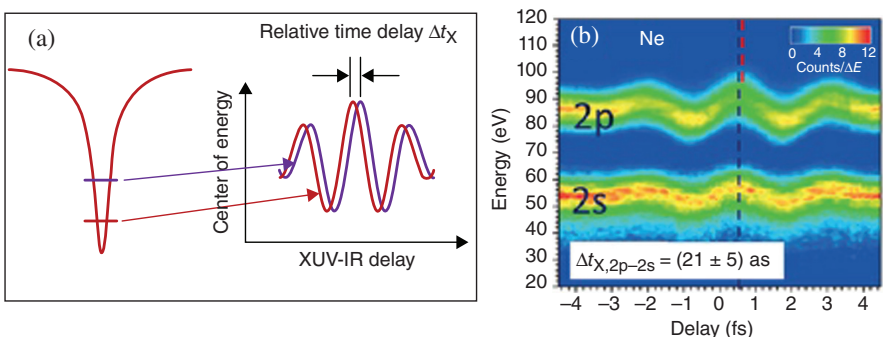
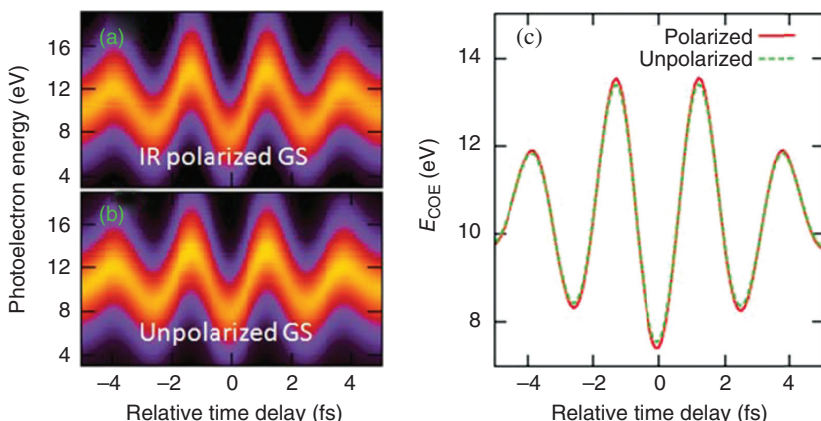


**FIGURE 13.9** (a) Illustration of the *relative* photoemission time delay,  $\Delta t_X$ , for photoionization from two energetically separate atomic levels. The two initial states yield energetically separated streaking traces in the photoelectron streaking spectrum.  $\Delta t_X$  is obtained from the phase difference between the centers of energy of the two traces. (b) Measured photoemission streaking spectrum for XUV photoionization of Ne. The *relative* photoemission time delay for emission out of 2s and 2p levels is determined as  $\Delta t_{X,2p-2s} = (21 \pm 5)$  fs. Adapted from Reference 53.

### XUV photoemission from ground state



### XUV photoemission from first excited state

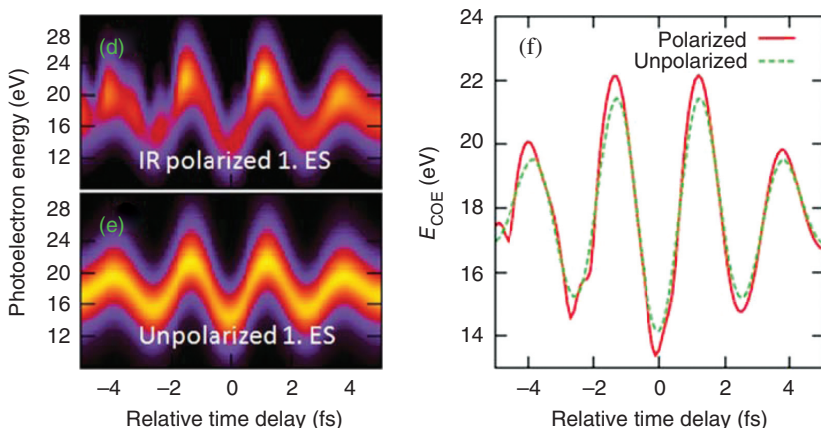


**FIGURE 13.11** The effect of initial-state perturbation (here referred to as “polarization”) by the IR streaking field on XUV photoemission from the ground state of an 1D model hydrogen atom for  $\hbar\omega_X = 25$  eV XUV pulses with a pulse length of 300 as. (a) Spectrogram including initial state polarization. (b) Spectrogram without initial state polarization. (c) Corresponding central energies  $E_{\text{COE}}(\tau)$  obtained as first moments in energy from the streaking traces. (d, e, f) Same as (a, b, c) for XUV photoionization from the first excited state of the model hydrogen atom. Adapted from Reference 80.

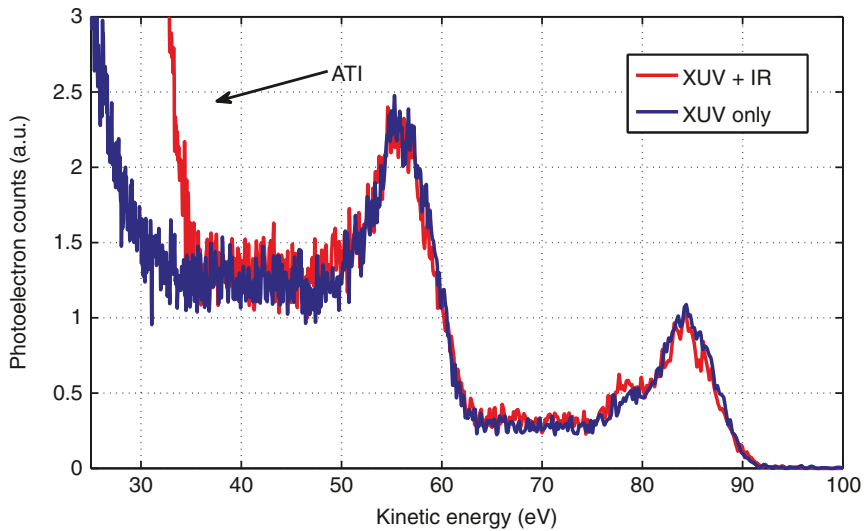


**FIGURE 13.15** Raw photoelectron spectra of tungsten (110) measured with (red curve) and without (blue curve) the presence of the probe NIR streaking field using 91 eV, XUV photons. The spectra show two distinct peaks originating from 5d/6sp valence and 4f/5p core levels at  $\sim$ 83 and  $\sim$ 56 eV, respectively. In the presence of the NIR probe field, there is an intense photoelectron signal below 35 eV induced by above threshold ionization (ATI). Each spectrum was obtained by integration over 60,000 laser pulses (from Reference 95 with permission of John Wiley & Sons).

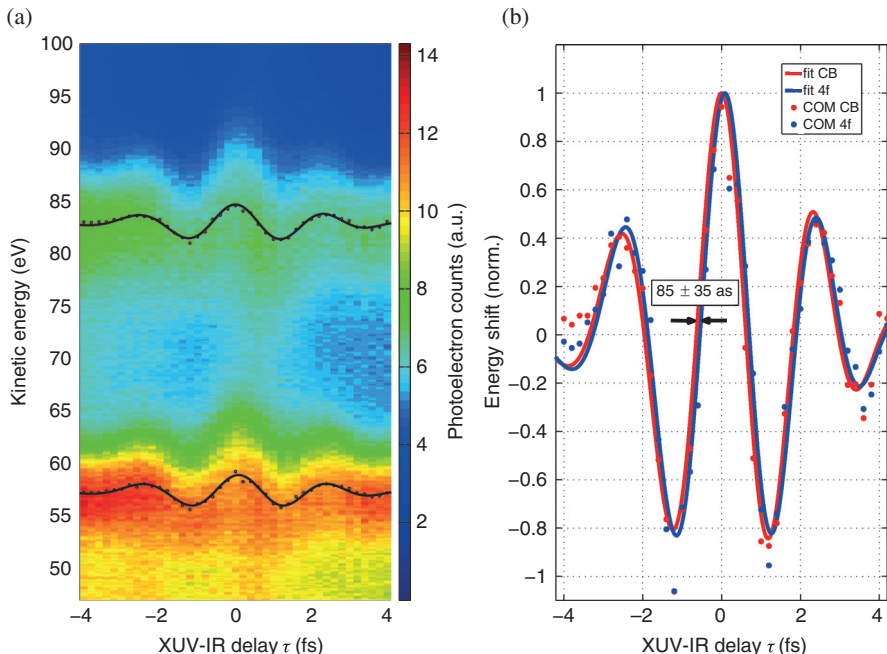


**FIGURE 13.17** (a) Raw attosecond streaking technique spectrogram of a tungsten (110) surface. Photoelectron intensities are given in arbitrary units. (b) Center-of-mass (COM) analysis of the spectrogram. The COM of both emission lines measured are given as dots, and a global fit to both COM traces is shown in solid lines (from Reference 96 with permission of John Wiley & Sons).

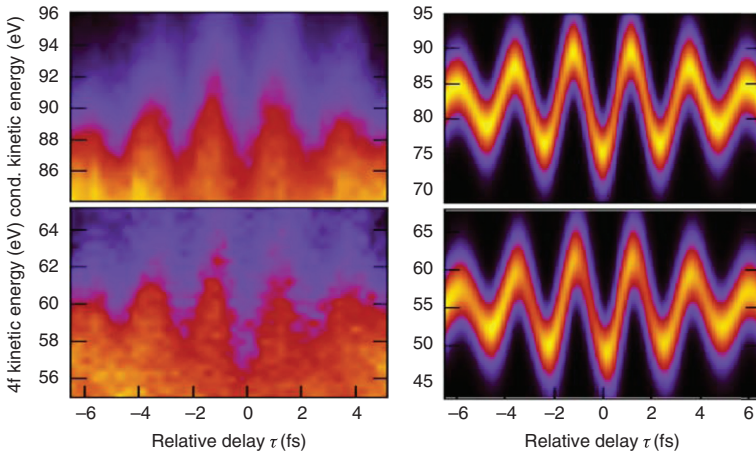


**FIGURE 13.18** Time-resolved, streaked photoelectron spectra for emission from the CB (top) and 4f-core levels (bottom) of a W(110) surface as a function of the delay between the XUV and IR pulses. Linear intensity scales. Experimental results of Cavalieri et al. [51] (left) in comparison with numerical simulations of Reference 4 (right). Reprinted with permissions of APS.

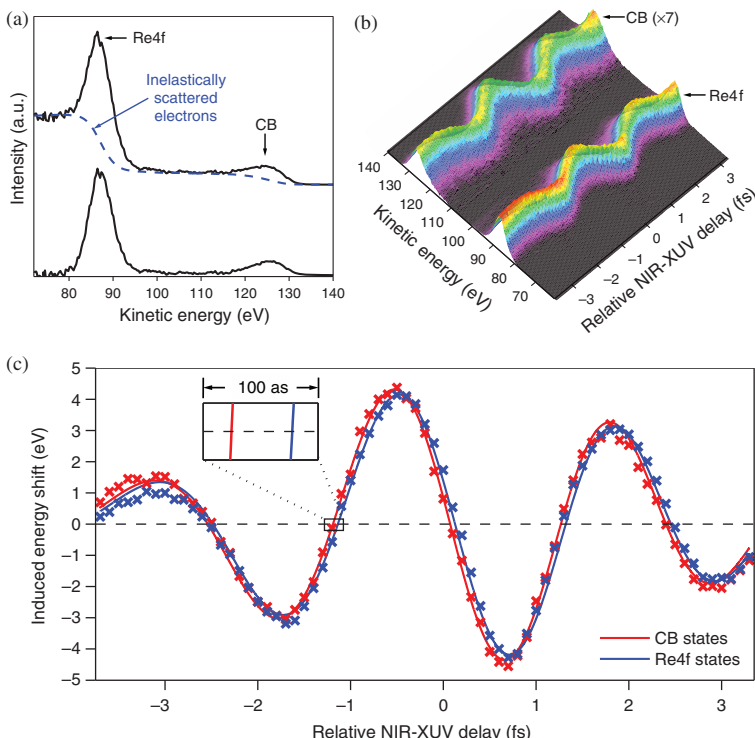


**FIGURE 13.20** Attosecond, time-resolved photoemission from the (0001) surface of rhenium. (a) Static photoelectron emission from rhenium (in the absence of the NIR streaking field) obtained with HH radiation filtered by a 6-eV (FWHM) bandwidth mirror centered near 125 eV. The background of inelastically scattered electrons (blue dashed line) is removed before the analysis. The full streaking spectrogram is shown in panel (b), with the CB intensity scaled by a factor of 7. The comparison of the first moments of the streaked electron distributions as a function of the NIR–XUV delay, shown in panel (c), reveals emission of the 4f photoelectrons from the metal surface delayed by 100 as compared to the photoelectrons released from the conduction-band states. (Adapted from Reference 96, with permission of John Wiley & Sons).

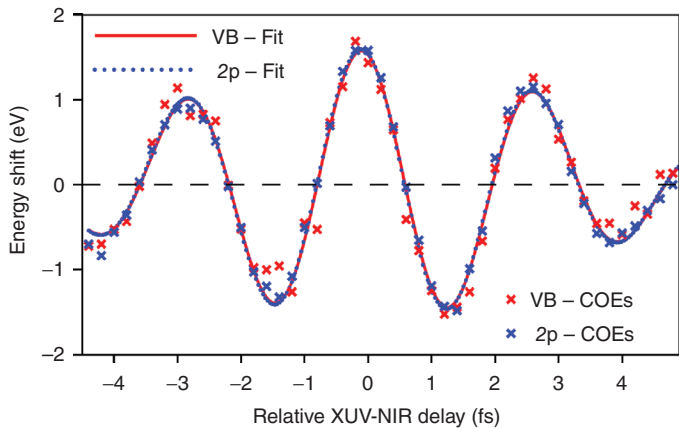


**FIGURE 13.21** Timing analysis of the VB and 2p core-level photoemission from Mg(0001). Calculated center-of-energies (COE) for the VB and 2p region of the spectrogram (depicted as crosses) are fitted to a pair of parameterized analytic functions describing the vector potential of the NIR streaking pulse. The absence of a relative shift between the fitted functions, shown as red solid line for the VB and blue dotted line for the 2p emission, provides evidence for a synchronous release of these electrons from the metal surface. Adapted from Reference 52.

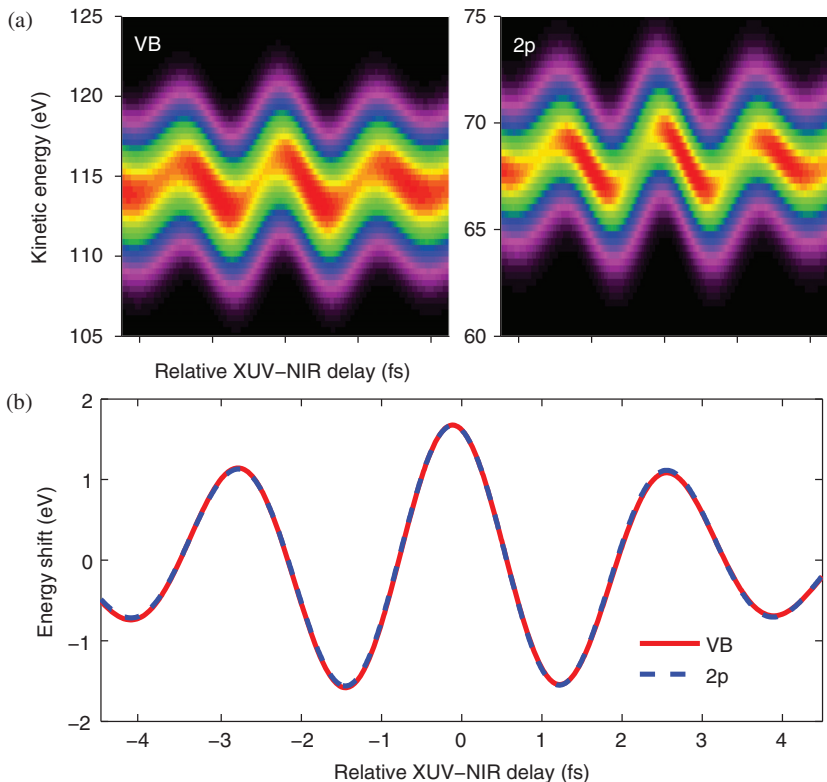


**FIGURE 13.22** (a) Calculated streaked photoemission spectrum for a Mg(0001) surface. The XUV-chirp rate is  $\beta = -2 \text{ fs}^{-2}$  and the NIR-field CEP is  $\phi = 1.22\pi$ . The MFPs are  $\lambda = 5.0 \text{ \AA}$  for VB photoelectron and  $\lambda = 4 \text{ \AA}$  for 2p-core level photoelectron. (b) Corresponding center-of-energy shift. The 2p-core level center-of-energy shift is multiplied by 1.09 for better comparison. Adapted from Reference 103.

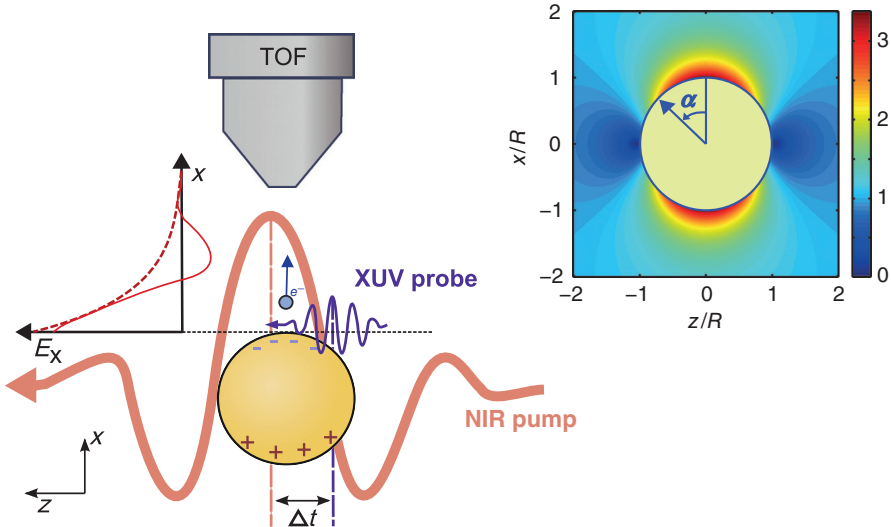


**FIGURE 13.27** Attosecond nanoplasmonic streaking principle illustrated for a spherical metal particle. An NIR pump pulse excites a localized surface plasmon in a metal nanoparticle, and a synchronized attosecond extreme-ultraviolet (XUV) pulse ejects photoelectrons. The field caused by the collective electron motion in the nanoparticle is imprinted in the kinetic energy of the electrons, which are measured by TOF spectroscopy. The inset shows the near-field around the nanoparticle as calculated by Mie theory in the  $y = 0$  plane through the center of the sphere [66]. Due to the symmetry of the plasmonic field in nanoparticles with diameters much smaller than the laser wavelength, the point of electron emission is uniquely defined by the angle  $\alpha$ . Reprinted from Reference 66 with copyright permission of APS.

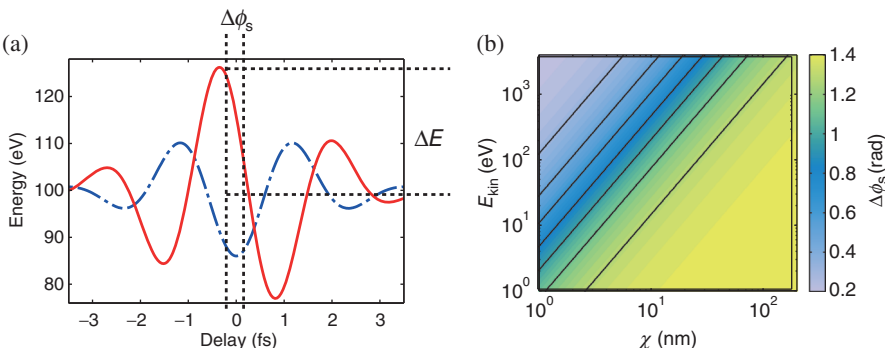


**FIGURE 13.28** (a) Phase shift  $\Delta\phi_s$  between the waveform apparent in the streaking spectrogram (red line) and the local near-field oscillation (blue dash-dotted line). (b) Phase shift  $\Delta\phi_s$  as a function of initial electron energy  $E_{\text{kin}}$  and spatial decay constant  $\chi$  for a fixed plasmonic decay constant of  $\tau_{\text{pl}} = 10$  fs and a laser wavelength of  $\lambda = 720$  nm [109]. The upper left corner ( $\Delta\phi_s$  close to zero) corresponds to the instantaneous streaking regime. The lower right corner ( $\Delta\phi_s$  close to  $\pi/2$ ) corresponds to the ponderomotive streaking regime.

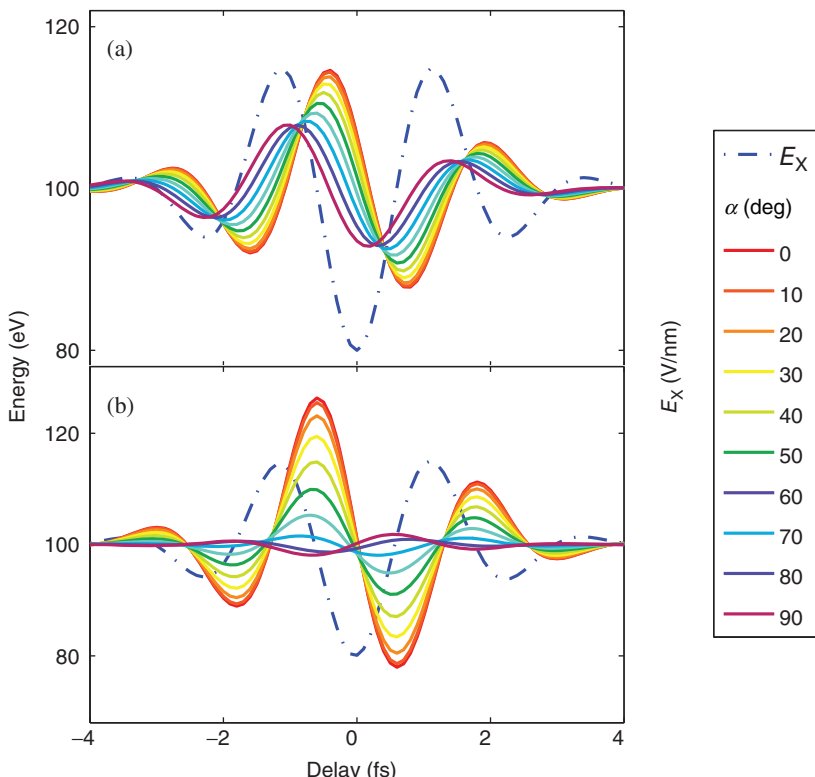


**FIGURE 13.29** Simulated streaking waveforms for electrons emitted at different positions (defined by the angle  $\alpha$  in Figure 13.27) on a Au sphere with a diameter of 10 nm (a) and 100 nm (b). The blue dash-dotted line indicates the driving field. Adapted from Reference 66 with copyright permission of APS.

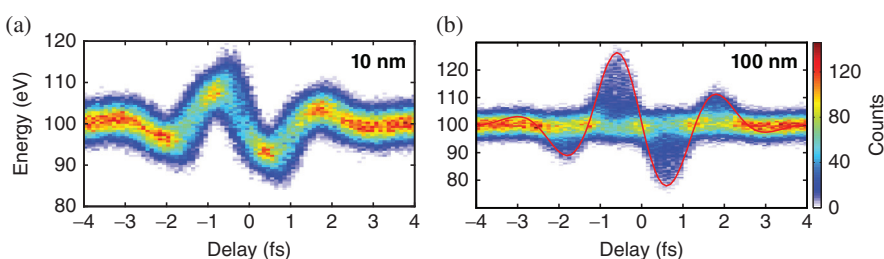


**FIGURE 13.30** Simulated streaking spectrograms for 10 nm (a) and 100 nm (b) Au spheres. The red line shows the contribution of electrons emitted on axis with the laser polarization vector. Reprinted from Reference 66 with copyright permission of APS.

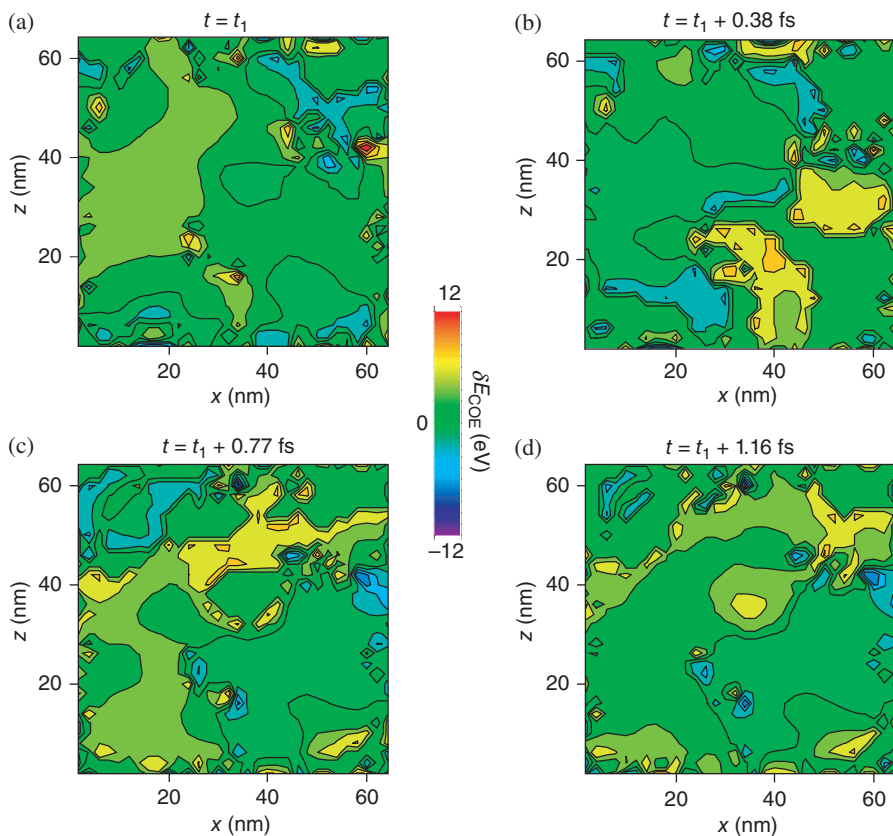


**FIGURE 13.32** Topographic color maps of the streaking energy shift  $\delta E_{\text{COE}}$ , of electrons emitted by an XUV pulse in the plane of this nanostructure. (a)–(d) Different times after excitation of the nanostructure by a 5.5-fs pulse at 800 nm. The time  $t_1$  corresponds to a time at which the near-field in the hotspot has reached a peak. Adapted from Reference 65 with copyright permission of *Nature*.